



**PHYSICAL CHEMISTRY 2021**

15<sup>th</sup> International Conference  
on Fundamental and Applied Aspects of  
Physical Chemistry

Proceedings  
Volume II

---

*The Conference is dedicated to the*

*30<sup>th</sup> Anniversary of the founding of the Society of Physical  
Chemists of Serbia*

*and*

*100<sup>th</sup> Anniversary of Bray-Liebhafsky reaction*

---

**September 20-24, 2021  
Belgrade, Serbia**

**Title:** Physical Chemistry 2021 (Proceedings) **ISBN** 978-86-82475-40-8

**Volume II: ISBN** 978-86-82475-39-2

**Editors:** Željko Čupić and Slobodan Anić

**Published by:** Society of Physical Chemists of Serbia, Studentski Trg 12-16, 11158, Belgrade, Serbia

**Publisher:** Society of Physical Chemists of Serbia

**For Publisher:** S. Anić, President of Society of Physical Chemists of Serbia

**Printed by:** "Jovan", <Printing and Publishing Company, 200 Copies

**Number of pages:** 6+388, Format A4, printing finished in December 2021

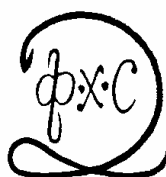
Text and Layout: "Jovan"

Neither this book nor any part may be reproduced or transmitted in any form or by any means, including photocopying, or by any information storage and retrieval system, without permission in writing from the publisher.

200 - *Copy printing*

## CONTENT

<i>Volume II</i>	
<i>Organizer</i>	IV
<i>Comittes</i>	V
<i>Organic Physical Chemistry</i>	345
<i>Material Science</i>	367
<i>Macromolecular Physical Chemistry</i>	487
<i>Environmental Protection, Forensic Sciences, Geophysical Chemistry, Radiochemistry, Nuclear Chemistry</i>	519
<i>Phase Boundaries, Colloids, Liquid Crystals, Surface-Active Substances</i>	633
<i>Complex Compounds</i>	643
<i>General Physical Chemistry</i>	655
<i>Pharmaceutical Physical Chemistry</i>	669
<i>Food Physical Chemistry</i>	679
<i>Physico-Chemical Analysis</i>	703
<i>Index</i>	725



# PHYSICAL CHEMISTRY 2021

*15<sup>th</sup> International Conference on  
Fundamental and Applied Aspects of  
Physical Chemistry*

*Organized by*

*The Society of Physical Chemists of  
Serbia*

*in co-operation with*

*Institute of Catalysis Bulgarian Academy of Sciences*

*and*

*Borekov Institute of Catalysis Siberian Branch of  
Russian Academy of Sciences*

*and*

*University of Belgrade, Serbia:*

*Faculty of Physical Chemistry  
Institute of Chemistry, Technology and Metallurgy  
Vinča Institute of Nuclear Sciences  
Faculty of Pharmacy*

*and*

*Institute of General and Physical Chemistry, Belgrade, Serbia*

## International Organizing Committee

**Chairman:** S. Anić (Serbia)  
**Vice-chairman:** M. Gabrovska (Bulgaria)  
A. A. Vedyagin (Russia)  
S. N. Blagojević (Serbia)

**Members:** N. Cvjetičanin (Serbia), S. M. Blagojević (Serbia), M. Daković (Serbia), J. Dimitrić Marković (Serbia), T. Grozdić (Serbia), Lj. Ignjatović (Serbia), D. Jovanović (Serbia), M. Kuzmanović (Serbia), D. Marković (Serbia), B. Milosavljević (USA), M. Mojović (Serbia), N. Pejić (Serbia), M. Petković (Serbia), A. Popović-Bjelić (Serbia), B. Simonović (Serbia), M. Stanković (Serbia), B. Šljukić (Serbia), G. Tasić (Serbia), S. Veličković (Serbia), N. Vukelić (Serbia)

## International Scientific Committee

**Chairman:** Ž. Čupić (Serbia)  
**Vice-chairman:** V. Bukhtiyarov (Russia)  
S. Todorova (Bulgaria)  
B. Adnađević (Serbia)

**Members:** S. Anić (Serbia), A. Antić-Jovanović (Serbia), A. Azizoglu (Turkey), R. Cervellati (Italy), G. Ćirić-Marjanović (Serbia), V. Dondur (Serbia), I. I. Grinvald (Russia), R. Jerala (Slovenia), M. Jeremić (Serbia), G. N. Kaluderović (Germany), E. Kiš (Serbia), A. V. Knyazev (Russia), Lj. Kolar-Anić (Serbia), U. Kortz (Germany), T. Kowalska (Poljska), A. Lemarchand (France), G. Lente (Hungary), Z. Marković (Serbia), S. Mentus (Serbia), K. Novaković (UK), N. Ostrovski (Serbia), V. Parmon (Russia), Z. Petkova Cherkezova-Zheleva (Bulgaria), M. Plavšić (Serbia), J. Savović (Serbia), G. Schmitz (Belgium), I. Schreiber (Czech), L. Schreiberova (Czech), D. Stanisavljev (Serbia), N. Stepanov (Russia), M. Stojanović (USA), E. Szabó (Slovakia), Zs. Szakacs (Romania), Z. Šaponjić (Serbia), Á. Tóth (Hungary), M. Trtica (Serbia), V. Vasić (Serbia), D. Veselinović (Serbia), V. Vukojević (Sweden)

## Local Executive Committee

**Chairman:** S. N. Blagojević  
**Vice-chairman:** A. Ivanović-Šašić  
N. Jović-Jovičić  
A. Stanojević

**Members:** M. Ajduković, I. N. Bujanja, A. Dobrota, J. Dostanić, D. Dimić, S. Jovanović, Z. Jovanović, D. Lončarević, M. Kragović, J. Krstić, B. Marković, S. Maćešić, J. Maksimović, S. Marinović, D. Milenković, T. Mudrinić, M. Pagnacco, N. Potkonjak, B. Stanković, I. Stefanović, G. Stevanović, A. Stoilković, M. Vasić

# SPONSORS

Ministry of Education, Science and Technological Development of the  
Republic Serbia

Institute of General and Physical Chemistry, Belgrade  
Belgrade Analysis d.o.o.

*G - Organic Physical Chemistry*



## ANTIRADICAL POTENCY OF CYNODONTIN TOWARD HYDROXYL RADICAL

J. Đorović Jovanović<sup>1</sup>, D. Milenković<sup>1</sup>, Ž. Milanović<sup>1,2</sup>, M. Antonijević<sup>1</sup> and Z. Marković<sup>1</sup>

<sup>1</sup>Department of Science, Institute for Information Technologies, University of Kragujevac, Jovana Cvijića bb, 34000 Kragujevac, Republic of Serbia  
e-mail: jelena.djorovic@uni.kg.ac.rs,

<sup>2</sup>Faculty of Science, University of Kragujevac, Radoja Domanovića 12, 34000 Kragujevac, Serbia.

### ABSTRACT

The antioxidant potency of cynodontin was studied in the presence of one of the most reactive free radical species, hydroxyl radical. This *in silico* study was done at the M06-2X/6-311++(d,p) level of theory. The geometry optimizations are performed in water and benzene, with an aim to simulate the polar and non-polar environment. The antiradical action of cynodontin *via* hydrogen atom transfer (HAT) and radical adduct formation (RAF) were determined.

### INTRODUCTION

The reactive chemical species can exceed the capacity of the endogenous protection system, and then the organism is found in the state known as oxidative stress (OS), which can damage biomolecules in the organism and cause numerous diseases. It can be reduced using natural and synthetic compounds identified as antioxidants. An accepted opinion is that the properties of antioxidants are of high interest in the prevention of various diseases such as cancer, inflammation, hypertension, and cardiovascular disorders [1]. One of the main characteristics of good antioxidants is fast radical-scavenging reactions.

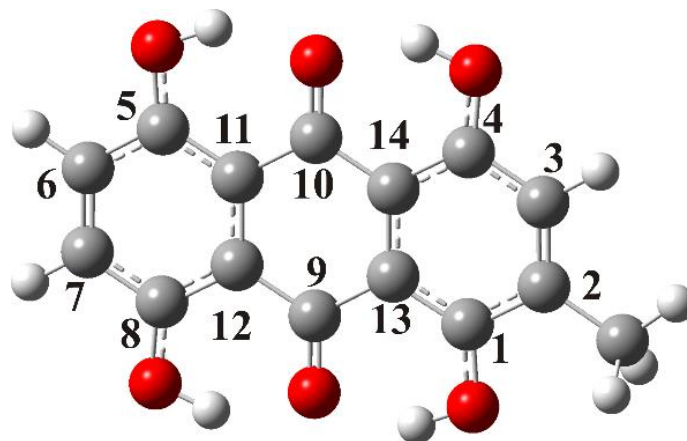


Figure 1. The labeled structure of cynodontin

Anthraquinones are a group of natural compounds predominant and represented by the red dyes kermes [2]. The main applications compounds from a group of anthraquinone found as dispersive, vat, and acid dyes, although they are used for the dyeing and printing of all types of textile materials. With increasing awareness of the damage caused to the environment by industry, the disposal of industrial effluent is becoming more costly and strictly regulated. Various fungi that produce

anthraquinones as secondary metabolites have the potential to be a source of a dyestu intermediate. This way of obtaining a dye can contribute to the control of malignant effluent and byproduct creation. In comparison with the commercially accessible hydroxyanthraquinones, most of these compounds possess an additional methyl group. Anthraquinone known as cynodontin (1,4,5,8-Tetrahydroxy-2-methyl-9,10-anthraquinone, Fig. 1) can be produced with a high percentage of purity. That allows it to be modified using a simple chemical step to a dye product, and this compound can be easily comparable with a commercially prepared analog. In this study are presented antioxidative properties of cynodontin, and their possibility to inactivate hydroxyl radical ( $\cdot\text{OH}$ ) *via* hydrogen atom transfer (HAT) and radical adduct formation (RAF) antioxidative mechanism.

## METHODS

Antioxidant potency can be estimated using various quantum-mechanical approaches [3]. The reaction between the free radical species and antioxidants can follow two different pathways: H-atom abstraction and radical adduct formation [4]. In this paper are studied and reported two different antiradical mechanisms: HAT (Eq. 1) and RAF (eq. 2).



The Gibbs free energy of these processes can be used as the first parameter in the determination of the preferred mechanistic pathway of antioxidative reaction. Generally speaking, HAT is a preferred reaction mechanism in a non-polar medium because it does not involve charge separation. Radical inactivation by the HAT mechanism (Eq. 1) is defined by the H-atom transfer from the examined compounds to the free radical species ( $\text{RO}\cdot$ ). Thermodynamic parameter,  $\Delta_r G_{\text{HAT}}$ , can be calculated using the following equation:

$$\Delta_r G_{\text{HAT}} = G(\text{A-O}\cdot) + G(\text{ROH}) - G(\text{A-OH}) - G(\text{RO}\cdot) \quad (3)$$

$$\Delta_r G_{\text{RAF}} = G(\text{A-OH-OR}\cdot) - G(\text{A-OH}) - G(\text{RO}\cdot) \quad (4)$$

Radical inactivation by the RAF mechanism (Eq. 2) is defined by  $\text{RO}\cdot$  addition to the examined compounds. Thermodynamic parameter,  $\Delta_r G_{\text{RAF}}$ , can be calculated using the Eq.4.

The optimized structure of the parent molecule of cynodontin and  $\text{HO}\cdot$  radical, corresponding radical cation, radicals, and anions were optimized by the DFT method at the M06-2X/6-311++G(d,p) level of theory. The software package Gaussian 09 is used for the calculations [5]. The CPCM solvation model is applied to evaluate the impact of polar and non-polar solvents (water and benzene). The values for solvation enthalpies of proton and electron are taken from the literature [6].

## RESULTS AND DISCUSSION

Our investigation was devoted to thermodynamic consideration of the reactions of HAT and RAF mechanism of antioxidant action. This examination aimed to establish exergonic reaction pathways of  $\text{OH}$  radical to determine the preferred mechanism of antioxidant action. The  $\cdot\text{OH}$  radical is produced during Fenton and Haber-Weiss reactions in an organism and represents one of the most potent radicals of biological importance.

**Table 1.** Gibbs energies ( $\text{kJ mol}^{-1}$ ) of the reactions (1) and (2) for cynodontin

Mechanism	Position		
		water	benzene
HAT	1	-110	-109
	4	-84	-101
	5	-105	-102
	8	-106	-103
RAF	1	-19	-20
	2	-59	-60
	3	-61	-61
	4	-61	-63
	5	-64	-65
	6	-52	-53
	7	-60	-60
	8	-59	-59
	11	-24	-27
	12	-17	-17
	13	-62	-64
	14	-22	-26

Examination of the HAT mechanism was focused on the abstraction of hydrogen atoms from phenolic groups. As for the RAF mechanism, the addition of the OH radical to the  $\text{sp}^2$  hybridized carbon atoms was simulated. The obtained results are presented in Table 1. It is apparent that the  $\Delta_r G$  values referring to the two solvents under investigation are in very good agreement with both investigated mechanisms of antiradical action. The results presented in Table 1 indicate HAT as thermodynamically favorable mechanism of antiradical action of cynodontin, since the very exergonic reactions are achieved with OH. On the other hand, the  $\Delta_r G$  values achieved for the RAF mechanistic pathways with OH are in all cases negative, but less negative than the values obtained for HAT mechanistic pathway.

## CONCLUSION

The *in silico* study of the antiradical capacity of cynodontin was studied in the presence of hydroxyl radical. The investigation was performed applying DFT method, and M06-2X/6-311++(d,p) level of theory. The antiradical action of cynodontin *via* HAT and RAF were determined in water and benzene. Thermodynamically, HAT is favorable mechanism of cynodontin, in both examined solvents. In addition, the obtained values for RAF indicate RAF as operative mechanistic pathway, also.

## Acknowledgement

The authors are grateful to the Ministry of Education, Science and Technological Development of the Republic of Serbia for financial support (Agreement No. 451-03-9/2021-14/200378).

**REFERENCES**

- [1] B. Halliwell, Free radicals and other reactive species in disease. e LS. 2001.
- [2] W.R. Taylor, J Mol Biol, 1986, 188, 2, 233-258.
- [3] R. Álvarez-Diduk, A. Galano, J Phys Chem B, 2015, 119, 3479-3491.
- [4] A. Galano, G. Mazzone, R. Alvarez-Diduk, T. Marino, J. R. Alvarez-Idaboy, N. Russo, Annu Rev Food Sci T, 2016, 7, 335-352.
- [5] M. J. Frisch, et al. Gaussian, Inc., Wallingford CT, 2013.
- [6] J. Tošović, S. Markovic, D. Milenkovic, Z. Marković, JSSCM, 2016, 10, 66-76.

## ANTIRADICAL ACTIVITY OF FOLIC ACID TOWARDS $\cdot\text{OH}$ AND $\cdot\text{OOH}$ RADICALS

Z. Marković, D. Milenković, J. Đorović, E. Avdović and M. Antonijević

*University of Kragujevac, Institute of Information Technologies, Department of Science, Jovana Cvijića bb, 34000 Kragujevac, Serbia. (zmarkovic@uni.kg.ac.rs)*

### ABSTRACT

Folic acid have been investigated theoretically for its ability to scavenge hydroxy and hydroperoxy radicals. Reaction enthalpies for the reaction of these molecules with selected radical species, related to three mechanisms of free radical scavenging activity (HAT, SET-PT and SPLET), are calculated using B3LYP-D3BJ/6-311+G(d,p) level of theory. Calculated energy requirements indicated preferred radical scavenging mechanisms in polar (water) and non-polar (benzene) solvents. Both mechanisms, HAT and SPLET, are suitable for reaction FA with  $\cdot\text{OH}$  in all solvents under investigations. On the other hand, in the reaction FA with  $\cdot\text{OOH}$ , the SPLET is possible mechanism in both solvents.

### INTRODUCTION

Folic acid (FA, vitamin B9) (Fig. 1) is water-soluble essential vitamin that is yellow-orange in colour and is known to aid in the metabolism of amino acids and is necessary for the biosynthesis of DNA and RNA [1]. This vitamin plays an important role in human health and disease processes [2]. The deficiency in FA has been ascribed to various disease processes including cancer, neurological dysfunction, and heart disease [3]. The antiradical activity of FA are related to their ability to transfer their phenolic H-atom to a free radical.

The reactive radical species in the radical scavenging mechanisms are inactivated by accepting a hydrogen atom from a NH of the FA. It has been recognized that this reaction proceeds via at least three different mechanisms: hydrogen atom transfer (HAT), single electron transfer followed by proton transfer (SET-PT) and sequential proton loss electron transfer (SPLET) [4-5]. The aim of present paper is to provide quantitative tools to determine the antiradical mechanisms of FA (Fig. 1) calculating the energy parameters for the reactions of these molecules with hydroxy and hydroperoxy radicals in different media. Calculated energy parameters may indicate which radical scavenging mechanism is thermodynamically preferred and point out active sites for radical inactivation. All three molecules are recognized as biologically very active.

### METHODS

The equilibrium geometry of FA (Fig. 1) was optimized by density functional theory (DFT) using global hybrid Generalized Gradient Approximation (GGA) functional B3LYP [6] with empirical dispersion corrections D3BJ (with Becke and Johnson damping) [7] in combination with the 6-311+G(d,p) basis set. Hybrid GGA B3LYP-D3BJ includes an empirical correction term proposed by Grimme [8]. The geometry optimization was carried out using Gaussian 09 package [9]. The structure was optimized at 298 K without any geometrical restrictions. The nature of the stationary points was determined by performing frequency analysis: the equilibrium geometries have no imaginary frequencies.

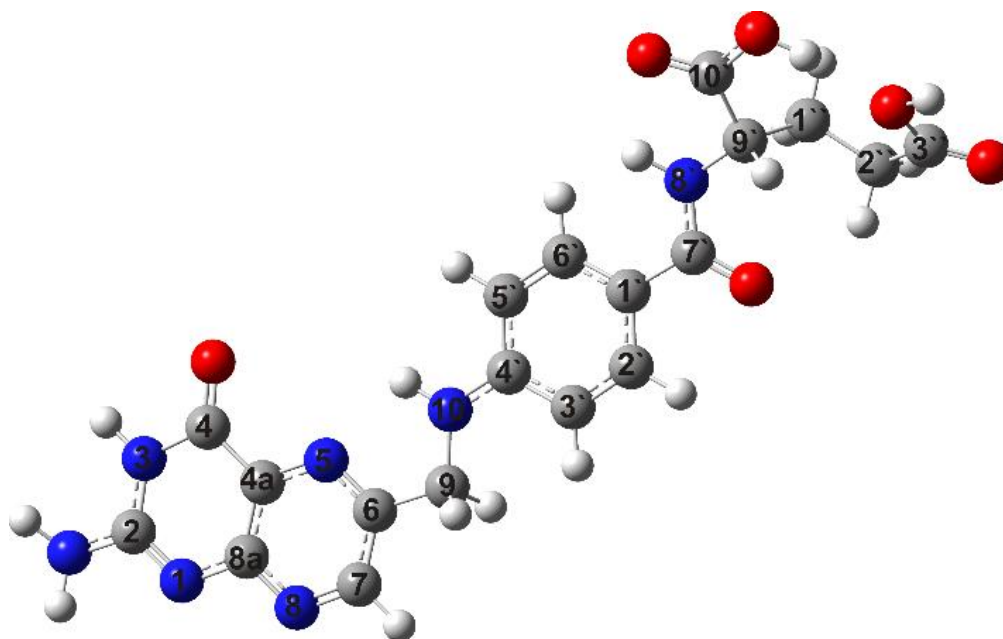
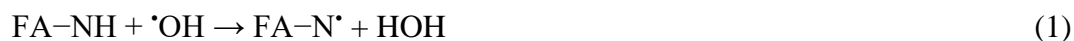


**Figure 1.** The optimized structures of folic acid and atomic numbering.

## RESULTS AND DISCUSSION

### *Antiradical mechanisms of Folic Acid (FA)*

In the radical scavenging mechanisms reactive radical species were inactivated by accepting a hydrogen atom from a NH group of the FA molecule. By reducing radical species FA become radicals themselves, which are less reactive and more stable than reduced ones. The following reactions describe this H atom transfer:



Reaction enthalpies related to the three radical scavenging mechanisms (HAT, SET-PT and SPLET) [10] were calculated by applying the B3LYP-D3BJ/6-311+G(d,p) level of theory. The species necessary to perform these calculations were generated from the most stable conformations of FA (Fig. 1). Which of the mechanisms is preferred can be estimated from the lowest value of  $\Delta H_{\text{BDE}}$ ,  $\Delta H_{\text{IP}}$ , and  $\Delta H_{\text{PA}}$ . The obtained results are presented in Table 1.

**Table 1.** Calculated reaction enthalpies (kJ/mol) for the reactions of FA with hydroxy and hydroperoxy radicals.

Site	B3LYP-D3BJ/6-311+G(d,p)									
	<i>Water</i>					<i>Benzene</i>				
	HAT $\Delta H_{\text{BDE}}$	SET-PT $\Delta H_{\text{IP}}$	SET-PT $\Delta H_{\text{PDE}}$	SPLET $\Delta H_{\text{PA}}$	SPLET $\Delta H_{\text{ETE}}$	HAT $\Delta H_{\text{BDE}}$	SET-PT $\Delta H_{\text{IP}}$	SET-PT $\Delta H_{\text{PDE}}$	SPLET $\Delta H_{\text{PA}}$	SPLET $\Delta H_{\text{ETE}}$
	36					245				
3 + $\cdot\text{OH}$	-77		-114	-104	27	-71		-315	-178	108
10 + $\cdot\text{OH}$	-116		-152	-16	-100	-112		-357	-90	-22
8 + $\cdot\text{OH}$	-57		-94	-28	-29	-47		-292	-82	34
	134					330				
3 + $\cdot\text{OOH}$	61		-73	-64	124	66		-265	-127	193
10 + $\cdot\text{OOH}$	22		-112	25	-3	25		-306	-39	64
8 + $\cdot\text{OOH}$	81		-53	12	68	89		-241	-31	120

The thermodynamic parameters ( $\Delta H_{\text{BDE}}$ , and  $\Delta H_{\text{PA}}$ ) presented in Table 1 indicate that FA react with hydroxy radical via both, HAT and SPLET mechanisms in all solvents under investigations. Since all  $\Delta H_{\text{BDE}}$  and  $\Delta H_{\text{PA}}$  values are similar both mechanisms are equally probable. As can be seen from Table 1, the N10–H group of FA is the most favorable site for homolytic N–H breaking in both solvents. On the other hand, the N3–H group is suitable for the heterolytic N–H bond breaking.

In the case of hydroperoxy radical, the reactions representing HAT mechanism are endothermic in all solvents (Table 1) indicating HAT as not possible for FA. The obtained  $\Delta H_{\text{PA}}$  values for the reaction of FA with hydroperoxy radical are negative or slightly positive implying the SPLET as possible mechanism in both solvents.

SET-PT mechanism proves to be thermodynamically unfavourable for all three molecules and in all solvents.

## CONCLUSION

It was established that calculated energy requirements indicate thermodynamically plausible radical scavenging mechanisms and point out the active site for radical inactivation. The obtained results show that investigated molecules can react with hydroxy radical via both, HAT and SPLET, mechanisms in all solvents under investigations. The N10–H group of FA is the most favorable site for homolytic, while the N3–H group is suitable for heterolytic the N–H bond breaking. Based on the theoretical calculations it is possible to conclude that FA has the potency of peroxy radical inactivation via SPLET mechanism. The SET-PT mechanism is found to be thermodynamically not possible in polar, as well as in non-polar solvent.

## Acknowledgement

This work was partially supported by the Ministry for Science of the Republic of Serbia (Agreement No. 451-03-9/2021-14/200378).

## REFERENCES

- [1] C. Chahidi, M. Aubailly, A. Momzikoff, M. Bazin, Photochem. Photobiol., 1981, 33, 641–649.
- [2] B. Kamen, In Seminars in oncology, 1997, 24, S18-30,
- [3] N. Wald, J. Sneddon, J. Densem, C. Frost, R. Stone, Lancet, 1991, 338, 131-137.
- [4] J. M. Mayer, Annu. Rev. Phys. Chem. 2004, 55, 363-90.

- 
- [5] D. Milenković, J. Đorović, S. Jeremić, J. M. Dimitrić Marković, E. H. Avdović, Z. Marković, J. Chem., 2017, 2017.
- [6] A. D. Becke, Phys. Rev. A., 1988, 38, 3098–3100.
- [7] E.R. Johnson, A.D. Becke, Chem. Phys. Lett., 2006, 432, 600–603.
- [8] S. Grimme, S. Ehrlich, L. Goerigk, J. Comput. Chem., 2011, 32, 1456–1465.
- [9] M. J. Frisch et al., Gaussian 09 (Revision D.01), Gaussian Inc.: Wallingford, CT, 2013.
- [10] J. Đorović, D. Milenković, L. Joksović, M. Joksović, Z. Marković, ChemistrySelect. 2019, 4, 7476-85.

## POTENTIAL INHIBITORY EFFECT OF COUMARIN PALLADIUM (II) COMPLEXES ON SARS-CoV-2 MAIN PROTEASE

Ž. Milanović<sup>1,2</sup>, E. Avdović<sup>2</sup>, M. Antonijević<sup>2</sup> and Z. Marković<sup>2</sup>

<sup>1</sup> University of Kragujevac, Faculty of Science, Department of Chemistry, Radoja Domanovića 12, 34000 Kragujevac, Serbia. (ziko.milanovic@pmf.kg.ac.rs)

<sup>2</sup> University of Kragujevac, Institute for Information Technologies, Department of Science, Jovana Cvijića bb, 34000 Kragujevac, Serbia.

### ABSTRACT

In this study, the inhibitory effect of the two previously synthesized palladium (II) complexes with chlorido-[(3-(1-(2-hydroxypropylamino)ethylidene)-chroman-2,4-dione)] and chlorido-[(3-(1-(2-mercaptoethylamino)-ethylidene)-chroman-2,4-dione)] on the SARS-CoV-2 main protease was evaluated. The investigation was carried out using molecular docking simulation. The results of this investigation indicate a potential inhibitory activity of coumarin derivatives on the SARS-CoV-2 main protease. Detailed description interactions between investigated compounds and protein can assist in the design of more specific and more potent antiviral drugs that can arrest the virus life cycle and progression of COVID 19 disease.

### INTRODUCTION

The new coronavirus disease 2019 (COVID-19) pandemic caused by severe acute respiratory syndrome (SARS-CoV-2), which rapidly spreads from its origin in the Wuhan province, is a global health emergency. An attractive drug target among coronaviruses is the main protease ( $M^{pro}$ , also called  $3CL^{pro}$ ) because of the crucial role in viral replication and transcription. Thus,  $3CL^{pro}$  could be a promising target to inhibit SARS-CoV-2 infection [1]. Coumarin and its derivatives comprise very large class of compounds found as naturally occurring secondary metabolites in the plant kingdom, bacteria and fungi.

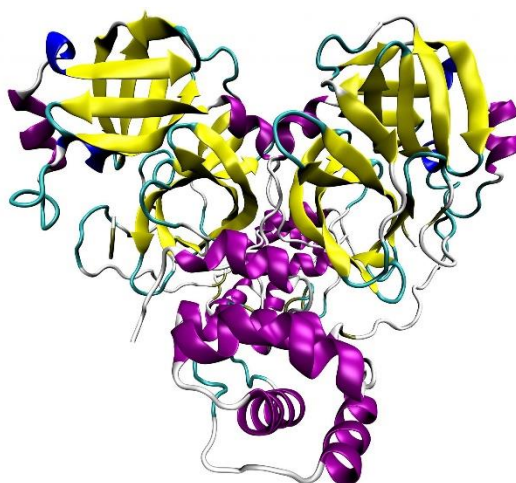


**Figure 1.** The X-Ray structure of the main protease ( $3CL^{pro}$ ) of the SARS-CoV-2 virus.

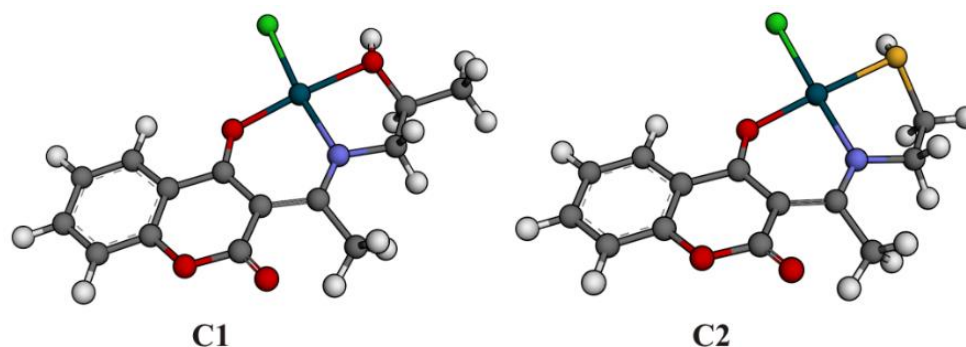


**Figure 2.** The structures of investigation compounds

These compounds have a different spectrum of biological and pharmacological activities. In the last decades, coumarins have received considerable attention as a lead structures for the discovery of orally bioavailable antiviral agents. A lot of structurally different coumarin derivatives analogs were found to display a remarkable array of inhibitory potential with different molecular targets for antiviral agents [2]. For this reason, we have applied a computational strategy, using a combination of virtual screening, molecular docking simulation, and ADME (absorption, distribution, metabolism, and excretion) analysis, aimed at identifying the possible inhibitory effect of previously synthesized coumarin palladium (II) complexes with chlorido-[(3-(1-(2 hydroxypropylamino)ethylidene)-chroman-2,4-dione)] (**C1**) and chlorido-[(3-(1-(2-mercaptoethylamino)-ethylidene)-chroman-2,4-dione)] (**C1**) for the non-covalent inhibition of the main protease  $3\text{CL}^{\text{pro}}$  of the SARS-CoV2 infections [3].

## METHODS

In order to study the interactions between the investigated compounds and main protease ( $3\text{CL}^{\text{pro}}$ ) of SARS-CoV-2 virus molecular docking simulation was carried out using the AutoDock 4.2 program package [4]. The ADME analysis was performed by the online server SwissADME. The three-dimensional crystal structure of the  $3\text{CL}^{\text{pro}}$  receptor was retrieved from RCSB Protein Data Bank with PDB code 6LU7 at resolution 2.16 Å [5]. The  $3\text{CL}^{\text{pro}}$  receptor was pretreated by deleting the non-protein parts (co-crystallized water molecules) as well as adding missing amino acid residues. The structures of the investigated compounds before docking simulation were optimized in the *Gaussian 09* program package at B3LYP-D3BJ/6-311++G (d,p) level of theory. The active site definition had been aligned to taken cristal structure co-crystallized with an N3 inhibitor ( $x=-20.186$ ,  $y=21.707$ ,  $z=64.591$  Å). The other docking parameters were selected using the standard protocols that are additionally explained in previous researches [6]. The calculation was done using the Lamarckian Genetic Algorithm (LGA) method.

## RESULTS AND DISCUSSION

Analyzing the physicochemical parameters (Table 1) it can be concluded that the investigated compounds have moderate solubility (Log *S*). The obtained values of  $t\text{PSA} < 140$  Å indicated that both compounds exhibit good permeability through the cell membrane as well as a high gastrointestinal absorption (GI, %ABS). A lower value for  $t\text{SPA}$  (75.96 Å) and a higher value for ABS (82.79 %) indicate that compound **C2** has better distribution and bioavailability in the human body then **C1**.

**Table 1.** Important physicochemical parameters: solubility (Log S), topological polar surface area (tPSA), absorption (%ABS), gastrointestinal absorption (GI), Lipinski rules.

Structure	Log S (ESOL)	tPSA Å	%ABS	GI absorption	Lipinski
C1	-4.53	94.53	76.38	High	Yes
C2	-4.05	75.96	82.79	High	Yes

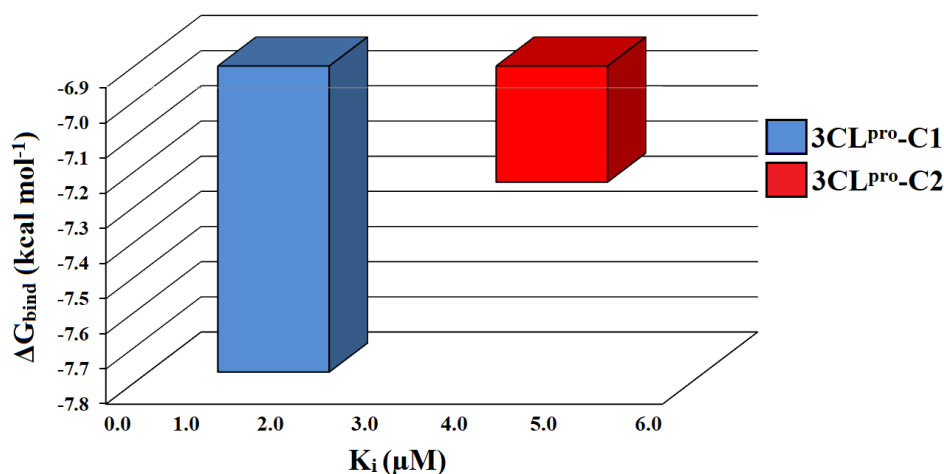
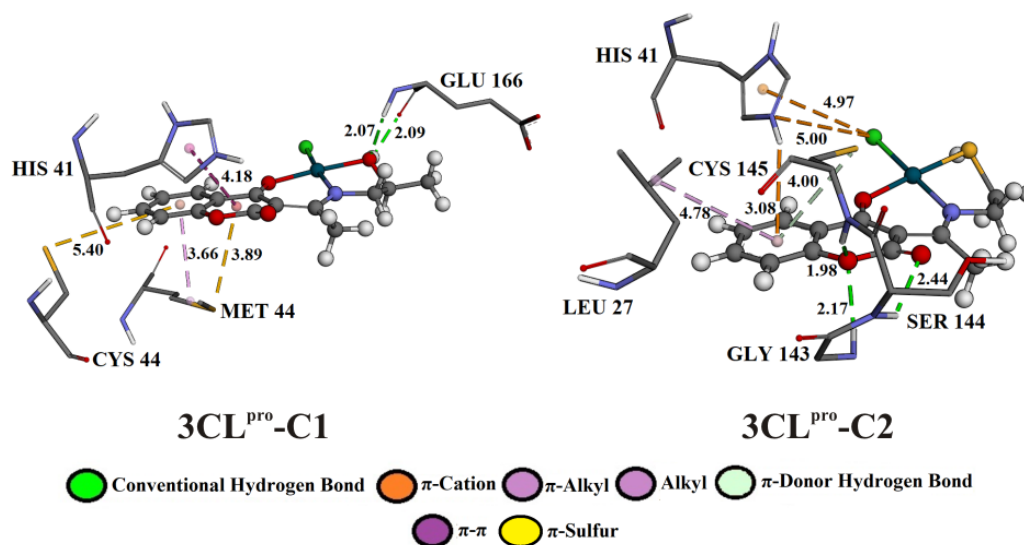
**Figure 3.** The important thermodynamic parameters: free energy binding ( $\Delta G_{\text{bind}}$ ) and constant of inhibition ( $K_i$ ).

Figure 3. shows the important thermodynamic parameters: free energy binding ( $\Delta G_{\text{bind}}$ ) and constant of inhibition ( $K_i$ ) of most stable protein-ligand complexes after molecular docking simulation. Both compounds show a pronounced inhibitory potential against the **3CL<sup>pro</sup>** protein of the SARS-CoV-2 virus. A more negative  $\Delta G_{\text{bind}}$  value and a lower  $K_i$  value indicate that compound **C1** ( $-7.77 \text{ kcal mol}^{-1}$ ,  $2.01 \mu\text{M}$ ) shows a better inhibitory effect against **3CL<sup>pro</sup>** protein than the **C2** ( $-7.23 \text{ kcal mol}^{-1}$ ,  $5.04 \mu\text{M}$ ) compound. The largest contribution of  $\Delta G_{\text{bind}}$  comes from conventional hydrogen bonds. In **3CL<sup>pro</sup>-C1** complex (Figure 4), -OH group of **C1**, which coordinates with Pd (II) ion, build bifurcated conventional hydrogen bonds with amino acid GLU 166 ( $2.07$ ,  $2.09 \text{ \AA}$ ). On the other hand, in **3CL<sup>pro</sup>-C2** complex, amino acids GLY 143 ( $2.17 \text{ \AA}$ ) and SER 144 ( $2.44 \text{ \AA}$ ) establish conventional hydrogen bonds with oxygen atoms of chroman ring of **C2**. In addition, both compounds build characteristic electrostatic ( $\pi$ -cation) and hydrophobic interactions ( $\pi$ -sulfur,  $\pi$ - $\pi$ ,  $\pi$ -alkyl) whose contributions to the  $\Delta G_{\text{bind}}$ , in this case, is negligible.



**Figure 4.** The best docking positions of **C1** (**3CL<sup>pro</sup>-C1**) and **C2** (**3CL<sup>pro</sup>-C2**) compounds to the **3CL<sup>pro</sup>** protein.

## CONCLUSION

Based on the results of our research, it was established that investigated compounds show significant bioavailability and inhibitory potency according to the **3CL<sup>pro</sup>** protein of the SARS-CoV-2 virus. Additionally, **C2** shows a more bioavailability while compound **C1** shows a more significant inhibitory activity.

## Acknowledgement

This work was partially supported by the Ministry of Science and Technological Development of the Republic of Serbia (Agreement No. 451-03-9/2021-14/200378).

## REFERENCES

- [1] G. Qu, X. Li, L. Hu, G. Jiang, *Environ Sci Technol*, 2020, 54, 3730–3732.
- [2] M. Z. Hassan, H. Osman, M. A. Ali, M. J. Ahsan, *Eur J Med Chem*, 2016, 123, 236-255.
- [3] E. Avdović, D. Stojković, V. Jevtić, M. Kostić, B. Ristić, Lj. H. Trajković, M. Vukić, N. Vuković, Z. Marković, I. Potočňák, S. Trifunović, *Inorg Chim Acta*, 2017, 466, 188-196.
- [4] G. M. Morris, R. Huey, W. Lindstrom, M. F. Sanner, R. K. Belew, D. S. Goodsell, A. J. Olson, *J Comput Chem*, 2009, 30, 2785–2791.
- [5] Z. Jin et al., *Nature*, 2020, 1-9.
- [6] E. Avdović, Ž. Milanović, M. Živanović, D. Šeklić, I. Radojević, Lj. Čomić, Z. Marković, *Inorg Chim Acta*, 2020, 504, 119465.

**THE BARRIERS TO ROTATION AROUND THE C=C BOND BY THE  
MEANS TO QUANTIFY THE  
PUSH–PULL EFFECT OF THE BROADER SERIES OF  
SELECTED 2-ALKYLIDENE-4-OXOTHIAZOLIDINES UNDER  
DIFFERENT SOLVENT CONDITIONS**

A. Rašović<sup>1</sup> and V. A. Blagojević<sup>2</sup>

<sup>1</sup>Center for Chemistry ICTM, University of Belgrade, Studentski trg 16,  
P. O. Box 473, 11000 Belgrade, Serbia (arasovic@chem.bg.ac.rs)

<sup>2</sup>Institute of Technical Sciences, Serbian Academy of Sciences and Arts, Knez-Mihailova 35/IV,  
P.O. Box 377, 11000 Belgrade, Serbia

**ABSTRACT**

In our previous work, based on the experimental and theoretical data of barriers to rotation around the C=C double bond of thiazolidine (*Z*)-**1a**, (*2E*, *5Z*)-**1e**, and (*E*)-**2b** that are determined under different solvent conditions, we showed that the *push–pull* effect of these compounds is not affected by the solvent (at least the two solvents studied). As the continuation of these studies, in this work we applied the same calculation procedure as we did for the (*Z*)-**1a**, (*2E*, *5Z*)-**1e**, and (*E*)-**2b** (solvents studied: chloroform and DMSO) to determine  $\Delta G^\ddagger$  of (*Z*)-**1b**, (*Z*)-**1c**, (*Z*)-**1d**, (*Z*)-**2a** and (*Z*)-**2c** (solvents studied: chloroform and DMSO) as well as of **1-2** (solvent studied: water). All these results showed that barriers to rotation ( $\Delta G^\ddagger$ ) proved to be an excellent parameter by the means to quantify the *push–pull* effect of selected thiazolidines under reliable experimental conditions.

**INTRODUCTION**

The *push–pull* effect, occurring by electron transfer from a donor (Don) to acceptor (Acc) groups, is the characteristic feature of different kinds of compounds known as *push–pull* alkenes. Consequently, as illustrated by the general structure of *push–pull* alkenes (Figure 1), this effect produces the polarization and reduction of the  $\pi$ -bond order of the C=C double bond of these type of compounds. Therefore, the barrier to rotation around the C=C double bond in *push–pull* alkenes could be employed to quantify the *push–pull* effect. To this,  $\Delta G^\ddagger$  is readily disclosed by dynamic NMR spectroscopy (DNMR) or can be theoretically calculated. Since the *push–pull* effect influences the chemical reactivity and dynamic behavior of *push–pull* alkenes, this topic attracted significant attention [1,2].

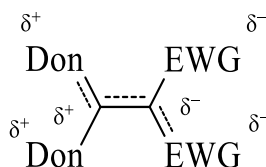
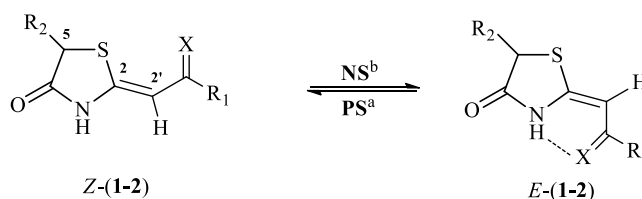


**Figure 1.** The general structure of *push–pull* alkenes.

The results of our previous work showed that all values of barriers to rotation around the C=C double bond, which we calculated for studied thiazolidine enamines (*Z*)-**1a**, (*2E*, *5Z*)-**1e**, and thiazolidine enaminothione (*E*)-**2b** under different solvent conditions, firmly follow their trend determined under experimental ones (Scheme 1) [3]. Moreover, these findings disclosed that the *push–pull* effect of these compounds is not affected by the solvent (at least the two solvents studied; chloroform for (*Z*)-**1a** → (*E*)-**1a** isomerization, and DMSO for (*2E*, *5Z*)-**1e** → (*2Z*, *5Z*)-**1e** and (*E*)-

**2b** → (*Z*)-**2b**, respectively) and the direction of isomerization (Scheme 1). As the continuation of studies of the efficiency of the  $\Delta G^\ddagger$  by the means to quantify the *push-pull* effect of 4-oxothiazolidines under different solvent conditions, in this paper we extending research interest on the broader series of thiazolidine derivatives, that is thiazolidine enaminones (*Z*)-**1b**, (*Z*)-**1c**, and (*Z*)-**1d** as well as thiazolidine enaminothiones (*Z*)-**2a** and (*Z*)-**2c**, by using the same calculation procedure to determine  $\Delta G^\ddagger$  as we did for (*Z*)-**1a**, (*2E*, *5Z*)-**1e** and (*E*)-**2b**. To check the limitation of the use of the  $\Delta G^\ddagger$  by increasing solvent polarity, we also treated the **1-2** by the same calculations protocol in water as the extremely polar solvent. All these compounds studied in this paper, whose configurational isomerizations are briefly explained in Scheme 1, possess two electron-donors (-NH and -S-) and one electron-acceptor ( $R_1CX = \text{COOEt}$ ,  $\text{COPh}$ ,  $\text{CSNH}_2$ ,  $\text{CO(S)NHPH}$  and  $\text{CO(S)NH(CH}_2\text{)Ph}$ ).



a) The polar solvents (PS) shifts equilibrium to the *Z* isomer due to the breaking the intramolecular hydrogen bond (IHB) in the *E*-counterpart.

b) In the nonpolar solvents (NS) the IHB is favored.

(*Z*)-**1a**:  $R_1 = \text{Ph}$ ;  $R_2 = \text{CH}_2\text{COOEt}$ ;  $X = \text{O}$

(*Z*)-**1b**:  $R_1 = \text{NHPH}$ ;  $R_2 = \text{CH}_2\text{COOEt}$ ;  $X = \text{O}$

(*Z*)-**1c**:  $R_1 = \text{NH(CH}_2\text{)Ph}$ ;  $R_2 = \text{H}$ ;  $X = \text{O}$

(*Z*)-**1d**:  $R_1 = \text{OEt}$ ;  $R_2 = \text{CH}_2\text{COOEt}$ ;  $X = \text{O}$

(*2E*, *5Z*)-**1e**:  $R_1 = \text{OEt}$ ;  $R_2 = \text{-CHCOOEt}$ ;  $X = \text{O}$

(*Z*)-**2a**:  $R_1 = \text{Ph}$ ;  $R_2 = \text{CH}_3$ ;  $X = \text{S}$

(*E*)-**2b**:  $R_1 = \text{NH}_2$ ;  $R_2 = \text{CH}_2\text{COOEt}$ ;  $X = \text{S}$

(*Z*)-**2c**:  $R_1 = \text{NH(CH}_2\text{)Ph}$ ;  $R_2 = \text{H}$ ;  $X = \text{S}$

**Scheme 1.** The configurational isomerization of 4-oxothiazolidines **1-2**.

## COMPUTATIONAL DETAILS

Geometry optimization and frequency analysis of *Z* and *E* isomers of studied compounds was conducted at the M06-2X/6-311G\*\* level, using the Gaussian 09 program package. Transition state structures were determined using the Synchronous Transit-Guided Quasi-Newton method at the M06-2X/6-311G\*\* level. To account for solvent effects, the structures of the three derivatives, **1-2**, were re-optimized in chloroform and dimethylsulfoxide along with their **TS**, using the continuum solvation COSMO model (conductor-like screening model). All transition state structures were characterized by an imaginary frequency, the vibrational mode of which corresponded to the rotation around the C(2)–C(2') bond [3].

## RESULTS AND DISCUSSION

Since the  $\Delta H^\ddagger$  and  $\Delta G^\ddagger$  values of selected thiazolidine derivatives **1-2** calculated for *Z* → *E* isomerizations in  $\text{CHCl}_3$  (weak polar solvent) and for *E* → *Z* isomerizations in DMSO (polar solvent) and water (extremely polar solvent), respectively, did not differ by more than  $6 \text{ kJ mol}^{-1}$  and they show the same trend, in Table 1 are presented only  $\Delta G^\ddagger$  values. The barriers span a broad range of  $\sim 105 \text{ kJ mol}^{-1}$  observed for chloroform and water to  $\sim 108 \text{ kJ mol}^{-1}$  observed for DMSO, being the lowest for (*Z*)-**2a** and the highest for (*Z*)-**1c** (entries 3 and 6). Based on these data (when *push-pull* effect increase, the  $\Delta G^\ddagger$  values decrease)  $R_1CX$  substituents can be ordered for all solvent conditions according to their electron-accepting ability as follows:  $\text{CSPH} > \text{CSNH}_2 \approx \text{CSNHCH}_2\text{CH}_2\text{Ph} > \text{COPh} > \text{CO}_2\text{Et} > \text{CONH(CH}_2\text{)Ph} > \text{CONHPH}$ . These results and conclusions therefrom greatly corroborate

with those previously published by us, concerning  $Z \rightarrow E$  and  $E \rightarrow Z$  isomerizations of **1-2** in vacuum [3].

Generally, solvents decrease  $\Delta H^\ddagger$  values because the more polar TS (due to the full charge separation) is more solvated than the less polar GS as follows: more polar solvent lower  $\Delta H^\ddagger$  values. Since the  $\Delta H^\ddagger$  and  $\Delta G^\ddagger$  values of selected thiazolidine derivatives **1-2** calculated for all single solvents studied are approximatively the same, the magnitude of  $\Delta S^\ddagger$  slightly affected barriers to rotations of the **1-2**, and therefore this rule could be valid when is also considered calculated  $\Delta G^\ddagger$  values of these compounds under different solvent conditions. Thus, as can be seen in Table 1, the calculated values of barriers to rotation slightly decrease with fewer exceptions in the following order:  $\Delta G^\ddagger$  (chloroform)  $>>$   $\Delta G^\ddagger$  (DMSO)  $>$   $\Delta G^\ddagger$  (water). This means that in this slight decreasing order of  $\Delta G^\ddagger$  values from chloroform to water, the differences of  $\Delta G^\ddagger$  values are "much lower" for the  $\Delta G^\ddagger$  (chloroform)/ $\Delta G^\ddagger$  (DMSO) relationship than those for the  $\Delta G^\ddagger$  (DMSO)/ $\Delta G^\ddagger$  (water) one. Although in theoretically simulated configuration isomerization the solvation effect is less expressed and has a minor impact on the activation entropy ( $\Delta S^\ddagger$ ), it should reflect realistic experimental conditions in terms of the proportional increase of the absolute values of the  $\Delta S^\ddagger$ . In this sense, the issue of validity could be related to the use of barriers to rotations by the means to quantify the *push-pull* effect of two or more thiazolidine derivatives when they are calculated under different solvent conditions. Thus, for the  $\Delta G^\ddagger$  (chloroform)/ $\Delta G^\ddagger$  (DMSO) and  $\Delta G^\ddagger$  (DMSO)/ $\Delta G^\ddagger$  (water) relationships, one can conclude that the  $\Delta G^\ddagger$  are showed to be an excellent parameter to quantify the *push-pull* effect of the selected thiazolidine derivatives **1-2** under reliable conditions compounds studied. On the other side, the relationship  $\Delta G^\ddagger$  (chloroform)/ $\Delta G^\ddagger$  (water) proves to be less useful for this purpose due to the water is much more polar than chloroform.

**Table 1.** The barriers to rotation ( $\Delta G^\ddagger$ , kJ mol<sup>-1</sup>) around the C=C double bond of studied thiazolidine derivatives **1-2** calculated for chloroform ( $Z/E$  isomerization), dimethylsulfoxide ( $E/Z$  isomerization) and water ( $E/Z$  isomerization).

Ent	Comp	Chloroform	DMSO	Water
		$\Delta G^\ddagger$	$\Delta G^\ddagger$	$\Delta G^\ddagger$
		$Z \rightarrow E$	$E \rightarrow Z$	$E \rightarrow Z$
1	(Z)- <b>1a</b>	154.4	149.1	145.3
2	(Z)- <b>1b</b>	180.2	175.4	172.0
3	(Z)- <b>1c</b>	181.6	180.3	178.7
4	(Z)- <b>1d</b>	164.2	162.1	161.4
5	(Z)- <b>1e</b>	174.9	169.1	167.7
6	(Z)- <b>2a</b>	76.3	72.1	73.3
7	(E)- <b>2b</b>	132.7	134.1	128.9
8	(Z)- <b>2c</b>	141.0	137.2	130.4

## CONCLUSION

In this work, we studied the efficiency of barriers to rotations to quantify *push-pull* effect of selected thiazolidines **1-2** under different solvent conditions. To this purpose, the  $\Delta G^\ddagger$  proved to be an excellent parameter under reliable conditions compounds studied.

***Acknowledgement***

This work was supported by the Ministry of Education, Science and Technological Development of the Republic of Serbia (Grant No: 451-03-9/2021-14/200026).

**REFERENCES**

- [1] J. Sandström, *Top. Stereochem.*, 1983, 14, 83-181.
- [2] E. Kleinpeter, *J. Serb. Chem. Soc.*, 2006, 71, 1-17.
- [3] A. Rašović, V. Blagojević, M. Baranac-Stojanović, E. Kleinpeter, R. Marković, D. M. Minić, *New J. Chem.*, 2016, 40, 6364-6373.

# THE ENTHALPY–ENTROPY COMPENSATION MECHANISM OBSERVED IN THE CONFIGURATIONAL ISOMERIZATION OF SELECTED 2-ALKYLIDENE-4-OXOTHIAZOLIDINES UNDER THE SAME AND DIFFERENT SOLVENT CONDITIONS

A. Rašović

*Center for Chemistry ICTM, University of Belgrade, Studentski trg 16,  
P. O. Box 473, 11000 Belgrade, Serbia (arasovic@chem.bg.ac.rs)*

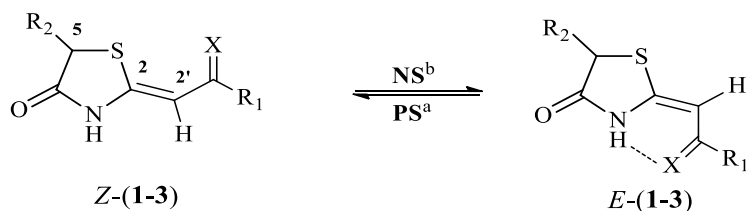
## ABSTRACT

The results of our previous work showed that barriers to rotation ( $\Delta G^\ddagger$ ) around the C=C double bond of thiazolidine derivatives (*Z*)-**1**, (*2E*, *5Z*)-**2**, and (*E*)-**3** can be employed as the very efficient parameter to quantify their *push–pull* effect under different solvent conditions. We explained this by enthalpy–entropy compensation (EEC), occurring on the relationship: weak polar solvent (CDCl<sub>3</sub>)/polar solvent (DMSO-*d*<sub>6</sub>). In this paper, it has been at the first time demonstrated that the thermodynamics of C=C double bond rotation of the (*Z*)-**1**, (*2E*, *5Z*)-**2**, and (*E*)-**3** follows the EEC. Thus, a linear plot between their activation enthalpy ( $\Delta H^\ddagger$ ) and entropy ( $\Delta S^\ddagger$ ) has been observed, showing enthalpy–entropy compensation (EEC), which is occurred for both under the same solvent conditions and different ones. This result indicated that the  $\Delta S^\ddagger$  and  $\Delta H^\ddagger$  could be employed to quantify the *push–pull* effect of 4-oxothiazolidines under the same solvent conditions.

## INTRODUCTION

The concept of enthalpy–entropy compensation (EEC) was introduced out by Constable [1]. Since that time, the EEC has been widely documented and discussed in the literature [2]. Closely related to this, from the data of our experimentally and theoretically studied configurational isomerization of selected thiazolidines (*Z*)-**1**, (*2E*, *5Z*)-**2**, and (*E*)-**3**, we previously concluded that the  $\Delta G^\ddagger$  proved to be an excellent parameter by means to quantify *push–pull* effect under different solvent conditions (at least the two solvents studied; CDCl<sub>3</sub> for (*Z*)-**1** → (*E*)-**1** isomerization, and DMSO-*d*<sub>6</sub> for (*2E*, *5Z*)-**2** → (*2Z*, *5Z*)-**2** and (*E*)-**3** → (*Z*)-**3** isomerizations, respectively) and the direction of isomerization (Scheme 1) [3]. Thus, all calculated and experimentally determined values of the  $\Delta G^\ddagger$  showed the correct trend in decreasing rotational barriers: **3** > **1** > **2**.

This work reports the plotting of activation entropy against activation enthalpy, whose experimentally determined data were previously reported by us [3]. The observed linear correlation between these magnitudes showed the enthalpy–entropy compensation (EEC) occurred for both under the same solvent conditions and different ones. This greatly supported our previous report, which showed that  $\Delta G^\ddagger$  proved to be an excellent parameter by the means to quantify the *push–pull* effect of the broader series of selected thiazolidines under reliable experimental conditions [4].



a) The polar solvents (PS) shifts equilibrium to the Z isomer due to the breaking the intramolecular hydrogen bond (IHB) in the E-counterpart.

b) In the nonpolar solvents (NS) the IHB is favored.

(Z)-**1**:  $R_1 = \text{Ph}$ ;  $R_2 = \text{CH}_2\text{COOEt}$ ;  $X = \text{O}$   
 (2E, 5Z)-**2**:  $R_1 = \text{OEt}$ ;  $R_2 = -\text{CHCOOEt}$ ;  $X = \text{O}$   
 (E)-**3**:  $R_1 = \text{NH}_2$ ;  $R_2 = \text{CH}_2\text{COOEt}$ ;  $X = \text{S}$

**Scheme 1.** The configurational isomerization of 4-oxothiazolidines **1-3**.

## EXPERIMENTAL DETAILS

The detailed experimental protocols associated with the monitoring of the stereodynamic behavior of the studied compounds **1-3** have been already reported by us [3]. As outlined in Figure 1, the activation entropy is plotted against activation enthalpy for rotation around the C(2)=C(2') double bond in 4-oxothiazolidines (Z)-**1**, (2E, 5Z)-**2** and (E)-**3** at 298 K for the same solvent conditions (DMSO- $d_6$ ) and different ones (CDCl<sub>3</sub> versus DMSO- $d_6$ ).

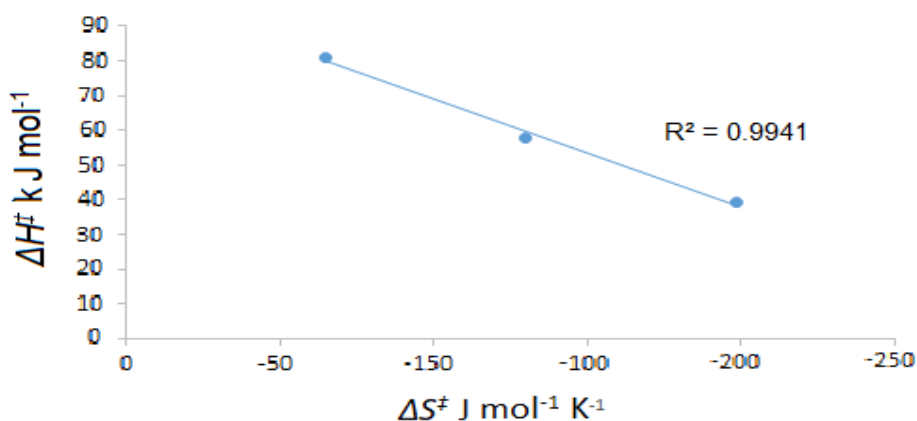


**Figure 1.** The plot of the  $\Delta H^\ddagger$  against the  $\Delta S^\ddagger$  for rotation around the C(2)=C(2') double bond in 4-oxothiazolidines established for the same solvent conditions and different ones ((2E, 5Z)-**2**, (E)-**3**/DMSO- $d_6$  versus (Z)-**1**/CDCl<sub>3</sub>).

## RESULTS AND DISCUSSION

The enthalpy-entropy compensation effect (or earlier named as the Barclay-Butler rule, the Meyer-Neldel rule, and others) has been found in a wide range of fields of chemistry, such as protein chemistry, lipid chemistry, nucleic acid chemistry, hydrogen bonding, proton transfer, enzyme binding, addition reaction and substitution reactions, and so on. The EEC has been characterized as a linear relationship between the logarithm of the preexponential factors and the activation energies, and between the enthalpies and entropies of activation of the Arrhenius equation, or between the enthalpy and entropy changes of the series of reactions [2].

The magnitudes of  $\Delta H^\ddagger$  and  $\Delta S^\ddagger$ , as the difference in enthalpy and entropy between transition (TS) and ground state (GS) structures, are influenced by structural changes within the molecule and by the

solvent. During the configurational isomerization, enthalpy increases and reaching the transition state becomes equal to  $\Delta H^\ddagger$ , when the C(2)=C(2') double bond is broken. Generally, solvents decrease  $\Delta H^\ddagger$  and  $\Delta S^\ddagger$  values because the more polar TS (due to the full charge separation) is more solvated than the less polar GS. Thus, if we compare  $E \rightarrow Z$  isomerizations of **2** and **3**, which are performed in the same solvent (DMSO- $d_6$ ) and at the same temperature (298 K), all activation parameters ( $\Delta G^\ddagger$ ,  $\Delta H^\ddagger$  and  $\Delta S^\ddagger$ ) indicate a decreased *push-pull* character in **2** (when *push-pull* effect increase, the  $\Delta G^\ddagger$ ,  $\Delta H^\ddagger$  and  $\Delta S^\ddagger$  values decrease; Table 2, entries 2 and 3), related to both the electronic properties of EWG (electron-withdrawing group attached at C(2') atom) and additional barrier-increasing effect of the C(5)=C(5')CO<sub>2</sub>Et moiety (Scheme 1). Furthermore, concerning their  $\Delta H^\ddagger$  and  $\Delta S^\ddagger$  values, the EEC effect, occurring for these compounds in the same solvent (DMSO- $d_6$ ), has been observed as follows: when activation entropy is lower (less favorable; compound **3**), activation enthalpy is decreasingly positive (more favorable; compound **3**), and vice versa.

Additionally, when is comparing the  $\Delta S^\ddagger$  values concerning the isomerization of (Z)-**1**, (2*E*, 5*Z*)-**3** and (E)-**3** under different solvent conditions and at the same temperature (298 K), they indicated an increased ordering in a solvent so to make activation entropy less favorable (more negative) when is decreased polarity of solvent from DMSO- $d_6$  (the (2*E*, 5*Z*)-**2**  $\rightarrow$  (2*Z*, 5*Z*)-**2** and (E)-**3**  $\rightarrow$  (Z)-**3** isomerizations) to CDCl<sub>3</sub> (the (Z)-**1**  $\rightarrow$  (E)-**1** isomerization). Consequently, looking at the same direction (from polar DMSO- $d_6$  to weak polar CDCl<sub>3</sub>), the  $\Delta H^\ddagger$  becomes more favorable (less positive). The other words, for the (Z)-**1**  $\rightarrow$  (E)-**1** isomerization (CDCl<sub>3</sub>), a significantly larger amount of ordering in the solvent is required (more negative  $\Delta S^\ddagger$  values) than for those performed in DMSO- $d_6$  to make favorable  $\Delta H^\ddagger$  (less positive) by increasing solvent/transition state interaction [3].

To above-explained, due to the enthalpy-entropy compensation effect, occurring for both under the same solvent conditions and different ones, the barriers to rotation around the C=C double bond of the selected thiazolidine derivatives **1-3** are not affected by the solvent (at least the two solvents studied) and the direction of isomerization (Scheme 1). Therefore, the resulting  $\Delta G^\ddagger$  are influenced only by structural changes within the **1-3**, spanning a rather narrow range of 3.6 kJ mol<sup>-1</sup> (Table 1), concurs with our previous estimation of the electron-withdrawing ability of substituents as CSNH<sub>2</sub> > CPh > CO<sub>2</sub>Et [3]. This could be explained as follows: the greater *push-pull* effect of thiazolidine, the greater similarity between its TS and GS, and lower  $\Delta G^\ddagger$ .

Finally, the great linear correlation (Figure 1;  $R^2 = 0.9941$ ) between activation enthalpy and entropy, achieved for the same solvent, as well as for different ones, is evidence showing that in the configurational isomerization of **1-3** the EEC occurred for both under the same solvent conditions and different ones. Consequently, the assumption that the resulting  $\Delta G^\ddagger$  are influenced only by structural changes within the **1-3** has been proved.

**Table 1.** The activation parameters ( $\Delta H^\ddagger$ ,  $\Delta S^\ddagger$  and  $\Delta G^\ddagger$ ) for rotation around the C(2)=C(2') double bond in 4-oxothiazolidines (Z)-**1**, (2*E*, 5*Z*)-**2** and (E)-**3** determined at 298 K.

Entry	Compound	Solvent	$\Delta H^\ddagger$ [kJ mol <sup>-1</sup> ]	$\Delta S^\ddagger$ [J mol <sup>-1</sup> K <sup>-1</sup> ]	$\Delta G^\ddagger$ [kJ mol <sup>-1</sup> ]
1	(Z)- <b>1</b>	CDCl <sub>3</sub>	39.3	-198.7	98.5
2	(2 <i>E</i> ,5 <i>Z</i> )- <b>2</b>	DMSO- $d_6$	80.9	-64.7	100.2
3	(Z)- <b>3</b>	DMSO- $d_6$	57.8	-130.2	96.6

## CONCLUSION

The excellent linear correlation between activation enthalpy and entropy has been achieved for the isomerization of **1-3** in the same solvent and different ones. They proved that enthalpy-entropy compensation occurred both under the same solvent conditions and different ones. Thus, the  $\Delta G^\ddagger$  are influenced only by structural changes of **1-3** (at least the two solvents studied).

## Acknowledgement

This work was supported by the Ministry of Education, Science and Technological Development of the Republic of Serbia (Grant No: 451-03-9/2021-14/200026).

## REFERENCES

- [1] F. H. Constable, *Proc. R. Soc. London (Ser. A)*, 1925, 108, 355-378.
- [2] L. Liu, Q.-X. Guo, *Chem. Rev.*, 2001, 101, 673-696.
- [3] A. Rašović, V. Blagojević, M. Baranac-Stojanović, E. Kleinpeter, R. Marković, D. M. Minić, *New J. Chem.*, 2016, 40, 6364-6373.
- [4] A. Rašović and V. A. Blagojević, The barriers to rotations around the C=C bond by the means to quantify *push-pull* effect of broader series of selected 2-alkylidene-4-oxothiazolidines under different solvent conditions: *Proceedings of the 15<sup>th</sup> International Conference on Fundamental and Applied Aspects of Physical Chemistry, September 20-24, Belgrade, Physical Chemistry, 2021.*

*H - Material Science*



## PHYSICOCHEMICAL CHANGES OF BIMETALLIC THIN FILM AFTER 300 fs/515 nm LASER IRRADIATIONS

B. Gaković<sup>1</sup>, D. Milovanović<sup>2</sup>, S.I. Kudryashov<sup>3</sup>, P.A Danilov<sup>3</sup>, A. Radulović<sup>2</sup>, P. Panjan<sup>4</sup> and A.A. Ionin<sup>3</sup>

<sup>1</sup>University of Belgrade, Vinča Institute of Nuclear Sciences,  
P.O.Box 522, 11001 Belgrade, Serbia. (biljagak@vin.bg.ac.rs)

<sup>2</sup>Institute of General and Physical Chemistry, Belgrade, Serbia

<sup>3</sup>Lebedev Physical Institute, 119991 Moscow, Russia

<sup>4</sup>Jožef Štefan Institute, 1000 Ljubljana, Slovenia

### ABSTRACT

The method that enables highly controlled non-contact morphological and composition modifications of materials is laser processing. In the case of ultra-short laser pulses, as femtosecond (fs) ones, this method allows extremely accurate modifications, on micrometer and even on nanometer scale. Results concerning physicochemical changes after precise ablation of bimetallic thin film (BMTF), by single fs laser pulses, are presented. We investigated influence of the variations in pulse energy on composition and morphology changes. For used range of single pulse energies, we registered ablation of the upper layer of BMTF without ablation of the substrate.

### INTRODUCTION

Aluminium (Al) and titanium (Ti) thin films (TFs) and their combinations are suitable for applications in nanotechnology. Treatment of these films can be handled by laser systems. The laser material treatment depends on several factors such as laser parameters (wavelength, pulse duration, pulse energy, etc.) and material characteristics (physicochemical properties, surface state, absorptivity, etc.). Up to now the individual thin films and their combinations have been studied regarding irradiation with short (ns) and ultra-short (ps and fs) laser pulses [1-4]. The most precise results are obtained with fs pulses that suppress the formation of a heat-affected zone, which is vital for ultrahigh precision fabrication.

### EXPERIMENTAL

The sample BMTF is composed of two layers, titanium (Ti) and aluminum (Al) that was used in the experiment. The first layer deposited on Si substrate was Ti, 50 nm thick and the second was Al, 10 nm thick [1]. In the text, the sample is denoted by Si/Ti/Al.

The fs laser irradiations of the BMTF were done with an ytterbium-doped fiber laser ( $\lambda = 515$  nm,  $\tau = 300$  fs) in the air (TEM<sub>00</sub> mode) [3]. Pulse energies values  $E_p$  varied from 0.02  $\mu$ J to 1.2  $\mu$ J. After irradiations, the sample was analyzed by optical microscopy, scanning electron microscopy (SEM), energy dispersive spectrometer (EDS) and non-contact profilometry.

### RESULTS AND DISCUSSION

The sample was irradiated by 10 laser pulses at different places of the TF surface and the presented results are expressed as the average values. The pulse energy was kept constant in each sequence of irradiation. Optical and SEM analyses confirmed almost identical spots on the surface that corresponds to the same pulse energy. At pulse energy ranged from 0.03  $\mu$ J up to 0.16  $\mu$ J circular craters with uniform topography bottom were registered, while higher pulse energy, from 0.32  $\mu$ J up to 1.2  $\mu$ J, produced circular craters with bottoms' topography comprised of values and peaks.

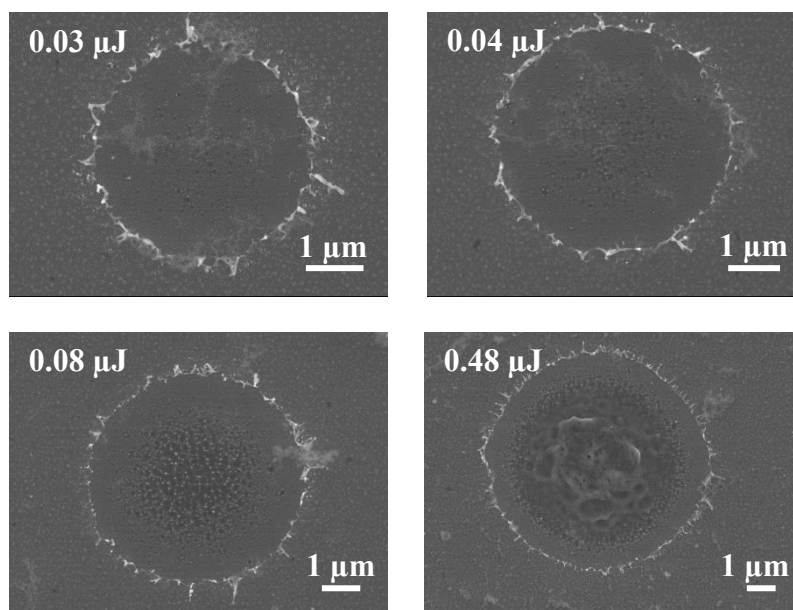


**Figure 1.** SEM micrographs of the surface morphology of Si/Ti/Al (50 nm-10 nm) after single fs pulse irradiations ( $E_p$  - pulse energy incorporated).

Qualitative and quantitative analyses of the modified areas were done by SEM and profilometry. Firstly, SEM study provided information about laser spots as diameters and morphology on the micrometre and nanometre levels. Characteristic morphology changes of the BMTF are presented on the SEM micrographs, Fig.1. The depth of the generated craters was measured by non-contact optical profilometry (Fig.2). At lower pulse energies the first layer and part of the second one were ablated without modification of the Si substrate. In the case of  $E_p = 0.03 \mu\text{J}$  and  $0.04 \mu\text{J}$  ablation depth ( $D$ ) values were comparable (Tab.1) and bottoms of craters were flat, while diameter value increased. Different morphology can be registered at higher pulse energies, such as  $E_p = 0.08 \mu\text{J}$  (Figs.1 and 2). The step like ablation appeared and value of the step depth  $d$  was close to previously found value of  $D$ . As the pulse energy further increases, the craters centre look similar to one produced by  $0.48 \mu\text{J}$  (Fig.1).

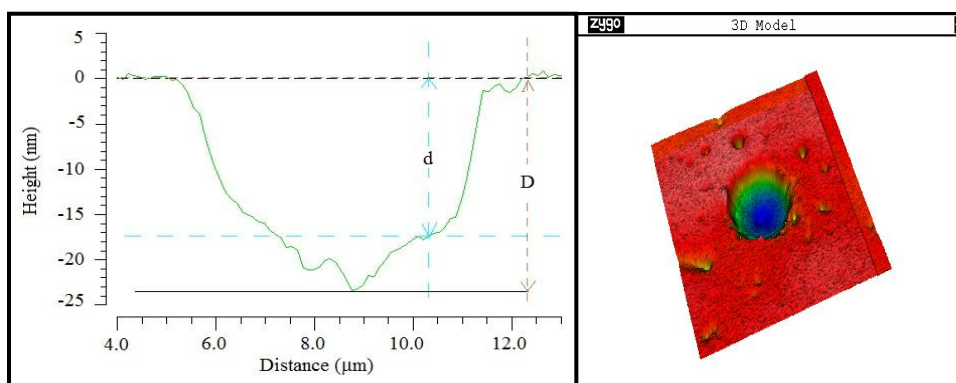


**Figure 2.** 2D and 3D profilometry of the crater created by a single pulse with  $E_p = 0.08 \mu\text{J}$  (SEM on Fig.1). Heights from the bottom and step to the surface of the BMTF are  $D = 24.3 \text{ nm}$  and  $d = 19.5 \text{ nm}$ , respectively.

**Table 1.** Compositional changes registered in the craters produced on the Si/Ti/Al after single fs pulse irradiation.

$E_p$ [ $\mu$ J]/	Al (w%)	Ti (w%)	Si (w%)	O (w%)	$D$ [nm]	$d$ [nm]
Thin film	0.24	1.82	95.58	2.37	-	-
0.03	-	1.86	95.26	2.88	19.0	
0.04	-	1.84	95.76	2.40	20.2	
0.08	-	1.41 <sup>C</sup>	96.05 <sup>C</sup>	2.55 <sup>C</sup>	24.3	19.5
		1.87 <sup>S</sup>	95.86 <sup>S</sup>	2.27 <sup>S</sup>		
0.48	-	1.00 <sup>C</sup>	97.49 <sup>C</sup>	1.52 <sup>C</sup>	> 60	
		1.86 <sup>S</sup>	95.31 <sup>S</sup>	2.83 <sup>S</sup>		

$D$ -the crater centre depth;  $d$  - the step depth; Concentration (w%) from the spot centre or from the first step is denoted with C or S, respectively.

Elemental compositions determined by the semi-quantitative EDS technique, of some of the created craters are shown in the Tab.1, from which one can see that: (i) non-zero concentration of Al was only present on the TF surface, (ii) nearly the same concentration of Ti in the crater area, at laser pulse energies of 0.03  $\mu$ J, 0.04  $\mu$ J and 0.06  $\mu$ J (last not shown in the Tab.1), (iii) at the first step regions of craters at pulse energies of 0.08  $\mu$ J and higher, a represent is 0.48  $\mu$ J, concentration of Ti was slightly lower, (iv) in the central areas of all craters produced by higher pulse energies than 0.48  $\mu$ J, average concentration of Ti was lower, but different from zero. In this experiment we determined a range of laser pulse energy values at which it was possible to ablate the upper Al layer from bimetallic thin film without removal of the entire film from the substrate.

## CONCLUSION

In this study we performed an experiment using thin nanolayer bimetallic film Si/Ti/Al and laser beam with pulse duration of 300 fs and wavelength of 515 nm. Irradiation was done in the air atmosphere, with the single laser pulses of different pulse energies. Morphological and compositional changes, after the single pulse irradiation, were examined with SEM, profilometry and EDS. In conclusion, single-shot femtosecond laser ablation of the film demonstrates energy-dependent selective removal of the first Al layer and only a part of Ti layer beneath depending on the pulse energy.

## Acknowledgement

This work was supported by STSM grant (No. CA17126-45334) given to B.Gaković by CA17126-TUMIEE to visit Lebedev Physical Institute Gas Lasers Lab., Quantum Radiophysics Division, Moscow, Russia and Ministry of Education, Science and Technological Development of Republic of Serbia, under contract No. 451-03-68/2020-14/ 200051.

This study was supported by the Russian Science Foundation (grant #16-12-10165).

## REFERENCES

- [1] S.M. Petrović, D. Peruško, B. Salatić, I. Bogdanović-Radović, P. Panjan, B. Gaković, D. Pantelić, M.Trtica, B. Jelenković, *Opt. Las. Tech.* **54**(2013)22.
- [2] A.A. Ionin, S.I. Kudryashov, S.V. Makarov, L.V. Seleznev, D.V. Sinitsyn, *Appl. Phys. A*, **117** (2014) 1757.

- [3] S.I. Kudryashov, B. Gaković, P.A. Danilov, S.M. Petrović, D. Milovanović, A.A. Rudenko, A.A. Ionin, *App. Phys. Lett.* **112** (2018) 02310.
- [4] B. Gaković, G.D. Tsibidis, E. Skoulas, S.M. Petrović, B. Vasić, E. Stratakis, *J. Appl. Phys.* **122** (2017) 223106.

## GRAPH-THEORY APPLIED TO THE SOLID SKELETON EVOLUTION IN SINTERING

B. M. Randjelovic and Z. S. Nikolic

*University of Niš, Faculty of Electronic Engineering,  
Aleksandra Medvedeva 14, 18000 Niš, Serbia (zoran.nikolic@ni.ac.rs).*

### ABSTRACT

Usually used methodology for modeling of microstructural evolution in sintering will be redefined by the introduction of the graph theory. Time- dependent evolution of graph data structure will be used for simulation of solid skeleton evolution induced by neck growth.

### INTRODUCTION

Many problems in mathematics, computer science, engineering, and technics, as well as in nature, can be described and modeled easily using graph theory. As one of the simplest but most popular and most applied branch of mathematics, it has a special advantage among others through simple mathematical approach, simple visualization and visual connection to the problems, and easy application of graph algorithms. In that sense, a simple mathematical approach and relatively simple visual connection of technological parameters and phenomena that characterize sintering can be very elegantly modeled by this methodology. If the problem of modeling the sintering process were completely mapped to graphs, then it would be possible to realize the more efficient simulation of microstructural evolution during sintering. Even more, it is also possible to use different algorithms for graphics operations (through matrices), as well as parallel algorithms for fast calculations on a large data set typical for multi-grain models with a huge number of grains.

### SOLID SKELETON TOPOLOGY

From the point of the theoretical investigation of sintering, an isolated solid grain can be mathematically represented by the domain of regular (spherical) shape,  $G^m = (\mathbf{r}_c^m, R_m)$ , where  $\mathbf{r}_c^m = (x_c^m, y_c^m, z_c^m)$  is position-vector of the center of the mass of the  $m$ -th grain of radius  $R_m$ .

During sintering, the microstructure is characterized by solid grains in contact with one another forming skeleton structure, where solid skeleton may be generally defined as series of connected solid grains arranged in a long chain. Such structure is always formed during either solid state sintering or liquid phase sintering [1].

Solid skeleton microstructure can be represented as a graph [2]. It is known that graphs have been used in many material science theoretical models ranging from molecular structure [3,4] to grain boundaries [5,6] and porous microstructure [7].

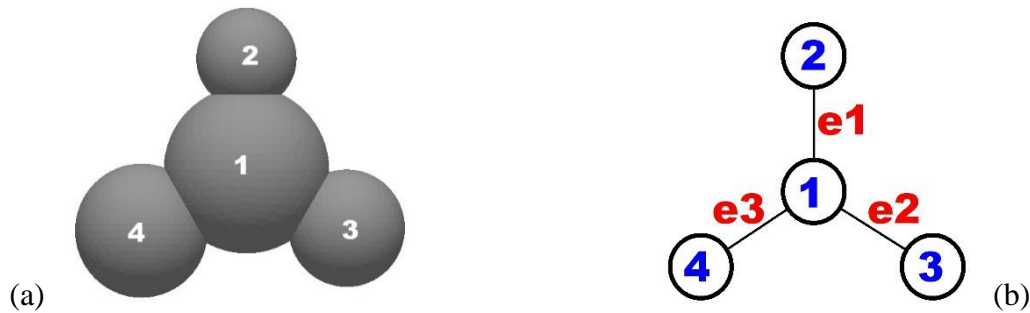


**Figure 1.** (a) Four-grain model; (b) Graph-based representation of four grain model with  $V = \{1,2,3,4\}$  and  $E = \{(1,2), (1,3), (1,4)\}$ .

A graph generally denoted with  $G(V,E)$  consists of the set of vertices (nodes)  $V$  and the set of edges  $E$ . A vertex can have any number of edges connected to it, where an edge connects exactly two vertices. The latter one represents *the graph structure unit* (in sintering: two grains connected by the neck). Taking into account the multi-grain model each grain can be replaced by a vertex and an edge between two connected grains  $G^a$  and  $G^b$  by the line segment between their centers with the length equals to the center-to-center distance  $\text{dist}(\mathbf{r}_c^a, \mathbf{r}_c^b) = \sqrt{(x_c^b - x_c^a)^2 + (y_c^b - y_c^a)^2 + (z_c^b - z_c^a)^2}$  (the Euclidean distance function). In Fig. 1b the grain model shown in Fig. 1a replaced by the corresponding discretized graph-based model.

For modeling the investigation of sintering through graph operations we will use two matrices that describe some graph properties: adjacency matrix and incidence matrix. *The adjacency matrix* of the corresponding graph is the matrix with real numbers of dimension, i.e.  $\mathbf{A} = \|a_{ij}\|_{n \times n}$ , where  $n$  is the number of vertices (number of grains), while the elements of the matrix

$$a_{ij} \equiv a_{ji} = \begin{cases} \text{dist}(G^i, G^j) & \text{for } i \neq j \text{ and domains in contact} \\ 0 & \text{for } i = j \text{ or no domains contact} \end{cases}$$

*The incidence matrix* of the corresponding graph is the binary matrix  $\mathbf{B} = \|b_{ij}\|_{m \times n}$ , where  $m$  is the number of edges, while the elements are defined as

$$b_{ij} \equiv b_{ji} = \begin{cases} 1 & \text{if vertex } j \text{ is incident with edge } i \text{ in graph} \\ 0 & \text{if vertex } j \text{ is not incident with edge } i \text{ in graph} \end{cases}$$

Computation of time-dependent graph structures will be constrained by geometrical limitation for two grains in contact with an observable dihedral angle. Once formed, grain contacts grow to satisfy the dihedral angle, and beyond that point, neck growth is paced by the rate of grain growth. During the neck growth, the adjacency matrix will be represented with time-dependent elements. For an idealized two-grain model (graph structure unit) undergoing sintering, the center-to-center distance is time-dependent, i.e.  $D_{ij}^t = \text{dist}(\mathbf{r}_c^i(t), \mathbf{r}_c^j(t))$ . The simulation approach will be based on the concept that sintering law  $f(D_{ij}^t)$  and sintering transformation [8] defined as  $a_{ij}(t) \equiv D_{ij}^{t+\Delta t} \mapsto D_{ij}^t - f(D_{ij}^t) \cdot \Delta t$  can be applied to each pair of contacting grains within the multi-grain model.

## RESULTS AND DISCUSSION

For system W-Ni we will assume that neck growth between tungsten grains results in a relative neck size to the grain size of about 0.4 after 1 h at the sintering temperature, similar to calculated value from conventional sintering models [9]. For simulation, we will apply an initial randomly generated model containing non-uniformly distributed domains of different radii (72 spherical tungsten grains, mean size 34.9  $\mu\text{m}$ , with all domain centers placed in a plane due to better visualization of graph structure evolution.

Figures 2a and 2b show computed microstructures for 10 min and 120 min, respectively, and Figs. 2c and 2d corresponding graphs. After a short sintering time and the formation of small necks between grains, movement of most isolated grains is complete and three graphs were established (Fig. 2c). The evolution of graph structure starts with the formation of many graph structure units (by the neck connected grains) and their motion and merging into a larger graph of connected graph structure units arranged in a long chain. During sintering connected grains continue to move and new grain contacts and grain growth lead to the formation of a completely connected stable graph structure (Fig. 2d). This graph appears to remain almost unchanged with sintering time beyond 120 min, suggesting thereby, that further neck growth promotes an equilibrium configuration for sintered microstructure characterized by a chain-like graph structure.

The evolution of graph structure given as a system of functions of topological parameters changes monotonically with time. The most important features of this approach are that the method can recognize and resolve topological constraints in large-scale random grain arrays. This approach does not need any special geometric assumptions and the evolution of graph structure is simulated using a set of simple local rules and overall neck growth law. A special advantage of our approach is in the possibility to use parallel algorithms for fast calculations on a large data set, such as multi-grain models with a large number of grains.

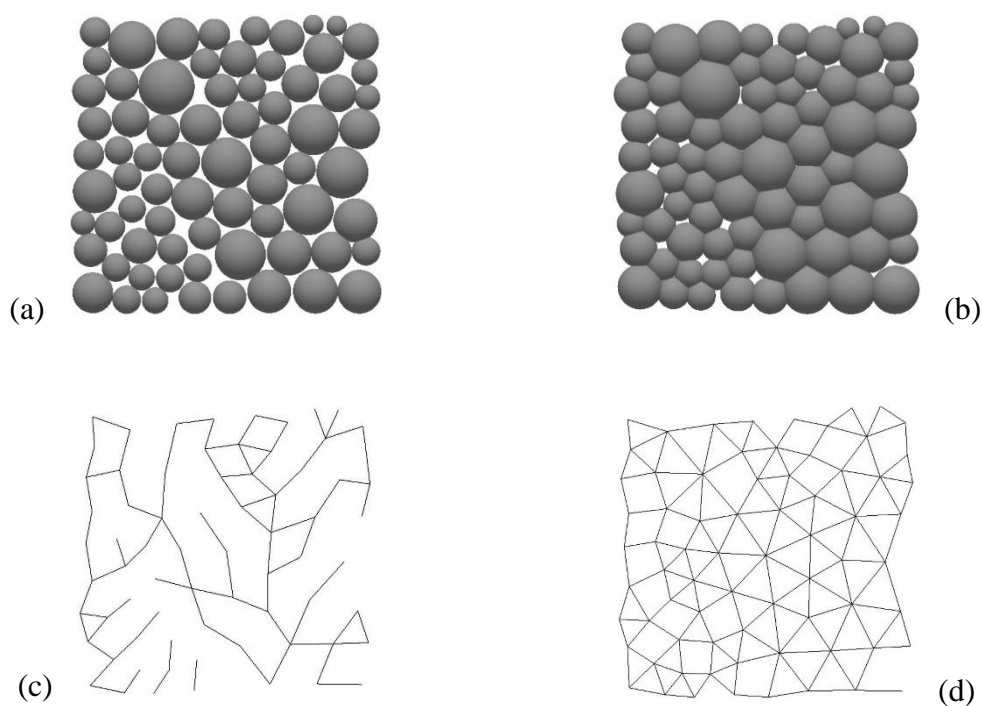


**Figure 2.** Computed microstructure (a) after 10 min. and (b) 120 min. with corresponding graph structures (c) and (d), respectively.

**REFERENCES**

- [1] D. F. Heaney, R. M. German, I. S. Ahn, *J. Mater. Sc.*, 1995, 30, 5808-5812.
- [2] P. Du, A. Zebrowski, J. Zola, B. Ganapathysubramanian, O. Wodo, *npj Comput. Mater.*, 2018, 4:50, 1-7.
- [3] V.A. Blatov, A.P. Shevchenko, D.M. Proserpio, *Cryst. Growth Des.* 2014, 14, 3576–3586.
- [4] B.G. Sumpter, D.W. Noid, *Macromol. Theory Simul.* 1994, 3, 363–378.
- [5] O.K. Johnson, J.M. Lund, T.R. Critchfield, *Acta Mater.* 2018, 146, 42–54.
- [6] M.M. Moghadam, J.M. Rickman, M.P. Harmer, H.M. Chan, *J. Appl. Phys.* 2015, 117, 045311.
- [7] A. Cecen, *ECS Trans.* 2011, 41, 679–687.
- [8] Z.S. Nikolic, *Math. Comp. Model.*, 2013, 57, 1060–1069.
- [9] R.M. German R M, *Powder Metall. Sci.* (Princeton: Metal Powder Industry Federation), 1994.

## A NUMERICAL APPROACH TO ESTIMATE INTERGRANULAR CAPACITANCE IN CERAMIC SINTERING

B. M. Randjelovic and Z. S. Nikolic

*University of Niš, Faculty of Electronic Engineering,  
Aleksandra Medvedeva 14, 18000 Niš, Serbia (zoran.nikolic@ni.ac.rs).*

### ABSTRACT

In this paper, a numerical method for predicting evolution of an intergranular capacitance during ceramic sintering will be defined. The contact between two grains undergoing sintering may be recognized as a structure that forms an intergranular capacitor whose capacitance changes as the neck grows by diffusion. It will be assumed that diffusion mechanisms responsible for material transport from the grain boundary to the neck are the volume and grain boundary diffusion only. The developed method will be applied for the computation of time-dependent intergranular capacitance during ceramic sintering of BaTiO<sub>3</sub> system.

### INTRODUCTION

Ceramic materials are of particular interest because of their unique and outstanding properties such as special electrical properties, superior mechanical properties, greater chemical stability, etc. In the last ten to twenty years, new high-performance ceramic materials have been developed as a result of an improved understanding of essential basic mechanisms, their microstructure evolution, and their final properties.

One way to gain a better understanding of common basic sintering mechanisms is by computer simulation using the appropriate numerical approach, because modeling by simulation enables the evolution of parameters to be followed throughout the sintering time and offers generally a framework within which experimental observations can be assessed.

In this paper we will propose a new interrelationship between electrical, geometrical, and technological parameters by introducing intergranular capacitance model, which will be based on an idealized two-grain model undergoing sintering. Microstructural evolution will be simulated by this model and a set of simple local rules and overall neck growth law which can be, in general, arbitrarily chosen. This approach will be used to enable the establishment of structural and electrical parameters of BaTiO<sub>3</sub> ceramics.

### MODEL TOPOLOGY

It is convenient to use a multi-grain model with a regular grain shape whose geometry requests to store only the position, orientation, and size of each grain. In that sense, a point in three-dimensional space  $\mathbf{R}^3$  will be characterized by the Cartesian coordinates  $(x, y, z)$ , and position-vector  $\mathbf{r} = (x, y, z)$ . Thus, the multi-grain structure will be now represented by the regular shape domain  $G^m = (\mathbf{r}_o^m, R_m)$ , where  $\mathbf{r}_o^m$  is position-vector of the center of the mass of the  $m$ -th grain of radius  $R_m$ .

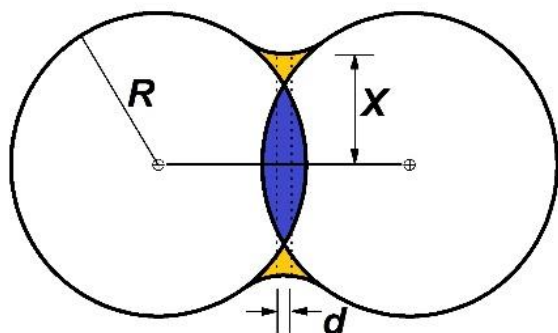


**Figure 1.** A two-dimensional two-grain model with equal-sized grains, as well as the scheme of an intergranular capacitor having dielectric thicknesses  $d$ , which is the result of material transport driven by the difference in surface curvature between sources and sinks.

Ceramics' microstructures show that two contacted grains make a structure that forms an intergranular capacitor whose structure depends on diffusion processes. The contact region defined by the neck radius  $x$  can be treated as a capacitor having dielectric thicknesses  $d$  (Fig. 1). Although diffusing atoms penetrate the neighboring grains and degrade the grain boundaries between contacting grains, the contact surface will be assumed as the circle of the area  $\pi x^2$ . Thus, the time-dependent capacitance per grain contact can be defined as  $C(t) = \varepsilon_0 \varepsilon_r \pi x^2(t)/d$ , where  $\varepsilon_0$  and  $\varepsilon_r$  are the dielectric constants of vacuum and the ceramic material and  $t$  is sintering time. Note that the exact calculation of the curvature differences involves the solution of time-temperature dependent diffusion equations. Assuming that the coordination number,  $N_C$ , has been conceived as the number of nearest neighbors of grain in the grain structure concerned, the total intergranular capacitance per grain will be estimated as,  $C_\Sigma(t) = N_C \cdot \overline{C(t)}$ , where  $\overline{C(t)}$  means the average value.

Taking into account an idealized two-grain sintering model and assuming that the center-to-center distance is defined as the Euclidean distance function [1],  $D_{ki} = \text{dist}(\mathbf{r}_o^k, \mathbf{r}_o^i)$ , time-dependent intergranular capacitance can be computed using sintering kinetic equation for simulation of neck growth by the iterative procedure [2],  $D_{ki}^{t+\Delta t} \mapsto D_{ki}^t - f(D_{ki}^t) \cdot \Delta t$  based on the concept of in advance defined sintering law  $f(\bullet)$ , where  $\Delta t$  is the time step. Note that the neck between the (contacting) grains forms as soon as the sintering begins, as well as that the neck growth continues until it about 40-50% of the grain size [3].

Sintered materials are in general characterized by connected microstructure that forms capacitor network ( $C_{NW}$ ), which always exists in ceramic sintering. Even more, the theoretical analysis [4] has shown that such a connected grain structure is favored. Such a network may be defined as series of connected domains arranged in long-chain,  $C_{NW} \mapsto \bigcup_{n=1}^N G^{s(n)}$ , where  $N$  is the number of domains included in NW and  $s(n)$  is the vector of their ordinal numbers. Within the network, the displacement of domain  $G^m$  induced by the neck growth can be modeled as the domain translation for a distance-vector  $\mathbf{q} = \{q_x, q_y, q_z\}$  accomplished through topological translation

$$G^m \mapsto G_{\mathbf{q}}^m = (x_o^m + q_x, y_o^m + q_y, z_o^m + q_z).$$

## RESULTS AND DISCUSSION

In this approach, the grain boundary will be treated as a transition region in which some atoms will not be exactly aligned with either grain and will be viewed as dielectric capacitors. We will also assume that grain boundaries can be considered as two-dimensional and with a finite thickness (a few lattice parameters in very pure metals to a few hundred angstroms in ceramics,  $\sim 0.3$ - $0.5$  nm).

In that sense, we will apply computer simulation for sintering of BaTiO<sub>3</sub>-ceramics assuming nearly constant dielectric thickness,  $d = 0.5$  nm, and the sintering law  $f(\bullet)$  with constant neck growth rate (e.g. relative neck size to grain size of about 0.4 after 1 h at the sintering temperature, similar to calculated value from conventional sintering models [5]).

For the simulation of the time-dependent capacitance of a ceramic sample, we will apply the multi-grain model in which interconnected grains, as explained above, may be replaced by capacitors. At the same time, the solid skeleton network must be replaced by the capacitor network.

Figure 2(a) demonstrates the evolution of the capacitor network and contact regions that determine intergranular capacitances. Figure 2(b) shows the overall time-dependent intergranular capacitance per grain in the sintering of the BaTiO<sub>3</sub>-ceramics multi-grain model. It can be seen that the electrical capacitance slowly increases according to time-dependent neck growth within the capacitor network. Note that this process is also characterized by appropriate densification manifested by a decrease in the center-to-center distance, and followed by relatively small grain rearrangement.

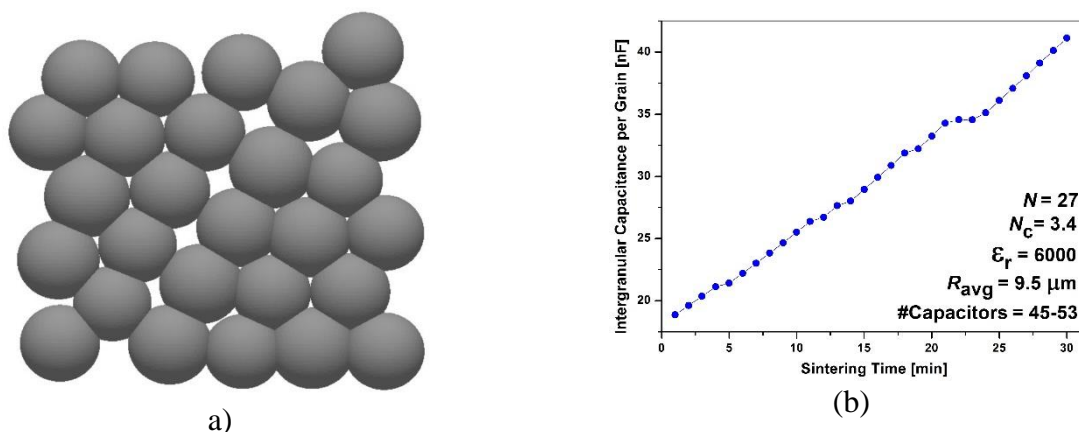


**Figure 2.** (a) Multi-grain model. (b) Time-dependent intergranular capacitance for sintering of BaTiO<sub>3</sub>-ceramics (initial number of capacitors was 45).

## CONCLUSION

The described model can be applied for the prediction of evolution of intergranular capacitance during ceramic sintering of real systems. Even more, a computer-based approach can be used to enable the establishment of interrelation between structural and electrical parameters, as well as to assist in the creation, modification, analysis, and optimization of new high-performance electronic ceramics materials.

## REFERENCES

- [1] Z. Liang, M.A. Ioannidis and I. Chatzis, *J Colloid and Interface Sci.* 221 (2000) 13–24.
- [2] Z.S. Nikolic, *Mathematical and Computer Modelling* 57 (2013) 1060–1069.
- [3] M.N. Rahman, *Sintering of Ceramics*. NY: CRC Press, 2007.
- [4] German R M and Liu Y 1996 *J. Mater. Sci. Engng.* 4 23
- [5] R.M. German, 1994 *Powder Metall. Sci.* (Princeton: Metal Powder Industry Federation).

## OCHRATOXIN A AND ZEARALENONE ADSORPTION BY SURFACTANT MODIFIED ZEOLITE

M. Marković<sup>1</sup>, A. Daković<sup>1</sup>, G. E. Rottinghaus<sup>2</sup>, M. Spasojević<sup>1</sup>, M. Obradović<sup>1</sup>, D. Smiljanić<sup>1</sup>

<sup>1</sup>*Institute for Technology of Nuclear and Other Mineral Raw Materials, Franše d' Epere 86, 11000 Belgrade, Serbia. (m.markovic@itnms.ac.rs)*

<sup>2</sup>*Veterinary Medical Diagnostic Laboratory, College of Veterinary Medicine, University of Missouri, Columbia, MO 65211, USA.*

### ABSTRACT

Cetylpyridinium chloride (CP) was used to modify the surface of the natural zeolite and adsorption of two mycotoxins, ochratoxin A (OCHRA) and zearalenone (ZEN) was investigated. The organozeolites were prepared with three different levels of CP (20, 50 and 100% of zeolite's external cation exchange capacity) and mycotoxin adsorption experiments were done at pH 3 and 7. Results showed that with increasing amounts of CP at the zeolitic surface, adsorption of OCHRA and ZEN increased, as well as with increasing amounts of solid phase in suspension. Adsorption of OCHRA was dependent of the form of OCHRA in solution while ZEN adsorption was pH independent. Maximum adsorption was obtained with the highest level of CP present at the zeolitic surface for both mycotoxins.

### INTRODUCTION

Mycotoxins are secondary metabolites produced by certain fungi that accumulate in maturing corn, cereals, and other food and feed crops. The most prevalent mycotoxins are aflatoxins, ochratoxins, fumonisins, zearalenone and the trichothecenes. Ochratoxin A (OCHRA) is a mycotoxin produced by *Aspergillus* and *Penicillium* species. It can cause nephrotoxicity, hepatotoxicity, neurotoxicity, teratogenicity and immunotoxicity in both human and animals. Chemical structure of OCHRA is presented in Figure 1(a). Zearalenone (ZEN) is a non-steroidal estrogenic mycotoxin produced by *Fusarium* species. Chemical structure of ZEN is presented in Figure 1(b). Due to its structural similarity to the naturally-occurring estrogens, it has strong estrogenic activity and causes infertility and abortion in livestock [1].

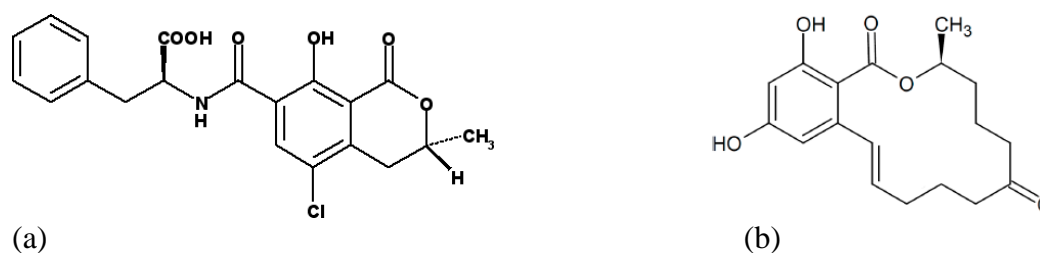


**Figure 1.** Chemical structures of OCHRA (a) and ZEN (b).

The most feasible and economical detoxification method is the use of adsorbents as feed additives. The aim is to sequester mycotoxins in the gastrointestinal tract avoiding their absorption by the organism. The natural aluminosilicate minerals, such as montmorillonite or zeolite, effectively bind aflatoxins *in vitro* and *in vivo* conditions. Nevertheless, the binding efficiency of these hydrophilic, negatively charged aluminosilicates to relatively non-polar and hydrophobic mycotoxins such as OCHRA and ZEN is low [2]. Modification of minerals with long chain organic cations (surfactants)

results in increased hydrophobicity of their surfaces and consequently higher affinity for hydrophobic organic molecules. Cetylpyridinium chloride (CP) is a surfactant widely used in pharmaceutical and cosmetic formulations as an antimicrobial preservative. It possesses a pyridine head group and a C16 alkyl chain.

In previous studies it was reported that modification of the natural zeolite clinoptilolite with different levels of surfactants – octadecyldimethylbenzyl ammonium chloride (ODMBA) or benzalkonium chloride (BC) increased adsorption of OCHRA and ZEN compared to unmodified clinoptilolite [3,4]. It was determined that adsorption of both mycotoxins increased with increasing amounts of surfactant at the zeolitic surface and that surfactants are active sites at which both mycotoxins are adsorbed.

Since adsorption of mycotoxins may be dependent on the type of surfactant, the aim of this research was to investigate if the natural zeolite modified with CP ions would be also efficient to adsorb OCHRA and ZEN.

## METHODS

Starting material was a zeolite-rich tuff from the Zlatokop deposit (Vranje, Serbia) containing primarily clinoptilolite (69%), with the smaller amounts of plagioclase and quartz. The cation exchange capacity (CEC) of the zeolitic tuff was 146 meq/100g, while the external cation exchange capacity (ECEC) was 10 meq/100g. The organozeolites were prepared by the following procedure: 10 g of zeolite was mixed with 100 mL of distilled water containing CP amounts equivalent to 20, 50 and 100% of its ECEC. The suspensions were stirred 10 min at 5000 rpm, and afterwards filtered, washed and dried at 60°C. Samples were denoted as ZCP-20, ZCP-50 and ZCP-100.

OCHRA and ZEN were obtained from Sigma-Aldrich Co. *In vitro* adsorption experiments were performed using the following procedure: duplicate aliquots of 0.1 M phosphate buffer (adjusted to pH 3 and 7) containing 2 ppm OCHRA or ZEN in solution (10 mL) were added to 15 mL Falcon polypropylene tubes to which had been added 20, 10, 5 or 2 mg of each adsorbent. The suspensions were shaken for 30 min at room temperature, then centrifuged at 13000 rpm for 5 min and 2 mL of the aqueous supernatant was removed for HPLC analysis. The percentage of OCHRA and ZEN bound was calculated from the difference between the initial and final concentration in the aqueous supernatant after equilibrium.

## RESULTS AND DISCUSSIONS

The organozeolites were obtained by cation exchange of inorganic cations at the zeolitic surface with CP surfactant.

OCHRA is a hydrophobic molecule which possesses carboxylic and phenolic functional groups (Figure 1a). Based on the dissociation constants of OCHRA,  $pK_{a1} = 3.5$  (carboxylic group) and  $pK_{a2} = 7$  (phenolic group), OCHRA is present in solution mainly in the anionic form at pH 3 and completely in the anionic form at pH 7. From chemical structure of ZEN (Figure 1b), it is evident that ZEN is a diphenolic compound with an estimated  $pK_{a1} = 7.62$ , suggesting that at pH 3 ZEN is mainly in the neutral form, while at pH 7 the phenolate anion is present in solution [4].

Previous results of OCHRA and ZEN adsorption by unmodified zeolite ( $C_0 = 2$  ppm,  $C_{\text{susp}} = 4$  g/L) showed 40% OCHRA adsorption and 7% ZEN adsorption at pH 3, and 3% OCHRA adsorption and 7% ZEN adsorption at pH 7 [3].

Results for OCHRA and ZEN adsorption by ZCPs at the constant initial mycotoxin concentration (2 ppm) and different amounts of solid phase in suspension at pH 3 and 7 are presented in Figures 2 and 3.

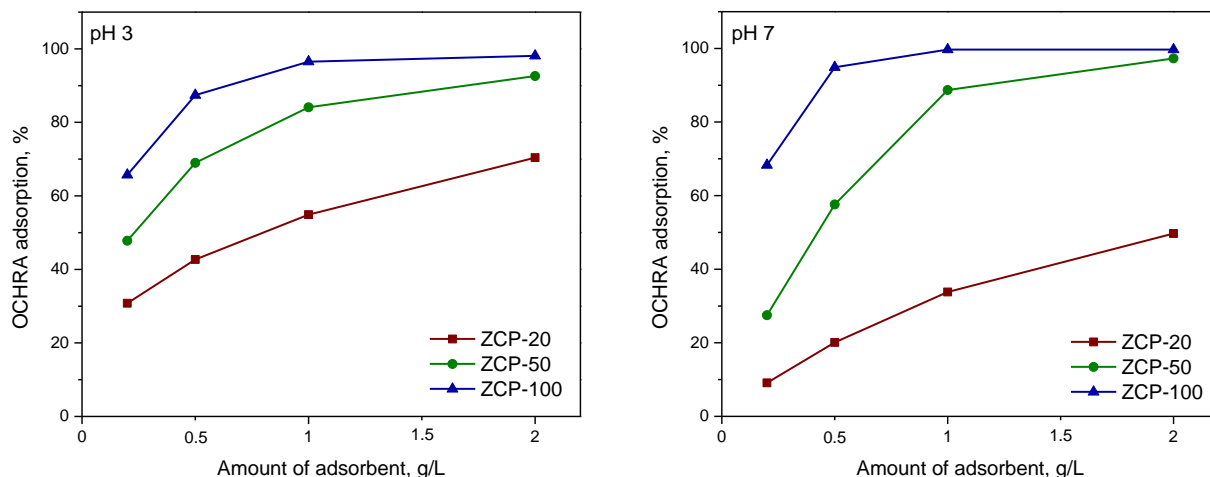


**Figure 2.** OCHRA adsorption by organozeolites (ZCP-20, ZCP-50 and ZCP-100) at pH 3 and 7.

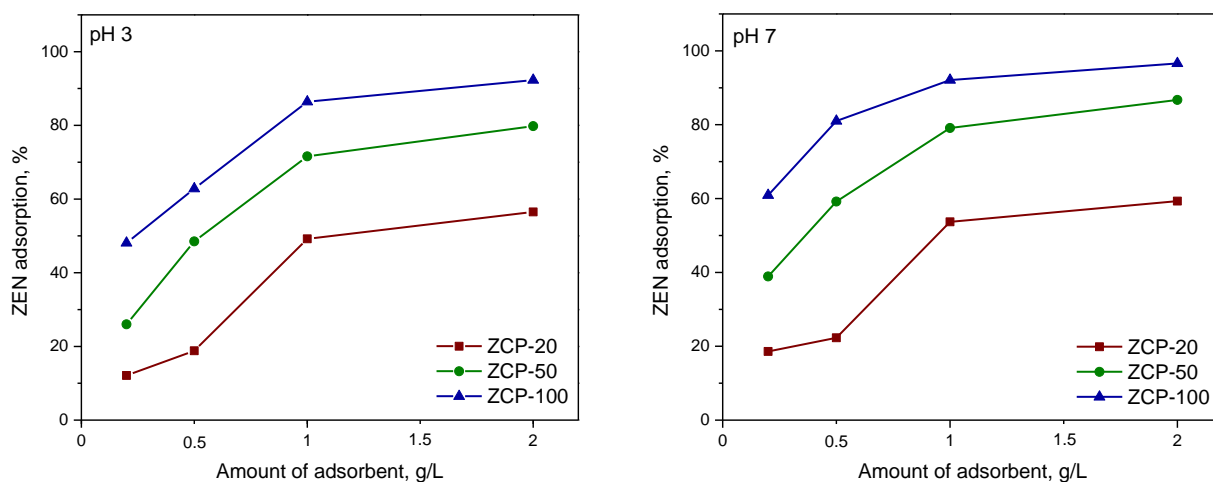


**Figure 3.** ZEN adsorption by organozeolites (ZCP-20, ZCP-50 and ZCP-100) at pH 3 and 7.

Presence of CP at the zeolitic surface significantly increased adsorption of both mycotoxins. At both pH values, the percentage of OCHRA and ZEN adsorption by ZCPs increased with increasing the amount of each adsorbent in suspension. This increase in adsorption of both mycotoxins can be interpreted with increasing number and availability of adsorption sites at the zeolitic surface. Also, at the same amount of solid phase in suspension, adsorption of OCHRA and ZEN increased with increasing the amount of surfactant at the zeolitic surface. For the lowest level of surfactant, ZCP-20, adsorption of OCHRA was much higher at pH 3 compared to pH 7. With increasing levels of surfactant at the zeolitic surface, differences in OCHRA adsorption at different pH values were less obvious. Compared to the previous results on OCHRA adsorption by unmodified zeolite it is obvious that some active sites are present at the zeolitic surface at pH 3 and together with CP surfactant are responsible for its adsorption. At pH 7, OCHRA is completely in the anionic form and due to the repulsion of the anionic OCHRA and negatively charged zeolitic surface only interactions to CP take place. ZEN adsorption by ZPCs showed similar values at pH 3 and 7 indicating that adsorption was

independent of the form of ZEN in solution and that only CP ions present at the zeolitic surface are responsible for ZEN adsorption.

It was previously mentioned that adsorption of mycotoxins by organozeolites may be dependent on the type of organic cation used for the modification of the zeolitic surface. Adsorption of ZEN and OCHRA was previously studied with zeolites modified with the same amounts of ODMBA [3] and BC [4] ions. Since the differences in adsorption of both mycotoxins are more visible when the amount of surfactant at the zeolitic surface is low, results on adsorption of ZEN and OCHRA by organozeolites with the lowest amount of all three surfactants (20% of ECEC value of zeolite) are compared. Organozeolite modified with ODMBA was denoted as OZ-2, while with BC was denoted as BZ-2 [3, 4].

For OCHRA, with the amount of adsorbent in suspension of 2 g/L, the following adsorption indexes were obtained: 70% for OZ-2, 60.9% for BZ-2 and 70.4% for ZCP-20 at pH 3, and 50% for OZ-2, 37.6% for BZ-2 and 49.7% for ZCP-20 at pH 7. This suggests that ZCP-20 was equally efficient as OZ-2, while BZ-2 was slightly less efficient to adsorb OCHRA.

At the same amount of adsorbent in suspension, ZEN adsorption was 72% for OZ-2, 61.9% for BZ-2 and 56.5% for ZCP-20 at pH 3. At pH 7, ZEN adsorption was 79%, 66.4% and 59.3% for OZ-2, BZ-2 and ZCP-20, respectively. This indicates that OZ-2 was more efficient for ZEN adsorption than BZ-2 and ZCP-20. Results confirmed that adsorption of both ZEN and OCHRA is dependent on the type of surfactant used for modification.

## CONCLUSION

The organozeolites were prepared by treatment of the natural zeolite clinoptilolite with different levels of CP and *in vitro* adsorption of OCHRA and ZEN at pH 3 and 7 was studied. Increased adsorption of OCHRA and ZEN with increasing amounts of surfactant confirmed that CP at the zeolitic surface is responsible for mycotoxin adsorption. Differences in OCHRA adsorption at different pH values showed that adsorption is dependent of the form of OCHRA in solution and that some active sites are present at the uncovered zeolitic surface. Adsorption of ZEN was pH independent suggesting that only interactions between CP and ZEN are responsible for its adsorption. Results showed that zeolite modified with CP could be good adsorbent as zeolites modified with ODMBA and BC for both OCHRA and ZEN.

## Acknowledgement

These experiments were funded by the Ministry of Education, Science and Technological Development of Republic of Serbia contract number: 451-03-9/2021-14/200023. Mycotoxin adsorption experiments were done at the Vet. Med. Diag. Lab., University of Missouri, Columbia, USA.

## REFERENCES

- [1] N. Zahra, N. Jamil, S.R. Ahmad, M.K. Saeed, I. Kalim, A. Sheikh, Pakistan J. Sci. Ind. Res. Ser. B Biol. Sci., 2019, **62**, 206–218.
- [2] P. Vila-Donat, S. Marín, V. Sanchis, A.J. Ramos, Food Chem. Toxicol., 2018, **114**, 246–259.
- [3] A. Daković, M. Tomašević-Čanović, V. Dondur, G.E. Rottinghaus, V. Medaković, S. Zarić, Colloids Surfaces B Biointerfaces, 2005, **46**, 20–25.
- [4] M. Marković, A. Daković, G.E. Rottinghaus, A. Petković, M. Kragović, D. Krajišnik, J. Milić, Colloids Surfaces A Physicochem. Eng. Asp., 2017, **529**, 7–17.

## CHEMICAL DOPING OF LANGMUIR-BLODGETT ASSEMBLED FEW-LAYER GRAPHENE FILMS WITH Li AND Au SALTS

I.R. Milošević<sup>1</sup>, B. Vasić<sup>1</sup>, A. Matković<sup>2</sup>, J. Vujin<sup>1</sup>

<sup>1</sup> *University of Belgrade, Institute of Physics Belgrade, Laboratory for 2D materials of Center for Solid State Physics and New Materials, Pregrevica 118, 11080 Belgrade, Serbia.  
(novovic@ipb.ac.rs)*

<sup>2</sup> *Institute of Physics, Montanuniversität Leoben, Austria*

### ABSTRACT

To implement large-area solution-processed graphene films in low-cost transparent conductor applications, it is necessary to have control over the work function (WF) of the film. In this study we demonstrate a straightforward single-step chemical approach for modulating the WF of graphene films with Li and Au salts. Li-based salts decrease the work function, while Au-based salts increase the work function of the entire film. As a result, this method allowed to tune the WF of graphene electrodes in a range of 0.7 eV.

### INTRODUCTION

Graphene has been identified as a promising material in electronics, especially as an electrode with the appropriate work function (WF). It can have two different roles as an electrode (as an anode and a cathode). The chemical vapor deposition (CVD) method has become the most common method for the production of large-area graphene films [1]. Still, simple and low-cost methods are needed for mass production. Liquid-phase exfoliation (LPE) is a promising way of obtaining large quantities of few-layer graphene sheets (GSs) in the solvent. In order to convert the dispersed GS into graphene thin films, the Langmuir-Blodgett assembly (LBA) technique could be used. Based on surface-tension induced self-assembly of nanoplatelets at the liquid-air interface or the interface of two liquids, LBA is a simple method for the production of large-scale, highly transparent, thin solution-processed graphene films [2-3].

To achieve the desired performance of the devices, tuning the electrodes' WF is very important. By modulating the WF, band-structure alignment at the interface can enhance the efficiency of carrier transport and lower contact resistance, thus improving the performance of the devices [4]. Chemical doping represents the effective method for tuning the WF by charge transfer between the GS films and dopants [5].

### METHODS

**Fabrication and doping of LPE GS films:** GS dispersion was prepared from graphite powder of initial concentration 18 mg/mL and solvent (N-methyl-2-pyrrolidone, NMP). The solution was sonicated in a low-power ultrasonic bath for 14 h. The resulting dispersion was centrifuged for 60 min at 3000 rpm immediately after the sonication. Stock standard solutions used for n-doping are 1 mg/mL LiCl, LiNO<sub>3</sub> and Li<sub>2</sub>CO<sub>3</sub> and for p-doping is the gold standard solution-H(AuCl<sub>4</sub>). By appropriate dilution of the stock solution with deionized water we obtained 0.1 mg/mL metal water solution which is then used in the doping process.

GS dispersion in NMP was used to fabricate transparent and conductive films by the LBA technique at a water-air interface [6]. A small amount of GS dispersion was added to the water-air interface and after the film was formed it was slowly scooped onto the target substrate (Figure 1). Applying the same process of fabricating the GS films and using the appropriate metal standard

solution instead of water, chemical doping was achieved (Figure 1). For WF measurements SiO<sub>2</sub>/Si wafer were used, as substrates.

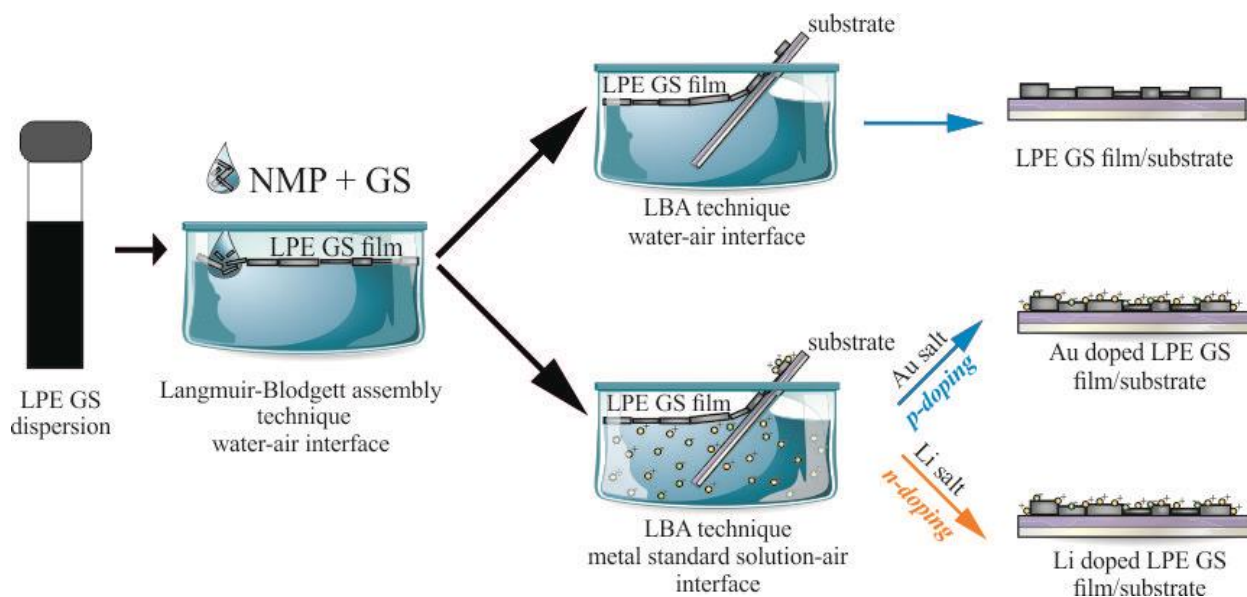


**Figure 1.** Schematic representation of the LPE GS film formation and its doping in the single-step process

**WF measurements for undoped and doped LPE GS films:** Kelvin probe force microscopy (KPFM), was employed in order to characterize changes in the electrical surface potential and corresponding Fermi level shifts due to doping. For this purpose, we measured the contact potential difference (CPD) between the AFM tip and the sample surface by using Pt covered NSG01/Pt probes with a typical tip curvature radius of 35 nm. For all samples, the CPD was measured on five  $5 \times 5 \mu\text{m}^2$  areas, and then averaged. The CPD is equal to the work function difference between AFM tip ( $WF_t$ ) and sample ( $WF_s$ ),  $CPD = WF_t - WF_s$ . The calibration of the  $WF_t$  was done by a standard procedure consisting of KPFM measurements on a freshly cleaved HOPG with a well-known work function of 4.6 eV [7]. The absolute value of the WF was calculated as  $WF_s = WF_t - CPD$ , where CPD is measured by KPFM for all, undoped and doped LPE GS films and presented in Figure 2.

## RESULTS AND DISCUSSION

Results for the values of the absolute WF are summarized in Figure 2. As can be seen, n-doping of graphene films is achieved by Li-based salts, whereas Au-based salt leads to p-doping.

According to Figure 2 (a), the maximal doping in both directions is similar, around 0.3-0.4 eV, finally providing a significant range of around 0.7 eV for the work function modulation of LPE GS films. The reported shift of the Fermi level is very similar to the other (comparable) systems in the literature. Compared with literature data of WF values changes [8] the same effect can be achieved, but advantages of our approach are fast and simple solution-based method for one-step fabrication and WF control of large-area graphene films.

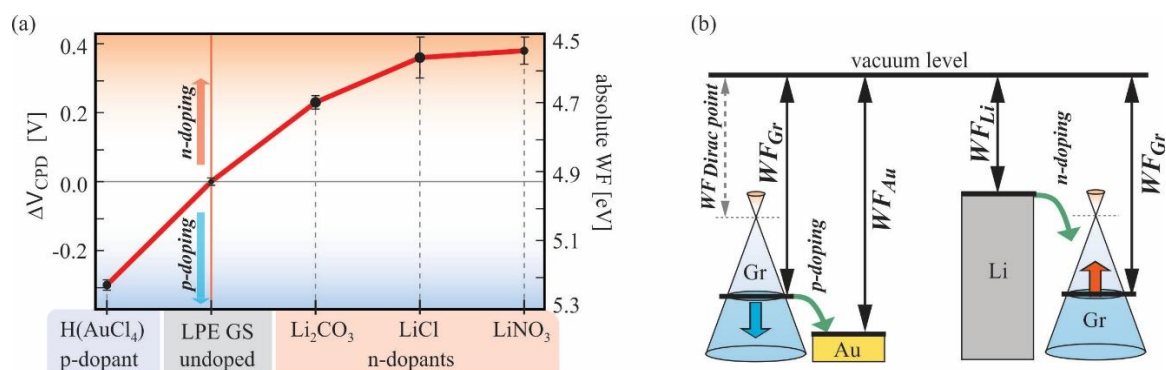


**Figure 2.** (a) Change in WF for doped LPE GS films for different dopants, in comparison to the undoped LPE GS film. (b) Schematic representation of the WF prior to the interaction (equal vacuum levels) for Au-based salt/graphene and Li-based salt/graphene.

The change of the WF due to the doping can be explained according to the schematic presentation in Figure 2 (b), illustrating Li (Au) as a lower (higher) work function material compared to GS films. Therefore, presence of Li-based salts results in a reduction of the WF of the entire film. This behavior can be interpreted as an increase in the Fermi level of GSs – compared to the value for the undoped films – indicating predominantly a charge transfer from Li-based salts to graphene (n-doping), as expected when considering that Li has lower WF than graphene (graphite). In contrast, the Au-based salt indicates charge transfer from graphene to Au-based salt and a relative reduction of the Fermi level in GSs (p-doping). It is also worth mentioning that the poly-crystalline nature of LPE based GS films, large amount of sheet edges and presence of the residual solvent (NMP) results in p-doped films [4]. Therefore, WF values are lower for the LPE-based films by at least 200 meV, than for the pristine exfoliated single-crystals [7]. p-type doping is also reflected on the WF of the reference samples (undoped LPE GS), and therefore on the whole accessible range for the WF modulation by this method. This was also highlighted in Figure 2 (b), where the  $WF_{Dirac\ point}$  depicts the case of undoped graphene [7]

## CONCLUSION

In our approach, we demonstrate a straightforward single-step method for forming and doping LPE GS films by metal standard solutions through charge transfer processes. Chemical doping of graphene allows to modulate its WF in a very large range (0.7 eV), and therefore potentially enables to use the same electrode material for both, the injection and the extraction of the electrons. Furthermore, solution-processed graphene films are in particular suited for the chemical modulations, since a large number of the sheet edges opens up many adsorption sites and enhances the doping effects when compared to many other types of graphene. Lithium nitrate (LiNO<sub>3</sub>) was selected as the best choice for n-type doping since it provides the largest WF modulation (by 400 meV).

## Acknowledgement

The authors acknowledge funding provided by the Institute of Physics Belgrade, through the grant by the Ministry of Education, Science, and Technological Development of the Republic of Serbia.

**REFERENCES**

- [1] Kwon, K.C. et al., *J. Mater. Chem. C*, 2013, **1**, 253–259.
- [2] Li, X. et al., *Nat. Nanotechnol.* **3**, 538–542 (2008).
- [3] Zheng, Q. et al., *ACS Nano*, 2011, **5**, 6039–6051.
- [4] Syu, J.-Y., *RSC Adv.*, 2016, **6**, 32746-32756.
- [5] Milošević, I.R. et al., *Sci. Report.*, 2020, **10:8476**, 1-12.
- [6] Matković, A. et al., *2D Mater.*, 2016, **3**, 015002.
- [7] Yu, Y. et al., *Nano Lett.*, 2009, **9**, 3430–3434.
- [8] Kwon, K. C., *J. Phys. Chem. C*, 2014, **118**, 8187–8193.

## INFLUENCE OF COBALT LOADING ON THE PHYSICAL-CHEMICAL PROPERTIES OF PILLARED CLAY - SUPPORTED COBALT

B. Milovanović, S. Marinović, Z. Vuković, M. Ajduković, G. Stevanović, P. Banković, T. Mudrinić

*University of Belgrade, Institute of Chemistry, Technology and Metallurgy,  
Njegoševa 12, 11000 Belgrade, Serbia. (biljana.milovanovic@ihtm.bg.ac.rs)*

### ABSTRACT

The aluminum pillared clay (AP) was synthesized and impregnated with various cobalt loadings (x%CoAP, x=1, 3, 5, and 10 wt.%) by incipient wetness impregnation method. All samples were characterized by using X-ray powder diffraction (XRPD), inductively coupled plasma optical emission spectroscopy (ICP-OES) and low temperature N<sub>2</sub> physisorption techniques. The chemical analysis confirmed the successful incorporation of cobalt in all impregnated samples. Nevertheless, only cobalt oxide (Co<sub>3</sub>O<sub>4</sub>) was identified for samples having higher cobalt contents. Furthermore, different cobalt loading was mainly affected the microporous region in such way that micropore surface area decreased with the increase of cobalt.

### INTRODUCTION

Pillared clays (PILC) as materials with permanent micro and/or mesoporosity and high surface area have been attracting considerably attention as catalytic support materials. Such interest rose from the fact that PILC can be easily prepared from the cheap, non-toxic and naturally available clays [1,2]. Recently, aluminum pillared clay-supported cobalt (CoAP) was found to be a promising catalyst for both catalytic oxidation of dye [2] and electrochemical determination of glucose [1]. In order to exploit the full potential of this catalyst, further optimization was requested. This paper discusses the influence of cobalt loading on physical-chemical properties of CoAP as the first step in designing a catalyst with optimal performance.

### EXPERIMENTAL

#### *Preparation of AP and x%CoAP samples*

Montmorillonite clay from the Source Clays Repository–The Clay Minerals Society, Wyoming, was used for pillaring. Pillaring solution with OH<sup>-</sup>/Al<sup>3+</sup> molar ratio of 2.0 was used for the synthesis of pillared clay. The detailed preparation of pillared clay was previously described [2]. The obtained pillared clay was denoted as AP. Cobalt was introduced into AP by impregnation using the incipient wetness impregnation method [3] in order to obtain Co-based catalysts (CoAP). The impregnation was performed by gradual addition of 0.89 cm<sup>3</sup> of 0.3, 1, 1.7, and 3.3 mol dm<sup>-3</sup> of Co<sup>2+</sup> solution in order to introduce 1 wt.%, 3 wt.%, 5 wt.%, and 10 wt.% of cobalt, respectively into AP powder. Then the samples were dried at 85 °C for 2 h and subsequently at 110 °C, overnight. The obtained samples were then calcined at 450 °C for 6 h and denoted as x%CoAP where x=1, 3, 5, 10 represents the weight percentage of cobalt.

#### *Characterization of AP, and x%CoAP samples*

The content of cobalt in x%CoAP samples was determined by ICP-OES technique using a iCAP 6500 Duo ICP Spectrometer (Thermo Fisher Scientific, Cambridge, UK). The samples were prepared by microwave digestion (Advanced Microwave Digestion System, ETHOS 1, Milestone) and analysed with iTEVA operating software. X-ray powder diffraction data of AP, and x%CoAP samples were obtained using a Philips PW 1710 X-ray powder diffractometer (CuK $\alpha$  radiation,  $\lambda = 0.1542$  nm).

Textural properties of samples were determined from the nitrogen adsorption/desorption isotherms at  $-196\text{ }^{\circ}\text{C}$  using a Sorptomatic 1990 Thermo Finnigan.

## RESULTS AND DISCUSSION

The ICP-OES results (Table 1) confirmed the incorporation of cobalt in the impregnated samples in amounts about 80% of theoretical. According to X-ray structural analysis (Fig. 1.) the presence of montmorillonite (Mt) and quartz (Q) was identified in all samples [4]. For samples impregnated with lower cobalt contents (up to 4.13 wt.%), no peaks related to cobalt oxide were detected. In contrast, the characteristic reflections of the cubic  $\text{Co}_3\text{O}_4$  phase at  $31.3^{\circ}$ ,  $36.9^{\circ}$  and  $59.4^{\circ}$  [4] were clearly visible in the diffractograms of the samples with higher cobalt content. Moreover, with the increase of cobalt content from 4.13 wt.% to 7.85 wt.% the intensity of all diffraction peaks corresponding to  $\text{Co}_3\text{O}_4$  increased.

Isotherms of all samples (Fig. 2.) belong to the II type with the H3 type of hysteresis loop for  $p/p_0 > 0.4$  characteristic for montmorillonite containing clays with aggregated planar particles and slit-shaped types of pores [2].

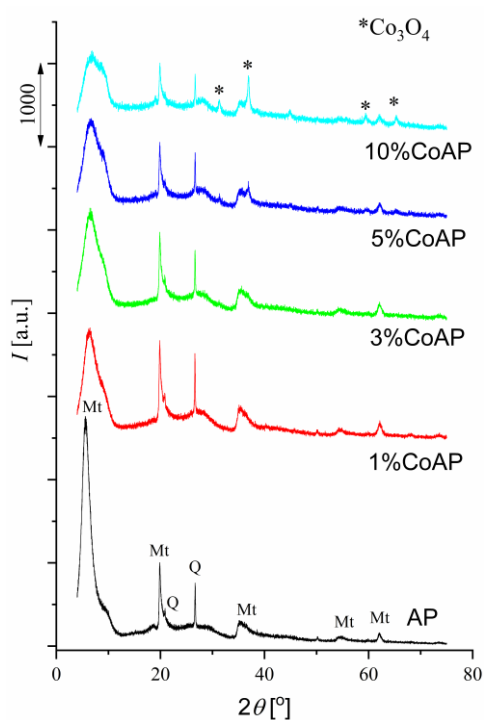


**Figure 1.** XRPD patterns of AP and x%CoAP samples

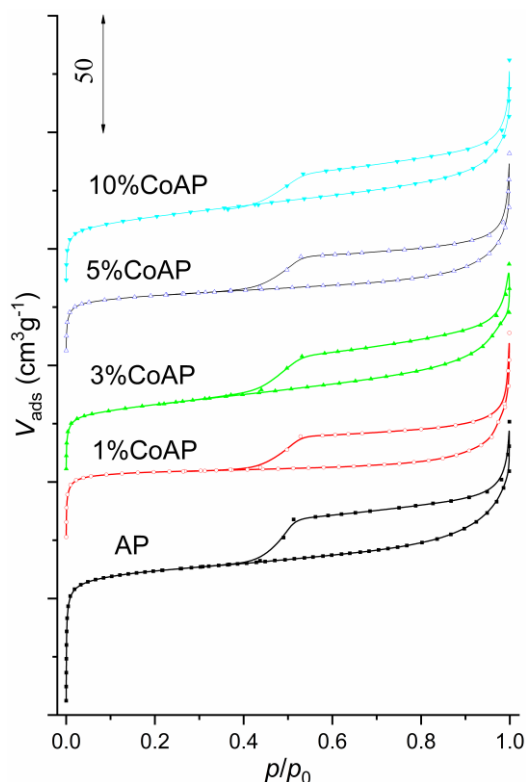


**Figure 2.**  $\text{N}_2$  adsorption-desorption isotherms of AP and x%CoAP samples

The highly developed mesoporous and microporous structure of pillared sample was affected by impregnation process. The impregnation with cobalt resulted in decrease of specific surface area in both mesoporous and microporous range of pores (Table 1). The process parameter that had the highest impact on textural properties was regime of heat treatment after impregnation since all cobalt impregnated samples had comparable values for the specific surface area. Differences in the surface area between samples impregnated with different amounts of cobalt are almost negligible in mesoporous region (with exception of  $S_{\text{BET}}$  for 1%CoAP and  $S_t$  for 10%CoAP). On the other hand,

in microporous region there is more noticeable trend. The specific surface area ( $S_{\text{mic}}$ ) decreased with the increase of cobalt loading.

Sample	Co content (wt.%)		$S_{\text{BET}}$ ( $\text{m}^2 \text{g}^{-1}$ )	$S_{\text{mic}}$ ( $\text{m}^2 \text{g}^{-1}$ )	$S_{\text{t}}$ ( $\text{m}^2 \text{g}^{-1}$ )
	theoretical	experimental			
AP	-	-	211	199	12
1%CoAP	1	0.79	146	133	13
3%CoAP	3	2.55	124	107	17
5%CoAP	5	4.13	123	109	14
10%CoAP	10	7.85	129	76	53

$S_{\text{BET}}$  – specific surface area (Brunauer, Emmett, Teller - 3 parameter equation);  $S_{\text{t}}$  – mesopore surface area t-Plot (Lippens and de Boer, using universal Harkins, Jura standard isotherm),  $S_{\text{mic}}$  – micropore specific surface ( $S_{\text{BET}} - S_{\text{t}}$ )

## CONCLUSION

This study continues our research devoted to development of the pillared clay - supported cobalt based catalysts (CoAP). It has been found that Co loading affected the phase composition and textural properties. The increase of cobalt loading above 4 wt.% favored the formation of  $\text{Co}_3\text{O}_4$ . The lower cobalt loading were not detected by XRPD as separate crystalline phases. Heat treatment after impregnation is probably responsible for the same derogation effect on textural properties (in both micro and mesopore region) of x%CoAP in comparison to AP. The cobalt content had impact only in microporous range. The specific surface area ( $S_{\text{mic}}$ ) decreased with the increase of the cobalt loading. Correlation between findings of this work and the catalytic performance of x%CoAP in two catalytic processes i.e. electrochemical oxidation of glucose and catalytic oxidation of dye is still ongoing.

## Acknowledgement

This work was financially supported by the Ministry of Education, Science and Technological Development of the Republic of Serbia (Grant No. 451-03-9/2021-14/200026).

## REFERENCES

- [1] Mudrinić T, Marinović S, Milutinović-Nikolić A, Jović-Jovičić N, Ajduković M, Mojović Z, et al. Novel non-enzymatic glucose sensing material based on pillared clay modified with cobalt. *Sensors Actuators B Chem* 2019;299:126976. <https://doi.org/https://doi.org/10.1016/j.snb.2019.126976>.
- [2] Marković M, Marinović S, Mudrinić T, Ajduković M, Jović-Jovičić N, Mojović Z, et al. Co(II) impregnated Al(III)-pillared montmorillonite–Synthesis, characterization and catalytic properties in Oxone® activation for dye degradation. *Appl Clay Sci* 2019;182:105276. <https://doi.org/https://doi.org/10.1016/j.clay.2019.105276>.
- [3] Pinna F. Supported metal catalysts preparation. *Catal Today* 1998;41:129–37. [https://doi.org/https://doi.org/10.1016/S0920-5861\(98\)00043-1](https://doi.org/https://doi.org/10.1016/S0920-5861(98)00043-1).
- [4] JCPDS, 1990. International Center for Diffraction Data. Joint Committee on Powder Diffraction Standards (JCPDS) , Swarthmore, USA, pp. 1990.

## MULTIFUNCTIONAL NANOCOMPOSITES BASED ON POLYMERS AND Ag NANOPARTICLES DESIGNED FOR DIFFERENT PURPOSE

U. Stamenović<sup>1</sup>, V. Vodnik<sup>1</sup>, D. Mašojević<sup>1</sup>, M. Otoničar<sup>2</sup>, and S. D. Škapin<sup>2</sup>

<sup>1</sup>*Vinča Institute of Nuclear Sciences – National Institute of the Republic of Serbia, University of Belgrade, 11351 Vinča, Belgrade, Serbia (una@vin.bg.ac.rs)*

<sup>2</sup>*Jožef Štefan Institute, Department of Advanced Materials, 1000 Ljubljana, Slovenia*

### ABSTRACT

In series of *in situ* aniline oxidative polymerization processes by silver ions ( $\text{Ag}^+$ ), and in the presence of polyvinylpyrrolidone (PVP) as an accelerator and stabilizer, six different SilverPolyaniline/Polyvinylpyrrolidone (AgPANI/PVP) nanocomposites were synthesized. With the variations in the synthetic conditions – pH adjustment, diversity in solvents, and molar ratios between components, differences in nanocomposites' structures, i.e., silver nanoparticles' (AgNPs) sizes and shapes, and PANI morphologies, were observed. Despite the same reactants are used in all polymerization processes, their direction/establishment are determined by environment (solvent, pH, reactants' concentrations) and components' oxidation potentials. These fast, simple and repeatable reactions yielded in dark powders, with differences in Ag content. As easily redispersible in water, these nanocomposites could find their value in the field of electrochemistry and/or as antimicrobial agents.

### INTRODUCTION

As hybrid materials with advanced characteristics and consequently applications from electrocatalytic to biomedical, nanomaterials based on metal nanoparticles and conducting polymers – i.e. nanocomposites, take a great deal of attention [1,2]. With the incorporation of metal nanoparticles throughout the polymer matrix, individual characteristics of each component become more pronounced, even new ones appear. There is a significant increase in specific surface area, compared to pure nanoparticles for example, allowing these materials larger contact superficies with the environment. Special concern should be committed to a simplification of the synthetic procedures considering these systems, so that within a few hours, and with as few reactants as possible, nanocomposite with satisfactory desired characteristics is obtained. Here we represent such systems – nanocomposites based on AgNPs and PANI, that have already proven to be great catalysts for oxygen reduction reaction (ORR) [3,4] and as antimicrobial agents [5].

### EXPERIMENTAL

A series of *in situ* oxidative aniline polymerization reactions were conducted in order of gaining AgPANI/PVP nanocomposites, denoted as AgPANI/PVP1–6. Varying molar ratios between components ( $\text{AgNO}_3$ , aniline and PVP), type of solvent (water and methanol), and pH of the reaction mixtures, affect synthetic conditions and therefore the characteristics of the final products. In the total volume of 20 ml  $\text{Ag}^+$  and PVP solutions in water or methanol, with or without pH adjusting (by  $\text{HNO}_3$ ), aniline monomer was added [3–5]. It was estimated for all reaction mixtures that stirring for 20 h at room temperature was enough for complete  $\text{Ag}^+$  reduction to AgNPs, and aniline polymerization to PANI, i.e. for the formation of nanocomposites. This was visualized by the change of color of the reaction mixtures from colorless or light yellow, through brown, to final dark green, indicative for PANI conductive form. Post-synthetic treatment included rinsing nanocomposites' dispersions with acetone, in order to remove PVP excess. Gained precipitates were dried at 30 °C, powdered, and finally characterized by an inductively coupled plasma atomic emission spectrometer

(ICP–AES), transmission electron microscopy (TEM), and field–emission scanning electron microscope (FE–SEM; Zeiss ULTRA plus). Synthetic conditions and Ag contents in each nanocomposite are presented in Table 1.

**Table 1.** Synthetic conditions and determined Ag content in nanocomposites by ICP– AES

Nanocomposite	Solvent	$c_{\text{Ag}^+}$ (M)	$c_{\text{PVP}}$ (M)	$c_{\text{aniline}}$ (M)	pH	Ag (wt%)
AgPANI/PVP1	water	0.12	0.12	0.04	11	3.4
AgPANI/PVP2	water	0.12	0.12	0.04	2	43.8
AgPANI/PVP3	methanol	0.12	0.12	0.04	11	35.4
AgPANI/PVP4	methanol	0.12	0.12	0.04	2	18.9
AgPANI/PVP5	water	0.12	0.06	0.04	2	22.5
AgPANI/PVP6	methanol	0.12	0.06	0.04	2	44.4

## RESULTS AND DISCUSSION

The reaction that is conducted between  $\text{Ag}^+$  and aniline monomer is a typical oxido– reduction reaction boiled down to the interaction among nitrogen atoms from amino groups in aniline units, and silver cations. As electron donors, nitrogen atoms reduce  $\text{Ag}^+$  to metallic Ag, transforming themselves at the same time into imine units, triggering the polymerization process. Since  $\text{Ag}^+$  has a low electrode potential (+0.8 V) insufficient for fast polymerization initiation, PVP molecules take part as a reaction accelerator, which will shorten the initiation phase to a couple of hours. Besides, PVP will affect the process of  $\text{Ag}^+$  reduction and formation of AgNPs, minimizing their agglomeration and macroscopic precipitation, through the steric hindrance effect. In general, for all six presented nanocomposites, the essence of their formation is aforementioned. However, the influence of experimental parameters, such are the type of medium, pH values of the reaction mixtures, and molar ratios of the components is, among all, evident through their structure/morphology (Figure 1).

With methanol used as a solvent (AgPANI/PVP3, 4, and 6),  $\text{Ag}^+$  reduction and formation of small nuclei, begins upon their dissolution (indicated by the light yellow coloration of the reaction mixture), while this step with water as solvent (AgPANI/PVP1, 2, and 5) is missing. After adding aniline into methanol's reaction mixtures, the reduction process of  $\text{Ag}^+$  and further growth of already formed small nuclei are continued, while in the case of water's reaction mixtures they just began. In addition, methanol is a less polar solvent than water, it decelerates  $\text{Ag}^+$  dissociation, their reduction, and nucleation, providing conditions for remained ions and formed nuclei to be arranged into larger structures. For example, triangular AgNPs, mostly truncated, with edge lengths ranged 50–150, and 25–140 nm in AgPANI/PVP4, and 6, respectively (Figure 1g, and k), were formed, compared to spherical AgNPs with a diameter around 7 nm in the case of AgPANI/PVP2 (Figure 1c). These spherical AgNPs are much smaller than those formed in AgPANI/PVP1 – around 120 nm (Figure 1a), with the same solvent (water) and molar ratios, but different pH (2 vs. 11). Namely, in the acidic environment the speed of nucleation is faster than the speed of particles' growth, resulting in the formation of smaller AgNPs. Similarly, acidic conditions in the case of AgPANI/PVP3 affect the formation of smaller, spherical AgNPs with an average diameter of 25 nm (Figure 1e), but methanol as solvent will, on the other side, decelerate reaction, allowing a certain degree of disorder, causing partial agglomeration, i.e. not so finely shaped NPs. When the amount of PVP is reduced (for example AgPANI/PVP5, Figure 1i), besides that NPs' growth is not limited enough, PVP role in particle shape control is decreased as well, meaning AgNPs grow in different crystallographic directions, they aggregate forming larger, polyhedron structures (140 nm for AgPANI/PVP5).

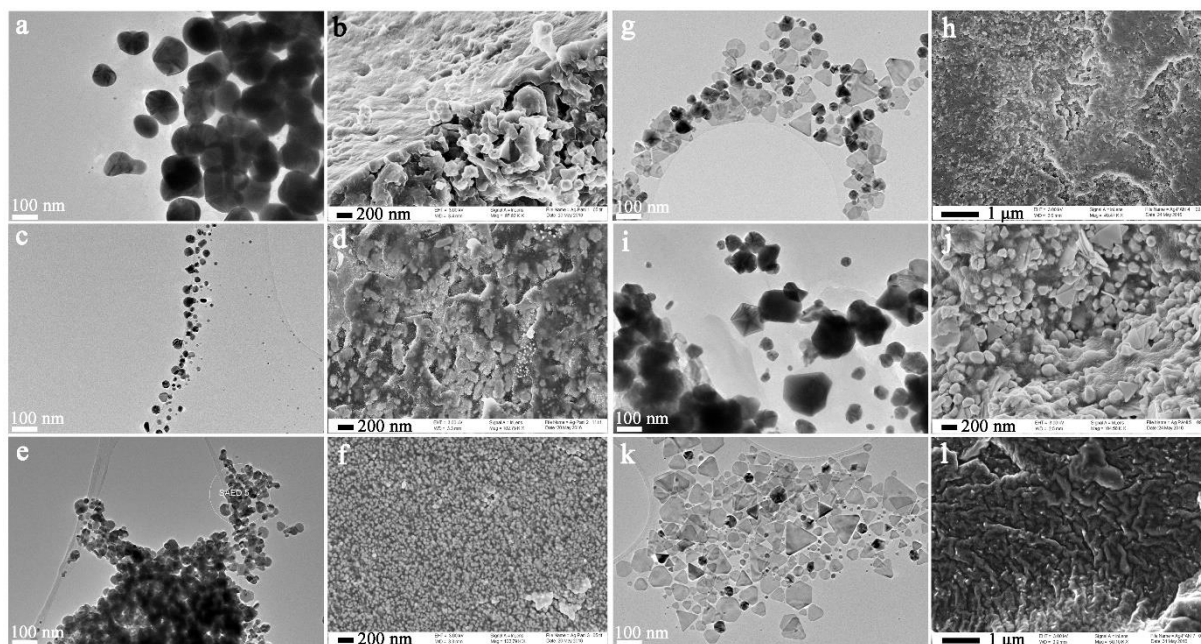


**Figure 1.** TEM and FE–SEM micrographs of AgPANI/PVP nanocomposites – a and b for AgPANI/PVP1, c and d for AgPANI/PVP2, e and f for AgPANI/PVP3, g and h for AgPANI/PVP4, i and j for AgPANI/PVP5, and k and l for AgPANI/PVP6.

Beside differences between AgNPs sizes and shapes in these nanocomposites, variations in PANI matrix morphologies are obvious as well, from granular morphology in AgPANI/PVP1, 2, 3, and 4 (Figure 1b, d, f, and h), through nanosheets in AgPANI/PVP5 (Figure 1j), to wrinkled morphology in AgPANI/PVP6 (Figure 1l). With lowering PVP concentration, the growth of granular PANI structures is reduced, making its growth in the form of nanosheets, through multiple point attachment to PVP, more pronounced. Additionally, in these conditions (lower PVP amount), when methanol is used as a solvent, PANI is gaining wrinkled morphology. PANI structure depends on PVP molecules organization in water. Assuming different types of organization of PVP in methanol, compared to water, one may say that PANI shape is a reflection of PVP organization in the surrounding medium.

In the continuation of our work, such designed AgPANI/PVP nanocomposites were further characterized by different physico–chemical methods (Ultraviolet–Visible, Fourier–Transform Infrared, and Raman spectroscopy, and X-ray powder diffraction), and examined for different purpose in electrochemical and biological areas [see Ref. 3–5]. Therefore, their electrocatalytic activities were investigated toward ORR, while their antimicrobial efficiencies were tested against most common pathogens – *Escherichia coli*, *Staphylococcus aureus*, and *Candida albicans* [3–5]. It was shown that the nanocomposites with the largest Ag content (AgPANI/PVP2, and 6) could be equally well used as catalysts and as antimicrobial agents [3–5]. Investigation of their antimicrobial potential and application as a powerful weapon against resistant microbial strains, have revealed proper inhibition of microbial growth, even at low composite concentrations (5 ppm) and short contact time (1 h) [5]. However, the electrocatalytic survey pointed out that the composites with the lowest Ag content (AgPANI/PVP1, and 4) have stood out with their appreciable activities and high ORR onset potentials [see Ref. 3,4]. Their possible applications in these fields are dependent, among all, on the composites' morphologies, size/shape of AgNPs and PANI structure, and Ag content. Surely, there is space for some more adjustments of synthetic conditions in order of designing AgPANI/PVP nanocomposites with more uniform and arranged particles' size and shape distribution throughout the PANI matrix.

## CONCLUSION

Preparation of all presented nanocomposites is simple and repeatable, resulting in high yield. However, eventhough there are small changes and adjustments of the synthetic parameters, differences between final products are evident through both morphologies – nanoparticles and polymer, together with the silver content. Direction and the establishment of these reactions are influenced and depended on the type of medium, molar ratios between components and their oxidation potentials, and pH. Nevertheless, the emphasis of presented nanocomposites is their multifunctionality and unique combination of properties, making them attractive as Pt-free electrocatalysts and/or effective in wastewater treatment and disinfectant production.

## Acknowledgement

The research was funded by the Ministry of Education, Science and Technological Development of the Republic of Serbia, via direct financing of Vinča Institute of Nuclear Sciences – National Institute of Republic of Serbia (contract number: 451–03–68/2020–14/200017).

## REFERENCES

- [1] E. Eskandari, M. Kosari, M.H.D.A. Farahani, N.D. Khiavi, M. Saeedikhani, R. Katal, M. Zarinejad, *Sep. Purif. Technol.*, 2020, **231**, 115901, 27pp.
- [2] E.N. Zare, P. Makvandi, B. Ashtari, F. Rossi, A. Motahari, G. Perale, *J. Med. Chem.* 2020, **63**, 1–22.
- [3] U. Stamenović, N. Gavrilov, I.Pašti, M. Otoničar, G. Ćirić–Marjanović, S.D. Škapin, M. Mitrić, V. Vodnik, *Electrochim. Acta*, 2018, **281**, 549–561.
- [4] U. Stamenović, V. Vodnik, N. Gavrilov, I.A. Pašti, M. Otoničar, M. Mitrić, S.D. Škapin, *Synth. Met.*, 2019, **257**, 116173, 9pp.
- [5] U. Stamenović, S. Davidović, S. Petrović, A. Leskovic, M. Stoiljković, V. Vodnik, *New J. Chem.*, 2021, DOI:10.1039/D1NJ02729H.

## MODIFIED CHITOSAN FOR RAPID FABRICATION OF MICROLENSES

B. Murić<sup>1</sup>, D. Pantelić<sup>1</sup>, M. Radmilović<sup>1</sup>, D. Grujić<sup>1</sup>, B. Zarkov<sup>2</sup>

<sup>1</sup> *Institute of Physics Belgrade, University of Belgrade, Pregrevica 118, 11080 Belgrade, Serbia  
(murić@ipb.ac.rs)*

<sup>2</sup> *Directorate for Measure and Precious Metals, Mike Alasa 14, 11000 Belgrade, Serbia*

### ABSTRACT

Chitosan was modified to prepare elastic, biocompatible, nontoxic, and ecofriendly material (MC) for rapid fabrication of microlenses. Concave, convex, aspheric microlenses (individual or arrays) are produced on the MC layer by direct laser writing at 488 nm. Microlenses can be used directly without chemical processing for different applications such as: medicine, sensors, cameras, security...

### INTRODUCTION

Microlenses are characterized by diameters from several micrometers up to nearly 1 mm and have a range of applications in microoptical devices, lab-on-a-chip, displays, sensors, smartphone cameras, artificial compound eyes, security [1-3]... Various methods were used for microlens fabrication, such as: hot embossing, direct laser writing, thermal reflow, photolithography, droplet process, and many other [4, 5]. Most of them are complex, and require use of the poisonous chemicals.

Chitosan is a partially deacetylated derivative of chitin, a natural polymer extracted from crustaceous shells. It is a linear polysaccharide composed of  $\beta$ -(1-4)-linked d-glucosamine and N-acetyl-d-glucosamine. Chitosan is insoluble in pure water and organic solvents. It dissolves in diluted acidic aqueous solutions where the solubility depends on pH and deacetylation degree. Chitosan as nontoxic, biocompatible and biodegradable can be used in biomedicine, bioengineering, food, pharmaceutical [6, 7]...

Our aim was to develop an ecofriendly, nontoxic, optically transparent, elastic, and durable material suitable for fabrication of microoptical components. In this paper, we present a simple and cheap method for preparing modified chitosan (MC) layer for microlenses fabrication. Microlenses, were produced on the MC layer by direct, focused blue laser radiation at 488 nm. Microlenses are produced rapidly and can be used for security, sensors, compound eyes, and so on without any additional chemical treatment.

### RESULTS AND DISCUSSION

The 2% chitosan solution was prepared by dissolving chitosan (low MW, 85% deacetylated) in acetic acid (1% aq. sol.) with stirring at 50°C, until a homogeneous solution is obtained.

A water solution composed with several active ingredients (plasticizers, humectants, and preservatives) was prepared, too. This solution (PS for short) contains: glycerol, sucrose, glucose, polysorbate 80, citric acid, and sodium benzoate in appropriate proportions. 0.2 ml of PS, and 0.1 ml anthocyanin food dye (E163) were further added per 1 ml of chitosan solution, with continued stirring. After complete dissolution the MC solution was centrifuged in order to remove all undissolved impurities. As a result, both mechanical and optical properties (such as: elasticity, durability and stability, optical transparency...) of the MC layer were improved [8].

The MC layer was prepared by the gravity settling method [9, 10], and dried in the dark overnight, under ordinary environmental conditions (the temperature about 25 °C and the relative humidity 50-60%). The thickness of the MC layer depends on the quantity of PS [8]. The layer thickness was

measured using a digital micrometer, and it was determined as the average of eight random layer locations measurements. In our experiments, the layer thickness was 100  $\mu\text{m}$ .

The absorption spectrum of MC layer was analyzed using a fiber-type spectrometer equipped with a tungsten-halogen lamp, and was observed that maximum absorption depends on the pH solution.

The microlenses were produced using a home-made laser writing device. The laser operating at 488 nm with maximal output power of 100 mW was focused on the MC layer, as schematically shown in Figure 1.

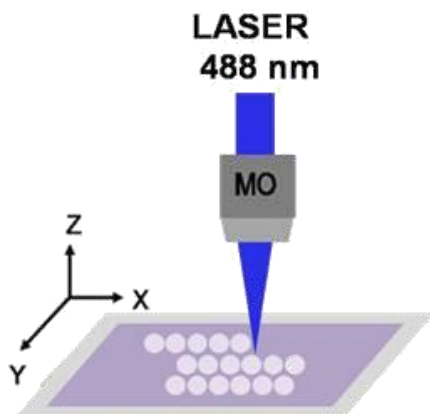


**Figure 1.** Microlenses array fabrication on the MC layer

The MC layer was mounted on a precise xy - linear translation stage used for the layer positioning with step resolution 25 nm and position repeatability of 2  $\mu\text{m}$ . The laser beam was focused with a microscope objective - MO (50 $\times$ 0.55NA) on the MC layer. Software controls and synchronizes operation of laser and coordinate table using a standard g-code [11]. The microlenses array is recorded lens by lens using the program which determines the microlens array parameters from the image file. By controlling the laser power, exposure time and distance among neighbor microlenses we were able to create concave or convex microlenses (individual or closely packed arrays).

The concave dip was formed on the MC layer by its controlled and local melting. Following the laser beam profile, the surface tension forces form a lens, without any waste.

Good quality positive microlenses were produced by making an arrangement of 8 polygonally positioned spots. The spherical surface in the polygon center acts as a convex (positive) microlens. The radius of curvature, as well as the corresponding focal length of microlenses can be controlled by the diameter of a polygon.

The concave or convex microlenses are obtained with good repeatability. An image of digit “-2” taken by a digital camera through the optical microscope and 5 $\times$ 5 MC convex microlens array is shown in Fig. 2 (the diameter of polygon was 25  $\mu\text{m}$ , while microlenses were fabricated using 50 mW of laser power and 200 ms exposure time).

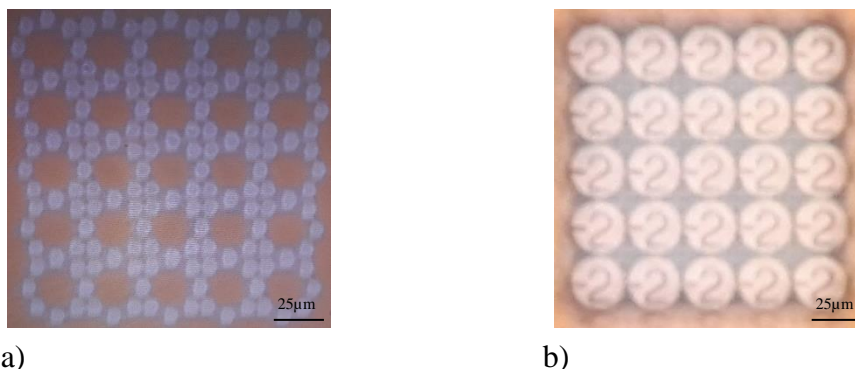


**Figure 2.** Reflection image of an array of 5 x 5 convex microlenses produced on the MC layer (a). Transmission image produced by the 5x5 convex microlenses produced on the MC layer (b)

Preliminary results have shown that MC layer elongation of 100% was obtained for the already mentioned PS concentration. Based on our previous research [11], we assume that the stress-strain behavior of the layer also depends on the PS concentration. The layer elasticity is very important for the fabrication of (adaptive) tunable microstructures.

## CONCLUSION

Chitosan was chemically modified to enable fabrication of microoptical components. The material is ecofriendly, nontoxic and suitable for a single-step rapid fabrication of microstructures by direct laser writing (blue radiation at 488nm).

Convex, concave, and aspherical microlenses can be used immediately, without additionally chemical treatment and waste. The individual and closely packed hexagonal or square arrays of microlenses show good optical and imaging properties. They can be used for a variety of applications such as: medical laser, optical sensors, light-field cameras, security, biological structure.

Improving the physicochemical properties of modified chitosan layer will be the focus of our future research.

## Acknowledgement

This paper was supported by the Ministry of Education, Science and Technological Development of the Republic of Serbia.

## REFERENCES

- [1] G. Lian, Y. Liu, K. Tao, H. Xing, R. Huang, M. Chi, W. Zhou, Y. Wu, *Micromachines* 2020, 11, 854.
- [2] F. Olivieri, M. Todino, S. Coppola, V. Vespini, V. Pagliarulo, S. Grilli, P. Ferrar, *Opt. Eng.* 2016, 55, 081319.
- [3] H. Jiang, S. Fraser, B. Kaminska, H. Porras, M. Raymond, *Adv. Opt. Materials* 2019, 7, 1900237.
- [4] J. M. Pavia, M. Wolf, E. Charbon *Opt. Express* 2014, 22, 4202-4213.
- [5] J. Tang, G. Qiu, X. Cao, Y. Yue, X. Zhang, J. Schmitt, J. Wang, *Lab Chip* 2020, 20, 2334.

- 
- [6] E. Melro, F. E. Antunes, G. J. da Silva, I. Cruz, P. E. Ramos, F. Carvalho, L. Alves, *Polymers* 2021,13, 13010001.
- [7] B. Tian, Y. Liu, *Polym Adv Technol.* 2020, 1–14.
- [8] B. Muric, D. Pantelic, D. Vasiljevic, B. Zarkov, B. Jelenkovic, S. Pantovic, M. Rosic, *Phys. Scr.* 2013, T157, 014018.
- [9] B. D. Muric, D. V. Pantelic, D. M. Vasiljevic, B. M. Panicé, *Appl. Opt.* 2007, 46 8527-8532.
- [10] B. Muric, D. Pantelic, D. Vasiljevic, B. Panic, *Opt. Mater.* 2008, 30, 1217-1220.
- [11] ISO 6983 - 1:2009(en) Automation systems and integration – Numerical control of machines - Program format and definitions of address words - Part 1: Data format for positioning, line motion and contouring control systems.

## SYNTHESIS OF CORE-SHELL NaYF<sub>4</sub>:Yb,Tm@TiO<sub>2</sub>-Acac MICRO- AND NANO-SIZED PARTICLES FOR EFFICIENT PHOTOCATALYSIS

S. Marković<sup>1</sup>, T.M. Machado<sup>2</sup>, I. Dinić<sup>1</sup>, Lj. Veselinović<sup>1</sup>, I. Janković-Častvan<sup>3</sup>, B.A. Marinković<sup>2</sup> and L. Mančić<sup>1</sup>

<sup>1</sup> Institute of Technical Sciences of SASA, Knez Mihailova 35/IV, 11000 Belgrade, Serbia  
(smilja.markovic@itn.sanu.ac.rs)

<sup>2</sup> Department of Chemical and Materials Engineering, Pontifical Catholic University of Rio de Janeiro (PUC-Rio), 22453-900, Rio de Janeiro, Brazil

<sup>3</sup> Faculty of Technology and Metallurgy, University of Belgrade, Karnegijeva 4, 11000 Belgrade, Serbia

### ABSTRACT

Micro- and nano-sized core-shell particles for efficient photocatalysis were successfully synthesized by a two step wet-chemical route. The core composed of up-converting (UC) NaYF<sub>4</sub>:Yb,Tm phase was prepared through EDTA assisted hydrothermal process, while the shell of anatase TiO<sub>2</sub> – Acetylacetonate (TiO<sub>2</sub>-Acac) charge-transfer complex was formed *via* a sol-gel method. During coating, the effect of polyvinylpyrrolidone (PVP) addition on the core and shell coupling was investigated. Two forms of core structures were obtained: hexagonal microprisms of β-NaYF<sub>4</sub>:Yb,Tm and α-NaYF<sub>4</sub>:Yb,Tm nanospheres, both coated with TiO<sub>2</sub>-Acac nanocrystals.

### INTRODUCTION

In the past decades, several methods have been tested for achieving efficient TiO<sub>2</sub>-based photocatalysis. The formation of hetero-junction, dye sensitization and metal/non-metal doping were used for extending absorption of TiO<sub>2</sub> toward the visible light range of solar spectrum. However, boosting photocatalytic efficiency is restricted due to the increase of electrons/holes recombination. To extend the light harvesting to the near-infrared (NIR) range of solar spectrum, we combined two extraordinary materials in a unique core-shell structure. NaYF<sub>4</sub>:Yb,Tm, used as a core, converts NIR to UV/VIS light, whereas TiO<sub>2</sub>-Acac charge-transfer complex, as a shell, absorbs the converted light, increasing in such way light harvesting. Up-conversion is the non-linear optical process which is most efficient in trivalent rare earth (RE<sup>3+</sup>)-doped NaYF<sub>4</sub> hexagonal phase. A suitable choice of sensitizer and activator ions, such as Yb<sup>3+</sup> and Tm<sup>3+</sup>, respectively, tunes UC emission toward blue and red part of spectra, *i.e.* toward wavelengths in which TiO<sub>2</sub>-Acac efficiently absorbs. We already showed that coupling of Acac on nanosized TiO<sub>2</sub> extends its absorption through visible spectral range due to altered optical band-gap to 1.4eV[1].

### METHODS

NaYF<sub>4</sub>:Yb,Tm particles with a nominal composition NaY<sub>0.78</sub>Yb<sub>0.2</sub>Tm<sub>0.02</sub> were hydrothermally synthesized from common rare earth nitrate precursor (0.01M) using the RE:F ratio of 14 and 7, respectively. Synthesis procedure is given in details elsewhere [2]. The as-obtained micro- and nano-sized UC particles were coated with TiO<sub>2</sub>-Acac using two methods. In both, the quantity of titanium tetraisopropoxide (TTIP) was calculated to be sufficient for formation of 50 and 10 nm thick shell on micro- and nano-sized particles, respectively, in accordance to sol-gel procedure described in [3]. In the first approach, 20 mg of UC particles were well dispersed in ethanol, using ultrasonic bath. Then acetilacetone (Acac:ethanol=1:10) and TTIP (TTIP:acac=1:2) were dropwise added under sonication. To accomplish the hydrolysis reaction, few drops of HNO<sub>3</sub> 0.307 M aqueous solution was added. Then the as-prepared sol was heated at 60 °C until complete solvent evaporation and the obtained

powder was thermally treated at 300 °C for 2h. In the second method, to explore the PVP use as coupling agent, the coating procedure was modified as followed: UC particles were firstly dispersed in 40ml of ethanol using ultrasonic bath. Then 0.5 g of PVP was added and the mixture was sonicated for 20 min. In a separate glass, 2 ml of TTIP was slowly added to 1.4 mL Acac/7 mL ethanol mixture under vigorous stirring. The obtained yellow solution was subsequently dropped into UC/PVP mixture and left overnight. The coated particles were collected through centrifugation at 7000 rpm and then, washed several times with ethanol and water. After drying, powder was subjected to a heat treatment at 300 °C for 2h. UC powders crystal structure were analyzed through X-ray powder diffraction (XRPD), using Bruker D8 Advance and Philips PW-1050 diffractometer. The morphology and surface properties of the particles, before and after coating, were investigated by field emission scanning electron microscopy (FE-SEM) and energy dispersive X-ray spectroscopy (EDS), using Mira Tescan 3X and Hitachi TM3000 SEM with Swift ED3000 detector, respectively.

## RESULTS AND DISCUSSION

The XRPD patterns of the  $\text{NaY}_{0.78}\text{Yb}_{0.2}\text{Tm}_{0.02}$  samples obtained using different  $\text{RE}^{3+}:\text{F}^-$  ratio (14 and 7) are presented in **Figure 1**. Higher content of fluoride anions lead to the direct crystallization of the thermodynamically stable hexagonal  $\beta$  phase (space group  $\text{P6}_3/\text{m}$ ; JCPDS file No. 16-0334), **Figure 1(a)**. With a decrease of the fluoride ions-content, the crystallization of the kinetically stable cubic  $\alpha$  phase (group  $\text{Fm-3m}$ , JCPDS file No. 77-2042) occurred, **Figure 1(b)**. The change in the crystal structure arrangement is followed by the change of the particles morphology. The  $\beta$ -phase appears as well-defined hexagonal prisms with the elongated c-axes, sized up to 3  $\mu\text{m}$ , while spherical particles of  $\alpha$  phase, smaller than 50 nm, are readily prepared from a precursor which comprises lower concentration of fluoride ions (insets in **Figure 1**).

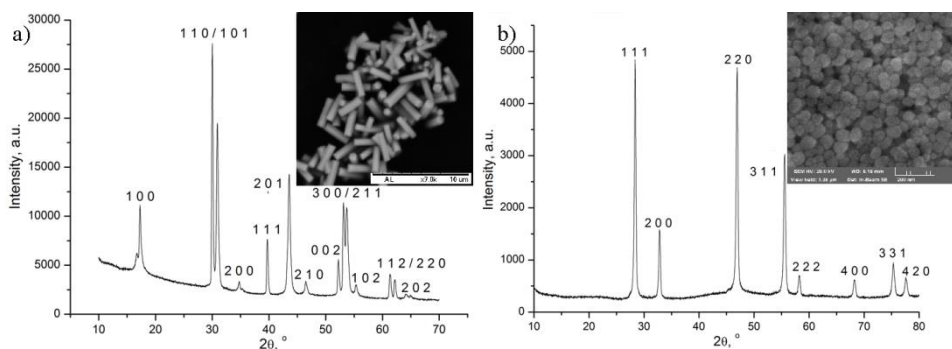


**Figure 1.** XRPD patterns and SEM images of  $\text{NaYF}_4:\text{Yb},\text{Tm}$  phases: a) hexagonal,  $\beta$ -phase and b) cubic,  $\alpha$ -phase.

**Figure 2** strongly suggests that core-shell  $\text{NaYF}_4:\text{Yb},\text{Tm}@\text{TiO}_2\text{-Acac}$  structures were obtained through the PVP free procedure, preserving initial particle morphology of both  $\text{NaYF}_4:\text{Yb},\text{Tm}$  phases. The presence of titanium ions at the particle surface is confirmed through EDS analysis of a single particle (in the case of micro-sized particles, Figure 2a) and on a group of nanoparticles (Figure 2b). The presence of the  $\text{TiO}_2\text{-acac}$  shell is additionally revealed by FTIR analysis of core-shell particles (not included here) which shown a characteristic band of  $\nu\text{C}=\text{C}(\text{Ti-Acac})$  group in the enolic form at  $1580\text{ cm}^{-1}$ . The addition of PVP prevents the shell formation over UC nanoparticles and entirely suppresses it when micro-sized UC particles are used as a core.

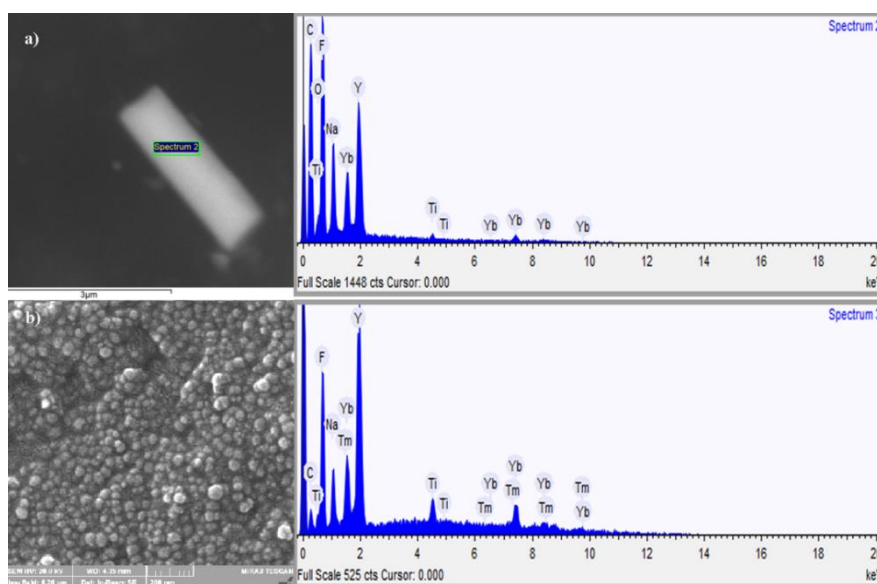


**Figure 2.** NaYF<sub>4</sub>:Yb,Tm@TiO<sub>2</sub>-Acac core-shell structures

## CONCLUSION

Micro- and nano-sized NaYF<sub>4</sub>:Yb,Tm@TiO<sub>2</sub>-Acac core-shell particles were successfully obtained through the combination of hydrothermal and sol-gel synthesis methods. The presence of UC core should improve the overall sensitivity of TiO<sub>2</sub>-Acac to the solar spectrum, intensifying its photocatalytic properties.

## Acknowledgement

This research was supported by the Science Fund of the Republic of Serbia, program DIJASPORA, #6421090, COSH-PHOTO and Ministry of Education, Science and Technological Development of Republic of Serbia (Contract No. 451-03-9/2021-14/200175). B.A.M. is grateful to CNPq for Research Productivity Grant. T.M. is grateful to CAPES for a post-doctoral scholarship (PNPD-88882.315335/2019-01).

## REFERENCES

- [1] L.A. Almeida, M. Habran, R. Santos Carvalho, M.E.H. Maia da Costa, M. Cremona, B.C. Silva, K. Krambrock, O.G. Pandoli, E. Morgado Jr and B.A. Marinkovic, *Catalysts*, 2020, 10, 1463-1481.
- [2] I. Z. Dinic, L. T. Mancic, M. E. Rabanal, K. Yamamoto, S. Ohara, S. Tamura, T. Koji, A. M. L. M. Costa, B. A. Marinkovic, O. B. Milosevic, *Advanced Powder Technology*, 2017, 28, 73-82.
- [3] M. Habran, P. I. Ponton, L. Mancic, O. Pandoli, K. Krambrock, M. E. H. Maia da Costa, S. Letichevskya, A. M. L. M. Costa, E. Morgado Jr., B.A. Marinkovic, *Journal of Photochemistry and Photobiology A: Chemistry*, 2018, 365, 133 – 144.

# THERMALLY INDUCED PHASE TRANSFORMATIONS AND THEIR INFLUENCE ON FUNCTIONAL PROPERTIES OF MULTICOMPONENT Fe-BASED AMORPHOUS ALLOYS

M. M. Vasić<sup>1</sup>, D. M. Minić<sup>2</sup>, D. M. Minić<sup>1</sup>

<sup>1</sup> Faculty of Physical Chemistry, University of Belgrade,

Studentski trg 12-16, 11000 Belgrade, Serbia (mvasic@ffh.bg.ac.rs)

<sup>2</sup> Military Technical Institute, Ratka Resanovića 1, 11000 Belgrade, Serbia

## ABSTRACT

In this work, results of the study of five multicomponent iron-based amorphous alloys are summarized and compared regarding their thermal stability, mechanism of thermally induced microstructural transformations and their effect on the functional properties of the alloys. The obtained informations can be significant for development of the materials with targeted properties.

## INTRODUCTION

Amorphous alloys are unique in terms of their short-range atomic ordering, due to which these materials possess isotropic physical and mechanical properties. The amorphous alloys based on iron attract a lot of attention owing to their combination of mechanical, electrical, magnetic and anticorrosion properties, which enables practical application in various fields [1]. Because of their thermodynamic and kinetic metastability, structure of the amorphous alloys is prone to transformations to the forms with higher stability. Such structural stabilization occurs through the processes of structural relaxation, crystallization and recrystallization, and can deteriorate or improve their functional properties. The aim of this work is to summarize and compare the results of the study of iron-based amorphous alloys with different chemical composition concerning their thermal stability and thermally induced phase transformations, including their influence on the functional properties of the alloys.

## EXPERIMENTAL

The subject of this work are iron-based amorphous alloys with the following compositions  $\text{Fe}_{81}\text{Si}_4\text{B}_{13}\text{C}_2$ ,  $\text{Fe}_{79.8}\text{Ni}_{1.5}\text{Si}_{5.2}\text{B}_{13}\text{C}_{0.5}$ ,  $\text{Fe}_{75}\text{Ni}_2\text{Si}_8\text{B}_{13}\text{C}_2$ ,  $\text{Fe}_{73.5}\text{Cu}_1\text{Nb}_3\text{Si}_{15.5}\text{B}_7$ , and  $\text{Fe}_{40}\text{Ni}_{40}\text{P}_{14}\text{B}_6$ , where the atomic percentages of individual elements are expressed as numbers in index. The studied alloys were prepared by melt-spinning method.

Differential scanning calorimetry (DSC) was performed in an inert atmosphere in the temperature range 25-750 °C, at constant heating rates. X-ray diffraction (XRD) analysis, with a Bragg-Brentano diffractometer, was used for the purpose of structural analysis of the alloy sample. Measurements were carried out at room temperature, using Co K $\alpha$  radiation. Thermally treated samples subjected to structural analysis were prepared by isothermal annealing of the alloy previously sealed in a quartz tube at different temperatures.

EG&G vibrating sample magnetometer was used for thermomagnetic measurements; electrical resistivity of the alloys was measured by utilizing the four-point method, while for determination of Vickers microhardness, a Anton Paar MHT-10 microhardness testing device was employed.

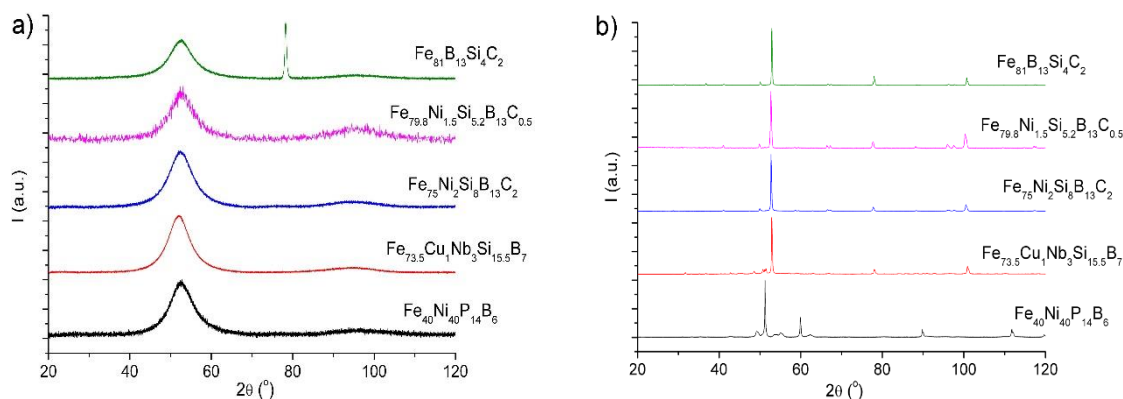


**Figure 1.** XRD diffractograms of the as-prepared alloys (a) (©2020, Originally published in ref [2] under CC BY 3.0 license); and crystallized alloy samples (b).

## RESULTS AND DISCUSSION

XRD analysis performed on the as-prepared alloy samples demonstrated completely or mostly amorphous structure, for all of the studied samples, Fig. 1a. Small amounts of the  $\alpha$ -Fe(Si) phase (JCPDS-PDF 06-0696) present in the  $\text{Fe}_{81}\text{Si}_4\text{B}_{13}\text{C}_2$  alloy resulted from the fact that its atomic fraction of iron is high, and the lack of another metal element in the composition, thus disobeying the empirical rule of more facile amorphization [2].

Thermal analysis using DSC was carried out to study the thermal stability and the temperature range of thermally induced microstructural transformations for the examined alloys, Fig. 2a, Table 1. The results revealed somewhat better thermal stability of the  $\text{Fe}_{79.8}\text{Ni}_{1.5}\text{Si}_{5.2}\text{B}_{13}\text{C}_{0.5}$  alloy in comparison with the other alloys studied herein, as a consequence of the optimal chemical composition, which involves two metals present in amount of around 80 at.% in total, and three non-metallic elements serving as amorphizers, present in amount of around 20 at.% in total.

**Table 1.** Temperatures of the crystallization onset ( $T_0$ ), phases formed during crystallization, and Curie temperatures ( $T_c$ ), for individual alloys. ©2020, Originally published in ref [2] under CC BY 3.0 license.

		$T_0$ ( $^\circ\text{C}$ )	$T_{c1}$ ( $^\circ\text{C}$ )	$T_{c2}$ ( $^\circ\text{C}$ )
$\text{Fe}_{81}\text{B}_{13}\text{Si}_4\text{C}_2$	$\alpha$ -Fe(Si), $\text{Fe}_3\text{B}$ , $\text{Fe}_2\text{B}$	500	420	730
$\text{Fe}_{79.8}\text{Ni}_{1.5}\text{Si}_{5.2}\text{B}_{13}\text{C}_{0.5}$	$\alpha$ -Fe(Si), $\text{Fe}_2\text{B}$	520	-	-
$\text{Fe}_{75}\text{Ni}_2\text{Si}_8\text{B}_{13}\text{C}_2$	$\alpha$ -Fe(Si), $\text{Fe}_3\text{B}$ , $\text{Fe}_2\text{B}$	500	430	740
	recrystallization	670		
$\text{Fe}_{73.5}\text{Cu}_1\text{Nb}_3\text{Si}_{15.5}\text{B}_7$	$\alpha$ -Fe(Si), $\text{Fe}_2\text{B}$	500	340	600
	$\text{Fe}_{16}\text{Nb}_6\text{Si}_7$ , $\text{Fe}_2\text{Si}$	670		
$\text{Fe}_{40}\text{Ni}_{40}\text{P}_{14}\text{B}_6$	$\alpha$ -(Fe,Ni),	380	360	480
	$\gamma$ -(Fe,Ni),			
	$(\text{Fe,Ni})_3(\text{P,B})$			

Microstructural transformations induced by thermal treatment included crystallization of different phases and recrystallization, Fig. 1b, Table 1. Crystallization of the examined alloys started with formation of the bcc-Fe crystals containing also Si and/or Ni, as a result of the bcc-Fe-like atomic configuration of the as-prepared alloy samples [2]. Crystalline phases  $\alpha$ -Fe(Si) and  $\text{Fe}_2\text{B}$  were the

final crystallization products of the alloys containing 73-81 at.%, while in the case of the  $\text{Fe}_{40}\text{Ni}_{40}\text{P}_{14}\text{B}_6$  alloy, phases  $\gamma\text{-(Fe,Ni)}$  and  $(\text{Fe,Ni})_3(\text{P,B})$  were present after annealing at the highest temperature (600 °C).

Functional properties of the studied alloys are influenced by their chemical composition and microstructure. The as-prepared alloys have relatively high microhardness values, over 900 HV [2, 3]. Thermally induced microstructural transformations changed microhardness values, Fig.2b, where the optimal microstructure (combined amorphous/nanocrystalline) with the highest microhardness was reached after annealing at 500-600 °C. According to thermomagnetic measurements [3], changes in magnetic moment followed the thermal effects observed by DSC measurements. The values of Curie temperature of the as-prepared alloys ( $T_{c1}$ ) and completely crystallized alloy samples ( $T_{c2}$ ) are given in Table 1. Similarities and differences in the Curie temperature values among individual alloys presented herein reflect specificities of their compositions. The ordered structure has lower electrical resistivity than the amorphous structure, resulting in decrease in electrical resistivity of the alloy samples after crystallization. Behavior of the completely crystallized samples during second thermal treatment was typical of electronic conductors [2].

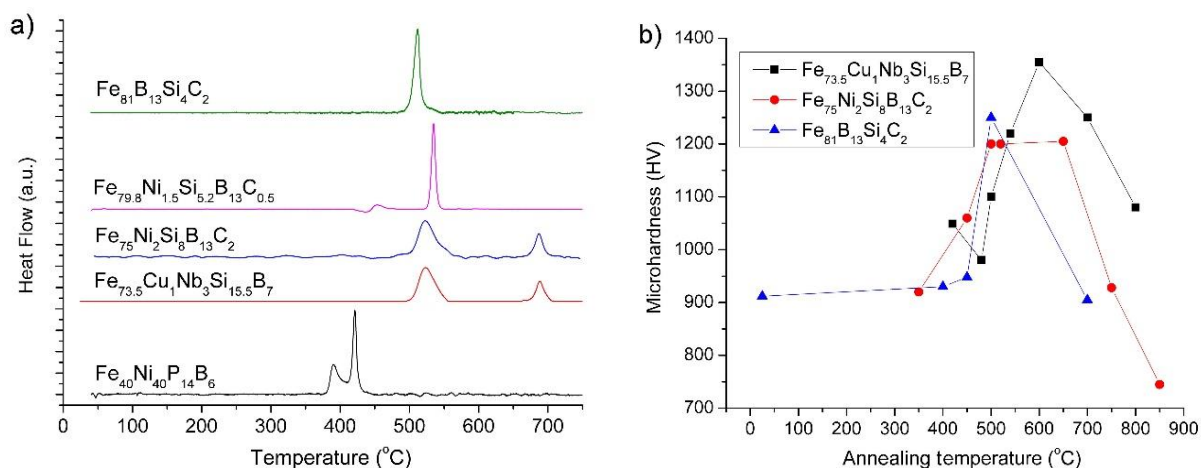


**Figure 2.** DSC curves of the studied alloys recorded at 5 °C/min (a), and microhardness values of several Fe-based alloys studied herein after annealing at different temperatures for 30 min (b); ©2020, Originally published in ref [2] under CC BY 3.0 license.

## CONCLUSION

The study of thermal stability and mechanism of thermally induced microstructural transformations of five multicomponent iron-based amorphous alloys demonstrated that slight differences in chemical composition can have a great influence on the alloy behavior. Thermally induced microstructural transformations strongly affect the mechanical, magnetic and electrical properties of the studied alloys.

## Acknowledgement

This work was financially supported by the Ministry of Education, Science and Technological Development of the Republic of Serbia (contract No. 451-03-9/2021-14/200146).

## REFERENCES

- [1] C. Suryanarayana, A. Inoue, *Int. Mater. Rev.*, 2013, 58, 131-166.
- [2] M. M. Vasić, D. M. Minić, D. M. Minić in: *Metallic glasses*, D. Minić, M. Vasić (Eds.), IntechOpen, London, 2020. Available from: <http://dx.doi.org/10.5772/intechopen.88260>

- [3] V. A. Blagojević, M. Vasić, B. David, D. M. Minić, N. Pizúrová, T. Žák, D. M. Minić, *Mater. Chem. Phys.*, 2014, 145, 12-17.

## INFLUENCE OF POLYOXOPALLADATES(II) ON ECTO-NUCLEOSIDE TRIPHOSPHATE DIPHOSPHOHYDROLASES

M. B. Čolović<sup>1</sup>, T. Ma<sup>2</sup>, X. Ma<sup>2</sup>, A. Isaković<sup>3</sup>, S. Misirlić-Denčić<sup>3</sup>, U. Kortz<sup>2</sup> and D. Z. Krstić<sup>4</sup>

<sup>1</sup>*Department of Physical Chemistry, "Vinča" Institute of Nuclear Sciences-National Institute of the Republic of Serbia, University of Belgrade, Serbia (colovicm@vin.bg.ac.rs)*

<sup>2</sup>*Department of Life Sciences and Chemistry, Jacobs University, Bremen, Germany*

<sup>3</sup>*Institute of Medical and Clinical Biochemistry, Faculty of Medicine, University of Belgrade, Serbia*

<sup>4</sup>*Institute of Medical Chemistry, Faculty of Medicine, University of Belgrade, Serbia*

### ABSTRACT

Polyoxopalladates (POPs) are discrete, anionic palladium(II)-oxo nanoclusters combining properties of polyoxometalates and palladium(II), and thus are highly promising for the development of novel antitumor metallodrugs. The aim of this study was to investigate *in vitro* the influence of three POP salts with approved anti-neuroblastoma action,  $\text{Na}_8[\text{Pd}_{13}\text{As}_8\text{O}_{34}(\text{OH})_6] \cdot 42\text{H}_2\text{O}$  (**Pd<sub>13</sub>**),  $\text{Na}_4[\text{SrPd}_{12}\text{O}_6(\text{OH})_3(\text{PhAsO}_3)_6(\text{OAc})_3] \cdot 2\text{NaOAc} \cdot 32\text{H}_2\text{O}$  (**SrPd<sub>12</sub>**), and  $\text{Na}_6[\text{Pd}_{13}\text{O}_8(\text{PhAsO}_3)_8] \cdot 23\text{H}_2\text{O}$  (**Pd<sub>13</sub>L**), on E-NTPDase activity using rat synaptic plasma membranes (SPMs) isolated from *Wistar* brain as a model system. Dose-dependent inhibition of E-NTPDases was obtained within concentration range  $2 \times 10^{-6}$  -  $1 \times 10^{-3}$  mol/L for all investigated POPs. Inhibition parameters, IC<sub>50</sub> value and Hill's coefficient,  $n_{\text{H}}$ , were determined by sigmoidal fitting the experimental results. The calculated IC<sub>50</sub> values were  $(1.08 \pm 0.25) \times 10^{-4}$ ,  $(1.19 \pm 0.13) \times 10^{-4}$ , and  $(2.06 \pm 0.88) \times 10^{-4}$  mol/L for **Pd<sub>13</sub>**, **SrPd<sub>12</sub>**, and **Pd<sub>13</sub>L**, respectively, indicating their similar inhibitory strengths. The  $n_{\text{H}}$  values were determined to be  $< 1$ , indicating negatively cooperative binding for all POPs studied. The observed inhibitory effect of these anti-neuroblastoma POPs on E-NTPDase activity suggest that the inhibition of E-NTPDases, the enzymes representing the major part of purinergic signaling, could be considered as a putative mechanism of antitumor action and a new strategy in the development of novel antitumor therapeutics.

### INTRODUCTION

Polyoxometalates (POMs) are discrete, negatively charged metal-oxo clusters of early *d*-block metal ions in high oxidation states, surrounded by oxygen atoms [1]. As many *in vivo* and *in vitro* studies revealed anticancer, antibacterial, antiviral, and antidiabetic activities of some POMs [2-4], their biological importance has considerably increased in recent years. Polyoxopalladates(II) (POPs) are discrete, anionic palladium(II)-oxo nanoclusters including properties of both polyoxometalates and palladium(II) whose complexes have been extensively studied as a promising alternative to platinum-based chemotherapeutics [5]. Ecto-nucleoside triphosphate diphosphohydrolases (ENTPDases) are plasma membrane bound enzymes that, in the presence of divalent cations ( $\text{Ca}^{2+}$  or  $\text{Mg}^{2+}$ ), hydrolyze extracellular nucleotides. E-NTPDases represent the major part of purinergic signaling, and elevated E-NTPDases levels are detected in cancer cells due to their abnormal cellular growth and proliferation. Thus, the inhibition of E-NTPDase activities could be considered as a new strategy in the development of novel antitumor therapeutics.

The aim of this study is to investigate *in vitro* the influence of three synthesized POPs with different capping groups or polyanions structures, arsenate-capped nanocube  $\text{Na}_8[\text{Pd}_{13}\text{As}_8\text{O}_{34}(\text{OH})_6] \cdot 42\text{H}_2\text{O}$  (**Pd<sub>13</sub>**), phenylarsenate-capped open shell  $\text{Na}_4[\text{SrPd}_{12}\text{O}_6(\text{OH})_3(\text{PhAsO}_3)_6(\text{OAc})_3] \cdot 2\text{NaOAc} \cdot 32\text{H}_2\text{O}$  (**SrPd<sub>12</sub>**), and phenylarsenate-capped nanocube  $\text{Na}_6[\text{Pd}_{13}(\text{AsPh})_8\text{O}_{32}] \cdot 23\text{H}_2\text{O}$  (**Pd<sub>13</sub>L**) (Figure 1), on E-NTPDase activity using rat synaptic

plasma membranes (SPMs) as a model system. Our previous research (results not published) demonstrated cytotoxic effects of these POPs to tumor human neuroblastoma cell line (SH-SY5Y), and POP-induced E-NTPDase inhibition might be a putative mechanism of the antitumor action.

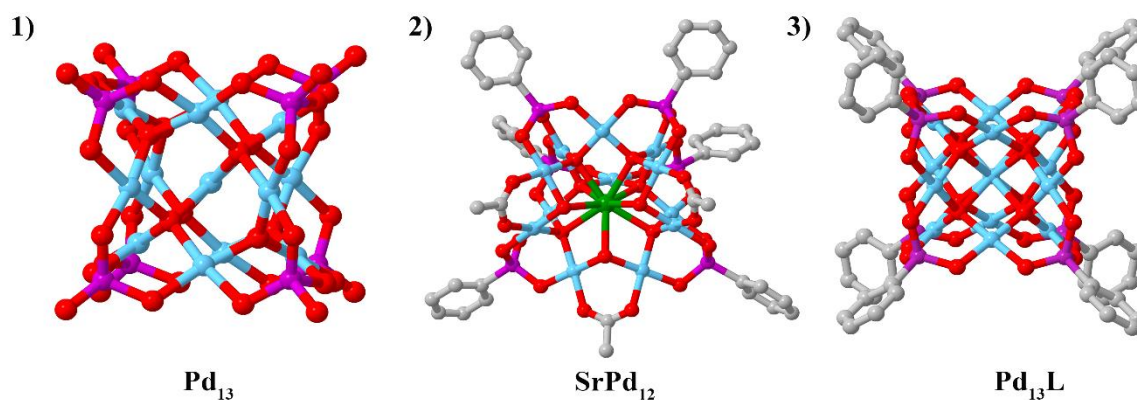


**Figure 1.** Structure of the studied polyoxopalladates **Pd<sub>13</sub>**, **SrPd<sub>12</sub>** and **Pd<sub>13</sub>L**. Color codes: light blue, Pd; green, Sr; purple, As; grey, C and red, O. Hydrogen atoms are omitted.

## EXPERIMENTAL

**Pd<sub>13</sub>**, **SrPd<sub>12</sub>**, and **Pd<sub>13</sub>L** were synthesized according to references [6], [7], and [8], respectively. SPMs were isolated from the whole brain of 3-month-old male *Wistar albino* rats according to the method of Cohen *et al.* [9], as modified by Towle and Sze [10], and stored at  $-70\text{ }^{\circ}\text{C}$  until used. The assay medium for SPM ENTDPase activity contained (in mmol/L): 50 Tris-HCl (pH 7.4), 5  $\text{MgCl}_2$ , 2 ATP and 150 mg/L SPM proteins. After preincubation for 15 min at  $37\text{ }^{\circ}\text{C}$  in the absence (control) or in the presence of the investigated compounds, the reaction was initiated by ATP addition and stopped after 30 min by adding 22  $\mu\text{L}$  ice cold of 6 mol/L HCl and immediate cooling on ice. The concentration of ADP liberated due to ATP hydrolysis was determined by a modified UPLC method [11, 12]. The mobile phase was composed of 4 mmol/L tetrabutylammonium hydroxide (TBAH) in 4 mmol/L phosphate buffer (phase A) and methanol (phase B) in the ratio 75:25. Flow rate was 0.25 mL/min, injection volume 10  $\mu\text{L}$ , and the column temperature  $40\text{ }^{\circ}\text{C}$ . The separation was monitored in a single wavelength mode at 254 nm.

## RESULTS AND DISCUSSION

The influence of **Pd<sub>13</sub>**, **SrPd<sub>12</sub>**, and **Pd<sub>13</sub>L** on SPM E-NTPDase activity was investigated within the concentration range from  $1 \times 10^{-7}$  to  $1 \times 10^{-3}$  mol/L. The results show that increasing concentrations of the investigated POPs induce an inhibition of the enzyme activity in a concentration-dependent manner (Figure 2). The dependence of the enzyme activity, expressed as a percentage of the control value (obtained without inhibitor), on inhibitor concentrations fits a sigmoidal function for all studied POPs.

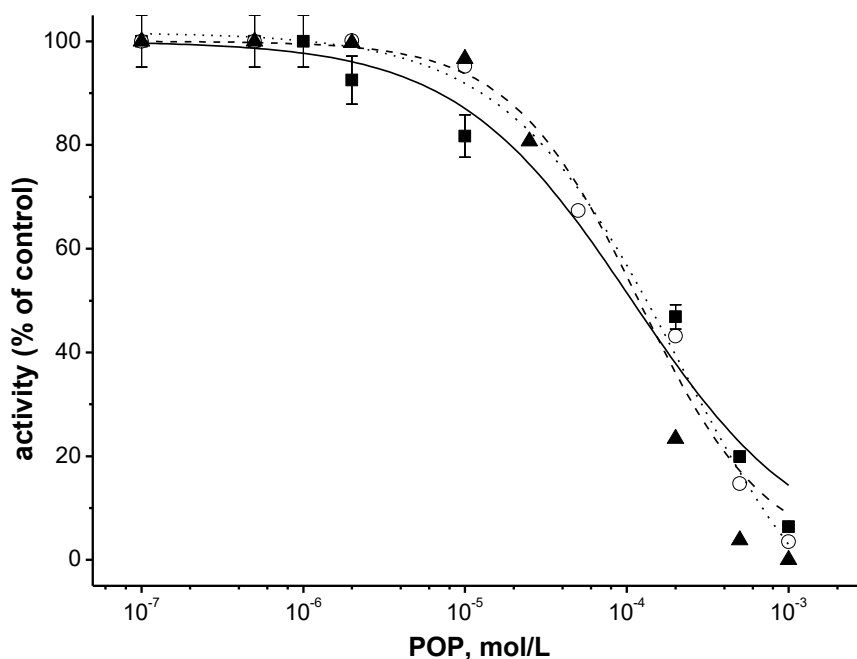


**Figure 2.** Concentration-dependent inhibition of SPM E-NTPDase activity induced by **Pd<sub>13</sub>** (solid squares), **SrPd<sub>12</sub>** (open circles), and **Pd<sub>13</sub>L** (solid triangles). The values are expressed as mean ± S.E.M.

Inhibition parameters, the concentrations of the investigated compounds with a capability to inhibit 50% of the enzyme after given exposure time ( $IC_{50}$  values) and Hill's coefficient,  $n_H$ , were determined by sigmoidal fitting. The calculated  $IC_{50}$  values were  $(1.08 \pm 0.25) \times 10^{-4}$ ,  $(1.19 \pm 0.13) \times 10^{-4}$ , and  $(2.06 \pm 0.88) \times 10^{-4}$  mol/L for **Pd<sub>13</sub>**, **SrPd<sub>12</sub>**, and **Pd<sub>13</sub>L**, respectively. Thus, it is obvious that **Pd<sub>13</sub>**, **SrPd<sub>12</sub>**, and **Pd<sub>13</sub>L** exhibited similar inhibitory potencies to SPM E-NTPDase. The highest investigated concentrations ( $1 \times 10^{-3}$  mol/L) resulted in almost complete inhibition of the enzyme activity for all POPs tested, whereas significant enzyme modulations were achieved at concentrations above  $2 \times 10^{-6}$  mol/L. The  $n_H$  values were  $< 1$ , indicating negatively cooperative enzyme-inhibitor binding for all POPs. The observed similar activities of the all-inorganic **Pd<sub>13</sub>** and the organically-modified **SrPd<sub>12</sub>** and **Pd<sub>13</sub>L** suggest that the introduced organic groups do not significantly affect the E-NTPDase sensitivity.

## CONCLUSION

The investigated POPs, **Pd<sub>13</sub>**, **SrPd<sub>12</sub>**, and **Pd<sub>13</sub>L**, showed concentration-dependent inhibitory effects on SPM E-NTPDase activity within the concentration range  $2 \times 10^{-6}$  -  $1 \times 10^{-3}$  mol/L, with similar inhibitory potencies ( $IC_{50} \approx 1 \times 10^{-4}$  mol/L). Since these POPs demonstrated cytotoxicity against human neuroblastoma cell line (SH-SY5Y), the observed E-NTPDase modulation might be considered as a possible mechanism of anti-neuroblastoma action of these promising drug candidates.

## Acknowledgement

This research was funded by the Ministry of Education, Science and Technological Development of the Republic of Serbia, through Grant Agreement with University of Belgrade, INN "Vinča" no. 451-03-9/2021-14/200017. The authors also gratefully acknowledge the bilateral project Serbia-Germany (no. 451-03-01038/2015-09/16, DAAD-PPP) and the CMST COST Action CM1203 (PoCheMoN). Figure 1 was generated with Diamond, version 3.2 (Crystal Impact GbR).

## REFERENCES

- [1] Pope, M.T.; Kortz, U. *Polyoxometalates Encyclopedia of Inorganic and Bioinorganic Chemistry*, 1<sup>st</sup> ed.; Wiley & Sons: New York, 2012.
- [2] Yamase, T. Polyoxometalates active against tumors, viruses and bacteria. *Prog. Mol. Subcell. Biol.*, **2013**, *54*, 65–116.
- [3] Čolović, M.B.; Lacković, M.; Lalatović, J.; Mougharbel, A.S.; Kortz, U.; Krstić, D. Polyoxometalates in biomedicine: update and overview. *Curr. Med. Chem.*, **2020**, *27*, 362–379.
- [4] Sun, T.; Cui, W.; Yan, M.; Qin, G.; Guo, W.; Gu, H.; Liu, S.; Wu, Q. Target delivery of a novel antitumor organoplatinum(IV)-substituted polyoxometalate complex for safer and more effective colorectal cancer therapy *in vivo*. *Adv. Mater.*, **2016**, *28*(34), 7397–7404.
- [5] Yang, P.; Kortz, U. Discovery and evolution of polyoxopalladates. *Accounts Chem. Res.*, **2018**, *51*, 1599–1608.
- [6] Chubarova, E.V.; Dickman, M.H.; Keita, B.; Nadjo, L.; Miserque, F.; Mifsud, M.; Arends, I.W.C.E.; Kortz, U. Self-assembly of a heteropolyoxopalladate nanocube:  $[\text{Pd}^{\text{II}}_{13}\text{AsV}_8\text{O}_{34}(\text{OH})_6]^{8-}$ . *Angew. Chem. Int. Edit.*, **2008**, *47*, 9542–9546.
- [7] Yang, P.; Xiang, Y.; Lin, Z.; Bassil, B.S.; Cao, J.; Fan, L.; Fan, Y.; Li, M.-X.; Jiménez-Lozano, P.; Carbó, J.J.; Poblet, J.M.; Kortz, U. (2014). Alkaline earth guests in polyoxopalladate chemistry: from nanocube to nanostar *via* an open-shell structure. *Angew. Chem. Int. Edit.*, **2014**, *53*(44), 11974–11978.
- [8] Izarova, N.V.; Dickman, M.H.; Biboum, R.N.; Keita, B.; Nadjo, L.; Ramachandran, V.; Dalal, N.S.; Kortz, U. Heteropoly-13-palladates(II)  $[\text{Pd}^{\text{II}}_{13}(\text{As}^{\text{V}}\text{Ph})_8\text{O}_{32}]^{6-}$  and  $[\text{Pd}^{\text{II}}_{13}\text{Se}^{\text{IV}}_8\text{O}_{32}]^{6-}$ . *Inorg. Chem.*, **2009**, *48*, 7504–7506.
- [9] Cohen, R.S.; Blomberg, F.; Berzins, K.; Siekevits, P.J. The structure of postsynaptic densities isolated from dog cerebral cortex. *Cell Biol.*, **1977**, *74*, 181–203.
- [10] Towle, A.C.; Sze, P.Y.J. Steroid binding to synaptic plasma membrane differential binding of glucocorticoid and gonadal steroids. *Steroid Biochem.*, **1983**, *18*, 135–143.
- [11] Sahoo, A.; Samanta, L.; Das, A.; Patra, K.S.; Chainy, B.N.G. Hexachlorocyclohexane-induced behavioural and neurochemical changes in rat. *J. Appl. Toxicol.*, **1999**, *19*, 13–18.
- [12] Čolović, M.; Krstić, D.; Petrović, S.; Leskovac, A.; Joksić, G.; Savić, J.; Franko, M.; Trebše, P.; Vasić, V. Toxic effects of diazinon and its photodegradation products. *Toxicol. Lett.*, **2010**, *193*, 9–18.

## INHIBITION OF ECTO-NUCLEOSIDE TRIPHOSPHATE DIPHOSPHOHYDROLASES BY POLYOXOPALLADATES WITH PROMISING ANTILEUKEMIC PROPERTIES

M. B. Čolović<sup>1</sup>, T. Ma<sup>2</sup>, X. Ma<sup>2</sup>, A. Isaković<sup>3</sup>, S. Misirlić-Denčić<sup>3</sup>, U. Kortz<sup>2</sup> and D. Z. Krstić<sup>4</sup>

<sup>1</sup>*Department of Physical Chemistry, "Vinča" Institute of Nuclear Sciences-National Institute of the Republic of Serbia, University of Belgrade, Serbia (colovicm@vin.bg.ac.rs)*

<sup>2</sup>*Department of Life Sciences and Chemistry, Jacobs University, Bremen, Germany*

<sup>3</sup>*Institute of Medical and Clinical Biochemistry, Faculty of Medicine, University of Belgrade, Serbia*

<sup>4</sup>*Institute of Medical Chemistry, Faculty of Medicine, University of Belgrade, Serbia*

### ABSTRACT

Polyoxopalladates(II) (POPs) are the largest subset of polyoxo-noble-metalates (PONMs), representing a class of discrete, anionic noble metal-oxo nanoclusters. In this study, the *in vitro* effects of two isostructural, fully inorganic POP salts containing tetravalent metal ions (Sn<sup>IV</sup> and Pb<sup>IV</sup>) incorporated inside the cubic Pd<sub>12</sub>-oxo host-shell, Na<sub>12</sub>[Sn<sup>IV</sup>O<sub>8</sub>Pd<sub>12</sub>(PO<sub>4</sub>)<sub>8</sub>]·43H<sub>2</sub>O (**SnPd<sub>12</sub>**) and Na<sub>12</sub>[Pb<sup>IV</sup>O<sub>8</sub>Pd<sub>12</sub>(PO<sub>4</sub>)<sub>8</sub>]·38H<sub>2</sub>O (**PbPd<sub>12</sub>**), which were found to exhibit considerable antileukemic effects, on E-NTPDase activity were investigated using rat synaptic plasma membranes (SPMs) as a model system. Concentration-dependent inhibition of E-NTPDases was observed within the concentration range  $5 \times 10^{-6}$  -  $2 \times 10^{-4}$  mol/L for both POPs. Inhibition parameters, half-maximum inhibitory concentrations (IC<sub>50</sub> values) and Hill's coefficients, n<sub>H</sub>, were determined by sigmoidal fitting the experimental results and Hill's analysis. The calculated IC<sub>50</sub> values were  $(6.59 \pm 1.09) \times 10^{-5}$  and  $(9.88 \pm 3.83) \times 10^{-5}$  mol/L for **SnPd<sub>12</sub>** and **PbPd<sub>12</sub>**, respectively. The calculated n<sub>H</sub> values were < 1, indicating negatively cooperative enzyme-inhibitor binding for both POPs. Accordingly, the confirmed antileukemic activities of **SnPd<sub>12</sub>** and **PbPd<sub>12</sub>** could be associated with the observed inhibition of E-NTPDases as a potential target of the antileukemic action of these promising drug candidates.

### INTRODUCTION

Polyoxopalladates(II) (POPs) are an important subset of polyoxo-noble-metalates (PONMs), representing a class of discrete, anionic noble metal-oxo nanoclusters [1]. Studies on biologically active polyoxometalates (POMs) have been mainly focused on classical POMs such as polyoxotungstates, -molybdates, and -vanadates, and various pharmacological properties such as antidiabetic, antimicrobial, and anticancer activities have been reported [2]. In addition, POPs belong to palladium(II)-based compounds whose complexes have been largely studied for last four decades as next-generation antitumor drug candidates [3]. Although the molecular mechanism of biological action has not been completely elucidated for many POMs, the inhibition of enzymes was reported to be responsible for many of their activities, especially those enzymes with extracellular binding sites such as phosphatases, kinases, sulfotransferases, sialyltransferases, and ecto-nucleotidases, which are mostly located on the plasma membrane and do not require membrane penetration [4]. Ecto-nucleoside triphosphate diphosphohydrolases (ENTPDases) are ecto-nucleotidases localized in cell membranes, which hydrolyze extracellular nucleoside tri-, di- and monophosphates such as ATP, ADP, and AMP. ENTPDases represent a major inactivating agent in purine-triphosphate signalling, and additionally ENTPDase activities were found to be increased in cancer cells [5], suggesting that these enzymes could be considered as targets of antitumor drug action.

The aim of this study was to investigate *in vitro* the effects of two isostructural all-inorganic phosphate-capped, cuboid-shaped POP hosts containing different tetravalent guest metal ions ( $\text{Sn}^{\text{IV}}$  or  $\text{Pb}^{\text{IV}}$ ),  $\text{Na}_{12}[\text{Sn}^{\text{IV}}\text{O}_8\text{Pd}_{12}(\text{PO}_4)_8]\cdot 43\text{H}_2\text{O}$  (**SnPd<sub>12</sub>**) and  $\text{Na}_{12}[\text{Pb}^{\text{IV}}\text{O}_8\text{Pd}_{12}(\text{PO}_4)_8]\cdot 38\text{H}_2\text{O}$  (**PbPd<sub>12</sub>**) (Figure 1), which were reported in our previous study [6] to exhibit considerable antileukemic effects against human acute promyelocytic cell line HL-60, on E-NTPDase activity using rat synaptic plasma membranes (SPMs) as a model system.

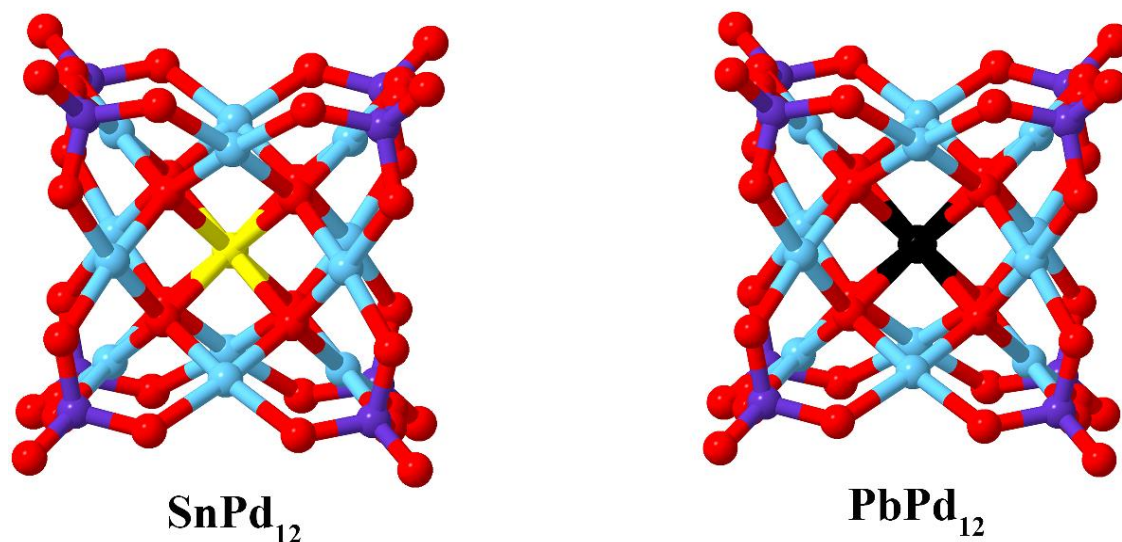


**Figure 1.** Structures of the investigated isostructural polyoxopalladates, **SnPd<sub>12</sub>** and **PbPd<sub>12</sub>**. Color codes: light blue, Pd; yellow, Sn; black, Pb; violet, P and red, O.

## EXPERIMENTAL

**SnPd<sub>12</sub>** and **PbPd<sub>12</sub>** were synthesized according to the published procedures [6]. SPMs were isolated from the whole brain of 3-month-old male *Wistar albino* rats according to the method of Cohen *et al.* [7], as modified by Towle and Sze [8], and stored at  $-70\text{ }^{\circ}\text{C}$  until used. SPM ENTDPase activity was determined following a previously established assay [9]. Briefly, the assay medium contained (in mmol/L): 50 Tris-HCl (pH 7.4), 5  $\text{MgCl}_2$ , 2 ATP and 150 mg/L SPM proteins. The SPMs were incubated at  $37\text{ }^{\circ}\text{C}$  in the absence (control) or in the presence of the investigated POPs for 15 min. Then, ATP was added to start the enzyme reaction that was allowed to proceed for 30 min. The enzyme reaction was stopped by adding 22  $\mu\text{L}$  of 6 mol/L ice cold HCl and immediate cooling on ice. The enzyme activity was followed *via* ADP liberated due to ATP hydrolysis. The ADP concentration was determined by a modified UPLC method [10, 11]. The mobile phase was composed of 4 mmol/L tetrabutylammonium hydroxide (TBAH) in 4 mmol/L phosphate buffer (phase A) and methanol (phase B) in the ratio 75:25. The flow rate was 0.25 mL/min, the injection volume 10  $\mu\text{L}$ , and the column temperature  $40\text{ }^{\circ}\text{C}$ . The separation was monitored in a single wavelength mode at 254 nm.

## RESULTS AND DISCUSSION

The influence of **SnPd<sub>12</sub>** and **PbPd<sub>12</sub>** on SPM E-NTPDase activity was investigated within the concentration range  $2 \times 10^{-7}$  -  $2 \times 10^{-4}$  mol/L. The results demonstrated that increasing concentrations of the investigated POPs induced an inhibition of the enzyme activity in a dose-dependent manner (Figure 2). The dependence of the enzyme activity, expressed as a percentage of the control value, on inhibitor concentrations was fitted with a sigmoidal function for both POPs.

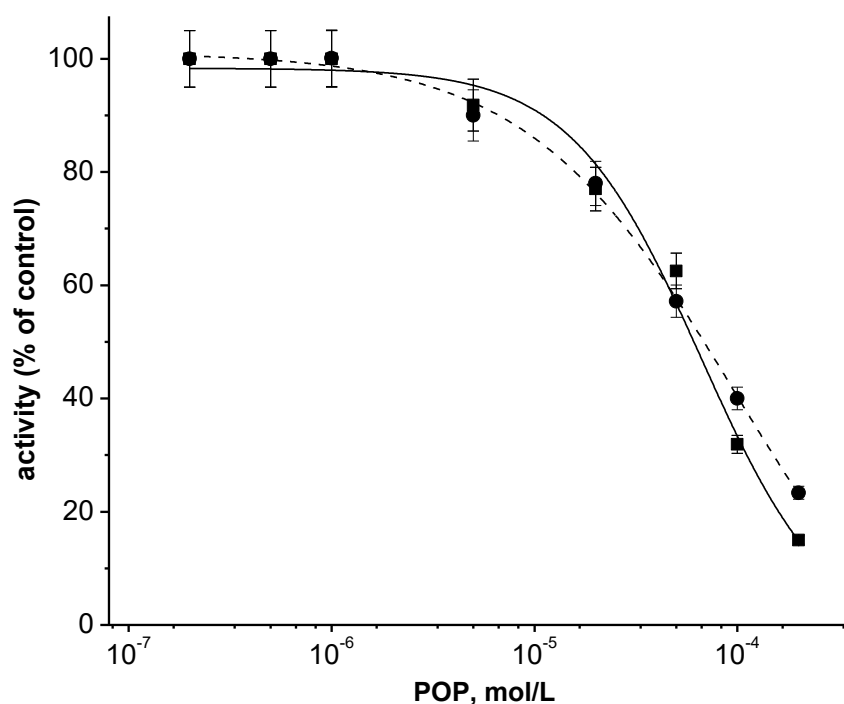


**Figure 2.** Concentration-dependent inhibition of SPM E-NTPDase activity induced by **SnPd<sub>12</sub>** (solid squares) and **PbPd<sub>12</sub>** (open circles). The values are expressed as mean ± S.E.M. Sigmoidal curves: **SnPd<sub>12</sub>** (solid line) and **PbPd<sub>12</sub>** (dashed line)

Inhibition parameters, half-maximum inhibitory concentrations ( $IC_{50}$  values) and Hill's coefficients,  $n_H$ , were determined by sigmoidal fitting of the experimental results and Hill's analysis. The obtained results indicated similar enzyme sensitivities toward **SnPd<sub>12</sub>** and **PbPd<sub>12</sub>**. The  $IC_{50}$  values were calculated as  $(6.59 \pm 1.09) \times 10^{-5}$  and  $(9.88 \pm 3.83) \times 10^{-5}$  mol/L for **SnPd<sub>12</sub>** and **PbPd<sub>12</sub>**, respectively. The highest tested concentration ( $2 \times 10^{-4}$  mol/L) induced approximately 80% decrease of the control activity for both POPs, and remarkable enzyme inhibitions were observed at concentrations  $\geq 5 \times 10^{-6}$  mol/L. The calculated  $n_H$  values were  $< 1$ , indicating negatively cooperative enzyme-inhibitor binding for both POPs. The observed similar inhibitory potencies of **SnPd<sub>12</sub>** and **PbPd<sub>12</sub>** to E-NTPDases are in accordance with their similar cytotoxic effects on tumor HL-60 cell line ( $IC_{50}$  (24h) =  $37.1 \pm 4.4$  and  $34.7 \pm 9.2$   $\mu$ mol/L for **SnPd<sub>12</sub>** and **PbPd<sub>12</sub>**, respectively) [6].

## CONCLUSION

The discrete, anionic, all-inorganic POPs, **SnPd<sub>12</sub>** and **PbPd<sub>12</sub>**, inhibited SPM E-NTPDase activity in a concentration-dependent manner within the range  $2 \times 10^{-7}$  -  $2 \times 10^{-4}$  mol/L, with similar inhibitory strength. Moreover, both POPs induced similar antileukemic effects against human acute promyelocytic cell line HL-60 [6]. Accordingly, the confirmed antileukemic activities might be associated with E-NTPDase inhibition, and E-NTPDases should be considered in further research as a potential target of the antileukemic action of these promising drug candidates.

## Acknowledgement

This research was funded by the Ministry of Education, Science and Technological Development of the Republic of Serbia (contract no. 451-03-9/2021-14/200017). The authors also gratefully

acknowledge the bilateral project Serbia-Germany (no. 451-03-01038/2015-09/16, DAAD-PPP) and the CMST COST Action CM1203 (PoCheMoN). Figure 1 was generated with Diamond, version 3.2 (Crystal Impact GbR).

## REFERENCES

- [1] Izarova, N.V.; Pope, M.T.; Kortz, U. Noble metals in polyoxometalates. *Angew. Chem. Int. Edit.*, **2012**, *51*(38), 9492–9510.
- [2] Čolović, M.B.; Lacković, M.; Lalatović, J.; Mougharbel, A.S.; Kortz, U.; Krstić, D. Polyoxometalates in biomedicine: update and overview. *Curr. Med. Chem.*, **2020**, *27*, 362–379.
- [3] Alam, M.N.; Huq, F. Comprehensive review on tumour active palladium compounds and structure–activity relationships. *Coord. Chem. Rev.*, **2016**, *316*, 36–67.
- [4] Stephan, H.; Kubeil, M.; Emmerling, F.; Müller, C.E. Polyoxometalates as versatile enzyme inhibitors. *Eur. J. Inorg. Chem.*, **2013**, *10*(11), 1585–1594.
- [5] Čolović, M.; Bajuk-Bogdanović, D.; Avramović, N.; Holclajtner-Antunović, I.; Bošnjaković-Pavlović, N.; Vasić, V.; Krstić, D. Inhibition of rat synaptic membrane  $\text{Na}^+/\text{K}^+$ -ATPase and ectonucleoside triphosphate diphosphohydrolases by 12-tungstosilicic and 12-tungstophosphoric acid. *Bioorgan. Med. Chem.*, **2011**, *19*(23), 7063–7069.
- [6] Yang, P.; Ma, T.; Lang, Z.; Misirlic-Dencic, S.; Isakovic, A.M.; Bényei, A.; Čolović, M.B.; Markovic, I.; Krstić, D.Z.; Poblet, J.M.; Lin, Z.; Kortz, U. Tetravalent metal ion guests in polyoxopalladate chemistry: synthesis and anticancer activity of  $[\text{MO}_8\text{Pd}_{12}(\text{PO}_4)_8]^{12-}$  ( $\text{M} = \text{Sn}^{\text{IV}}$ ,  $\text{Pb}^{\text{IV}}$ ). *Inorg. Chem.*, **2019**, *58*(17), 11294–11299.
- [7] Cohen, R.S.; Blomberg, F.; Berzins, K.; Siekevits, P.J. The structure of postsynaptic densities isolated from dog cerebral cortex. *Cell Biol.*, **1977**, *74*, 181–203.
- [8] Towle, A.C.; Sze, P.Y.J. Steroid binding to synaptic plasma membrane differential binding of glucocorticoid and gonadal steroids. *Steroid Biochem.*, **1983**, *18*, 135–143.
- [9] Krstić, D.; Čolović, M.; Bošnjaković-Pavlović, N.; Spasojević-de Bire, A.; Vasić, V. Influence of decavanadate on rat synaptic plasma membrane ATPases activity. *Gen. Physiol. Biophys.*, **2009**, *28*, 302–308.
- [10] Sahoo, A.; Samanta, L.; Das, A.; Patra, K.S.; Chainy, B.N.G. Hexachlorocyclohexane-induced behavioural and neurochemical changes in rat. *J. Appl. Toxicol.*, **1999**, *19*, 13–18.
- [11] Čolović, M.; Krstić, D.; Petrović, S.; Leskovac, A.; Joksić, G.; Savić, J.; Franko, M.; Trebše, P.; Vasić, V. Toxic effects of diazinon and its photodegradation products. *Toxicol. Lett.*, **2010**, *193*, 9–18.

## CYTOGENOTOXICITY ASSESSMENT OF POLYOXOPALLADATES(II) AS PROMISING ANTILEUKEMIC DRUG CANDIDATES

M. B. Čolović<sup>1</sup>, G. Gajski<sup>2</sup>, M. Gerić<sup>2</sup>, T. Ma<sup>3</sup>, X. Ma<sup>3</sup>, U. Kortz<sup>3</sup> and D. Z. Krstić<sup>4</sup>

<sup>1</sup>Department of Physical Chemistry, "Vinča" Institute of Nuclear Sciences-National Institute of the Republic of Serbia, University of Belgrade, Serbia ([colovicm@vin.bg.ac.rs](mailto:colovicm@vin.bg.ac.rs))

<sup>2</sup>Institute for Medical Research and Occupational Health, Zagreb, Croatia

<sup>3</sup>Department of Life Sciences and Chemistry, Jacobs University, Bremen, Germany

<sup>4</sup>Institute of Medical Chemistry, Faculty of Medicine, University of Belgrade, Serbia

### ABSTRACT

Polyoxopalladates(II) (POPs) are discrete, anionic palladium(II)-oxo nanoclusters that possess features of both conventional polyoxometalates (POMs) and palladium(II), which were shown to exhibit promising antitumor properties. In this study, *in vitro* cyto- and genotoxicity evaluation was performed on normal non-target human blood cells using two isostructural POPs with tetravalent metal ions (Sn<sup>IV</sup>, Pb<sup>IV</sup>) encapsulated in the cuboid Pd<sub>12</sub>-oxo host, Na<sub>12</sub>[SnO<sub>8</sub>Pd<sub>12</sub>(PO<sub>4</sub>)<sub>8</sub>]·43H<sub>2</sub>O (**SnPd<sub>12</sub>**) and Na<sub>12</sub>[PbO<sub>8</sub>Pd<sub>12</sub>(PO<sub>4</sub>)<sub>8</sub>]·38H<sub>2</sub>O (**PbPd<sub>12</sub>**), with confirmed *in vitro* antileukemic actions against HL-60 cell line. For this purpose, whole blood samples were exposed to the POPs, at concentrations of  $\approx$  IC<sub>50</sub> (24 h) values, resulting in cytotoxicity in HL-60 cells for 24 h at 37 °C. The cytotoxicity studies were performed on human peripheral blood mononuclear cells which were stained with acridine orange and ethidium bromide, and then viewed under a fluorescence microscope. The genotoxicity was tested in whole blood by the alkaline comet assay (microgel electrophoresis). The results of the cytotoxicity evaluation and the comet assay demonstrated that none of the tested POPs, within the investigated concentration range 12.5 – 50  $\mu$ M, resulted in a statistically significant modulation of blood cell viability as well as DNA damage, expressed as % of tail DNA (relative increase of tail DNA), compared to the untreated controls. Therefore, the promising antileukemic drug candidates, **SnPd<sub>12</sub>** and **PbPd<sub>12</sub>**, can be considered as selective and safe from a cytogenotoxicity point of view.

### INTRODUCTION

Numerous palladium(II) complexes have been synthesized and tested against various tumor cells *in vitro* and *in vivo* in order to find an appropriate alternative to platinum(II)-based antitumor drugs as most frequently prescribed chemotherapeutics [1]. Polyoxopalladates (POPs) are another group of palladium(II)-based compounds, which are discrete, anionic palladium-oxo clusters and hence belong to the class of polyoxometalates (POMs)[2]. POMs were also reported to exhibit different biological activities including significant cytotoxic action against various types of malignant cells *in vitro* and *in vivo* [3]. However, toxicity studies revealed adverse effects after *in vivo* POM application, which could limit their potential application in biomedicine [4].

Taking into account that the development of novel drugs requires an assessment of their safety, the aim of this study was to evaluate the cytogenotoxicity of two POPs containing tetravalent metal ion guests (Sn<sup>IV</sup> and Pb<sup>IV</sup>), Na<sub>12</sub>[SnO<sub>8</sub>Pd<sub>12</sub>(PO<sub>4</sub>)<sub>8</sub>]·43H<sub>2</sub>O (**SnPd<sub>12</sub>**) and Na<sub>12</sub>[PbO<sub>8</sub>Pd<sub>12</sub>(PO<sub>4</sub>)<sub>8</sub>]·38H<sub>2</sub>O (**PbPd<sub>12</sub>**) (Figure 1), towards normal non-target cells by employing cell viability and the comet assays on human peripheral blood cells (HPBCs). **SnPd<sub>12</sub>** and **PbPd<sub>12</sub>** were reported in our previous study [5] to exhibit cytotoxicity against human acute promyelocytic cell line HL-60 (IC<sub>50</sub> (24h) = 37.1  $\pm$  4.4 and 34.7  $\pm$  9.2  $\mu$ M for **SnPd<sub>12</sub>** and **PbPd<sub>12</sub>**, respectively), and can therefore be regarded as potential antileukemic metallodrugs.

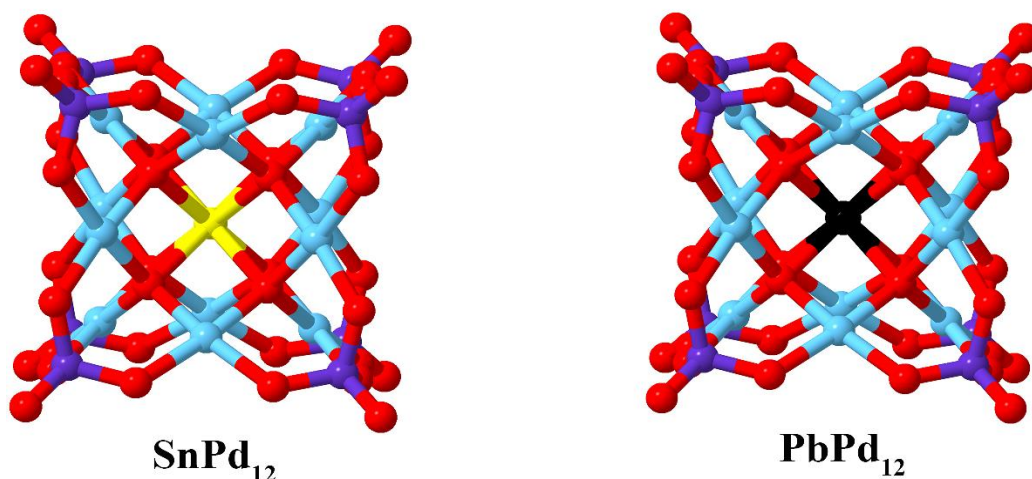


**Figure 1.** Structure of the investigated POPs **SnPd<sub>12</sub>** and **PbPd<sub>12</sub>**. Color codes: light blue, Pd; yellow, Sn; black, Pb; violet, P and red, O.

## EXPERIMENTAL

**SnPd<sub>12</sub>** and **PbPd<sub>12</sub>** were prepared according to the published procedures [5]. The cytotoxicity of the POPs in peripheral blood mononuclear cells (PBMCs) was determined by differential staining with acridine orange and ethidium bromide and by fluorescence microscopy [6]. Briefly, whole blood samples obtained from a healthy female donor were treated with the POPs, and then incubated at 37 °C for 24 h. The PBMCs were isolated by the histopaque density gradient centrifugation method, and the slides were prepared using 200 µL of PBMCs and 2 µL of stain (acridine orange and ethidium bromide). A total of 100 cells per repetition were examined with an epifluorescence microscope (Olympus BX51, Tokyo, Japan). The cells were divided in two categories: live cells with a functional membrane and with uniform green staining of the nucleus and dead cells with uniform red staining of the nucleus. Alkaline comet assay for genotoxicity evaluation was essentially carried out as described by Singh *et al.* [7]. After the exposure to different POP concentrations for 24 h, 5 µL of whole blood was embedded into an agarose matrix and subsequently lysed (2.5 M NaCl, 100 mM EDTANa<sub>2</sub>, 10 mM Tris, 1% sodium sarcosinate, 1% Triton X-100, 10% DMSO, pH 10) overnight at 4 °C. After the lysis, the slides were placed into an alkaline solution (300 mM NaOH, 1 mM EDTANa<sub>2</sub>, pH 13) for 20 min at 4 °C to allow DNA unwinding and subsequently electrophoresed for 20 min at 1 V/cm. Finally, the slides were neutralized in 0.4 M Tris buffer (pH 7.5) for 5 min 3 times, stained with ethidium bromide (10 µg/mL) and analyzed at 250× magnification using an epifluorescence microscope (Zeiss, Göttingen, Germany) connected through a camera to an image analysis system (Comet Assay II; Perceptive Instruments Ltd., Haverhill, Suffolk, UK). One hundred randomly captured comets from each slide were examined.

## RESULTS AND DISCUSSION

For the cytogenotoxicity evaluation of **SnPd<sub>12</sub>** and **PbPd<sub>12</sub>** whole blood samples were treated with three different POP concentrations (12.5, 25, and 50 µM) inducing cytotoxic effects against HL-60 cells during 24 h treatment [5].

The effect of **SnPd<sub>12</sub>** and **PbPd<sub>12</sub>** on the viability in human PBMCs after 24 h exposure is presented in Figure 2. It can be seen that the cell viability, expressed as a percentage of untreated control, was not significantly affected with respect to the corresponding control at all investigated concentrations for both POPs. Even the highest concentration applied (50 µM  $\approx$  1.5 × IC<sub>50</sub>(24 h) for HL-60) did not result in cytotoxic action.

The degree of DNA damage, a genotoxicity indicator expressed as % of tail DNA, dependent on **SnPd**<sub>12</sub> and **PbPd**<sub>12</sub> concentrations is presented in Figure 3. Similar to cytotoxicity, no statistically significant difference in the amount of DNA strand breaks compared to the corresponding control samples was observed for both **SnPd**<sub>12</sub> and **PbPd**<sub>12</sub>, regardless of the concentrations tested.

Since both **SnPd**<sub>12</sub> and **PbPd**<sub>12</sub> did not induce cytogenotoxic effect on normal non-target HPBCs at the concentrations ( $\approx$  IC<sub>50</sub> values) inducing considerable antileukemic effects, they should be considered in further research as promising, low toxic, and selective antileukemic drug candidates.

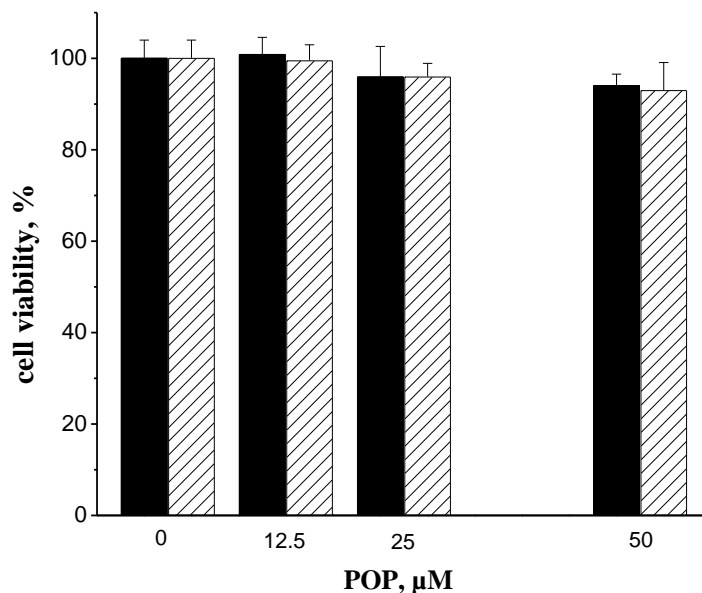


**Figure 2.** The effects of **SnPd**<sub>12</sub> (solid symbol) and **PbPd**<sub>12</sub> (sparse pattern) on the viability in human peripheral blood mononuclear cells (PBMCs) after 24 h treatment. \*Statistically significant compared to the corresponding control ( $p < 0.05$ ).

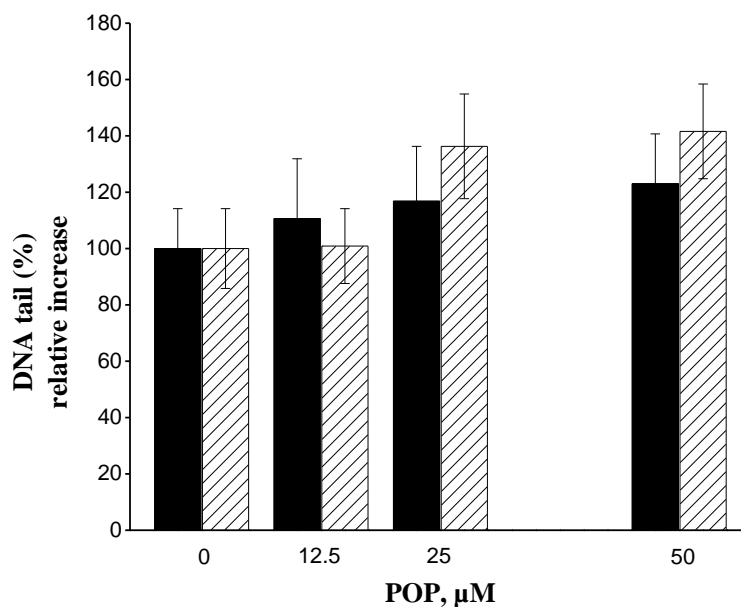


**Figure 3.** The effects of **SnPd**<sub>12</sub> (solid symbol) and **PbPd**<sub>12</sub> (sparse pattern) on DNA damage in human peripheral blood cells (HPBCs) after 24 h treatment. \*Statistically significant compared to the corresponding control ( $p < 0.05$ ).

## CONCLUSION

The obtained cytotoxicity results indicated that neither **SnPd<sub>12</sub>** nor **PbPd<sub>12</sub>**, within the concentration range 12.5 – 50  $\mu\text{M}$ , induced statistically significant alterations of cell viability compared to the control. Moreover, the results of the comet assay showed that none of the tested POPs at concentrations  $\leq 50 \mu\text{M}$  resulted in a statistically significant relative increase of tail DNA. Accordingly, both **SnPd<sub>12</sub>** and **PbPd<sub>12</sub>** could be considered as promising, selective, and safe antileukemic drug candidates from a cytogenotoxicity point of view.

## Acknowledgement

This research was funded by the Ministry of Education, Science and Technological Development of the Republic of Serbia (contract no. 451-03-9/2021-14/200017) and the Institute for Medical Research and Occupational Health, Zagreb, Croatia. The authors also gratefully acknowledge the bilateral project Serbia-Germany (no. 451-03-01038/2015-09/16, DAAD-PPP) the CMST COST Action CM1203 (PoCheMoN), the bilateral project Serbia-Croatia (no. 337-00-205/2019-09/19), and the COST Action CA16113 (CliniMARK). Figure 1 was generated with Diamond, version 3.2 (Crystal Impact GbR).

## REFERENCES

- [1] Alam, M.N.; Huq, F. Comprehensive review on tumour active palladium compounds and structure–activity relationships. *Coord. Chem. Rev.*, **2016**, *316*, 36–67.
- [2] Izarova, N.V.; Pope, M.T.; Kortz, U. Noble metals in polyoxometalates. *Angew. Chem. Int. Edit.*, **2012**, *51*(38), 9492–9510.
- [3] Čolović, M.B.; Lacković, M.; Lalatović, J.; Mougharbel, A.S.; Kortz, U.; Krstić, D. Polyoxometalates in biomedicine: update and overview. *Curr. Med. Chem.*, **2020**, *27*, 362–379.
- [4] Čolović, M.B.; Medić, B.; Četković, M.; Kravić Stevović, T.; Stojanović, M.; Ayass, W.W.; Mougharbel, A.S.; Radenković, M.; Prostran, M.; Kortz, U.; Krstić, Z. Toxicity evaluation of two polyoxotungstates with anti-acetylcholinesterase activity. *Toxicol. Appl. Pharm.*, **2017**, *333*, 68–75.
- [5] Yang, P.; Ma, T.; Lang, Z.; Misirlic-Dencic, S.; Isakovic, A.M.; Bényei, A.; Čolović, M.B.; Markovic, I.; Krstić, D.Z.; Poblet, J.M.; Lin, Z.; Kortz, U. Tetravalent metal ion guests in polyoxopalladate chemistry: synthesis and anticancer activity of  $[\text{MO}_8\text{Pd}_{12}(\text{PO}_4)_8]^{12-}$  ( $\text{M} = \text{Sn}^{\text{IV}}$ ,  $\text{Pb}^{\text{IV}}$ ). *Inorg. Chem.*, **2019**, *58*(17), 11294–11299.
- [6] Atale, N.; Gupta, S.; Yadav, U.; Rani, V. Cell-death assessment by fluorescent and nonfluorescent cytosolic and nuclear staining techniques. *Microscopy-JPN*, **2014**, *255*(1), 7–19.
- [7] Singh, NP.; McCoy, M.T.; Tice, R.R.; Schneider, E.L. A simple technique for quantitation of low levels of DNA damage in individual cells. *Exp. Cell. Res.*, **1988**, *175*(1), 184–191.

## SILVER DODECATUNGSTOPHOSPHATE/BEA ZEOLITE ADSORBENTS FOR PESTICIDE REMOVAL

D. Janićijević<sup>1</sup>, A. Jevremović<sup>1</sup>, B. Nedić Vasiljević<sup>1</sup>, S. Uskoković-Marković<sup>2</sup>,  
M. Milojević-Rakić<sup>1</sup> and D. Bajuk-Bogdanović<sup>1</sup>

<sup>1</sup>University of Belgrade-Faculty of Physical Chemistry, 11000 Belgrade, Serbia.  
(anka@ffh.bg.ac.rs)

<sup>2</sup>University of Belgrade-Faculty of Pharmacy, 1100 Belgrade, Serbia.

### ABSTRACT

Composite materials consisting of the silver salt of dodecatungstophosphoric acid and BEA zeolite are developed in order to obtain material with material of superior adsorption properties for pesticide removal from water. A two-step impregnation with variable constituent mass ratios was employed as a synthesis procedure. Composites are investigated by Fourier-transform Infrared (FTIR) spectroscopy, and results are compared with their adsorption capacities for glyphosate herbicide. A spectroscopic analysis reports the interaction of the BEA zeolite network with the silver salt of tungstophosphoric acid with evenly distributed adsorption sites in the investigated composites. The amount of glyphosate removed from water suspension was 243 mg/g of composite material.

### INTRODUCTION

Glyphosate, N-(phosphonomethyl) glycine, is one of the most widely used herbicides in the world. Glyphosate is often in the public spotlight due to its potential carcinogenic effects. However, as a total herbicide for the control of rhizome weeds, as well as annual and perennial grass and broadleaf weeds on agricultural sites, glyphosate is increasingly present in the environment. The possibility of remediation of soil and water by continuous removal of pesticide residues is often in the focus of materials design for pollutant removal. Zeolites are one of the most promising host materials for association with various active constituents as they are a family of highly ordered systems with pores, which, along with high specific surface and negatively charged framework, enable the introduction of metal cations. Excellent adsorption and catalytic properties have previously been established for BEA zeotype comprising hybrid materials [1]. Particular emphasis is placed on heteropoly acids and their salts used as the active phase [2]. Additional improvement can be achieved by the introduction of silver ions, as it previously enabled improvement in antimicrobial [3] and catalytic [4] performance in addition to superior adsorption properties. Composites consisting of BEA zeolite and silver salt tungstophosphoric acid (AgWPA) are prepared by a two-step impregnation method and investigated by infrared spectroscopy. This report is, to the best of our knowledge, the first contribution of BEA/AgWPA composites for glyphosate removal.

### METHODS

BEA Zeolite (Si/Al = 12.5) was purchased from Zeolyst International and transformed to the HBEA form. Dodeca-tungstophosphoric acid, WPA, was synthesized according the procedure described in the literature [5]. A WPA silver salt (AgWPA) was prepared *in situ* on zeolite by the two-step impregnation method. The detailed sample preparation procedure was given previously [3,4]. In essence, three suspensions, in a total volume of 40 mL, comprised 1 g of HBEA, and appropriate amounts of silver-nitrate and WPA calculated to obtain the intended mass % AgWPA relative to the mass of the zeolite (10, 25 and 50 %). The prepared composites are denoted as B/AgWPA-1, B/AgWPA-2 and B/AgWPA-3. The Fourier-transform Infrared (FTIR) spectra of samples were

recorded with an iS20, Nicolet spectrometer (Thermo Scientific), in the range from 4000 to 400  $\text{cm}^{-1}$  with 2  $\text{cm}^{-1}$  resolution employing KBr pellet technique.

Adsorption of glyphosate on B/AgWPA composites was recorded in a batch system that comprised 5 mL of glyphosate standards (0.1–4.0 g/L) and 10 mg of composite samples. The amount of glyphosate present in equilibrium is measured by a Bischoff high-performance liquid chromatography (HPLC) system. The stationary phase was a Partisil SAX column (Whatman, Inc). The glyphosate determination was performed at 200 nm using UV/VIS Lambda 1010 detector. The mobile phase was phosphate buffer: methanol (96:4, pH = 1.9) and was pumped at a flow rate of 2.3 mL/min. The nonlinear fit of adsorption data was performed in the Python 3.9 programming language.

## RESULTS AND DISCUSSION

Fig. 1 shows B/AgWPA composites spectra, as well as the spectra of bulk AgWPA and BEA, given for comparison. Samples B/AgWPA-1 and B/AgWPA-2 express matching spectra with a broad band at 962  $\text{cm}^{-1}$  with a shoulder at 947  $\text{cm}^{-1}$  and a very weak one at 900  $\text{cm}^{-1}$ . Compared to the AgWPA spectra, the  $\text{W}=\text{O}_d$  band is broad and red-shifted while the  $\text{W}-\text{O}_b-\text{W}$  band is blue-shifted with diminished intensity. This means that the Keggin anion distortion is due to the interaction between Keggin oxygens and H/Ag on the zeolite surface. The B/AgWPA-3 spectrum, with the highest salt content, is different from the other two composites, which indicates the existence of AgWPA agglomerates. Possible interaction of the AgWPA and zeolite framework is hydrogen bonding in which the Keggin anion has a distorting effect owing to the interaction between its oxygen atoms and H/Ag, on the zeolite surface [3].

The Langmuir, Freundlich and Langmuir–Freundlich isotherm models are typically used to fit the equilibrium sorption data. However, in the case of pollutants adsorption, an increasing number of studies consider S-shaped isotherms [6]. Modelling adsorption data, therefore, requires equations with flexible parameters, such as the recently re-applied Krishnamurti isotherm [7]. The binding of adsorbate molecules on a support is based on a cooperative adsorption model when already adsorbed molecules facilitate the successive binding of new molecules in adjacent positions [6]. An isotherm is given as three parameter equation  $q=N_0/(1+k_1 \cdot \exp(-k_2 \cdot C))$  where  $q$  is concentration of the adsorbed phase and  $N_0$  is a total number of molecules that can be adsorbed per unit mass of adsorbent, while  $C$  is equilibrium concentration.

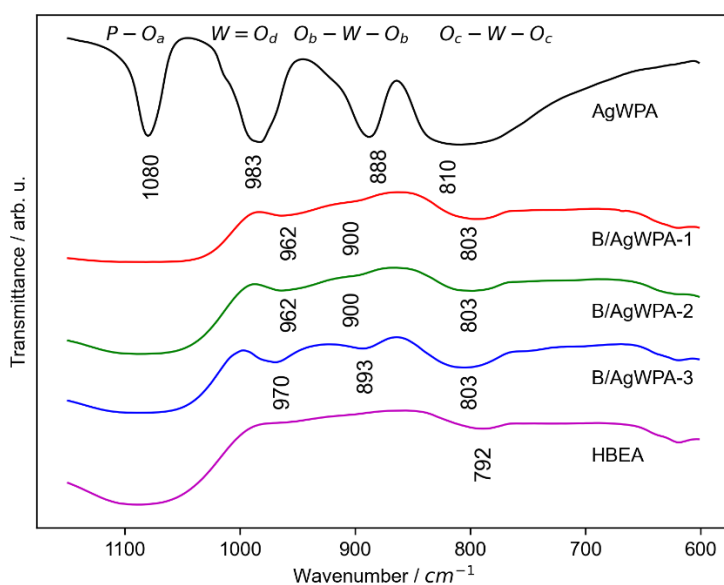


**Figure 1.** FTIR spectra of B/AgWPA composites, HBEA zeolite and bulk AgWPA

Application of the original Krishnamurti isotherm on adsorption data modelling is given in Fig. 2. Fitting results have good correlation coefficients,  $R^2$  values being in the range 0.976 - 0.999. Comparing the influence of the amount of AgWPA active phase on the adsorption capacity in composite materials, greater efficiency in pesticide removal is obtained with increasing AgWPA content, as the lowest value was found for starting zeolite (114.3 mg/g). The highest amount of glyphosate adsorbed was detected for the B/AgWPA-2 sample - 243 mg/g of composite (of the projected 260 per fitting parameter  $N_0$ ), which is the highest amount we were able to achieve in our adsorption studies on various designed hybrid materials. For the high efficiency of this type of functionalized materials, both components must have centers active in adsorption.

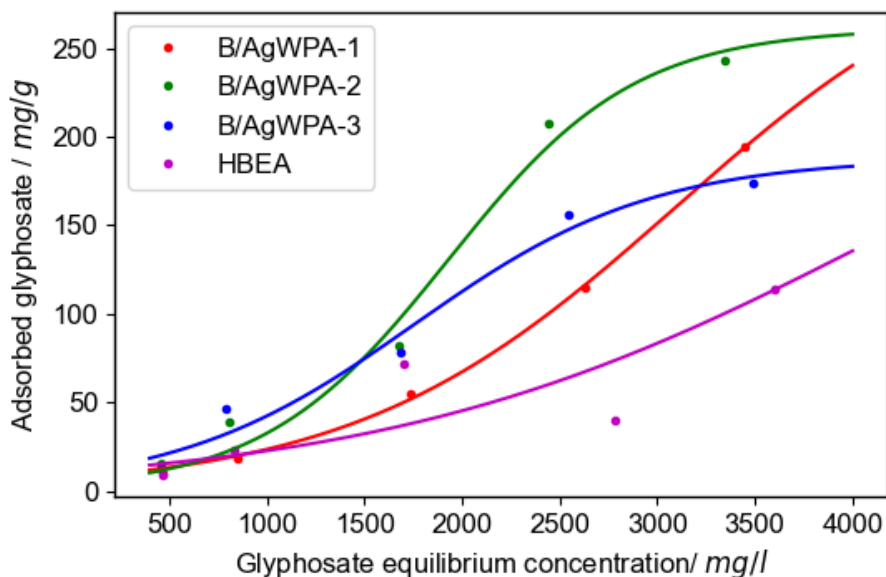


**Figure 2.** Adsorption isotherms of B/AgWPA composites and starting HBEA zeolite.

## CONCLUSION

Advanced composites of BEA zeolite and silver tungstophosphate were synthesized with three mass ratios of zeolite and AgWPA by two-step impregnation. The highest activity for glyphosate removal was found for the sample with 25 % AgWPA content. This synthesis method enables the efficient formation of AgWPA at the zeolite surface, without agglomeration, which assists in testing for application in the removal of water pollutants from the environment.

## Acknowledgement

This work was supported by the Ministry of Education, Science and Technological Development of the Republic of Serbia (Grants no. 451-03-9/2021-14/200146 and 451-03-9/2021-14/200161).

## REFERENCES

- [1] A. Jevremović, P. Bober, M. Mičušík, J. Kuliček, U. Acharya, J. Pflieger, M. Milojević-Rakić, D. Krajišnik, M. Trchová, J. Stejskal and G. Ćirić-Marjanović, *Microporous Mesoporous Mater.*, 2019, 287, 234–245.
- [2] B. Nedić Vasiljević, M. Obradović, D. Bajuk-Bogdanović, M. Milojević-Rakić, Z. Jovanović, N. Gavrilov and I. Holclajtner-Antunović, *J. Environ. Sci.*, 2019, 81, 136–147.

- 
- [3] D. Jančićević, S. Uskoković-Marković, D. Ranković, M. Milenković, A. Jevremović, B. Nedić Vasiljević, M. Milojević-Rakić and D. Bajuk-Bogdanović, *Sci. Total Environ.*, 2020, 735, 139530.
- [4] D. Jančićević, S. Uskoković-Marković, A. Popa, B. Nedić Vasiljević, A. Jevremović, M. Milojević-Rakić and D. Bajuk-Bogdanović, *Chem. Pap.*, 2021, 75, 3169–3180.
- [5] M. De Oliveira, U. P. Rodrigues-Filho and J. Schneider, *J. Phys. Chem. C*, 2014, 118, 11573–11583.
- [6] K. Krishnamurti, *Proc. Indian Acad. Sci. - Sect. A*, 1951, 33, 92–96.
- [7] K. H. Chu, *Sep. Purif. Technol.*, 2021, 259, 118079.

## IRON MODIFIED Y AND ZSM ZEOLITES AS PERSPECTIVE ECOFRIENDLY ADSORBENTS

A. Jevremović, A. Stanojković, B. Nedić Vasiljević M. Milojević-Rakić

*University of Belgrade-Faculty of Physical Chemistry, 11000 Belgrade, Serbia.  
(anka@ffh.bg.ac.rs)*

### ABSTRACT

This study investigated Y and ZSM-5 zeolites, important materials for a large number of different adsorption processes, modified with iron through an aqueous ion-exchange method, using dilute solutions of ferric citrate and ferrous oxalate. An Atomic Force Microscopy was employed for the analysis of zeolite microcrystalline surfaces. Acetamiprid, a neonicotinoid insecticide was chosen as a pollutant due to its extreme toxicity to bees and the negative impact on the environment. Characterization of material showed that crystal structure both zeolites is well defined and remained unchanged after the modification. Removal of acetamiprid from the water solution reached its maximum of 100 mg/g with Y citrate- and oxalate- modified samples, while citrate-modified ZSM-5 sample had the highest adsorbed amount of 38 mg/g.

### INTRODUCTION

Due to the globally increase in food production, mass use of pesticides has led to significant consequences, not only on public health, but also on the nutritional quality of food. Improper application of pesticides affects the entire ecosystem, they reach the food chain, polluting the soil, air and surface water. Increasingly, humans acute exposure to pesticides has been linked to a wide range of immunosuppression, the development of allergies and autoimmune diseases [1,2]. In addition to various techniques, adsorption is the most widespread technique for removal of different pollutants, as it is simple and efficient in the purification of surface and wastewaters. Porous zeolite-based materials have adopted their large specific surfaces, high levels of adsorption as well as low initial prices, and are good candidates for efficient adsorbents of ions and organic matter [3]. The numerous studies showed that oxidation processes are effective for the degradation of organic compounds, including pesticides. Heterogeneous Fenton oxidation, for example iron species immobilized on solid supports such as zeolites, is one of the most appealing oxidation processes owing to the utilization of environmental friendly reagents ( $\text{Fe}^{2+}$  and  $\text{H}_2\text{O}_2$ ) [4]. Bearing in mind that adsorption is the first step of any heterogeneous catalytic process, we examined the adsorption capacity of the synthesized iron modified zeolite.

Acetamiprid, a neonicotinoid insecticide works as a selective participant for the nicotinic acetylcholine receptors in insects. Previously, acetamiprid removal was investigated on surfactant functionalized zeolites, before and after tannic acid adsorption [5].

As far as we know, this is the first time to test adsorption this pesticide on iron modified zeolite .

### METHODS

FAU ( $\text{SiO}_2/\text{Al}_2\text{O}_3=5.2$ ) and ZSM-5 ( $\text{SiO}_2/\text{Al}_2\text{O}_3=23$ ) were purchased from *Zeolyst International*, ferric citrate and ferrous oxalate were purchased from *Sigma Aldrich* and acetamiprid (99 %) was obtained from *Chemical Agrosava*. Solutions of ferric citrate or ferrous oxalate were made as follows: 2 g of ferric citrate or ferrous oxalate were mixed with 2 L of water, and heated for several hours until dissolved. 10 g of zeolites was suspended in 0.7 L of the ferric citrate/ferrous oxalate solutions. Samples were stirred for 7 days at room temperature. Thereafter, the samples were filtered, washed with water and dried at 110 °C for 2 h. AFM tapping-mode images were obtained on a NTEGRA

Prima microscope (NT–MDT Spectrum Instruments, Russian Federation). A small amount of zeolite sample was dispersed in the water at room temperature and left to air–dry to a thin layer. An aluminium-coated N–type doped silicon AFM probe (NT–MDT) with a force constant of 3,5 N/m and the resonant frequency of 75 kHz was used. All images were obtained using the Nova Px program with the integrated ScanT™ module. An evaluation was performed using the P9 Data Processing software for image analysis. Adsorption of acetamiprid on zeolites was carried out by shaking 50 mg in 5 ml of acetamiprid standards (0.1–1.0 g/L) at room temperature for 1 h. Samples were centrifuged (5 min, 13.4 rpm) and the concentrations of acetamiprid was determined using by Bischoff high-performance liquid chromatography (HPLC) system. The stationary phase was Pronto SIL C18 AQ PLUS column (Whatman, Inc.). The acetamiprid determination was performed at 250 nm using UV/VIS Lambda 1010 detector. The mobile phase was a mixture of water/acetonitrile (50:50, in a volume ratio).

## RESULTS AND DISCUSSION

In Figure 1, AFM micrographs of Y zeolite and Fe-citrate forms of Y and ZSM-5 zeolite are shown. Crystal faces, edges and small crystal fragments are clearly visible. The sharpness of the crystal structure remained unchanged after the modification with iron ions. The surface structures can vary and has a different size which can reach hundreds of nanometers, combined with areas with different surface shapes. In Figure 2, the percentage of adsorbed pesticide as a function of the concentration of standard is presented for Y and ZSM-5 zeolites and their modified forms (citrate forms FeC-Y and FeC-ZSM, oxalate forms FeO-Y and FeO-ZSM). As it can be seen, Y samples adsorbed the complete pesticide content (100 mg/g), in a 1 h period.

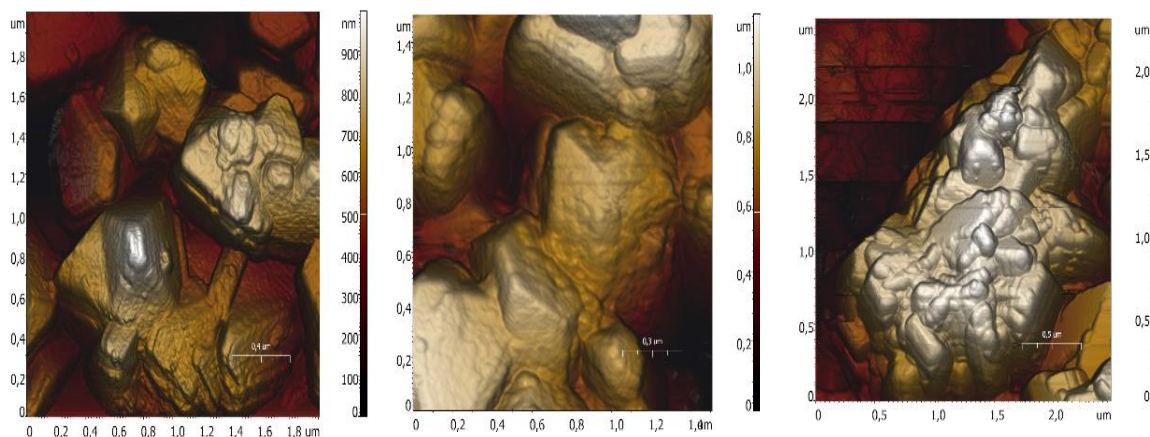


**Figure 1.** AFM micrographs FeC-Y (left), Y (in the middle) and FeC-ZSM (right)

Compared to Y samples, in the ZSM-5 series, the modified forms showed higher adsorption capacity than the zeolite itself, where FeC-ZSM showed the highest adsorbed amount of pesticide, 38 mg/g. The Fe introduction in zeolites leads to adverse effect, for Y zeolite, the presence of metal cation did not lead to adsorption improvement although the acetamiprid was retained by zeolite in a substantial amount. Further increase in concentration may lead to observable differences.

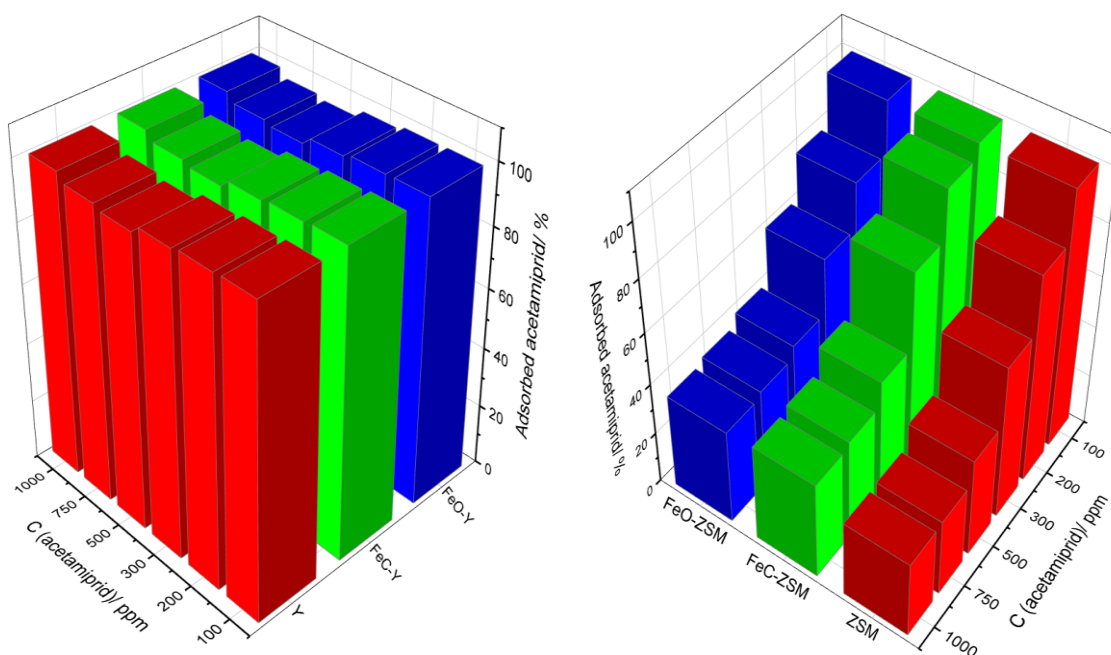


**Figure 2.** The percent of adsorbed acetamiprid onto Y samples (left) and ZSM-5 samples (right)

## CONCLUSION

Y and ZSM-5 zeolites were modified with ferric citrate and ferrous oxalate using an ion-exchange method and proved to be good candidates for the removal of the pesticide acetamiprid. For the first time, investigated materials were characterized with Atomic Force Microscopy. The zeolite modification by introducing Fe into extra-framework zeolite positions, in the case of Y zeolite, did not lead to an observable effect on adsorption sites in relation to the starting zeolite. On the other hand, in the ZSM-5 series, a significant influence of the synthesis method on the adsorption properties was observed. The presence of Fe in zeolite samples allows further removal of acetamiprid pesticide by catalytic decomposition in the presence of hydrogen peroxide.

## Acknowledgement

This work was supported by the Ministry of Education, Science and Technological Development of the Republic of Serbia (Grants no. 451-03-9/2021-14/200146).

## REFERENCES

- [1] A. Hedstrom, Ion exchange of ammonium in zeolites: a literature review, *Journal of Environmental Engineering: ASCE* **127** (2001) 673–681.
- [2] S.B. Wang, H.W. Wu, Environmental-benign utilization of fly ash as low-cost adsorbents, *Journal of Hazardous Materials*, **136** (2006), 482–501.
- [3] S. Wang, Y. Peng, Natural zeolites as effective adsorbents in water and wastewater treatment, *Chemical Engineering Journal*, **156** (2010) 11–24.
- [4] M. Milojević-Rakić, D. Bajuk-Bogdanović, B. Nedić Vasiljević, A. Rakić, S. Škrivanj, Lj. Ignjatović, V. Dondur, S. Mentus, G. Ćirić-Marjanović, Polyaniline/FeZSM-5 composites- Synthesis, characterization and their high catalytic activity for the oxidative degradation of herbicide glyphosate, *Microporous & Mesoporous Materials* **267** (2018) 68–79.
- [5] A. Jevremović, N. Božinović, D. Arsenijević, S. Marmakov, B. Nedić Vasiljević, S. Uskoković-Marković, D. Bajuk-Bogdanović, M. Milojević-Rakić, Modulation of cytotoxicity by consecutive

adsorption of tannic acid and pesticide on surfactant functionalized zeolites, *Environmental Science: Processes & Impacts*, **22** (2020), 2199-2211.

## SWELLING BEHAVIOR OF Ag-POLY(NiPAAm/IA) HYDROGEL NANOCOMPOSITES: INFLUENCE OF TEMPERATURE AND pH

J. Spasojević, A. Radosavljević, N. Nikolić and Z. Kačarević-Popović

*Vinča Institute of Nuclear Sciences - National Institute of the Republic of Serbia, University of Belgrade, Mike Petrovića Alasa 12-14, 11351 Vinča, Belgrade, Serbia (jelenas@vin.bg.ac.rs)*

### ABSTRACT

In this work, swelling behavior of dual responsive Ag-poly(NiPAAm/IA) hydrogel nanocomposites, obtained by  $\gamma$ -irradiation induced synthesis, was investigated. Poly(NiPAAm/IA) hydrogels belong to the class of smart materials with thermo- and pH-sensitivity. Accordingly, swelling behavior was examined at two temperatures (25°C and 37°C) in three buffer solutions (pH 2.2; 4.5 and 6.8). Swelling and diffusion properties of investigated hydrogels were affected by polymer matrices composition, presence of AgNPs and environmental factors, such as temperature and pH of swelling media.

### INTRODUCTION

In the past decade, development of polymer-based smart materials, that can autonomously change their physical and/or chemical properties when exposed to external stimuli, is one of the fastest growing areas in materials sciences. The gel 3D structure, porosity, swelling behavior and stability, makes hydrogels suitable for many applications [1].

A special class of hydrogels shows an active and significant response to small changes in the surrounding environment, and they are called stimuli responsive or intelligent materials. Among them, thermo- and pH-sensitive polymers are the most frequently studied. Poly(N-isopropylacrylamide), (PNiPAAm), is one of the most investigated thermo-sensitive polymer with a sharp lower critical solution temperature (LCST) at around 32°C, which can be adjusted by addition of hydrophilic ionic comonomers, such as itaconic acid (IA). In this case, the thermo-sensitivity of PNiPAAm-based hydrogels can be controlled by pH value of the external media [2].

On the other side, silver nanoparticles (AgNPs) possess antimicrobial activity and have found many applications in field of medicine and pharmaceuticals, due to their capability to release silver ions in a controlled manner. Incorporation of AgNPs into crosslinked polymer matrix represents a promising solution for stabilization and distribution problem, which limit their usage [3].

The aim of this work is to investigate the swelling behavior of Ag-poly(NiPAAm/IA) hydrogel nanocomposites, obtained by  $\gamma$ -irradiation induced synthesis. The swelling properties were examined at two temperatures (25°C and 37°C), below and above LCST, in three buffer solutions (pH 2.2; 4.5 and 6.8). The thermo- and pH-sensitivity are investigated because the temperature and pH are two factors that are most often changed in physiological, biological and chemical systems.

### EXPERIMENTAL

The investigated Ag-P(NiPAAm/IA) hydrogel nanocomposites were synthesized according to the previously reported procedure [4]. Briefly, the hydrogel nanocomposites were synthesized by two-step  $\gamma$ -irradiation induced processes. In the first step, simultaneous copolymerization and crosslinking of P(NiPAAm/IA) hydrogels, with weight ratios 100/0 (S0), 98.5/1.5 (S1), 97/3 (S2) and 95.5/4.5 (S3), were conducted. Then, in the second step, *in situ* reduction of Ag<sup>+</sup> ions and formation of AgNPs within the hydrogels were performed in order to obtain Ag-S0, Ag-S1, Ag-S2 and Ag-S3 hydrogel nanocomposites, respectively.

The swelling behavior of investigated hydrogels was examined at two temperatures (25°C and 37°C) in three buffer solutions: H<sub>3</sub>PO<sub>4</sub>/KH<sub>2</sub>PO<sub>4</sub> (pH 2.2), CH<sub>3</sub>COOH/CH<sub>3</sub>COONa (pH 4.5) and NaOH/KH<sub>2</sub>PO<sub>4</sub> (pH 6.8). Swelling process of hydrogels was monitored gravimetrically by measuring mass of swollen hydrogel at predetermined time intervals ( $m_t$ ), until the initial mass of xerogel ( $m_0$ ) was equilibrated ( $m_{eq}$ ). The swelling degree was calculated as  $SD = (m_t - m_0)/m_0$ , and the equilibrium swelling degree ( $SD_{eq}$ ) was determined by replacing  $m_t$  with  $m_{eq}$ . All swelling experiments were performed in triplicate.

## RESULTS AND DISCUSSION

In previous investigation [4], series of thermo- and pH-sensitive Ag-P(NiPAAm/IA) hydrogel nanocomposites were prepared by  $\gamma$ -irradiation technique, with the content of AgNPs around 0.027 wt%. It was shown that increasing of IA content (from 0 to 4.5 wt%) in polymer matrices induce decrease in gel content and degree of crosslinking, and increase in pore size. As a consequence, an increase in AgNPs diameter from 8 nm for Ag-S0 up to 16.5 nm for Ag-S2 occurs. These NPs decreased  $SD_{eq}$  of Ag-P(NiPAAm/IA) hydrogel nanocomposites, in water at 25°C, in comparison with P(NiPAAm/IA) hydrogels. Incorporation of AgNPs enables fine tuning of volume phase transition temperature (VPTT) and improving the mechanical properties of hydrogel nanocomposites. Moreover, incorporation of AgNPs into P(NiPAAm/IA) hydrogels causes the appearance of antibacterial effect against gram-positive and gram-negative bacteria [4].

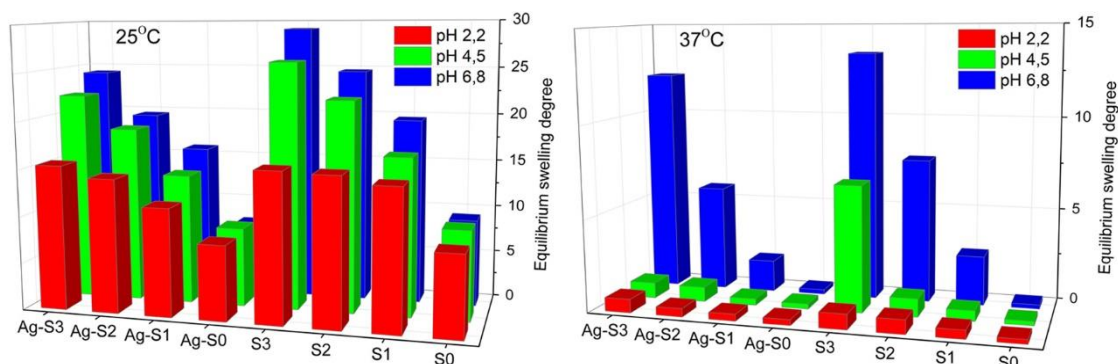


**Figure 1.** Equilibrium swelling degree of hydrogels, P(NiPAAm/IA) and Ag-P(NiPAAm/IA) nanocomposites, at 25°C and 37°C in three buffer solutions (pH 2.2; 4.5 and 6.8).

All investigated samples shows typical three-stage swelling curves (not presented here): the amount of absorbed water increased quickly at initial swelling stage, then increased slowly and at the end of process, when the osmotic and elastic forces become equal, reached equilibrium [3]. Fig. 1 shows dependence of  $SD_{eq}$  of investigated hydrogels on temperature and pH value of swelling medium, and the thermo- and pH-sensitivity are evident. As can be seen, at 25°C (below LCST), the non-ionic (S0 and Ag-S0) hydrogels swelled, but there was not a significant pH dependence of the  $SD_{eq}$ . In contrast, the  $SD_{eq}$  of the copolymeric hydrogels was strongly dependent on the pH value of swelling medium and on the concentration of ionizable groups in the network. Increasing the IA content (matrices from S0 to S4) as well as increasing of pH value causes an increase in water uptake and  $SD_{eq}$ . The incorporation of IA into polymer network lead to an increase in electrostatic repulsive force between charge sites on carboxylate (COO<sup>-</sup>) ions upon their partially or complete dissociation ( $pK_{a1}$  3.85 and  $pK_{a2}$  5.44) and enhance a more extended configuration [5]. On the other hand, the swelling capacity of hydrogel nanocomposites (samples from Ag-S0 to Ag-S4) decrease, compared with matrices from S0 to S4, probably due to partial restriction of segmental motion of the polymer chain caused by presence of AgNPs. At 37°C (above LCST), the thermo-sensitivity of PNiPAAm is

dominant and investigated hydrogels are in the collapsed state [2]. The higher values of  $SD_{eq}$  are evident only in buffer solution with pH 6.8, when the dissociation is complete and hydrophilic interactions caused by presence of IA are dominant. Below the LCST, a hydration shell around the hydrophobic groups is formed by hydrogen bonding between the hydrophilic groups in the side chains and water, causing water uptake and swelling of the PNiPAAm. The increase of the external temperature above the LCST, leads to scission of the H-bonds and hydrophobic interactions prevail, causing the leaching of water and collapsing of PNiPAAm, indicating the occurrence of phase separation and volume change. The VPTT of PNiPAAm-type hydrogel can be changed and adjusted by copolymerization. In investigated systems, by increasing of IA content increase the VPTT from 30°C up to around 42°C [2,4].

Furthermore, swelling kinetics and diffusion properties of investigated hydrogel were investigated. In order to determined swelling mechanism of hydrogels, a simple and effective power-law approach was used to calculate the kinetic parameters of water diffusion into polymer network using equation  $SD/SD_{eq}=kt^n$ , where  $k$  is the kinetic constant related to the structure of network and the penetrant,  $n$  is the diffusion exponent which describes transport mode of the penetrant and  $t$  is the time. Generally, three models of diffusion mechanism were accepted: (i) Fickian or Case I diffusion ( $n \leq 0.5$ ), (ii) non-Fickian or anomalous diffusion ( $0.5 < n < 1$ ) and (iii) Case II diffusion ( $n = 1$ ) [2-4].

**Table 1.** Swelling and diffusion parameters for hydrogels, P(NiPAAm/IA) and Ag-P(NiPAAm/IA) nanocomposite, at 25°C in three buffer solutions.

S <sub>i</sub>	pH	SD <sub>eq</sub>		k×10 <sup>2</sup> (1/min)		n		D <sub>Early</sub> ×10 <sup>8</sup> (cm <sup>2</sup> /s)		D <sub>Late</sub> ×10 <sup>8</sup> (cm <sup>2</sup> /s)		D <sub>Etter</sub> ×10 <sup>8</sup> (cm <sup>2</sup> /s)	
		S <sub>i</sub>	Ag-S <sub>i</sub>	S <sub>i</sub>	Ag-S <sub>i</sub>	S <sub>i</sub>	Ag-S <sub>i</sub>	S <sub>i</sub>	Ag-S <sub>i</sub>	S <sub>i</sub>	Ag-S <sub>i</sub>	S <sub>i</sub>	Ag-S <sub>i</sub>
S0	2.2	8.50	7.95	1.06	1.57	0.73	0.61	4.08	2.27	3.71	3.14	4.25	3.5
S1		14.71	11.46	0.61	1.45	0.80	0.62	3.47	2.26	3.56	2.94	2.50	1.27
S2		15.54	14.22	1.92	1.96	0.65	0.56	5.47	2.42	5.35	3.07	3.44	2.56
S3		15.75	15.41	2.11	2.12	0.62	0.55	5.60	2.12	6.25	2.45	12.2	3.29
S0	4.5	9.45	8.37	1.16	1.92	0.66	0.57	2.77	2.76	6.33	3.34	3.11	3.14
S1		16.58	13.81	1.59	2.17	0.65	0.55	4.58	2.63	3.96	3.22	3.42	2.71
S2		22.20	18.64	2.77	1.91	0.57	0.61	5.39	3.87	4.98	3.17	4.51	3.70
S3		26.01	22.19	1.82	1.52	0.65	0.64	5.33	3.46	4.79	3.05	3.21	5.68
S0	6.8	9.16	7.57	1.22	1.88	0.66	0.59	3.35	2.19	7.90	8.94	2.77	4.13
S1		19.60	15.85	2.22	2.13	0.59	0.58	4.35	2.52	4.21	2.72	3.42	2.51
S2		24.07	19.54	2.59	2.25	0.59	0.56	5.21	3.94	4.60	7.31	3.66	3.65
S3		29.19	24.29	2.87	2.84	0.55	0.52	4.81	5.18	4.84	3.50	3.21	4.55

According to the results presented in Table 1, it is evident that at 25°C all investigated hydrogels showed non-Fickian diffusion, indicating that both diffusion and polymer relaxation processes control the fluid transport. On the other hand, at 37°C hydrogels show Fickian diffusion at pH 2.2 and 4.5 (Table 2), indicating that polymer chains relaxation control the swelling process, which is in accordance with the fact that due to hydrophobic interaction the polymer network is in collapsed state. At pH 6.8 the swelling medium diffusion follows non-Fickian mechanism. Incorporation of AgNPs into matrices has no significant influence on the values of  $n$  and  $k$ , indicating that there is no change in diffusion model and structural properties of hydrogels.

The diffusion coefficients ( $D$ ) were determined by three approximations: the early-time approximation ( $D_{Early}$ ) valid in the range  $SD/SD_{eq} < 0.6$ , the late-time approximation ( $D_{Late}$ ) valid in the range  $SD/SD_{eq} > 0.6$  and Etters approximation ( $D_{Etter}$ ) valid in the range  $0 < SD/SD_{eq} < 1$  [3, 4]. The calculated values of diffusion coefficients are listed in Table 1 and Table 2.

**Table 2.** Swelling and diffusion parameters for hydrogels, P(NiPAAm/IA) and Ag-P(NiPAAm/IA) nanocomposite, at 37°C in three buffer solutions.

S <sub>i</sub>	pH	SD <sub>eq</sub>		k×10 <sup>2</sup> (1/min)		n		D <sub>Early</sub> ×10 <sup>8</sup> (cm <sup>2</sup> /s)		D <sub>Late</sub> ×10 <sup>8</sup> (cm <sup>2</sup> /s)		D <sub>Etter</sub> ×10 <sup>8</sup> (cm <sup>2</sup> /s)	
		S <sub>i</sub>	Ag-S <sub>i</sub>	S <sub>i</sub>	Ag-S <sub>i</sub>	S <sub>i</sub>	Ag-S <sub>i</sub>	S <sub>i</sub>	Ag-S <sub>i</sub>	S <sub>i</sub>	Ag-S <sub>i</sub>	S <sub>i</sub>	Ag-S <sub>i</sub>
S0	2.2	0.24	0.31	12.07	20.79	0.38	0.20	16.9	8.39	8.94	9.45	3.65	3.97
S1		0.47	0.37	0.05	2.94	0.26	0.48	2.42	2.85	2.72	7.16	3.24	2.69
S2		0.76	0.45	11.13	20.12	0.27	0.21	1.75	7.33	7.79	5.84	2.52	3.89
S3		0.82	0.74	7.66	10.24	0.33	0.29	3.59	2.11	3.48	7.62	2.40	3.80
S0	4.5	0.23	0.27	18.85	22.15	0.25	0.20	6.49	9.84	6.47	6.54	2.96	3.36
S1		0.56	0.35	14.58	5.36	0.33	0.42	13.7	12.4	8.92	8.02	3.48	7.91
S2		0.98	0.80	5.64	9.27	0.44	0.26	5.68	1.18	5.78	7.08	1.10	3.95
S3		6.80	0.84	1.47	10.34	0.47	0.35	3.99	8.11	3.46	7.85	4.83	2.98
S0	6.8	0.22	0.24	8.37	9.88	0.58	0.59	6.44	11.6	6.39	9.45	6.20	5.70
S1		2.65	1.71	2.85	10.13	0.58	0.58	5.81	2.24	5.00	8.94	5.04	3.83
S2		7.75	5.75	3.10	3.62	0.64	0.50	11.8	5.02	12.5	5.47	8.25	8.63
S3		13.47	12.17	2.03	2.55	0.64	0.54	6.07	4.15	6.02	8.30	3.45	3.63

From the presented results it can be noticed that there is some changes in the values of  $D_{Early}$ ,  $D_{Late}$  and  $D_{Etter}$  suggesting that the diffusion rate of swelling medium is altered for the applied experimental conditions, due to a change in the balance of hydrophobic and hydrophilic interactions caused by composition of polymer matrices. Among three applied approximation, the Etters approximation showed the best fit with the experimental results. The incorporation of AgNPs into the polymer network generally causes a decrease of water diffusion coefficients in the case of hydrogel nanocomposites, compared with hydrogel matrices. Such results are consistent with Reinhart and Peppas theory, according to which the lower swelling degree lead to lower diffusion coefficients of swelling medium [6].

## CONCLUSION

Swelling and diffusion properties of investigated hydrogels were affected by polymer matrices composition, presence of AgNPs and environmental factors, such as temperature and pH of swelling media. The obtained results showed that swelling capacity of hydrogels at 25°C increased with increasing of IA content and pH value of swelling medium, while at 37°C hydrophobic interactions prevail and all hydrogels are in collapsed state, except at pH 6.8. Incorporation of AgNPs causes decrease of swelling capacity. The obtained values of diffusion coefficient suggest that the diffusion rate of swelling medium changes with experimental conditions, due to a change in balance of hydrophobic and hydrophilic interactions caused by composition of polymer matrices.

## Acknowledgement

This work was supported by the Ministry of Education, Science and Technological Development of the Republic of Serbia (contract number: 451-03-68/2020-14/200017).

## REFERENCES

- [1] L. Tang, L. Wang, X. Yang, Y. Feng, Y. Li, W. Feng, Progress in Materials Science, 2021, 115, 100702.
- [2] M. Kalagasidis Krušić, M. Ilić, J. Filipović, Polymer Bulletin, 2009, 63, 197-211.
- [3] J. Krstić, J. Spasojević, A. Radosavljević, A. Perić-Grujić, M. Đurić, Z. Kačarević-Popović, S. Popović, Journal of Applied Polymer Science, 2014, 40321.
- [4] J. Spasojević, A. Radosavljević, J. Krstić, D. Jovanović, V. Spasojević, M. Kalagasidis-Krušić, Z. Kačarević-Popović, European Polymer Journal, 2015, 69, 168-185.
- [5] R.C. Weast, Handbook of Chemistry and Physics, CRC Press, Cleveland, 1975.
- [6] C. Reinhart, N. Peppas, Journal of Membrane Science, 1984, 18, 227-239.

## EFFECT OF SINTERING TEMPERATURE ON THE COMPRESSIVE STRENGTH AND MICROSTRUCTURE OF GLASS FOAM MADE FROM WASTE MATERIALS

V. Savić<sup>1</sup>, S. Matijašević<sup>1</sup>, V. Topalović<sup>1</sup>, J. Nikolić<sup>1</sup>, S. Smiljanić<sup>2,3</sup>, S. Zildžović<sup>1</sup>, S. Grujić<sup>2</sup>

<sup>1</sup>*Institute for Technology of Nuclear and Other Mineral Raw Materials, Franchet d'Esperey 86, 11000, Belgrade, Serbia (v.savic@itnms.ac.rs)*

<sup>2</sup>*University of Belgrade, Faculty of Technology and Metallurgy, Karnegijeva 4, 11000, Belgrade, Serbia*

<sup>3</sup>*Institute "Jožef Stefan", Jamova cesta 39, 1000 Ljubljana, Slovenia*

### ABSTRACT

Glass foams were produced from a green beer bottle and sugar beet factory lime (SBFL) as the foaming agent. The sintering temperature was in the 750-900 °C range. Porosity and compressive strength were determined. Results showed that glass foam sintered at 750 °C has the best compressive strength and even distribution of pores throughout the volume of the sample. With the increase of temperature from 800 to 900 °C compressive strength was improved while porosity has slightly dropped. Pores with diameters greater than 1000 µm were formed due to pore agglomeration. Obtained glass foams have properties comparable to commercial ones.

### INTRODUCTION

Glass foams are lightweight porous material used in sound and thermal insulation [1]. In the preparation of glass foam, the glass powder is mixed with a foaming agent. The mixture is then heated above the glass-softening temperature, where sintering of the glass powder and release of gases from the foaming agent occurred [2]. Gases from the foaming agent can be released by redox reactions or by thermal decomposition. In foaming by redox reaction, foaming is induced by carbon oxidation [3, 4]. Another way for gas release is the thermal decomposition of the foaming agent, most commonly CaCO<sub>3</sub>, where CO<sub>2</sub> is formed, and CaO is incorporated into the molten glass mass and acts as a glass modifier, altering the viscosity of the molten glass [1, 5]. Recently, there is an increased interest in researches where CaCO<sub>3</sub> rich wastes are used as a foaming agent for glass foam production [6, 7]. In this research discarded green beer bottle is used as a glass matrix and SBFL is used as a foaming agent. SBFL is CaCO<sub>3</sub> rich waste generated during the purification of diffusion juice in a sugar factory. The possibility of obtaining foam glass with properties comparable to commercial ones, using only waste materials, was investigated [1].

### METHODS

The green beer bottle was used as a glass raw material. It was milled into fine particles with TENCAN planetary mill at 400 rpm for 30 min. Obtained glass powder was sieved to obtain glass powder particles size under 50 µm. SBFL was used as a foaming agent. SBFL was dried in an oven at 110 °C, then crushed in an agate mortar and sieved to particles size under 50 µm. The chemical compositions of the glass and SBFL were determined using gravimetric and spectroscopic methods (AAS Analyst 300).

Glass powder (1 g) was mixed with 1% of SBFL in an agate mortar and then uniaxially pressed in a laboratory hydraulic press at 20 MPa with the addition of 5% H<sub>2</sub>O as a binder. The obtained samples were 15 mm in diameter and 3 mm thick. Samples were heated at the selected temperature (750, 800, 850, and 900 °C) for 30 min using the heating rate of 10 °C min<sup>-1</sup> in an electric furnace (Carbolite CWF 13/13) and then cooled in the air.

The porosity of samples was calculated using equation (1)

$$\varepsilon = (1 - \rho_g / \rho_t) \times 100 \quad (1)$$

where  $\rho_g$  is geometrical density determined using an analytical balance and a caliper, and  $\rho_t$  is a true density determined by the pycnometer method with distilled water as medium fluid. The mechanical strength of the samples is determined by compression tests (KS model). Tests were performed on three samples.

The microstructure of the glass foam samples was examined using a scanning electron microscope (MIRA3 XM TESCAN).

## RESULTS AND DISCUSSION

Table 1. shows the results of the chemical analysis of the green bottle glass.

**Table 1.** Chemical analysis of bottle glass

Oxide	SiO <sub>2</sub>	Al <sub>2</sub> O <sub>3</sub>	CaO	MgO	Na <sub>2</sub> O	Fe <sub>2</sub> O <sub>3</sub>	MnO	Cr <sub>2</sub> O <sub>3</sub>
mass %	71.9	2.46	10.2	2.10	12.7	0.42	0.01	0.11

The chemical composition of glass is typical for container soda-lime glasses. Chemical analysis of SBFL shows that it consists of 69.21% CaCO<sub>3</sub>.

In figure 1 is shown the temperature effect on the compressive strength and porosity of glass foam. It can be seen that the highest porosity (94.81±0.64 %) and the lowest compressive strength (0.31±0.1 MPa) has sample sintered at 800 °C. With the temperature increase, the porosity drops, and the compressive strength is increased. The compressive strength of the sample sintered at 750 °C is the highest, and porosity is comparable to commercial glass foams (85-95%) [1].

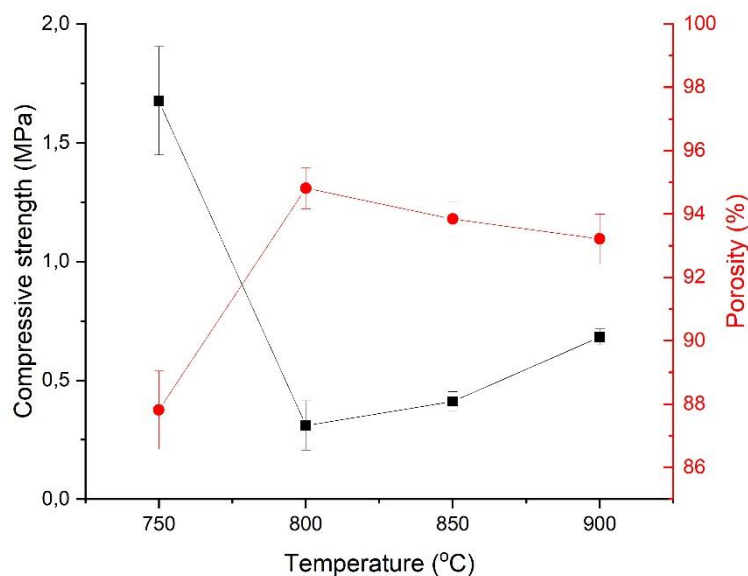


**Figure 1.** Temperature effect on the compressive strength and porosity of glass foams.

In figure 2 are shown SEM micrographs of obtained glass foams.

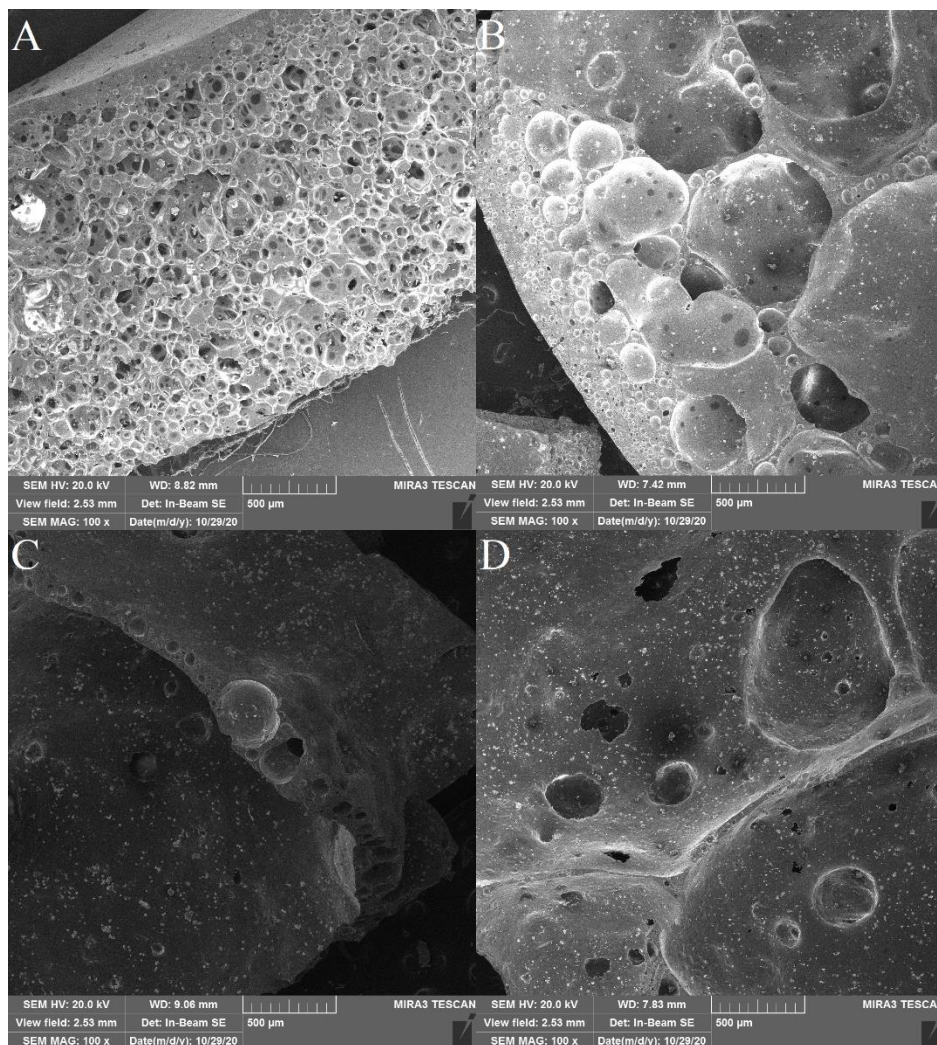


**Figure 2.** SEM Micrographs of glass foam sintered at A- 750 °C, B- 800 °C, C- 850 °C and D- 900 °C

Figure 2 shows that glass foam sintered at 750 °C forms pores with a diameter up to 200  $\mu\text{m}$ . The sample has a more evenly pore size distribution throughout volume than samples sintered at higher temperatures. At higher temperatures pore agglomeration occurs that leads to the formation of pores with a diameter greater than 1000  $\mu\text{m}$ . The compressive strength of glass foam is under the strong influence of uneven pore size.

## CONCLUSION

Glass foam has been successfully prepared using only secondary raw materials. The best compressive strength and the evenest microstructure has glass foam sintered at 750 °C, with properties similar to commercial glass foam products. In temperature range from 800 to 900 °C the compressive strength increases, while porosity slightly drops.

**Acknowledgement**

This research was supported through the Ministry of Education and Science of the Republic of Serbia, grant contract No.: 451-03-9/2021-14/200135 and 451-03-9/2021-14/200023.

**REFERENCES**

- [1] G. Scarinci, G. Brusatin, E. Bernardo in: Cellular Ceramics: Structure, Manufacturing, Properties and Applications, M. Scheffler, P. Colombo (Eds.), Wiley-VCH Verlag, Weinheim, 2005.
- [2] J. König, R. R. Petersen, Y. Yue, D. Suvorov, *Ceram. Int.*, 2017, 43, 4638-4646
- [3] E. Bernardo, R. Cedro, M. Florean, S. Hreglich, *Ceram. Int.*, 2007, 33 963–968.
- [4] A.S. Llaudis, M.J.O. Tari, F.J.G. Ten, E. Bernardo, P. Colombo, *Ceram. Int.*, 2009, 35, 1953–1959.
- [5] N.M.P. Low, *J. Mater. Sci.*, 1981, 16, 800–808.
- [6] H.R. Fernandes, F. Andreola, L. Barbieri, I. Lancellott, M.J. Pascual, J.M.F. Ferreira, *Ceram. Int.*, 2013, 39 (8), 9071–9078.
- [7] M. T. Souza, B. G.O. Maia, L.B. Teixeira, Karine G. de Oliveira, A. H.B. Teixeira, A. P. N. de Oliveira, *Process Saf Environ*, 2017, 3, 60-64.

## RADIOLYTIC SYNTHESIS AND CHARACTERIZATION OF ANTIBACTERIAL Ag-(PVA/PVP) HYDROGEL NANOCOMPOSITES

N. Nikolić, J. Spasojević, A. Radosavljević, Z. Kačarević-Popović

*Vinča Institute of Nuclear Sciences - National Institute of the Republic of Serbia, University of Belgrade, Mike Petrovića Alasa 12-14, 11351 Vinča, Belgrade, Serbia (nnikolina@vin.bg.ac.rs)*

### ABSTRACT

This paper describes the synthesis of nanocomposite systems of different compositions based on biocompatible polymers and antibacterial silver nanoparticles (AgNPs). The synthesis of hydrogel matrices of poly(vinyl alcohol) (PVA) and poly(*N*-vinyl-2-pyrrolidone) (PVP), as well as their combinations, was performed by gamma irradiation induced process. In the second step, *in situ* synthesis of AgNPs was performed by reducing silver ions, also using gamma irradiation, within previously synthesized matrices. Polymer matrices were characterized by swelling examination and scanning electron microscopy (SEM). The optical and microstructural properties of nanocomposites were analyzed by UV-Vis spectroscopy and X-ray diffraction (XRD), respectively. The antibacterial potential of the synthesized systems was confirmed by the diffusion test method on Gram-positive and Gram-negative bacteria.

### INTRODUCTION

Hydrogel nanocomposites represent a specific group of materials with a complex structure of crosslinked polymer chains capable to stabilize metal nanoparticles. They integrate two different components into one material with unique physicochemical and biological properties, that none of the building blocks possess [1, 2]. Hydrogels are hydrophilic multi-component systems consisting of three-dimensional networks of polymer chains. This structure provides unique swelling behavior and the capability to absorb a large amount of surrounding medium without dissolving.

Poly (vinyl alcohol) (PVA) and poly (*N*-vinyl 2-pyrrolidone) (PVP) are synthetic, water-soluble polymers with excellent transparency and biocompatibility, that make them suitable for wide range of application. Due to their stable 3D structure, porosity, swelling capacity, biodegradability, non-toxicity and good mechanical properties, which are widely variable and easily adjusted, hydrogels have attracted a considerable attention for many applications in the field of medicine and pharmaceuticals. Because they are soft materials that contain a significant amount of water, they simulate specific properties of human skin and tissues [3].

The presence of metal NPs can improve the existing characteristics of hydrogels and add new, unusual chemical, physical and mechanical properties. Silver nanoparticles (AgNPs) with their specific catalytic, optical, and antimicrobial properties stand out as the most common synthesized type of nanoparticles. Nanocomposite systems based on AgNPs and crosslinked polymer matrices (hydrogels) have great potential applications as antimicrobial biomaterials. Thanks to porosity of polymer network and liquid-filled pores, hydrogels represent a good platform for nucleation, growth and stabilization of synthesized AgNPs [4, 5].

The radiation-chemical method is a "green" method of synthesis of hydrogel nanocomposites without additional chemical agents (crosslinkers, initiators, inhibitors, and catalysts), which eliminates the problem of their removal at the end of the process. For the biomedical application, the main advantage of this method is the possibility of synthesis and sterilization of the material in one technological step [1, 5].

The aim of this study was investigation of the physico-chemical, optical and structural characteristics of PVA/PVA hydrogels and Ag-(PVA/PVP) hydrogel nanocomposites, as well as their antibacterial activity, for potential biomedical application.

## EXPERIMENTAL

The 5 wt% aqueous solutions of PVA and PVP were dissolved, mixed in a different PVA/PVP weight ratios (1:0, 1:1, 0:1) and exposed to gamma irradiation ( $^{60}\text{Co}$  source, dose rate 0.5 kGy/h up to the total absorbed dose of 25 kGy) to induce crosslinking and formation of the polymer network. Obtained PVA/PVP hydrogels were dried to the constant mass and then extracted in distilled water for 7 days, in order to remove the uncrosslinked polymer. Extracted hydrogels were dried again to the constant weight to determine the weight fraction of gel. The percentage gelation was found to be 91.9% for the ratio 1:0, 97.3% for the ratio 1:1, and 95.5% for the ratio 0:1. The prepared PVA/PVP hydrogels were immersed in argon saturated solution containing silver nitrate ( $1 \times 10^{-2}$  mol/dm<sup>3</sup>) and 2-propanol (0.2 mol/dm<sup>3</sup>) for 48 hours, and then exposed to gamma irradiation (dose rate 10 kGy/h up to the total absorbed dose of 18 kGy) to achieve *in situ* reductions of silver ions and generation of AgNPs. Optical and microstructural properties of Ag-(PVA/PVP) hydrogel nanocomposites were examined by UV-Vis spectroscopy and X-ray diffraction (XRD), respectively. The morphology of the polymer network was investigated by SEM analysis. Swelling processes of investigated systems were monitored in phosphate buffer (pH 7.4) at 37°C, while the antibacterial properties were investigated using the agar diffusion test method. Suspensions of strains (*Escherichia coli* and *Staphylococcus aureus*) were mixed with the top agar layer and samples were placed on it. Incubation was performed at 37°C for 48 h and the appearance of inhibition zones was monitored.

## RESULTS AND DISCUSSION

PVA/PVP hydrogels were obtained by using gamma irradiation method, which induced crosslinking of polymer chains and the formation of a stable 3D polymer structure. The internal morphology was examined by using SEM analysis (Fig. 1a), which confirmed the expected porous, sponge like structure.

UV-Vis spectroscopy is used to confirm the presence of AgNPs inside the polymer matrix. The obtained absorption spectra (Fig. 1b) clearly indicate the presence of characteristic surface plasmon resonance (SPR) bands of AgNPs, centered in the range of 390 - 420 nm, indicating the formation of spherical particles with nanometer dimension. Based on the obtained absorption spectra, the average radius of the nanoparticles can be determined by the full width at half maximum (FWHM) of their corresponding SPR band using the equation  $r = V_f / (\Delta\omega_{1/2})$ , where  $r$  is the particle radius,  $V_f$  is the Fermi velocity of the metal, and  $\Delta\omega_{1/2}$  is the FWHM for the SPR band [5]. The values of the average AgNPs radius obtained by the UV-Vis experimental spectra are presented on Fig. 1b.

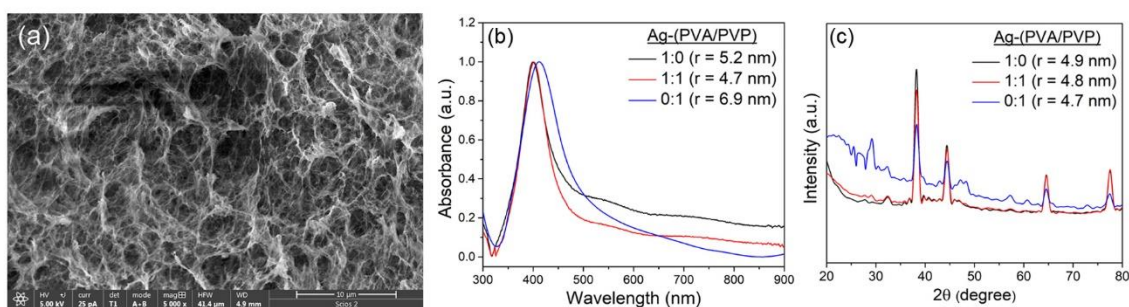


**Figure 1.** SEM micrographs of PVA/PVP (1:1) hydrogel (a), UV-Vis absorption spectra (b) and XRD patterns of investigated samples (c).

The XRD patterns of Ag-(PVA/PVP) xerogel nanocomposites are shown in Fig. 1c. The diffraction maxima correspond to Bragg reflections with crystal planes (111), (200), (220), (311), and (222). Indexed crystal planes attribute to the face-centered cubic (*fcc*) crystal structure of AgNPs, and the absence of silver oxide peaks indicates the existence of pure silver. According to the Scherrer's equation [1], the radius of the crystalline domain size was found to be about 4.8 nm. This result corresponds to the results obtained from UV-Vis spectroscopy.

The results obtained by monitoring the swelling process show that the swelling capacity of the hydrogels tends to increase with an increasing PVP content in hydrogel matrices. PVA/PVP hydrogels, possess hydroxyl, amide, and carbonyl groups with hydrophilic character. The amide group in PVP is a more hydrophilic compared to the other functional groups. Therefore, with the increase of PVP content in hydrogels, there is an increase in the degree of swelling (Fig. 2a). On the other hand, the incorporation of AgNPs leads to a decrease in swelling capacity (Fig. 2b). This can be explained by electrostatic or coordinate interactions between metal NPs and polymer functional groups, which act as an additional crosslinking.

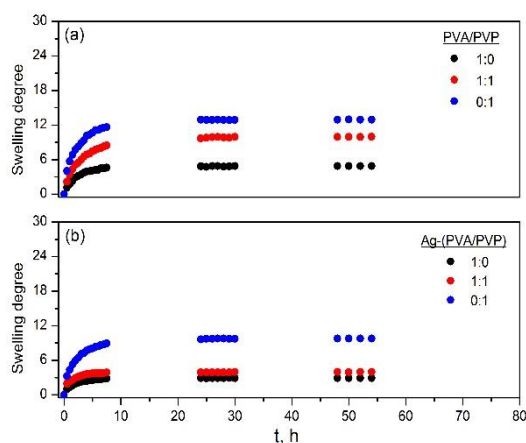


**Table 1.** Characteristic parameters obtained from swelling measurements.

	Sample	$SD_{eq}$	$n$	$D \times 10^6$ , $cm^2/min$
PVA/PVP	1:0	4.9	0.64	6.67
	1:1	9.9	0.57	4.74
	0:1	12.9	0.54	4.86
Ag-(PVA/PVP)	1:0	2.9	0.48	6.65
	1:1	4.0	0.28	5.16
	0:1	9.8	0.43	5.17

**Figure 2.** Swelling curves of PVA/PVP hydrogels (a) and Ag-(PVA/PVP) hydrogel nanocomposites (b).

Specific parameters of the swelling process: equilibrium swelling degree ( $SD_{eq}$ ), characteristic exponent ( $n$ ) and diffusion coefficient ( $D$ ) for examined systems are presented in Table 1. According to the results, it is evident that hydrogel matrices showed non-Fickian diffusion ( $0.5 \leq n \leq 1$ ), indicating that both diffusion and polymer relaxation processes controlled the fluid transport. On the other hand, the value of  $n \leq 0.5$  indicates the Fickian mechanism of diffusion for hydrogel nanocomposites, which means that the rate of polymer chains relaxation is significantly slower than the rate of the diffusion [5].

It is well known that AgNPs attract great attention due to their capability to release silver ions in a controlled manner, which leads to a powerful antibacterial activity against a large number of bacteria. The antibacterial potential of Ag-(PVA/PVP) nanocomposites was investigated by disc diffusion method against Gram-negative (*Escherichia coli*) and Gram-positive (*Staphylococcus aureus*) bacteria. After incubation for 48 h at 37°C, an obvious clear zone appeared around the both disc specimens (Fig. 3), indicating the absence of microbial growth. The diameter of inhibition zone for *E. coli* is slightly larger (1-3 mm) than that for *S. aureus* (0.5-1.5 mm), and for the Ag-(PVA/PVP) nanocomposites with the polymer ratio 1:1. This suggests the reaching of the minimum inhibitory concentrations of released silver around the Ag-(PVA/PVP) hydrogel nanocomposite specimens, which is in agreement with the previous investigation [6, 7].



**Figure 3.** Antibacterial activity of Ag-(PVA/PVP) hydrogel nanocomposite against *Escherichia coli* and *Staphylococcus aureus* (sample 7 - ratio 1:0 and sample 8 - ratio 1:1).

## CONCLUSION

In this investigation, a series of PVA/PVP hydrogels, and Ag-(PVA/PVP) hydrogel nanocomposites were successfully synthesized by gamma irradiation induced process. The obtained high percentages of gel fraction indicate that the chosen gamma irradiation method is suitable for hydrogel nanocomposites synthesis. UV-Vis analysis confirmed that all nanocomposite samples showed absorption band peaking at the wavelength value around 400 nm, confirming the presence of spherical AgNPs, with calculated radii value from 4.7 - 6.9 nm. The X-ray diffraction data are consistent with the face-centered cubic (*fcc*) crystal structure of bulk metallic Ag, with the mean radius around 4.8 nm. SEM analysis confirmed expected porous internal morphology, while swelling studies show high swelling capacity, depending on comonomer ratio and presence of AgNPs within the polymer network. The obtained results show an increase a swelling capacity with higher PVP content, while incorporation of AgNPs causes a decrease in swelling capacity. Finally, a good antibacterial activity on Gram-positive and Gram-negative bacteria, makes those hydrogel systems interesting for a wide range of biomedical applications.

## Acknowledgement

This work was supported by the Ministry of Education, Science and Technological Development of the Republic of Serbia (contract number: 451-03-68/2020-14/200017).

## REFERENCES

- [1] M. Eid, M. B. El-Arnaouty, M. Salah, E. S. Soliman, E. S. A. Hegazy, *Journal of Polymer Research*, 2012, 19, 9835.
- [2] W. Gao, Y. Zhang, Q. Zhang, L. Zhang, *Annals of Biomedical Engineering*, 2016, 44, 2049-2061.
- [3] H. L. A. El-Mohdy, S. Ghanem, *Journal of Polymer Research*, 2009, 16, 1-10.
- [4] M. T. S. Alcântara, N. Lincopan, P.M. Santos, P.A. Ramirez, A.J.C. Brant, H.G. Riella, A.B. Lugão, *Radiation Physics and Chemistry*, 2019, 165, 108369.
- [5] J. Spasojević, A. Radosavljević, J. Krstić, D. Jovanović, V. Spasojević, M. Kalagasidis-Krušić, Z. Kačarević-Popović, *European Polymer Journal*, 2015, 69, 168-185.
- [6] J. Krstić, J. Spasojević, A. Radosavljević, A. Perić-Grujić, M. Đurić, Z. Kačarević-Popović, S. Popović, *Journal of Applied Polymer Science*, 2014, 131, 40321.
- [7] Ž. Jovanović, A. Radosavljević, J. Stojkowska, B. Nikolić, B. Obradović, Z. Kačarević-Popović, V. Mišković-Stanković, *Polymer Composites*, 2014, 35, 217-226.

## THE INFLUENCE OF HYDROCHLORIC ACID ON THE FEATURES OF SBA-15 PARTICLES

M. Kokunešoski<sup>1</sup>, Z. Bašćarević<sup>2</sup>, S. Ilić<sup>1</sup>, A. Valenta-Šobot<sup>1</sup>, A. Grce<sup>1</sup>, M. Pošarc-Marković<sup>1</sup>  
and A. Šaponjić<sup>1</sup>

<sup>1</sup> *University of Belgrade, Vinca Institute of Nuclear Sciences, Institute of National Importance for the Republic of Serbia, Mike Petrovica Alasa 12-14, Vinca, 11000 Belgrade, Serbia (majako@vin.bg.ac.rs)*

<sup>2</sup> *University of Belgrade, Institute for Multidisciplinary Research, Kneza Višeslava 1, 11030 Belgrade, Srbija*

### ABSTRACT

The template method synthesis of both SBA-15 materials with elongated and spherical particles was performed using a surfactant Pluronic P<sub>123</sub>. The HCl (p.a.) was used to synthesize material with elongated particles connected in chain structures grouped into shapes resembling sheaves of wheat. In the synthesis of spherical SBA-15 with diameters ranging from 0.5 to 2 μm, a spent HCl solution which was obtained after chemical treatment of clay was used where the dominant presence of the spheres was confirmed by the SEM method. In addition to the methods mentioned above, XRD, EDS and FTIR methods characterize SBA-15 materials.

### INTRODUCTION

The silicates have attracted a great deal of interest in the past decades because of their use in catalysis, separations, sensors, drug delivery, and optical devices. Many efforts have been devoted to the synthesis of silica spheres of defined size and pore diameter because the control of the particle morphology and pore size of mesoporous silica could open up new possibilities for its application as packing material in chromatography or as an easy-to-handle form for catalytic purposes [1-3]. Different morphologies of the SBA-15, such as fibres, platelets, spheres, monoliths, films, etc., can be synthesized by varying the reaction conditions during synthesis [4]. Silica spheres were obtained via a two-step synthesis process by using a triblock copolymer Pluronic P<sub>123</sub> as a template in combination with an HCl solution used after use in the chemical treatment of clay.

### METHODS

Both samples of SBA-15 were synthesized according to the standard procedure [5] by using Pluronic P<sub>123</sub> (non-ionic triblock copolymer, EO<sub>20</sub>PO<sub>70</sub>O<sub>20</sub>, BASF) as a surfactant and tetraethoxysilane (TEOS, 98%) as a source of silica. A 4.0 g sample of Pluronic P<sub>123</sub> was dissolved in 30 ml of distilled water and 120 g of 2M HCl solution and stirred at 35 °C for 1.5 h. 8.5 g of TEOS were added dropwise into the solution and vigorously stirred at the same temperature for 1.5 h. According to the proposed method [5], the mixture was aged at 35 °C for 20 h and then at 80 °C for 48 h. The final products were filtered, washed with 600 ml of distilled water, and dried at room temperature. Calcination was carried out in flowing air by slowly increasing the temperature from room temperature to 500 °C for 8 h and keeping it at 500 °C for 6 h to decompose triblock copolymer. In the synthesis of SBA-15 with elongated particles (SBA-15/E), HCl (p.a.) was used. In the synthesis of SBA-15 with spherical particles (SBA-15/S), a spent HCl solution after chemical treatment of clay was used (spent HCl solution) [6]. Methods SEM, XRD, EDS and FTIR were employed to characterize the phases, functional groups and microstructure of the obtained samples are described elsewhere [4,7,8].

## RESULTS AND DISCUSSION

The SEM micrographs of the SBA-15 materials are shown in Figure 1.

The material SBA-15/E consists of many elongated particles of relatively uniform sizes (up to  $1\ \mu\text{m}$ ). These elongated particles are aggregated into wheat like structures. Similar chain agglomerate structures were reported in the literature [5]. The spherical particles of (SBA-15/S), with diameters ranging approximately from  $0.5$  to  $2\ \mu\text{m}$ , are presented in Figure 1. The form and the size of the grains depend on the form and dimensions of the micelle, which was formed from the surface-active substance as a template [9]. Earlier research presented that Pluronic P<sub>123</sub> has never formed spheres only due to powerful hydrophobic forces that lead to the formation of elongated cylindrical silicate-surfactant micelles that are aggregated into wheat-like structures [10]. According to the literature data, various ionic species in the spent HCl solution could promote the formation of spherical particles [11]. Spheric SBA-15 is synthesized using the ionic surfactant cetyltrimethylammonium bromide (CTAB) under acidic condition [2]. Instead of using surfactant CTAB, we have demonstrated that sphere SBA-15/S can be obtained using a spent HCl solution.

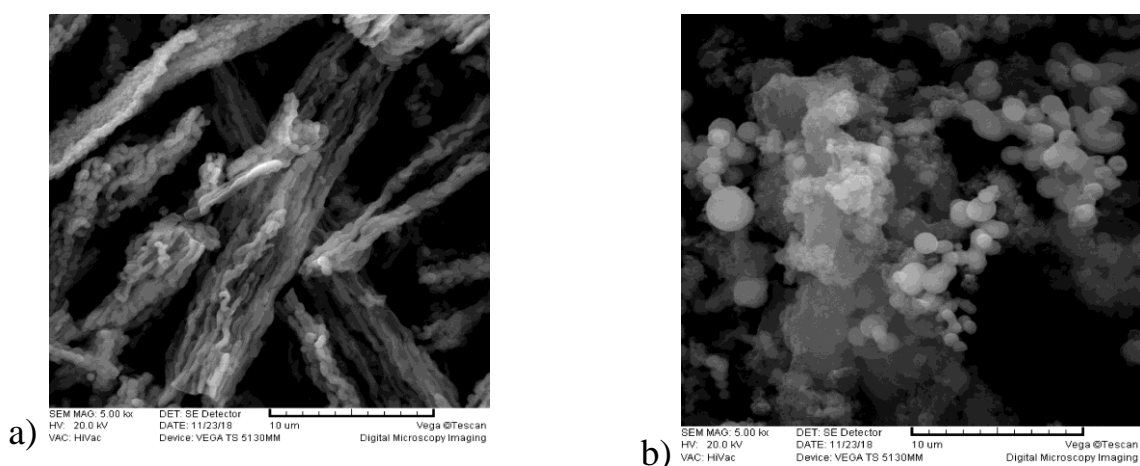


**Figure 1.** SEM micrographs of: a) SBA-15/E and b) SBA-15/S.

The EDS analysis showed that the particles of both test materials consist of  $\text{SiO}_2$ . The XRD analysis confirmed the presence of amorphous  $\text{SiO}_2$  in the investigated samples. For SBA-15/E, the EDS analysis and diffractogram are presented elsewhere [4]. Figure 2. presents the FT-IR spectrums of SBA-15 with elongated and spherical particles. The FT-IR spectrums of both investigated SBA-15 materials are very similar. Bands at  $1054$  and  $797\ \text{cm}^{-1}$  belong to asymmetric and symmetric stretching vibrations of the Si-O-Si framework, respectively. The weak absorption, which peaks at  $557$  and  $441\ \text{cm}^{-1}$  could possibly be attributed to Si-O deformation. A weak band at  $956\ \text{cm}^{-1}$  represent Si-OH vibration [12–15].

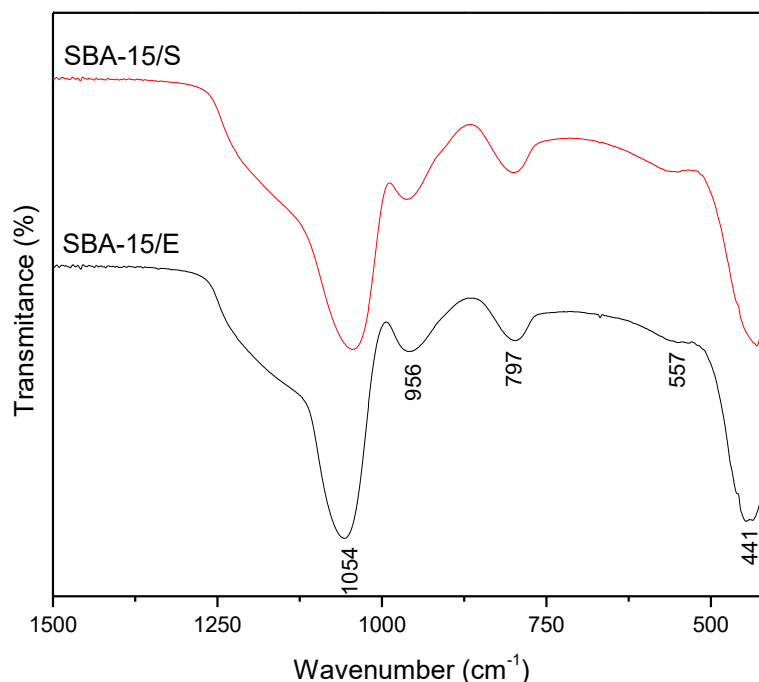


**Figure 2.** FT-IR spectra of: SBA-15/E and SBA-15/S.

## CONCLUSION

The SBA-15 spheres were successfully synthesized. Investigations in this paper show that the differences in the structures of synthesized SBA-15 materials closely depend on the origin of reactants used in the synthesis of SBA-15. The spent HCl solution after use in chemical treatment of clay was used to synthesize SBA-15 spheres. The synthesis of spherical particles with diameters ranging approximately from 0.5 to 2  $\mu\text{m}$  was promoted by various ionic species from spent HCl solution instead of using a commercial ionic surfactant.

## Acknowledgement

This research was funded by the Ministry of Education, Science and Technological Development of the Republic of Serbia. Grant no. 451-03-9/2021-14/200017

## REFERENCES

- [1] Y. Ma, L. Qi, J. Ma, Y. Wu, O. Liu, H. Cheng, *Colloids and Surfaces A: Physicochem. Eng. Aspects* 2003, **229**, 1-8.
- [2] D. Zhao, J. Sun, Q. Li, and G. D. Stucky *Chem. Mater.*, 2000, **12**, 275-279.
- [3] S. Kingchok, S. Pornsuwan, *J. Porous Mater.* 2020, **27**, 1547-1557.
- [4] M. Kokunešoski, Z. Baščarević, Z. Rakočević, A. Šaponjić, Dj. Šaponjić, D. Jordanov, B. Babić, *Science of Sintering* 2018, **50**, 111-121.
- [5] D. Zhao, J. Feng, Q. Huo, N. Melosh, G. H. Fredrickson, B. F. Chmelka, G. D. Stucky, *Science* 1998, **279**, 548-552.
- [6] M. Kokunešoski, A. Šaponjić, V. Maksimović, M. Stanković, M.

- Pavlović, J. Pantić, J. Majstorović, *Ceram.Int.* 2014, **40**, 14191-14196.
- [7] M. Kokunešoski, J. Gulicovski, B. Matović, B. Babić, *J. Optoelectron.* 2009, **11**, 1656-1659.
- [8] M. Kokunešoski, J. Gulicovski, B. Matović, M. Logar, S.K. Milonjić, B. Babić, *Mater. Chem. Phys.* 2010, **124**, 1248-1252.
- [9] V.L. Zholobenko, A.Y. Khodakov, M. Impéror-Clerc, D. Durand, I. Grillo, *Adv. Colloid Interface Sci.* 2008, **142**, 67-74.
- [10] C. Yu, J. Fan, B. Tian, D. Zhao, *Chem. Mater.* 2004, **16**, 889-898.
- [11] P.H.K. Charan, G.R. Rao, *J. Chem. Sci.* 2015, **127**, 909-919.
- [12] A. Burneau, O. Barres, J.P. Gallas, J.C. Lavalley, *Langmuir* 1990, **6**, 1346-1372.
- [13] J.P. Gallas, J.C. Lavalley, *Langmuir* 1991, **7**, 1235-1240.
- [14] K.C. Vrancken, P. van Der Voort, I. Gillis D'Hamers, E.F. Vansant, P.J. Grobet, *J. Chem. Faraday Trans.* 1992, **88**, 3197-3200.
- [15] S.V. Nitta, V. Pisupatti, A. Jain, P.C. Wayner, W.N. Gill, J.L. Plawsky, *Vac. Sci. Technol. B* 1999, **17**, 205-212.

## MESOPOROUS SILICA DECREASE CELL VIABILITY *IN VITRO* IN DOSE DEPENDENT MANNER

A. Valenta Šobot, J. Filipović Tričković, A. Šaponjić, S. Ilić,  
A. Grce, Dj. Katnić and M. Kokunešoski

*Department of Physical Chemistry; VINČA Institute of Nuclear Sciences, National Institute of the Republic of Serbia, University of Belgrade, Mike Petrovića Alasa 12-14, 11001 Belgrade, Republic of Serbia (ana\_v.s@vin.bg.ac.rs)*

### ABSTRACT

Mesoporous silica renders chemical and mechanical stability under biological conditions, but due to its physicochemical properties, could be potentially harmful to exposed cells. The aim of the current study was to estimate SBA-15 (concentration of 50, 100 and 250  $\mu\text{g/mL}$ ) impact on human peripheral blood mononuclear cells to induce cyto- and genotoxicity *in vitro* after 72 h treatment, as well as lipid peroxidation in serum samples *ex vivo*. SBA-15 mesoporous silica treatment impact on cell viability was performed by XTT assay, lipid peroxidation was estimated by determining malondialdehyde and 4-hydroxyalkenals levels and genotoxicity by micronucleus assay. SBA-15 treatments displayed genotoxic potential at the lowest concentration, while highest tested concentration led to decrease of cell viability and increase of lipid peroxidation. Chemical modification of SBA-15 material that could influence its physicochemical properties could be useful way to lower its toxicity.

### INTRODUCTION

Santa Barbara Amorphous (SBA-15) mesoporous silica was synthesized and characterized by a well-ordered hexagonal structure with a uniform pore size up to 6 nm [1]. Their high surface areas enable large pharmaceutical adsorption capacities referring to high application potential. Biocompatibility, low toxicity and the presence of micropores, promote their application as carriers in drug formulations of prolonged release [2]. Despite all named quality properties, it was shown that 24 h exposure to 10 - 80  $\mu\text{g/mL}$  of SBA-15 caused oxidative stress, i.e., increased reactive oxygen species (ROS) in the cell culture medium, in a concentration dependent manner. Increased ROS production could provoke cyto- and genotoxicity by altering important cellular macromolecules, which is why initial toxicity screening is very important. Moreover, impurities that could be introduced into mesoporous silica during the production process, such as catalysts, could display intrinsic toxicities [3]. Thus, the aim of the present study was to estimate potential cyto- and genotoxicity of SBA-15 and their relation to oxidative damage.

### METHODS

SBA-15 is synthesized according to the standard procedure [4], by using Pluronic P<sub>123</sub> (non-ionic triblock copolymer, EO<sub>20</sub>PO<sub>70</sub>O<sub>20</sub>, BASF) as a surfactant and tetraethoxysilane (TEOS, 98 %) as a source of silica [4]. Peripheral blood samples were obtained from three healthy donors [5]. Aliquots of heparinized whole blood were set up for cytokinesis-block micronucleus assay (CBMN) [6]. Samples were centrifuged at 400 x g, plasmas were collected, and sediments diluted in PBS and used for further peripheral blood mononuclear cells (PBMC) separation by Ficoll™ density gradient media. PBMC were resuspended in RPMI 1640 medium supplemented with 1 % penicillin-streptomycin, 10 % fetal bovine serum (FBS) and 5  $\mu\text{g/mL}$  phytohemagglutinin (PHA-M) mitogen for the stimulation of cell proliferation. Plasma samples were used as a medium for oxidative capacity estimation. Whole blood, PBMC and plasma samples were treated with increasing concentrations of SBA-15 (50, 100, 250  $\mu\text{g/mL}$  and untreated control) for 72 h at standard cell culture conditions, i.e.

37 °C 5 % CO<sub>2</sub>. Viability XTT assay was performed according to Roehm et al. [7]. From plasma samples, lipid peroxidation products (LPP) assay was done according to Tsikas [8]. All experiments were set up in duplicates and repeated three times. Statistical analysis was done using ANOVA test and Pearson correlation coefficient. Data are presented as the mean percentage  $\pm$  SD, relative to control.

## RESULTS AND DISCUSSION

Increase in cell proliferation was induced only by the lowest tested SBA-15 concentration. Upon 100  $\mu$ g/mL SBA-15 treatment no impact on cell viability was detected, while the highest tested concentration of SBA-15 (250  $\mu$ g/mL) significantly reduced cell viability (Figure 1.). The lowest tested SBA-15 concentration had no impact on LPP values, while higher SBA-15 concentrations elevated LPP in dose dependent manner (Figure 1.). However, the lowest concentration led to a significant increase in micronuclei formation by almost 50 % (Figure 2.), while other two concentrations didn't significantly affect MN frequency. Viability rates correlate positively with micronucleus frequency ( $p < 0.01$ ;  $r = 0.702$ ), indicating that genotoxicity assessment of SBA-15 treatments could rely on a number of cells that past cell division, and that higher concentration didn't display genotoxic effect due to more pronounced cytotoxicity.

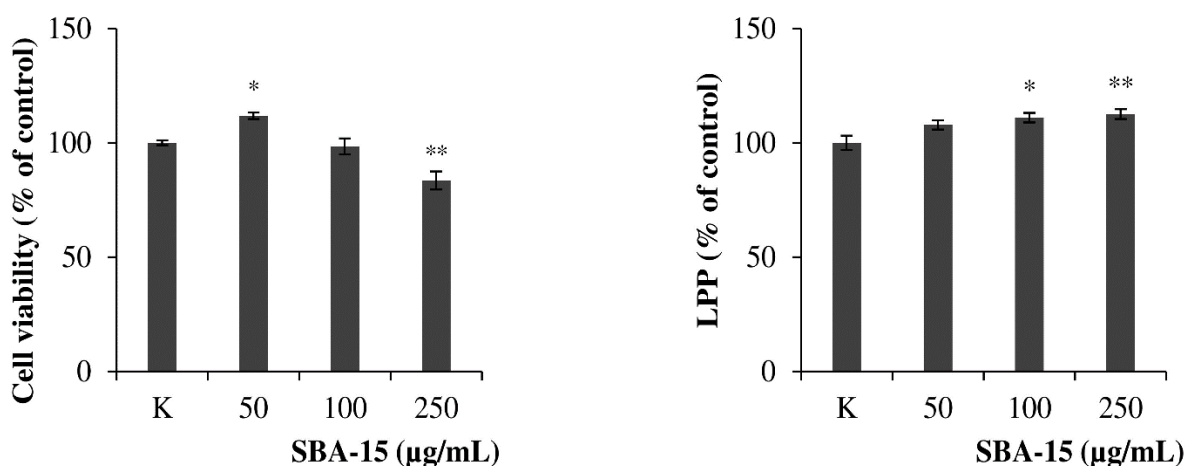


**Figure 1.** Cell viability (left) and level of lipid peroxidation products (right), expressed as percentage of control. Level of significance is marked as \*  $p < 0.05$ , \*\*  $p < 0.01$ .

Physicochemical properties of test materials that can contribute to their toxic effects include particle size and shape, crystal structure, chemical composition, surface area, surface chemistry, surface charge, and porosity [9]. Since size of SBA-15 aggregate prevents cellular uptake (Figure 2.), mechanical damage induced by its rod-like shaped structure could be the factor contributing to its cytotoxicity. Rise of LPP could be indicative of oxidative damage that also affects the cell viability, and presumably contributes to decreased cellular survival in higher concentration treatments. Detected changes in all of the tested parameters could arise from potentially present impurities that tail SBA-15 synthesis and concentration increment. Sodium, zinc, potassium, aluminum, calcium, magnesium, and iron were reported as abundant in SBA-15 [3].

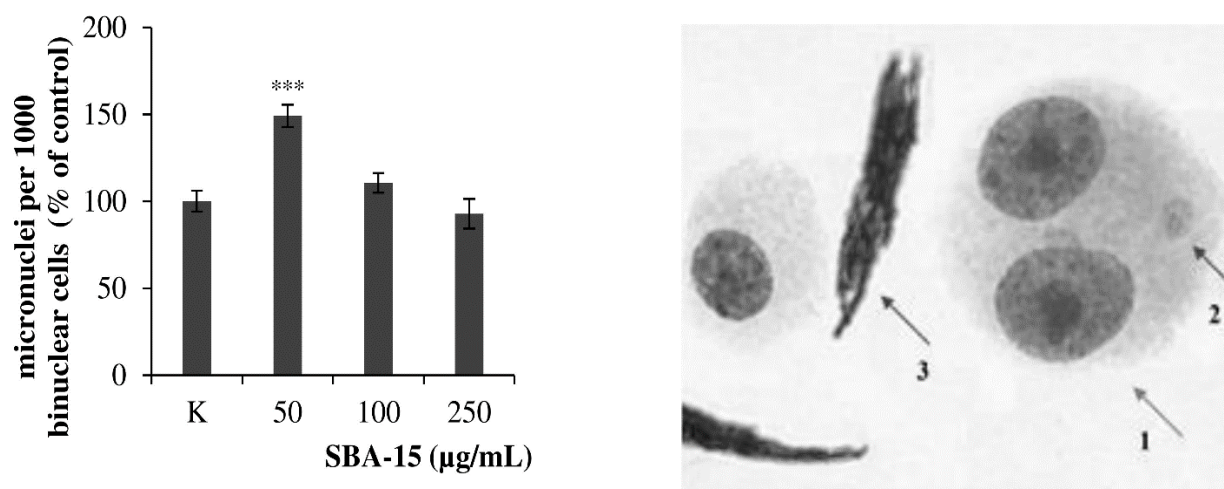


**Figure 2.** Frequency of micronuclei expressed as percentage of control. Level of significance is marked as \*\*\*  $p < 0.001$  (left); Representative photomicrograph of binuclear cell (1), with micronuclei (2) and rod-like SBA-15 structure (3), (right).

## CONCLUSION

SBA-15 treatments displayed genotoxic potential and decreased cell viability. Additional test should be performed to exclude potential influence of trace impurities that could contribute to SBA-15 toxic influence. Modification of SBA-15 material that could influence its shape without changing surface area potentially could be useful way to lower toxicity.

## Acknowledgement

The research was funded by the Ministry of Education, Science and Technological Development of the Republic of Serbia (454-03-9/2021-14/200017).

## REFERENCES

- [1] M. Kokunešoski, J. Gulicovski, B. Matović, B. Babić, *Journal of Optoelectronics and Advanced Materials*, 2009, **11**, 1656-1659.
- [2] M. Moritz, M. Laniecki, *Powder technology*, 2012, **230**, 106-111.
- [3] H.-M. Chiang, K.-Y. Cho, L.-X. Zeng, H.-L. Chiang, *Materials*, 2016, **9**(5), 350.
- [4] D. Zhao, J. Feng, Q. Huo, N. Melosh, G. H. Fredrickson, B. F. Chmelka, G. D. Stucky, *Science*, 1998, **279**, 548-552.
- [5] Parliament of the Republic of Serbia, Law on health care, *Official Gazette of the Republic of Serbia*, 2019, **25**, 112.
- [6] M. Fenech, *Mutation Research / Fundamental and Molecular Mechanisms of Mutagenesis*, 1993, **285**(1), 35-44.
- [7] NW. Roehm, GH. Rodgers, SM. Hatfield, AL. Glasebrook, *Journal of Immunological Methods*, 1991, **142**(2), 257-265.
- [8] D. Tsikas, *Analytical biochemistry*, 2017, **524**, 13-30.
- [9] J. Jiang, G. Oberdörster, P. Biswas, *Journal of Nanoparticle Research*, 2009, **11**, 77-89.

## MICROWAVE ASSISTED SYNTHESIS OF POLYANILINE/PULLULAN (PANI/PULL) COMPOSITE

I. N. Bubanja<sup>1</sup>, B. Lončarević<sup>2</sup>, M. Lješević<sup>2</sup>, D. Stanisavljev<sup>1</sup>, V. Beškoski<sup>3</sup>, G. Gojgić-Cvijović<sup>2</sup>, D. Bajuk-Bogdanović<sup>1</sup> and M. Gizdavić-Nikolaidis<sup>4</sup>

<sup>1</sup> Faculty of Physical Chemistry, University of Belgrade, Studentski trg 12-16, Belgrade, Serbia (itana.bubanja@ffh.bg.ac.rs)

<sup>2</sup> Department of Chemistry, Institute of Chemistry, Technology and Metallurgy, University of Belgrade, Njegoševa 12, Belgrade, Serbia

<sup>3</sup> University of Belgrade-Faculty of Chemistry, Department of Biochemistry, Studentski trg 12-15, Belgrade, Serbia

<sup>4</sup> Department of Molecular Medicine and Pathology, Faculty of Medical and Health Sciences, the University of Auckland, Auckland 1023, New Zealand

### ABSTRACT

Microwave assisted synthesis of polyaniline modified by pullulan (PANI/Pull) composite was performed by aniline oxidation with potassium iodate. The PANI/Pull composite was characterized using ATR-FTIR technique. FTIR spectra confirm presence of both components in PANI/Pull composite. Antimicrobial evaluation of PANI/Pull material performed by using a qualitative disk diffusion method on *Candida albicans* (*C. albicans*) culture showed very high sensitivity to PANI/Pull composite. Observed FTIR and antifungal activity represent a promising results especially for potential biomedical applications of PANI/Pull composite.

### INTRODUCTION

Growing interest in modification of conducting polymers with biopolymers is due to the fact that a simple procedure can be used to couple the properties of both, conducting polymers and biopolymers, in order to develop materials with improved characteristics [1]. As a conducting polymer, polyaniline (PANI) has achieved great attention due to its high electrical conductivity, unique redox properties, simple preparation and doping procedure, low cost, and therefore it has found a wide range of applications [1,2]. Besides mentioned, it has been shown that PANI represents a novel antimicrobial agent that is active against a broad range of bacteria and thus has a potential applications in food safety and biomedicine as an infection control coatings [3].

The aim of our work was to modify PANI by pullulan to obtain novel and improved composite. Thanks to pullulan's biocompatibility, non-toxicity, biodegradability and wide range of applicability (as low-calorie food additive, packaging material, usage in target drug therapy, tissue engineering, wound healing etc.) [4,5] this polysaccharide biopolymer seemed to be a good candidate as a potential PANI modifier.

In this paper, MW assisted copolymerization of aniline with pullulan using potassium iodate ( $\text{KIO}_3$ ) as an oxidant was conducted.

### METHODS

**MW Assisted Synthesis.** Microwave synthesis of PANI/Pull composite was performed in CEM reactor (CEM Discover 300-W single mode reactor operating at 2.45 GHz). Since the key part of our experiments was to keep a constant temperature as well as an irradiation power during the synthesis, it was carried out in specially designed double jacket reaction vessel which was connected to an external cooling circulating thermostat. For temperature measurements a fiber optic temperature sensor was used. Also, to achieve uniform temperature, the sample was mixed by magnetic stirring

at 400 rpm. Absorbed MW power,  $P$  was calculated from:  $P = C \cdot m \cdot (\Delta T/\Delta t)_i$ , where  $C$  represents heat capacity and its value is approximated with the value for pure water of  $4.18 \text{ J/g}^\circ\text{C}$ ,  $m$  is mass of the solution and  $(\Delta T/\Delta t)_i$  is estimated from the linear temperature increase throughout initial heating period during which dissipation of heat by the external thermostat was small. From mentioned calorimetric method the absorbed power for 80 W emitted power,  $P$  and its standard deviation were calculated from six replicates  $P = (10.0 \pm 0.5) \text{ W}$ . With this experimental design the temperature of the reaction mixture before addition of aniline was maintained at  $(26 \pm 2)^\circ\text{C}$ . PANI/Pull composite was prepared by aniline oxidation with potassium iodate. In 12 mL of an aqueous solution of 1.25 M hydrochloric acid, 0.432 g  $\text{KIO}_3$  and 0.343 g pullulan (or 70 wt% relative to aniline) were added. After initial heating period and when temperature reached constant value aniline (0.480 mL or 0.490 g) was added to HCl,  $\text{KIO}_3$  and pullulan mixture. MW synthesis was carried out for 10 min. The PANI/Pull product was obtained by centrifugation. Product was washed thoroughly with 1.25 M HCl aqueous solution, deionized water and acetone to eliminate impurities and low molecular weight oligomers. The product was dried in oven at  $40^\circ\text{C}$  overnight.

**FTIR characterization.** The ATR-FTIR spectra were recorded using Thermo Scientific Nicolet iS20 FT-IR spectrophotometer. A sample was placed in direct contact with an infrared attenuated total reflection (ATR) diamond crystal. All FTIR spectra were collected in the wavenumber range of  $1800\text{--}600 \text{ cm}^{-1}$  by co-adding 32 scans with a resolution of  $4 \text{ cm}^{-1}$ .

**Antimicrobial activity.** The qualitative antimicrobial evaluation of PANI and PANI/Pull materials was performed using a disk diffusion method [6] with reference culture of fungal strain *C. albicans* (ATCC 24433). Fungal inoculum was adjusted to the concentration of  $1\text{--}2 \cdot 10^6 \text{ CFU/mL}$ , and 100  $\mu\text{L}$  were seeded in Petri dishes containing Malt agar, followed by placing 1 mg of PANI and PANI/Pull materials on top of it. The Petri plates were incubated at  $28^\circ\text{C}$  for 48 h.

## RESULTS AND DISCUSSION

Obtained PANI/Pull composite was characterized using ATR-FTIR technique. Besides composite, pure PANI was synthesized as well under the same experimental conditions. The characteristic peaks observed in the FT-IR spectra of PANI/Pull composite give valuable information regarding to the possible interactions between pullulan and PANI. At Figure 1. the ATR-FTIR spectra of PANI (a), PANI/Pull composite (b) and pure pullulan (c) is shown. The spectrum of PANI/Pull composite exhibits bands characteristic of PANI as well as of pullulan which confirms the presence of both components in the composite. For pure PANI (Fig. 1(a)), the characteristic bands [2] attributed to C-C stretching quinoid band, C-C stretching benzenoid band, C-N stretching benzenoid band, band of deprotonated PANI and out-of-plane bending vibration of C-H on para distributed ring appear at  $1575$ ,  $1492$ ,  $1296$ ,  $1138$  and  $826 \text{ cm}^{-1}$  respectively. The strongest band at  $993 \text{ cm}^{-1}$  in the spectrum of pullulan (Fig. 1(c)) corresponds to glycosidic linkages [7]. The most prominent changes of the spectrum of the PANI/Pull composite (Fig. 1(b)), in comparison to the spectrum of the pure PANI, is the red shift of peaks at  $1575$  and  $1492 \text{ cm}^{-1}$  (quinonoid (Q) and benzenoid (B) ring-stretching vibrations, respectively) to  $1554$  and  $1458 \text{ cm}^{-1}$  and the increase in absorption at about  $1000 \text{ cm}^{-1}$ , due to the presence of pullulan during the polymerization of aniline. Also, the band at  $1296 \text{ cm}^{-1}$ , observed in the PANI spectrum attributed to C-N stretching of secondary amine, is significantly weakened and shifted to  $1287 \text{ cm}^{-1}$  in the spectrum of composite. Qualitative antimicrobial evaluation of PANI and PANI/Pull materials was performed using a disk diffusion method on *C. albicans* culture.

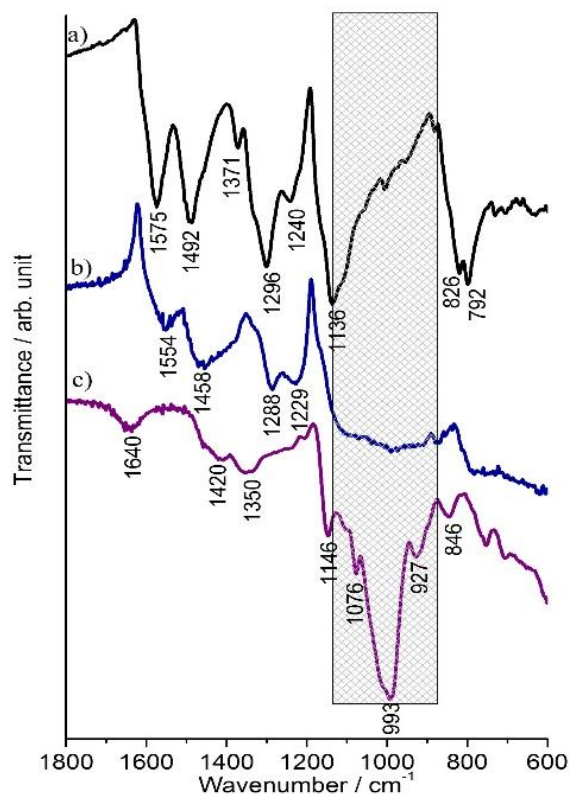


**Figure 1.** The ATR-FTIR spectra of PANI (a), PANI/Pull composite (b) and pure pullulan (c).

Even though slightly larger inhibition zone was obtained for PANI/Pull composite, obtained results suggest a high sensitivity of *C. albicans* to both PANI and PANI/Pull composite, indicating the antifungal activity of novel material.

## CONCLUSION

PANI/Pull composite was synthesized by MW assisted method under constant irradiation power and temperature. FTIR spectra confirmed the presence of both components, pure PANI and pullulan, in the PANI/Pull composite. Qualitative antimicrobial test showed that PANI/Pull has a high antifungal effect against *C. albicans*. Even though obtained results from FTIR and antimicrobial evaluation are promising, especially for potential biomedical application, further investigations are required.

## Acknowledgement

This work was partially supported by Ministry of Education, Science and Technological Development of Republic of Serbia (Grant No: 451-03-9/2021-14/200146, 451-03-9/2021-14/200168, 451-03-9/2021-14/200026)

## REFERENCES

- [1] J. S. Karthika, B. Vishalakshi and J. Naik, *Int. J. Biol. Macromol.*, 2016, **82**, 61-67.
- [2] M. Gizdavic-Nikolaidis, G Bowmaker and Z Zujovic in: *The synthesis, physical properties, bioactivity and potential applications of polyanilines*, Cambridge Scholar Publishing, Newcastle upon Tyne, UK 2018.
- [3] J. Robertson, M. Gizdavic-Nikolaidis, M. K. Nieuwoudt and S. Swift, *PeerJ*, 2018, e5135.
- [4] V. D. Prajapati, G. K. Jani and S. M. Khanda, *Carbohydr. Polym.*, 2013, 95(1), 540-549.

- [5] M. B. Coltelli, S. Danti, K. De Clerk, A. Layyeri and P. Morganti, *J. Funct. Biomater.*, 2020, **11**(1), 20.
- [6] M. Goodfellow and D. Minnikin (Eds.), *Chemical methods in bacterial systematics*, Academic Press, London, UK 1985.
- [7] K. I. Shingel, *Carbohydr. Res.*, 2002, **337**(16),1445-1451.

## SYNTHESIS AND CHARACTERIZATION OF NEW CERIUM DOPED PHOSPHATE TUNGSTEN BRONZE

T. Maksimović<sup>1</sup>, Lj. Joksović<sup>1</sup>, P. Tančić<sup>2</sup>, J. Maksimović<sup>3</sup>, J. Senčanski<sup>4</sup>,  
M. Pagnacco<sup>5\*</sup> and Z. Nedić<sup>3</sup>

<sup>1</sup>Faculty of Science, Department of Chemistry, University of Kragujevac, Radoja Domanovića 12, 34000 Kragujevac, Serbia.

<sup>2</sup>Geological Survey of Serbia, Rovinjska 12, 11000 Belgrade, Serbia

<sup>3</sup>Faculty of Physical Chemistry, University of Belgrade, Studentski trg 12-16, 11000 Belgrade, Serbia

<sup>4</sup>University of Belgrade, Institute of General and Physical Chemistry, Studentski trg 12-15, 11000 Belgrade, Serbia.

<sup>5</sup>University of Belgrade, Institute of Chemistry, Technology and Metallurgy, Njegoševa 12, 11000 Belgrade, Serbia. (\*corresponding author e-mail [maja.pagnacco@nanosys.ihtm.bg.ac.rs](mailto:maja.pagnacco@nanosys.ihtm.bg.ac.rs))

### ABSTRACT

Cerium doped phosphate tungsten bronze (Ce-PWB) was synthesized by phase transformations of  $\text{CePW}_{12}\text{O}_{40}\times 6\text{H}_2\text{O}$  (Ce-6-PWA) salt. The solid-solid transformations of Keggin's anion of this salt, including dehydration processes and bronze's formation are finished at about 600 °C. The constructions of Ce-6-PWA and Ce-PWB were characterized by thermal analysis (TGA and DTA), X-ray powder diffraction (XRPD), and Fourier-transform infrared spectra (FTIR).

### INTRODUCTION

The general formula of heteropoly acids of Keggin's type can be presented as  $\text{H}_{(8-x)}\text{XM}_{12}\text{O}_{40}\times n\text{H}_2\text{O}$  (where x is the oxidation number of X and n = 6-31) [1-3]. HPA has been a matter of interest in basic and applied science for more than a century because of its high protonic conductivity at room temperature [3]. Based on our previously performed examinations [4], in this work we have synthesized cerium doped phosphate tungsten bronze starting from 12-tungstophosphoric heteropoly acid with Keggin's structure. Tungsten bronzes, as inert inorganic solids, with alkali, alkaline earth, or rare earth ions have been extensively investigated due to their electronic and magnetic features [5]. The construction of phosphate tungsten bronzes can be described as a  $\text{ReO}_3$ -type structure and represents a gathering of  $\text{WO}_6$  units repeated along three bearings by sharing corners [6]. Ce-PWB has been synthesized for the first time to obtain information about its structure, chemical properties, and practical usage. The potential practical application of Ce-PWB is in its installation in portable rechargeable batteries and as catalysts for the oxidation process in fuel cells, as well as in photocatalysis.

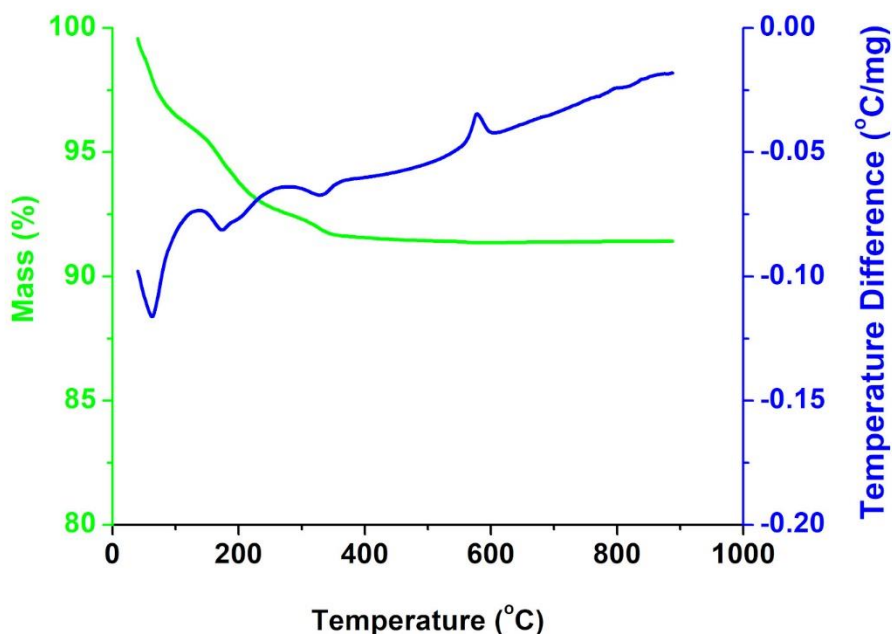
### METHODS

For the preparation of Ce-PWB, as a starting material is used 12-tungstophosphoric heteropoly acid  $\text{H}_3\text{PW}_{12}\text{O}_{40}\times 29\text{H}_2\text{O}$  (29-PWA), which was first transformed into heteropoly acid 6-hydrate  $\text{H}_3\text{PW}_{12}\text{O}_{40}\times 6\text{H}_2\text{O}$  (6-PWA), by heating of 29-PWA in a kiln at 80 °C. The salt Ce-6-PWA is prepared by ionic exchange of  $\text{H}^+$  ion in 6-PWA with cerium ion. By heating of Ce-6-PWA, the Keggin's structure is destroyed and Ce-PWB is formed. Thermal examinations were performed in a stream of nitrogen, using a TA Instruments SDT 2960 Simultaneous DSC-TGA scanning rate (10 °C  $\text{min}^{-1}$ ), in a temperature range from room temperature to 900 °C. For obtaining X-ray powder diffraction (XRPD) pattern it is used a Rigaku Ultima4 automated diffractometer with Cu tube, operating at 40 kV and 40 mA. The diffraction data were collected in the 2 $\theta$  Bragg angle ranges from

10° to 90°, counting for 2 deg min<sup>-1</sup> at every 0.05° steps. The XRPD measurements were performed ex-situ at room temperature (23 °C). FTIR spectra of Ce-6-PWA and Ce-PWB were recorded on a Thermo Scientific Nicolet iS20 Instrument, using the KBr pellet technique with 32 scans and 4 cm<sup>-1</sup> resolution.

## RESULTS AND DISCUSSION

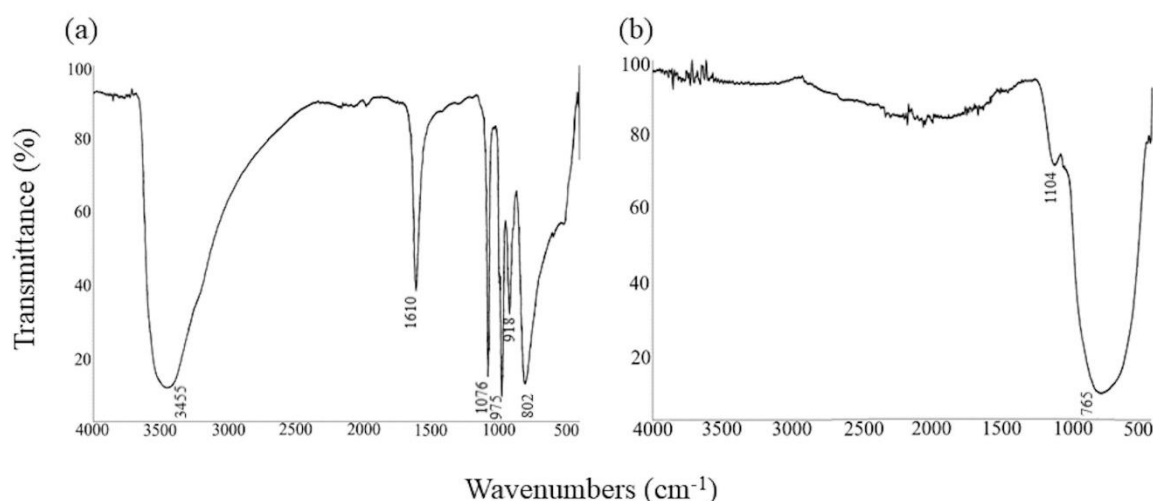
The constituted Ce-PWB, as well as the intermediate, Ce-6-PWA are characterized. The results of the thermal analysis of Ce-6-PWA in a temperature range from room temperature to 900 °C are presented in Fig.1. The DTA curve represented in blue color shows three endothermic peaks at 50 °C, 180 °C and 340 °C and one exothermic at about 600 °C. When the sample loses molecules of water anhydrous phase of Ce-6-PWA is formed. The solid-solid transformations of Keggin's anion and formation of the Ce-PWB have happened during the exothermic process. XRPD pattern of Ce doped phosphate tungsten bronze (Ce-PWB), with appropriate inter-planar spacing, is shown in Table 1. The observed data for Ce-PWB are analogical to those obtained for PWB crystallized as monoclinic at temperature conditions of 750 °C [7]. FTIR spectra of Ce-6-PWA and Ce-PWB at room temperature are represented in Fig. 2. In the Ce-6-PWA spectrum are noticeable the characteristic bands of molecule H<sub>2</sub>O ( $\nu = 3455\text{ cm}^{-1}$  and  $\delta = 1610\text{ cm}^{-1}$ ), PO<sub>4</sub> tetrahedral ( $\nu_3 = 1076\text{ cm}^{-1}$  and  $\nu_1 = 975\text{ cm}^{-1}$ ), WO<sub>6</sub> octahedral ( $\nu = 918\text{ cm}^{-1}$ ). The destruction of Keggin's ions and bronze's formation happens in the process of calcination and is shown in Fig 2 b). The small intensity band  $\nu_3$  (1104 cm<sup>-1</sup>) is characteristic for the PO<sub>4</sub> group, while the very strong band at about 800 cm<sup>-1</sup> is characteristic for the WO<sub>6</sub> octahedron. Phosphorus is in the form of PO<sub>4</sub> at a very small percentage relative to WO<sub>6</sub>. However, there is also the possibility of building a mixed network consisting of WO<sub>6</sub> octahedra and PO<sub>4</sub> tetrahedra in Ce doped PWB.



**Figure 1.** DTA and TGA curves of Ce-6-PWA.

**Table 1.** Observed inter-planar spacing ( $d$ , in Å) and intensities ( $I$ , in %) of Ce-PWB, in comparison with PWB

Ce-PWB		PWB		
$d$	$I$	$D$	$I$	$h k l$
		3.84	41	0 0 2
3.743(2)	100	3.75	100	0 2 0
3.099(6)	10	3.11	6	-1 1 2
2.663(1)	68	2.68	40	-2 0 2
		2.64	26	2 0 2
2.173(2)	17	2.17	14	-2 2 2
		2.01	2	2 1 3
1.877(4)	9	1.87	11	-1 0 4
		1.81	4	-1 1 4
1.678(1)	23	1.67	15	-2 1 4
1.534(1)	14	1.53	9	2 4 2
		1.49	3	-1 4 3
1.330(3)	4			
1.253(2)	7			

**Figure 2.** FTIR spectra of: (a) Ce-6-PWA and (b) Ce-PWB.

## CONCLUSION

The conditions for thermally phase transformation of cerium salt of 12-tungstophosphoric heteropoly acid to obtain new cerium phosphate tungsten bronze, have been studied in the present work. The new material (Ce-PWB), synthesized from Keggin's anion structure as a precursor, is formed and characterized by TGA, DTA, XRPD, FTIR.

## Acknowledgement

This work was supported by the Serbian Ministry of Education, Science and Technological Development (Grant Numbers 451-03-9/2021-14/200122, 451-3-9/2021-14/20146 and 451-03-9/2021-14/200026).

## REFERENCES

[1] O. Nakamura, T. Kodama, J. Ogino, I. Miyake, Chem. Letters, 1979, 1, 17-18.

- 
- [2] K. D. Kreuer, M. Hampele, K. Dolde, A. Rabenau, *Solid State Ionics*, 1988, 28-30, 589-593.
- [3] U. B. Mioč, M. R. Todorović, M. Davidović, Ph. Colomban, I. Holclajtner-Antunović, *Solid State Ionics*, 2005, 39, 3005-3017.
- [4] T. V. Maksimović, J. P. Maksimović, Lj. G. Joksović, Z. P. Nedić, Maja C. Pagnacco, *Hemijska industrija*, 2018, 72, 275-283.
- [5] M. T. Pope, K. Wassermann, M. Salmen, J. D. Dann, H.J. Lunk, *Journal of Solid State Chemistry*, 1999, 149, 378-383.
- [6] P. Rousset, P. Labbé, D. Groult, *Acta Crystallographica B*, 2000, 56, 377-391.
- [7] U. Mioč, R. Dimitrijević, M. Davidović, Z. Nedić, M. Mitrović, Ph. Colomban, *Journal of Materials Science*, 1994, 29, 3705-3718.

## EVALUATION OF PERFORMANCE OF DISPERSION CORRECTED DENSITY FUNCTIONALS FOR TTF-TTF STACKING INTERACTIONS

I. S. Veljković<sup>1</sup>, D. P. Malenov<sup>2</sup> and S. D. Zarić<sup>2</sup>

<sup>1</sup> University of Belgrade – Institute of Chemistry, Technology and Metallurgy – National Institute of the Republic of Serbia, Njegoševa 12, 11000 Belgrade, Serbia (ivana.veljkovic@ihm.bg.ac.rs)

<sup>2</sup> University of Belgrade – Faculty of Chemistry, Studentski trg 12-16, 11000 Belgrade, Serbia.

### ABSTRACT

CCSD(T)/CBS energies for stacking interactions between two tetrathiafulvalene molecules were used as benchmark data to evaluate the performance of dispersion corrected density functionals in calculating the interaction energies. The results showed that the best functional for TTF-TTF stacking is B2PLYP-D3 with 6-311++G\*\* basis set, which successfully reproduces gold standard CCSD(T)/CBS interaction energies. M06L-D3 functional with 6-311++G\*\* basis set consistently underestimates interaction energies, giving potential energy curves of accurate shapes.

### INTRODUCTION

Tetrathiafulvalene and its derivatives are well-known group of molecules with remarkable electron donor and redox properties. These properties make TTF and its derivatives a key element in designing of organic electrically conducting materials [1]. TTF unit is very often an integral part of different materials with electrical, magnetic and optical properties, especially in systems able to act as molecular machines [1-4].

Our previous research demonstrated that there is a large number of stacking interactions between two TTF molecules in crystal structures from Cambridge Structural Database, while the energies of these interactions are very strong, the strongest having the CCSD(T)/CBS interaction energy of -9.96 kcal mol [5]. Although this method gives the most reliable results [6] and is referred to as gold standard of quantum chemistry, it is highly time consuming and computationally expensive.

In this work, we made an effort in finding an efficient and at the same time computationally less demanding method for calculations of TTF-TTF stacking energies. We performed benchmark analysis to evaluate the performance of dispersion corrected density functionals for TTF-TTF stacking, in order to find the method that gives accurate interaction energies and/or potential energy curves of correct shapes.

### METHODS

All calculations were performed using the Gaussian09 program package. The geometry of the TTF monomer was optimized using the B97xD density functional and the def2-TZVP basis set and confirmed as a true minimum by performing the calculations of vibrational frequencies. For several stacking geometries (Figure 1) CCSD(T) interaction energies at the complete basis set (CBS) were calculated by applying the triple-quadrupole extrapolation scheme proposed by Helgaker [7].

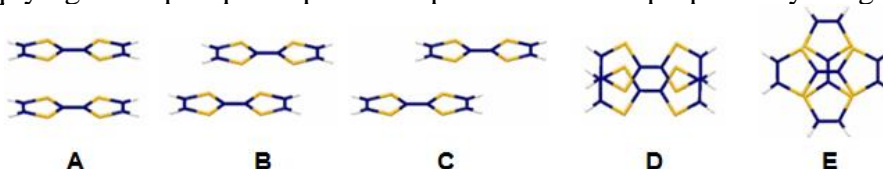


**Figure 1.** Tetrathiafulvalene dimers used to obtain interaction energies at the CCSD(T)/CBS level of theory.

Interaction energies obtained by CCSD(T)/CBS calculations were used for comparison with interaction energies obtained by different combinations of density functionals and basis sets. To assess which level of theory gives good agreement with the CCSD(T)/CBS results, the parameters RMSE (root mean square error) and SESD (signed error standard deviation) were calculated by applying the formulas:

$$RMSE = \sqrt{\frac{\sum_{i=1}^n SE_i^2}{n}} \quad SESD = \sqrt{\frac{\sum_{i=1}^n (SE_i - AVG)^2}{n-1}}$$

where  $n$  is the number of tested TTF dimers ( $n = 5$ ),  $SE$  is signed error, and  $AVG$  is average (signed) error.

## RESULTS AND DISCUSSION

The calculated CCSD(T)/CBS interaction energies for dimers A–E (Figure 1) are -4.97, -9.49, -6.30, -8.15, and -5.68 kcal/mol, respectively [5]. In the first part of our benchmark study, several basis sets: 6-31G\*\*, 6-31++G\*\*, 6-311++G\*\*, cc-pVTZ, aug-cc-pVDZ, def2-SVP, def2-TZVP, def2-TZVPP; were combined with common DFT methods with dispersion correction: B2PLYP-D3, B3LYP-D3, TPSS-D3,  $\omega$ B97xD, BLYP-D3. The results obtained with 6-311++G\*\* basis set were in best agreement with CCSD(T)/CBS interaction energies, and this basis set was then used for further testing with larger number of density functionals. Table 1 contains the list of all the functionals, as well as the values of statistical parameters used to assess their performance when combined with 6-311++G\*\* basis set.

**Table 1.** List of dispersion corrected density functionals used with 6-311++G\*\* basis set to calculate TTF-TTF stacking, with values of RMSE and SESD parameters of their performance against CCSD(T)/CBS level.

method	RMSE [kcal/mol]	SESD [kcal/mol]	method	RMSE [kcal/mol]	SESD [kcal/mol]
B2PLYP-D3	0.26	0.13	M06-D3	1.41	0.40
B97-D3	2.24	0.36	M052X-D3	1.31	0.41
$\omega$ B97xD	1.62	0.43	M062X-D3	1.27	0.86
B3LYP-D3	0.27	0.21	M06L-D3	0.85	0.28
BLYP-D3	0.75	0.28	M06HF-D3	0.87	0.81
TPSS/TPSS-D3	0.48	0.37	M05	6.37	1.56
PBEPBE-D3	0.99	0.71	M06	1.79	0.36
PBE0-D3	0.81	0.47	M052X	3.48	0.56
BPBE-D3	1.96	0.86	M062X	2.11	0.92
B3PW91-D3	1.19	0.41	M06L	1.93	0.28
M05-D3	1.30	0.85	M06HF	2.58	0.96

Statistical analysis showed that the B2PLYP-D3 functional with the 6-311++G\*\* basis set shows excellent agreement with all obtained CCSD(T)/CBS energy values. In addition to low RMSE (0.26

kcal/mol), the value of the SESD is only 0.13 kcal/mol (Table 1). Therefore, this combination of method and basis set can be considered the best for calculating potential energy curves of TTF-TTF stacking (Figure 2).

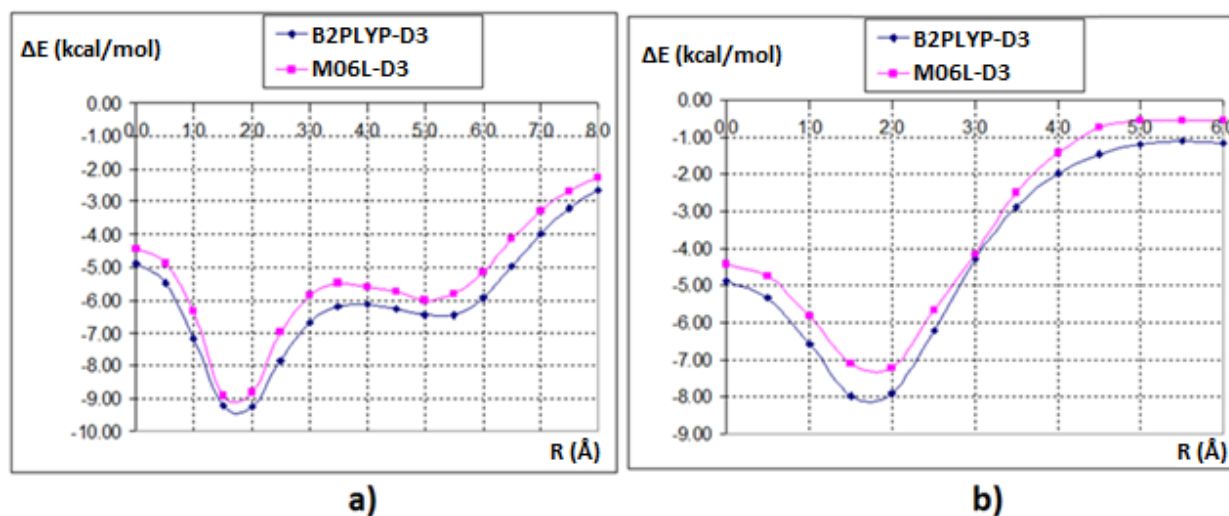


**Figure 2.** Potential energy curves for TTF–TTF stacking along the longer  $C_2$  axis of TTF (a, includes geometries A–C in Figure 1) and along the shorter  $C_2$  axis of TTF (b, includes geometries A and D in Figure 1). The curves were calculated with B2PLYP-D3 (blue) and M06L-D3 (pink) methods, using 6-311++G\*\* basis set.

In addition to B2PLYP-D3, B3LYP-D3 with 6-311++G\*\* basis set also gives reasonably accurate energies of TTF-TTF stacking (Table 1). Although high RMSE values for BLYP-D3, M06L-D3 and M06L indicate that they are not able to give correct energies, their low SESD values indicate underestimating of interaction energies with excellent consistency (Table 1). The curves calculated with M06L-D3 method using 6-311++G\*\* basis set are therefore of very similar shapes to those calculated at the most accurate B2PLYP-D3/6-311++G\*\* level (Figure 2), giving correct geometries of potential curve minima.

## CONCLUSION

The energies of stacking interactions between two neutral TTF molecules were calculated using different combinations of DFT functionals and basis sets and compared to gold standard CCSD(T)/CBS energies. It was shown that the B2PLYP-D3 with 6-311++G\*\* basis set is excellent and computationally inexpensive functional for reproducing the benchmark data. M06L-D3 functional with 6-311++G\*\* basis set systematically underestimates the benchmark energies, but with high level of consistency, implying that it can be used for calculations of potential energy curves of accurate shapes. Some other studied methods are reliable in reproducing the CCSD(T)/CBS data, but with certain degree of inconsistency.

## Acknowledgement

This work was supported by the Serbian Ministry of Education, Science and Technological Development (Grant No. 451-03-9/2021-14/200026 and 451-03-9/2021-14/200168).

## REFERENCES

- [1] N. Martín, *Chem. Commun.*, 2013, **49**, 7025 – 7027.
- [2] F. G. Brunetti, J. L. López, C. Atienza, N. Martín, *J. Mater. Chem.*, 2012, **22**, 4188 – 4205.

- 
- [3] H. Jiang, X. Yang, Z. Cui, Y. Liu, H. Li, W. Hu, C. Kloc, *CrystEngComm*, 2014, **16**, 5968 – 5983.
- [4] M. Bendikov, F. Wudl, D. F. Perepichka, *Chem. Rev.*, 2004, **104**, 4891 – 4946.
- [5] I. S. Antonijević, D. P. Malenov, M. B. Hall, S. D. Zarić, *Acta Crystallographica B75*, 2019, 1 – 7.
- [6] J. A. Pople, M. Head-Gordon, K. Raghavachari, *J. Chem. Phys.* 1987, **87**, 5968 – 5975.
- [7] T. Helgaker, W. Klopper, H. Koch, J. Noga, *J. Chem. Phys.*, 1997, **106**, 9639.

## CHARACTERIZATION OF PRODUCTS OF PROLONGED HEMATOXYLIN AUTOXIDATION IN ALKALINE AQUEOUS SOLUTION

M.G. Nikolić<sup>1</sup>, S.C. Živanović<sup>2</sup>, N.S. Krstić<sup>1</sup> and G.M. Nikolić<sup>3</sup>

<sup>1</sup> *University of Niš, Faculty of Sciences and Mathematics, Department of Chemistry, Višegradaska 33, 18000 Niš, Serbia*

<sup>2</sup> *Research Centre for Biomedicine, Faculty of Medicine, University of Nis, Bulevar Dr Zorana Đinđića 81, 18 000 Niš, Serbia*

<sup>3</sup> *Department of Chemistry, Faculty of Medicine, University of Niš, Bulevar Dr Zorana Đinđića 81, 18 000 Nis, Serbia (goranhem@yahoo.com)*

### ABSTRACT

The products of prolonged autoxidation of hematoxylin in alkaline aqueous solution were characterized by infrared (IR) spectroscopy, matrix-assisted laser desorption/ionization - time-of-flight mass spectrometry (MALDI-TOF MS), and electron spin resonance (ESR) spectroscopy. The IR data indicated that polymerization has occurred during this process. This was confirmed by the MALDI-TOF MS data, which also gave some insight into the degree of polymerization under our experimental conditions. The ESR data revealed that obtained products contain stable oxygen-centered radicals. This material has characteristics resembling natural and synthetic humic acid-like substances.

### INTRODUCTION

Hematoxylin (7,11b-dihydroindeno[2,1-c]chromene-3,4,6a,9,10(6H)-pentol) is a naturally occurring polyphenol with a long history of use, most prominently as a basis of dyes applied in cytology and histochemistry [1]. Additionally, polymers of hematoxylin have found new and interesting applications in constructing electrodes for biosensors [2, 3] and synthesis of gold and silver nanoparticles [4, 5].

Having in mind that interest in hematoxylin and its polymers is not decreasing [6], we decided to prepare and characterize material obtained *via* prolonged hematoxylin autoxidation in alkaline aqueous solution.

### EXPERIMENTAL

*Materials and methods:* Hematoxylin (>95%) was purchased from Merck, Germany, and used without further purification. Sodium hydroxide, hydrochloric acid, trifluoroacetic acid (TFA), and acetone (all p.a. grade) were purchased from Sigma-Aldrich, USA. All solutions were prepared with deionized water. IR measurements (neat, attenuated total reflectance) were carried out on a Thermo Nicolet 6700 FTIR instrument with the spectral resolution of 2 cm<sup>-1</sup>. ESR measurements were performed at room temperature on an X-band EMX spectrometer (Bruker, Germany) using 2 mm quartz tube cell for solid samples. The main ESR settings were as follows: microwave frequency – 9.85 GHz, modulation frequency – 100 kHz, modulation amplitude – 2 G, and time constant – 0.64 msec. Samples for MALDI-TOF MS analysis were prepared using the dried droplet method. Five milligrams of sample were dissolved in acetone and mixed with an equal amount of 0.1% TFA. The solution (0.5 µL) was applied on the sample plate and allowed to dry for 15 min at room temperature. MALDI-TOF MS experiments were performed on an Autoflex speed instrument (Bruker Daltonics, Germany) operating in linear positive and negative mode in the *m/z* range from 300 to 2000 Da. A solid-state, Nd:YAG 355 nm SmartBeam, laser with a frequency of 1000 Hz was used for ionization. Typically, spectra were acquired by accumulating signals from 2000 laser shots at 4 different spots.

*Autoxidation product preparation:* Hematoxylin (1g, 3.3 mmol) was dissolved in 20 mL of deionized water, and pH was adjusted to 9.0 with 1M NaOH solution. The solution was stirred in an open round bottom flask without direct exposure to sunlight for 72 h. The pH of the solution was adjusted to approximately 2 by adding 1M HCl. After additional 48 h without stirring, dark brown product precipitated, and it was vacuum filtered, washed with 100 mL of 0.1M HCl, and dried for 24h at 60 °C.

## RESULTS AND DISCUSSION

In the IR spectrum of a product of hematoxylin autoxidation (Figure 1b) the number of individual absorption bands noticeably decreased when compared to the IR spectrum of pure hematoxylin (Figure 1a). In addition, broadening of absorption bands indicates that some degree of polymerization has occurred during the autoxidation process.

MALDI-TOF mass spectra of hematoxylin autoxidation products have not been, to the best of our knowledge, previously reported in the literature. For spectrum recorded in the negative mode (Figure 2a) the largest detected ion was at 1090 Da, and the most intensive fragments in the spectrum were found in the mass range from 300 to 900 Da. Spectrum recorded in the positive mode (Figure 2b) generally has lower peak intensities, but revealed the existence of some additional fragments ranging in mass from 1090 up to 1666 Da. Although the detailed analysis of MALDI-TOF MS data has to be postponed for some future paper, it is clear that there is the possibility that under our experimental conditions at least five hematoxylin units might condense to form the product of autoxidation.

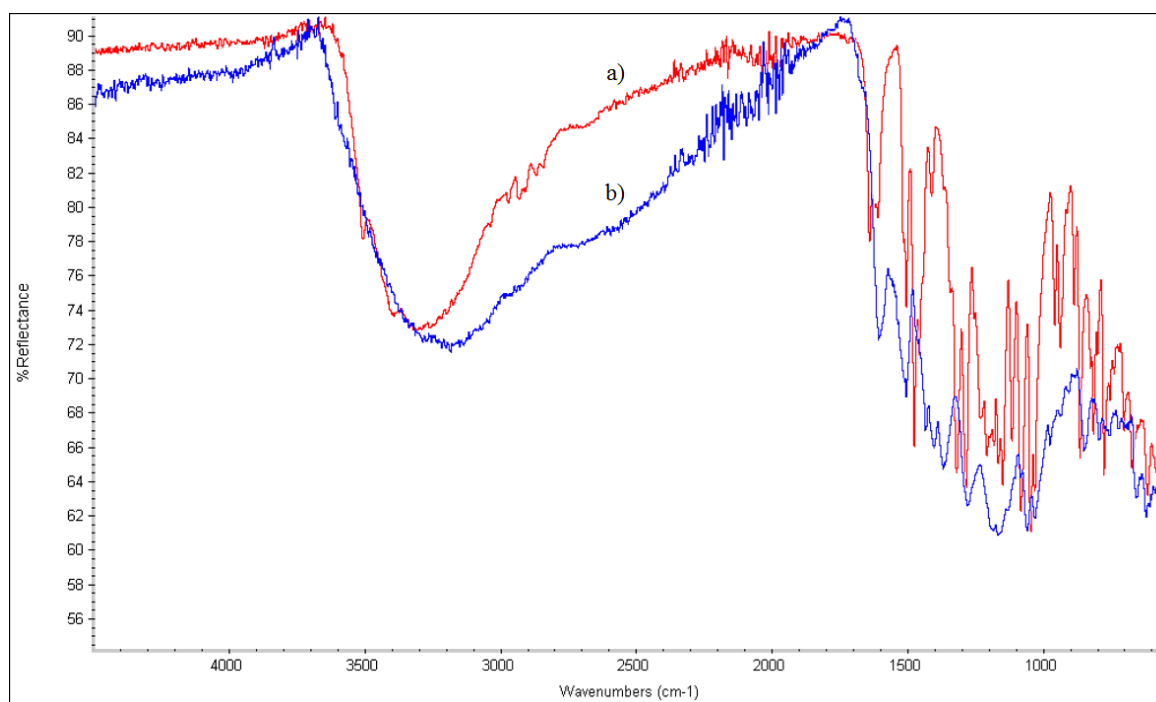


**Figure 1.** IR spectra of hematoxylin (a) and products of hematoxylin autoxidation (b).

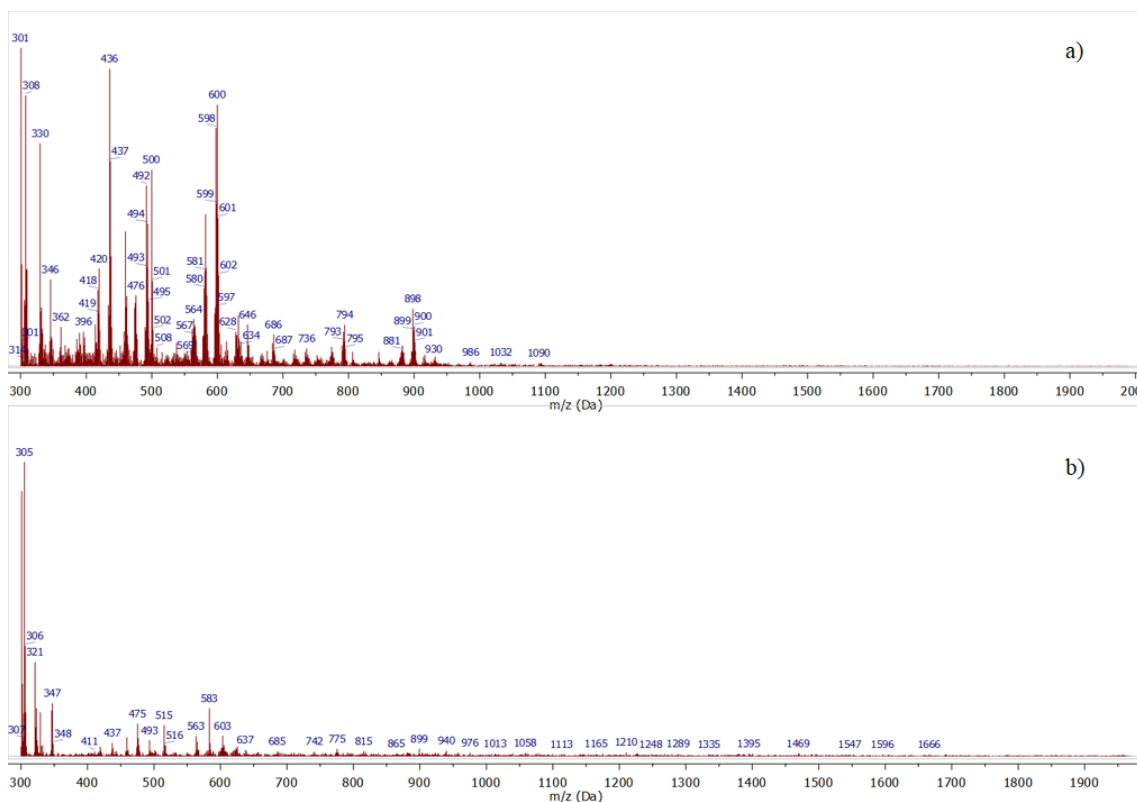


**Figure 2.** MALDI-TOF mass spectra of hematoxylin autoxidation products recorded in negative (a) and positive mode (b).

The ESR spectrum of hematoxylin autoxidation products consisted of only one, slightly asymmetric, signal with the linewidth of 3.63 G and  $g$ -value of 2.0042. According to the literature, these spectral characteristics are in agreement with the data for oxygen-centered radical species in natural humic acids and synthetic humic acid-like substances [7]. The ESR parameters of hematoxylin autoxidation products stored in the dark at room temperature remained stable during the time period of 4 months, which is expected for a system that contains oxygen centres adjacent to aromatic structures.

## CONCLUSION

IR, MALDI-TOF MS, and ESR data revealed that prolonged autoxidation of hematoxylin in alkaline aqueous solution leads to the formation of polymerization products containing stable oxygen-centered radicals. Comparison of our results with the literature data led us to the conclusion that obtained material bears great resemblance in its characteristics to the natural and synthetic humic acid-like substances.

## Acknowledgement

This work was supported by the Ministry of Education, Science and Technological Development of the Republic of Serbia, Contract No. 451-03-9/2021-14/200124.

## REFERENCES

- [1] M. Titford, *Biotech. Histochem.*, 2005, **80**, 73-78.
- [2] A.Samide, B. Tutunaru, G. Bratulescu, *J. Appl. Polym. Sci.*, 2013, **130**, 687-697.
- [3] D.G. Dilgin, H.İ. Gökçel, *Anal. Methods*, 2015, **7**, 990-999.

- [4] V.A. Litvin, B.F. Minaev, *Mater. Chem. Phys.*, 2014, **144**, 168-178.
- [5] V.A. Litvin, B.F. Minaev, *Spectrochim. Acta A*, 2013, **108**, 115-122.
- [6] C.J. Cooksey, *Biotech. Histochem.*, 2021, **96**, 242-249.
- [7] V.A. Litvin, B.F. Minaev, G.V. Baryshnikov, *J. Mol. Struct.*, 2015, **1086**, 25-33.

## DIELECTRIC PROPERTIES OF PULSED LASER DEPOSITED NANOSCALE LaNi<sub>5</sub> THIN FILMS

R. Todoran, D. Todoran, Zs. Szakacs

*Technical University of Cluj Napoca, North University Center of Baia Mare, Baia Mare, Maramures, Romania. (szakacsz@yahoo.com)*

### ABSTRACT

Dielectric properties of pulsed laser deposited, nanoscale LaNi<sub>5</sub> alloy layers, on glass or SiO<sub>2</sub> substrate are described using the complex dielectric function. The UV-Vis-IR spectral behavior of this function is studied separately for its real  $\epsilon_1$  (the dielectric constant or dielectric permittivity), and imaginary part  $\epsilon_2$  (the dielectric loss function). The obtained absolute reflectance spectra were processed using the Kramers–Krönig formalism, so that the real and imaginary parts of the complex dielectric function could be computationally determined, also leading to the calculation of the electron loss functions  $-\text{Im } \epsilon^{-1}$ . This study reveals the layer thickness and deposition substrate dependent optical and electrical properties of the produced nanoscale LaNi<sub>5</sub> structures.

### INTRODUCTION

Rare earth element (REE) compounds are undeniably of paramount importance in modern technologies, proven by the number of theoretical and practical application studies published. Lanthanum is the prototype of its group of transition metals. Probably its best-known application is for Hydrogen storage in AB<sub>5</sub> type alloys with Ni [1,2].

### MATERIALS AND METHODS

The materials and methods used in our study were thoroughly described previously [2,3]. LaNi<sub>5</sub> thin films, obtained by previously prepared bulk LaNi<sub>5</sub>, were deposited using laser induced vaporization in a low-pressure Ar filled deposition chamber on lime-glass or silica substrates using a 30MW ruby laser. Deposition substrates were positioned 3-5cm away from the LaNi<sub>5</sub> bulk sample holder with a 10-15° tilt from perpendicular direction. The film thickness was measurements using an interferometric optical microscope and a Na lamp's 588.995 nm wavelength, which also allowed the observation of the insular deposition pattern. The films used in our study were determined to have the following thicknesses: 4.5 nm, 22 nm, 38 nm, 42 nm on glass substrate, and 36 nm on SiO<sub>2</sub> substrate. Their quality-check was done using XRD.

Absolute differential reflectance and transmittance values of the deposited films, without the substrate's contribution, were obtained at the HeNe laser's 632.8 nm wavelength. Relative differential single-beam reflectance spectroscopy of deposited samples, in the UV-Vis-NIR-MIR domain was done for wavelengths between 200–950 nm UV-Vis-NIR and 2.5–25  $\mu\text{m}$  MIR using a Specord M40, respectively a Specord 75IR spectrophotometer. Interpolation bridged the gap over the two spectra, and an  $1/a^\nu$ -type law extrapolated the data to down 125 nm, where  $\nu$  is the photon frequency, and the dimensionless coefficient  $a$  was determined using two lines from the Lyman series of a deuterium lamp and a LiF window. These data were processed to compute the refractive index  $n$  and the extinction coefficient  $k$  using the Kramers-Krönig formalism which was successfully used by us before [2-4].

Knowing that  $\varepsilon = (n+ik)^2$  one could determine the real and imaginary parts of the complex dielectric function. For the interpretations of the obtained graphical representations of  $\varepsilon_1$  (the dielectric constant or dielectric permittivity) and  $\varepsilon_2$  (the dielectric loss function) and of the electron loss functions  $-\text{Im} \varepsilon^{-1}$  and  $-\text{Im}(1 + \varepsilon)^{-1}$ , one took into consideration both 2D and 3D electronic models, as before [3]. We still use the notation around a van Hove singularity as defined in [3] so that: maximal values are of type M<sub>0</sub>, minimal ones are M<sub>2</sub> type, while the M<sub>1</sub> and M<sub>3</sub> types represent, decreasing respectively increasing behaviors with different slopes. Sharp peaks in the electron loss functions indicate resonances of free-electron plasma with the external electro-magnetic field.

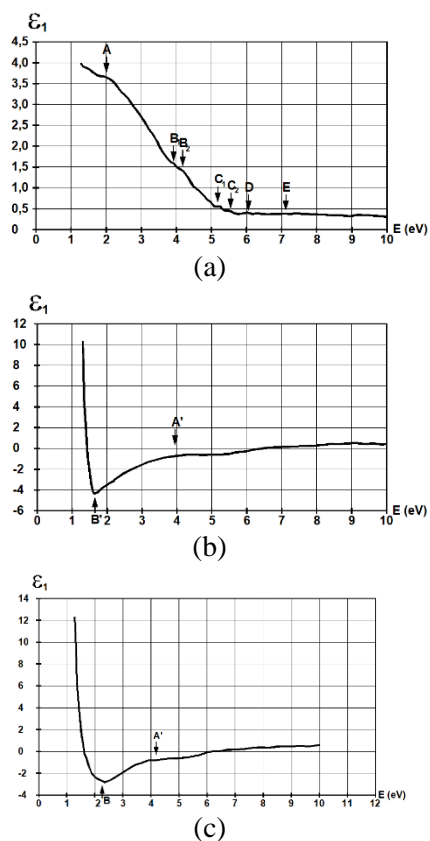


**Figure 1.** The dielectric constant's spectral behavior for film thicknesses of (a) d=4.5nm, (b) d=42nm deposited on glass substrate, and for the (c) d=36nm film on SiO<sub>2</sub> substrate

### RESULTS AND DISCUSSIONS

Behavior of the dielectric constant distribution  $\varepsilon_1(E)$ , can be observed in Fig. 1, for different nanometer scale film thicknesses. The thinnest film exhibits weak then sharp increase as the energy decreases, characteristic to insular deposition patterns. The marked particularities designate van Hove singularities. Increased film thickness from 36nm to 42nm leads to the minimum's displacement towards lower energies, explained by increase in the concentration of free electrons trapped in the surface layers.

In the region between cca. 1.5-6eV, where the dielectric permittivity has negative values, the absorption coefficient  $k$  has much higher values than the refraction index  $n$  indicating optical electronic transitions of bound electrons. The wide hump at around 4eV can be also observed in the other optical functions and it corresponds to electronic transitions from high density levels at a value of around 4eV below the Fermi level.[3]

The behavior of the dielectric loss function  $\varepsilon_2$  can be viewed in fig. 2.

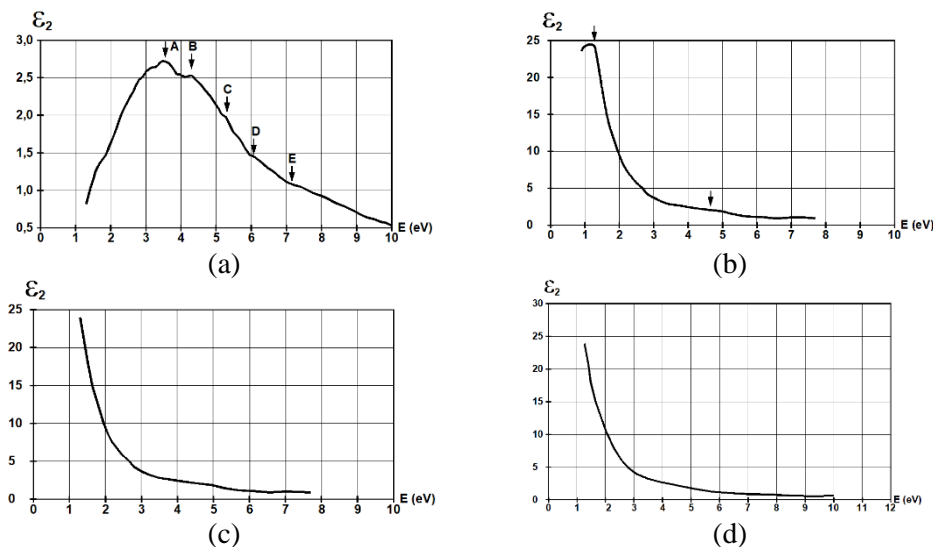


**Figure 2.** The dielectric loss function’s spectral behavior for film thicknesses of (a)  $d=4.5\text{nm}$ , (b)  $d=38\text{nm}$ , (c)  $d=42\text{nm}$  on glass and (d)  $d=36\text{nm}$  on  $\text{SiO}_2$  substrate

A striking feature change can be observed in figures 2(a) to 2(c). While the first figure exhibits feature characteristic to semiconductors, this maximum is displaced towards lower energies, then it disappears completely. The last figure shows high concentrations of free charge carriers in the 40nm and 36 nm thick films on glass and  $\text{SiO}_2$  substrates. One can correlate the maxima observed for the thinnest deposited film with the optical energy absorptions which occur at energies around  $A(\hbar\omega=3.7\text{eV})$ ,  $B(\hbar\omega=4.6\text{eV})$ ,  $A(\hbar\omega=5.4\text{eV})$ ,  $A(\hbar\omega=6.2\text{eV})$ ,  $A(\hbar\omega=7.3\text{eV})$ . Because the free energy concentration is low, optical transitions may occur also between completely occupied levels from the bulk to energies above the Fermi level whose level occupancy number is in turn lowered by capture of free electrons in surface states. For film thicknesses above a couple of tens of nanometers one can observe the characteristic behavior of optical interactions with free charge carriers. The remaining increase in this function at low energies demonstrates that we still deal with insular deposition with bigger isles. The behavior of the electron loss functions can be seen in Fig. 3.

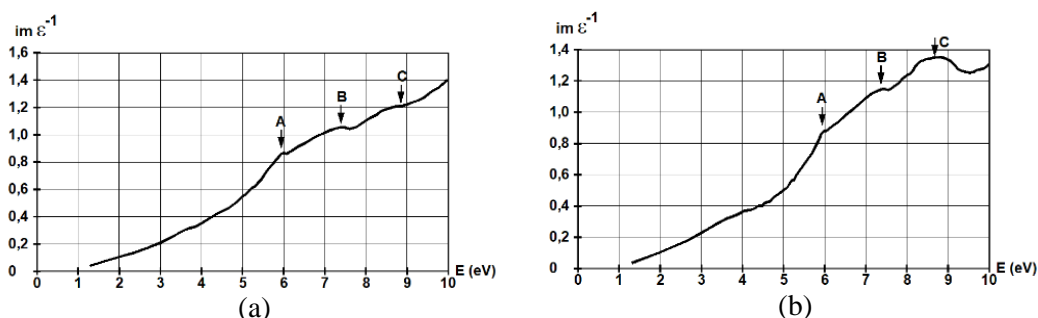


**Figure 3.** The electron loss function  $-\text{Im } \epsilon^{-1}$  spectral behavior for film thicknesses of (a)  $d=22\text{nm}$ , (b)  $d=42\text{nm}$  deposited on glass

The first electronic loss function represents energy losses of fast electrons. One observes the increase of this function, indicating vibrations of electron plasma with resonance at energies over the

studied domain, modulated by three maxima. The increase of the maximum C indicates that electron energy lost in collisions with free electrons increases with the electron's energy.

### **CONCLUSION**

The present work describes dielectric properties of LaNi<sub>5</sub> thin films deposited using laser induced vaporization on lime and silica glass substrates. In the case of the thinnest film the allowed interband transitions are revealed which are smeared by free electron DoS for the thicker films. Inter-insular hopping, with increasing isle surfaces and decreasing inter-insular distances is also observed.

### ***Acknowledgement***

The authors acknowledge the support from JINR Dubna-TU Cluj-Napoca joint research projects.

### **REFERENCES**

- [1] L. Schlapbach, A. Züttel, Nature, 2001, **414**, 353
- [2] D. Todoran, R. Todoran, Zs. Szakacs, E.M. Anitas, Materials, 2018, **11**, 1475.
- [3] D. Todoran, R. Todoran, Zs. Szakacs, Russ. J. Phys. Chem A, 2019, **93**, 2858.
- [4] R. Todoran, D. Todoran, Zs. Szakacs, Russ. J. Phys. Chem A, 2015, **89**, 2422.

## ALKYLAMMONIUM CLAY BASED NANOCOMPOSITES VS. ALKYLAMMONIUM-MODIFIED LIGNOCELLULOSIC MATERIALS IN ADSORPTION OF CONGO RED

N. Velić<sup>2</sup>, M. Stjepanović<sup>2</sup>, I. Ilić<sup>1</sup>, M. Habuda-Stanić<sup>2</sup> and  
N. Jović-Jovičić<sup>1</sup>

<sup>1</sup>*University of Belgrade – IChTM, National Institute, Center for Catalysis and Chemical Engineering, Njegoševa 12, 11000 Belgrade, Republic of Serbia*

<sup>2</sup>*Josip Juraj Strossmayer University of Osijek, Faculty of Food Technology Osijek, Franje Kuhača 20, Osijek, Republic of Croatia*

### ABSTRACT

In this study, lignocellulose waste materials and smectite clay were modified into adsorbents with surface free ammonium groups. Poplar waste biomass and brewer's spent grain were chemically modified. Smectite based adsorbents were obtained by intercalation of biopolymer chitosan and hexadecyl trimethylammonium (HDTMA<sup>+</sup>) cations in smectite structure. The samples were characterized by using X-ray diffraction, elemental analysis and FTIR spectroscopy. The adsorbents were tested for removal of azo dye Congo Red (CR). The concentration of CR was analyzed before and after adsorption test using Thermo Electron Nicolet Evolution 500 UV-VIS spectrophotometer in wavelength range from 250 – 800 nm. It was estimated that adsorption isotherms of CR for all investigated adsorbents showed best fit with Langmuir adsorption model.

### INTRODUCTION

During the last decades, the materials with free surface (alkyl)ammonium groups were recognized as promising adsorbents [1, 2] since these groups can electrostatically interact with anionic sites present in numerous pollutants. The industrial and agricultural waste (i.e. lignocellulosic waste) and low-cost clays are in the research focus since these raw materials can be converted to very efficient adsorbents using relatively simple modification methods [2, 3]. In this work, lignocellulosic waste materials and smectite were modified into adsorbents with free surface ammonium groups. The obtained materials were evaluated as adsorbents of anionic synthetic dye Congo Red.

### EXPERIMENTAL

Poplar waste biomass (PWB, wood shavings and sawdust), donated by "Hrvatske šume d.o.o." and brewers' spent grain (BSG), provided by "Osijek Brewery d.o.o." were subjected to chemical modification according to the previously described procedure [3]. The samples were denoted as mPWB and mBSG, respectively. The 2 μm fraction of smectite (Bogovina, Serbia) with cation exchange capacity (CEC) of 0.633 mmol g<sup>-1</sup> was used as a host material for intercalation of chitosan (av. M<sub>w</sub> = 342,500 g mol<sup>-1</sup>, Sigma-Aldrich) and hexadecyl trimethylammonium (HDTMA) bromide, Alfa-Aesar Chemical. The common procedure [4] was applied to obtain 2H-S with HDTMA<sup>+</sup>: CEC ratio 2:1. The previously described procedure [5] was used to obtain a sample with chitosan (C-S).

The synthetic dye –Congo Red (CR), (Carlo Erba) was used as test model pollutant in adsorption tests.

The smectite samples were characterized using a Rigaku SmartLab automatic multipurpose X-ray diffractometer (Cu anode, λ=0.1542 nm), while elemental analysis (Perkin Elmer CHNS/O analyzer, Series II) and FTIR spectroscopy (Cary 630, Agilent Technologies) were used for lignocellulosic samples characterization.

The adsorption isotherms for CR were obtained in a batch system at 25 °C using a thermostated shaker (Memmert WNE14/ SV 1422). The CR concentration after adsorption was estimated by Thermo Electron Nicolet Evolution 500 UV-VIS spectrophotometer at  $\lambda_{\max}=496$  nm. All adsorption experiments were conducted in duplicate, and the mean values were reported.

## RESULTS AND DISCUSSION

The XRD spectra of 2H-S and C-S showed the presence of smectite as main mineral (> 90 mass %) with only a small amount of quartz. According to literature data, the obtained  $d_{001}=2.02$  nm and 2.08 nm for C-S and 2H-S, respectively, indicated that interlamellar space of smectite was fulfilled with bi-layer arrangement of chitosan [5] and pseudo-three molecular arrangement of HDTMA<sup>+</sup> [4]. These forms of intercalated organic species provide the presence of free ammonium groups [4, 5].

The elemental CHN analysis showed the increase in nitrogen content of both modified lignocellulosic materials compared to unmodified waste materials (from 0.21 to 8.93% and from 3.6 to 10.17% for mPWB and mBSG, respectively), which is in accordance with the literature [2, 3]. FTIR spectra of unmodified and modified lignocellulosic samples revealed the presence of a large number of hydroxyl groups that are, among others, mainly engaged in the adsorption processes. Furthermore, FTIR spectra of mPWB and mBSG showed a shift in vibration frequency of some groups and the appearance of new bands associated with quaternary ammonium groups introduced by modification procedure (quaternisation).

The adsorption isotherms of CR dye on modified lignocellulosic waste materials (mPWB and mBSG) are given in Fig 1a, while adsorption isotherms of CR on smectites based composites (2H-B and C-B) are given in Figure 1b. Equilibrium was reached for shorter times, but 240 min was taken as adsorption time sufficient for all processes to reach adsorption maximum. Adsorption isotherms for mPWB and mBSG showed similar uptake of CR, with  $q_e \sim 50$  mg g<sup>-1</sup> (Fig 1a), while values of  $q_e$  were  $\sim 100$  mg g<sup>-1</sup> and  $\sim 300$  mg g<sup>-1</sup> for C-S and 2H-S, respectively. The superior adsorption properties of 2H-S can be explained by the formation of *pseudo-tri* molecular arrangement of intercalated HDTMA<sup>+</sup>, providing a high amount of surface available ammonium groups as active adsorption sites.

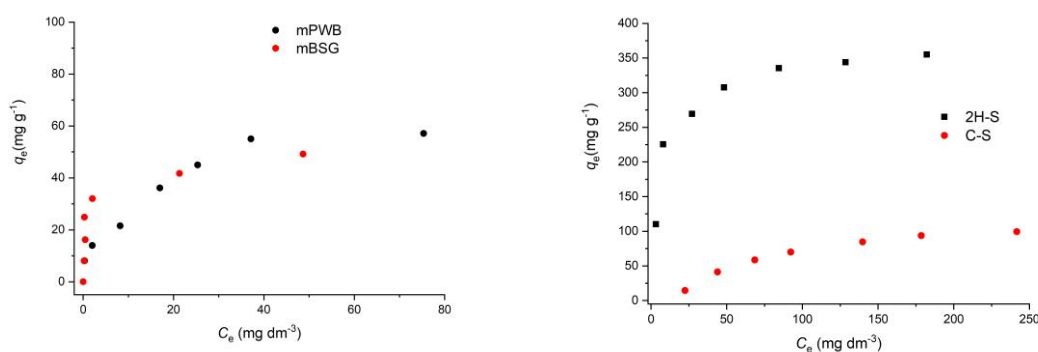


**Figure 1.** Adsorption isotherms of CR on a) mPWB and mBSG; b) 2H-B and C-B.

Adsorption conditions:  $C_0=25, 50, 75, 100, 150, 200$  and  $250$  mg dm<sup>-3</sup>;

$m_{\text{ads}}=10$  mg of 2H-S and C-S and 150 mg of mPWB and mBSG ;  $t_{\text{eq}}=240$  min.

The adsorption data were fitted with Langmuir and Freundlich models, and corresponding constants are given in Table 1.

**Table 1.** Langmuir and Freundlich parameters

Samples	Freundlich parameters			Langmuir parameters		
	$K_F$ ( $\text{dm}^3\text{g}^{-1}$ )	n	$R^2$	$q_{\text{max}}$ ( $\text{mg g}^{-1}$ )	$K_L$ ( $\text{dm}^3\text{mg}^{-1}$ )	$R^2$
mPWB	12.25	2.65	0.956	70.33	0.069	0.960
mBSG	23.10	5.51	0.904	47.00	1.52	0.917
C-B	5.18	1.81	0.952	154.70	0.0083	0.984
2H-B	127.96	4.81	0.865	357.56	0.1588	0.963

For all investigated adsorbents, the correlation coefficient in the Langmuir model is closer to unity and therefore, can be regarded as the more appropriate model.

## CONCLUSION

Adsorbents with free ammonium groups as active sites were tested in batch adsorption study of Congo Red (CR) dye removal. Lignocellulosic waste materials (poplar waste biomass and brewers' spent grain) were chemically modified in order to introduce ammonium groups. The introduction of  $-\text{NH}_3^+$  groups in lignocellulosic adsorbents was confirmed by CHN analysis and FTIR. The intercalation of chitosan and hexadecyl trimethylammonium ( $\text{HDTMA}^+$ ) in smectite structure in smectite based adsorbents was confirmed by XRD analysis. The adsorption processes for all investigated adsorbents could be described by the Langmuir adsorption model. Although HDTMA-smectite had superior adsorption properties toward CR, chemically modified poplar waste biomass, brewers' spent grain as well as chitosan-smectite composite represent a green alternative to conventional alkylammonium-smectites and could be successfully applied in treatment of moderate-loaded effluents.

## Acknowledgement

This work was financially supported by the Ministry of Education, Science and Technological Development of the Republic of Serbia (Grant No. 451-03-68/2020-14/200026) and Osijek-Baranja County, the Republic of Croatia (Project "Research on the use of lignocellulosic waste materials from agricultural and food production as adsorbents").

## REFERENCES

- [1] R. Zhu, Q. Zhou, J. Zhu, Y. Xi, H. He, *Clays Clay Miner.*, 2015, **63**, 199–221.
- [2] A. Keränen, T. Leiviskä, B.Y. Gao, O. Hormi, J. Tanskanen, *Chem. Eng. Sci.*, 2013, **98**, 59–68.
- [3] M. Stjepanović, N. Velić, A. Lončarić, D. Gašo-Sokač, V. Bušić, M. Habuda-Stanić, *J. Mol. Liq.*, 2019, **285**, 535-544.
- [4] N.P. Jović-Jovičić, A.D. Milutinović-Nikolić, M.J. Žunić, Z.D. Mojović, P.T. Banković, I.A. Gržetić, D.M. Jovanović, *J. Contamin. Hidr.*, 2013, **150**, 1–11.
- [5] M. Darder, M. Colilla, E. Ruiz-Hitzky, *Chem. Mater.*, 2003, **15**, 3774–3780.

## KINETIC AND ISOTHERM STUDIES OF BIOSORPTION PROCESS OF COPPER IONS FROM WATER

N. Velinov, M. Kostić, J. Mitrović, M. Radović Vučić, M. Petrović, S. Najdanović and A. Bojić

University of Niš, Faculty of Sciences and Mathematics, Department of Chemistry, Višegradaska 33, 18000 Niš, Serbia. (nena.velinov@yahoo.com)

### ABSTRACT

The chemically modified lignocellulosic biomass with  $\text{Al}_2\text{O}_3$  (LC- $\text{Al}_2\text{O}_3$ ) was tested as a new sorbent for the removal of copper (Cu(II)) ions from aqueous solution in batch conditions. As a lignocellulosic base material woodchips from an oak tree (*Quercus robur*) were used. To define the kinetic and equilibrium isotherm, experimental data were analyzed by pseudo-first-order and pseudo-second-order kinetic models and Langmuir and Freundlich isotherm models. Sorption kinetics followed pseudo-second-order model suggesting that surface reaction was the rate-limiting step. Equilibrium experimental results are the best fitted by the Langmuir isotherm model. The maximal sorption capacities of the biosorbent for removal of Cu(II) ions was  $15.38 \text{ mg g}^{-1}$ . According to the experimental data results, LC- $\text{Al}_2\text{O}_3$  seems to be an alternative and effective biosorbent for the removal of Cu(II) ions from aqueous solution.

### INTRODUCTION

Currently, with the rapid increase of industries, problem with water pollution has become progressively serious. Among all pollutants enclosed in industrial wastewater, heavy metals are considered one of the most hazardous compounds for the environment [1]. Copper (Cu(II)) is present in the wastewater of several industries, such as metal cleaning and plating baths, paper and pulp, refineries, fertilizer, and wood preservatives and it is highly toxic. The excessive intake of Cu(II) leads to severe mucosal irritation, capillary damage, hepatic and renal damage, central nervous problems, gastrointestinal irritation and changes in the liver and kidney [2].

In wastewater treatment technology, various techniques have been used for Cu(II) ions removal. Among these, biosorption using inactive and dead biomasses as sorbents, has emerged as a promising technique as compared to other methods of wastewater treatment in terms of cost, the simplicity of design and operation, availability, effectiveness, insensitivity to toxic substances and potential metal recovery [3].

In this paper, application of a chemically modified lignocellulosic biomass with a small amount of  $\text{Al}_2\text{O}_3$  (LC- $\text{Al}_2\text{O}_3$ ) for removal of Cu(II) ions from water was studied. As a lignocellulosic base material woodchips from an oak tree (*Quercus robur*) were used. In order to study the kinetic and equilibrium the sorption process, the experimental data were analyzed by pseudo-first order and pseudo-second order kinetic models and Langmuir and Freundlich isotherm models.

### METHODS

*Quercus robur* woodchips were fractionated by size and washed with deionized water. Ten grams of the biomass was acid treated (0.3 M  $\text{HNO}_3$ ) to remove bio-accumulated metals, then alkali treated (1 M NaOH) in the period of 60 min. After that the material was mixed with solution of 1 g of  $\text{Al}(\text{NO}_3)_3 \cdot 9\text{H}_2\text{O}$  dissolved in  $100 \text{ cm}^3$  of deionized water and the suspension was stirred for 0.5 h at  $25.0 \pm 0.5^\circ\text{C}$ . After that the solution was evaporated. The obtained material was washed with deionized water, and treated by trimethylamine, then washed with deionized water until neutral pH and dried at  $55 \pm 1^\circ\text{C}$  for 5h. This material was abbreviated as LC- $\text{Al}_2\text{O}_3$ .

Kinetic and isotherm studies were performed by preparing solutions with the initial concentration of Cu(II) ions in the range from 5.0 to 100.0 mg dm<sup>-3</sup>, and mixing the solutions with 2.0 g dm<sup>-3</sup> of the sorbent at pH 5.0 and 25.0°C till equilibrium. The aliquots of the solution were taken before the sorption started, and after particular periods of time. The concentrations of Cu(II) ions in the solution were determined by an atomic adsorption spectrometer Analyst AA 300 (PerkinElmer, USA). All parameters were evaluated with the non-linear regression method by means of OriginPro 2016 software (OriginLab Corporation, USA).

## RESULTS AND DISCUSSION

### Sorption kinetics

The pseudo-first-order kinetic model describes the rate of sorption, which is proportional to the number of unoccupied binding sites of the sorbent [4]. The pseudo-second-order kinetic model is based on equilibrium sorption, which depends on the amount of solute sorbed on the surface of sorbent and the amount sorbed at equilibrium [5]. The equations and parameters of the above-mentioned kinetics models, along with their values and corresponding  $r^2$ , are presented in Table 1.

In the nonlinear equations of the pseudo-first-order and pseudo-second-order kinetic models (Table 1)  $k_1$  (min<sup>-1</sup>) is the first order rate constant,  $k_2$  (g mg<sup>-1</sup> min<sup>-1</sup>) is the second-order-rate constant,  $q_t$  and  $q_e$  (mg g<sup>-1</sup>) are the amounts of Cu(II) ions sorbed at time  $t$  and at equilibrium, respectively.

**Table 1.** Kinetic parameters for Cu(II) ions sorption onto LC-Al<sub>2</sub>O<sub>3</sub>.

	$c_0$ (mg g <sup>-1</sup> )	5.0	10.0	20.0	50.0	100.0
	$q_e, \text{exp}$ (mg g <sup>-1</sup> )	2.48	4.96	9.72	13.89	15.75
<b>Pseudo-First Order Model</b>						
	$q_e, \text{cal}$ (mg g <sup>-1</sup> ) ±	2.44 ±	4.69 ±	9.11±	13.26 ±	14.93 ±
	standard error	0.08	0.16	0.31	0.45	0.51
$q_t = q_e(1 - e^{-k_1 t})$	$k_1$ (min <sup>-1</sup> ) ±	0.219 ±	0.085 ±	0.077 ±	0.071 ±	0.069 ±
	standard error	0.031	0.012	0.011	0.010	0.009
	$r^2$	0.989	0.989	0.987	0.987	0.987
<b>Pseudo-Second Order Model</b>						
	$q_e, \text{cal}$ (mg g <sup>-1</sup> ) ±	2.56 ±	5.19 ±	10.17 ±	14.89 ±	16.38 ±
	standard error	0.06	0.13	0.25	0.37	0.40
$q_t = \frac{q_e^2 k_2 t}{1 + k_2 q_e t}$	$k_2$ (g mg <sup>-1</sup> min <sup>-1</sup> ) ±	0.365 ±	0.113 ±	0.099 ±	0.090 ±	0.090 ±
	standard error	0.030	0.011	0.01	0.009	0.009
	$r^2$	0.998	0.999	0.999	0.999	0.999

As can be seen from the data presented in Table 1, the determined values of  $q_e$  for both models showed similarity with the experimental values, but in the case of pseudo-second-order model, they are closer to the experimental  $q_e$  values. Obtained determination coefficients for pseudo-second-order model (Table 1) is relatively higher than the determination coefficients for pseudo-first-order model. The obtained data showed that pseudo-second-order model better fitted experimental data due to a higher determination coefficient and better matching of experimental and calculated  $q_e$  values suggesting that the sorption process depends on the solute amount sorbed on the sorbent surface and the solute amount at equilibrium [5].

### Sorption isotherm

The Langmuir model assumes that the uptake of adsorbate occurs on an energetically homogeneous surface by monolayer adsorption without any interaction between adsorbed species [6]. The Freundlich empirical adsorption isotherm equation is based on adsorption on a heterogeneous surface where the stronger binding sites are occupied first, and that the binding strength decreases with the increasing degree of site occupation [7]. The equations and parameters of the above-mentioned isotherm models, along with their values and corresponding  $r^2$ , are presented in Table 2.

In the nonlinear equations of the Langmuir and Freundlich isotherm models  $q_e$  is the amount of sorbate sorbed at equilibrium ( $\text{mg g}^{-1}$ ),  $c_e$  is the equilibrium concentration of the sorbate in solution ( $\text{mg dm}^{-3}$ ),  $q_m$  is the maximum sorption capacity ( $\text{mg g}^{-1}$ ),  $K_L$  is a Langmuir constant related to the energy of sorption,  $K_f$  is Freundlich constant related to the sorption capacity and  $1/n$  is Freundlich exponent related to the intensity of sorption.

**Table 2.** Isotherm parameters for Cu(II) ions sorption onto LC- $\text{Al}_2\text{O}_3$ .

Model	Equation	Parameter	Value
Langmuir model	$q_e = q_m \frac{K_L c_e}{1 + K_L c_e}$	$q_m$ ( $\text{mg g}^{-1}$ )	15.38
		$K_L$ ( $\text{dm}^3 \text{mg}^{-1}$ )	5.26
		$r^2$	0.995
Freundlich model	$q_e = K_F c_e^{1/n_F}$	$K_F$ ( $\text{mg g}^{-1}$ ) <sup>1/n</sup>	8.45
		$n$	6.14
		$r^2$	0.843

The Langmuir model gives better fit to the experimental data due to the higher determination coefficient ( $r^2 > 0.99$ ) and thus, the nature of sorption of Cu(II) ions on the sorbents is more compatible with Langmuir assumptions about the monolayer sorption of the investigated pollutant on the sorbent, and after saturation of this layer, no further sorption took place. The maximum biosorbent capacity determined from the Langmuir isotherm model was  $15.38 \text{ mg g}^{-1}$  (Table 2), which is consistent with the experimental value.

### CONCLUSION

A new biosorbent based on chemical modification of oak woodchips with  $\text{Al}_2\text{O}_3$  was synthesized. The sorption process followed the pseudo-second-order model indicating that chemical reaction can be involved in the biosorption process of Cu(II) ions LC- $\text{Al}_2\text{O}_3$ . The Langmuir isotherm model showed the best fit to experimental data in describing the sorption of Cu(II) ions. The maximal sorption capacities for Cu(II) ions of the LC- $\text{Al}_2\text{O}_3$  biosorbent is  $15.38 \text{ mg g}^{-1}$ . In addition, LC- $\text{Al}_2\text{O}_3$  possesses other benefits, like cost-effectiveness and easy sorbent preparation, making it a promising material for the removal of heavy metals from water and wastewaters.

### Acknowledgement

The authors would like to acknowledge financial support from the Ministry of Education, Science and Technological Development of the Republic of Serbia (Agreement No 451-03-9/2021-14/200124).

### REFERENCES

- [1] S.C. Doney, Science, 2010, **328**, 1512 – 1516.
- [2] R. Gündogan, B. Acemioglu, M.H. Alma, J. Colloid Interface Sci., 2004, **269**, 303 – 309.

- [3] T.V. Nguyen, S. Vigneswaran, H.H. Ngo, et al., *J. Hazard. Mater.*, **182**, 2010, 723 – 729.
- [4] S. Lagergren, *K. Sven. vetensk.akad. handl.*, 1898, **24**, 1 – 39.
- [5] Y.S. Ho, G. McKay, *Process. Saf. Environ. Prot.*, 1998, **76**, 183 – 191.
- [6] I. Langmuir, *J. Am. Chem. Soc.*, 1918, **40**, 1361 – 1403.
- [7] H.Z. Freundlich, *J. Phys. Chem.*, 1906, **57A**, 385 – 470.

## THE EFFECTIVE REMOVAL OF REACTIVE DYE BY USING LAYERED DOUBLE HYDROXIDE

M. Kostić, N. Velinov, M. Radović Vučić, M. Petrović, S. Najdanović, D. Bojić and A. Bojić

*University of Niš, Faculty of Sciences and Mathematics, Department of Chemistry, Višegradska 33, 18000 Niš, Serbia. (nena.velinov@yahoo.com)*

### ABSTRACT

In this investigation, a layered double hydroxide (M-LDH) was synthesized by using the co-precipitation reaction. The morphology characteristics of the M-LDH were examined by SEM. It was found that the M-LDH was consisted of shards, nearly spherical particles with the size distribution of approximately 25 nm. The efficiency of the M-LDH for removal of reactive blue 19 (RB19) was evaluated by two parameters: contact time and initial dye concentration. The increase in contact time led to an increase in the sorption capacity, reaching equilibrium in approximately 120 min. The sorption capacity increased from 162.8 to 343.7 mg g<sup>-1</sup> with the increase in initial dye concentrations from 100 to 400 mg dm<sup>-3</sup>. Finally, the prepared M-LDH had the amenability to operate efficiently in the sorption of dyes from water.

### INTRODUCTION

The use of synthetic dyes has been increased in the various industries such as textile, leather, cosmetic, paper, printing, plastic, rubber, pharmaceutical and food [1]. Dyes in water environment decrease the depth of light penetration, inhibit the growth of the animal and plant life and cause toxicity to aquatic life. The reactive dyes are one of the most common used synthetic dyes in the mentioned industries. The reactive blue 19 (RB19) dye is very often used in the textile industry [2]. RB19 may have mutagenic properties due to the presence of electrophilic vinylsulfone groups [3]. The removal of dyes from water and wastewater is currently one of the major problems faced by the world today. Various physical, chemical, biological, radiation and electrochemical treatment methods (coagulation/flocculation, reverse osmosis, membrane filtration and advance oxidation processes) have been used for removal of dyes from water and wastewater. The sorption processes offer significant advantages in removing of dyes from waste effluents because of low costs, simplicity of design and ease of operation in relation to traditional methods. Disadvantages of sorption processes are cost-intensive recycling steps of sorbents, as well as storage of used sorbent when it is impossible to recycle.

In this study, a layered double hydroxide (M-LDH) was chemically synthesized based on iron, copper and nickel and applied for sorption of RB19. The surface morphology of the sorbent was obtained by using scanning electron microscopy (SEM). The effects of contact time and initial dye concentration on sorption process were studied.

### MATERIALS AND METHODS

All chemicals were of reagent grade and used without further refinement. HNO<sub>3</sub>, NaOH, NaCl, FeCl<sub>3</sub>·H<sub>2</sub>O, FeCl<sub>2</sub>·4H<sub>2</sub>O, NiCl<sub>2</sub>·6H<sub>2</sub>O, CuCl<sub>2</sub>·2H<sub>2</sub>O and RB19 were purchased from Merck (Darmstadt, Germany). All solutions were prepared with deionized water (18MΩ).

The M-LDH was prepared by the hydrothermal process, by using co-precipitation reaction. FeCl<sub>3</sub>·6H<sub>2</sub>O, FeCl<sub>2</sub>·4H<sub>2</sub>O, CuCl<sub>2</sub>·2H<sub>2</sub>O and NiCl<sub>2</sub>·4H<sub>2</sub>O were used for preparing the M-LDH in molar ratio 2:1:1:1, respectively. Mentioned reagents are dissolved in 0.1 M HCl solution. The solution was heated to 80 °C with a reflux condenser and mixed by agitating and ultrasonication in period of 1 h. After 1 h, 2 M NaOH solution was added dropwise to pH of about 10 at 80 °C with

vigorous stirring and agitating with ultrasonication with refluxing. The suspension with obtained brown colored precipitate was continuously stirred and agitated with ultrasonication in the next hour. After one hour, the suspension should settle for 2 h without stirring, ultrasonication and heating. The precipitate was washed several times with hot deionized water over a Büchner funnel. Finally, the prepared precipitate was dried at 90 °C for 24 h.

The working standard solutions of RB19 were prepared just before use by dilution of the stock solutions with concentration 1000 mg dm<sup>-3</sup>. The morphology of the nanosorbent surface was analyzed by SEM (Hitachi SU8030). The concentrations of RB19 in the solution were determined by UV–vis technique, using the spectrophotometer Shimadzu UV–vis 1650 PC.

The sorption capacity  $q_t$  (mg g<sup>-1</sup>) was determined by using the equation 1:

$$q_t = \frac{c_0 - c_t}{m} \times V \quad (1)$$

where  $c_0$  and  $c_t$  are the initial and final concentrations of the dye in solution (mg dm<sup>-3</sup>),  $V$  is the solution volume (dm<sup>3</sup>) and  $m$  is the mass of the sorbent (g).

## RESULTS AND DISCUSSION

The nominal magnifications of x300 and x1000 were used during imaging the samples and additional magnifications of x20000 and x70000 were used to examine the fine structure of the material.

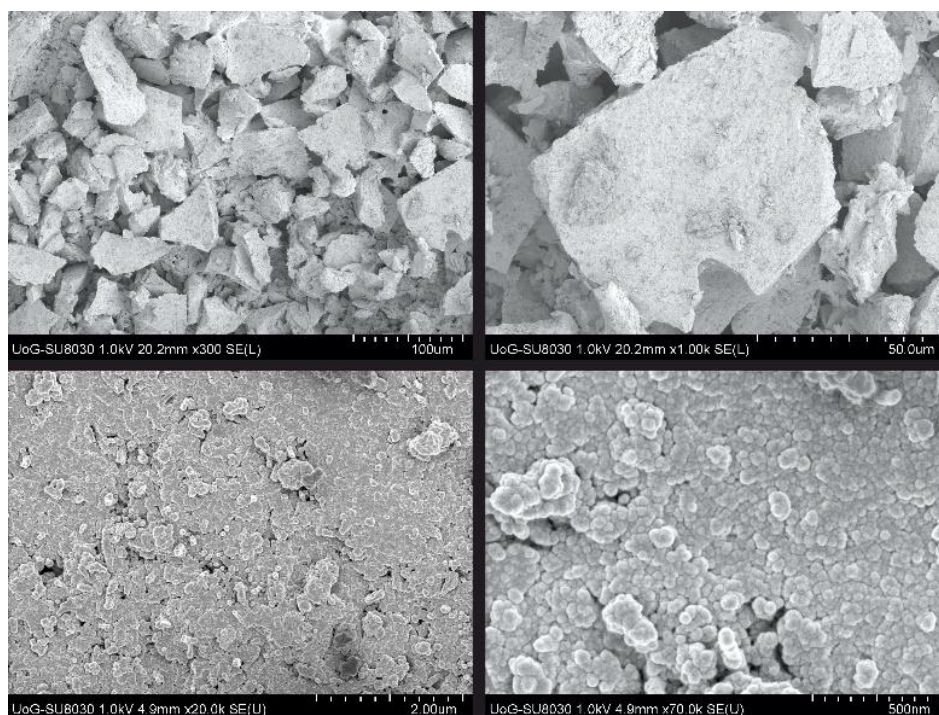


**Figure 1.** SEM micrographs for M-LDH.

SEM micrographs showed in Figure 1 confirmed the presence of agglomerated particles with nonuniform size. The M-LDH was consisted of shards which were approximately 50  $\mu\text{m}$ . There could be noticed nearly spherical particles with the size distribution of approximately 25 nm. The sample was highly textured showing the shards which were aggregated of smaller particles.

To define the influence of contact time on the sorption capacity of the sorbents the effect of contact time on the sorption of RB19 was studied (Figure 2).

Figure 2 showed that increasing of contact time led to rapid increase in the sorption capacity, in the first 60 min. After that, the sorption capacity gradually increased, reaching equilibrium for approximately 120 min, because all available sites were covered and there was no active site available for binding.

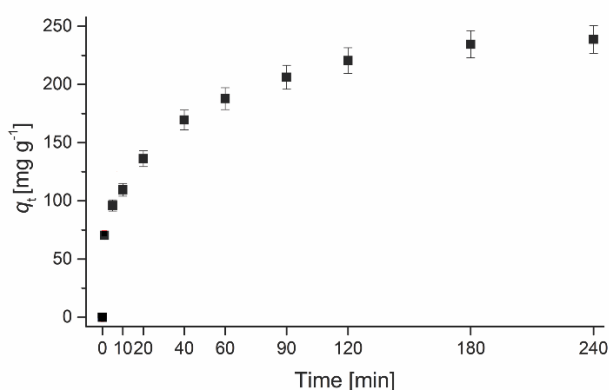


**Figure 2.** Results of effects of contact time on the sorption of RB19 on M-LDH ( $c_0$ : 200  $\text{mg dm}^{-3}$ ; sorbent dose: 0.6  $\text{g dm}^{-3}$ , steering speed: 280 rpm, temperature: 20  $^{\circ}\text{C}$ ).

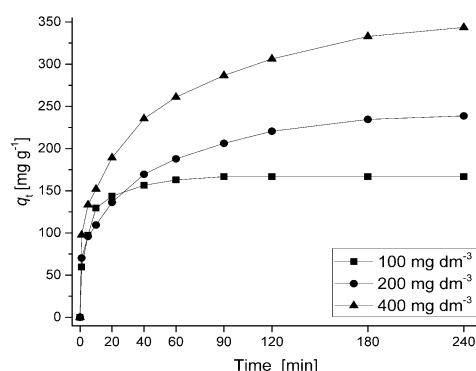


**Figure 3.** Effect of initial concentration on RB19 removal using M-LDH (sorbent dose: 0.6  $\text{g dm}^{-3}$ , steering speed: 280 rpm, temperature: 20  $^{\circ}\text{C}$ ).

The results from Figure 3 indicated that the sorption capacity increased with increase in initial dye concentrations. The increase in sorption capacity could be explained by growing effect of driving force (the concentration gradient) [4]. The contrary to that, surface saturation increased with increasing of RB19 concentration, so that the efficiency of RB19 removal decreased due to diminishing loading capacity of the M-LDH. It could also be seen that the M-LDH was very effective in removing of RB19. The sorption capacity reached value of 343.7  $\text{mg g}^{-1}$ .

## CONCLUSION

The metal nanosorbent M-LDH was synthesized. The morphology and the removal of RB19 from water were investigated. The morphological investigations showed that the M-LDH has a porous structure with spherical particles that are sized about 25 nm. The time required to reach equilibrium is below 120 min. The experimental sorption capacity is 343.7  $\text{mg g}^{-1}$ . Therefore, the investigated M-LDH can be recommended as an efficient sorbent for the treatment of water and wastewater.

## Acknowledgement

The authors would like to acknowledge financial support from the Ministry of Education, Science and Technological Development of the Republic of Serbia ((Agreement No 451-03-9/2021-14/200124).

**REFERENCES**

- [1] V. K. Garg, R. Kumar, R. Gupta, *Dyes and Pigments*, 2004, 62, 1–10.
- [2] J. E. B. McCallum, S. A. Madison, S. Alkan, R. L. Depinto, R. U. R. Wahl, *Environmental Science and Technology*, 2000, 34, 5157–5164.
- [3] N. A. Fathy, S. E. El-Shafey, O. I. El-Shafey, W. S. Mohamed, *Journal of Environmental Chemical Engineering*, 2013, 1, 858–864.
- [4] D. Hu, L. Wang, *Journal of the Taiwan Institute of Chemical Engineers*, 2016, 64, 227–234.

## DEGRADATION OF PESTICIDE 2,4-D WITH UV-ACTIVATED PEROXYDISULFATE AND HYDROGEN PEROXIDE

J. Mitrović, M. Radović Vučić, N. Velinov, M. Petrović, M. Kostić, D. Bojić and A. Bojić

*University of Niš, Faculty of Sciences and Mathematics, Department of Chemistry, Višegradska 33, 18000 Niš, Serbia. (nena.velinov@yahoo.com)*

### ABSTRACT

Two advanced oxidation processes based on combination of UV light irradiation with potassium peroxydisulfate and with hydrogen peroxide were employed for the degradation of pesticide 2,4-D in aqueous media. The influence of operating parameters, such as initial pH and concentration of the oxidant reagents, was investigated. Under the optimal operational conditions, complete degradation of pesticide 2,4-D was achieved after 15 and 30 min of treatments for UV/H<sub>2</sub>O<sub>2</sub> and UV/S<sub>2</sub>O<sub>8</sub><sup>2-</sup> process, respectively.

### INTRODUCTION

The increase in the type and concentration of pollutants in aquatic systems or urban/industrial effluents, mostly related to anthropogenic activities, generated the need for innovative strategies for water remediation. Advanced oxidation processes (AOPs) are generally proposed as the most promising and effective methods for the treatment of water containing organic pollutants [1].

The agricultural sector has been considered as one of the major worldwide source of water pollution due to the excessive use of pesticides to increase agricultural production [2]. It has been reported that herbicide 2,4-dichlorophenoxyacetic acid (2,4-D) can seriously alter soil water quality and contaminate surface waters, adversely affecting human and animal life due to its disruptive effect on the hormonal system and its potential carcinogenic effects [3].

Hence, this research was focused on the activation of hydrogen peroxide and peroxydisulfate by UV irradiation for the oxidative degradation of 2,4-D herbicide. The degradation efficiency of herbicide was evaluated at different key operational parameters, such as initial solution pH and initial concentration of applied oxidant.

### METHODS

Analytical grade 2,4-dichlorophenoxyacetic acid, sodium peroxydisulfate (Na<sub>2</sub>S<sub>2</sub>O<sub>8</sub>, reagent grade), hydrogen peroxide (H<sub>2</sub>O<sub>2</sub>, reagent grade), sodium hydroxide and hydrochloric acid were purchased from Sigma Aldrich (USA).

All degradation experiments were performed in a batch photoreactor equipped with ten low pressure mercury lamps, emitting at 254 nm (Philips, Holland). Degradation experiments were conducted with 100 mL of working solution, containing desired initial concentration of pesticide and oxidant and with appropriate initial pH value, in glass Petri dishes. The samples were taken from the reaction mixture at defined intervals and the residual pesticide concentration was determined by high performance liquid chromatography (Dionex UltiMate 3000, Thermo Scientific, SAD). Wavelength of UV detection was 228 nm and the chromatographic column Zorbax Eclipse Plus C18 (2.1 x 150 mm, 5 µm, Agilent Technologies, SAD) was used. The mobile phase consisted of 60:40 v/v methanol/0.1% formic acid. The flow rate was 0.5 mL min<sup>-1</sup> and the volume of injection 10 µL.

## RESULTS AND DISCUSSION

The initial experiments were carried out in the presence of the only oxidant ( $\text{H}_2\text{O}_2$  or  $\text{S}_2\text{O}_8^{2-}$ ), under UV irradiation only and with a combination of oxidant and UV light (UV/ $\text{H}_2\text{O}_2$  or UV/ $\text{S}_2\text{O}_8^{2-}$ ).

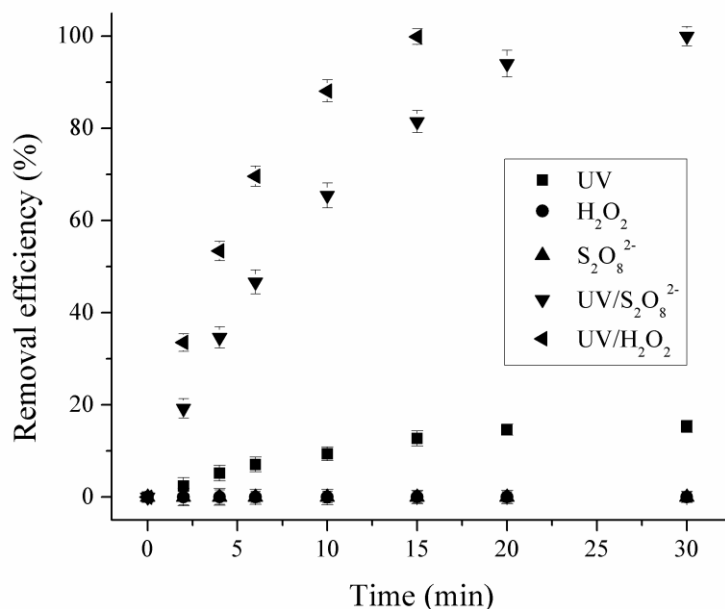


**Figure 1.** Removal efficiency of pesticide 2,4-D after treatment with UV irradiation,  $\text{H}_2\text{O}_2$ ,  $\text{S}_2\text{O}_8^{2-}$ , UV/ $\text{S}_2\text{O}_8^{2-}$  or UV/ $\text{H}_2\text{O}_2$ .  $c_0(2,4\text{-D}) = 30 \text{ mg dm}^{-3}$ ,  $c_0(\text{S}_2\text{O}_8^{2-}) = 1 \text{ mmol dm}^{-3}$ ,  $c_0(\text{H}_2\text{O}_2) = 0.4 \text{ mmol dm}^{-3}$ ,  $\text{pH } 2 \pm 0.1$ .

Results showed that there are no changes in the removal efficiency when experiments were carried out with oxidants alone (Fig.1). Removal efficiency increased to 15% after 30 min of irradiation when UV-C light only was applied probably because 2,4-D pesticide is not stable in water solution under the direct UV-C photolysis. The complete removal of the 2,4-D pesticide occurred when the solution was irradiated with UV-C light in the presence of  $\text{H}_2\text{O}_2$  for 15 min, while treatment of 30 min was needed for removal of pesticide with UV/ $\text{S}_2\text{O}_8^{2-}$  process. The activation of peroxydisulfate anions or hydrogen peroxide with the UV-C light, and formation of reactive species, probably sulfate ( $\text{SO}_4^{\cdot-}$ ) and hydroxyl radicals ( $\cdot\text{OH}$ ), significantly enhanced removal of pesticide 2,4-D.

### *The effect of initial concentration of oxidant*

The effect of initial oxidant concentration on the removal of 2,4-D was studied in the concentration range from 0.5 to 4  $\text{mmol dm}^{-3}$  of  $\text{S}_2\text{O}_8^{2-}$  and from 0.1 up to 0.6  $\text{mmol dm}^{-3}$  of peroxide (Table 1). For both processes (UV/ $\text{H}_2\text{O}_2$  and UV/ $\text{S}_2\text{O}_8^{2-}$ ) removal efficiency increased with increasing in initial oxidant concentration. The enhancement in removal efficiency of 2,4-D pesticide can be attributed to the increasing in rate of  $\text{SO}_4^{\cdot-}$  and  $\cdot\text{OH}$  radicals formation as the concentration of  $\text{S}_2\text{O}_8^{2-}$  or  $\text{H}_2\text{O}_2$  increased.

**Table 1.** Removal of pesticide 2,4-D with UV/S<sub>2</sub>O<sub>8</sub><sup>2-</sup> and UV/H<sub>2</sub>O<sub>2</sub> process under different experimental conditions

$c_0(2,4-D)$ (mg dm <sup>-3</sup> )	$c_0(S_2O_8^{2-})$ (mmol dm <sup>-3</sup> )	$c_0(H_2O_2)$ (mmol dm <sup>-3</sup> )	pH	$k_{app}$ (min <sup>-1</sup> )
The effect of initial oxidant concentration				
30	0.5	0	2	0.056
30	1.0	0	2	0.111
30	2.0	0	2	0.167
30	4.0	0	2	0.304
30	0	0.1	3	0.066
30	0	0.2	3	0.112
30	0	0.4	3	0.238
30	0	0.6	3	0.306
The effect of initial pH value				
30	1	0	2	0.134
30	1	0	3	0.047
30	1	0	5	0.046
30	1	0	7	0.04
30	1	0	9	0.038
30	1	0	10	0.036
30	0	0.2	2	0.212
30	0	0.2	3	0.112
30	0	0.2	5	0.02
30	0	0.2	7	0.083
30	0	0.2	9	0.082
30	0	0.2	10	0.086

### *The effect of initial pH*

The results revealed that the removal of pesticide 2,4-D with the both studied processes (UV/S<sub>2</sub>O<sub>8</sub><sup>2-</sup> and UV/H<sub>2</sub>O<sub>2</sub>) is more favorable in the acidic conditions, in the comparison to the neutral and basic (Table 1). Pseudo-first rate constant dropped significantly for both processes when initial pH value raised from 2.0 up to 3.0, while with further rising in initial pH value up to 10.0, a slight drop of rate constant was obtained. Due to the acid catalyzed decomposition of peroxydisulfate at lower pH values, a greater amount of SO<sub>4</sub><sup>•-</sup> radicals would be generated in UV/S<sub>2</sub>O<sub>8</sub><sup>2-</sup> system so that degradation efficiency might be improved [4]. In the case of UV/H<sub>2</sub>O<sub>2</sub> system, the decrease in 2,4-D removal with an increase in initial pH can be explained based on the two competing processes: the production of the hydroxyl radicals and the scavenging of hydroxyl radicals by hydroperoxide ion [5]. Moreover, H<sub>2</sub>O<sub>2</sub> decomposes in the neutral to basic pH range producing oxygen molecules and loses its characteristics as an oxidant [5].

### CONCLUSION

Oxidative degradation of pesticide 2,4-D was insignificant with direct UV-C irradiation, while with the addition of oxidant (H<sub>2</sub>O<sub>2</sub> or S<sub>2</sub>O<sub>8</sub><sup>2-</sup>) degradation efficiency increased significantly. The degradation rates decreased with the increase of initial pH of solution for both treatment processes. Due to the increasing in rate of reactive radicals formation, initial concentration of both oxidants has positive influence on removal efficiency of pesticide 2,4-D.

**Acknowledgement**

The authors would like to acknowledge financial support from the Ministry of Education, Science and Technological Development of the Republic of Serbia (Agreement No 451-03-9/2021-14/200124).

**REFERENCES**

- [1] P. Devi, U. Das, A. K. Dalai, *Sci. Total Environ.*, 2016, **571**, 643 – 657.
- [2] A. Chenchana, A. Nemancha, H. Moumeni, J. M. Doña Rodríguez, J. Araña, J. A. Navío, O. González Díaz, E. Pulido Melián, *Appl. Surf. Sci.*, 2019, **467** – **468**, 1076 – 1087.
- [3] M. Kermani, F. Mohammadi, B. Kakavandi, A. Esrafil, Z. Rostamifasih, *J. Phys. Chem. Solids*, 2018, **117**, 49 – 59.
- [4] S. Dhaka, R. Kumar, M. A. Khan, K. J. Paeng, M. B. Kurade, S. J. Kim, B. H. Jeon, *Chem. Eng. J.*, 2017, **321**, 11 – 19.
- [5] J. Sharma, I. M. Mishra, V. Kumar, *J. Environ. Manage.*, 2015, **156**, 266 – 275.

## CELL ADHESION CHARACTERISTICS OF POLYURETHANE-MESOPOROUS SILICA NANOPARTICLE COMPOSITE MATERIALS

M. V. Pergal<sup>1</sup>, J. Brkljačić<sup>2</sup>, G. Tovilović-Kovačević<sup>2</sup>, M. Špirkova<sup>3</sup>, I. D. Kodranov<sup>4</sup>, D. D. Manojlović<sup>4</sup> and N. Ž. Knežević<sup>5</sup>

<sup>1</sup> *University of Belgrade, Institute of Chemistry, Technology and Metallurgy, Njegoševa 12, 11000 Belgrade, Serbia. (marijav@chem.bg.ac.rs)*

<sup>2</sup> *Department of Biochemistry, Institute for Biological Research "Siniša Stanković", National Institute of Republic of Serbia, University of Belgrade, 142 Despot Stefan Blvd, 11060 Belgrade, Serbia.*

<sup>3</sup> *Institute of Macromolecular Chemistry CAS (IMC), Heyrovsky Sq. 2, 16206 Prague 6, Czech Republic.*

<sup>4</sup> *Faculty of Chemistry, University of Belgrade, Studentski trg 12-16, 11000 Belgrade, Serbia. ikodranov@gmail.com*

<sup>5</sup> *BioSense Institute, University of Novi Sad, Dr Zorana Djindjica 1, Novi Sad 21000, Serbia. (nknezevic@biosense.rs)*

### ABSTRACT

Surface characteristics and biocompatibility of new nanocomposites based on polyurethane network and mesoporous silica nanoparticles (PUMSNs) were investigated. Surface topography and roughness coefficient were studied by AFM. Biocompatibility with endothelial cells and cytotoxicity of the PUNs were assessed using MTT (3-[4,5-dimethylthiazol-2-yl]-2,5-diphenyl-tetrazolium bromide) and cell adhesion assays. The addition of MSNs into polyurethane network led to improvement of surface properties, as well as exhibited promising characteristics regarding adhesion of cells, toward potential application in coating for medical devices.

### INTRODUCTION

In recent years, polyurethane (PU) has shown strong potential for biomedical applications due to its adjustable design of chemical structures and appropriate mechanical properties [1]. Poly(dimethylsiloxane) (PDMS) has been widely used in biological and chemical research, owing to its chemical inertness, optical transparency, biocompatibility, nontoxicity, permeability to gases and rapid prototyping capabilities [1]. To improve the properties of conventional PU coatings, a newer approach has been developed to manipulate the coating properties by modifying the macromolecular architecture using branched polymer, such as hyperbranched polymers, as precursors [2]. These polymers show unique physical properties like low melt and solution viscosity, low degree of chain entanglement and high solubility, due to their high branching, large number of end group functionalities, compact and globular structure. Polyurethane nanocomposites (PUN), with excellent mechanical properties and biocompatibility, are good candidates for use as coatings on medical devices and implants. Also, mesoporous silica nanoparticles (MSNs) have specific properties, such as good biocompatibility, large specific surface area, uniform pore size distribution, ability for various surface functionalization, excellent thermal stability and strength, meaning they are useful for biomedical applications [3]. Recent expansion in research on new biomaterials has contributed to the ability to create PU materials with desired physical, chemical and biological properties for specific purposes, thanks to the knowledge of how these polymers' structures influence their properties. Most physiologically relevant interactions between material and biological system occur at the interface, so crucial requirement for every biomaterial is biocompatibility of its coating [4]. The enhancement of physicochemical properties and biocompatibility of PU materials as medical implants remains an

important challenge. In the present study, new nanocomposites based on crosslinked polyurethane and MSNs (PU-MSNs) were prepared through *in situ* two-step polymerization method. Surface properties of PU-MSNs and their interaction with endothelial cells were evaluated for potential biomedical applications.

## METHODS

Nanocomposites based on polyurethane network and MSNs with 50 wt.% PDMS segment were prepared by *in situ* two-step polymerization in solution (NMP/THF) using  $\alpha,\omega$ -dihydroxy-ethylene oxide-poly(dimethylsiloxane)-ethylene oxide (PDMS; abcr GmbH;  $M_n = 1000$  g/mol), 4,4'-methylenediphenyl diisocyanate (MDI; Sigma-Aldrich) as monomers and hyperbranched polyester of the second pseudo generation (BH-20; Polymer Factory;  $M_n = 1780$  g/mol). The synthesis procedure for nanocomposite films is analogous to our previously published procedure [4]. Non-functionalized and surface-functionalized (with 3-(trihydroxysilyl)propyl methylphosphonate (PHMSN) and 2-[methoxy(polyethyleneoxy)6-9propyl]trimethoxysilane (PEOMSN)) MSNs were used as the nanofillers in the concentration of 1 wt.% in the PU-MSN materials. The study of microphase-separated structure and topography of prepared PU-MSN films was carried out by a commercial atomic force microscope (Dimension Icon, Bruker), equipped with the SSS-NCL probe Super Sharp Silicon<sup>TM</sup>-SMP-Sensor (NanosensorsTMSwitzerland); spring constant  $35 \text{ Nm}^{-1}$ , resonant frequency  $\approx 170 \text{ kHz}$ ). The measurements were done at ambient temperature, in the tapping mode AFM technique. Endothelial cell adhesion on the surface of PU-MSN films was examined by a computer-based Carl Zeiss Axiovision microscope as previously described by Pergal et al. [4]. Briefly, different concentrations of EA.hy926 cells were seeded into 96-microwell plate and 3-[4,5-dimethylthiazol-2-yl]-2,5-diphenyl-tetrazolium bromide (MTT) test was performed 48 h post-seeding. The results were presented as percent of the control value obtained from cells grown without sample film, taken as 100%.

## RESULTS AND DISCUSSION

AFM images of the surface topology were used to characterize the PU nanocomposites with different types of MSNs and AFM image of selected PU-PHMSN film is presented in Fig. 1a. Surface roughness values increase in order PU-PHMSN ( $R_q = 60 \text{ nm}$ ), PU-MSN ( $R_q = 118 \text{ nm}$ ), and PU-PEOMSN ( $R_q = 192 \text{ nm}$ ). The samples with higher  $R_q$  values showed a rougher surface of the prepared nanocomposites.

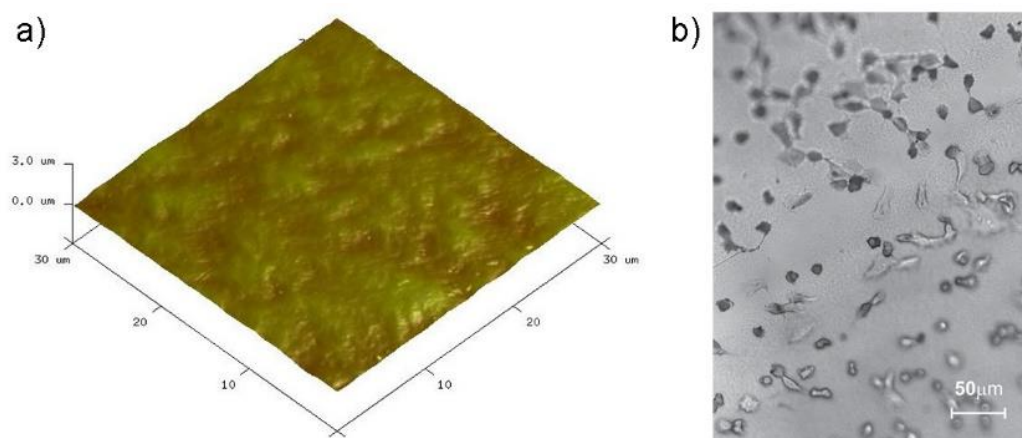


**Figure 1.** PU-PHMSN: a) 3D AFM image and b) photograph of cell attachment

To assess biocompatibility of novel PU-MSNs, cell viability and cell adhesion tests were carried out using human EA.hy926 cell line (Fig. 1b). Influence of incubation with nanocomposites on cell viability was evaluated by MTT assay. The reduction in cell viability ( $41.0 \pm 8.1\%$  for PU-PHMSN;  $51.4 \pm 9.4\%$  for PU-MSN and  $56.3 \pm 4.7\%$  for PU-PEGMSN) can indicate a lower number of cells on the surface of investigated materials in relation to the control surface (polystyrene; cell viability on control sample was 100%), probably as a consequence of moderate EA.hy926 cells attachment on the surface of PU-MSN films. Although MTT test was not sensitive enough to show differences between the prepared materials, probably because of the high respiratory activity of cells grown around the films, the micrographs detected subtle distinction in cell attachment among investigated films. The cell adhesion and growth appeared to depend on the microphase separation and surface roughness. The prepared PU-MSNs with higher microphase separation and surface roughness showed enhanced endothelial cells attachment. In addition, cell morphology was preserved on the surface of PU-MSN films. The density of adhered cells was the highest on PU-PEOMSN ( $2345 \pm 615$  cells/mm<sup>2</sup>) followed by PU-MSN ( $1645 \pm 301$  cells/mm<sup>2</sup>) and PU-PHMSN ( $1500 \pm 518$  cells/mm<sup>2</sup>). The level of the endothelial cell attachment on PU-MSNs films was in the range from 47.0 (for PU-PHMSN) to 55.1% (for PU-PEOMSN), which is higher as compared to some commercial PU i.e. ElastEon™ (31.4%). Prepared nanocomposites indicated improved endothelial cell attachment as compared to PU based on tri-block pre-polymer poly( $\epsilon$ -caprolactone)-*block*-poly(dimethylsiloxane) macrodiol [4].

## CONCLUSION

A series of polyurethane nanocomposites with different type of MSNs was successful prepared. The PUMSN materials with higher surface roughness values showed enhanced endothelial cells attachment. Prepared nanocomposites favored endothelial cells adhesion and growth, indicating good biocompatibility. The results of this study indicate that prepared PUMSN materials can be considered as biocompatible materials with potential applications in biomedical fields, in particular as a new coating for medical implants.

## Acknowledgement

This work was financially supported by the Ministry of Education, Science and Technological Development of the Republic of Serbia within Serbian-French Bilateral Project No. 337-00-8/2020-04 (2020-2021) and Ministry of Foreign Affairs of the Republic of France. The authors would like to thank the Ministry of Education, Science and Technological Development (Grant No: 451-03-9/2021-14/200026; 451-03-9/2021-14/200358; 451-03-9/2021-14/200168; 451-03-9/2021-14/200007) and the Czech Science Foundation (No: 18-03932S).

## REFERENCES

- [1] R. Vermette, H. J. Griesser, G. Laroche, R. Guidoin, *Biomedical Applications of Polyurethanes*; Landes Bioscience, Austin, TX, 2001.
- [2] M. V. Pergal, J. V. Džunuzović, R. Poręba, M. Steinhart, M. M. Pergal, V. V. Vodnik, M. Špírková, *Ind. Eng. Chem. Res.* 2013, 52, 6164-6176.
- [3] N. Knežević, N. Ilić, V. Đokić, R. Petrović, Đ. Janačković, *ACS Appl. Mater. Inter.* 2018, 10, 20231-20236.
- [4] M. V. Pergal, V. V. Antić, G. Tovilović, J. Nestorov, D. Vasiljević-Radović, J. Djonlagić, *J. Biomater. Sci. Polym. E.* 2012, 23, 1629-1657.

## THERMAL CHARACTERIZATION OF POLYURETHANE/SILVER FERRITE NANOCOMPOSITES

M. V. Pergal<sup>1</sup>, B. P. Dojčinović<sup>1</sup>, I. D. Kodranov<sup>2</sup>, S. Ostojić<sup>3</sup>, M. Ognjanović<sup>4</sup>, D. Stanković<sup>2</sup> and B. Antić<sup>4</sup>

<sup>1</sup> *University of Belgrade, Institute of Chemistry, Technology and Metallurgy, Njegoševa 12, 11000 Belgrade, Serbia. (marijav@chem.bg.ac.rs)*

<sup>2</sup> *Faculty of Chemistry, University of Belgrade, Studentski trg 12-16, 11000 Belgrade, Serbia. ikodranov@gmail.com*

<sup>3</sup> *Institute of General and Physical Chemistry, University of Belgrade, Studentski trg 12-16, Belgrade, Serbia.*

<sup>4</sup> *The Vinca Institute of Nuclear Sciences, University of Belgrade, POB 522, Belgrade, Serbia.*

### ABSTRACT

The novel polyurethane composite films were prepared using *in situ* polymerization method in the presence of silver ferrite nanoparticles (1 wt.%). Preparation, structure, and thermal characterization of polyurethane/silver ferrite nanocomposites (PUFNCs) were investigated. The study of the effect of soft segment content (from 30 to 60 wt.%) on the structure and thermal properties was performed using FTIR, DSC, TGA and TEM analyses. The higher thermal stability was detected for PUFNCs with higher soft segment content. The glass transition of the hard segment ( $T_{gHS}$ ) of PUFNCs increased with decreasing soft segment content due to higher crosslinking density.

### INTRODUCTION

Polyurethane nanocomposites (PUNCs) have received widespread attention due to their improved physicochemical properties compared with the pure polyurethane (PU) [1]. It is currently accepted that attractive interactions between the PU and the nanoparticles may promote homogeneous dispersion [1]. The most challenging task in construction of PUNCs is to achieve a good dispersion of nanoparticles into a PU matrix, as these tend to agglomerate [1]. Surface modification is one of the pathways to reduce the agglomeration tendency of the nanoparticles. Ferrite nanoparticles possess unique properties, such as uniform size distribution, less agglomeration, good biocompatibility, and stability in the biological medium. The good mechanical properties and blood compatibility of PUNCs, moreover, have made them major candidates for medical devices [2]. Poly(dimethylsiloxane) (PDMS) has been incorporated into PUs to produce a non-cytotoxic materials with enhanced degradation resistance and *in vivo* biostability [2]. PUs based on PDMS are particularly suitable for the development of cardiovascular implants, such as vascular grafts, catheters, artificial heart-assisting devices, etc [2]. However, bacterial colonization on the medical device surface often occurs, frequently causing bloodstream infections in patients [3]. Several metal ions show antimicrobial activity due to their ability to affect bacterial protein synthesis by the coordination of protein active site residues or by binding to bacterial ribosomal subunits. Silver has been widely employed as an effective non-resistance-inducing agent able to prevent medical device-related infections when incorporated in polymers [3]. Conventional approaches mainly consist of the deposition of metallic silver on the polymer surface, or direct incorporation of silver ions, the active species of silver into the polymer [3].

In this paper, preparation, structure, and thermal properties of novel polyurethane/ferrite composites (PUFNCs) using low amount of silver ferrite (1 wt.%) as fillers were studied. The synthesized PUFNCs have a great deal of attention from scientific community, due its unique

properties (good thermal, mechanical and surface properties) and applications (as coatings for medical devices and implants).

## METHODS

Polyurethane nanocomposites based on polyurethane network and silver ferrite were prepared by *in situ* polymerization method as previously described [4]. PUFNCs were prepared using  $\alpha,\omega$ -dihydroxy-poly(dimethylsiloxane) (PDMS; ABCR;  $M_n = 1000$  g/mol), 4,4'-methylenediphenyl diisocyanate (MDI; Sigma-Aldrich) as monomers and hyperbranched polyester of the second pseudo generation as crosslinking agent (BH-20; Polymer Factory;  $M_n = 1780$  g/mol) [4]. The soft PDMS segment was varied from 30 to 60 wt.%. Silver ferrite was used as the nanofillers in the concentration of 1 wt.% in nanocomposites. The silver ferrite ( $\text{AgFeO}_2$ ) nanoparticles modified with poly(ethylene oxide) was prepared by co-precipitation/microwave hydrothermal method.

FTIR spectra were recorded on ATR Nicolet 380 FTIR spectrometer. Differential scanning calorimetry (DSC) was carried out on a TA DSC Q1000 thermal analyzer. The DSC scans were recorded under a dynamic nitrogen atmosphere ( $50 \text{ cm}^3/\text{min}$ ), in the temperature range from  $-90$  to  $260$  °C, at a heating and cooling rate of  $10$  and  $5$  °C/min, respectively (two scans were run for each sample). The thermal stability was determined by thermogravimetric (TG) analysis, using TA TGA Q500 instrument in nitrogen atmosphere, at heating rate of  $10$  °C/min.

## RESULTS AND DISCUSSION

FTIR analysis was performed to study the structure of the obtained PUFNC films. The FTIR spectra of the selected PUFNCs are displayed in Fig. 1. The absence of unreacted isocyanate absorption peaks at  $2270 \text{ cm}^{-1}$  relieved that the presence of silver ferrite nanoparticles did not negatively affect the formation of the urethane groups.

The characteristic stretching frequencies of the prepared PUFNCs appeared at  $3320\text{--}3450 \text{ cm}^{-1}$  ( $\nu_{\text{N-H}}$ ),  $2960$ ,  $2945$ , and  $2865 \text{ cm}^{-1}$  ( $\nu_{\text{sym}}$  and  $\nu_{\text{asym}}$  of C-H),  $1645\text{--}1735 \text{ cm}^{-1}$  ( $\nu_{\text{C=O}}$ ),  $1535$  and  $1260 \text{ cm}^{-1}$  ( $\nu_{\text{C-N}} + \delta_{\text{N-H}}$ , i.e., amide II and amide III bands),  $1016$  and  $1080 \text{ cm}^{-1}$  ( $\nu_{\text{Si-O-Si}}$  and  $\nu_{\text{C-O-C}}$ ),  $1597$  and  $1415 \text{ cm}^{-1}$  ( $\nu_{\text{(C=C)arom}}$ ), and  $790 \text{ cm}^{-1}$  ( $\rho_{\text{C-H}}$  in  $\text{SiCH}_3$ ). In FTIR spectra of PUFNCs, two bands at lower frequency range i.e., one strong band at  $\sim 450 \text{ cm}^{-1}$  and one very weak band at  $\sim 510 \text{ cm}^{-1}$ . An FTIR band at  $\sim 450 \text{ cm}^{-1}$  could be assigned to stretching vibration of Ag-O, while the appeared FTIR band at  $\sim 510 \text{ cm}^{-1}$  could be ascribed to stretching vibration of Fe-O [5].

Thermogravimetric curves of the selected PUFNC films are given in Fig. 2 and results are presented in Table 1. Thermal stability increased with increasing soft (PDMS) segment content. DTG curves of PUFNC films are characterized with three steps (Table 1; 5<sup>th</sup> column). The first one, DTG peak, is more pronounced, and belongs to the degradation of hard domains (the urethane links scission), while the second and third process (shoulders in DTG curves) are assigned to the decomposition of ester and soft segments (PDMS).

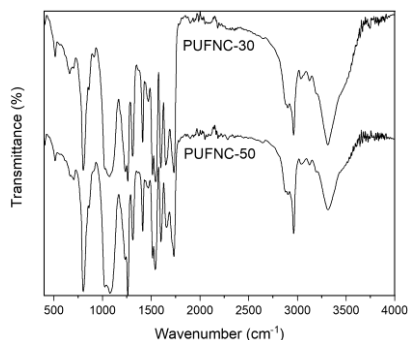


**Figure 1.** FTIR spectra of PUFNCs.

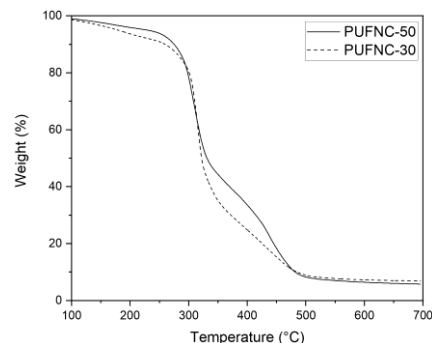


**Figure 2.** TGA of the selected PUFNCs.

Thermal characteristics of PUFNCs were investigated by DSC. The first heating DSC curves of PUFNC films show glass transition temperature of the hard (MDI-BH20) segment ( $T_{gHS}$ ). The  $T_{gHS}$  values ranged from 49 to 56 °C (Table 1) and increased with decreasing soft segment content. The obtained results are attributed to the higher of cross-linking density in materials with lower soft segment content, that cause more restricts the molecular motion of the polymer chains and leads to the increase in  $T_{gHS}$ .

**Table 1.** The soft segments content (SSC), characteristic temperatures of thermal degradation, and glass transition temperature of the hard segment ( $T_{gHS}$ ), determined by DSC, of PUFNC films

Sample	SSC, wt. %	$T_{10}$ , °C	$T_{50}$ , °C	$T_{max}$ , °C	$T_{gHS}$ (DSC), °C
PUFNC-30	30	260	322	316/343//445	56
PUFNC-40	40	265	324	314/352/450	54
PUFNC-50	50	275	332	309/357/440	52
PUFNC-60	60	270	343	308/326/452	49

Incorporation of PEG coated  $AgFeO_2$  nanoparticles in PU was examined by High-angle annular dark-field scanning transmission electron microscopy (HAADF-STEM) using a JEOL ARM 200CF electron microscope equipped with JEOL Centurio EDXS and Quantum ER Gatan GIF dual-EELS systems. A micrograph of PUFNC-30 composite is shown in the Fig. 3. Bright spots indicate that nanoparticles of  $AgFeO_2$  are a few nanometer is size, spherical shape and random distributed in polymer.

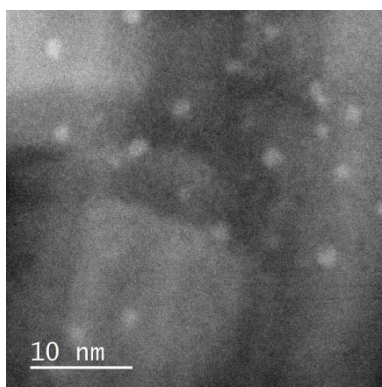


**Figure 3.** HAADF/STEM images of PUFNC-30.

## CONCLUSION

A series of novel PU nanocomposites with different soft segment content was successfully obtained by addition of 1 wt% of silver ferrite nanoparticles using *in situ* polymerization method. The thermal stability increased with increasing soft segment content. The  $T_{gHS}$  values increased with decreasing soft segment content due to higher crosslinking density. The obtained results confirmed the existence of interaction between the silver ferrite nanoparticles and hard segments of PUFNCs.

## Acknowledgement

The authors would like to thank the Ministry of Education, Science and Technological Development (Grant No: 451-03-9/2021-14/200026). We thank Prof. Goran Drazic for performing HAADF/STEM measurements.

## REFERENCES

- [1] M. V. Pergal, I. S. Stefanović, R. Poręba, M. Steinhart, P. Jovančić, S. Ostojić, M. Špírková, Ind. Eng. Chem. Res., 2017, 56, 4970-4983.
- [2] R. Vermette, H. J. Griesser, G. Laroche, R. Guidoin, Biomedical Applications of Polyurethanes; Landes Bioscience, Austin, TX, 2001.
- [3] I. Francolini, L.D 'Ilario, E. Guaglianone, G. Donelli, A. Martinelli, A. Piozzi, Acta Biomater., 2010, 6, 3482-3490.
- [4] M. V. Pergal, J. V. Džunuzović, R. Poręba, S. Ostojić, A. Radulović, M. Špírková, Prog. Org. Coat., 2013, 76, 743-756.
- [5] S. M. Hosseini, H. Hosseini-Monfared, V. Abbasi, M. R. Khoshroo, Inorg Chem Commun., 2016, 67, 72-79.

*J - Macromolecular Physical  
Chemistry*



## MODIFICATION OF TOKAT RESADIYE BENTONITE WITH CATIONIC SURFACTANT

V. Teofilović<sup>1</sup>, J. Pavličević<sup>1</sup>, T. Erceg<sup>1</sup>, N. Vukić<sup>2</sup>, O. Govedarica<sup>1</sup>, D. Lacin<sup>3</sup>, A. Z. Aroguz<sup>4</sup>

<sup>1</sup>University of Novi Sad, Faculty of Technology Novi Sad, Bul. cara Lazara 1, 21000 Novi Sad, Serbia. (vesnateofilovic@uns.ac.rs)

<sup>2</sup>University of Kragujevac, Faculty of Technical Sciences, Svetog Save 65, 32000 Čačak, Serbia.

<sup>3</sup>Istanbul University-Cerrahpasa, Engineering Faculty, Department of Geological Engineering, 34320, Avcilar, Istanbul, Turkey.

<sup>4</sup>Istanbul University-Cerrahpasa, Engineering Faculty, Chemistry Department, 34320, Avcilar, Istanbul, Turkey.

### ABSTRACT

The large bentonite reserves in Turkey are presently mined as very important raw materials for different industries. Application areas of bentonites vary, depending on kinds and amounts of its constituents such as smectites and non-clay minerals. In order to enhance the efficiency of Tokat Resadiye bentonite as a filler in polymer matrix, its modification with cationic surfactant, cetyltrimethylammonium bromide, was investigated in this study. The modified bentonite was examined by X-ray diffraction and Attenuated total reflectance fourier transform infrared spectroscopy.

### INTRODUCTION

Bentonite is a 2:1 type aluminosilicate, with a large surface area and surface energy, which ensure good adsorption properties. Due to the presence of high amount of exchangeable cations between layers, bentonites are naturally hydrophilic. In order to add bentonite into different polymer composites, its surface should be organically modified to hydrophobic, which is usually done by exchanging the occupation of sites on the bentonite surface with organic cations [1]. Bentonites have been found widespread within the Bereketli member of the Cretaceous Resadiye Formation, central Anatolia (Turkey). These bentonites were hypothesized to have been formed by the in-situ alteration of parent rhyolitic, dacitic, and trachyandesitic pyroclastics, in a shallow marine environment, during early diagenesis shortly after deposition. Tokat Resadiye bentonite may be used to prepare organoclays, pillared clays, electrodes, clay-polymer nanocomposites, as well as for drilling, casting, food and tire industries [2].

### MATERIALS AND METHODS

The clay mineral was obtained from the Tokat Resadiye area in Turkey. Cation exchange capacity (CEC) is 75 meq/100 g. Chemical structure is following: 57.1% SiO<sub>2</sub>, 16.8% Al<sub>2</sub>O<sub>3</sub>, 2.6% Na<sub>2</sub>O, 3.4% CaO, and 3.8% Fe<sub>2</sub>O<sub>3</sub> and 15.2% loss on ignition (LOI) value, with trace amount of impurities such as illite, quartz, mica, feldspar, calcite, etc. Organic modification of bentonite was performed using cationic surfactant cetyltrimethylammonium bromide (CTAB) (Sigma-Aldrich). The clay was crushed in a mortar, wet sieved with distilled water through a 63 μm sieve, and dried at 105 °C until constant weight. After drying, it was crushed again in the mortar. 10 g of clay was dispersed in 1 l of distilled water by continuous stirring for 3 h. After that, the clay was left overnight to settle down. After vacuum filtration, clay was added to 1.8 g CTAB in 1 l of distilled water. The clay/CTAB aqueous solution was continuously mixed for 5 h at constant temperature (25 °C). The concentrate solution was left for 1 h to settle down and then vacuumed filtered to remove the solid part. The solid product (modified clay) was washed with distilled water until no bromide ions were found from the

filtrate by 0.1 M  $\text{AgNO}_3$  solution. The crystallographic structure of the bentonite samples was determined using powder X-ray diffractometry (Rigaku MiniFlex600, with  $\text{CuK}\alpha$  radiation at a scan rate of  $2\theta = 0.01^\circ/\text{s}$ ). The chemical structure of samples was studied by attenuated total reflectance Fourier transform infrared spectroscopy (ATR-FTIR) (Shimadzu IRaffinity-1S instrument in the range of  $400$  to  $4000\text{ cm}^{-1}$  and resolution of  $4\text{ cm}^{-1}$ ).

## RESULTS AND DISCUSSION

The powder XRD pattern for an unoriented sample is given in Fig. 1. When montmorillonite type clays are treated with polar organics (ethylene glycol, glycerol, CTAB, etc.), the polar organics entering between the layers cause the clays to swell. This situation in XRD analyzes is observed as follows: when the clay swells, the d-distance increases, shifting towards the low  $2\theta$  angle side (left), according to Bragg's law ( $n\lambda = 2d\sin\theta$ ), since there is an inversely proportional relationship between the d-value, which is the distance between the layers, and the  $2\theta$  angle. As the  $2\theta$  angle increases, the d-value decreases; also, when the  $2\theta$  angle decreases, the d-value increases. Therefore, when the clay mineral swells, the peak of the clay shifts to the left as the d-distance will increase. Since the XRD recording started from  $2\theta = 5^\circ$ , in the figure 1, the swelling of galleries, can't be observed clearly. If the XRD recording had been started from  $2\theta = 3^\circ$  instead, the leftward shift would clearly be seen due to swelling in the bentonite clay treated with polar organic (CTAB). However, certain left shift is observed, which can confirm the modification of clay.

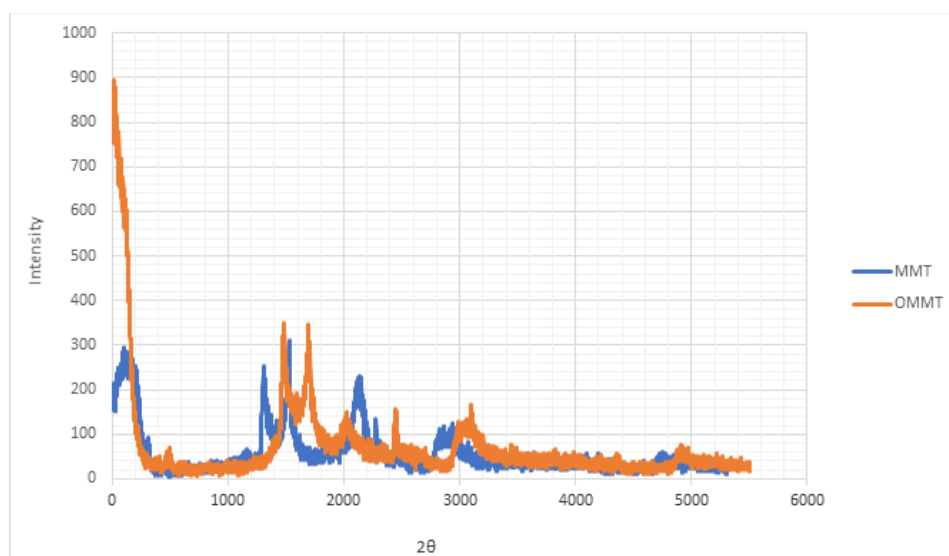


**Figure 1.** Results of XRD analyses of unmodified Resadiye bentonite (MMT) and Resadiye bentonite modified with CTAB (OMMT)

FTIR was used for identifying formation of new bonds in the modified bentonites in comparison to unmodified ones. This analysis also helped to confirm the success of the modification procedure applied in this study. Tyagi et al, 2006 studied the FTIR spectra of Indian MMT and attributed FTIR bands to certain interactions [3].

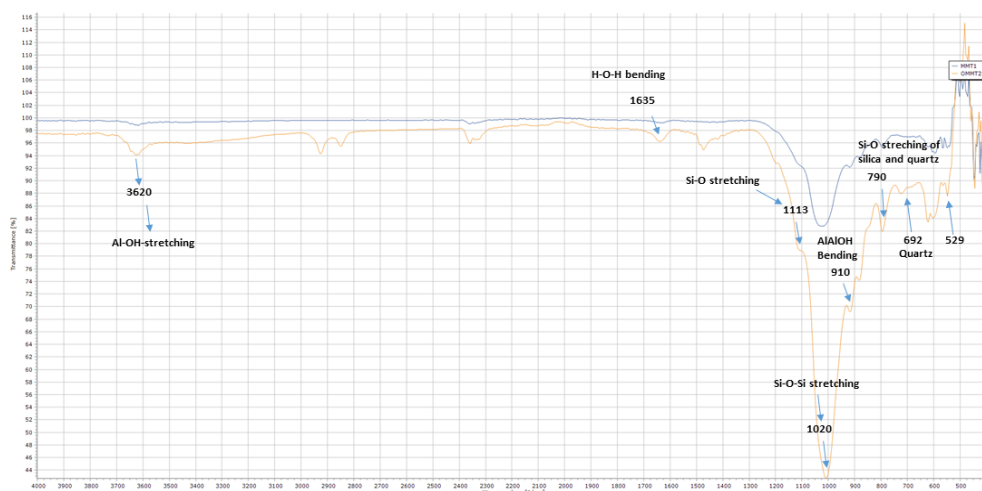


**Figure 2.** FTIR spectra of unmodified Resadiye bentonite (MMT) and Resadiye bentonite modified with CTAB (OMMT)

In FTIR spectrum of MMT (Fig. 2), the band near  $3620\text{ cm}^{-1}$  is attributed to OH group bound with  $\text{Al}^{+3}$  in bentonite, which is a characteristic peak for MMT with high amount of Al in the octahedra. Free water of bentonite are associated with bands near  $3440\text{ cm}^{-1}$  and  $1639\text{ cm}^{-1}$  which are attributed to stretching and bending vibrations of OH groups of water. A characteristic band of MMT at  $1114\text{ cm}^{-1}$  shows Si-O out-of-plane stretching vibration. The band at  $1033\text{ cm}^{-1}$  is attributed to Si-O in-plane stretching and the band at  $529\text{ cm}^{-1}$  Si-O bending vibrations. Bending vibration of hydroxyl groups with Al (AlAlOH) is registered at  $910\text{ cm}^{-1}$ , while the band at  $871\text{ cm}^{-1}$  is attributed to AlFe-OH. Moreover, the band at  $696\text{ cm}^{-1}$  shows the presence of quartz in the bentonite [3-5].

## CONCLUSION

Bentonite clays can find many applications, but in order to use them as fillers in polymer composites, their surface should be organically modified from hydrophilic to hydrophobic. In this paper, the bentonite clay obtained from Tokat Region in Turkey was organically modified with cetyltrimethylammonium bromide. The successful modification of Tokat bentonite was confirmed by XRD and FTIR analyses.

## Acknowledgement

This work was supported by the Scientific Research Fund of the Istanbul University-Cerrahpaşa (Project code: BAP-20755), and by the Ministry of Education, Science and Technological Development of the Republic of Serbia (Grant no. 451-03-9/2021-14/200134).

## REFERENCES

- [1] V. Teofilović, J. Pavličević, O. Bera, M. Jovičić, J. Budinski-Simendić, K. M. Szécsényi, A. Aroguz, The preparation and thermal properties of chitosan/bentonite composite beads, *Hem. Ind.* 68, 653, 2014.
- [2] F. E. Özgüven et al, Characterization of a bentonite and its permanent aqueous suspension, *JOTCSA*, 7(1): 11-18, 2020.
- [3] B. Tyagi, C. D. Chudasama, R. V. Jasra, Determination of Structural Modification in Acid Activated Montmorillonite Clay by FT-IR Spectroscopy, *Spectrochimica Acta Part A*, 64, 273–278, 2006.

- [4] H. A. Patel, R. S. Somani, H. C. Bajaj, R. V. Jasra, Preparation and Characterization of Phosphonium Montmorillonite with Enhanced Thermal Stability, *Applied Clay Science*, 35, 194–200, 2007.
- [5] T. Seyidođlu, Purification and Modification of Bentonite and its use in Polypropylene and Linear Low Density Polyethylene Matrix Nanocomposites, Middle East Technical University, PhD Thesis, 329, 2010.

## FABRICATION of CS/PAA/Bnt as pH RESPONSIVE HYDROGEL FOR DRUG DELIVERY APPLICATIONS

V. Teofilović<sup>1</sup>, B. Agan<sup>2</sup>, J. Pavličević<sup>1</sup>, D.Lacin<sup>3</sup>  
A. Z. Aroguz<sup>2</sup>

<sup>1</sup>University of NoviSad, Faculty of Technology Novi Sad, bul. cara Lazara 1, 21000 Novi Sad, Serbia. (vesnateofilovic@uns.ac.rs)

<sup>2</sup>Istanbul University-Cerrahpasa, Engineering Faculty, Chemistry Department, 34320, Avcilar, Istanbul, Turkey.

<sup>3</sup>Istanbul University-Cerrahpasa, Engineering Faculty, Department of Geological Engineering, 34320, Avcilar, Istanbul, Turkey.

### ABSTRACT

The purpose of this work was to prepare Chitosan/Polyacrylic acid/Bentonite (CS/PAA/Bnt) as drug carrier for controllable drug delivery and highly-effective drug release. The materials used for preparation were bentonite (Bnt) clay, chitosan (CS) and acrylic acid (AA). The model drug for analyzing drug delivery and release kinetics was pantoprazole. The FTIR results confirmed that the drug active agent was successfully loaded into the prepared drug carriers. The swelling properties of the drug carriers were examined in buffer solutions at different pH values. The controlled pantoprazole release properties of the prepared samples showed that the release of the drug active reagent from drug carriers is pH-sensitive. The kinetics of the drug release was examined by fitting the experimental data to the first order kinetic. CS/PAA/Bnt hydrogels were shown to be capable of carrying pantoprazole and can potentially be used in drug delivery systems.

### INTRODUCTION

The drug delivery systems have become increasingly important since the production of a new drug is very expensive and takes a long time. Several different techniques are used in oral drug release systems, such as adsorption and coating, pellet technique, hydrogels, tablets, microbeads, core shell technique, etc [1]. pH-sensitive drug release systems release drugs in the stomach by responding to gastric low pH [2]. In order to make them compatible with the living organisms, hydrogels as drug carriers are preferably prepared using biopolymers and other natural substances, like clays. Clays have high surface energy, which reflects in high adsorption capacity, and ability to load high amounts of active substance, which provides them an important role in drug carrier systems. Due to hydrophilic surface, clays can't intercalate with polymers, therefore, they should be organically modified, usually by ion exchange reaction by using organic cations as alkylammonium ions [3]. Chitosan is a biodegradable, natural polymer, and is widely used in many scientific studies in pharmaceutical and medical fields due to its non-toxicity and biocompatibility properties. Pantoprazole is a proton pump inhibitor (PPI) used to treat gastric acid-base disturbances. It is effective at reducing gastric acidity and thereby regulating gastric pH [4]. The aim of this study is to prepare a drug carrier for controllable drug delivery and release. The materials used in this work were prepared by adding bentonite (Bnt) and acrylic acid to chitosan (CS) in order to improve the adsorptive capacity of chitosan.

### METHODS

Modification of Bentonite was detailly explained in previous paper [5].

*The preparation of chitosan/poly acrylic acid/bentonite (CS/PAA/Bnt)*

Chitosan (0,25g) was dissolved in 15 ml acetic acid solution (1%) at 65 °C in an inert atmosphere. 0,2 g of modified clay (120 mesh) previously dispersed in 20 ml of distilled water was added to the

chitosan solution. 1,68 g of Acrylic acid (AA)/potassium peroxydisulfate (KPS) as initiators (10/1) (wt/wt) were added to the mixture. After continuous stirring, a homogenous mixture was obtained. The resultant solution was poured into a Teflon petri dish and dried until constant weight at ambient temperature.

### Swelling of the samples

The swelling of the samples can be estimated as the mass swelling in distilled water and in buffer solutions. The swelling percentage were calculated as;

$$\text{Swelling (\%)} = \frac{W_s - W_d}{W_d} \times 100 \quad (1)$$

$W_s$ : the swollen weight of composite at time  $t$ ,  $W_d$ : the dry weight of composite

Approximately 0.01 g of samples were used for swelling experiments. The samples kept in distilled water were taken for a certain time and weighed after removing excess water. The amount of swelling (%) was estimated by Eq1.

### Kinetic studies

*First order Kinetics*: A first-order kinetic indicates that the drug release rate is linearly dependent on the concentration (Eq. 2).

$$\ln C_t = -k_1 t + \ln C_0 \quad (2)$$

Where  $C_0$  is the initial drug concentration and  $C_t$  is the concentration of drug at any time.  $k_1$  is the first order rate constant.

### Drug loading and release

0,50 g of the CS-PAA/Bnt sample was added to the 100 ml drug solution (0,2 g/L) and kept at 25°C for 5h. The absorbance values of the drug solution during loading and releasing process were measured by UV-spectrophotometer.

## RESULTS AND DISCUSSION

The structural and morphological characterization of the prepared samples was analyzed by FTIR.

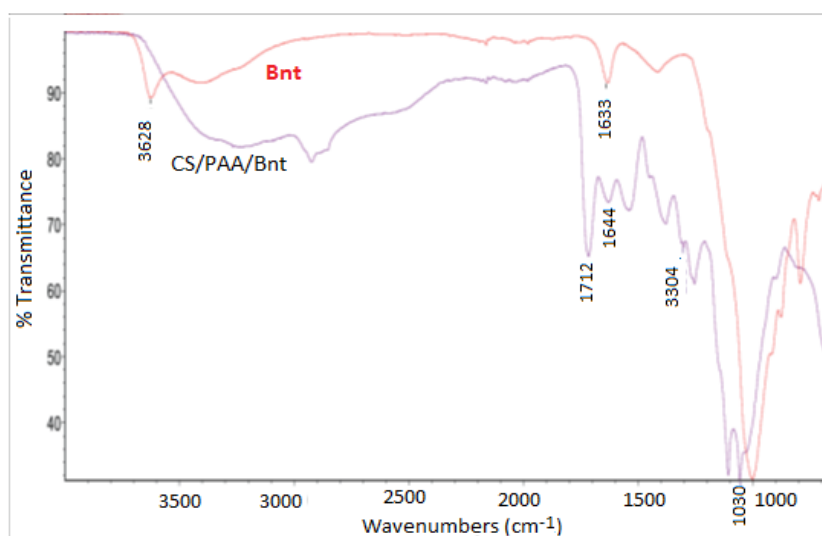


**Fig 1:** The FTIR spectra of bentonite and CS/PAA/Bnt

The structural characterization of the prepared sample and Bnt were given in Fig.1. The peaks observed in the 1000-792 $\text{cm}^{-1}$  range are the -OH in the tetrahedral and octahedral structures of the clay. It shows Si-O peaks with bending vibrations. Si-OH peak in the 1000  $\text{cm}^{-1}$  region of clay shifted a little to the left (1030  $\text{cm}^{-1}$ ) in the CS/PAA/Bnt sample. These results imply that clay compatible enters into the polymer structure.

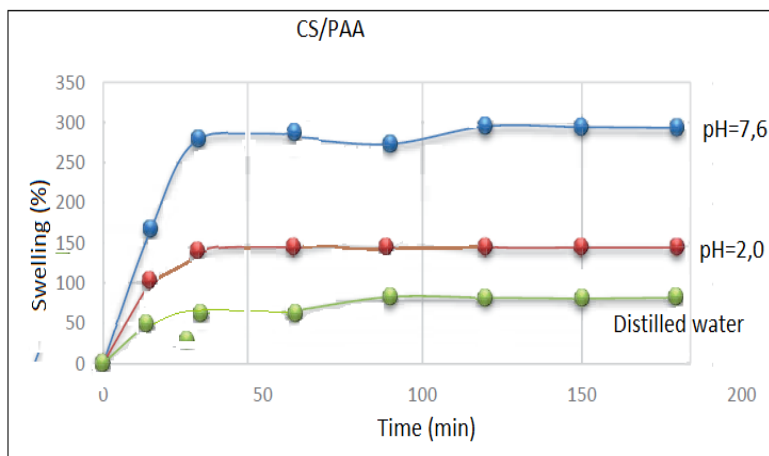


**Figure 2:** Swelling behavior of the CS/PAA/Bnt sample in different pH solution

The swelling behavior of the CS/PAA/Bnt samples was examined and the results were given in Fig 3. The maximum swelling of the samples was obtained at pH = 7,6. This situation can be explained by the repulsion among the hydrophilic groups (-COO<sup>-</sup>) in the sample. The-COO- groups on the prepared sample were protonated in acidic media, and then led to small water absorbency and swelling. With increasing pH of external solution, -COO-groups in acrylic acids are ionized gradually, which enhance electrostatic repulsion, and then enhance swelling capacity as reported Zhang et. al [6].

Results of kinetic studies showed that the drug release kinetics of Pantaprazole fitted to the first order kinetic ( $R = 0,9942$ ) and it is linearly dependent on the concentration.

## CONCLUSION

In this work CS/PAA/Bnt sample was successfully prepared as scaffold for the drug release system. The swelling behavior was examined and the highest swelling value were observed at the pH 7,6 solution. The loading and release properties have shown that the release kinetics follows first order. It has been shown that the prepared sample is effective for loading and carrying pantoprazole. It can potentially be used in oral drug delivery systems.

## Acknowledgement

This work was supported by the Scientific Research Fund of the Istanbul University-Cerrahpaşa. Project code: BAP-20755, and by the Ministry of Education, Science and Technological Development of the Republic of Serbia (Grant no. 451-03-9/2021-14/200134).

## REFERENCES

- [1] P. W. S. Heng, *Controlled release drug delivery systems*, in *Pharm. Dev. Technol.* **23**, Taylor and Francis Ltd, (2018).
- [2] T. Yoshida, T. C. Lai, G. S. Kwon and K. Sako, *pH- and ion-sensitive polymers for drug delivery*,

- Expert Opin. Drug Deliv.* **10**, NIH Public Access, (2013) 1497.
- [3] C. Aguzzi, P. Cerezo, C. Viseras and C. Caramella, *Use of clays as drug delivery systems: Possibilities and limitations*, *Appl. Clay Sci.* **36**, Elsevier, (2007) 22.
- [4] A. Z. Aroğuz, V. Teofilovic, J. Budinski-Simendic, *Highly Swollen Composite Hydrogel for Investigation of Pantoprazole Release Profile*, in *IUPAC-FAPS 2017*, (2017).
- [5] V. Teofilović, J. Pavličević, T. Erceg, N. Vukić, O. Govedarica, D. Lacin, A. Z. Aroguz, *Modification of tokat resadiye bentonite with cationic surfactant*, *Physical Chemistry 2021* (2021).
- [6] J. Zhang, L. Wang, A. Wang, *Reparation and properties of chitosan- g-poly(acrylic acid)/montmorillonite superabsorbent nanocomposite via in situ intercalative polymerization*, *Industrial Engineering Chemistry Research*, **46**: 2497-2502, (2007).

## SYNTHESIS AND CHARACTERIZATION OF EDTA FUNCTIONALIZED MACROPOROUS GLYCIDYL METHACRYLATE BASED COPOLYMER

B. M. Marković<sup>1</sup>, T. T. Tadić<sup>1</sup>, I. S. Stefanović<sup>1</sup>, J. V. Džunuzović<sup>1</sup>, Lj. T. Suručić<sup>2</sup>, Z. P. Sandić<sup>3</sup> and A. B. Nastasović<sup>1</sup>

<sup>1</sup> *University of Belgrade - Institute of Chemistry, Technology and Metallurgy, Njegoševa 12, 11000 Belgrade, Republic of Serbia. (bojana.markovic@ihtm.bg.ac.rs)*

<sup>2</sup> *University of Banja Luka, Faculty of Medicine, Save Mrkalja 14, Banja Luka, Republic of Srpska, B&H*

<sup>3</sup> *University of Banja Luka, Faculty of Natural Science and Mathematics, Mladena Stojanovića 2, Banja Luka, Republic of Srpska, B&H*

### ABSTRACT

A novel functionalized macroporous poly(glycidyl methacrylate-co-ethylene glycol dimethacrylate), (pSGE-eda-EDTA) copolymer was obtained by two-step functionalization with ethylene diamine (EDA) and ethylenediaminetetraacetic acid (EDTA). The initial copolymers, as well as functionalized samples, were characterized by Fourier transform infrared spectroscopy (FTIR), scanning electron microscopy (SEM), mercury porosimetry and elemental analysis. Additionally, the content of amino and carboxyl group, as well as the point of zero charge (pH<sub>PZC</sub> value), were determined.

### INTRODUCTION

Macroporous crosslinked copolymers based on glycidyl methacrylate (GMA) are very attractive for metal sorption from waste solutions as sorbents, due to the presence of epoxy groups that can easily be transformed into various functional groups [1]. Due to the seriousness of the pollution problem, the use of multidentate ligands attached to the polymers for the removal and regeneration of transition metals from aqueous waste streams is the objective of extensive scientific research [2]. Since the most transition metal ions are four or five coordinating in complexation with many ligands, it could be expected that multidentate ligands attached to polymers could have better complexing abilities in comparison to the other polymer ligands. The objective of this study was to produce a novel coordination polymer bearing different functional groups (in this case, amino, carboxyl and hydroxyl groups) with porous structure tunable by variation of reaction conditions and reaction mixture content.

### EXPERIMENTAL

Macroporous crosslinked copolymer pSGE (with 20 wt% of ethylene glycol dimethacrylate) was synthesized by suspension copolymerization in the presence of inert component [1]. Further, two-step functionalization of pSGE (particles with average diameter of 0.15–0.30 mm) was performed with consecutive reactions with EDA and EDTA. Firstly, pSGE (10.0 g), EDA (25.0 g) and toluene (250 ml) were mixed at 80 °C for 6 h. The sample (pSGM-eda) was filtered and washed with ethanol and dried at 40 °C. Then, the modified sample pSGE-eda (10.0 g), EDTA (45.0 g) and distilled water (375 ml) were stirred 80 °C for 6 h. The final sample (pSGM-eda-EDTA) was washed with ethanol and dried at 40 °C.

FTIR spectra were taken in ATR (attenuated total reflection) mode using a Nicolet 380 spectrometer with a Smart Orbit™ ATR attachment (wavenumber range 400–4000 cm<sup>-1</sup>, resolution 2 cm<sup>-1</sup>). The scanning electron microscopy analysis (SEM) was done on JEOL JSM-6460LV instrument. The samples were coated with gold in high-vacuum evaporator prior measurements. The pore size distributions of samples were determined by a high-pressure mercury intrusion porosimeter

Carlo Erba Porosimeter 2000 (Washington, USA, software Milestone 200). The elemental analysis (C, H and N content) of the samples was performed by using the Vario EL III device (GmbH Hanau Instruments, German). The content of amino and carboxyl groups in obtained functionalized copolymers was determined by acid-base titration [1,3]. The method of gradual change of pH value (drift method) was used to determine the point of zero charge ( $\text{pH}_{\text{PZC}}$ ) [1].

## RESULTS AND DISCUSSION

Figure 1 shows the FTIR spectra of copolymer and functionalized copolymers. In the FTIR spectrum of pSGE-eda, the absorption bands at  $3341\text{ cm}^{-1}$  (O-H and N-H stretching vibrations),  $1561\text{ cm}^{-1}$  and  $1641\text{ cm}^{-1}$  (N-H bending vibrations of primary and secondary amino groups) and  $756\text{ cm}^{-1}$  (N-H wagging vibrations) were observed [1]. For the pSGE-eda-EDTA, two new peaks at  $1405\text{ cm}^{-1}$  and  $1630\text{ cm}^{-1}$  appeared, corresponding to the C-N stretching vibrations and asymmetric stretching vibration of the C=O groups of amides [4,5]. These bands confirmed that pSGE copolymer was successfully functionalized with EDA and EDTA.

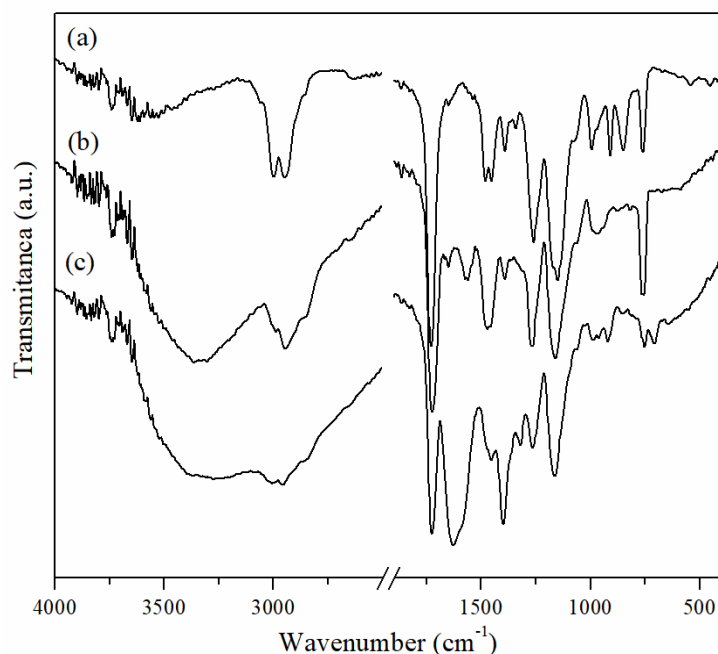


**Figure 1.** FTIR spectra of (a) pSGE, (b) pSGE-eda and (c) pSGE-eda-EDTA

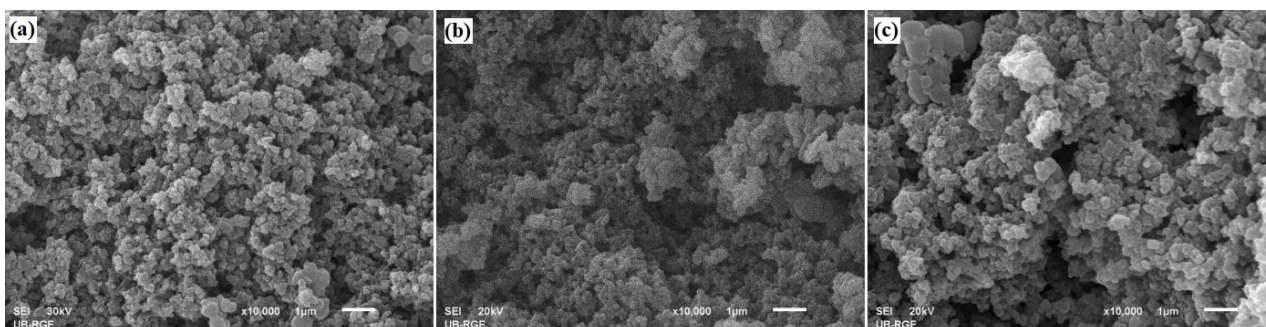
The values of specific pore volume ( $V_s$ ), specific surface area ( $S_{Hg}$ ) and pore diameter corresponding to the half of pore volume ( $d_{V/2}$ ) of pSGE, pSGE-eda and pSGE-eda-EDTA were determined from the cumulative pore volume distribution curves and presented in Table 1. The two-step functionalization leads to the sample pSGE-eda-EDTA with almost 1.5 times larger pore diameter and 60% reduction in  $S_{s,Hg}$  values compared to the initial, non-functionalized pSGE.

**Table 1.** Relevant porosity parameters of indicated samples.

Sample	$V_p$ ( $\text{cm}^3/\text{g}$ )	$S_{Hg}$ ( $\text{m}^2/\text{g}$ )	$d_{V2}$ (nm)
pSGE	1.20	44	204
pSGE-eda	0.95	37	253
pSGE-eda-EDTA	0.82	27	294

Figure 2 presents SEM micrographs of cross-section of the particle for selected copolymers. It can be noticed that all samples have a porous structure. A large number of clusters of congregated globules separated by channel-like cavities are clearly visible.

The results of the elemental analysis (Table 2) were used to verify the preparation of functionalized copolymers, as well as the calculated content of amino groups in pSGE-eda and pSGE-eda-EDTA.

**Figure 2.** SEM microphotographs of particle cross-section for (a) pSGE, (b) pSGE-eda and (c) pSGE-eda-EDTA (magnification 10000 $\times$ ).

The difference of nitrogen content and concentrations of amino groups obtained for pSGE-eda and pSGE-eda-EDTA, indicates the successful functionalization. Also, the value of carboxyl groups concentration for pSGE-eda-EDTA (4.2 mmol/g) confirms the introduction of EDTA onto pSGE-eda.

**Table 2.** Elemental analysis, amino ( $C_{AG}$ ) and carboxyl groups ( $C_{COOH}$ ) concentration of functionalized copolymers.

Sample	Found (%)			$C_{AG}^a$ (mmol/g)	$C_{AG}^b$ (mmol/g)	$C_{COOH}^b$ (mmol/g)
	C	H	N			
pSGE-eda	50.9	8.4	7.4	5.2	2.1	-
pSGE-eda-EDTA	45.6	7.6	7.8	5.6	1.8	4.2

<sup>a</sup> Calculated from the elemental analysis

<sup>b</sup> Obtained by acid-base titration

The  $\text{pH}_{\text{PZC}}$  values of pSGE-eda-EDTA were  $\sim 5.8$ , which is lower than those of pSGE ( $\sim 6.4$ ) and pSGE-eda ( $\sim 6.7$ ). These results could be a consequence of the functionalization, which introduced more amino and carboxyl groups on the surface of pSGE-eda-EDTA.

## CONCLUSION

In this study, a novel pSGE-eda-EDTA copolymer was successfully synthesized. FTIR and elemental analysis confirmed the introduction of EDTA onto pSGE-eda. The porosity of copolymers was proved by SEM analysis, while results of mercury porosimetry indicated the predominant presence of a macroporous structure in all three samples.

**Acknowledgement**

This work was financially supported by the Ministry of Education, Science and Technological Development of the Republic of Serbia (Grant No. 451-03-9/2021-14/200026).

**REFERENCES**

- [1] B.M. Marković, Z.M. Vuković, V.V. Spasojević, V.B. Kusigerski, V.B. Pavlović, A.E. Onjia, A.B. Nastasović, *Journal of Alloys and Compounds*, 2017, **705**, 38-50.
- [2] B.L.Rivas, B.F. Urbano, J. Sánchez, *Frontiers in Chemistry*, 2018, **6**, Article ID 320.
- [3] CY Wen, JY Sun, *ChemistrySelect*, 2017, **2**, 10885 – 10888.
- [4] M. Soleimani, M.G. Afshar, A. Sedghi, *International Scholarly Research Notices*, 2013, **2013**, Article ID 674289.
- [5] F. Zhao, E. Repo, D. Yin, L. Chen, S. Kalliola, J. Tang, E. Iakovleva, K.C. Tam, M. Sillanpää, *Scientific Reports*, 2017, **7**, Article ID 15811.

## THERMAL PROPERTIES OF POLYURETHANE-CLAY NANOCOMPOSITES

I. Stefanović<sup>1</sup>, J. Džunuzović<sup>1</sup>, B. Marković<sup>1</sup>, T. Tadić<sup>1</sup>, A. Nastasović<sup>1</sup>,  
E. Džunuzović<sup>2</sup> and C. Marega<sup>3</sup>

<sup>1</sup>University of Belgrade, Institute of Chemistry, Technology and Metallurgy,  
Njegoševa 12, 11000 Belgrade, Serbia. (ivan.stefanovic@ihtm.bg.ac.rs)

<sup>2</sup>University of Belgrade, Faculty of Technology and Metallurgy, Karnegijeva 4, 11120 Belgrade,  
Serbia.

<sup>3</sup>University of Padova, Department of Chemical Sciences, via Marzolo 1, 35131 Padova, Italy.

### ABSTRACT

Two samples of poly(urethane-siloxane) nanocomposites (PUNs), based on 4,4'-diphenylmethane diisocyanate (MDI) and 1,4-butanediol (BD) as the comonomers of the hard segments (HS) and  $\alpha,\omega$ -dihydroxyethoxy propyl poly(dimethylsiloxane) (EO-PDMS) as the part of the soft segments (SS), were prepared by *in situ* polymerization. HS content of the prepared PUN samples were 10 and 20 wt%. Organomodified montmorillonite clay (Cloisite 30B<sup>®</sup>) was used as nanofiller (1 wt%) for poly(urethane-siloxane)s. Prepared PUNs have good thermal stability, and they represent semicrystalline polymers.

### INTRODUCTION

Segmented polyurethanes (PUs) are polymers constructed of alternating flexible polyol parts that represent soft segments and rigid urethane parts which represent hard segments. By careful selection of diisocyanates, as well as polyols and chain extenders, it is possible to obtain PUs with a wide range of physical and chemical features that are quite important for a variety of applications [1]. Moreover, properties of PUs are also affected by the utilized composition of HS and SS, their chemical structure and obtained molecular weight. Although these PUs have significant number of advantages, it is still unsatisfactory when it comes to their heat resistance and thermal properties. In order to improve these properties, PUN can be prepared by using poly(dimethylsiloxane) (PDMS) as polyol and different clay nanoparticles as nanofillers [2].

### EXPERIMENTAL

Two samples of PUNs based on  $\alpha,\omega$ -dihydroxyethoxy propyl poly(dimethylsiloxane) (EO-PDMS) (ABCR,  $M_n = 1000$  g/mol) and organically modified montmorillonite clay (Cloisite 30B<sup>®</sup>), with different HS content (10 and 20 wt%, samples PUN10 and PUN20, respectively), were prepared by *in situ* two-step polyaddition reaction in THF/DMAc solution (1/1, v/v). In the first step, MDI, PDMS and delaminated clay were mixed in order to prepare -NCO-prepolymer with addition of catalyst dibutyltin dilaurate, and in the second step BD was added to the reaction mixture at 60 °C for 6 h. The PUN films were prepared by placing reaction mixtures in the Teflon<sup>®</sup> dishes, followed by their drying in air and vacuum oven for 24h at 50 °C and 24h at 40 °C, respectively.

The thermogravimetric analysis (TG) was carried out on a TA SDT 2960 instrument that was calibrated with Curie temperature standard materials (with well-known Curie temperatures) and melting point standards (Ni and Zn). The TG measurements were recorded under N<sub>2</sub> and air atmosphere, in the range from 25 to 700 °C and at a heating rate of 10 °C/min. Differential scanning calorimetry (DSC) was carried out on a Perkin-Elmer DSC6 thermal analyzer. The DSC measurements were performed under N<sub>2</sub> flow, using weighted samples (~5 mg) in Al pans and in the temperature range from -20 to 220 °C, at a heating and cooling rate of 10 °C/min.

## RESULTS AND DISCUSSION

The thermal stability of the prepared PUNs was investigated by TG analysis under nitrogen and air atmosphere. The obtained TG and derivative TG (DTG) curves are shown in Figure 1, while characteristic degradation temperatures are listed in Table 1.

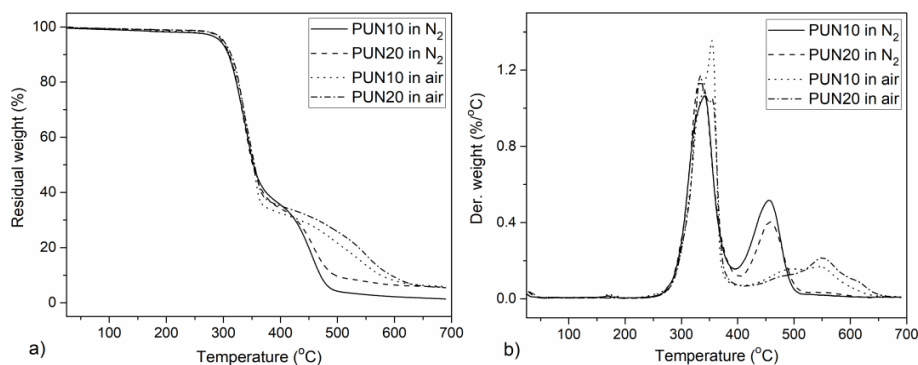


**Figure 1.** a) TG and b) DTG curves of the prepared PUNs in nitrogen and air atmosphere.

From the obtained TG results, thermal degradation of the PUN10 starts after 294 and 295 °C, in nitrogen and air atmosphere, respectively.  $T_{10\%}$  values were 309 °C for PUN10 and 311 °C for PUN20 in nitrogen, and 311 °C for PUN10 and 314 °C for PUN20 in air atmosphere. From these results, it is concluded that PUNs exhibit slightly greater thermal stability in air than in a nitrogen atmosphere. Moreover, sample with higher content of HS exhibit greater thermal stability. According to the DTG curves (Figure 1b), thermal degradation occurs as a three- or four-step process in nitrogen and air atmosphere, respectively. In the first step, in the range from 332 to 341 °C and from 354 to 355 °C in nitrogen and air atmosphere, respectively, the urethane bonds start to decompose. In the second step, in the range from 457 to 458 °C and from 483 to 493 °C in nitrogen and air atmosphere, respectively, ether bonds inside PDMS start to break down. In the third step, the decomposition of the aromatic rings occurred in the range from 553 to 557 °C and from 547 to 549 °C in nitrogen and air atmosphere, respectively [3]. Degradation of the PUNs in the air atmosphere is more complex due to the one more additional peak-shoulder at ~ 600 °C, which originates from oxidation of the PDMS and creation of complex silicate structures.

**Table 1.** TG results of the prepared PUNs in nitrogen and air atmosphere.

Sample	$T_{5\%}$ (°C)	$T_{10\%}$ (°C)	$T_{50\%}$ (°C)	$T_{90\%}$ (°C)	DTG <sub>max</sub> (°C)
PUN10 <sup>a)</sup>	294	309	353	470	341/457/553
PUN20 <sup>a)</sup>	298	311	351	495	332/458/557
PUN10 <sup>b)</sup>	295	311	353	576	354/493/547/603
PUN20 <sup>b)</sup>	301	314	355	594	355/483/549/604

a) Recorded under nitrogen atmosphere

b) Recorded under air atmosphere

In order to investigate thermal properties of the prepared PUNs, differential scanning calorimetry (DSC) was performed. The obtained DSC curves are shown in Figure 2. The glass transition ( $T_g$ ), melting ( $T_m$ ) and crystallization ( $T_c$ ) temperatures, as well as the enthalpy of melting ( $\Delta H_m$ ) and crystallization ( $\Delta H_c$ ), were determined and summarized in Table 2.

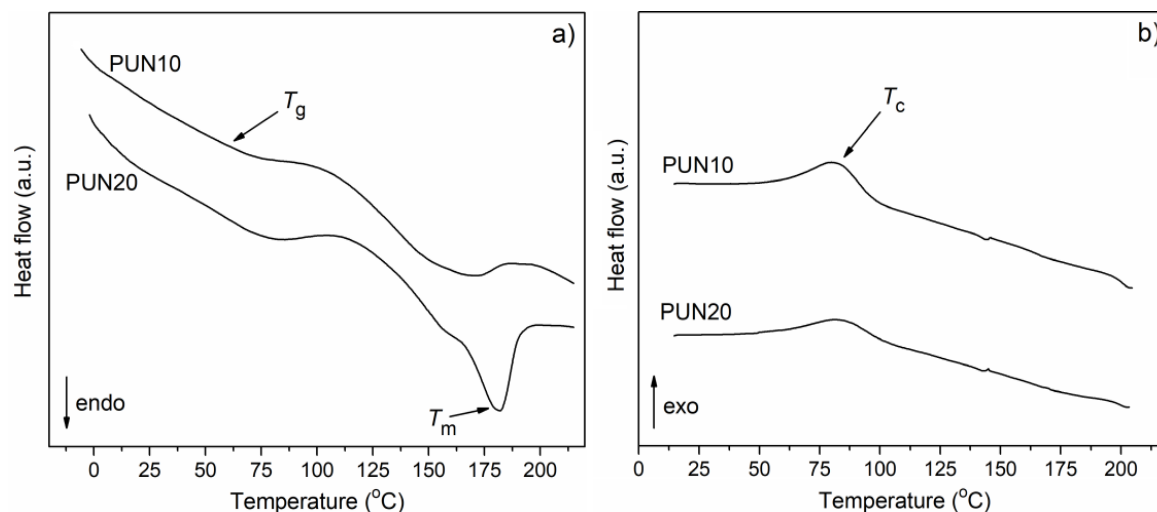


**Figure 2.** DSC curves of the prepared PUNs recorded during a) the second heating and b) cooling run.

DSC curves of PUNs have only one peak which appeared during the heating and cooling run, corresponding to the melting and crystallization, respectively, of the HS (MDI-BD). Also, PUNs have one  $T_g$  that belongs to the HS and obtained  $T_g$  values are higher than values reported for the neat copolymer, resulting from the addition of clay nanoparticles [3]. According to the results presented in Table 2, all values, except  $\Delta H_c$ , increased with increasing HS content in the prepared PUNs. This was caused by better ordering of the hard domains which are formed from the longer MDI-BD units. The crystallinity degrees ( $X_c$  and  $X_{cHS}$ ) were calculated based on the group contribution method [4]. Total crystallinity degrees ( $X_c$ ) are lower than theoretical values, which indicates that these HS could not crystallize completely, partly because of the addition of clay nanoparticles and partly due to the incorporation of HS into the amorphous phase.

**Table 2.** DSC results (glass transition ( $T_g$ ), melting ( $T_m$ ) and crystallization ( $T_c$ ) temperatures, the enthalpy of melting ( $\Delta H_m$ ) and crystallization ( $\Delta H_c$ ), total crystallinity degree ( $X_c$ ) and crystallinity degree of the HS ( $X_{cHS}$ )) of the prepared PUNs.

Sample	$T_g$ (°C)	$T_m$ (°C)	$T_c$ (°C)	$\Delta H_m$ (J/g)	$\Delta H_c$ (J/g)	$X_c$ (%)	$X_{cHS}$ (%)
PUN10	41.4	162.9	82.8	3.54	2.46	3.88	17.81
PUN20	54.1	181.4	84.3	10.20	1.99	11.18	30.47

## CONCLUSION

Two PUN samples with different HS content, based on MDI, PDMS, BD and clay Cloisite 30B<sup>®</sup>, were successfully prepared. TG analysis showed that these PUNs have good thermal stability, while DSC analysis showed that they are semicrystalline polymers.

## Acknowledgement

This work was financially supported by the Ministry of Education, Science and Technological Development of the Republic of Serbia (Grants No. 451-03-9/2021-14/200026).

**REFERENCES**

- [1] I. Stefanović, M. Špírková, S. Ostojčić, P. Stefanov, V. Pavlović, M. Pergal, *Applied Clay Science*, 2017, **149**, 136–146.
- [2] S. Taheri, G.M.M. Sadeghi, *Applied Clay Science* 2015, **114**, 430–439.
- [3] M.V. Pergal, I.S. Stefanović, D. Gođevac, V.V. Antić, V. Milačić, S. Ostojčić, J. Rogan, J. Djonlagić, *Journal of the Serbian Chemical Society*, 2014, **79**, 843–866.
- [4] D.W Van Krevelen, *Properties of Polymers*, Amsterdam: Elsevier, 1990.

## INVESTIGATION OF SORPTION BEHAVIOUR OF Cu(II) AND Pb(II) ONTO A NOVEL EDTA MODIFIED COPOLYMER

T. T. Tadić<sup>1</sup>, B. M. Marković<sup>1</sup>, I. S. Stefanović<sup>1</sup>, J. V. Džunuzović<sup>1</sup>,  
Z. P. Sandić<sup>2</sup>, Lj. T. Suručić<sup>3</sup> and A. E. Onjia<sup>4</sup>

<sup>1</sup> University of Belgrade - Institute of Chemistry, Technology and Metallurgy, Njegoševa 12, 11000 Belgrade, Republic of Serbia (tamara.tadic@ihtm.bg.ac.rs)

<sup>2</sup> University of Banja Luka, Faculty of Natural Science and Mathematics, Mladena Stojanovića 2, Banja Luka, Republic of Srpska, B&H

<sup>3</sup> University of Banja Luka, Faculty of Medicine, Save Mrkalja 14, Banja Luka, Republic of Srpska, B&H

<sup>4</sup> University of Belgrade, Faculty of Technology and Metallurgy, Karnegijeva 4, Belgrade, Republic of Serbia

### ABSTRACT

A new metal-chelating glycidyl methacrylate based macroporous copolymer with ethylenediaminetetraacetic acid functions was tested as a potential Cu(II) and Pb(II) ions sorbent from aqueous solutions. The sorption was studied in non-competitive batch experiments, by varying initial pH and metal concentration, contact time and temperature. Pseudo-first and pseudo-second order model, as well as Bangham, intra-particle and liquid film diffusion models were used to determine the nature of sorption kinetics and the rate of limiting step. Equilibrium sorption data were analyzed with Langmuir, Freundlich, Temkin and Elovich isotherm models.

### INTRODUCTION

Lead and copper are the common heavy metal ions discharged from electroplating industries and battery manufacturing [1]. Polymer-based Cu(II) and Pb(II) sorbents are good alternative in comparison to clays, activated carbon and biosorbents, due to their large surface area, appropriate particle size distribution, chemical and mechanical strength [3]. As known, EDTA forms stable chelates with metal ions via metal-oxygen carboxylate and metal-nitrogen bonds [4]. The purpose of this study was to investigate possible synergetic effect of incorporation of multidentate ligand into macroporous polymer and adjustable porous structure on the sorption of Cu(II) and Zn(II) from single aqueous solutions.

### EXPERIMENTAL

Sorption of Cu(II) and Pb(II) onto chelating sorbent was carried out in non-competitive batch conditions with a dose of sorbent of 10 g/L. The effect of initial pH (1 – 5), temperature (298 – 343 K), contact time (0 – 180 min) and initial metal concentration (0,0005 – 0,15 mol/dm<sup>3</sup>) was studied. For pH adjustment, 1 mol/dm<sup>3</sup> HCl and 1 mol/dm<sup>3</sup> NaOH solutions were used. At the predetermined time intervals sample aliquots were withdrawn, and analyzed with ICP-OES (Perkin Elmer, Model ICP 400). All experiments were repeated in triplicate or more if necessary.

### RESULTS AND DISCUSSION

Figure 1 and 2 summarize the influence of initial pH and concentration, contact time and temperature on the Cu(II) and Pb(II) ions sorption. For all investigated sorption parameters, considerably higher affinity of sorbent towards Pb(II) than Cu(II) was observed. These results are a consequence of the Pb(II) smaller hydrated radius.

As seen from Figure 1a, both Cu(II) and Pb(II) sorption capacities are strongly dependent on the pH value with the maximum  $Q_t$  values at pH 4 and pH 5 for Cu(II) and Pb(II), respectively. The  $Q_t-t$  (Figure 1b) dependence for Pb(II) clearly shows two stages of the sorption process. Up to 30 minutes, a rapid  $Q_t$  increase was observed, followed by a gradually increase up to ca. 1350 mg/g after 30 minutes. On the otherside, Cu(II) sorption capacity gradually increased, reaching equilibrium value of ca. 450 mg/g after 30 minutes.

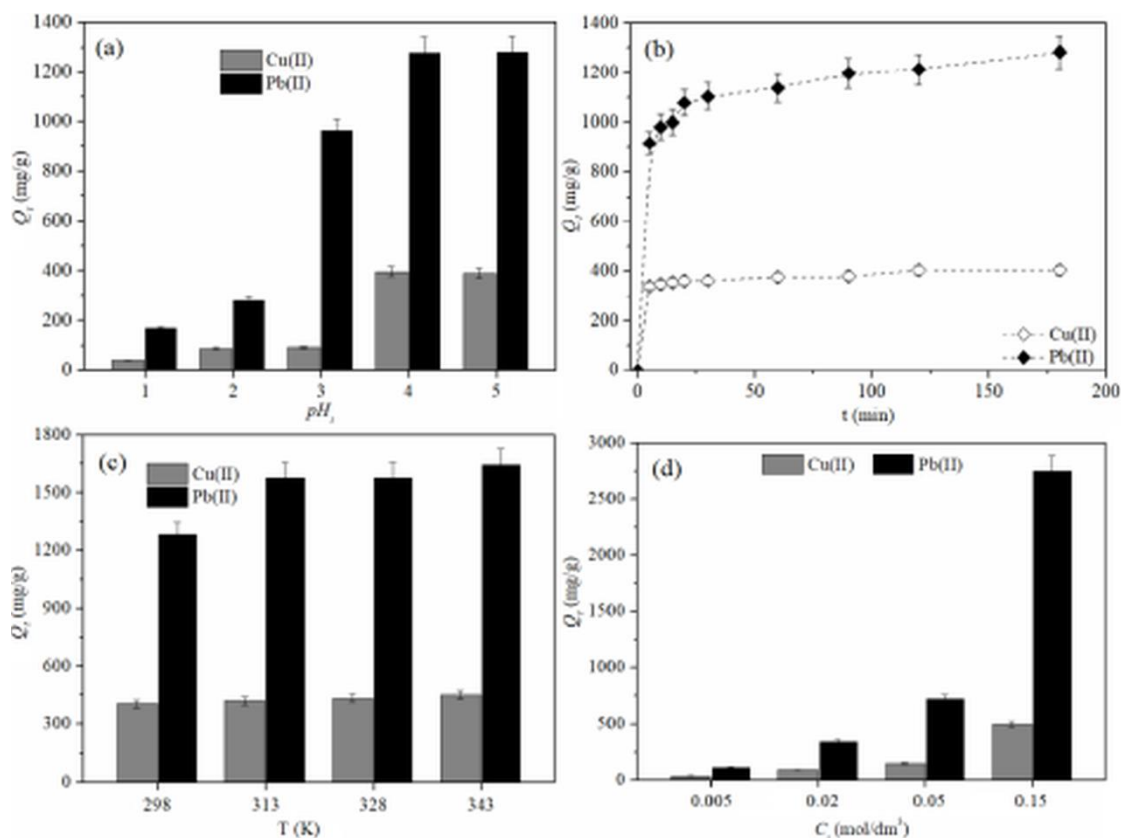


**Figure 1.** Effect of (a) initial pH, (b) contact time, (c) temperature and (d) initial concentration on the sorption capacity of Pb(II) and Cu(II)

On the otherside, Cu(II) sorption capacity gradually increased, reaching equilibrium value of ca. 450 mg/g after 30 minutes. It was observed (Figure 1c) that the capacity of sorption increased slightly along with the increasing temperature. The sorption capacity also increased with increasing the initial metal concentration (Figure 1d). The observed behavior can be attributed to the increase in the number of metal ions to the fixed quantity of adsorbents used in this study.

For analysis of the kinetic data, pseudo-first order model, pseudo-second order model, as well as Bangham, intra-particle and liquid film diffusion model were used [4]. The results are presented in Table 1. The highest correlation coefficient ( $R^2 > 0.99$ ) and the  $Q_e^{\text{calc}}$  value (400 and 1282 mg/g) approximating to  $Q_e^{\text{exp}}$  (405 and 1284 mg/g), indicate the pseudo-second order model is the best fit for Cu(II) and Pb(II) sorption. Also, the high  $R^2$  values ( $> 0.9$ ) for intra-particle diffusion and liquid film diffusion model suggest the simultaneous influence of pore and film diffusion. This was

expected, since chelating sorbent has a high value of pore diameter corresponding to the half of pore volume ( $d_{V/2} = 294$  nm).

**Table 1.** Kinetic parameters for Cu(II) and Pb(II) sorption onto chelating sorbent

	Cu(II)	Pb(II)
$Q^{\text{exp}}$ (mg/g)	405	1284
Pseudo-first order model		
$k_1 \cdot 10^2$ (1/min)	1.49	1.375
$Q_e^{\text{calc}}$ (mg/g)	84.58	323.35
$R^2$	0.961	0.944
Pseudo-second order model		
$k_2 \cdot 10^3$ (g/mg min)	0.07	0.17
$Q_e^{\text{calc}}$ (mg/g)	400	1282
$R^2$	0.999	0.998
Bangham diffusion model		
$\alpha$	0.09	0.15
$k_B \cdot 10^3$ (g/mg min)	1.78	1.69
$R^2$	0.952	0.979
Intra-particle diffusion model		
$k_{1id}$ , (mg/g min <sup>0.5</sup> )	10.12	67.75
$C_{1id} \cdot 10^2$ (mg/g)	302.36	762.53
$R^2$	0.995	0.942
$k_{2id}$ (mg/(g min <sup>0.5</sup> ))	6.851	22.32
$C_{2id}$ (mg/g)	314.14	978.60
$R^2$	0.983	0.988
Liquid film diffusion model		
$k_{fd}$ , (1/min)	0.02	0.01
$C_{fd}$ ,	-1.57	-1.38
$R^2$	0.962	0.944

**Table 2.** Isotherm parameters for Cu(II) and Pb(II) sorption

	Cu (II)	Pb(II)
Langmuir isotherm model		
$Q_{\text{max}}$ (mg/g)	1011	5000
$K_L \cdot 10^4$ (L/mg)	2.65	3.07
$R^2$	0.864	0.977
Freundlich isotherm model		
$K_F$ (L <sup>n</sup> mg <sup>1-n</sup> /g)	0.94	32.36
$N$	1.31	1.28
$R^2$	0.998	0.997
Temkin isotherm model		
$K_T \cdot 10^3$ (L/mg)	6.88	10.13
$b_T$ , (kJ/mol)	17.95	3.80
$R^2$	0.876	0.879
Elovich isotherm model		
$K_E$ (L/mg)	0.99	1.00
$Q_{mE}$ (mg/g)	667	3135
$R^2$	0.816	0.970

In this study, Langmuir, Freundlich, Temkin and Elovich isotherm models were used for equilibrium data analysis. The results are shown in Table 2. According to the high  $R^2$  values (>0.99), the Freundlich model provided a better fit than the other used models. These results suggested that reversible sorption played a significant role in the Cu(II) and Pb(II) sorption process.

## CONCLUSION

The sorption behavior of Cu(II) and Pb(II) onto chelating sorbent was investigated from aqueous solution. All the investigated sorption parameters have more pronounced effect on Pb(II) than Cu(II) sorption. The sorption of both metal ions followed the pseudo-second order kinetic model, with unambiguous influence of pore and film diffusion. Equilibrium data fitted best with Freundlich isotherm model.

## Acknowledgement

This work was financially supported by the Ministry of Education, Science and Technological Development of the Republic of Serbia (Grant No. 451-03-9/2021-14/200026 and 451-03-9/2021-14/200135).

**REFERENCES**

- [1] W. Zhan, C. Xu, G. Qian, G. Huang, X. Tang, B. Lin, *RSC Advances*, 2018, **8**, 18723-18733.
- [2] G. Zhao, X. Wu, X. Tan, X. Wang, *The Open Colloid Science Journal*, 2010, **4**, 19-31.
- [3] A. Mehdinia, M. Salamat, A. Jabbari, *Scientific Reports*, 2020, **10**, Article ID 3279.
- [4] I. Jilal, S. El Barkany, Z. Bahari, O. Sundman, A. El Idrissi, Mohamed Abou-Salama, A. Romane, C. Zannagui, H. Amhamdi, *Carbohydrate Polymers*, 2018, **180**, 156–167.

## POLYMER-SACCHARIDE CONJUGATES

### I. THERMODYNAMICS OF TREHALOSE- LIVING CELL MEMBRANE INTERACTIONS

M.M. Plavsić<sup>1,2</sup>, D.S. Savić<sup>1</sup>, S.A.Žerajić<sup>1</sup>, Lj. B. Nikolić<sup>1</sup>

<sup>1</sup> *University of Niš, Faculty of Technology, Bulevar Oslobođenja 124, Leskovac,* <sup>2</sup>*The Academy for High Technical Education, Belgrade (milankaplav@gmail.com)*

#### ABSTRACT

This is the first in a series of papers, on unusual properties and high structural complexity of systems, based on conjugations of disaccharides with different polymeric entities, all been missed for a long time. Here we present interaction analyzes of trehalose, as living cell heat- and desiccation-protectant, in parallel with comparable features of trehalose 6-phosphate, and pullulan. Modeling and computer simulations, based on both main approaches- experimental, from yeast cell lines, and - theoretical, from thermodynamics, statistical mechanics and quantum-mechanics foundations of modern physical chemistry, are presented. Here, at the start for the series, focus will be mainly on supramolecular structures of such systems.

#### INTRODUCTION

Interest for supramolecular polymer systems (SUPLS) has grown highly last years, both in fundamental and application areas: [I,1-5]. Nowadays the investigations are induced also by the pandemic problems, but the synergetic cooperation and developments of polymer science, microbiology, molecular biology and biophysical chemistry in that direction, were proposed already by Linus Pauling, exactly 70 years ago:[I,6]. Interestingly, the incentive in both periods, the one of early ideas emerging, and nowadays fast development, are related to virus issues, and vaccines: [I,1-3.6], but the promising results extend to much broader areas: *nano*-technology and materials science, biology and bio-medicine, bio-engineering and pharmacy, etc.: [I,1-10]. Of course, the number of basic principles had been already established considering complex RNA-systems, but the way from heuristic discovering at the very start, to nowadays accepted theoretical principles, has been long lasting, hard process, with lot of diversity: [I, 7]. Last forty years, the efforts have been fruitfully extended to protein-systems, than DNA-systems, and much later to synthetic approaches of modern Systemic Chemistry: [I,8]. But, the third main group of biopolymers, polysaccharides, had been waiting asides, very long time, to enter the field. It is surprising, because some of them are the most abundant biopolymers on Earth, and some request much simpler chemistry and morphology elaboration, than the chains of previous types. Moreover, polysaccharide in combination with some disaccharides (e.g. trehalose) into SUPLS, have very interesting thermal and diffusive features, convenient for industry: [I,8-10,III,1]. But, there is an additional, important, aspect: some of mentioned SUPLS, e.g. those with trehalose, have very interesting, quite unusual, even paradoxical and astonishing features! First data on trehalose appeared already in 1832 (Wiggers), but Berthelot, (who was than the leading person in both, catalysis and biochemistry), was the one who isolated it from trehala (the product of wheat plants) and gave it the name, and no wonder, that pretty soon after, appeared the first publications on enzymatic processes dealing with trehalose (TRH) in yeast cells. But, the interest for it and its derivate (e.g. trehalose 6-phosphate (TH-6P)) decreased in the long period after, due to the long lasting opinion in bio-medical sciences, that such saccharides serve only as food storage reserve, and as some adjuncts for connective tissues. But in 1970s become clear that yeast cells produce under stress significant amount of TRH, to survive under heat-, cold-, osmosis- and desiccation- stresses: [I,7]. In parallel become clear that TH-6P has high influence upon the

growth and development of plants, and serves as essential signal metabolite in plants, rivaling any other signaling molecule including major phytohormones: [I,7]. Moreover, TRH has been found as the protectant in anhydrobiotes of very different kind, some even belonging to different biological kingdoms. But just the reverse hierarchy of disaccharide influences was also found e.g. some other (e.g. sucrose, or pullulan segment-mers) have similar protective functions as trehalose, (but with much less efficiency), all of them to the same cell (strain): [I,9,10]. But, surprisingly, TH-6P, supposed to be closest of the species to TRH, has no such abilities [I,10]. How to explain such discrepancies? There is a number of independent theories, from different scientific fields, (microbiology, chemistry, molecular biology) but neither can explain all phenomena (observed by different approaches, from those different sciences). In our opinion, the reason for all of that, is the existence of some other component (or components and factors) been conjugated with TRH into some type of fine detailed supramolecular structures of the cells!?

## METHODS

To confirm assumptions from the Introduction, and contribute in resolving important issues of cell surviving under severe stress conditions, we performed both, experimental and theoretical investigations of yeast components performances, which are able to participate in chemical and physical changes during dehydration of the cell, and in parallel, monitor, heating, cooling and diffusion effects on them, to extract corresponding structures, as candidates for SUPLS, been supposed in Introduction. The importance of cell membrane as a barrier to environmental stresses is well known and accepted, so obviously it should be the starting point for studying influences described. But both, complexity of membrane structure and changes, and also specificity of SUPLS formation, indicate needs for a factorization of interactions involved, to recognize the main players. The extensive pull of data on cell membrane structure and new results on SUPLS self-assembling, provide possibilities for preliminary computer simulations of possible interactions, depending on topology, and principles of thermodynamics and quantum mechanics. Using that, we have investigated dominant interactions of corresponding components in vitro, by spectroscopic methods (FTIR, UV etc.) and then in vivo, estimated survival of cells under predicted resulting conditions. Then, we have returned to computer calculation for fine tuning details of interactions, been hard, of still impossible to detect experimentally, under present conditions so, to model them with Auto Dock, Vine, DSV-studio-visualization etc., and obtain a comprehensive view of the process. The results are to be presented in systematic series of papers- this one is the first of them. But, preliminary results indicate that this first step had already to be splatted into two subparts (a) the analyses of TRH interactions with membrane phospholipids (PHL) (b) the interactions of TRH with membrane enzymes of high vital importance.

## RESULTS AND DISCUSSION

From the numerous phenomena observed in THR- membrane interactions described previously, as those of most obvious structural selectivity and sensitivity but, also most convenient for first system simulation, we have chosen, for the start to analyze the differences of TRH and TH-6P, in interactions with membrane PHL. Constitutional similarity: both, between THR and TH-6P, and also similarity of TH-6P and PHL active groups, would indicate the highest compatibility, and following protective ability, as described previously, of TH-6P with PHL and the yeast cell as the whole. But, Experimental results show just the opposite relations. Why? Three main reasons could be supposed: (a) there are some steric hindrances that are in control of those interactions, but TRH is free of them, in some way (b) there exist some constellation of interactions of three, (not two type members) controlling the system, so the third, hindered one, has a selectivity and power, to control the system (c) There are some very fine, SUPS features but selective enough, to give TRH, as a part of SUPS, a priority over

other disaccharides, in some way. To find the right direction for investigations that follow in Parts II and III, among the possible interactions mentioned, we calculated dimer energy maps of Flory's type: [I,12], for THR and TH-6P (presented in Part III in detail) analyzing possible conformations, to be than fitted into disaccharide - membrane PHL modeling by docking simulations and calculation interaction energies of TRH-PHL pairs. Energies obtained are used for formulation of partition function:  $Z = \sum \exp(-\beta \mu \cdot \mathbf{n}_{TRH}) (N_{PHL})^{n_{TRH}} [\exp(-\beta E_{int} \cdot \mathbf{n}_{TRH})]$  of Einstein-Debye type for regular lattices: [I,11,12] and in combination with Flory-Huggins lattice-model [I,11,12],  $\Delta \mu / RT = \ln \Phi_{TRH} + (1-y^{-1})(1-\Phi_{TRH}) + \chi(1-\Phi_{TRH})^2$ , to estimate differences of sorbent activity  $ASR = \exp(\Delta \mu / RT)$ . The results of calculations indicate that TRH changes conformation as it approaches PHL layer. It interacts with lipid head-group, so its O-no.2 and O-no.3(or O-no.3 and O-no.4) atoms align and build hydrogen bonds with PHL phosphate groups and O-no.6 is the most mobile one, but mostly inactive, according to CHARM dynamics simulations. It may explain both: why no.6-site of TRH usually does not interact with lipid head-groups, and why TH-6H cannot at all. (Because of hindrances at ring-6-position TH-6H cannot align other hydroxyl groups, and interact with lipids in a way as it THR does, in its favorable position). But, more general conclusions require analysis of other membrane vital interactions, e.g. of some enzymes with THR, which may change their structure and activity during desiccation of yeast, what will be, as comprehensive activity, analyzed in detail, and presented as **SUMMARY CONCLUSIONS** in Part III.

**REFERENCES** (of the Part I, have notations [I,1] for Part II : [II,1], etc.)

- [I,1] B. G-C. Andersson,...J.Valezuela, *Nature Com.* 2021 v.467, 230--241.
- [I,2] P. Pender, ...C.Bock, E. Tomazou, *NatureCom.* 2021, 467, 445-461.
- [I,3] V. Leung,..C.Filipe, *Nature* 2019, 598, 440-451
- [I,4] D. Corradini,...H.E. Stanley, *Nature* 2013, 218, 1038-1047
- [I,5] P. Abudula,...S. Bencherif, *Frontiers in Chem.*2020, 6, 816-827
- [I,6] L Pauling, R. Corey, H. Branson, *Proc. Nat .Acad. Sci. USA*, 37, 205-211
- [I,7] B.. Alberts,...J. D. Watson, *Molecular Biology of the Cell*, Taylor & Francis N.Y 1994
- [I,8] Venetian Commission EU, *Compilations of Venice Commission and reports concerning development of Systemic Chemistry* 2006.
- [I,9] A. D. Elbein,...D. Carroil, *Glycobiology* 2003, 13, 17R-27R.
- [I,10] T. Hottiger,...A. Wiemken, *Eur. J. Biochem*1994, 219, 187-193.
- [I,11] S.F. Sun, *Physical Chemistry of Macromolecules*, Wiley, N.Y. 2004.
- [I,12] P.J. Flory, *Statistical Mechanics of Chain Molecules*, 2.Ed. Hanser, Vienna, 1989.

**POLYMER-SACCHARIDE CONJUGATES**  
**II. HEAT AND MASS TRANSFER THROUGH COATING-CELL MEMBRANES OF**  
**PULLULAN FIBERS, SUPPORTED BY TREHALOSE AND POSSIBLE APPLICATIONS**  
**IN VACCINE PRODUCTION**

M.M. Plavšić<sup>1,2</sup>, D.S. Savic<sup>1</sup>, D.M. Đorđević<sup>1</sup>, M.B. Plavšić<sup>3</sup>

<sup>1</sup>University of Niš, Faculty of Technology, Bulevar Oslobođenja 124, Leskovac, <sup>2</sup>Academy of High Technical Studies, Belgrade (milankaplav@gmail.com) <sup>3</sup>Belgrade University TMF

**ABSTRACT**

The results obtained in Part I indicate that for excellent cell protective effects obtained by trehalose, are required contributions of some additional substances involved in a kind of supramolecular structure with it, what has been proposed also by other authors, but what that can be, is unknown. To contribute solving the problem, we consider here possible role of pullulan, also used for protection by some fungi, but in completely different way.

**INTRODUCTION**

In the previous paper of this series (with the same main title and assigned as Part I) we have considered some unusual impacts of disaccharides, in particular trehalose (TRH) upon cell membranes, (providing to them heat- cold- and desiccation-protection e.g. for yeast cells). We made some comparisons of these phenomena to nowadays known behavior, of supra- molecular systems (SUPS), trying to relate such interesting properties to some theoretical explanations, or at least to contribute to its rational interpretations, because of the diversities, still present in the opinion about such problems. Here we consider polysaccharides, e.g. pullulan (PLU), the polymer of very similar local structure to TRH, which is also used by some of the microorganism for the same purpose as it, but the way they apply it to protect themselves, is very different of that applied with TRH. Obviously, heat-, oxygen dissolution(OD)-, desiccation- protection, are important for all living beings, especially now in focus, due to climate changes and lack of drinking water in some part of the world. So the issues are very general, and the field they belong, i.e. heat and mass transport phenomena is nowadays the part of fundamental engineering education worldwide:[I,8,III, 1-4]. But, the research related to bio-systems, seems at present, to be mainly focused on micro- and nano- details of cell structure, with a silent aspect of the approach that standard engineering methods are here of low, or no use. On the other hand, just this year, pandemic raised issues about thermal condition (deep cold chain at -80°C, or -20°C or refrigerator conditions at -4°C, or contra: T=+40°C, for a number of SUPS, or even varying temperatures for just one, the same system, in medical use : [I,1-3,III,1-4]. In short, effective values of heat conduction coefficient  $\lambda_{EF}$ , through polymer materials can be described as a sum of contribution of conduction in solid phase ( $\lambda_{CS}$ ), conduction in a fluid phase(gas or liquid in pores) ( $\lambda_{FL}$ ),and radiation through pores ( $\lambda_{RAD}$ ) [III,3] so,  $\lambda_{EF} = (\lambda_{CS} + \lambda_{FL} + \lambda_{RAD})$ . It warns us immediately, on importance of scaling considerations to determine which mechanism is in control in given situation: [III,4]. The system density is one of the benchmarks, as criteria used for the first help. But with polymer membranes, the situation is more complicated. The dimensional anisotropy, i.e. very high ratio of surface to thickness sizes, provides for such thin layers proportionality between eff. conductivity and **porosity**:  $\lambda_{EF} \sim \Phi$ , in the first approximation. So as the optimal solution nowadays, seems to be fibrillar structure of the membrane. It provides variation in layer porosity, what further provides variation of  $\lambda_{CG}$  coefficient dominating than transmission phenomena, together with effective diffusion coefficient  $D_{ef}$  For example, we know nowadays, that some microorganisms produce coating layers of micro-fibril structure, coating themselves, with fibers, organized in

addition, in some kind of textures and/or networks over cell membranes. In that way, the fiber structure could provide in parallel with mechanical protection, the control of the layer porosity and conductivity of mass and heat, as well. Such layers have been discovered at *Aureobasidium pullulans* (AUBPU) by Bernier 1958, with its structure further elaborated by Bender 1959: [III,1]. The PLU is linear polymer of maltotriose units, connected by  $\alpha(1\rightarrow4)$  glycosidic bond, whereas consecutive maltotriose units are connected to each other by  $\alpha(1\rightarrow6)$  glycosidic linkages. Later were discovered more than ten microorganisms producing  $\beta$ -glucans as only exocellular product: [III,1]. The structure morphology of all of them is rather complex, especially in formation pullulan fiber structures around the cell, but AUBPU is most successful in formation of fibrous layers coating itself, for the protection, as mentioned. It is the only one, used nowadays for commercial production of PLU (as food protectant and additive, pharmaceutical and cosmetic component, etc.) and most studied, of all of them, by far. Still, there is no accepted model for PLU-way of cell protection, although the interest for better understanding principles of membrane coating by polysaccharides, both fundamentally and applicative, grows fast. Here we propose a simple model for approximate evaluation of heat- and mass- transport parameters through PLU-fiber layers, coating a cell membrane.

**METHODS**

As a starting point of the model, we use well known, and broadly accepted, design methods for polymer fiber waving structures of macro- fabrics, and investigate possible analogy with micro structures, scaling step by step, the fiber size, structure, and corresponding change in properties from macro-size: [III,3] to micro-fibrillar level:[III,1], presented schematically in Fig.1.

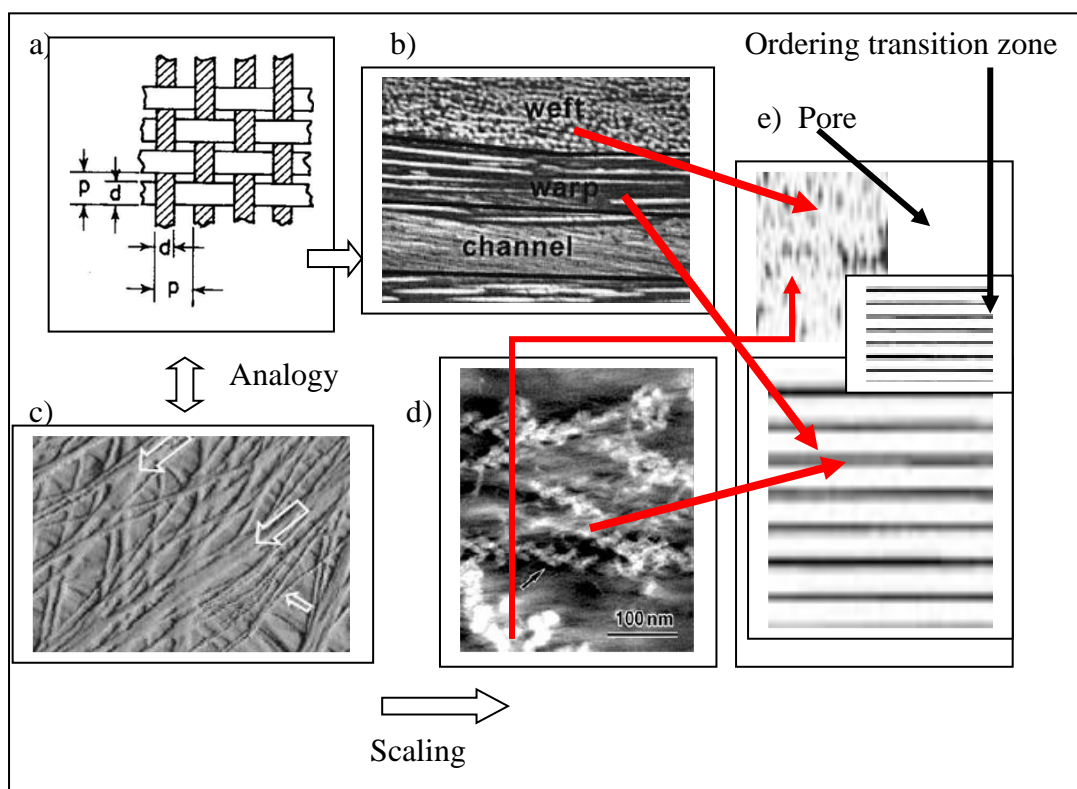


**Figure.1.** The analogy between structures of macro-fiber constructions of textile fabrics and micro fibrillar pullulan structures at cell walls

In Fig.1(a) is presented common textile, two shuttle weave macro layer, and in (b) corresponding fibrillar micro-structure, with layers oriented in two directions. In (c) is represented micro structure of PLU-layer with micro-fibers approximately also oriented in two directions, and in d) the cross-cut of PLU cell- membrane covering layer, with some longitudinally and some transversally oriented fibrils relative to the cutting plane. In (e) is schematic representation valid for both structures, with main geometry parameters, and a number of simplifications, but useful for the further analyses.

Obviously, the fiber organization into tow- or warp- or bundle- structures and their relative orientation, ordering and packing into higher level structures of layers for different purposes in nature and industry are complex process but, here is in focus just the free space between the fibers important for both, heat eff. conductivity and porosity. But, the main parameter for quantification the process here is permeability- $\kappa_f$  of the layer as the proportionality factor between the instant flux through porous medium  $q_{FL}$  and pressure drop  $\Delta p$ , as described by Darcy, and later extended by Navies and Stocks, long before Transport Phenomena as the science was established. According to Darcy's law  $q = -(\kappa/\eta)\nabla p$ , where  $\eta$  is dynamic viscosity. Later, the theory has been extended in several directions, using advances in both, in physics and engineering of the transport phenomena, because the permeability depends fundamentally on porosity  $\Phi$  of the fibrous layer, which depends further on the fiber order parameter  $L_{FB}$  of the system, which is function of the space distribution of (rigid) segments of fiber macromolecules (e.g. pulullane-maltotrioses in terms of Kuhn theory): [I,11-12] So, the system description is obtained by Legendre series:  $N(\theta) = \sum(n+1/2)[\langle L_{FB} \rangle][\langle L_{FB}(\cos\theta) \rangle]$ . But, it can be significantly simplified for fiber bundles, due to their cylindrical symmetry. So, as a practical measure of fiber layer order:  $\langle L_{FB}(\cos\theta) \rangle = (1/2)(3 \cos^2 \theta - 1)$ .

## RESULTS AND DISCUSSION

To quantify evaluation of PLU desiccation protective ability is necessarily to estimate its porosity, permeability and their interdependence, but in last 200 years no such analytical relation is found in general form, in spite of efforts, because of versatility of possible layer structures. But for particular geometries it is possible, so we made a model relating  $\kappa$ - $\Phi$ , and even  $L$ , for fibril-layer structure in the form:  $\kappa_f = [(2L + 1) \Phi^3] / (3 c \xi^2)$  where  $c$  is the constant from Kozeny theory, and  $\xi$  is ratio of pore surface to their volume. Using PUL-data for layer change with air humidity, (RH: 70%-->0%) [III, 6], than  $\kappa$  change from  $\kappa_e = 258 \text{ mL } \mu\text{m m}^{-2} (24 \text{ h}) \text{ atm}^{-1}$  to 1.43 (same-dimens.) for the layer thickness normalised to 1  $\mu\text{m}$ , we obtain high change in porosity:  $\Phi_{70\%} = 2.47 \Phi_{0\%}$ , supposing practically the same ratio  $\xi$ , because fibres didn't change. But some changes in bundle orientation are possible. Although there is very few data on microfibrillar order factors, Petersburg Acad. Sci. Inst. Polym. Group published just for pullulan fibrillar structures  $L_{FB} = -0.012$  in the range  $\pm 0.0033$ . Further conclusions on the PLU permeability, porosity changes, and structure in general, will be given (together with REFERENCES as SUMMARY CONCLUSIONS in Part III of this series).

## POLYMER-SACCHARIDE CONJUGATES

### III. THE PROTECTIVE CONTROL OF CELL MEMBRANE ACTIVITIES BY TREHALOSE WITH PULLULAN

M.M. Plavšić<sup>1,2</sup>, D.S. Savić<sup>1</sup>, S.R. Savić<sup>1</sup> and S. A. Žerajić<sup>1</sup>

<sup>1</sup> University of Niš, Faculty of Technology, Bulevar Oslobođenja 124, Leskovac,

<sup>2</sup>The Academy of Applied Technical Studies Belgrade (milankapla@gmail.com)

#### ABSTRACT

Several possible protection mechanisms yeast cells use against desiccation, based on present theories and available experimental results are simulated, compared, evaluated, using molecular modeling, and analyzed in terms of present general theories on supramolecular polymer systems.

#### INTRODUCTION

In the previous papers of this series (with the same main title and assigned as Part I and II) are considered microorganisms heat- cold- and desiccation protection by saccharide trehalose (in Part I) and polysaccharide pullulan (in Part II). The chemical activity of both substances is very similar, although their properties at cells differ, e.g. in action scaling, due to the difference in size, as the first: [III,1-4]. But, there is also an essential difference in the mechanisms the cells apply by using those molecules for protection, as is described in previous papers of the series (e.g. yeast strain *Saccharomyces cerevisiae* (YSC) produces under stress the large amount of trehalose (TRH) and accumulates it in its membrane, where it generates different interactions protecting the cell, but fungus *Aureobasidium pullulans* (AUBPU) excretes pullulan (PLU) outside of the cell, to cover itself with polymer protective layer. But, if the mechanisms so differ (chemical impact of TRH in YST vs. physical barrier impact of protective PLU layer of AUBPU), why AUBPU still produces also some amount of TRH in parallel with PLU, under stress? Also some authors claim much better protection of pharmaceuticals with mixing PLU with TRH into materials for the capsule production. But most important paradox, or most interesting fact, is that some anhydrobiotes protect themselves without use of either TRH or PLU: [III,1,5]?! The only answer to it, we can propose now is: the point is in principles on which the protection mechanism works, not just the components that perform it. Those two substances fit the best into this process, but if we understand the mechanism, the other substances may be also used with some adjustment, or even the protective mechanism itself extended to other living beings!? But, what is the key, to trace the regularity staying behind all of that, so different phenomena, if it's still hard, to take the control over them!? According to the results published, it is related to cell membrane structure and function. Obviously, under stress membrane is the first to fight, but expected to keep cell integrity till the end of the fight, exposing meanwhile numerous changes, due to those stresses. With excess of fluids in the cell it swells, with shortage of water it shrinks and wrinkles, to adduce. But, "there is no life without water", so we are face here some very fundamental phenomena, and must consider them in general terms, first. So, the statement "there is no life without water", is here not correct as a starting point. Much better formulation is "life functions arise with coupling water with the macromolecules" [III,7]. But, what kind of the coupling changes can desiccation produce? Two hypotheses exist for now (better to say two groups of theories, but neither can cover all the phenomena and answer all the issues mentioned): (a) the water replacement hypothesis (e.g. TRH replaces water in the membrane, possible as we described in Part I) (b) the water entrapment hypothesis, e.g. with protective layer of PLU, as a barrier for water and heat transport, as described on Part II, and also, used now in pharmaceutical industry, or for food protection, and also for cosmetics- with some modification. Recently, some of the medical products

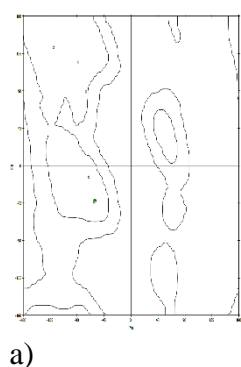
were also modified, (e.g. capsules, vaccine carrier etc.) using TRH with PLU together in the material: [I,2-5,III,8,12. It is similar to phenomena that AUBPU, already protected by PLU layer, produce some amount of TRH, under stress. On the other hand, some papers report on much better results for TRH as the protector, when it is in the presence of some proteins, in the system. So looking for the third factor of the mechanism, we consider also two possibilities (1) contribution of some molecules of the third kind to the mechanism, activated by TRH or/and PLU (2) contribution of some other type of interaction to the process as a whole, much easier performed when TRH and PLU act together.

## METHODS

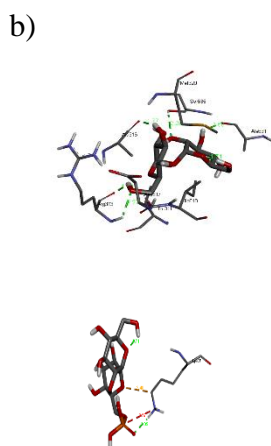
Considering hypothesis-(1), can be also two possibilities for the third component of the protecting mechanism proposed, in fact, that are two types of participants in the cell defense at the membrane, against desiccation stress: proteins located in this area and membrane phospholipids (PHL), themselves. Among these proteins we see some enzymes, controlling the processes of vitally importance for cell metabolism and vitally functions in general, as ATPase class, e.g.  $H^+$ -ATPase ( $H^+A$ ) in YST, in E1 and E2 forms: [I,7]. Similar structure has  $Na^+/K^+$ -ATPase (NKA) (the first been discovered and now target of digitalis glycosides used for treatment of heart conditions) and also  $H^+/K^+$ -ATPase (HKA) (also inhibited with modern drugs for preventing the excess production of stomach acid). So it can be expected, that the inhibition of  $H^+A$  similar to the other two ATPase mentioned blocking, will slow down functions of the cell under stress, or temporally stop those vitally functions (that need water) and so decrease its consumption of water and survive desiccation stresses. But how can be verified inhibitory actions upon ATPase, in situations in which TRH or PUL act? The first member of the ATPase family was discovered accidentally by physician J.C Skou in 1957, who -enthusiastic for biology, investigated leg nerves of crabs, what broth him The Nobel Prize 40 years later, for fundamental contribution in chemistry! But people in medicine and labs of similar kind, still had been waiting for its practical use, anthill appeared the first energy landscape conformational maps, for tracing mechanisms of such supramolecular systems of very complicated architecture, another 40 years ago: [I,2-5,7,12]. But, last years significant progress is achieved, mainly due to both, sophisticated computer modeling programs, and cryo-electron microscopy experiments. In this contribution we use docking programs, to elucidate possible mechanism of inhibition ATPase functions by saccharides (e.g. AutoDock-Vine, DSV, LAMMPS, etc.)

## RESULTS AND DISCUSSION

In Fig.1a-b-c are presented conformational relations of TRH and TH-6P, as discussed in Part I. In Fig.2 are added some of the results on their possible configuration adjustments in interactions with ATPase. As the first supposition is considered their possible roles as inhibitors in analogy to NKA inhibited by CSe (i.e. steroid skeleton substituted with saccharide moiety, at positions C-17 and C-3) as mentioned previously. Of course, there are significant differences in size and rigidity of those two entities, but according to nowadays experience the mechanism for regulation NKA activity is based on conformational changes governing ATP binding and thus reducing activity of all P-ATPase. Moreover according to results published last years there are redly identifiable sequence similarities between proteolipid subunits among the ATP classes suggesting a fundamental similarity between the catalytic mechanisms saved during evolution. So the binding site of modulators is regularly located in M domain among  $M_1$ - $M_{10}$  helices, with the highest affinity in the P-E2 state (with released  $Na^+$  and not yet bond  $K^+$  in NAK). So, besides preventing catalytic activity, can modulators also to stabilize E2 conformation, and prevent collapse of active cavity, due to membrane shrinkage because of drying.



a)



b)



c)

**Figure 1.** TRH conformations**Figure 2.** TRH - ATPase interactions

## CONCLUSIONS

It follows that protective role of TRH can be preservation of some cell vital functions and not just inhibition of enzyme activity (in the course of desiccation). TRH can both, to fill the active ATP cavity and replace water at the protein surface there and at all cell proteins, in cooperation with PLU layer, and moreover extend the layer into a network-like structure with polar PHL ester groups. Indeed, there are several experimental papers indicating not inhibition, but stabilization of ATPase of YST by TRH: [III,8-11] in Post -Albers cycle and productions of the food-protective layers of TRH with alginates, what are the polysaccharides as well as PLU. Also is proposed the superposition model of hydrogen TRH interactions with PHL dipole vectors, pointing to needs of more membrane dipoles orientation and ordering data, besides the ester group dipole vector angle: [III,12]

## REFERENCES (all have additional mark III- by quoting e.g. : [III,1])

- [1] N. P. Elinov, Himija Mikrobnih Polisakharidov, Mir, Moskov (in Russian) 2017.
- [2] R.B. Byrd, W.E. Stewart, E.N. Lightfoot, Transport Phenomena, Wiley, N.Y. 1960..
- [3] T Bergman, F. Incorpera, Fundamentals of Heat and Mass Transfer 7<sup>th</sup>, edn. Wiley N.Y. 2011.
- [4] P.G. deGennes, Scaling Concept in Polymer Physics, Cornell Un. N.Y. 1979
- [5] S. Rattnakumar, A. Tunnacliffe, FEMS Yeast Res. 2006, **6**, 802-813
- [6] S. Farris at al. J., Appl. Polym. Sci. 2014, **131**, 40539-40551
- [7] P. J. Flory, Lecture of the Nobel Laureate, Nobel Foundation Stockholm 1974.
- [8] C. Fagundas Felix at al., Eur. J. Biochem. 1999, **266**, 660-664.
- [9] I. Pajic-Ljakovic, V. Ilic, B. Bugarski, M.B. Plavsic, Eur. Biophys. J. 2019, **39**, 789-800.
- [10] C. Lambruschini at al. Langmuir 2000, **16**, 5467-5470.
- [11] A. Das at al. Int. J. Biological Macromolecules, 2019, **127**, 365-375
- [12] E. Saiz, J.P. Hummel, P.J. Flory, M.B. Plavsic, J. Phys. Chem. 1981, 3211-3217



*K - Environmental Protection,  
Forensic Sciences,  
Geophysical Chemistry,  
Radiochemistry,  
Nuclear Chemistry*



## UPTAKE AND ACCUMULATION OF Pb AND Ni IN SPRUCE AND DOUGLAS-FIR TREE-RINGS AND BARK

I.R. Milošević<sup>1</sup>, S. Živković<sup>2</sup>, M. Momčilović<sup>2</sup>, Ž. Višnjic-Jeftić<sup>3</sup>, M. Veselinović<sup>4</sup>, I. D. Marković<sup>5</sup> and D. M. Marković<sup>1</sup>

<sup>1</sup> *University of Belgrade, Institute of Physics Belgrade, Laboratory for 2D materials of Center for Solid State Physics and New Materials, Pregrevica 118, 11080 Belgrade, Serbia.  
(novovic@ipb.ac.rs)*

<sup>2</sup> *University of Belgrade, Institute of Nuclear Sciences Vinča, Mike Petrovića Alasa 12-14, 11351 Belgrade, Serbia.*

<sup>3</sup> *Institute for Multidisciplinary Research, University of Belgrade, Kneza Višeslava 1, 11090 Belgrade, Serbia.*

<sup>4</sup> *Institute of Forestry, Kneza Višeslava 3, 11090 Belgrade, Serbia.*

<sup>5</sup> *Worldwid Clinical Trials, Omladinskih brigada 90b, 11070 Belgrade, Serbia.*

### ABSTRACT

Modern development and increasing urbanisation, have production of a wide range of different pollutants, as a side effect. Trees in particular are emerging as an active factor receiving pollution. In a two-year study, we exposed spruce (*Picea abies* Karst.) and Douglas-fir (*Pseudotsuga menziesii* Mirb.) seedlings to elevated concentrations of Pb and Ni by adding these elements in the soil. Their concentrations as well as Mn and Zn concentrations in soil, tree-rings and bark were determined with Inductively Coupled Plasma- Optical Emission Spectrometry (ICP-OES). Analyses showed an increase of Pb and Ni in examined plant parts (tree-rings and bark) for both tree species, especially for Douglas-fir tree-ring.

### INTRODUCTION

Among different types of pollutants, heavy metals are the most significant ones, because they are very toxic even at very low concentrations and could not be degraded naturally. Higher plants have emerged as a valuable tool enabling information about environmental pollution and different parts of trees have been used to monitor heavy metal contamination in the environment e.g. leaves/needles, bark, and tree-rings [1-4]. The bioavailability of metals for plants is controlled by plant's requests for micronutrients and their capacity to absorb and eliminate toxic elements. Generally, it is expected that the uptake increases, as the concentration of the metal ions in the external solution increases. The influence of heavy metals on the accumulation in tree-rings and bark is an area that is faintly investigated, especially in the form of a field experiment.

### METHODS

The field experiment was conducted in Livada 1 Street in Kaluđerica, Belgrade, Serbia. The seedlings of spruce (*Picea abies* L.) and Douglas-fir (*Pseudotsuga menziesii* Mirb.), 5 years old, were obtained from the Institute of Forestry in Belgrade. They were planted in May 2017 and were arranged in six groups containing four seedlings in each group with a 1m distance. From January to May seedlings of spruce and Douglas-fir were watered (five times in total) with Pb and Ni in parallel experiments (I experiment- 2 g/L of Pb, 0.5 g/L of Ni and II experiment- 1 g/L of Pb, 0.25 g/L of Ni. Metal solutions were prepared from their nitrate salts and tap water was used for the metal solution preparation.). The third group of seedlings was taken as a control group. Spruce and Douglas-fir seedlings were cut in May 2019. Bark was taken as a separate sample. Soil samples were collected from the base of each tree at 0-20 cm depth. Tree disk, bark and soil were digested using an Advanced Microwave Digestion

System (ETHOS 1, Milestone, Italy). Also, the pH of the soil was determined. The content of elements (Pb, Ni, Mn and Zn) in each sample, prepared as diluted aqueous solutions, has been determined by using a Thermo Scientific iCAP 7400duo Series instrument for ICP-OES.

In order to simplify the display of the results, spruce sampled at this location for the first experiment will have the abbreviated name 'SI' and Douglas-fir 'DI', for the second experiment 'SII' and 'DII' and in the case of control 'SC' and 'DC', respectively.

## RESULTS AND DISCUSSION

Mean Pb and Ni concentrations in soil, tree-rings and bark of spruce and Douglas-fir seedlings treated by metal solutions, were presented in Table 1. Also, mean Mn and Zn concentrations in plant parts and soil can be seen, as well as pH of the corresponding soil. Mn and Zn were examined because they are, among other elements, essential for higher plants and have several functions in plants. They weren't externally added in this field experiment

**Pb concentration:** From Figure 1, it can be seen that the Pb content in the soil increases. Compared to the control sample, the increase is about 40 and 24 times for SI and SII, respectively. This implies an elevation of Pb concentration in tree-rings of SI (2.8 times) and bark for SI (2.8 times) and SII (1.1 times), compared to control.

In the case of Douglas-fir, it was noticed that with the increase of Pb concentration in the soil (28 and 16 times, compared to control), the content in tree-rings (7 and 4 times) and bark (4 and 2 times) also increases (Figure 1).

**Ni concentration:** Increased Ni concentration in soil samples (3 (SI) and 2 (SII) times; 2.5 (DI) and 2 (DII) times compared to control) also have a direct effect on increasing the concentration in both tree-rings and bark (Figure 1).

**Mn and Zn concentration:** Although the soil has not been treated with these elements a very small difference between experiments comparing to control. For both examined tree species some unusual behaviour can be seen in these experiments. Their concentrations in tree-rings and bark were slowly lowered (except for the Mn concentration in Douglas-fir bark, where an increase can be seen) for the concentrations of SI and SII compared to control despite their slightly increased concentration in the soil (Mn (15%, 12%) and Zn (9%, 6%); Mn (12%, 12%) and Zn (15%, 7%)). This soil concentration increase could be the consequence of the soil pH decrease (SI- 0.1; SII- 0.2; and in DI- 0.1; DII- 0.3) [2]. The decrease of Mn and Zn in plant parts could be explained as a consequence of the competition between various metals in the course of their uptake by roots and by a disturbance of uptake mechanism [5].

**Table 1.** Mean Pb, Ni, Mn and Zn (n=4) concentrations in soil, tree-rings and bark of spruce and Douglas-fir seedlings (ppm), as well as, corresponding soil pH.

	Pb			Ni		
	soil	tree-rings	bark	soil	tree-rings	bark
SI	827±56	0.41±0.05	4.73±0.55	278±16	0.34±0.03	2.71±0.16
SII	505±30	<0.15	1.87±0.09	199±9	0.29±0.04	1.78±0.09
SC	21±1	<0.15	1.67±0.10	88±4	0.24±0.03	1.09±0.09
DI	634±30	1.06±0.10	2.44±0.13	226±11	0.73±0.06	1.13±0.06
DII	369±19	0.61±0.08	1.28±0.06	182±9	0.40±0.03	1.03±0.06
DC	23±1	<0.15	0.68±0.05	89±4	<0.04	0.36±0.04
	Mn			Zn		
	soil	tree-rings	Bark	soil	tree-rings	Bark
SI	950±43	8.23±0.46	18.70±1.36	128±6	18.01±0.91	67.86±3.90
SII	923±42	8.41±0.49	23.41±1.88	125±5	21.53±0.96	73.36±4.44
SC	823±42	9.22±0.57	28.85±1.85	118±7	28.41±1.62	100±5
DI	951±43	3.38±0.23	13.69±0.92	131±7	5.36±0.37	22.02±1.85
DII	954±43	2.63±0.20	12.03±0.55	122±5	3.52±0.19	24.98±1.44
DC	852±46	5.00±0.27	8.71±0.44	113±5	7.66±0.38	30.35±1.62
	SI	SII	SC	DI	DII	DC
Soil pH	6.7±0.05	6.6±0.05	6.8±0.05	6.90±0.05	6.7±0.05	7.0±0.05

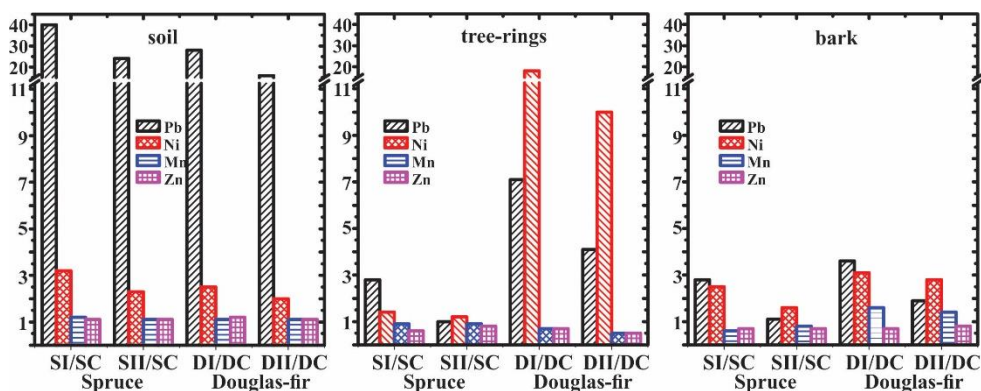


**Figure 1.** Concentration ratios between first-I and second-II experiment with control-C in soil, tree-rings and bark, for spruce and Douglas-fir.

**CONCLUSION**

All trees have survived the experiments (in these extreme conditions) and grew at a normal rate with no indications of metal toxicity. The addition of other metals (Pb and Ni) to soil leads to their increased accumulation in the body of tree-rings and bark, and the decrease of essential elements (Mn and Zn). Although every element uptake is a complex process, tree-rings of spruce and Douglas-fir

react on elevated concentrations in the soil and can give information about environmental pollution. Bark was also influenced by the Pb and Ni elevated concentrations in the soil.

### ***Acknowledgement***

The authors acknowledge funding provided by the Institute of Physics Belgrade and Institute of Nuclear Sciences Vinča, through the grant by the Ministry of Education, Science, and Technological Development of the Republic of Serbia.

### **REFERENCES**

- [1] Aničić, M. et al., *Ecological Indicators*, 2011, **11**, 824–830.
- [2] Marković, D.M. et al., *Environ. Sci. Pollut. Res.*, 2013, **20**, 136-145.
- [3] Turkyilmaz, A. et al. *Environ. Sci. Pollut. Res.*, 2019, **26**, 5122–5130.
- [4] Yousaf, M. et al., *Water Air Soil Pollut.*, 2020, **231:382**, 1-9.
- [5] Seregin, I. V., Kozhevnikova, A.D., *Russ. J. Plant Physiol.*, 2006, **53**, 257–277.

## ADSORPTION OF IBUPROFEN BY SURFACTANT MODIFIED KAOLIN

M. Obradović<sup>1</sup>, A. Daković<sup>1</sup>, G. E. Rottinghaus<sup>2</sup>, M. Spasojević<sup>1</sup>, M. Marković<sup>1</sup>, D. Smiljanić<sup>1</sup>,  
D. Krajišnik<sup>3</sup>

<sup>1</sup>*Institute for Technology of Nuclear and Other Mineral Raw Materials, Franše d' Eperre 86, 11000 Belgrade, Serbia. (m.obradovic@itnms.ac.rs)*

<sup>2</sup>*Veterinary Medical Diagnostic Laboratory, College of Veterinary Medicine, University of Missouri, Columbia, MO 65211, USA.*

<sup>3</sup>*Department of Pharmaceutical Technology and Cosmetology, University of Belgrade, Faculty of Pharmacy, Vojvode Stepe 450, 11221 Belgrade, Serbia.*

### ABSTRACT

In this paper, results of ibuprofen (IBU) adsorption by organokaolins obtained by modification of the natural kaolin (KR) with surfactant - hexadecyltrimethyl ammonium bromide (H) are presented. Two different amounts of surfactant were used for modification of KR (50 and 90% of kaolin's cation exchange capacity). Samples are denoted as HKR-50 and HKR-90. Adsorption of IBU on organokaolins was investigated with different initial drug concentrations (2 – 20 mg/L) in phosphate buffer at pH 7. Compared with KR which has no affinity to adsorb IBU, modification of KR with H improved adsorption of this drug. Results showed that adsorption of IBU increased with increasing of the amount of surfactant in organokaolins as well as with increasing of the initial concentration of the drug in solution. Adsorption of IBU by both adsorbents followed nonlinear isotherms and from the Langmuir model, the maximum adsorption capacities were 2.05 mg/g for HKR-50 and 3.12 mg/g for HKR-90.

### INTRODUCTION

Pharmaceuticals are a large group of emerging contaminants extensively used in human health; therefore, they often occur in the aquatic environment. These substances are becoming a concern due to their high environmental persistence and possible negative effects on human health and aquatic ecosystems. Emerging contaminants could be hazardous even at their low concentrations. Measured concentrations of non-steroidal anti-inflammatory drugs (NSAIDs) can vary from several ng/L to even mg/L in case of the effluents from the pharmaceutical industry [1,2]. Wastewater treatment plants effluents represent major sources of pharmaceuticals in the aquatic environment since many of them are not significantly removed and flow into receiving water sources [3]. Thus, finding a low cost method for eliminating pharmaceuticals from water is required. Several treatment methods like advanced oxidation processes, membrane techniques, adsorption, and constructed wetlands are usually used for removal of pharmaceutical from water systems. Among all of these methods, adsorption is the most promising approach for removal of emerging contaminants because of its low cost, highly efficient and has simple operating design.

IBU is the one of the most common NSAIDs, widely used in treatment of rheumatic disorders, pain and fever. Thus, it is frequently found in water systems [4]. Chemical structure of IBU ((2RS)-2-[4-(2-methylpropyl)phenyl]propanoic acid) is presented in Figure 1.

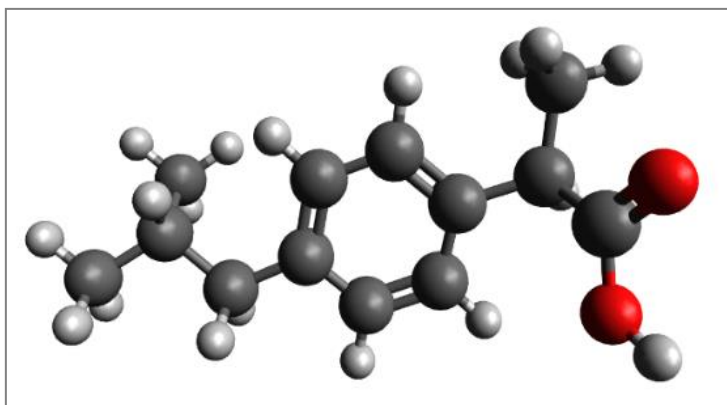


**Figure 1.** Chemical structure of IBU (Colour code: C: grey, H: light grey, O: red)

Zeolites and clays are usually used as adsorbents for removal of different pollutants. These minerals are aluminosilicates that possess hydrated exchangeable inorganic cations which make their surface hydrophilic. Accordingly, they are less able to bind relatively nonpolar - like most of the pharmaceuticals are. In order to adsorb these relatively nonpolar molecules, modification of minerals is required. It is reported that surfactant modified zeolites are effective adsorbents for removal of drugs – diclofenac sodium, ibuprofen and ketoprofen from water systems [3,5]. It was also shown that organoclays modified with cationic surfactants are efficient in removing organic compounds from aqueous solutions [6]. Surfactant modified montmorillonite and kaolinite have been considered for removal of relatively low polar molecules from water solutions. For example, adsorption of phenol by montmorillonite and kaolinite modified with two surfactants - hexadecyltrimethylammonium bromide (H) and phenyltrimethylammonium bromide (PTMA) was studied by Alkaram et al. [7]. They reported that both clays modified with surfactants were much more effective in phenol removal than unmodified samples.

The aim of this work is to modify the natural kaolin, non-swelling clay with low cation exchange capacity (CEC) with two different amounts of surfactant (H) and to investigate if obtained materials would be efficient to remove IBU (as representative of NSAIDs) from aqueous solution.

## METHODS

Starting material used in this study was a sample of the natural kaolin (Rgotina, Serbia) - KR. XRD analysis showed that the main mineral in KR is kaolinite with smaller amounts of quartz and mica [8,9]. The raw material was used without any further purification for the preparation of the organokaolins and subsequent IBU adsorption experiments. The total CEC of KR is 6 meq/100g [9].

Two organokaolins were prepared by mixing of KR suspensions with two different amounts of surfactant H (Sigma-Aldrich Co) solution that is equivalent to 50 % and 90 % of KR cation exchange capacity. Suspensions were stirred at 5000 rpm for 10 min at 50°C, then filtered, rinsed with distilled water and dried. Organokaolins were denoted as HKR-50 and HKR-90.

IBU (Sigma-Aldrich Co) standard solution was prepared in methanol with concentration of 1000 mg/L. In order to obtain isotherms, stock solutions of the drug in the concentration range from 2 to 20 mg/L in phosphate buffer at pH 7 were prepared. Experiments were performed by shaking 5 mg of HKR-50 or HKR-90 with 10 mL of each drug solution for 30 min at room temperature. Then mixtures were centrifuged and supernatants were collected for analysis. The concentrations of the IBU before and after adsorption were determined by HPLC.

## RESULTS AND DISCUSSION

IBU is hydrophobic molecule, practically insoluble in water, freely soluble in acetone, methanol and methylene chloride. It dissolves in dilute solutions of alkali hydroxides and carbonates (Ph. Eur.). Adsorption experiments were performed at pH 7, at which IBU exists in anionic form (IBU  $pK_a=4.4$ ). Natural KR has a negative hydrophilic surface and hydrated inorganic cations, therefore it is not efficient in removal of hydrophobic molecules. In the preliminary experiment, it was confirmed, that the KR has no affinity to adsorb IBU. The results of adsorption of IBU by HKR-50 and HKR-90 are presented in Figure 2. It can be noticed, that adsorption of IBU increased with increasing of the amount of surfactant in the organokaolins. Also, adsorption of IBU by both adsorbents increased with increasing of the initial drug concentration.

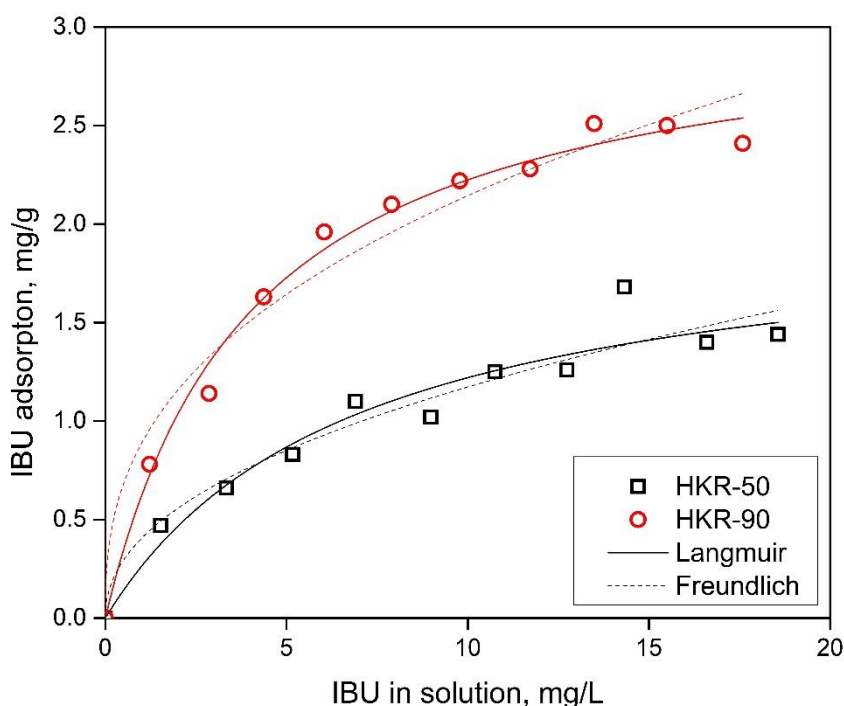


**Figure 2.** IBU adsorption by HKR-50 and HKR-90 at pH 7

The results showed that the presence of hydrophobic surfactant molecules in organokaolins increased IBU adsorption, indicating that surfactant molecules at the organokaolins surface are active sites responsible for drug adsorption.

For both adsorbents, nonlinear isotherms were obtained, thus Langmuir and Freundlich isotherm models were used to fit the equilibrium adsorption data. Parameters of the Langmuir and Freundlich isotherms are presented in Table 1. A better fit of experimental data was obtained with the Langmuir model. From the Langmuir model, the calculated values for IBU maximum adsorption capacities were 2.5 mg/g for HKR-50 and 3.12 mg/g for HKR-90. The low values of  $K_L$  (0.147 L/mg for HKR-50 and 0.248 L/mg for HKR-90) implied that binding between IBU and organokaolins was strong. Nonlinear isotherms obtained for adsorption of IBU by two organokaolins suggest complex adsorption mechanism which probably includes partitioning of the hydrophobic part of IBU into the surfactant alkyl chains as well as interactions between positive “heads” from H molecules at the kaolin surface and negatively charged IBU.

**Table 1.** Characteristic parameters of IBU adsorption isotherms

	Langmuir			Freundlich		
	$q_m$ (mg/g)	$K_L$ (L/mg)	$r^2$	$n$	$K_F$ (L/mg)	$r^2$
<b>HKR-50</b>	2.05	0.147	0.937	2.161	0.404	0.935
<b>HKR-90</b>	3.12	0.248	0.989	2.608	0.887	0.964

## CONCLUSION

Results reported in this paper demonstrated that modification of the KR with surfactant H improved adsorption of IBU, a representative of NSAIDs. Two amounts of surfactant were used for modification of KR. Adsorption of IBU increased with increasing amounts of surfactant in the organokaolins and also with increasing of the initial drug concentration. The presence of hydrophobic surfactants at the KR surface increased IBU adsorption, thus these adsorbents may be suitable materials for removal of IBU from contaminated water.

## Acknowledgement

These experiments were funded by the Ministry of Education, Science and Technological Development of Republic of Serbia Contact numbers: 451-03-68/2020-14/200023 and 451-03-9/2021-14/200161. Ibuprofen adsorption experiments were done at the Vet. Med. Diag. Lab., University of Missouri, Columbia, USA.

## REFERENCES

- [1] J.C.G. Sousa, A.R. Ribeiro, M.O. Barbosa, M.F.R. Pereira, A.M.T. Silva, *J. Hazard. Mater.*, 2018, **344**, 146–162.
- [2] S. Terzić, I. Senta, M. Ahel, M. Gros, M. Petrović, D. Barcelo, J. Müller, T. Knepper, I. Martí, F. Ventura, P. Jovančić, D. Jabučar, *Sci. Total Environ.*, 2018, **399**, 66–77.
- [3] D. Smiljanić, B. de Gennaro, F. Izzo, A. Langella, A. Daković, C. Germinario, G.E. Rottinghaus, M. Spasojević, M. Mercurio, *Microporous Mesoporous Mater.*, 2020, **298**, 110057.
- [4] C. Sophia A., E.C. Lima, *Ecotoxicol. Environ. Saf.*, 2018, **150**, 1–17.
- [5] F. Izzo, M. Mercurio, B. De Gennaro, P. Aprea, P. Cappelletti, *Colloids Surf. B Biointerfaces*, 2019, **182**, 110380.
- [6] D.I. Song, S.S. Won, *Environ. Sci. Technol.*, 2005, **39**, 1138–1143.
- [7] U.F. Alkaram, A.A. Mukhlis, A.H. Al-Dujaili, *J. Hazard. Mater.*, 2009, **169**, 324–332.
- [8] M. Spasojević, A. Daković, G.E. Rottinghaus, M. Obradović, D. Krajišnik, M. Marković, J. Krstić, *Appl. Clay Sci.*, 2021, **205**, 106040.
- [9] V. Rakić, N. Rajić, A. Daković, A. Auroux, *Microporous Mesoporous Mater.*, 2013, **166**, 185–194.

## SOLID-PHASE EXTRACTION OF ESTROGEN HORMONES FROM WATER USING MULTI-WALLED CARBON NANOTUBES AS SORBENT

D. Prokić<sup>1</sup>, M. Vukčević<sup>2</sup>, M. Maletić<sup>1</sup>, I. Janković-Častvan<sup>2</sup> and T. Đurkić<sup>2</sup>

<sup>1</sup> *Innovation Center of the Faculty of Technology and Metallurgy, Karnegijeva 4, 11000 Belgrade, Serbia. (dprokic@tmf.bg.ac.rs)*

<sup>2</sup> *University of Belgrade, Faculty of Technology and Metallurgy, Karnegijeva 4, 11000 Belgrade, Serbia.*

### ABSTRACT

Multi-walled carbon nanotubes were employed as a sorbent for solid-phase extraction of estrogen hormones (estrone, 17 $\beta$ -estradiol, and 17 $\alpha$ -ethinylestradiol) from water solution. The solid-phase extraction (SPE) method was optimized by choosing an appropriate mass of the sorbent, volume, and initial pH of hormone water solution, as well as by choosing an appropriate organic solvent for extraction. Based on the obtained hormone recoveries, the following SPE conditions were chosen as optimal: 100 cm<sup>3</sup> of hormone water solution at initial pH adjusted to 10; 20 mg of the sorbent; and methanol-dichloromethane mixture as elution solvent. Recoveries obtained under the optimal conditions ranged from 70.56 % for estrone, to 81.23 % for 17 $\alpha$ -ethinylestradiol, with a relative standard deviation from 9.92 to 18.74 %.

### INTRODUCTION

Steroid estrogens are a group of endocrine-disrupting compounds (EDCs) which, even present in very low concentration (ng/l) [1], can have different adverse effects on living organisms [2]. The principal way in which these compounds reach the environment is through municipal wastewater [3]. Since these compounds are present in very low concentrations in the environment, their detection requires the development of an efficient isolation and preconcentration technique.

Multi-walled carbon nanotubes have been used so far as sorbents for many environmental pollutants, due to high adsorption capacity, the wide pH range of application, and the possibility of surface chemistry modification [4]. This paper aimed to examine the possibility of using multi-walled carbon nanotubes as sorbent for solid-phase extraction (SPE) of estrone (E1), 17 $\beta$ -estradiol (E2), and 17 $\alpha$ -ethinylestradiol (EE2) from water solution. To obtain high recovery values of the SPE method, the following parameters were optimized: volume and initial pH of hormone solution, the mass of sorbent, and type of organic solvent for hormone elution.

### MATERIALS AND METHODS

Multi-walled carbon nanotubes (MWCNTs) (Sigma-Aldrich, USA), with the specific surface area of 252 m<sup>2</sup>/g ( $S_{\text{meso}} = 236 \text{ m}^2/\text{g}$ ,  $S_{\text{micro}} = 16 \text{ m}^2/\text{g}$ ,  $V_{\text{micro}} = 0.0749 \text{ cm}^3/\text{g}$ ) were used as SPE sorbent for extraction of selected hormones [4]. Applied SPE procedure included: conditioning of SPE cartridges (3 cm<sup>3</sup>) loaded with MWCNTs, passing the water solution of the hormones (with an appropriate volume and pH values) through the cartridges, drying under vacuum for 10 min, elution of hormones with suitable organic solvent, followed by evaporation to dryness under N<sub>2</sub>, and reconstitution with 1 cm<sup>3</sup> of methanol. The SPE process was optimized to obtain the highest recoveries by choosing an appropriate mass of the sorbent (20, 50, 100 mg), volume (25, 50, 100 cm<sup>3</sup>) and pH (5-11) of hormone water solution, as well as organic solvent (methanol - MeOH, acetonitrile - ACN, dichloromethane/methanol mixture - DCM/MeOH) for hormones extraction.

## RESULTS AND DISCUSSION

The recoveries of the SPE method using a different mass of MWCNTs sorbent: 20, 50, and 100 mg, are summarized in Table 1. Since sorbent mass does not have a significant influence on the extraction efficiency, the lowest mass of material was chosen for the following experiments.

SPE method was also optimized by choosing an appropriate volume of hormone water solution (Table 2).

According to the results shown in Table 2, the highest recoveries for all tested hormones were obtained for the volume of 100 cm<sup>3</sup>, and this volume was chosen as optimal.

Results obtained for optimization of organic solvent are presented in Table 3. The highest recoveries for estrone and 17 $\beta$ -estradiol were gained using DCM/MeOH, while the best result for 17 $\alpha$ -ethinylestradiol was achieved with methanol. The mixture DCM/MeOH was chosen as the optimal organic solvent for the simultaneous extraction of all hormones.

**Table 1.** Recoveries (%) of SPE method obtained using different mass of sorbent

Hormone	Sorbent mass (mg)		
	20	50	100
Estrone	63.9	63.0	63.5
17 $\alpha$ -ethinylestradiol	69.3	68.9	66.2
17 $\beta$ -estradiol	52.6	51.7	54.2

**Table 2.** Recoveries (%) of SPE method obtained using different volume of hormone water solution

Hormone	Volume (cm <sup>3</sup> )		
	25	50	100
Estrone	32.1	56.1	60.7
17 $\alpha$ -ethinylestradiol	40.9	84.2	97.4
17 $\beta$ -estradiol	34.4	64.9	74.7

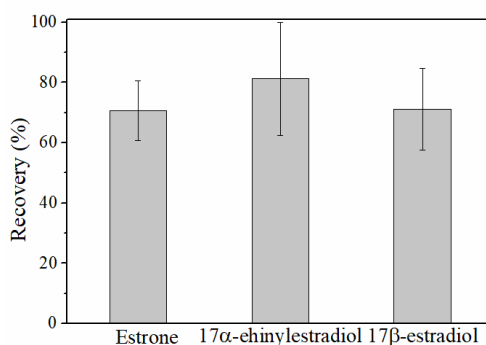
**Table 3.** Recoveries (%) of SPE method obtained using different organic solvents

Hormone	Solvent		
	Acetonitrile	Methanol	DCM/MeOH
Estrone	49.4	30.9	62.6
17 $\alpha$ -ethinylestradiol	61.6	79.2	60.3
17 $\beta$ -estradiol	33.9	23.1	57.6

Recoveries of the SPE method, obtained by examining the influence of initial pH values of the hormone solution are given in Table 4. The pH 10 was chosen as optimal, due to the highest recoveries obtained for all hormones.

**Table 4.** Recoveries (%) of SPE method at different pH of hormone water solution

Hormone	pH						
	5	6	7	8	9	10	11
Estrone	51	63	49	70	49	72	78
17 $\alpha$ -ethinylestradiol	56	63	48	68	46	85	79
17 $\beta$ -estradiol	50	62	49	62	46	71	65

**Figure 1.** Recoveries of examined hormones obtained using optimized SPE method

The optimum conditions obtained for hormone extraction were the following: 100 cm<sup>3</sup> of water hormone solution with initial pH value adjusted to 10 was passed through the cartridges loaded with 20 mg of MWCNTs, and DCM/MeOH mixture was used as elution solvent.

The optimized SPE method was applied for hormones extraction from water, and obtained recoveries with relative standard deviation are given in Figure 1. Satisfactorily high results were obtained, as recoveries ranged from 70.56 % for estrone, to 81.23 % for 17 $\alpha$ -ethinylestradiol, with relative standard deviation from 9.92 to 18.74 %.

## CONCLUSION

In this study, MWCNTs were used as sorbents for SPE of estrogen hormones. Parameters of the SPE method were optimized in order to get optimal sorbent mass, volume, and initial pH value of hormone water solution, as well as an optimal organic solvent for elution. Optimized SPE method involves extraction of hormones from 100 cm<sup>3</sup> of water solution, with pH adjusted to 10, using cartridges packed with 20 mg of multi-walled carbon nanotubes, and the mixture of dichloromethane/methanol as elution solvent for hormones extraction. Applying the optimized SPE procedure, high recoveries for estrone, 17 $\beta$ -estradiol and 17 $\alpha$ -ethinylestradiol were achieved, which indicates that MWCNTs can be used as an efficient sorbent for hormone extraction from water.

## Acknowledgement

The research was funded by the Ministry of Education, Science and Technological Development of the Republic of Serbia (Contract No. 451-03-9/2021-14/200135 and Contract No. 451-03-9/2021-14/200287).

**REFERENCES**

- [1] M. Auriol, Y. Filali-Meknassi, R.D. Tyagi, C.D. Adams, R.Y. Surampalli, *Process Biochem.*, 2006, **41**, 525–539.
- [2] M. Adeel, X. Song, Y. Wang, D. Francis, Y. Yang, *Environ. Int.*, 2017, **99**, 107–119.
- [3] H. Hamid, C. Eskicioglu, *Water Res.*, 2012, **46**, 5813–5833.
- [4] B. Lalović, T. Đurkić, M. Vukčević, I. Janković-Častvan, A. Kalijadis, Z. Laušević, M. Laušević, *Environ. Sci. Pollut. Res.*, 2017, **24**, 20784–20793.

## ENVIRONMENTAL RISK OF HEAVY METAL CONTAMINATION IN URBAN SEDIMENTS: A STUDY IN THE CITY OF BELGRADE, SERBIA

G. Dević,<sup>1</sup> M. Ilića<sup>1</sup>, S. Miletić<sup>1</sup>, M. M. Vrvic<sup>2</sup>

<sup>1</sup> *University of Belgrade, Institute of Chemistry, Technology and Metallurgy, Njegoševa 12, 11000 Belgrade, Serbia. (gordana.devic.@ihtm.bg.ac.rs and gdevic@chem.bg.ac.rs)*

<sup>2</sup> *Faculty of Chemistry, University of Belgrade, Studentski trg 12-16, 11000 Belgrade, Serbia.*

### ABSTRACT

Concentrations of 10 potentially toxic trace elements were measured in soil samples collected from 18 sites in urban areas of Belgrade, the capital and the largest city in Serbia. Samples were analysed in order to assess the extent of soil contamination and to distinguish natural and anthropogenic input. The results demonstrated a general Zn, Pb, and Cd enrichment in surface samples, hence, after comparison with guidelines, it has been determined that there is a potential risk for human health. In the surface and buried samples, traces of copper were detected. The highest concentrations of Cr ( $121 \pm 12.3$  mg/kg) and Ni ( $94.9 \pm 12.6$  mg/kg) were found at a sediment depth of 2m and should be ascribed to geogenic sources. The results of HCA and PCA analysis supported a natural origin of Co, Cu, Mn, Cr, and Ni, while Cd, Zn, and Pb originated from anthropogenic inputs.

### INTRODUCTION

Contamination with toxic and potentially toxic trace elements has a significant impact on the quality of the environment.

Mobilization of trace elements in the biosphere under the influence of human activities has become an important process in the geochemical cycle of these elements. It has become particularly pronounced in urban areas, where different sources release amounts of toxic elements in the atmosphere, waterways, soil and sediments. In this way, toxic elements become important tracers of environmental pollution. Environmental concerns have resulted in a large number of articles on toxic and potentially toxic elements in the urban environment of many cities around the world [1-3]. Soil sampling strategies have been established across Europe for the protection of the continent's soils. However, for the territory of the Republic of Serbia, there are still no such strategies for systematically monitoring of soil, which would include collection of samples from the entire territory of Serbia in the same calendar year. The aim was to investigate the spatial distribution of toxic and potentially toxic trace elements in order to identify the sources of pollutants, evaluate the degree of sediment contamination, improve their monitoring in the analysed area and assess the human and environmental risk. Human and environmental risks were assessed by comparing the results with Serbian and Dutch soil quality references, as well as available data in the literature.

### METHODS

For this study, a total of 45 sediment samples from 18 locations in the urban area of new belgrade, including the Thermal power plant complex, covering of 0.3 km<sup>2</sup>, were selected. Sampling was carried out in May 2015. A large number of investigated sites is located near the Sava River and reservoirs for diesel fuel and mazut, while a smaller number of sites is located in the hinterland of the urban areas (residential block), but all sites are in the high traffic zone, near Belgrade–Novi Sad Highway, which is a part of the Pan-European corridor X.

The concentrations of heavy metals were measured using methods described by Sakan et al.[4] After three-acid total digestion (HCl, HNO<sub>3</sub>, and HF), the total concentrations of Cd, Co, Cu, Cr, Fe,

Mn, Zn, Pb, Ni, and V were determined using an atomic emission spectrometer with an inductively coupled plasma iCAP-6500 Duo (Thermo Scientific, Loughborough, United Kingdom).

## RESULTS AND DISCUSSION

It's done descriptive statistics (mean with standard deviation, median, maximum and minimum) for the variables in 45 sediment samples and together with the background values and with Serbian[5] and Dutch[6] legislation (Table 1). The maximum values for Cd, Zn, and Pb were greater than respective upper baseline concentration, which may suggest contamination in the investigated sediments.

On the other hand, concentrations of Co, Cr, Cu Ni, V, Fe and Mn in the analysed samples were largely similar to the baseline concentrations, which suggest that these elements can be treated as their background levels in samples. Comparison of the values of metal concentrations with the baseline concentration indicated that the urban sediments of New Belgrade are polluted with "traffic-related metals" (Pb, Zn and Cd). Their increased concentrations could probably be related to the rising urban population that relies on automobiles as the main means of transportation, and, of course, the existence of storage tanks for oil products in this alluvial area of Belgrade. According to the Serbian legislation for trace elements in sediments, some samples of urban sediments (surface samples) exceeded the maximum permissible value for Zn (614.97 mg/kg) and Pb (190 mg/kg) and the maximum values of these metals were also greater than the upper baseline concentrations. This enrichment could only be explained by some local accidental source on these sites. The concentrations of Cd (16% of all samples) and Cr (86% of all samples) exceeded the Serbian limit values and the maximum values of Cd were greater than upper baseline concentrations. According to the Netherlands Standard, 100% of the examined samples were polluted with V and Ni, 22% were polluted with Cr, 11% were polluted with Pb, 4% were polluted with Cd and 2% with Zn. The intervention values are representative of the level of contamination above which there is a serious case of contamination. The obtained Zn, V, Cd, Cu and Co concentrations were not sufficiently high to require remediation. The nickel contents always exceeded both Serbian and Dutch sediment quality values and 86% of samples had high concentrations of Cr, but the baseline concentrations for these metals were not exceeded. The Ni and Cr contents correlated closely with each other and carried similar information. The high Ni and Cr contents are believed to be of geogenic origin, coming from Quaternary eolian and alluvial sediments.[1-3] Similar conclusions concerning the origin of these contaminants were also reached in other studies worldwide. The slight increase in the maximum concentration of V compared to baseline level found in some of the studied surface sediments, could be the result of airborne emissions from storage tanks for crude oil and oil products (mainly gasoline, diesel fuel and mazut). Cadmium, lead and to a lesser extent zinc, are the key factors impairing the quality of the urban sediment in the area of the Thermal Power Plant New Belgrade, which has more than 200,000 residents. The results from spatial PCA/FA suggested that most of the variations could be explained by a set of natural and anthropogenic pollutions.

**Table 1.** Descriptive statistics of the total element contents (mg/kg) of 45 sediment samples analyzed in this study.

	Cd	Co	Cr	Cu	Fe	Mn	Ni	Pb	Zn	V
Mean	2.42	20.97	111.9	19.34	24900	589.2	88.6	60.1	105	127
Standard deviation	0.73	4.47	20.3	11.1	5673	126	17	27.4	84	60.3
Median	2.5	20.5	112.9	18.5	22900	565	89.9	59	90.5	115
Minimum	1	15.99	37	5.5	17400	395	50	20	1	49.9
Maximum	4	36.99	150.9	30.9	32400	925	139.9	190	615	299.9
The national limits <sup>a</sup>	0.8	9	100	36			35	85	300	42
Dutch standard target/intervention values <sup>b/c</sup>	1/12	9/24	100/3 80	36/190			35/210	85/530	140/72 0	42/250
Background values	0.23- 2.8	19.5- 28.5	71.2- 168	11.5- 23.8	16000- 32100	261- 890	55.7- 135	19-161	55.3- 133	56.4- 225

<sup>a</sup>The national limits- Official Gazette of Serbia (2018-2019)

<sup>b</sup>Target values-Dutch standard target values (VROM, 2000)

<sup>c</sup>Intervention values - Dutch standard intervention values (VROM, 2000)

## CONCLUSION

This study explored environmental pollution by potentially toxic elements in the urban area of the Thermal Power Plant in New Belgrade, which has more than 200,000 residents. The sediment samples contained higher potentially toxic metals concentrations (Pb, Zn and Cd) than the baseline concentrations, suggesting great dynamics of natural and anthropogenic processes in this alluvion region. Chemometric methods were successively applied to evaluate the spatial variations in sediment quality and identify sources in all the investigated sites, which indicated that different methods complement and validate each other.

Road traffic was identified as the main source of anthropogenic potentially toxic metals, especially lead, cadmium and zinc. In addition, industrial activity in this region, especially thermal power plant, was identified as the source of V in some samples. The high Ni and Cr contents are believed to be of geogenic origin, coming from Quaternary eolian and alluvial sediments. Considering the Dutch quality standard, the target values for Cd, Pb, Cr, Ni, and V were exceeded in the majority of the analysed samples, indicating samples polluted above the baseline levels, but not above the intervention values.

## Acknowledgement

The authors would like to thank the Ministry of Education, Science and Technological Development (Grant No:III 43004).

## REFERENCES

- [1] Manta, D. S.; Angelone, M.; Bellanca, A.; Neri, R.; Sprovieri, M. Heavy Metals in Urban Soils: A Case Study from the City of Palermo (Sicily), Italy. *Sci. Total Environ.* 2002, 300, 229–243.
- [2] Madrid, L.; Díaz-Barrientos, E.; Madrid, F. Distribution of Heavy Metal Contents of Urban Soils in Parks of Seville. *Chemosphere* 2002, 49, 1301–1308.

- 
- [3] Biasioli, M.; Barberis, R.; Ajmone-Marsan, F. The Influence of a Large City on Some Soil Properties and Metals Content. *Sci. Total Environ*, 2006, 356, 154
- [4] Sakan, Sanja, Devic, Gordana, Relic, Dubravka, Andjelkovic, Ivan, Sakan, Nenad, Dordevic, Dragana. (2014). Evaluation of sediment contamination with heavy metals: the importance of determining appropriate background content and suitable element for normalization. *Environmental geochemistry and health*. 37. 10.1007/s10653-014-9633-4.
- [5] Regulation on Limit Values of Pollutants, Harmful and Hazardous Materials in The Land ("Official Gazette of RS", no. 30/2018 and 64/2019)
- [6] Dutch VROM. "The Circular on Target Values and Intervention Values for Soil Remediation," Dutch Ministry of Housing, Spatial Planning and Environment (VROM), 2000.

# POLYCYCLIC AROMATIC HYDROCARBONS (PAHS) IN TWO HYDROGEOCHEMICAL DIFFERENT SEDIMENTARY ENVIRONMENTS OF THE TERTIARY KREPOLJIN BROWN COAL BASIN, SERBIA

G.Devic<sup>1</sup> and M. Pergal<sup>2</sup>

<sup>1</sup>*University of Belgrade, Institute of Chemistry, Technology and Metallurgy National Institute of the Republic of Serbia, Njegoševa 12, 11000 Belgrade, Serbia*

<sup>2</sup>*Faculty of Chemistry, University of Belgrade, Studentski trg 12-16, Belgrade 11000, Serbia*

## ABSTRACT

The sediments of the coal-bearing series of the Tertiary Krepoljin Brown Coal Basin have been investigated and presented in this manuscript. The samples of the intercalated mixed sediments (pieces of coal in clays, sandstones and shales) originate from two hydrogeochemically differing sedimentary environments: the illitemontmorillonitic (IM), and the calcitic (Ct) environment. The abundances of 16 polycyclic aromatic hydrocarbons (PAHs) on the priority list of the United States Environmental Protection Agency (U.S. EPA) have been determined in 10 analyzed sediment samples. The concentrations of  $\Sigma$ PAHs in sediments ranged from 449 to 10585  $\mu\text{g/L}$ . A total of 8 of 16 PAHs, including B[a]A, Chry, B[b]F, B[k]F, B[a]P, IP, DB[a,h]A, and B[g,h,i]P, are regarded as potentially carcinogenic, indicating a higher possibility of occurrence of adverse ecological effect. High molecular-weight (HMW) PAHs are predominant in all sediments, but carcinogenic PAHs are predominant in sediments of Ct environment ( $550\mu\text{gL}^{-1}$ ). Freshwater sediments show a lower sulfur content ( $\Sigma 346\pm 19.9\mu\text{M/g}$  for IM samples, and  $402\pm 56.28\mu\text{M/g}$  for Ct samples), with organic sulfur dominating. The molar ratio of H/C play a role in the changing process in the total PAHs, followed by the molar ratio of O/C and carbon content. Non-existence of the correlation between N/C ratio and other parameters indicates unspecific changes which accompany original terrestrial organic matter.

## INTRODUCTION

Polycyclic aromatic hydrocarbons (PAHs) are a group of persistent and toxic organic pollutants that occur in environmental matrices worldwide [1].

Many studies have suggested that polycyclic aromatic hydrocarbons (PAHs) are environmental immunosuppressive contaminants.

Native PAHs in coal are of particular interest in environmental research since coal has been mined on a global scale for centuries at quantities reaching approx. 5 billion tons in 2005 [2].

Numerous environmental polycyclic aromatic hydrocarbon (PAH) sources have been reported in literature, however, unburnt coal is considered only rarely. It can carry native PAH concentrations up to hundreds, in some cases, thousands of mg/kg. The molecular structures of extractable compounds from coals consist mostly of 2–6 polyaromatic condensed rings, linked by ether or methylene bridges carrying methyl and phenol side chains. The extractable phase may be released to the aquatic environment, be available to organisms, and thus be an important PAH source. PAH concentrations and patterns in coals depend on the original organic matter type, as well as temperature and pressure conditions during coalification. The environmental impact of native unburnt coal bound PAH in soils and sediments is not well studied, and an exact source apportionment is hardly possible [2].

Here we describe the sediments from the Krepoljin Brown Coal Basin which are exploited in the small mine in East Serbia. These coals are in the low maturity range with good preservation of organic compounds. The aims of the study were as follows: (1) to investigate the concentration of PAHs in two hydrogeochemical different sedimentary environments of the Tertiary Krepoljin brown coal basin, Serbia and (2) to evaluate the potential ecological risk of PAHs.

Besides, the results provide information that is essential for establishment and implementation of sustainable and safe practices to manage and dispose of coals in the Krepoljin brown coal Basin and other coal-polluted regions.

## METHODS

A suite of 10 sediment samples was collected from the Tertiary Krepoljin brown coal basin, Serbia. The older coal-bearing series from boreholes, J-98 and J-99 (44° 15' 17" and 21° 36' 16") of the Krepoljin Basin were investigated.

The samples comprise the sedimentary sequences from the underlayers to the overlayers, including several sublayers of coal and the mixed sediments, MS (clays and sandstones containing coal fragments). According to the abundance of minerals, the following main sedimentary environments were distinguished: (1) the illite-montmorillonitic, IM and (2) calcitic environment, Ct.

Ultimate (organic carbon, elemental ratio H/C, O/C, N/C),  $\Sigma S$  analysis and soluble organic matter were performed following the previous paper [3].

*Polycyclic aromatic hydrocarbons* The obtained concentrated extracts of aromatic hydrocarbons were analyzed for the presence of the following 16 US Environmental Protection Agency (EPA) priority PAHs: naphthalene (Nap), acenaphthylene (Acy), acenaphthene (Acp), fluorene (Flr), phenanthrene (Phen), anthracene (Ant), fluoranthene (Fl), pyrene (Pyr), chrysene (Chr), benzo(a)-anthracene (BaA), benzo(b)fluoranthene (BbF), benzo(k)-fluoranthene (BkF), benzo(a)pyrene (BaP), dibenzo(a,h)anthracene (DahA), indeno(1,2,3-c,d)pyrene (IcdP), and benzo(g,h,i)perylene (BghiP). Analysis of concentrated extracts was conducted using an Agilent Technologies gas chromatograph with mass selective detector (GC/MSD) 7890A/5975C, Agilent Technologies ChemStation for instrument control and chromatogram data processing, and capillary column (Agilent Technologies HP5-MS; 30-m length, 0.25-mm inner diameter, and 0.25- $\mu\text{m}$  film layer), with He gas (5.0 specification, Linde Gas) as the carrier gas at constant flow rate of 1.5 mLmin<sup>-1</sup>.

## RESULTS AND DISCUSSION

The mean  $\pm$  standard deviation (SD), of individual PAHs calculated from data collected on all 10 tested samples are shown in Table 1. The distributions of individual PAHs showed variations. These variations are important to recognize in environmental assessments in which the contributions of PAHs derived from particulate coal must be reconciled versus PAHs derived from other sources. Generally, the observed PAH levels are high. The concentration of  $\Sigma\text{PAHs}$  in sediments ranged from 449 to 10585  $\mu\text{g L}^{-1}$ . Not only do the amounts of total PAHs in the samples vary, but also their distribution patterns vary based on the contents of the two-ring, three-five-ring, and six-ring PAHs. Four-ring PAHs were the most abundant constituent in all samples (50% of the total PAHs on average), followed by five + six-ring PAHs averaging 25%.

A total of 8 of 16 PAHs, including B[a]A, Chry, B[b]F, B[k]F, B[a]P, IP, DB[a,h]A, and B[g,h,i]P, are regarded as potentially carcinogenic. Our study also showed that B[a]A was the major compound in total PAHs and total carcinogenic PAHs in sediments from the IM and Ct samples. The benzo[a]anthracene is publicly regarded as the strongly carcinogenic matter. The mean concentration of B[a]A in sediments from the IM samples was  $152.52 \pm 75.394 \mu\text{g kg}^{-1}$ , while in Ct samples  $171.491 \pm 93.01$ , indicating a higher possibility of occurrence of adverse ecological effect. Low rank coals/sediments were dominated by high molecular PAHs (HMW PAHs). Pearson's correlation matrix was used to explore the possible relationships between PAHs in sediments with ultimate analysis and sulfur species. The sulfur content in coal is widely regarded as an indicator of the paleoenvironmental conditions under which the precursor peat accumulated. Freshwater sediments show a lower sulfur content ( $\Sigma 345.98 \pm 19.9 \mu\text{M/g}$  for IM samples, and  $402.18 \pm 56.28 \mu\text{M/g}$  for Ct samples), with organic sulfur dominating. Corg-content in the calcitic sediments (Ct) seems to be lower than in the clay-matrix I-M sediments but the difference is not statistically significant due to

the wide ranges of individual values. The molar ratio of H/C and less O/C play a role in the changing process in the PAHs. Non-existence of the correlation between N/C ratio and other parameters indicates unspecific changes which accompany original organic matter.

**Table 1.** Mean values with standard deviations of individual PAHs for two investigated sedimentation environments

	IM samples	Ct samples
Naphthalene	23.608±0.161	23.63±0.158
Acenaphthylene	31.95±0.289	31.91±0.135
Acenaphthene	29.487±0.211	29.448±0.241
Fluorene	25.698±0.107	26.056±0.691
Phenanthrene	43.990±2.47	45.354±3.88
Anthracene	16.736±1.310	17.021±1.98
Fluoranthene	94.160±55.83	69.34±56.20
Pyrene	93.021±45.373	56.790±31.873
Benzo[a]anthracene	152.52±75.394	171.491±93.01
Chrysene	68.840±30.253	76.71±36/660
Benzo[b]fluoranthene	20.850±13.143	35.116±33.582
Benzo[k]fluoranthene	33.449±14.678	49.737±38.167
Benzo[a]pyrene	37.951±6.714	42.483±33.100
Dibenzo[a,h]anthracene	12.801±3.670	12.061±20.676
Benzo[g,h,i]perylene	14.940±0.751	17.548±2.458
Indeno[1,2,3-cd]pyrene	7.494±0.915	9.040±3.00
H/C	1.156±0.08	1.167±0.178
O/C	0.331±0.041	0.575±0.105
N/C	0.0121±0.007	0.0123±0.003

## CONCLUSION

The 16 PAHs on the U.S. EPA priority list have been determined in 10 sediment samples from Krepoljin coal Basin from Serbia, using Soxhlet extraction and GC-MS. The results show that the total amount of PAHs ranged from 449 to 10585  $\mu\text{g L}^{-1}$ , of sediments in two hydrogeochemical different sedimentary environments (on a dry basis). Our study showed that B[a]A was the major compound in total PAHs and total carcinogenic PAHs in sediments from the IM and Ct samples. The mean concentration of B[a]A in sediments from the IM samples was 152.5±75.4  $\mu\text{g L}^{-1}$ , while in Ct samplers 171.5±93.01  $\mu\text{g L}^{-1}$ . The benzo[a] anthracene is publicly regarded as the strongly carcinogenic matter, indicating a higher possibility of occurrence of adverse ecological effect. Hydrogeochemical different sedimentary environments of the Tertiary Krepoljin brown coal basin, contains lower sulfur values (till 402.2±56.3  $\mu\text{M/g}$ ), with organic sulfur dominating. Corg-content in the calcitic sediments (Ct) seems to be lower than in the clay-matrix I-M sediments but the difference is not statistically significant due to the wide ranges of individual values. The molar ratio of H/C and less O/C play a role in the changing process in the PAHs. Non-existence of the correlation between N/C ratio and other parameters indicates unspecific changes which accompany original organic matter.

**Acknowledgement**

The authors would like to thank the Ministry of Education, Science and Technological Development (Grant No: 146008).

**REFERENCES**

- [1] Stout SA, Emsbo-Mattingly S. Concentration and character of PAHs and other hydrocarbons in coals of varying rank – Implications for environmental studies of soils and sediments containing particulate coal. *Org Geochem* 2008; 39: 801–19.
- [2] C. Achten, T. Hofmann. Native polycyclic aromatic hydrocarbons (PAH) in coals – A hardly recognized source of environmental contamination. *Science of the Total Environment*, 2008, 407,2461-2475.
- [3] Devic, G, Popovic, Z. Biomarker and micropetrographic investigations of coal from the Krepoljin Brown Coal Basin Serbia. *International Journal Of Coal Geology*, 2013, 105; 48-59.DOI:10.1016/j.coal.2012.11.010

## REMOVAL EFFICIENCY OF ARTIFICIAL SWEETENERS IN WASTEWATER TREATMENT PLANTS IN SERBIA

E. Gvozdić<sup>1</sup>, I. Matić Bujagić<sup>2</sup>, T. Đurkić<sup>3</sup> and S. Grujić<sup>3</sup>

<sup>1</sup> *Innovation Centre of the Faculty of Technology and Metallurgy, Karnegijeva 4, 11000 Belgrade, Serbia.*

<sup>2</sup> *Department of Environmental Engineering and Occupational Safety, Belgrade Polytechnic College, Academy of Applied Technical Studies Belgrade, Katarine Ambrozić 3, 11000 Belgrade, Serbia.*

<sup>3</sup> *University of Belgrade, Faculty of Technology and Metallurgy, Karnegijeva 4, 11000 Belgrade, Serbia. (svetlana.grujic@tmf.bg.ac.rs)*

### ABSTRACT

Artificial sweeteners have been recognized as high-priority emerging contaminants that cause great concern due to unknown environmental behavior and long-term ecotoxicological impact on water resources. Wastewater treatment plants are not designed to remove these pollutants and consequently they are continuously introduced into the aquatic environment. This paper describes investigation of four artificial sweeteners, highly abundant in urban wastewater, and their removal rate in wastewater treatment plants in Serbia, in order to assess the efficiency of the treatment to reduce their environmental inputs. For this purpose, influent and effluent wastewater samples from two treatment plants were extracted and analyzed using liquid chromatography–tandem mass spectrometry.

### INTRODUCTION

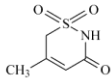
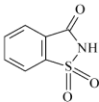
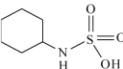
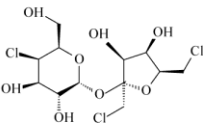
Artificial sweeteners are widely utilized as sugar substitutes in human diets and animal feeds due to their high-intensity sweetness and low caloric value [1]. Following ingestion, a large percentage of these compounds are excreted in an unchanged form [2]. As a result of wastewater effluents and untreated municipal wastewater discharges, traces of these substances have been reported in natural waters [1, 3]. Furthermore, with the increasing use of various artificial sweeteners, the long-term risks to human health and the environment resulting from continuous exposure to low levels of these compounds remain largely unknown. For that reason, artificial sweeteners are recently recognized as high-priority emerging contaminants [1]. Due to their high persistence, ubiquitous occurrence in aquatic ecosystems and incomplete removal in wastewater treatment plants (WWTPs), artificial sweeteners can be used as powerful tracers of sewage pollution [3]. Current wastewater treatments are a combination of physical, chemical and biological processes for the removal of different pollutants. However, even the most effective treatments have limited ability to completely remove all existing contaminants [3, 4]. As a consequence, WWTP effluents are a major point source of many environmental pollutants, including artificial sweeteners.

The aim of this work was to determine the levels of acesulfame, saccharin, cyclamate and sucralose in influent and effluent wastewater of two WWTPs in Serbia and their removal efficiency in order to evaluate the impact of the treatment on quality of the water resources. Due to high sensitivity and selectivity, liquid chromatography with tandem mass spectrometry (LC–MS/MS) is the method of choice for detection of traces of artificial sweeteners in complex wastewater samples.

### METHODS

The physico-chemical properties of the selected artificial sweeteners are presented in Table 1.

**Table 1.** Chemical structures and physico-chemical properties of the selected artificial sweeteners: molecular weight ( $M_w$ ), octanol-water partitioning coefficient ( $K_{ow}$ ) and water solubility at 25 °C (WS)

Artificial sweetener (formula)	Chemical structure	$M_w$ (g mol <sup>-1</sup> )	$\log K_{ow}^a$	WS <sup>a</sup> (mg L <sup>-1</sup> )
Acesulfame (C <sub>4</sub> H <sub>5</sub> NO <sub>4</sub> S)		163.1	-1.33	9.1×10 <sup>5</sup>
Saccharin (C <sub>7</sub> H <sub>5</sub> NO <sub>3</sub> S)		183.1	0.45	789.2
Cyclamate (C <sub>6</sub> H <sub>12</sub> NO <sub>3</sub> S)		179.2	-1.61	1.0×10 <sup>6</sup>
Sucralose (C <sub>12</sub> H <sub>19</sub> Cl <sub>3</sub> O <sub>8</sub> )		397.6	-1.00	2.3×10 <sup>4</sup>

<sup>a</sup> Source: ChemSpider database; <http://www.chemspider.com/>

Sewage influent as well as effluent samples were collected from two municipal wastewater treatment plants in Serbia, with the population equivalents of 25,000 (WWTP1) and 2,000 (WWTP2). Conventional treatment processes of the two treatment plants include primary precipitation coupled with secondary biological activated sludge treatment. Sampling was performed over a time range of 4 hours and composite samples were taken.

The wastewater samples were filtered through 1–3 µm glass fiber filters and prepared for the analysis using solid-phase extraction (SPE). In a SPE procedure, a 50 mL of the water sample, with pH adjusted to 3.0, was loaded onto Oasis HLB cartridge (200 mg/6 mL) from Waters, USA. Sweeteners were eluted with 10 mL of methanol and extract was evaporated and reconstituted to 0.5 mL.

LC analysis was performed using Dionex UltiMate 3000 HPLC system (Thermo Fisher Scientific, Waltham, US). The chromatographic separation was carried out on Luna® C8 (3.0 mm × 150 mm, 3 µm) column. Mobile phase consisted of (A) deionized water, (B) methanol and (C) 0.1 mol L<sup>-1</sup> aqueous solution of ammonium acetate. The mass spectra were recorded by LTQ XL (Thermo Fisher Scientific) linear ion trap mass spectrometer using electrospray ionization (ESI) in the negative ionization mode.

## RESULTS AND DISCUSSION

All investigated artificial sweeteners were found at high levels in influents of both treatment plants (up to 9631 ng L<sup>-1</sup> for cyclamate), with WWTP1 showing much heavier wastewater burden reflecting the number of inhabitants in the investigated area (Table 2). For both WWTPs, very low removal efficiency of acesulfame was noted (19.8% and 0.3%, respectively). These results are in accordance with other authors who indicated that acesulfame, along with sucralose, was the most persistent sweetener in wastewater treatment [3, 4]. For this reason, both can be used as chemical markers for tracing municipal wastewater contamination in the aquatic environment. In our study, only WWTP2 showed low elimination rate of sucralose (21.4%), while WWTP1 was more efficient in sucralose removal (64.5%). The highest removal efficiency in both WWTPs was achieved for cyclamate (68.8 % and 94.1%, respectively). The results of similar studies showed that the highest removal rates were

usually obtained for cyclamate and saccharin (up to 94%) [3, 4]. However, our results for elimination of saccharin showed that WWTP1 was less efficient (28.9%), whereas WWTP2 showed higher elimination potential (69.5%). Biodegradation is considered a key mechanism for elimination of artificial sweeteners in biological wastewater treatment, while sorption plays a minor role due to their high water solubility [1].

**Table 2.** Concentrations of artificial sweeteners detected in influents and effluents and removal efficiency (RE)

Artificial sweeteners	Concentration $\pm$ SD (ng L <sup>-1</sup> )		RE (%)	
	Influent	Effluent		
WWTP1	Acesulfame	5436 $\pm$ 176	4365 $\pm$ 225	19.8
	Saccharin	7080 $\pm$ 452	5033 $\pm$ 511	28.9
	Cyclamate	9631 $\pm$ 337	3009 $\pm$ 198	68.8
	Sucralose	7174 $\pm$ 111	2544 $\pm$ 178	64.5
WWTP2	Acesulfame	1600 $\pm$ 98	1596 $\pm$ 127	0.3
	Saccharin	3800 $\pm$ 301	1200 $\pm$ 117	69.5
	Cyclamate	1700 $\pm$ 88	100 $\pm$ 12	94.1
	Sucralose	1400 $\pm$ 95	1100 $\pm$ 85	21.4

## CONCLUSION

The determined high levels of selected artificial sweeteners in both influent and effluent samples and low or incomplete removal in WWTPs indicate continuous contamination of the aquatic environment in Serbia with these substances. Only in the case of cyclamate, high removal rate was determined. Nevertheless, the results have confirmed importance and crucial impact of municipal wastewater treatment on the quality of the water resources and reduction of environmental inputs of the pollutants.

## Acknowledgement

This work was supported by the Ministry of Education, Science and Technological Development of the Republic of Serbia (Contract no. 451-03-9/2021-14/200287 and 451-03-9/2021-14/200135).

## REFERENCES

- [1] J. Luo, Q. Zhang, M. Cao, L. Wu, J. Cao, F. Fang, C. Li, Z. Xue, Q. Feng, *Science of the Total Environment*, 2019, 653, 1149–1160.
- [2] A. G. Renwick, *Xenobiotica*, 1986, 16, 1057–1071.
- [3] M. Scheurer, H.-J. Brauch, F. T. Lange, *Analytical and Bioanalytical Chemistry*, 2009, 394, 1585–1594.
- [4] B. Subedi, K. Kannan, *Environmental Science and Technology*, 2014, 48, 13668–13674.

## VISCOSE-BASED ACTIVATED CARBON MATERIAL FOR MALATHION REMEDIATION

T. Tasić <sup>1</sup>, N. Potkonjak <sup>2</sup> and T. Lazarević-Pašti <sup>2</sup>

<sup>1</sup> *University of Belgrade, Faculty of Physical Chemistry, Studentski Trg 12, 11000 Belgrade, Serbia.*

<sup>2</sup> *University of Belgrade, VINČA Institute of Nuclear Sciences - National Institute of the Republic of Serbia, Mike Petrovica Alasa 12-14, 11000 Belgrade, Serbia. (lazarevictlj@yahoo.com)*

### ABSTRACT

Extensive use of the malathion invokes the development of efficient procedures for its elimination from the environment. Viscose-based activated carbon material was used for malathion removal from water. It was shown that 1 g of investigated material is capable to adsorb 0.727 g of malathion. Also, the toxicity of all samples was decreased after the treatment with the adsorbent.

### INTRODUCTION

Organophosphorus pesticides (OPs) play an important role in the improvement of agricultural production by controlling various diseases. A common application of OPs in agriculture also leads to high-level OP residues in food and the environment, which is highly undesirable. Their toxic effects of OPs are related to the irreversible inhibition of the enzyme acetylcholinesterase (AChE) [1].

Malathion (Figure 1) is a pesticide widely used in agriculture and public health pest control programs, such as mosquito eradication. It is the most commonly used organophosphate insecticide in the USA. Malathion exhibits moderate to high toxicity. Absorption or ingestion of malathion into the human body results in its transformation to malaoxon, which is significantly more toxic [1].

Efficient new methods for removal of OPs are necessary to decrease the level of these compounds in food and the environment. So far, various adsorbents have been applied to remove malathion from wastewaters, such as activated carbon, rice husk, activated rice husk, bagasse fly-ash from sugar industry waste, clays and organ clays [2]. Carbon materials gave promising results as adsorbents for the OPs removal [1, 3]. Considering the interaction of OPs with carbon materials, the interactions with  $\pi$  conjugated systems and functional groups present on the materials' surface play very important roles [3]. Various plant materials, being easily accessible, economically and environmentally friendly, are gaining increasing importance as precursors for the production of cheaper activated carbon (AC) with specific structure and properties.

In this contribution, viscose-based AC material was considered as adsorbent for the malathion removal from water. In addition, we assess the toxicity of the samples after the treatment to exclude the transformation of malathion to more toxic products.

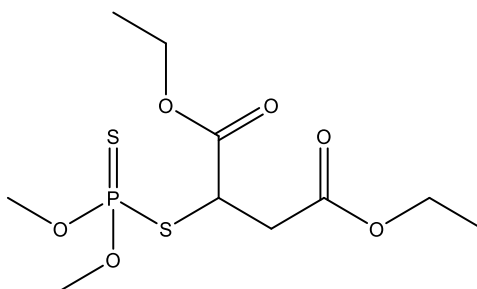


**Figure 1.** Structure of malathion.

## METHODS

Viscose fibers were dried for 24 h at 90 °C and then impregnated for 15 min in 11.4 mM solution of diammonium hydrogen phosphate (DAHP). After spin-drying for 15 min, the impregnated fibers were stored in the drying cabinet at 90 °C for 24 h. Then, the fibers were carbonized under a nitrogen atmosphere with a heating rate of 1.0 °C min<sup>-1</sup> and held isothermally for 20 min at 850 °C. Afterward, the carbonized fibers were activated in a rotary kiln at 870 °C for 165 min in a CO<sub>2</sub>-flow of 80 L h<sup>-1</sup>. The adsorbent was dispersed in double-distilled water (0,1 mg mL<sup>-1</sup>), and the desired amount of OP stock solution was added to provide the targeted concentration of adsorbent and OP. The vessel containing the adsorbent + OP mixture was placed on a laboratory shaker and left overnight at 25 °C to ensure that equilibrium was reached. After that, the mixture was centrifuged for 10 min at 14500 rpm, and the supernatant was filtered through a nylon filter membrane. The concentration of OP was determined using UPLC analysis [2]. Control experiments were performed identically but without adsorbent. AChE activity was assayed according to modified Ellman's procedure [3].

## RESULTS AND DISCUSSION

In order to investigate the process of adsorption, 0.1 mg cm<sup>-3</sup> adsorbent was incubated with malathion in the concentration range from 5×10<sup>-5</sup> to 5×10<sup>-3</sup> M for 24 h at 25 °C. The concentration of adsorbed malathion was calculated as a difference between its initial concentration (C<sub>0</sub>) and the concentration of malathion measured with UPLC after removing the adsorbent. The results are presented in Figure 2. Experimental results were fitted with the Hills equation to determine the specific parameters of adsorption. It was shown that the maximal concentration of malathion adsorbed on 0.1 mg cm<sup>-3</sup> adsorbent is 2.2×10<sup>-4</sup> M. From those data, it was calculated that 1 g of investigated material is capable of adsorbing 0.727 g of malathion. In comparison to literature data, this value is rather high [4].

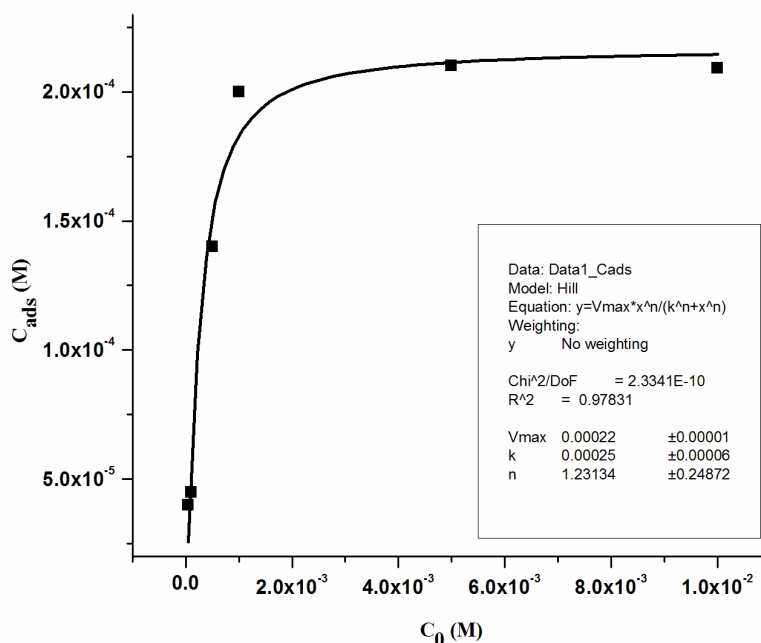


**Figure 2.** Dependence of the concentration of adsorbed malathion on its initial concentration after the incubation with 0.1 mg cm<sup>-3</sup> adsorbent for 24 h at 25 °C.

The samples were also tested in terms of their ability to inhibit the activity of AChE before and after the treatment with adsorbent. Results obtained are presented in Table 1. In all cases, the activity of AChE is increased after the incubation with adsorbent. Results have suggested that the treatment of water contaminated with malathion is successful in terms of its detoxification, and there are no more toxic products formed.

**Table 1.** AChE activity (% of control) of the malathion solutions in the concentration range from  $5 \times 10^{-5}$  to  $5 \times 10^{-3}$  M before and after the treatment with  $0.1 \text{ mg cm}^{-3}$  adsorbent.

$C_0 / \text{M}$	AChE activity / % of control	
	before the treatment	after the treatment
$5 \times 10^{-5}$	51	100
$1 \times 10^{-4}$	45	80
$5 \times 10^{-4}$	10	46
$1 \times 10^{-3}$	0	37
$5 \times 10^{-3}$	0	15

## CONCLUSION

Viscose-based activated carbon material was used for malathion removal from water. It was shown that 1 g of investigated material is capable of adsorbing 0.727 g of malathion. Also, the toxicity of all samples was decreased after the treatment with the adsorbent. Remediation of malathion using the selected adsorbent was successful.

## Acknowledgement

This work was partially supported by the Ministry for Science of the Republic of Serbia (Grant no. 451-03-9/2021-14/200017).

## REFERENCES

- [1] T. Lazarević-Pašti, I. Pašti, B. Jokić, B. Babić, V. Vasić, RSC Advances, 2016, 6 (67), 62128-62139.
- [2] M. Mirković, T. Lazarević-Pašti, A. Došen, M. Čebela, A. Rosić, B. Matović, B. Babić, RSC Advances, 2016, 6 (15), 12219-12225.
- [3] T. Lazarević-Pašti, V. Aničijević, M. Baljzović, D. Vasić Aničijević, S. Gutić, V. Vasić, N. Skorodumova, I. Pašti, Environmental Science: Nano, 2018, 5 (6), 1482-1494.
- [4] T. Momić, T. Lazarević-Pašti, U. Bogdanović, V. Vodnik, A. Mraković, Z. Rakočević, V. Pavlović, V. Vasić, Journal of Nanomaterials, 2016, 2016, art. no. 8910271.

## GRAPHENE OXIDE AS AN ADSORBENT FOR DIMETHOATE REMOVAL FROM WATER

V. Anićijević<sup>1</sup>, N. Potkonjak<sup>2</sup> and T. Lazarević-Pašti<sup>2</sup>

<sup>1</sup>University of Belgrade, Faculty of Physical Chemistry, Studentski Trg 12, 11000 Belgrade, Serbia.

<sup>2</sup>University of Belgrade, VINČA Institute of Nuclear Sciences - National Institute of the Republic of Serbia, Mike Petrovica Alasa 12-14, 11000 Belgrade, Serbia. (lazarevictlj@yahoo.com)

### ABSTRACT

Nowadays, the use of organophosphate pesticide dimethoate is widespread. Dimethoate is toxic for mammals, so efficient procedures for its elimination from the environment are necessary. We used graphene oxide for dimethoate removal from water. It was shown that 1 g of investigated material is capable of adsorbing  $8.8 \times 10^{-3}$  mol of dimethoate. A satisfactory agreement of experimental results with the Langmuir isotherm model suggests the monolayer adsorption on the homogenous surface.

### INTRODUCTION

Organophosphorus pesticides (OPs) have been used globally since the first introduction of synthetic insecticide parathion for crop protection in 1944. Their high stability, environmental endurance, poor biodegradability and extensive usage led to pesticide accumulation in our environment, particularly in water [1].

Dimethoate (Figure 1) is a very powerful pesticide. It has harmful effects on the health of humans and animals because of its toxicity even at low concentrations (liver, endocrine organs, lymphatic system, chronic renal disease, parathyroid hyperplasia, oxidative stress, DNA damage in rainbow trout, and a skin irritant). World Health Organization classified it as "moderately hazardous" with a guideline value of  $6 \mu\text{g dm}^{-3}$  in drinking water. However, due to oxidation, dimethoate transforms to omethoate (Figure 1), its oxo analog, which is more toxic than dimethoate. Omethoate could also be found in the environment due to the presence of various oxidizing agents. Therefore, systematic work is needed to develop new methods for efficient dimethoate and omethoate removal from the environment [1].

One of the main strategies for the removal of pesticides from water is the adsorption on different types of materials. Numerous studies can be found in the literature reporting OPs adsorption on mineral surfaces, carbon-based materials, and nanoparticles [2-4]. Since the discovery of graphene in 2004, it has attracted overwhelming attention due to its unique chemical and physical properties compared to other graphitic forms [2]. Functionalization of graphene with molecules that have water solubility and affinity toward target analysts improves the selectivity of adsorbents and prevents aggregation. Based on this idea, diverse derivatives of graphene have been reported and applied to environmental protection, especially graphene oxide and reduced graphene oxide.

In this contribution, graphene oxide was considered as an adsorbent for the removal of dimethoate from water. In addition, we evaluate experimental results with the Langmuir isotherm model to determine the specific parameters of the adsorption process.

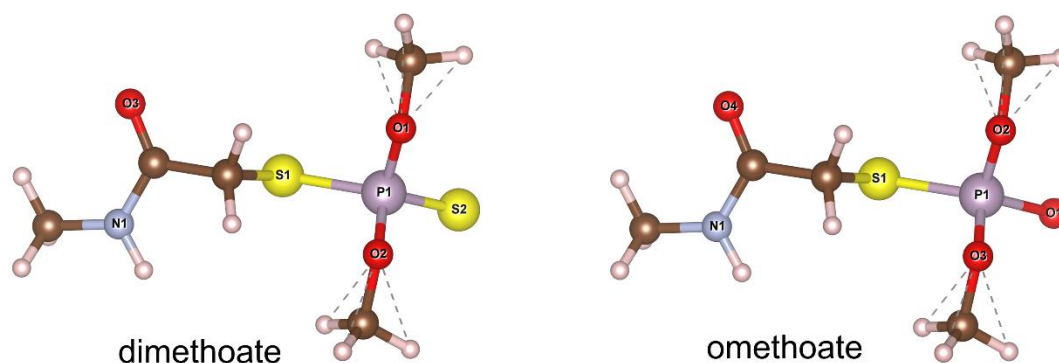


**Figure 1.** The structure of dimethoate and omethoate.

## METHODS

Graphene oxide (GO) was dispersed in double-distilled water ( $0.01$  and  $0.05 \text{ mg cm}^{-3}$ ), and the desired amount of dimethoate stock solution was added to provide the targeted concentration of adsorbent and OP. Then, the vessel containing the mixture of GO and dimethoate was placed on a laboratory shaker and left overnight at  $25 \text{ }^\circ\text{C}$  to ensure that equilibrium was reached. After equilibration, the mixture was centrifuged for 10 min at 14500 rpm, and the supernatant was filtered through a nylon filter membrane. The concentration of dimethoate was determined using Waters ACQUITY ultra performance liquid chromatography (UPLC) system coupled with a tunable UV detector. Chromatographic separations were run on an ACQUITY UPLC™ BEH C18 column with the dimensions  $1.7 \text{ }\mu\text{m}$ ,  $100 \text{ mm} \times 2.1 \text{ mm}$  (Waters). The analyses of dimethoate solutions were done under isocratic conditions with the mobile phase consisting of 10% acetonitrile and 90% water (v/v). The eluent flow rate was  $0.2 \text{ cm}^3 \text{ min}^{-1}$ , and the injection volume was  $10^{-5} \text{ dm}^3$ . Optical detection of dimethoate was done at 200 nm. Under the described conditions, the retention time of dimethoate was  $1.73 \pm 0.05 \text{ min}$ . Control experiments were performed identically but without adsorbent.

## RESULTS AND DISCUSSION

In order to investigate the process of adsorption,  $0.01$  and  $0.05 \text{ mg cm}^{-3}$  of GO was incubated with dimethoate in the concentration range from  $1 \times 10^{-5}$  to  $1 \times 10^{-3} \text{ M}$  for 24 h at  $25 \text{ }^\circ\text{C}$ . The concentration of adsorbed dimethoate was calculated as a difference between its initial concentration ( $C_0$ ) and the equilibrium concentration ( $C_e$ ) of dimethoate measured with UPLC after removing the adsorbent. Adsorption capacity ( $q_e$ ) represents the equilibrium concentration of dimethoate *per* 1 g of GO. Experimental results were evaluated by the Langmuir isotherm model [3] to determine the specific parameters of adsorption. The results are presented in Figure 2. and Table 1.

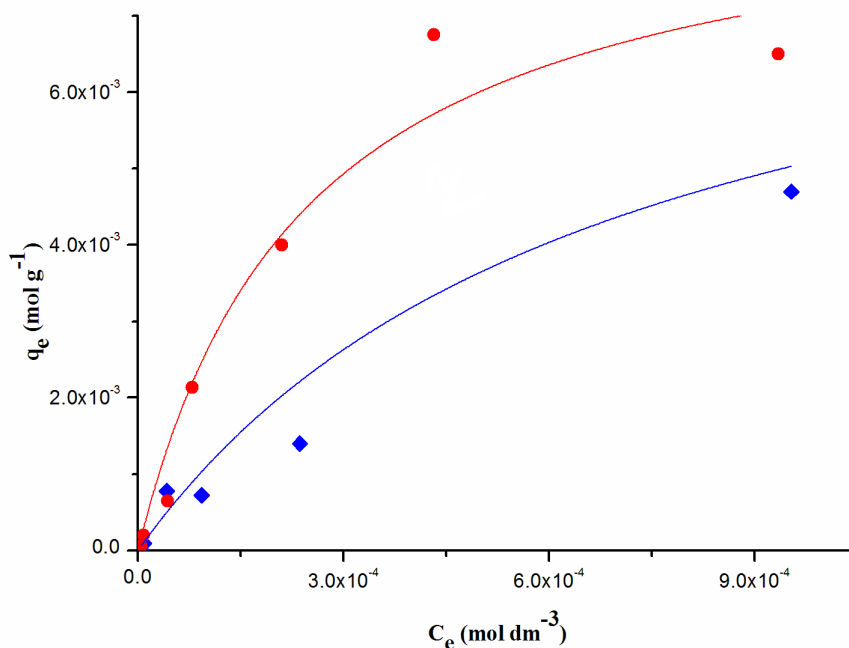


**Figure 2.** Experimental data for 0.01 (rhombus) and 0.05 (circles) mg mL<sup>-1</sup> GO fitted with the Langmuir adsorption isotherm.  $q_e$  (mol g<sup>-1</sup>)

From the data presented in Table 1, it can be concluded that a satisfactory agreement, the coefficient of determination ( $R^2$ ), was achieved in both cases with the Langmuir model. Also, the maximum adsorption capacity ( $q_{\max}$ ) and the Langmuir constant ( $K_L$ ) were calculated. Results obtained suggest complete monolayer coverage on the GO homogenous surface. It was shown that 1 g of GO is able to adsorb  $8.8 \times 10^{-3}$  mol of dimethoate. In comparison to literature data, this value is considerably higher [4].

**Table 1.** Parameters of the Langmuir isotherm model: the maximum adsorption capacity ( $q_{\max}$ ), the Langmuir constant ( $K_L$ ) and the coefficient of determination ( $R^2$ ) for a GO concentration of 0.01 and 0.05 mg mL<sup>-1</sup>.

Parameters	0.01	0.05
Graphene oxide (mg mL <sup>-1</sup> )	0.01	0.05
$q_{\max}$ (mol dm <sup>-3</sup> g <sup>-1</sup> )	$(8.7 \pm 3.4) \times 10^{-3}$	$(8.9 \pm 1.2) \times 10^{-3}$
$K_L$ (dm <sup>3</sup> mol <sup>-1</sup> ) <sup>n</sup>	$(1.5 \pm 1.1) \times 10^4$	$(4.1 \pm 1.5) \times 10^4$
$R^2$	0.9452	0.9530

## CONCLUSION

Graphene oxide was used for dimethoate removal from water. It was shown that 1 g of graphene oxide is capable of adsorbing  $8.8 \times 10^{-3}$  mol of dimethoate. A satisfactory agreement of experimental results with the Langmuir isotherm model suggests the monolayer adsorption on the homogenous surface. The removal of dimethoate from water was successfully done by using graphene oxide.

**Acknowledgement**

This work was partially supported by the Ministry for Science of the Republic of Serbia (Grant no. 451-03-9/2021-14/200017).

**REFERENCES**

- [1] T. Mitrović, S. Lazović, B. Nastasijević, I. Pašti, V. Vasić, T. Lazarević-Pašti, *Journal of Environmental Management*, 2019, 246, 63-70.
- [2] T. Lazarević-Pašti, V. Anićijević, M. Baljozović, D. Vasić Anićijević, S. Gutić, V. Vasić, N. Skorodumova, I. Pašti, *Environmental Science: Nano*, 2018, 5 (6), 1482-1494.
- [3] V. Anićijević, T. Lazarević-Pašti, V. Vasić, D. Vasić Anićijević, *Applied Sciences*, 2021; 11(9), 4014-4028.
- [4] T. Momić, T. Lazarević-Pašti, U. Bogdanović, V. Vodnik, A. Mraković, Z. Rakočević, V. Pavlović, V. Vasić, *Journal of Nanomaterials*, 2016, 2016, art. no. 8910271.

## DOES HUMIFICATION TAKE PLACE DURING BIODEGRADATION OF PETROLEUM HYDROCARBON?

J. Avdalović<sup>1</sup>, N. Lugonja<sup>1</sup>, K. Joksimović<sup>1</sup>, M. Lukić<sup>2</sup>, J. Milić<sup>1</sup>,  
Z. Lopičić<sup>3</sup>, J. Milojković<sup>3</sup>

<sup>1</sup>University of Belgrade, Institute of Chemistry, Technology and Metallurgy,  
Njegoševa 12, 11000 Belgrade, Serbia. (jelena.avdalovic@ihtm.bg.ac.rs)

<sup>2</sup>University of Belgrade, Faculty of Chemistry, Studentski trg 12-16, 11000 Belgrade, Serbia.

<sup>3</sup>Institute for Technology of Nuclear and Other Mineral Raw Materials, Bulevar Franš d'Eperea 86,  
Belgrade, Serbia

### ABSTRACT

The aim of this paper was to study using an active consortium of zymogenic microorganisms for *ex situ* biodegradation of a petroleum hydrocarbon, along with simultaneous monitoring of the humification process.

In this study, the biopile (B) and control biopile (CB) for *ex situ* bioremediation consisted of soil polluted with petroleum and its derivatives. The initial level of total petroleum hydrocarbon (TPH) in the B and CB was 26 g kg<sup>-1</sup>. At the end of the study, TPH were reduced to 4 g kg<sup>-1</sup> in B, but only to 24 g kg<sup>-1</sup> in the CB. The starting material contained 2.79% of humic acids (HAs) while at the end of study, HAs in the B had increased to 3.88%, in contrast, in CB, only a very small increase of HAs, to 2.90% was noted. Also, the quality of humification was monitored by determining parameters such as HAs/FAs (the humic acid/fulvic acid ratio) and HI (C<sub>HAs</sub>/TOC).

The current results show undoubtedly that humification occurred during biodegradation of petroleum hydrocarbon.

### INTRODUCTION

The accumulation of waste materials of various origins causes increased pollution of the environment. Petroleum and its derivatives such are one of the major and most dangerous pollutants of soil. Biodegradation is a method of reducing petroleum pollution that has been widely used in recent years. Biodegradation is based on the natural capacity of microorganisms to degrade or transform toxic substances from the environment into harmless products [1].

Some scientists [2] believe that during biodegradation of polycyclic aromatic hydrocarbons (PAH), humin-like substances can be produced. This possibility could be a very important factor in the usefulness of bioremediating polluted soils, because humic substances are a key element in soil quality.

Fractionation of humic substances into humic acids (HAs), fulvic acids (FAs) and humin is based on their solubility in alkaline and acid dilute solutions. The FAs compose the fraction soluble in both alkali and acid dilute solutions. The HAs are soluble in alkali but not in acid, while the humin fraction is insoluble in both alkaline and acid conditions [3].

Some authors have proposed one indicator of humification based on monitoring the concentration of HAs [4], whereas others think that the quality of humification can be evaluated by determining HAs/FAs= C<sub>HAs</sub>/C<sub>FAs</sub> (the humic acid/fulvic acid ratio) [5] and HI (C<sub>HAs</sub>/C<sub>X</sub>100) [6], C<sub>HAs</sub>, C<sub>FAs</sub> and C are, respectively, the dissolved organic carbon in the HAs, in the FAs and the total organic carbon in the solid material.

The aim of this study was to investigate the relationship between bioremediation and humification processes and to determine quantitative changes of humic substances isolated during bioremediation of soil polluted with petroleum and its derivatives.

## METHODS

The biopile (B) and control biopile (CB) for *ex situ* bioremediation consisted of soil polluted with petroleum and its derivatives. Both (biopile and control biopile) contained added sawdust to increase the water holding capacity and aeration, and as an alternative source of carbon, BioSolve®CLEAR, to increase dispersion of petroleum hydrocarbons in water, and to increase the contact surface between microorganisms and lipophilic pollutants. Sources of nitrogen, phosphorus and potassium were added for biostimulation. During bioremediation, the B was watered, turned and mixed every 10 d to maintain the required moisture and aeration levels. Finally, an enriched consortium of hydrocarbon-degrading microorganisms was added every two weeks to enhance microbial activity on B. This pilot bioremediation study lasted 90 days.

The content of total petroleum hydrocarbon (TPH) in the sample was extracted as per method ISO 16703 [7]. The results were calculated according to dry matter.

The microorganisms were determined as previously described [8].

The determination of HAs and humification parameters were determined as previously described [9].

## RESULTS AND DISCUSSION

The initial level of TPH in the B was  $26 \text{ g kg}^{-1}$ . At the end of the study, TPH were reduced to  $4 \text{ g kg}^{-1}$  in B, but only to  $24 \text{ g kg}^{-1}$  in the CB. The number of naturally-occurring hydrocarbon-degrading microorganisms in CB was  $3.1 \times 10^3 \text{ CFU g}^{-1}$ , and the number of hydrocarbon-degrading microorganisms in B was  $7.7 \times 10^9 \text{ CFU g}^{-1}$ , at the end of the *ex situ* bioremediation process. The starting material contained 2.79% HAs, while at the end of study, HAs in the B had increased to 3.88%; in contrast, in CB, only a very small increase of HAs, to 2.90, was noted.

The parameters which describe and quantify the humification processes during bioremediation process are shown in Figure 1.

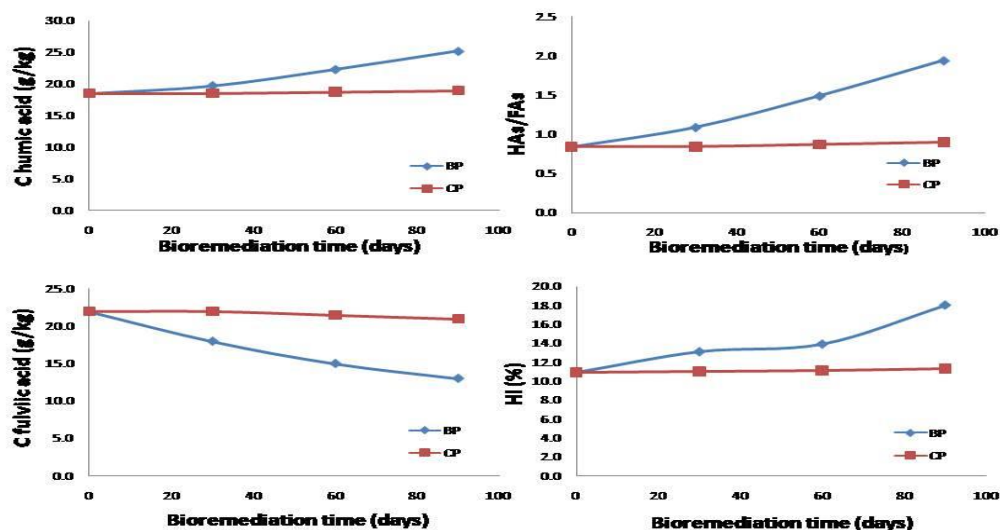


**Figure 1.** The parameters which describe the humification processes

Compared to HAs, FAs are relatively mobile, available and immature fractions. To some extent, microorganisms could utilize the readily available organic substance (i.e., FAs) as the energy source. In addition, the unstable humic components (i.e., FAs) could be converted to stable components (i.e.,

HAs). Therefore, FAs concentration was decreased, and HAs concentration was increased during bioremediation. The humification indexes (including HAs/FAs and HI) accurately indicate the degree of humification. Among them, the HAs/FAs ratio is widely used to describe the relative sequestration speed of HAs and FAs. The increase of HI suggested the enhancement of the structural complexity of humic substances [6]. With the process of bioremediation, the HAs/FAs ratio and HI had increased (Fig. 1).

## CONCLUSION

The results obtained show that humification occurs during the bioremediation. It is probably a result of the fact that organic compounds which are the most resistant to biodegradation can be transformed and incorporated into materials analogous to humic substances. It is believed, that residual materials, after the process of biodegradation of petroleum and its derivatives, are not a serious danger for environment, on the contrary, the humic acids formed generally contribute to improvement of the environment.

## Acknowledgement

This work was financially supported by the Ministry of Education, Science and Technological Development of the Republic of Serbia (Grant no. 451-03-9/2021-14/200026 and Grant no. 451-03-9/2021-14/200023).

## REFERENCES

- [1] F. Gomez, M. Sartaj, *Int. Biodeter. Biodegr.*, 2014, 89, 103-109.
- [2] B.P. Ressler, H. Kneifel, J. Winter, *Appl. Microbiol. Biot.* 1999, 53, 85-91.
- [3] F.J. Stevenson, *Humus chemistry: genesis, composition, reactions*, Wiley, New York, 1994.
- [4] P. Castaldi, G. Alberti, R. Merella, P. Melis, *Waste Manage.*, 2005, 25, 209-213.
- [5] M. Domeizel, A. Khalil, P. Prudent, *Bioresour. Technol.*, 2004, 94, 177-184.
- [6] Z. Zhang, Y. Zhao, T. Yang, Z. Wei, Y. Li, Y. Wei, X. Chen, L. Wang, *Bioresour. Technol.* 2019, 291, 121882.
- [7] ISO 16703, *Soil quality – Determination of content of hydrocarbon in the range C10 to C40 by gas chromatography*, Geneva, 2004.
- [8] G.D. Gojgić-Cvijović, J.S. Milić, T.M. Šolević, V.P. Beškoski, M.V. Ilić, L.S. Djokić, T.M. Narančić, M.M. Vrvic, *Biodegradation*, 2012, 23, 1-14.
- [9] T. Jednak, J. Avdalović, S. Miletić, L. Slavković-Beškoski, D. Stanković, J. Milić, M. Ilić, V. Beškoski, G. Gojgić-Cvijović, M.M. Vrvic, *Int. Biodeter. Biodegr.*, 2017, 122, 47-52.

## DYNAMICS OF DIESEL BIODEGRADATION BY *PLANOMICROBIUM* SP ISOLATED FROM PETROLEUM CONTAMINATED SOIL

J. Milić<sup>1</sup>, J. Avdalović<sup>1</sup>, T. Šolević Knudsen<sup>1</sup>, M. Ilić<sup>1</sup>, N. Lugonja<sup>1</sup> and M.M. Vrvic<sup>2</sup>

<sup>1</sup>University of Belgrade, Institute of Chemistry, Technology and Metallurgy, Njegoševa 12, 11000 Belgrade, Serbia. (jelena.avdalovic@ihtm.bg.ac.rs)

<sup>2</sup>BREM GROUP Ltd, Str. Oslobođenja 39b, 11090 Belgrade, Serbia

### ABSTRACT

A direct consequence of the use of fossil fuels is the environmental contamination during production, processing and distribution. Microbial biodegradation is efficient technique for cleaning contaminated areas which follows the principles of sustainability. This paper presents the dynamics of biodegradation of hydrocarbon fractions of diesel D2, using *Planomicrobium* sp. RNP01 isolated from the area contaminated with petroleum pollutants. The obtained results showed that after 30 days of biodegradation of diesel D2 significant degradation is achieved, with almost complete degradation of *n*-alkanes and decrease in the amount of sesquiterpane.

### INTRODUCTION

A direct consequence of the use of fossil fuels is the environmental contamination by petroleum hydrocarbons during production, processing and distribution. Decontamination of polluted sites is based on physical, chemical and biological principles, with the aim of making the process as energy efficient as possible and to produce as little waste as possible. Methods that use biological principles are increasingly taking precedence over other methods because they are using natural pathways for degradation of hydrocarbons, producing almost no waste, and have possibility of use direct solar energy to achieve optimal temperature for microorganism's metabolism [1]. This paper presents the dynamics of biodegradation of hydrocarbon fractions of a petroleum derivate diesel D2, using a bacterial strain *Planomicrobium* sp. RNP01 isolated from the area contaminated with petroleum pollutants.

### METHODS

Biodegradation of diesel D2 by *Planomicrobium* sp. RNP01 was tested in laboratory conditions, in Erlenmeyer flasks with microbiological medium and diesel D2 as only source of carbons. Erlenmeyers were incubated for 30 days at 28°C and 200 rpm [2]. Decrease in total petroleum hydrocarbons (TPH) content was monitored every ten days. Dynamics of diesel fuel biodegradation was monitored by gravimetric analysis of TPH and gas chromatographic-mass spectrometric (GC-MS) analysis of diesel D2. The control was prepared and treated at the same way as sample, but did not contain microorganism.

### RESULTS AND DISCUSSION

Gravimetric analysis of TPH content revealed the fastest rate of biodegradation in the first 10 days of experiment (53% TPH biodegraded), and after that the process was slowed down. In the next 10 days, bacteria biodegraded around 16% of TPH, and during the third 10 days of experiment, 14% of TPH has been biodegraded. In total, *Planomicrobium* sp. RNP01 achieved biodegradation of 83,1% of diesel D2 during 30 days.

### GC-MS analysis of biodegradation of saturated diesel D2 hydrocarbons

The dominant compounds of the hydrocarbon fraction at the start were *n*-alkanes and the isoprenoids pristane and phytane. GC-MS analysis indicated a gradual decrease of *n*-alkanes and isoprenoids over 30 days. After 30 days, *n*-alkanes and isoprenoids of lower number of C atoms (C<sub>11</sub>-C<sub>19</sub>) could not be observed, which indicated their complete degradation. *n*-Alkanes and isoprenoids with a larger number of C atoms (max peak at C<sub>21</sub>) were dominant (Figure 1).

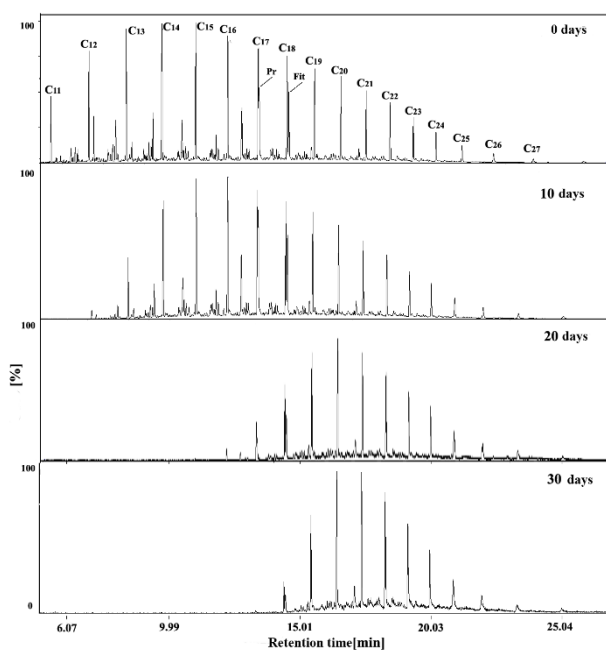


**Figure 1.** TIC chromatograms of degradation of the hydrocarbon fractions by the *Planomicrobium* sp. RNP01 after 10, 20 and 30 (Pr - pristane, Phyt - phytane)

### GC-MS analysis of alkane and isoprenoid fractions during biodegradation of diesel D2

The chromatogram of *n*-alkanes and isoprenoids (m/z 57) is characterized by the presence of *n*-alkanes in the range C<sub>11</sub>-C<sub>27</sub> with uniform distribution of even and odd homologues (Figure 2).

By comparing the chromatogram of alkanes in sample after 20 days of the experiment and start, it can be concluded that *n*-alkanes lower than C<sub>20</sub> were significantly removed due to the biodegradation activity of *Planomicrobium* sp. RNP01. Pristane could no longer be identified. Phyt/n-C<sub>18</sub> ratio slightly decreased (0.82) but the abundance of both, Phyt and n-C<sub>18</sub> was affected by biodegradation. According to the obtained results, biodegradation of *n*-alkanes started already in the first ten days of the experiment, while the degradation of isoprenoids began after 10 days of the experiment.

After 30 days of the experiment, the degradation extended to all homologues lower than C<sub>21</sub> including both, *n*-alkane and isoprenoids. Alkanes and isoprenoids with lower number of C atoms were completely degraded and the peak fragmentogram shifted to C<sub>21</sub>.

### GC-MS analysis of sesquiterpenes during biodegradation of diesel D2

Polymethyl-substituted decalins or decahydronaphthalenes (C<sub>14</sub>-C<sub>16</sub> bicyclic alkanes), commonly known as sesquiterpenes are bicyclic petroleum biomarkers and represent the largest group of biomarkers within the terpenoid class. Compared to other components in petroleum, including *n*-alkanes and most aromatic compounds, those biomarkers show greater resistance to degradation by microorganisms [3]. For lighter petroleum derivatives where most diesel and jet fuels are included, the refining process removes most high molecular weight biomarkers from the initial crude oil blend. Because of that, tetracyclic and pentacyclic terpanes are in low content, while sesquiterpenes are concentrated in these fractions [4]. Sesquiterpenes were monitored in m/z 123 ion fragmentogram and ion confirmation could be obtained in m/z 179, m/z 193 and m/z 207 ion fragmentograms (Figure 3).

The obtained results showed that after 10 days of the experiment there was some change in the abundance of the first five sesquiterpanes in the chromatogram. This group of compounds, although very resistant to biodegradation, was degraded between the 10th and 20th day of biodegradation by the action of *Planomicrobium sp.* RNP01.

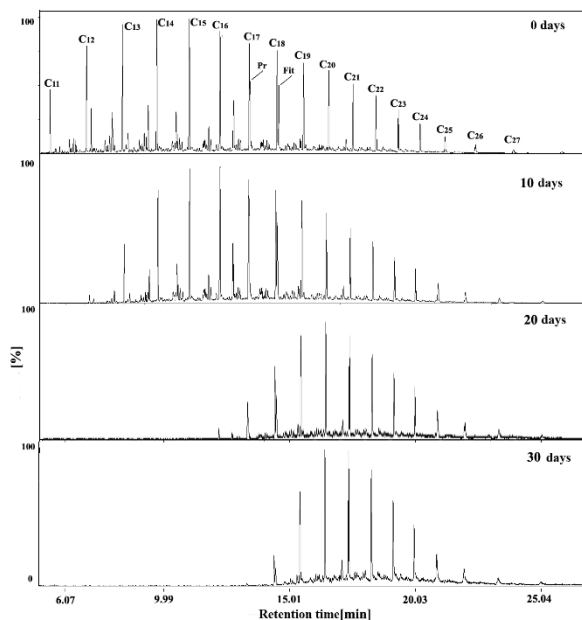


**Figure 2.** GC-MS fragmentograms of *n*-alkanes and isoprenoids (*m/z* 57) of hydrocarbon fractions by the *Planomicrobium sp.* RNP01 (Pr-pristane, Phyt-phytane)

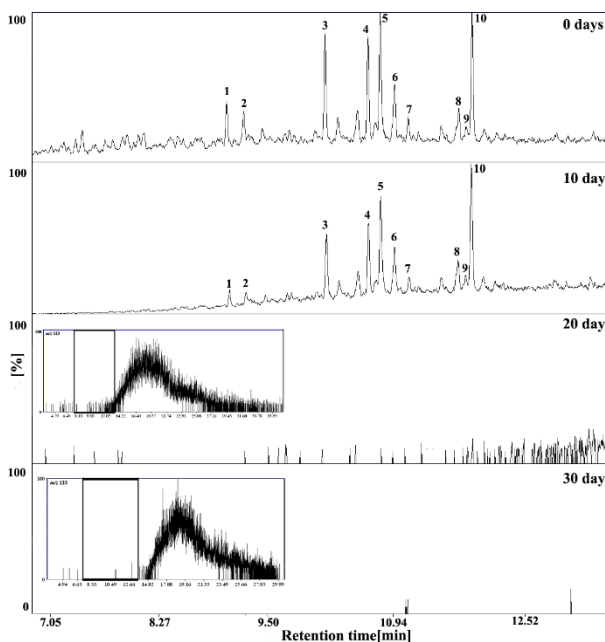


**Figure 3.** GC-MS fragmentograms (*m/z* 123) of sesquiterpane fraction after 10, 20 and 30 days by the action of *Planomicrobium sp.* RNP01

## CONCLUSION

The obtained results showed that after 30 days of biodegradation of diesel D2 by the *Planomicrobium sp.* RNP01 significant degradation was achieved, with complete degradation of sesquiterpanes and decrease in the amount of *n*-alkanes lower than C<sub>21</sub>. Pristane and phytane were almost completely degraded, so it can be concluded this bacterial strain has the ability to degrade these two biomarkers as well.

## Acknowledgement

This work was supported by Ministry of Education, Science and Technological Development of Republic of Serbia (Grant No: 451-03-9/2021-14/200026).

## REFERENCES

- [1] C.C.Azubuike, C.B.Chikere, G.C.Okpokwasili, Bioremediation: An Eco-friendly Sustainable Technology for Environmental Management, 2019.
- [2] J.Milić, J. Avdalović, T.Šolević Knudsen, G.Gojgić Cvijović, T.Jednak, M.M.Vrvić, Chem. Ind. Chem. Eng. Q., 2016,**22**, 293–299.

- [3] M. Ilić, M. Antić, V. Antić, J. Schwarzbauer, M.M. Vrvic B, Jovančićević, *Environ. Chem. Lett.*, 2011, **9**, 133–140
- [4] Z. Wang, M. Fingas, C. Yan.g B. Hollebhone, *Fuel Chem.*, 2004, **49**, 331.

## THE REDUCED COMPTON WAVELENGTH AND THE ENERGY-POSITION/MOMENTUM-TIME-UNCERTAINTIES

P. I. Premović

Laboratory for Geochemistry, Cosmochemistry and Astrochemistry,  
University of Niš, P.O. Box 224, 18000 Niš, Serbia

### INTRODUCTION

The Compton scattering is an elastic collision of the x-ray or gamma photons with free electrons (or loosely bound valence shell electrons). This scattering is demonstrated in Fig. 1. In this communication, we are combining *Heisenberg's uncertainty principle* and the Compton scattering. *Note, that some of the expressions (including their derivations) of this communication can be found in modern physics textbooks.*

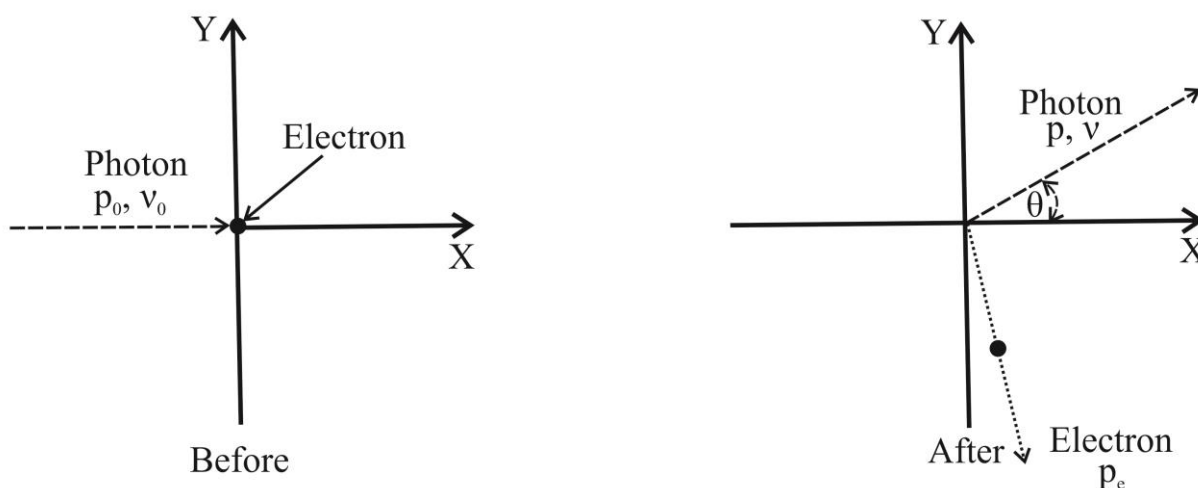


**Figure 1.** Schematic representation of Compton scattering, in which an incoming photon scatters from an electron at rest.

### DERIVATIONS AND DISCUSSION

The electron of the rest mass  $m_e$  has the rest energy of  $E_r = m_e c^2$ . The Compton scattered electron (hereinafter the Compton electron) possesses relativistic kinetic energy, the relativistic speed  $v_e$  and the linear momentum  $p_e = m_e v_e$ .

Before scattering, let the photon move along the positive x-axis having an energy  $E_0 = h\nu_0$ , frequency  $\nu_0$ , wavelength  $\lambda_0$  and linear momentum  $p_0 = h\nu_0/c$ , where  $h$  ( $= 6.63 \times 10^{-34}$  J s) is the Planck constant and  $c$  ( $= 2.99792 \times 10^8$  m s $^{-1}$ ) is the speed of light. After scattering, the photon moves at an angle  $\theta$  off the x-axis with an energy  $E = h\nu$ , frequency  $\nu$ , wavelength  $\lambda$  and momentum  $p = h\nu/c$ . The conservation of linear momentum of the electron after the collision yields,

$$p_e^2 = p_0^2 + p^2 - 2p_0 p \cos\theta.$$

The conservation of energy gives,

$$(p_e c)^2 = (h\nu_0 - h\nu)^2 + 2m_e c^2 (h\nu_0 - h\nu).$$

Combining these two expressions leads to the standard Compton formula  $\lambda - \lambda_0 = (h/m_e c)(1 - \cos \theta)$ . Here  $h/m_e c$  is called the standard Compton wavelength of the electron,  $\lambda_c$ , and it has a value of  $2.43 \times 10^{-12}$  m. This formula supposes that the scattering occurs in the rest frame of the electron. The energy  $h\nu_0$  of the incident photon with this wavelength is equal to the rest mass energy  $m_e c^2$  of the electron. In the following discussion, we will take the reduced Compton wavelength  $\lambda_{rc} = \hbar/m_e c$  ( $= 3.87 \times 10^{-13}$  m), where  $\hbar$  ( $= h/2\pi = 1.05 \times 10^{-34}$  J s) is the reduced Planck constant.

If the Heisenberg uncertainty principle holds for the Compton electron<sup>1</sup> then

$$\Delta p_e \Delta x_e \geq \hbar.$$

This inequality can be expressed as:

$$\Delta p_e \Delta x_e = a \hbar \quad \dots \quad (1),$$

where  $a \geq 1$ . In this case, quantum mechanics predicts that the uncertainty in position of the Compton electron  $\Delta x_e$  must be greater than the reduced Compton wavelength  $\hbar/m_e c$  or  $\Delta x_e > \lambda_{rc} = \hbar/m_e c$ .<sup>2</sup> Accordingly, we can write

$$\Delta x_e = a \hbar / m_e c \quad \dots \quad (2)$$

where  $a > 1$ .

If the uncertainty in energy  $\Delta p_e$  of the Compton electron is higher than  $m_e c$  then the uncertainty in its energy  $\Delta E_e$  ( $> m_e c^2$ ) would be high enough to create an electron-positron pair. Suppose that

$$\Delta p_e = b m_e c \quad \dots \quad (3),$$

where  $b \leq 1$ . Thus for the Compton electron the momentum-position expression we can be written as

$$\Delta p_e \Delta x_e = b a \hbar \quad \dots \quad (4)$$

with  $b a = a$ , see equation (1).

By differentiating the relativistic equation for the total energy  $E_e$  of the Compton electron  $E_e^2 = (p_e c)^2 + (m_e c^2)^2$ , we obtain

$$\Delta E_e = v_e \Delta p_e \quad \dots \quad (5).$$

If we multiply both sides of equations (5) with  $\Delta x_e$  and using equation (4) we get

$$\Delta E_e \Delta x_e = v_e \Delta p_e \Delta x_e = b a \hbar v_e \quad \dots \quad (6).$$

According to Special relativity, the speed of the Compton electron  $v_e$  cannot be greater than  $c$ . It is reasonable to assume that  $1 \leq a \leq 2^3$  and that  $v_e$  is relativistic when is = or > than  $0.5c$ . In this case  $b a v_e < 2c$ . So equation (6) can be rewritten

<sup>1</sup> This is a crucial assumption. In general, it is worth mentioning that the lower limit of  $\hbar/2$  for  $\Delta p \Delta x$  is rarely attained; more usually  $\hbar$  even  $h$ .

<sup>2</sup> Since the standard Compton wavelength  $\lambda_c$  ( $= h/m_e c$ ) and the de Broglie wavelength ( $\lambda_{DB} = h/m_e v$ ) are both greater than  $\lambda_{rc}$  ( $= \hbar/m_e c$ ). So, if  $\Delta x_e > \lambda_{DB}$  or  $> \lambda_c$  then  $\Delta x_e > \lambda_{rc}$ .

<sup>3</sup> It is reasonable to expect that  $1 < a \leq 2$ .

$$\Delta E_e \Delta x_e < 2\hbar c \dots \quad (7).$$

Recently, employing the uncertainty relation for momentum-position, we have derived the same energy-position uncertainty expression for a relativistic particle with the speed  $v \geq 0.5c$  [1]. This derivation was based on the same two assumptions as above for the Compton electron, and these are A) the *speed of light*  $c$  is independent of the motion of the observer, as postulated by Special relativity and B)  $1 \leq a \leq 2$ .

We also derived the expression for the momentum-time position for a relativistic particle with the speed  $v \geq 0.5 c$  [1]:

$$\Delta p_p \Delta t > \hbar/c \dots \quad (8).$$

The energy time-uncertainty relation for the Compton electron is

$$\Delta E_e \Delta t \geq \hbar \dots \quad (9).$$

As we derived above  $\Delta E_e = v_e \Delta p_e$ . So, relation (9) can be rewritten

$$v_e \Delta p_e \Delta t > \hbar \dots \quad (10).$$

Since the speed of the Compton electron  $v_e$  after interaction with the photon cannot be greater than  $c$ . In this case (10) we arrive at

$$\Delta p_e \Delta t > \hbar/c.$$

Thus, inequality (8) holds for the Compton electron.

As we pointed out in footnote 1 the value of  $\hbar/2$  is seldom attained; the values  $\hbar$  and  $h$  are more common. Thus, the energy-position expression [7] can be written as  $\Delta E_e \Delta x_e < \hbar c$  or  $\Delta E_e \Delta x_e < 2\hbar c$ . Similarly, the momentum-time expression [8] can be reformulated as  $\Delta p_e \Delta t > \hbar/2c$  or  $\Delta p_e \Delta t > \hbar/c$ .

## REFERENCE

[1] P. I. Premović, The General Science Journal, March 2018.

## RADIOACTIVITY IN SOIL AND MOSSES FROM NP ĐERDAP IN 2019

A. Čučulović<sup>1</sup>, J. Stanojković<sup>1</sup>, R. Čučulović<sup>2</sup>, N. Radaković<sup>3</sup>, S. Nestorović<sup>3</sup> and D. Veselinović<sup>4</sup>

<sup>1</sup>*University of Belgrade, Institute for the Application of Nuclear Energy – INEP, Banatska 31b, 11080 Zemun, Serbia. (anas@inep.co.rs)*

<sup>2</sup>*University of Union Nikola Tesla, Faculty of Business and Law, 11000 Belgrade, Serbia.*

<sup>3</sup>*Public Company Đerdap National Park, Kralja Petra I 14a, 19220 Donji Milanovac, Serbia.*

<sup>4</sup>*University of Belgrade, Faculty of Physical Chemistry, Studentski trg 12-16, P. Box 137, 11000 Belgrade, Serbia.*

### ABSTRACT

In June 2019, 18 soil samples and 20 moss samples were collected from 3 regions on the territory of National Park Đerdap. The radionuclide content (Bq/kg) in soil (moss) was: <sup>137</sup>Cs 3.5-496 (5.5-908), <sup>40</sup>K 36.4-918 (136-493), <sup>226</sup>Ra 7.8-45.0 (4.2-34.1), and <sup>232</sup>Th 8.2-59.5 (1.7-22.2). The external gamma dose rate (nGy/h) in 2019 on the territory of NP Đerdap is in the range from 22.4 to 93.6, average value 50.0. Values of the external gamma dose were in the range of the expected values and close to the average values in the world. The mean value of annual effective dose ( $10^{-5}$  Sv) in the NP Đerdap is  $6.12 \times 10^{-5}$  and is lower than the mean value on the world level of  $7.00 \times 10^{-5}$  Sv.

### INTRODUCTION

There are five natural parks (NP) in Serbia, and the Đerdap is one of them since 1974, with an area of 63.350 ha. It is located in the Northeast of Serbia on the boundary with Romania.

All organisms of planet Earth are exposed to radiation that is classified by place of origin into earth and cosmic. Sources of ionization radiation by their genesis and occurrence in the environment are classified as: natural, anthropogenic and radioactive waste. Natural radionuclides (<sup>40</sup>K, <sup>232</sup>Th, <sup>226</sup>Ra, <sup>238</sup>U...) are formed during the nucleosynthesis process and have a long half-life and different physical, geochemical properties, half-life types, radiation intensities, isotropic prolific quantities, occurrence method and geochemical cycles [1]. Anthropogenic radionuclides are enhanced or created due to human activity. The <sup>137</sup>Cs anthropogenic radionuclide to the greatest extent entered the environment in Serbia after the accident in the Chernobyl nuclear power plant in the Ukraine in 1986. Mosses are widespread, long-lived, easy accessible and good bioindicators of pollution of the environment as they adopt nutrients from the atmosphere by dry and moist desorption through weakly or no developed cuticles.

### EXPERIMENTAL

Investigations performed on the territory of NP Đerdap in the last few years have shown that the radionuclide content in moss and its substrate is not homogenous. In June 2019 18 soil samples and 20 moss samples were collected from 18 locations in NP Đerdap, from three regions: Tekija (Đerdap, 48; Crni vrh 1, 17, 59; Štrbačko korito 47, 59), Donji Milanovac (Pecka bara 25, 41; Boljetinka 58, 66, 81; Boljetinska reka 2, 9, 10) and Dobra (Leva reka 13c, 29a, 30, 52a). In the laboratory the samples were cleaned from visible impurities dried, homogenized and packed in Marinelli vessels with a volume of 0.5 and 1L. They were sealed with paraffin and left for at least four weeks to ensure equilibrium between <sup>226</sup>Ra and its decay products prior to radioactivity measurements. A semiconducting germanium high purity detector of the n-type produced by ORTEC - AMETEK, USA, with 8192 channels, resolution 1.65 keV and relative efficiency of 34% at 1.33

MeV for  $^{60}\text{Co}$  was used for detection. All samples were measured for 60000 s. Activity concentrations of  $^{226}\text{Ra}$  and  $^{232}\text{Th}$  were determined by their decay products  $^{214}\text{Bi}$ ,  $^{214}\text{Pb}$  and  $^{228}\text{Ac}$ , respectively. The  $^{40}\text{K}$  activity was determined based on the gamma line at 1460 keV and  $^{137}\text{Cs}$  at 661.6 keV. The total standard error of the method was estimated to be about 20%. Gamma-spectral analysis was performed with the Gamma Vision 32 software package. The external gamma dose rate and the annual effective dose the calculations were performed according to recommendations of UNSCEAR [2].

## RESULTS AND DISCUSSION

The results obtained from measuring the content of radionuclides in investigated soil and moss samples collected in 2019 on the territory of NP, including values of the external gamma dose rate  $D$  (nGy/h) and annual effective dose  $D_E$  ( $10^{-5}$  Sv) are given in Table 1. The average value (Bq/kg) of the radionuclide content in soil collected on the territory of NP Đerdap (Tekija, Donji Milanovac, Dobra) was:  $^{137}\text{Cs}$  185 (156, 211, 174),  $^{40}\text{K}$  438 (460, 496, 289),  $^{226}\text{Ra}$  29.0 (35.8, 26.7, 23.1) and  $^{232}\text{Th}$  30.4 (35.4, 28.7, 26.2), and that is within the range of average values in soil in the world [2]. In moss it was:  $^{137}\text{Cs}$  142 (170, 171, 26.8),  $^{40}\text{K}$  224 (234, 234, 187),  $^{226}\text{Ra}$  13.7 (14.7, 15.9, 6.5) and  $^{232}\text{Th}$  8.2 (7.8, 9.6, 5.1), that is in the range determined in our previous research [3]. The external gamma dose rate (nGy/h) in 2019 on the territory of NP Đerdap (Tekija, D. Milanovac, Dobra) is in the range from 22.4 (28.3, 22.4, 24.5) to 93.6 (70.9, 93.6, 54.0), average value 50.0 (57.1, 50.3, 38.5). Values of the external gamma dose were in the range of the expected values and close to the average values in the world. The annual effective dose ( $10^{-5}$  Sv) in 2019 was from 2.75 to 11.48, and they are the same order of magnitude as values determined on other locations in our country [4]. The mean value of  $D_E$  in the NP Đerdap is  $6.12 \times 10^{-5}$  Sv.

**Table 1.** Radionuclide content (Bq/kg) in soil and moss samples and also values of the external gamma dose rate and annual effective dose  
(**MU**-Management unit, **S**-Sample, **M**-Moss, **Soil**-Soil)

No	S	MU division	<sup>137</sup> Cs	<sup>40</sup> K (Bq/kg)	<sup>226</sup> Ra	<sup>232</sup> Th	D (nGy/h)	D <sub>E</sub> (10 <sup>-5</sup> ) (Sv)
1	Soil	Đerdap	23.6	575	42.8	45.0	70.9	8.7
1a	M	48	34.6	493	4.6	14.4	---	---
2	Soil	Crni vrh	348	184	19.1	19.6	28.3	3.5
2a	M	1	820	162	6.9	4.3	---	---
3	Soil	C. vrh	152	441	41.3	39.0	61.0	7.5
3a	M	17	35.2	174	14.0	15.1	---	---
4	Soil	C. vrh	3.5	471	24.5	26.5	47.0	5.8
4a	M	59	45.8	244	34.1	9.2	---	---
5	Soil	Štrbačko	207	499	45.0	39.3	65.3	8.0
5a	M	korito 47	53.6	160	20.6	1.7	---	---
6	Soil	Š. korito	201	588	42.2	43.0	70.0	8.6
6a	M	59	33.6	171	7.7	2.1	---	---
7	Soil	Pecka	39.7	602	39.4	40.5	67.8	8.3
7a	M	bara 25	59.0	237	19.3	15.3	---	---
8	Soil	P. bara	164	918	41.9	59.5	93.6	11.5
8a	M	41	16.8	189	6.5	9.7	---	---
9	Soil	Boljetinka	340	437	25.9	20.9	42.8	5.3
9a	M	58	115	225	12.0	6.1	---	---
9b	M		106	163	20.0	7.6	---	---
10	Soil	Boljetinka	130	634	29.4	29.4	57.8	7.1
10a	M	66	59.7	293	20.7	8.5	---	---
11	Soil	Boljetinka	438	80.6	19.1	18.0	23.1	2.8
11a	M	81	908	136	4.6	6.5	---	---
11b	M		112	160	24.5	8.9	---	---
12	Soil	Boljetinsk	22.5	624	35.8	43.0	68.5	8.4
12a	M	a reka 2	109	306	14.7	21.6	---	---
13	Soil	B. reka	58.8	333	7.8	8.2	22.4	2.8
13a	M	9	23.2	396	15.9	5.4	---	---
14	Soil	B. reka	496	341	14.1	9.8	26.7	3.3
14a	M	10	201	231	21.0	6.2	---	---
15	Soil	Leva reka	452	36.4	18.9	23.6	24.5	3.0
15a	M	13c	71.2	185	5.6	3.7	---	---
16	Soil	Leva reka	68.2	350	17.7	22.2	36.2	4.4
16a	M	29a	15.4	159	10.4	3.0	---	---
17	Soil	Leva reka	168	369	21.5	23.4	39.5	4.8
17a	M	30	15.0	175	4.2	4.1	---	---
18	Soil	Desna	9.3	400	34.1	35.7	54.0	6.6
18a	M	reka 52/a	5.5	229	5.8	9.7	---	---

## CONCLUSION

Measured results show that all samples contained natural radionuclides ( $^{40}\text{K}$ ,  $^{226}\text{Ra}$  and  $^{232}\text{Th}$ ) and the produced radionuclide  $^{137}\text{Cs}$ . High values of Pearson coefficients for radionuclides Ra-Th (0.925) in soil indicate their common origin and strong linear bond. The values of Pearson coefficients for K-Ra (0.690) and K-Th (0.765) indicate their medium connectivity. Values of the strength of the absorbed gamma radiation dose and the yearly effective dose from external exposure to gamma radiation based on the content of natural radionuclides in soil were in the range of the expected values and close to the average values in the world.

## Acknowledgement

This work was financed by the Ministry for Education, Science and Technological Development of the Republic of Serbia (Grants no. III43009).

## REFERENCES

- [1] D. Veselinović, I.A. Gržetić, Š.A. Đarmati, D. Marković, Stanja i procesi u životnoj sredini, Fizičko-hemijski osnovi zaštite životne sredine, knjiga I, Udžbenici Fizičke hemije, Fakultet za fizičku hemiju, Univerzitet u Beogradu, Beograd, 1995.
- [2] UNSCEAR Sources and Effects of Ionizing Radiation. Annex B: Exposure from natural radiation sources. United Nations, New York, 2000.
- [3] A. Čučulović, R. Čučulović, M. Sabovljević, M.B. Radenković, D. Veselinović, Arch. Hig. Rada Toksikol., 2016, 67, 31-37.
- [4] Republika Srbija, Agencija za zaštitu od jonizujućih zračenja i nuklearnu sigurnost Srbije, Izveštaj o sistematskom ispitivanju sadržaja radionuklida u zemljištu u 2014 godini, Beograd, 2015.

## MULTI-WAVELENGTH LIGHT ABSORPTION ANALYSIS OF BLACK CARBON IN FINE FRACTION OF SUBURBAN AEROSOL

M. Radenković<sup>1</sup>, D. Topalović<sup>1</sup>, R. Radić<sup>2</sup> and M. Govedarica<sup>3</sup>

<sup>1</sup> *University of Belgrade, Vinča Institute of Nuclear Sciences, National Institute of the Republic of Serbia, University of Belgrade,*

*Mike Petrovica Alasa 12-14, Belgrade, Serbia. (mirar@vin.bg.ac.rs)*

<sup>2</sup> *Republic Hydrometeorological Service of Republic of Srpska, Put Banjalučkog odreda b.b. 78000 Banja Luka, Bosnia and Herzegovina*

<sup>3</sup> *General Hospital Vrbas, Dr Milana Cekica bb. 21640 Vrbas, Serbia*

### ABSTRACT

A multi-wavelength light absorption of black carbon (BC) in fine aerosol particulate matter was analyzed to estimate BC contribution coming from different emission sources to receptor site in Banja Luka suburb. Analysis was performed at 140 daily PM<sub>2.5</sub> samples collected on PTFE filters. Blank and exposed filters were irradiated by monochromatic light in range 405-1050 nm and related intensity attenuation due to absorption by BC present in aerosol deposits have been recorded. Obtained results and relationships between light- and mass- absorption coefficients and their dependence on the PM<sub>2.5</sub> deposit characteristics allowed differentiation between BC dominantly coming from fossil fuel combustion and BC formed in biomass burning emissions that is valuable information for PMF receptor modeling.

### INTRODUCTION

Black carbon (BC) is a product of incomplete combustion of fossil fuels or a biomass burning emissions into atmosphere from both natural and anthropogenic sources. It is a leading contributor to expecting worldwide climate change due to its sunlight absorption and warming effects and cause of significant risks for exposed population health. [1]

Main approaches in BC analysis are based on the thermal and optical properties of carbon species. The method used in this study is relying on a mass absorption coefficient determination which is a strong function of the light wavelength, size, refraction and density of the BC particles, all depending on the dominant emission source at the receptor site. Main advantage of the multi-wavelength light absorption analysis is a possibility to distinguish BC portion coming from fossil fuel combustion and BC formed as a result of biomass burning.

### METHODS

PM<sub>2.5</sub> samples (140) have been collected 24 hours, every third day on 47 mm diameter PTFE filters by Sven Leckel MVS6 air samplers with air flow 2.3 m<sup>3</sup>/h at suburban monitoring site in Banja Luka (H<sub>s</sub>=175m φ=44.75N, λ=17.24E) for one year. Following PM<sub>2.5</sub> mass concentrations gravimetrically measurements, blank and exposed filters were irradiated by LED light sources at 405, 465, 525, 639, 870, 940 and 1050 nm wavelengths. Beam attenuation due to absorption by BC present in filter deposits have been recorded as the intensity of transmitted light, using the multi-wavelength absorption black carbon instrument (MABI). [2] The light beam attenuation is defined by the light absorption coefficient ( $b_{\text{abs}}$ ) value for each wavelength, given by equation:

$$b_{\text{abs}}[\text{Mm}^{-1}] = 100 \frac{A[\text{cm}^2]}{V[\text{m}^3]} \ln \left[ \frac{I_0}{I} \right], \quad (1)$$

where  $A$  is exposed filter surface ( $\text{cm}^2$ ),  $V$ -air volume ( $\text{m}^3$ ),  $I_0$ -intensity of transmitted light for blank filter,  $I$ -intensity of transmitted light for exposed filter with  $\text{PM}_{2.5}$  deposit.

Light absorption coefficient is correlated with mass absorption coefficient  $\varepsilon$  ( $\text{m}^2/\text{g}$ ) by relation:

$$\varepsilon[\text{m}^2/\text{g}] = b_{\text{abs}}[\text{Mm}^{-1}] / \rho[\text{g}/\text{cm}^3]. \quad (2)$$

Finally, the black carbon  $BC$  [ $\mu\text{g}/\text{m}^3$ ] have been determined by:

$$BC [\mu\text{g}/\text{m}^3] = \frac{10^5 A[\text{cm}^2]}{\varepsilon[\text{m}^2/\text{g}]V[\text{m}^3]} \ln \left[ \frac{I_0}{I} \right], \quad (3)$$

for each wavelength. Fitting of  $\varepsilon$  values based on light transmission experimental results for each wavelength in compare with central of 639 nm, allowed us to determine coefficients related to filter type, aerosol fraction characteristics and light wavelength and to estimate BC origin in the  $\text{PM}_{2.5}$  deposit. [2]

## RESULTS AND DISCUSSION

In the first phase of study, mass absorption coefficients,  $\varepsilon$  ( $\text{m}^2/\text{g}$ ), have been determined at each applied wavelength and related BC was calculated by equation (3). Linear regression between  $\ln[I_0/I]$  for 639 nm and other wavelengths have shown high correlation with coefficient of determination  $R^2 > 0.95$ . Similar time series of  $BC$  [ $\mu\text{g}/\text{m}^3$ ] in 2016/2017 for 7 wavelengths have shown seasonal variations with highest values in heating seasons as expected. Coefficient of determination for BC and  $\text{PM}_{2.5}$  mass concentration was  $R^2 = 0.47$ .

Already known that black carbon formed in combustion at low temperatures show better absorption at low wavelengths, while the one coming from high temperature processes show dominant absorption in infrared spectral area, it would be preferable for BC source identification to form a difference:

$$Diff = BC|_{\lambda=405 \text{ nm}} - BC|_{\lambda=1050 \text{ nm}}. \quad (4)$$

Fig. 1 shows annual variations of BC at central wavelength 639 nm and difference given by equation (4). Differences of these values in heating and non-heating seasons are very pronounced but not exclusive. During the summer,  $Diff$  value is near zero, indicating high temperature combustion probably coming from diesel engines as dominant source of emission at the monitoring site. Generated particles in that case have smaller diameter [3]. In the heating season,  $Diff > 0$ , meaning that dominant BC sources might be a low-temperature processes like biomass burning coming from individual heating units. Obtained results are in accordance with data on high share of old diesel vehicles in Banja Luka's sector and prevailing use of coal for domestic heating as well as in the energy sector.

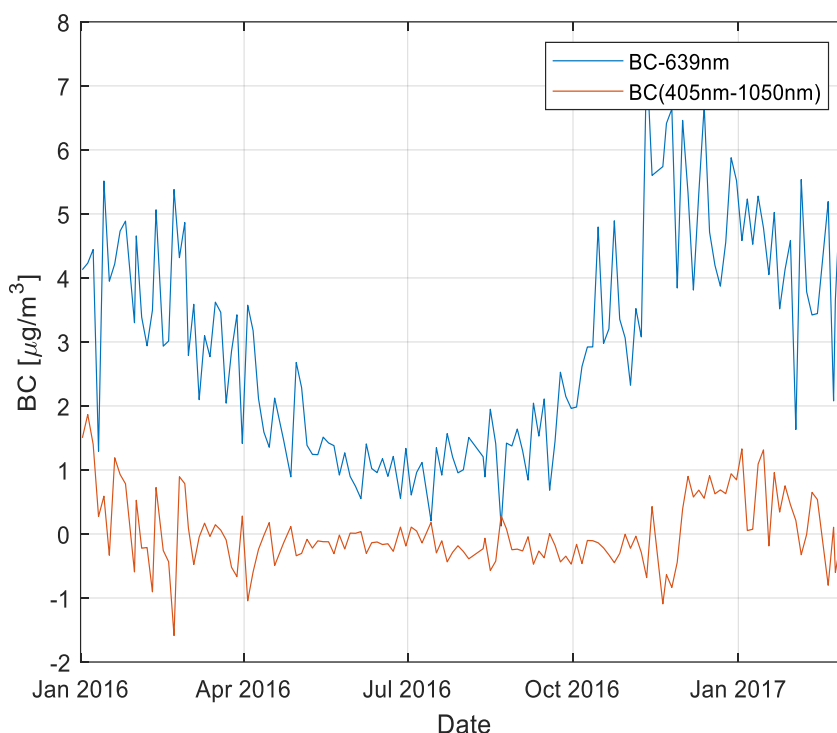


**Figure 1.** Time series of BC mass concentration at 639 nm and  $Diff = BC_{405nm} - BC_{1050nm}$

These estimations are valuable for receptor modeling like source apportionment by positive matrix factorization (EPA PMF) based on quantitative data of about 20 major and trace elements obtained by EDXRF non-destructive measurements. Since more information on carbon species, organic compounds and ions would significantly improve PMF solutions, further chemical techniques should be additionally applied to extend input database. The multi-wavelength light absorption analysis gives valuable data on BC content in  $PM_{2.5}$  deposit on PTFE filter media providing it in whole for other analytical techniques. Based on these results air pollution mitigation measures at the receptor site may be undertaken with more confidence.

## CONCLUSION

Main advantage of multi-wavelength light absorption analysis of black carbon in fine aerosol particulate matter is possibility of differentiation between black carbon coming from fossil fuels combustion and from biomass burning sources that is valuable additional information for source apportionment modeling. In addition, it is complementary with non-destructive nuclear analytical techniques like EDXRF and PIXE for elemental analysis of fine aerosol fraction sampled at PTFE filter media so that  $PM_{2.5}$  deposit stay available for further analysis.

## Acknowledgement

This study was done with support of IAEA TC in the frame of RER1015 regional European project and with support of the Serbian Ministry of Education, Science and Technological Development.

## REFERENCES

- [1] Mathijs J. H. M. Harmsen et al, Climatic Change, 2020, 163, 1519-1538.

- [2] M. Manohar, A. Atanacio, D. Button, D. Cohen, Atmospheric Pollution Research, 2021, 12(4), 133-140.
- [3] Y. Wu, T. Cheng, L. Zheng, Environmental Research Letters, 2020, 15, 094051.

## IMPACT OF PHARMACEUTICAL LEVELS IN UNTREATED WASTEWATER ON BELGRADE RIVER WATER QUALITY

Lj. Tolić Stojadinović <sup>1</sup>, S. Grujić <sup>2</sup>, N. Antić <sup>2</sup> and T. Đurkić <sup>2</sup>

<sup>1</sup> *Innovation Centre of the Faculty of Technology and Metallurgy, Karnegijeva 4, 11000 Belgrade, Serbia.*

<sup>2</sup> *University of Belgrade, Faculty of Technology and Metallurgy, Karnegijeva 4, 11000 Belgrade, Serbia. (svetlana.grujic@tmf.bg.ac.rs)*

### ABSTRACT

In the city of Belgrade, raw sewage is discharged directly into the Sava and the Danube rivers affecting the quality of river water. To determine the level of this impact, eight frequently used and detected pharmaceuticals were selected for the study. A previously developed method for analysis of pharmaceuticals in different water matrices was used. Sample extracts were analyzed by liquid chromatography-tandem mass spectrometry, using the electrospray ionization technique. The most commonly detected analytes in both municipal wastewater and surface water were carbamazepine, known for its high environmental stability, and diclofenac, known as having high acute ecotoxicity. The dilution effect, noted for most of the detected drugs, was not as pronounced with diclofenac, indicating a higher risk for aquatic organisms.

### INTRODUCTION

Pharmaceuticals are among the most important environmental contaminants because of their increasing production and extensive use. They are widely used in human and veterinary medicine and are continuously released into the environment through many human activities and the pharmaceutical industry. However, legal limits of pharmaceuticals in environmental waters have not been established yet, although they are commonly found in surface water at levels that may be harmful to aquatic organisms [1, 2]. Furthermore, there is still limited information on long-term effects of trace levels of pharmaceuticals in the environment. Municipal wastewater is the most significant source of these contaminants in the aquatic environment [1]. Since Belgrade does not have a wastewater treatment plant, raw sewage is discharged directly into rivers the Sava and the Danube through many sewage channels.

The aim of this work was to collect data on the concentrations of selected pharmaceuticals in Belgrade wastewater and corresponding receiving river water in order to determine the impact level of untreated sewage on the surface water quality in Belgrade. Liquid chromatography coupled to tandem mass spectrometry (LC-MS/MS), as the most extensively used technique for the determination of trace levels of contaminants in water matrices, will be employed for this purpose.

### METHODS

Commonly used and frequently detected pharmaceuticals were selected for the study: trimethoprim, sulfamethoxazole, azithromycin, erythromycin (antibiotics); carbamazepine, lorazepam, diazepam (sedatives); and diclofenac (nonsteroidal anti-inflammatory drug, NSAID). A previously developed method for the determination of pharmaceuticals in different water matrices was applied [3]. In short, water samples were prepared using solid-phase extraction: 100 mL of the sample (pH = 6) was loaded on the Oasis HLB cartridges (Waters, USA), analytes were eluted with 10 mL of methanol-dichloromethane (1:1) mixture, and the extract was evaporated and reconstituted to the volume of 1.0 mL. As for the LC-MS/MS analysis, Dionex UltiMate 3000 HPLC system (Thermo Fisher

Scientific, Waltham, US) coupled with the linear ion trap mass spectrometer (Thermo Fisher Scientific) was used. The chromatographic separation of compounds was achieved on a reverse-phase Zorbax Eclipse® XDB–C18 column, 75 mm × 4.6 mm ID and 3.5 µm particle size. The mobile phase consisted of methanol, water, and 10% acetic acid. The mass spectrometric analysis was performed using the electrospray ionization technique in the positive mode.

Wastewater samples were collected from three sewage discharges in Belgrade, while the corresponding receiving river water samples were collected downstream (Figure 1).



**Figure 1.** Sampling sites of wastewater (W1–W3) and surface water (S1–S3).

## RESULTS AND DISCUSSION

All investigated pharmaceuticals were detected in Belgrade municipal wastewater, at concentration levels ranging from 54 ng L<sup>-1</sup> (for azithromycin, Table 1) to as high as 1184 ng L<sup>-1</sup> (for sulfamethoxazole). Wastewater sample W1, collected at the discharge with the highest sewage inflow, showed trace levels of all selected analytes. The most frequently detected pharmaceuticals, found in all river water samples, as well as in all wastewater samples, were diclofenac and carbamazepine. In ecotoxicity studies of diclofenac, it was determined that it has high acute toxicity for aquatic organisms, the highest within the NSAID group [2]. As for carbamazepine, studies have shown that it is among the most persistent pharmaceuticals in the environment [4].

**Table 1.** Pharmaceuticals detected in Belgrade municipal wastewater (W1–W3) and corresponding surface water (S1–S3) samples.

Pharmaceuticals	Concentration (SD), ng L <sup>-1</sup>					
	W1	S1	W2	S2	W3	S3
Trimethoprim	122(12)	– <sup>a</sup>	–	–	482(72)	–
Sulfamethoxazole	122(19)	–	–	–	1184(152)	12(1)
Azithromycin	318(48)	8(1)	54(4)	3(0)	–	–
Erythromycin	133(22)	–	266(34)	–	–	–
Carbamazepine	274(44)	27(4)	313(30)	24(3)	127(25)	56(3)
Lorazepam	171(24)	–	84(3)	–	77(10)	–
Diazepam	163(22)	–	–	–	–	–
Diclofenac	442(73)	263(10)	579(64)	370(9)	782(156)	252(12)

<sup>a</sup>–: not detected

Our results have shown that there is evident contamination of the aquatic environment in Belgrade as a consequence of untreated wastewater discharge. In river water samples collected downstream from the corresponding sewage discharges, significantly lower levels of detected pharmaceuticals were found or drug traces could not be detected, indicating an intense dilution effect (Table 1). However, in the case of diclofenac, the dilution effect was not as pronounced, leading to a higher risk for river organisms. In addition, when aquatic species are continuously exposed to trace levels of contaminants over a long period of time, negative effects slowly accumulate and major changes occur when the cumulative level of these effects is reached [1]. Moreover, the mixtures of drug traces occurring in the environment may have an even greater impact than can be expected from the cumulative effects of individual substances.

## CONCLUSION

The study has shown that the discharge of untreated municipal wastewater significantly affects the quality of river water in Belgrade. All investigated pharmaceuticals were detected in wastewater samples, and 50% of the drugs were found in corresponding surface water samples. Although the dilution effect was generally very pronounced, the exception in the case of diclofenac led to a higher risk for aquatic organisms because this drug has high acute toxicity.

## *Acknowledgement*

This work was supported by the Ministry of Education, Science and Technological Development of the Republic of Serbia (Contract no. 451-03-9/2021-14/200287 and 451-03-9/2021-14/200135).

## REFERENCES

- [1] C. Daughton, T. Ternes, *Environ. Health Perspect.*, 1999, 107, 907–938.
- [2] K. Fent, A. Weston, D. Caminada, *Aquat. Toxicol.*, 2006, 76, 122–159.
- [3] S. Grujić, T. Vasiljević, M. Laušević, *J. Chromatogr. A*, 2009, 1216, 4989–5000.
- [4] M.J. Benotti, B.J. Brownawell, *Environ. Pollut.*, 2009, 157, 994–1002.

## DOES EXPOSURE TO A SINGLE DOSE OF MICROPLASTIC REPRESENTS A HEALTH RISK?

I. Guševac Stojanović<sup>1</sup>, D. Drakulić<sup>1</sup>, A. Todorović<sup>1</sup>, N. Filipović<sup>2</sup>, Z. Stojanović<sup>2</sup>

<sup>1</sup> VINČA Institute of Nuclear Sciences - National Institute of the Republic of Serbia, University of Belgrade, Mike Petrovića Alasa 12-14, 11351 Belgrade, Republic of Serbia. (igusevac@vinca.rs)

<sup>2</sup> Institute of Technical Sciences of SASA, Knez Mihailova Street 35/4, Belgrade, Republic of Serbia.

### ABSTRACT

Worldwide pollution with plastic debris represents tremendous environmental issue. Small particles originated from plastic bottles exert various effects in organisms when exposed chronically, while the effects of a single exposure are completely unknown. Thus, to test their potential health impact, male Wistar rats were exposed by oral gavage to a single dose of microplastic particles (MP) derived from polyethylene terephthalate (PET) bottles (1.4, 35 or 125 mg/kg with median diameter of 85 µm). Food and water intakes were monitored, and neurological and clinical tests were conducted. Obtained results point to lower food and water intakes in groups that received two higher MP doses indicating to interference with normal digestion. None of three used MP doses provoked neurological and clinical impairments either due to short-term exposure and/or lack of MP cumulative effect. Overall, presented results indicate that exposure to a single dose of MP can initiate health issues.

### INTRODUCTION

Even though the environmental pollutants are recognized as a major threat to a human health, little is achieved in global reduction of their omnipresence. One of these hazardous materials is biochemically inert polyethylene terephthalate (PET), widely used due to its low-cost production and long durability. Under certain conditions, PET can be fragmented into smaller pieces, including microplastic particles (MP) that are smaller than 5 mm. It appears that particles less than 150 µm in diameter could penetrate tissues and accumulate in organs, including brain [1].

Numerous studies reported that fishes exposed to MP exert alterations in behaviour (such as hypoactivity, erratic movements, seizures), body weight and length along with histological changes of organs and tissues [2]. In contrast to the relatively abundant MP studies in aquatic organisms, only few of them have been conducted to investigate the impact of these particles in mammals. They revealed that exposure to MP results in their uptake and presence in the gut, liver and kidneys of the mice [3] and could lead to decrease in body, liver, and body fat weights, disorders in energy metabolism, inflammation and neurotoxicity [2].

Given that a behavioural disruptions (such as alterations regarding activity levels, potential anxiogenic effects, depression-like behaviours and altered cognitive functions) can arise as a consequence of organism's chronic exposure to small sized particles [1], it is of great importance to test whether a single ingested dose of MP, that correlates to daily ingested dose in humans [4], could impact victuals consumption, sensory-motor functions and factors of acute toxicity in rats. The parameters of interest were assessed 24 h after a single MP exposure to provide new insights of potential health risks upon acute MP ingestion.

### METHODS

Microplastic particles were produced by filing PET bottles of worldwide famous soft drink brand which were thoroughly washed with distilled and Milli-Q water. Produced MP sawdust was sifted through laboratory sieve with mesh size of 160 µm and MP images were captured by optical microscope B-500MET (Optika, Ponteranica, Italy). Furthermore, FTIR (ATR) measurements were

performed on Nicolet Nexus spectrometer (Thermo Fisher Scientific, Waltham, USA) to identify chemical composition of samples and Malvern Mastersizer laser diffraction particle size analyser (Malvern, Worcestershire, UK) was used for additional characterisation of MP.

Research procedures conducted on animals were approved by the Ethical Committee for the Use of Laboratory Animals of VINČA Institute of Nuclear Sciences - National Institute of the Republic of Serbia, University of Belgrade, Republic of Serbia (protocol authorization number 323-07-03460/2021-05) and were in accordance with European Communities Council Directive (2010/63/EU).

Young adult male *Wistar* rats (300–350 g, n = 4 per group) were randomly divided in five groups: intact animals, used as controls (I); rats that received 2,5 ml of Milli-Q (Q); rats that received MP in dose 1.4 mg/kg (P1)/35 mg/kg (P2)/125 mg/kg (P3). Microplastic particles were dispersed in 2.5 ml of Milli-Q and the dose was calculated by multiplying human dose to correction factor (Km, 6.2 for rats) [3], [4]. All treatments were applied in a single dose by oral gavage. The food and water intakes were measured 24 h following the treatments.

Serious of non-invasive neurological and clinical tests were conducted 24 h after the treatment to evaluate potential sensory-motor deficits and possible signs of acute toxicity [5], [6]. The neurological test included scoring of following sensory-motor parameters: consciousness (0–1 point), respiration (0–1), spontaneous activity (0–3), forepaw outstretching (0–2), climbing (0–1), visual placing (0–1), cage grasp (0–1), gait posture (0–2), geotaxis (0–1), hearing and pacing/circling (0–1). Total score of neurological tests was expressed as the sum of average scores of all investigated parameters and graded on the scale of 0 to 15. The clinical test assessed: agitation, convulsion, piloerection, sleepiness and lethargy. Parameters were valued as – (no effect), + (mild effect), ++ (moderate effect) and +++ (major effect). In pre-treatment control testing, none of the animals exhibited any physiological deficit. All assessments were performed by the researcher blinded to experimental setup.

Obtained data were analysed by One-way analysis of variance followed by Tukey's *posthoc* test using GraphPad Prism 6 Software (San Diego, USA). Results are presented as a percentage of the mean of the values in I group  $\pm$  SEM (standard error of the mean). p value of 0.05 is considered significant.

## RESULTS AND DISCUSSION

Beside magnitude of organism exposure to small size particles, a variety of factors could influence their neurotoxicity and it appears that it may be also strongly affected by particle characteristics such as size and shape.

Images obtained by the optical microscope revealed that MP are of irregular shape with higher aspect ratios (whiskers, bundles of whiskers) (**Figure 1A**). Compared with data, FTIR spectra confirmed that samples are PET MP and laser diffraction analysis showed that specimens are composed of MP with median diameter of 85  $\mu\text{m}$  ( $d_{10} = 35 \mu\text{m}$  and  $d_{90} = 170 \mu\text{m}$ ) (**Figure 1B**).

Chemically inert MP larger than 150  $\mu\text{m}$ , most likely, when ingested cannot be absorbed by surrounding tissues. Before reaching the intestinal epithelium, MP pass through different compartments of the gastrointestinal tract which might affect MP surface parameters and physicochemical properties. However, the particles' stability minimizes the possibilities of enzymatic or chemical MP degradation and probably, no major MP decomposition occurs during ingestion. Nonetheless, it is considered that particles less than 150  $\mu\text{m}$  in diameter could be uptaken by epithelial lining of the gut by phagocytosis and further transported around the body by lymphatic and circulatory systems possibly reaching, among other tissues, the brain [1].

According to the obtained results, no change in any investigated parameter was observed between I and Q groups, indicating that oral gavage treatment *per se* does not affect investigated parameters. Comparing to I/Q groups, rats in P2 and P3 groups were consuming less food and water

( $p < 0.05$  for P2 and  $p < 0.01$  for P3, respectively) pointing out that MP treatment with higher doses decreased consumption of victuals (**Figure 2A** and **2B**). These findings might indicate that certain amount of MP was retained in digestive tract and animals had a false sense of satiation. Food and water intakes are usually positively correlated, and being highly controlled processes under the influence of hormones, enzymes and various regulatory mechanisms, their reduction in this study might point to health issues.

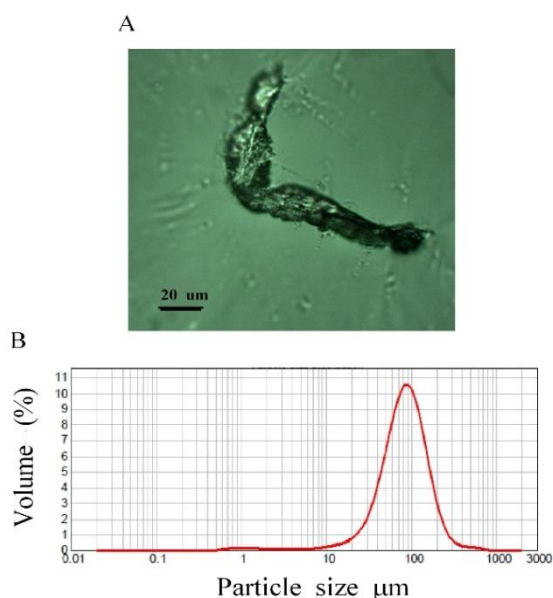


**Figure 1.** Microplastic particles characterisation **A)** Specimens are of irregular shape with higher aspect ratios (whiskers, bundles of whiskers) **B)** Specimens are composed of microplastic particles with median diameter of 85 µm ( $d_{10} = 35$  µm and  $d_{90} = 170$  µm).

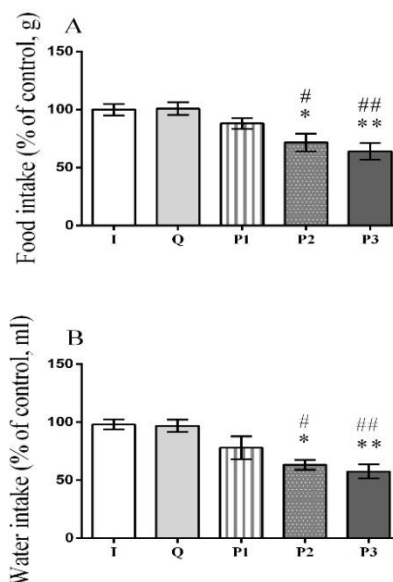


**Figure 2.** Food and water intake of rats 24 h after receiving single dose of microplastic **A)** Food intake **B)** Water intake. Data are presented as % of control  $\pm$  SEM of  $n = 4$  animals per group. Statistical analysis was performed using one-way ANOVA followed by Tukey's post hoc test (\* $p < 0.05$ , \*\* $p < 0.01$  P2/P3 vs I and # $p < 0.05$ , ## $p < 0.01$  P2/P3 vs Q).

Considering the size of particles used in this study, there might be a possibility that at least some of the MP were uptaken and transported within the body, reaching various organs and tissues. Thus, batteries of relevant neurological and clinical tests were used to examine whether an acute MP exposure represents a health risk. Although results of neurological testing revealed subtle decrement of sensory-motor functions in groups that received MP comparing to I and Q groups, these changes were not sufficient to make statistical difference (**Table 1**). Moreover, no changes were detected among these 5 groups regarding clinical scoring, either (**Table 1**) since rats were not anxious, sleepy, lethargic nor displayed sudden, irregular movements. Observed lack of MP impact on neurological and clinical scoring could be attributed to acute exposure of rats to MP and absence of cumulative effect. However, taking all results into account, there is a possibility that proposed MP specimens might be transported throughout the body inducing health issues. Thus, additional investigations are needed to elucidate mechanism of MP acting in mammals with emphasis on clarification whether and by what terms single dose of MP provokes health issues.

**Table 1.** Results of neurological (assessed by alterations in sensory-motor functions) and clinical tests scoring 24 h after treatments

Experimental group/test	I	Q	P1	P2	P3
Sensory- motor functions	100 ± 0.25	100 ± 0.25	98.31 ± 0.29	96.6 ± 0.48	94.92 ± 0.71
Clinical signs	-	-	-	-	-

## CONCLUSION

Since MP have pervaded the ecosystems, exposure to these particles and their accumulation will probably only increase with time. Although acute MP exposure had no effect on sensory-motor functions and did not induced acute toxicity, due to reduced water and food intakes that are reported in current study, it can be assumed that MP might lead to health issues. Further research regarding pathologic mechanisms at cellular and tissue levels, as well as on the long-term effects of tissue accumulation, are necessary.

## Acknowledgement

This work was supported by the Ministry for Science of the Republic of Serbia (451-03-9/2021-14/200175, 451-03-9/2021-14/200017 - 0902102 and 451-03-9/2021-14/200017 - 0902107).

## REFERENCES

- [1] M. Rafiee, L. Dargahi, A. Eslami, E. Beirami, M. Jahangiri-Rad, S. Sabour, F. Amereh, *Chemosphere*, 2018, 193, 745–753.
- [2] C. Q. Y. Yong, S. Valiyaveetill, B. L. Tang, *International Journal of Environmental Research and Public Health*, 2020, 17 (5), 1509.
- [3] M. Prüst, J. Meijer, R. H. S. Westerink, *Particle and Fibre Toxicology*, 2020, 17 (1).
- [4] K. Senathirajah, S. Attwood, G. Bhagwat, M. Carbery, S. Wilson, T. Palanisami, *Journal of Hazardous Materials*, 2021, 404 (Pt B), 124004.
- [5] A. Nair, S. Jacob, *Journal of Basic and Clinical. Pharmacy*, 2016, 7(2), 27-31.
- [6] M. Zaric, D. Drakulić, M. Dragić, I. Guševac Stojanović, N. Mitrović, I. Grković, J. Martinović, *Neuroscience*, 2019, 410, 128–139.
- [7] D. Dekanski, B. Spremo-Potparević, V. Bajić, L. Živković, D. Topalović, D. Sredojević, V. Lazić, J. Nedeljković, *Food and chemical toxicology : an international journal published for the British Industrial Biological Research Association*, 2018, 115, 42–48.

## POTENTIAL USE OF SLAG GENERATED FROM LIGNITE COMBUSTION IN HITTING PLANTS

A. Nedeljković<sup>1\*</sup>, N. Nišić<sup>1</sup>, I. Kandić<sup>1</sup>, N. Ristić<sup>2</sup>, M. Stojmenović<sup>1</sup>, J. Gulicovski<sup>1</sup>, and M. Kragović<sup>1</sup>

<sup>1</sup>*Department of Materials, "VINČA", Institute of Nuclear Sciences-National Institute of the Republic of Serbia, University of Belgrade, Serbia, Mike Petrovića Alasa 12-14, 11000 (andrijana.nedeljkovic@vin.bg.ac.rs)*

<sup>2</sup>*University of Niš, Faculty of Civil Engineering and Architecture, Aleksandra Medvedeva 14, 18000 Niš, Serbia*

### ABSTRACT

This paper presents the examination of potential application of slag, obtained from lignite combustion process in heating plant in Valjevo, Serbia, as a replacement for cement in mortars and concrete production. Waste slag was characterized with X-Ray Diffraction Analysis, Field Emission Scanning Electron Microscopy and Gamma spectrometric analysis, while its application possibility was investigated with testing Pozzolan activity Strength activity index, Activity index and Water requirement. The aim of this study is to determine under what conditions the slag could successfully replace cement in construction industry in certain percentages. Based on presented results it was concluded that, after mixing with silicate fume, waste slag can be used for the purpose mentioned. Optimal proportion of cement replacement is 20% -: 18% of slag and 2% of silica fume.

### INTRODUCTION

Coal is combustible dark-brown sedimentary rock of organic origin. Because of its capability to burn, it is used as a fossil fuel and represents a main source of energy in present-day society. It consists mostly of carbon and hydrocarbon, but also there are other elements such as sulphur, oxygen and nitrogen [1]. Coal is widely used for the purpose of electricity and heat generation, cement, steel, and alloys production as well as in other processes and industries.

Depending on the degree of coalification that has occurred, there are different types of coal: peat (precursor to coal), bituminous, subbituminous, lignite and anthracite, while the graphite known as "dead carbon" is the last grade of organic substance transformation of coal [2]. Coal Combustion Residues (CCRs) refer to the residues produced during the combustion of coal that include fly ash, bottom ash, slag, fluidized bed combustion ash and other solid fine particles [3].

In comparison with other types of coal, lignite has the lowest carbon content, therefore lowest calorific value and makes up the largest share of Serbian coal reserves. Despite its low quality, lignite is the most common fuel in Serbian heating facilities because of compatibility with present technology and is widely available with considerable price. In Serbia, heating plants supply about 25% of population with heat, which is generated from lignite combustion. However, these processes produce a lot of waste, such as slag and ash, which is followed by emissions of a number of harmful substances that potentially can cause substantial air, soil and water pollution. Some of them are sulfur and aluminum oxides as well as heavy metals such as wolfram, cadmium, lead, mercury, lime etc.

Slag is hard and durable waste matter with particles uniform in size and high resistance to surface wear, which contains different undesirable elements in small shares that can endanger the environment and cause population health issues. The use of waste slag in industry is currently in early phase in Serbia. Each year in Serbia millions of tons of slag and ash are produced in heating plants and disposed in landfills as waste products. Due to that the negative effects of their disposal in high amounts, environmental pollution is at increase in recent years. Reuse of waste slag in construction

industry is of great potential and could come up as a possible solution for reducing the amount of waste disposed and, therefore its negative impact on environment. However, this aspect is still underdeveloped and not many studies were performed in this field. To derive the best possible way of slag usage, it must be examined and treated in accordance with results obtained.

In this study for the purpose of waste slag characterization, different physical – chemical and physical mechanical techniques were used: X-Ray Diffraction Analysis (XRD), Field Emission Scanning Electron Microscopy (FESEM), Gamma Spectrometry Analysis with gamma index determination and testing of the pozzolan activity.

## METHODS

The slag samples were taken from landfill in Valjevo, Serbia. For further examination, samples were homogenized, dried and crushed so the particle size was 100% below 63  $\mu$ m. For assessment and monitoring of the phase composition of slag samples the X-Ray Diffraction Analysis (XRD) was used. The X-Ray diffract or Philips, PW-1710 with curved graphite monochrome and scintillation counter was used for investigations. Intensities of diffracted  $CuK\alpha$  ( $\lambda=1.54178\text{\AA}$ ) were measured at room temperature in 0-02  $^\circ$ /s in range from 4 to 65  $^\circ$ 2 $\theta$ . Voltage of 40 kV and power of 30 mA was used for measuring. The morphology of the slag samples was determined on Tescan Mira 3 XMU field emission scanning electron microscopy (FESEM). The samples were coated with gold using sputter coater Polaron SC503 Fision Instrument prior to SEM analysis. For gamma-ray measurement, prepared sample of slag was placed in 125 ml PVC cylindrical box. The detector was calibrated using the coal and soil matrix in identical cylindrical boxes spiked with common mixture of gamma-ray emitters ( $^{241}\text{Am}$ ,  $^{109}\text{Cd}$ ,  $^{139}\text{Ce}$ ,  $^{57}\text{Co}$ ,  $^{60}\text{Co}$ ,  $^{137}\text{Cs}$ ,  $^{113}\text{Sn}$ ,  $^{85}\text{Sr}$ , and  $^{88}\text{Y}$ ) certified by CMI [4]. The sample was measured in close to detector geometry by means of HPGe spectrometer - Canberra GX5019, with 55% relative efficiency and 1.9 keV resolutions for  $^{60}\text{Co}$  at 1332.5 keV [5].

The gamma index ( $I$ ) was obtained according to formula (1):

$$I = \frac{c(\text{Ra}^{226})}{300 \text{ Bq/kg}} + \frac{c(\text{Th}^{232})}{200 \text{ Bq/kg}} + \frac{c(\text{K}^{40})}{3000 \text{ Bq/kg}} \quad (1)$$

where  $C(\text{Ra}^{226})$  is specific activity of  $\text{Ra}^{226}$  in Bq/kg,  $C(\text{Th}^{232})$  is specific activity of  $\text{Th}^{232}$  in Bq/kg, and  $C(\text{K}^{40})$  is specific activity of  $\text{K}^{40}$  in Bq/kg.

Preparation of the cement mixtures was conducted with addition of different amounts of the slag and silicate fume as it is presented in Table 1. Replacement of cement (in total) was: P 10 (10 %), P 15 (15 %), P 20 (20 %) and P 25 (25 %).

Pozzolanic activity was determined according to Standards SRPSB.C1.018, ASTM C311 - C311-13, EN 450-1, EN 450-1 Annex B, EN 196-3.

**Table 1.** Amounts of cement replaced with waste slag and silica fume

replacement cement	P 10	P 15	P 20	P 25
slag	9 %	13 %	18 %	22 %
silicate fume	1 %	2 %	2 %	3 %

## RESULTS AND DISCUSSION

The sample of slag was examined with XRD Analysis on polycrystal specimen (powder). The presence of minerals/phases such as: quartz, olivine, magnetite, pyrite, tridymite, feldspars was affirmed while the other minerals were less represented. Among feldspars, the most common were plagioclase feldspars, much more than alkali feldspars. Slag's degree of crystallinity was low [6].

FESEM analysis was used for examination of the slag morphology and surface properties. The micrographs were obtained with a magnification of 5000 and 40000x and are presented in Figure 1. As it can be seen, slag is mainly constituted of irregularly shaped flat plates of different size of about up to 100 μm.

Radiation risk by definition presents the probability for an individual to experience a certain harmful effect as a result of exposure to ionizing radiation. In order to assess the radiation risk, concentrations of activity of natural radionuclides Ra<sup>226</sup>, Th<sup>232</sup> and K<sup>40</sup> must be determined. The values of specific activity of certain radionuclides, obtained by gamma spectrometric analysis are shown in Table 2.

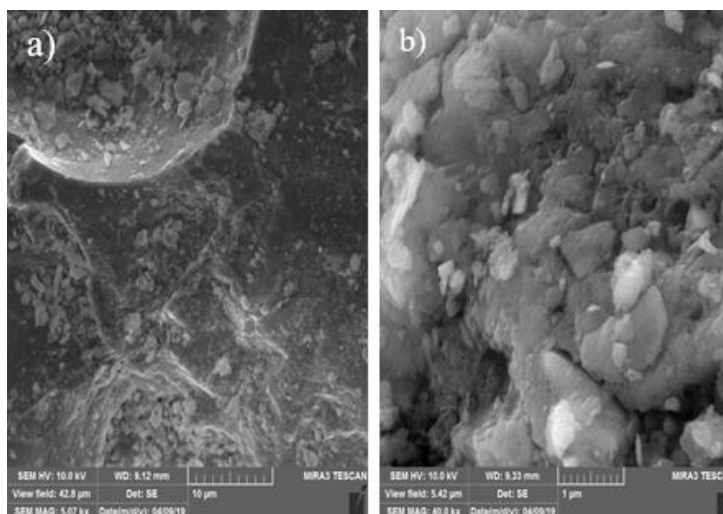


**Figure 1.** SEM photographs of slag sample taken with different magnification; a) 5.00kx and b) 40kx

**Table 2.** Specific activity of radionuclides

Radionuclide	Specific activity (Bq/kg)
K <sup>40</sup>	238 ± 12
Ra <sup>226</sup>	88.3 ± 6.3
Th <sup>232</sup>	65.9 ± 3.6

The gamma index (I) refers to the radiation dose, above the usual radiation exposure in the open space, in a building constructed of the material for which the index is calculated. The gamma index has a recommended limit value, I = 1, reported in Article 15 of the Regulation about limitations of radionuclides content in drinking water, foodstuffs, fodder, medicaments, items of general use, construction materials and other goods put in traffic. Based on the results of specific activity of radionuclides, gamma index was calculated using equation 1 and obtained value was I = 0.7. Therefore the gamma index of waste slag is under the recommended limit and does not represent a radiological risk on environment [7].

After characterization, waste slag was tested for application in cement industry as a replacement component in concrete and mortar production.

The analysed parameters included determination of activity index, water requirement, setting time and soundness. From results it can be concluded that parameters such as Initial and final setting time as well as Soundness satisfied criteria prescribed by the standards, while Strength activity index, Activity index and Water requirement do not satisfy requirements prescribed by the Standards. Namely, the values of Strength activity index (SAI) (28 days – 67 %) and Activity index (90 days - 76 %) were lower in comparison with Standard (Strength activity (>75 % for 28 days) and Activity index for 90 days >85 %), while the value of Water requirement (113 %) was higher than value prescribed by the Standards ASTM C311-C311-13 and EN 450-1 (<95 %), what indicates that slag in present raw form could not be used as a cement replacement. Because of that additional actions were performed. Since it is well known that silicate fume possesses good pozzolanic properties, it was used as an addition to the slag in order to increase slags pozzolanic activity and improve its properties.

The results for samples Activity index with different slag and silicate fume ratios for 28 and 90 days are shown in Table 3. According to standard requirements (EN 450-1 p. 5.3.2), limit value for activity index for 28 days is 75%, and for 90 days is 85%. Values for all samples for 28 days were in

intervals (82 ÷ 95) % and for 90 days in intervals (81÷93) %. Considering the goal of incorporating as much slag as possible, sample P 20, where the cement is replaced with 18 % slag and 2 % silicate fume had a best performance.

**Table 3.** Activity index of mixed samples of slag and silicate fume

P 10		Activity index P 15		P 20		P 25	
28 days	90 days	28 days	90 days	28 days	90 days	28 days	90 days
95 %	93 %	91 %	89 %	87 %	85 %	82 %	81 %

## CONCLUSION

XRD analysis showed that the slag sample mostly appears in amorphous form and possess very low crystalline. According to FESEM analysis it can be concluded that the surface of slag mainly is consisted of irregularly shaped particles with the diameters mainly of 1 µm. Radiological examination presented that gamma index of analysed slag sample was 0.7 which is not of radiological risk for the environment.

Results based on overall analysis of slag samples from heating plant in Valjevo, Serbia indicate that slag in raw form doesn't show pozzolan activity since Strength activity index (SAI), Activity index, and Water requirement do not meet criteria prescribed by the standards. As a solution, the silicate fume was added to the slag, which enhanced its characteristics.

From presented results, it may be suggested that the waste slag could be used in construction industry, as a cement replacement in mortars and concrete production, but only after addition of the silica fume. Results showed that it is justified to replace cement with slag in the amount up to 20 %. In that case, the ratio of the constituents in the mixture is: cement/ slag/ silica fume = 80/18/2 %.

## Acknowledgement

The research was funded by the Ministry of Education, Science and Technological Development of the Republic of Serbia.

## REFERENCES

- [1] M. Blander, S. Sinha, A. Pelton, G. Eriksson, Argonne National Laboratory, 2011, 315
- [2] P. Nikolić, D. Dimitrijević, Ugalj Jugoslavije - geologija i proizvodno razvojni potencijali ležišta i rudnika uglja, DP „Pronalazaštvo“, Beograd, 1990.
- [3] Mills, S. J. (2011). Global perspective on the use of low quality coals. *IEA Clean Coal Centre*, 180, 1-2.
- [4] CMI, (2012). Radioactive Standard, ER X, Cert. No 9031-OI-427/12. Czech Metrology Institute, Prague.
- [5] Kandić, A., Vukanac, I., Djurašević, M., Novković, D., Šešlak, B., Milošević, Z. 2012. On the long-term stability of calibration standards in different matrices. *Applied Radiation and Isotopes*, 70(9), 1860-1862.
- [6] Nedeljković, A., Stojmenović, M., Gulicovski, J., Ristić, N., Milićević, S., Krstić, J., Kragović, M. (2020). Waste Slag from Heating Plants as a Partial Replacement for Cement in Mortar and Concrete Production. Part I—Physical–Chemical and Physical–Mechanical Characterization of Slag. *Minerals*, 10(11), 992.]
- [7] Official Gazette of the Republic of Serbia, 2018. Regulation on limits of radionuclide content in drinking water, foodstuffs, feeding stuffs, drugs, items of general use, building materials and other goods to be placed on the market. Official Gazette of the Republic of Serbia 36/2018-54.

## BLACK INORGANIC PIGMENTS OBTAINED FROM WASTE MATERIALS

A. Devečerski, K. Kumrić, S. Stanković, M. Egerić, M. Omerašević, S. Krstić, R. Vujasin

*"Vinča" Institute of Nuclear Sciences - National Institute of the Republic of Serbia, University of Belgrade, Belgrade, Serbia. (kkumric@vinca.rs)*

### ABSTRACT

Hazardous industrial wastes are the most common source of environmental pollution. Waters originating from unregulated landfills and places of inadequate disposal of this type of wastes can pollute the water sources and affect the human health. In this study, electroplating waste sludge (ES) and various Fe-rich wastes were used as starting materials for the synthesis of inorganic pigments. Obtained black  $\text{Cr}_{1.3}\text{Fe}_{0.7}\text{O}_3$  pigments possess adequate properties required for use as inorganic pigments.

### INTRODUCTION

Inorganic pigments are widely applied due to the many of their advantages: high chemical and temperature stability, non-toxicity, resistance to the influence of UV radiation, and as such, can be used for external uses: facades, roofs, wall and floor tiles [1,2]. The waste sludge used in this study comes from an electroplating plant (nickel, chromium, zinc, etc.) and belongs to toxic industrial wastes class. It has already been used [3] as a raw material for the synthesis of black inorganic pigment through the reaction with commercially available  $\text{Fe}_2\text{O}_3$  (p.a. purity). Despite expectations that a spinel ( $\text{FeCr}_2\text{O}_4$ ) black pigment will be obtained, it was found that a mixed Fe/Cr oxide ( $\text{Cr}_{1.3}\text{Fe}_{0.7}\text{O}_3$ ) was obtained instead. However, its color and non-toxicity indicate the possibility for his commercial use. In this study, we tried to replace previously used p.a.  $\text{Fe}_2\text{O}_3$  with a various Fe-rich wastes as cheaper raw materials, thus fully following the principles of circular economy.

### EXPERIMENTAL

The ES investigated in this study was collected from an open-air basin containing 40t of historical sludge from the Cr/Ni-plating plant of "PPT TMO" Technological and metallurgical processing factory, Trstenik, Serbia. As a Fe-source, following waste materials, in the form of the powders, were used in this study: Fe-waste from the metal processing industry (FeW1); Fe-waste from the steel plant (FeW2); Rust, scraped from the iron/steel items that were exposed to atmospheric conditions for a longer period (FeW3).

Characterization of the Cr/Ni plating sludge and products obtained from it, included determination of chemical composition (XRF), main crystalline phases (XRD), color of the samples (UV/VIS, NIR) expressed in  $L^*a^*b^*$  values and toxicity level (leaching test, performed according to DIN-38414-S4, to determine the metals mobility under the neutral conditions [4]).

### RESULTS AND DISCUSSION

The sludge in liquid form was taken from a basin at five different spots and then thoroughly mixed while in liquid state. Sludge was then dried at 110 °C and the mass of the dry residue was measured. It was found that water content in sludge is about 91.5 wt%. Chemical composition of the dried sludge is shown in Table 1 and it represents average value of five different samples.

**Table 1.** Chemical composition of the dried ES determined by XRF

	Cr	Fe	P	Zn	Ni	Cu	Pb	Si	Elements in traces
Conc. (wt%)	62.93	11.79	9.20	6.51	3.58	2.62	1.75	1.36	0.26

From the XRD patterns (not shown) of the dried (110 °C) and calcined (600 °C) Fe-wastes, following was observed: all reflections in the XRD pattern of the dried FeW1 waste can be ascribed to Fe<sub>2</sub>O<sub>3</sub> phase (JCPDS No. 33-0664). XRD patterns of dried FeW2 waste showed reflections of the Fe<sub>2</sub>O<sub>3</sub> phase and Fe<sub>3</sub>O<sub>4</sub> phase (JCPDS No. 19-0629). XRD patterns of dried FeW3 waste showed reflections of the species that are known as the rust constituents: FeO-OH (JCPDS No. 76-2301), Fe(OH)<sub>3</sub> (JCPDS No. 38-0032) and Fe<sub>3</sub>O<sub>4</sub>. After the calcination at 600 °C, XRD patterns of all Fe-wastes showed reflections originating only from the Fe<sub>2</sub>O<sub>3</sub> phase, indicating that all the wastes constituents were transformed into the Fe<sub>2</sub>O<sub>3</sub> during the calcination process. Moisture content i.e. weight loss after drying at the 110 °C were 0 wt% for FeW1, 0 wt% for FeW2 and 2.2 wt% for FeW3. Weight losses after the calcination at 600 °C were 0 wt% for FeW1, 0 wt% for FeW2 and 6.6 wt% for FeW3.

By varying the amount of the Fe-waste added into the ES, it was found that for all Fe-wastes, 30 wt% is amount that is sufficient to transform ES into the black pigment.

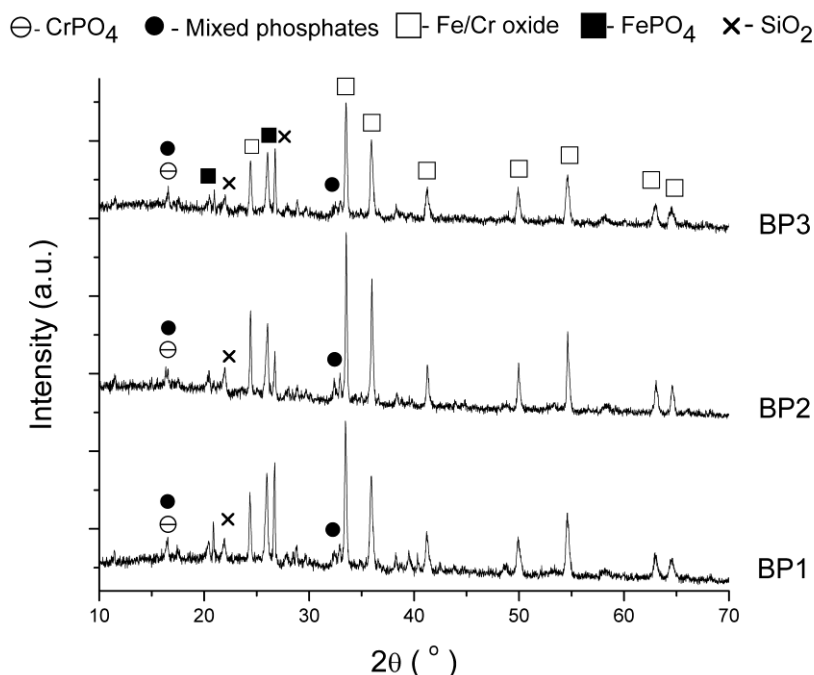


**Figure 1.** XRD patterns of the black pigments obtained after the calcination of various ES/Fe mixtures at 1000 °C (2h): BP1 – ES/30wt% FeW1; BP 2 – ES/30wt% FeW2; BP 3 - ES/30wt% FeW3.

As can be seen from Fig. 1, CrPO<sub>4</sub> and mixed phosphates phases, which are characteristic for unreacted ES, almost completely disappeared. Dominant phase in all pigments was Fe<sub>0.7</sub>Cr<sub>1.3</sub>O<sub>3</sub> mixed oxide, followed by FePO<sub>4</sub> and SiO<sub>2</sub> phases. Also, there were no reflections characteristic for the bulk/metallic Fe or Fe<sub>2</sub>O<sub>3</sub> phase, which indicated that all Fe was bounded either in Fe<sub>0.7</sub>Cr<sub>1.3</sub>O<sub>3</sub>

mixed oxide structure or in  $\text{FePO}_4$  structure. Color of all the samples was black without brown domains in it.

Color of the pigments was estimated by UV/VIS spectroscopy and Table 2 shows the colorimetric coordinates of some pigments. As one can see, values for  $L^*a^*b^*$  coordinates are in accordance with the literature, or even better. ( $L = 100 =$  white color;  $L = 0 =$  black color).

**Table 2.** The colorimetric coordinates of black pigments

	$L^*$	$a^*$	$b^*$
BP1	38.00	0.44	-1.99
BP2	38.29	0.22	-2.24
BP3	38.35	0.48	-2.04
Commercial black pigment [1]	33,0	1	0
Commercial black pigment [3]	28,8	-1,2	0,7

Level of toxicity, i. e. the leaching test, was conducted according to DIN-38414-S4 standard, which is most commonly found in the literature regarding the synthesis of pigments from waste materials. The metal concentrations in eluates were determined by the AAS method (Atomic Absorption Spectroscopy) and the results are shown in Table 3.

**Table 3.** Metal content (mg/l) in eluates obtained after the leaching test

	<b>Cr</b>	<b>Ni</b>	<b>Pb</b>	<b>Zn</b>	<b>Fe</b>	<b>Cu</b>	<b>pH</b>
ES dried at 110 °C	10,5	75	0,1	194	69	9,1	4,5
BP1	<0,01	<0,2	<0,5	<0,1	0,32	<0,1	7,7
BP2	<0,01	<0,2	<0,5	0,11	<0,3	<0,1	7,1
BP3	<0,01	<0,2	<0,5	<0,1	<0,3	<0,1	6,9
<i>Allowed concentrations*</i>	<i>0,05 - 1</i>	<i>0,04 - 1</i>	<i>0,05 - 1</i>	<i>0,4 - 5</i>	/	<i>0,2 - 5</i>	<i>4 - 13</i>

\* - EU Council Decision 2003/33/EC; first value refers to the “*Inert*” and second to the “*Non-hazardous*” classification of materials

## CONCLUSIONS

Following the principles of the circular economy, black  $\text{Fe}_{0.7}\text{Cr}_{1.3}\text{O}_3$  pigments were obtained using only the waste materials (electroplating sludge and Fe-rich wastes). The obtained products show no leaching of toxic metals, have color comparable to those of commercial pigments and thus have potential commercial application.

## Acknowledgement

This research was supported by the Ministry of Education, Science and Technological Development of the Republic of Serbia.

**REFERENCES**

- [1] W. Hajjaji M.P. Seabra, J.A. Labrincha, J. Hazard. Mater., 2011, **185**, 619 - 625.
- [2] G. Costa V.P. Della, M.J. Ribeiro, A.P.N. Oliveira, G. Monrós, J.A.Labrincha, Dyes and Pigments, 2008, **77**, 137 - 144.
- [3] A. Devečerski, K. Kumrić, J. Ilić, R. Vujasin, M. Omerašević, L. Slavković-Beškoski, Lj. Matović.14th Int. Conf. on Fundamental and Applied Aspects of Physical Chemistry, Belgrade, 2018, 809 – 812.
- [4] A.P. Galvin J. Ayuso, J.R. Jiménez, F. Agrela, Waste Management, 2012, **32**, 88 - 95.

## DEVELOPMENT AND VALIDATION OF A SPE-HPLC-DAD METHOD FOR THE DETERMINATION OF SELECTED PESTICIDES IN WATER SAMPLES

K. Kumrić, R. Vujasin, M. Egerić, Đ. Petrović, K. Stanković, A. Devečerski and Lj. Matović

*"Vinča" Institute of Nuclear Sciences – National Institute of the Republic of Serbia, University of Belgrade, Belgrade, Serbia. (kkumric@vinca.rs)*

### ABSTRACT

An analytical method based on solid-phase extraction (SPE) using coconut shell activated carbon (CSAC) as a low-cost adsorbent and high performance liquid chromatography with diode array detector (HPLC-DAD) was developed and validated for the determination of four varying polarity pesticides in water samples. SPE procedure was optimized and under the optimized conditions the proposed method was validated. The method exhibited good linearity, satisfactory precision (1.4 – 5.1%), high enrichment factor, good recovery and low limits of detection (0.025 – 0.039  $\mu\text{g}/\text{dm}^3$ ). Optimized method was used to determine selected pesticides in tap water samples. The recoveries ranged from 58.2% to 105.3%, with low relative standard deviations. The obtained results indicated that the proposed SPE-HPLC-DAD method could be efficiently used for the determination of the selected pesticides in environmental water samples at trace levels.

### INTRODUCTION

Pesticides released from agricultural practices are an important class of pollutants due to their widespread use, toxicity, persistence, polar nature and water solubility. Trace level determination of pesticides in aqueous samples comprises a sample preparation procedure for the simultaneous extraction and preconcentration, and high performance instrumental techniques (usually gas and liquid chromatography) for quantification [1]. Development of sample preparation methods is often difficult, since the pesticides possess diverse physicochemical properties, which are the consequence of their chemical structures. Current sample preparation methods for pesticides determination in aqueous samples mainly include liquid-liquid extraction (LLE) [2, 3], solid-phase extraction (SPE) [4, 5], liquid-phase microextraction (LPME) [6] and solid-phase microextraction (SPME) [7]. Among them, SPE has been widely used for the preconcentration of pesticides due to high enrichment efficiency, low consumption of organic solvents, simplicity, ease of automation and operation.

Activated carbons have been widely used as adsorbents in SPE owing to their large surface area, high adsorption capacity, porous structure and selective adsorption. These materials can be prepared from variety of carbonaceous materials such as coal, wood, agricultural or industrial wastes. In recent years there has been an increasing interest in using low-cost and abundantly available agricultural waste materials, such as sugar cane bagasse, orange peel, rice husk, pistachio shell etc., as precursors for the preparation of carbon materials. Coconut shell is also a potential precursor for the production of low-cost activated carbon due to its excellent natural structure and low ash content, and provide a potentially cheap alternative to existing commercial carbons.

The aim of this study was to develop, optimize and validate an efficient SPE procedure based on CSAC as a low-cost adsorbent for the simultaneous extraction and preconcentration of the selected pesticides (imidacloprid (Imi), acetamiprid (Ace), simazine (Sim) and linuron (Lin)) from aqueous solutions prior to their determination by HPLC-DAD. The applicability of the developed SPE-HPLC-DAD method to the analysis of four targeted pesticides in tap water samples was tested and discussed.

## METHODS

Coconut shell activated carbon was obtained from Traylor corporation (Kruševac, Serbia), while pesticides Imi, Ace, Car, Sim and Lin were obtained from Fitofarmacija (Zemun, Serbia). Stock solutions of the pesticides ( $100 \text{ mg/dm}^3$ ) were prepared in methanol, and working solutions were prepared by appropriate dilution of the stock solutions with deionized water. Tap water sample was collected from our laboratory after it has flowed for 10 min at a very fast flow rate. The sample was filtered through a Millipore filter of  $0.45 \mu\text{m}$  pore size and stored in glass bottle at  $4^\circ\text{C}$ .

SPE cartridges were prepared by placing 50 mg of CSAC into an empty cartridge. Polyethylene upper and lower frits were placed at each end of the cartridge to hold the adsorbent packing in place. The column was connected to a peristaltic pump. The sample solutions spiked with the selected pesticides were passed through the column at a controlled flow rate. Then, the pesticides retained on the column were eluted with an adequate eluent. The HPLC analysis of the selected pesticides was performed using an Agilent 1100 liquid chromatographic system (Agilent Technologies, USA) with Zorbax XDB-C<sub>18</sub> column ( $4.6 \times 250 \text{ mm}$ ,  $3.5 \mu\text{m}$  particle size) and DAD detector at wavelengths: 220 nm (Sim), 254 nm (Ace and Lin) and 270 nm (Imi). The mobile phase was a mixture of methanol (A) and deionized water (B) and the gradient elution profile was as follows: 0.0 min 43% A and 57% B, 7 min 60% A and 40% B, 10 min 70% A and 30% B, 14 min 72% A and 28% B, and 20 min returned to the initial composition. Flow rate and sample volume were  $0.7 \text{ cm}^3/\text{min}$  and  $20 \mu\text{L}$ .

## RESULTS AND DISCUSSION

The optimization of SPE method using CSAC as an adsorbent included the investigation of the parameters that may affect the performance of SPE procedure, such as the type and volume of the eluent, sample pH, the flow rate of sample loading and the sample volume. Based on the obtained results, the following optimal conditions were used for the SPE-CSAC method: sample volume of  $500 \text{ cm}^3$  at pH 5.5;  $6 \text{ cm}^3$  of dichloromethane (DCM) as eluent; flow rate of sample and eluent  $3.8$  and  $1 \text{ cm}^3/\text{min}$ .

Under the optimized conditions, the proposed SPE-CSAC method in combination with HPLC-DAD determination was validated in terms of linear ranges, limits of detection (LODs) and limits of quantification (LOQs), and precisions. Linearity was tested by spiking Milli-Q water with each of the pesticide at six concentration levels ranging from  $0.025$  to  $1 \mu\text{g/dm}^3$ . The obtained results are given in Table 1.

**Table 1.** Analytical parameters for the SPE-CSAC method for determination of pesticides.

Analyte	Linear equation	$R^2$	LOD ( $\mu\text{g/dm}^3$ )	LOQ ( $\mu\text{g/dm}^3$ )	RSD (%)
Imi	$y = 19.6 + 1386.4 x$	0.9984	0.025	0.084	1.9
Ace	$y = 18.5 + 600.2 x$	0.9981	0.028	0.092	1.4
Sim	$y = 1.5 + 1049.7 x$	0.9984	0.025	0.083	5.1
Lin	$y = -1.9 + 551.7 x$	0.9963	0.039	0.129	2.1

As can be seen in Table 1, the developed method demonstrated good linearity with the determination coefficients ( $R^2$ ) between 0.9963 and 0.9984. The LODs and LOQs, calculated at a signal to noise ratio of 3 ( $S/N = 3$ ), i.e. 10 ( $S/N = 10$ ), were in the range  $0.025 - 0.039 \mu\text{g L}^{-1}$  and  $0.083 - 0.129 \mu\text{g L}^{-1}$ , respectively. These detection limits are below the legal tolerance level for each individual pesticide in drinking water ( $0.1 \mu\text{g L}^{-1}$ ) according to the EU Directive on water quality (98/83/EC). Precision of the method was investigated by performing three replicate analyses of the samples spiked with  $0.1 \mu\text{g L}^{-1}$  of each pesticide and the relative standard deviations (RSDs, %) varied

from 1.4 - 5.1%. These results clearly indicated that the SPE method based on CSAC as adsorbent has a high potential in the analysis of pesticides at trace levels in water samples.

The proposed SPE-HPLC-DAD method based on CSAC adsorbent was then applied to the analysis of four targeted pesticides in tap water samples collected in our laboratory to test its applicability. Tap water samples were simultaneously spiked with each of the selected pesticides at two concentration levels (0.05 and 0.25  $\mu\text{g}/\text{dm}^3$ ) and then analyzed by the developed method. Typical chromatograms obtained from unspiked tap water sample and tap water samples spiked with the selected pesticides at the concentrations of 0.05 and 0.25  $\mu\text{g}/\text{dm}^3$  are shown in Fig. 1. Recoveries ranged between 58.2% and 105.3%, and RSDs were between 1.9 and 5.7% (Table 2). The obtained results showed that matrix interferences of the analyzed environmental water samples had no influence on the recoveries of four targeted pesticides.

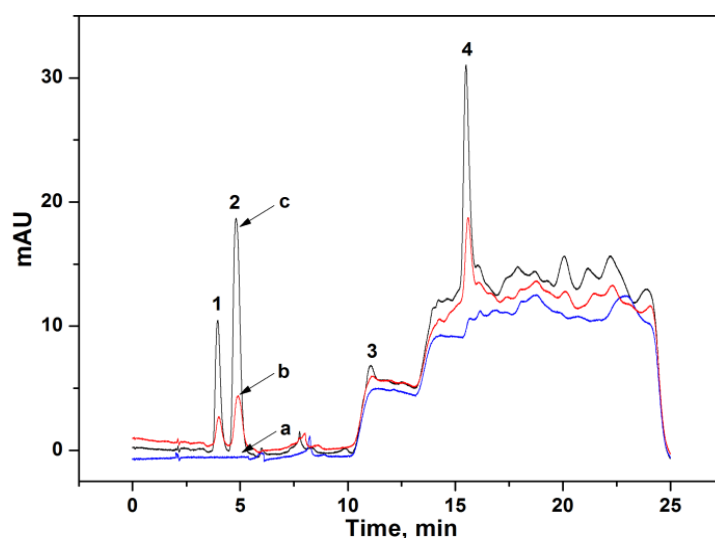


**Figure 1.** Chromatograms of extracted pesticides from a) unspiked tap water, b) and c) spiked tap water samples with 0.05 and 0.25  $\mu\text{g}/\text{dm}^3$ , respectively, after SPE-CSAC procedure under optimized conditions. Peak identification: 1) Imi, 2) Ace, 3) Sim and 4) Lin.

**Table 2.** Recoveries of the selected pesticides from spiked tap water samples after the SPE-CSAC preconcentration procedure (n = 3).

Analyte	Tap water samples		
	Concentration added ( $\mu\text{g L}^{-1}$ )	R (%)	RSD (%)
Imi	0.05	94.1	2.3
	0.25	97.6	2.1
Ace	0.05	98.3	2.8
	0.25	98.7	1.9
Sim	0.05	102.7	5.7
	0.25	105.3	4.8
Lin	0.05	58.2	3.2
	0.25	63.5	2.4

## CONCLUSION

In the present work, CSAC was successfully applied for the preconcentration of selected pesticides in water samples. Under the optimized conditions, satisfied recoveries, wide linear ranges, low LODs

and low RSDs were observed. Thus, it can be concluded that the developed SPE-HPLC-DAD method based on CSAC as a low-cost adsorbent has a large potential as an inexpensive and efficient sample preparation method, which could be widely used in the future for the determination of varying polarity pesticides at trace levels in environmental water samples.

#### ***Acknowledgement***

The research was funded by the Ministry of Education, Science and Technological Development of the Republic of Serbia.

#### **REFERENCES**

- [1] J. J. Villaverde, B. Sevilla-Morán, C. López-Goti, J. L. Alonso-Prados, P. Sandín-España, *Trends in Analytical Chemistry*, 2016, 80, 568-580.
- [2] D. A. Lambropoulou, T. A. Albanis, *Analytical and Bioanalytical Chemistry*, 2007, 389, 1663-1683.
- [3] Y. R. Tahboub, M. F. Zaater, Z. A. Al-Talla, *Journal of Chromatography A*, 2005, 1098, 150-155.
- [4] M. Li, J. Wang, C. Jiao, C. Wang, Q. Wu, Z. Wang, *Journal of Chromatography A*, 2016, 1469, 17-24.
- [5] S. Meseguer-Lloret, S. Torres-Cartas, M. Catalá-Icardo, E. F. Simó-Alfonso, J. M. Herrero-Martínez, *Analytical and Bioanalytical Chemistry*, 2017, 409, 3561-3571.
- [6] J. Zhang, H. K. Lee, *Journal of Chromatography A*, 2006, 1117, 31-37.
- [7] R. Carabias-Martínez, C. García-Hermida, E. Rodríguez-Gonzalo, L. Ruano-Miguel, *Journal of Separation Science*, 2005, 28, 2130-2138.

## DEVELOPMENT OF CHITOSAN-BASED HYDROGEL BEADS FOR HEAVY METALS REMOVAL FROM AQUEOUS SOLUTIONS

K. Stanković, Đ. Petrović, I. Telečki, R. Vujasin, Lj. Matović, A. Devečerski, K. Kumrić

*"Vinča" Institute of Nuclear Sciences – National Institute of the Republic of Serbia, University of Belgrade, Belgrade, Serbia. (kkumric@vinca.rs)*

### ABSTRACT

Chitosan and its modified forms have received great attention as potential adsorbents due to its outstanding adsorption characteristics toward removal of various toxic heavy metal ions from aqueous solutions. In this work, porous chitosan hydrogel beads (CHB) and CHB cross-linked with glutaraldehyde (GLA) and citric acid (CA) were synthesized and used for investigation of its adsorption performances toward the removal of Pb(II), Cu(II), Zn(II), Cd(II) and Cr(VI) ions from water in batch and dynamic systems. Maximum removal was achieved in the pH ranges of 4.0 - 6.5 and 2.0 - 3.5 for divalent cations and Cr(VI) oxyanion, respectively. The equilibrium adsorption data were best fitted by the Langmuir isotherm model. Based on the optimal conditions, the fixed-bed breakthrough curves for the removal of the studied metal ions from the aqueous solutions using fixed-bed columns were experimentally evaluated, as well as theoretically predicted using COMSOL Multiphysics software.

### INTRODUCTION

Hydrogels are three-dimensional polymeric networks that swell in contact with water but maintaining their structural integrity. Natural biopolymers, such as chitosan, are well-developed as the matrix to fabricate hydrogels to meet different demands [1]. Favorable characteristics of chitosan, such as resource abundance, non-toxicity, biodegradability and existence of sufficiently active sites ( $-NH_2$  and  $-OH$ ) for adsorption of various pollutants, make chitosan-based hydrogels the promising biosorbents for the removal of heavy metal ions from aqueous solutions. Chitosan-based hydrogels have numerous advantages compared to raw, powdery chitosan, including decrease crystallinity, high porosity and large pore sizes, which may facilitate a fast diffusion of heavy metal ions toward a large number of internal  $-NH_2$  and  $-OH$  functional groups of the adsorbent [2, 3]. Besides, chitosan-based hydrogels in the form of uniform beads are convenient for utilization in continuous fixed-bed columns.

The aim of the present study was to (1) synthesize chitosan-based hydrogel beads (CHB) and modified CHB with glutaraldehyde (GLA) and citric acid (CA) and (2) investigate its adsorption performance toward the removal of Pb(II), Cu(II), Zn(II), Cd(II) and Cr(VI) ions from aqueous solutions in batch and dynamic systems. Batch adsorption experiments were conducted to evaluate the effect of the initial solution pH and initial metal ion concentrations on the removal efficiency of the studied metal ions. The equilibrium adsorption data were analyzed using Langmuir and Freundlich isotherm models. Finally, the adsorption process using CHB-GLA-CA as adsorbent was studied in a continuous laboratory-scale fixed-bed column. The obtained breakthrough curves for the removal of the studied metal ions from the aqueous solutions were experimentally evaluated, as well as theoretically predicted using COMSOL Multiphysics software pack. The COMSOL software enables analysis of hydrodynamic behavior of breakthrough curves and its application to scale-up for real continuous systems.

## METHODS

Chitosan powder with medium molecular weight (100 – 300 kDa) and deacetylation degree higher than 90% was purchased from Acros Organics (Belgium), while GLA solution and CA were purchased from Sigma-Aldrich (USA). Preparation of chitosan adsorbent in the form of hydrogel beads was done by dissolving 1 g of chitosan powder in 40 cm<sup>3</sup> of 2 wt% of acetic acid solution. Then, the obtained solution was dropped into 1 mol/dm<sup>3</sup> NaOH solution to form uniform chitosan beads (CHB). In order to form CHB-GLA-CA hydrogel beads, chitosan solution was firstly mixed with 0.025% GLA for 4 h and then was dropped into 1 mol/dm<sup>3</sup> NaOH. The formed CHB and CHB-GLA were kept in the NaOH solution for the next 24 h. Afterwards, CHB and CHB-GLA were rinsed with deionized water until neutral pH was reached. Secondly, CHB-GLA beads were immersed in aqueous 1% (w/v) CA solution for 24 h. The CHB-GLA-CA beads were repeatedly washed with deionized water to wash out the non-reacted CA. Finally, both types of wet hydrogel beads (CHB and CHB-GLA-CA) were dried using freeze-drying and stored for further use.

Batch adsorption experiments were carried out at room temperature by mixing 0.05 g of adsorbent (either CHB or CHB-GLA-CA) with 25 cm<sup>3</sup> of Pb(II), Cu(II), Zn(II), Cd(II) and Cr(VI) solutions in closed plastic bottles. The samples were shaken on the laboratory shaker (Heidolph, Germany) for 240 min at the stirring speed of 150 rpm. The effect of pH was studied by changing pH of the adsorption solution containing either 12.5 mg/dm<sup>3</sup> each of the investigated divalent cations (Pb(II), Cu(II), Zn(II), Cd(II)) or 10 mg/dm<sup>3</sup> of Cr(VI) oxyanions. pH was adjusted in the range 2 – 7 either with 0.1 mol/dm<sup>3</sup> HNO<sub>3</sub> or 0.1 mol/dm<sup>3</sup> NaOH. Adsorption isotherms were investigated in the concentration range from 2.5 to 400 mg/dm<sup>3</sup> at pH 5.1 for divalent cations, i.e. 2.5 for Cr(VI) oxyanions. The concentration of heavy metal ions was determined with a polarography system 797 VA Computrace analyser (Metrohm, Switzerland) by using the Metrohm's procedures for the voltammetric determination of (1) zinc, cadmium, lead and copper in water samples No. 231/2 e and (2) Cr(VI) ions in water samples No. 116/3 e.

Continuous fixed-bed experiments were performed in plastic column of 20 cm in height and internal diameter of 19.6 mm with perforated support at the bottom and top of the column. The column was packed with 0.5 g of CHB-GLA-CA, bed height was 21 mm. Feed solution was introduced to the top of the column at the flow rate of 1.2 cm<sup>3</sup>/min via a peristaltic pump. The samples of the heavy metal ions solutions were gathered at specified time intervals to determine the concentration of investigated metal ions by 797 VA Computrace analyser. The obtained experimental results were compared with the theoretical values obtained from the solution of the Advection Dispersion Reaction (ADR) equation using COMSOL Multiphysics software.

## RESULTS AND DISCUSSION

Solution pH is one of the most important adsorption parameters that may affect both the surface properties of the adsorbent and ionic forms of metal ions in the solution, and consequently contribute to a greater or lesser efficiency of adsorption process. In order to study the influence of the initial solution pH on Pb(II), Cu(II), Zn(II), Cd(II) and Cr(VI) removal by CHB and CHB-GLA-CA, the adsorption experiments were performed in the pH range of 2 to 7 at an initial metal ion concentrations of 12.5 mg/dm<sup>3</sup> for divalent cations, i.e. 10 mg/dm<sup>3</sup> for Cr(VI) oxyanions, and solid to liquid ratio of 2 g/dm<sup>3</sup>.

As shown in Fig. 1a, removal efficiency,  $E$  (%), of Cu(II) ions increased with increasing pH of the solution and reached a maximum value of 99.8% in the pH range from 4.5 to 6.5. Lower removal efficiency of Cu(II) ions at pH < 4.5 can be explained by the competition between protons and Cu(II) ions for the adsorption sites. Further, the protonation of amine groups and carboxylic groups in CHB-GLA-CA induced electrostatic repulsion of Cu(II) cations. At higher pHs, the negative charge density on the chitosan surface and the dissociation degree of –OH groups increases resulting in higher

removal of Cu(II) cations due to the electrostatic interaction with Cu(II) ions. Similar behavior was observed for the other three metal cations. The maximum removal efficiency of Pb(II), Zn(II) and Cd(II) was 95.1, 34.4 and 37.5%, respectively. For the investigated metal cations, pH value of 5.1 was selected as optimal for further adsorption experiments.

In contrast to heavy metal cations, Cr(VI) oxyanion showed (Fig. 1b) maximum removal efficiency of 98.5% at pH < 3. At low pH values, the surface of both adsorbents would be surrounded by the hydronium ions which enable the interaction of Cr(VI) oxyanions with binding sites of the CHB and CHB-GLA-CA adsorbents by electrostatic attraction forces. As the pH increased, the overall surface charge on the adsorbents became negative and adsorption of Cr(VI) ions decreased. pH 2.5 was used in further Cr(VI) adsorption experiments.

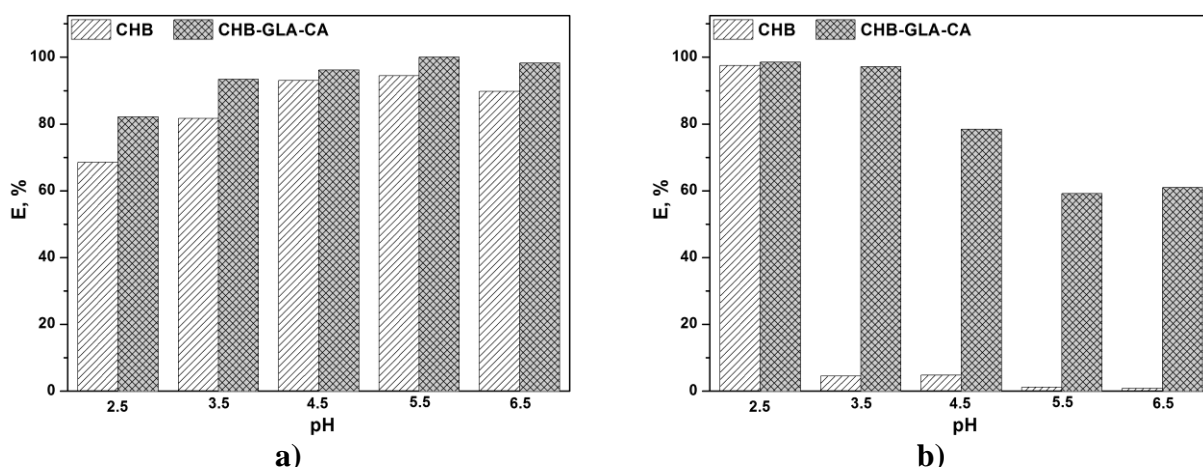


**Figure 1.** Effect of pH on the removal efficiency of a) Cu(II) and b) Cr(VI) ions using CHB and CHB-GLA-CA as adsorbents.

Under the optimized pH conditions for Pb(II), Cu(II), Zn(II), Cd(II) and Cr(VI) adsorption onto CHB and CHB-GLA-CA, the experimental data obtained for the adsorption equilibrium of investigated metal ions at different initial metal ion concentrations were analyzed using the Langmuir and the Freundlich isotherm models. The obtained results showed that the Langmuir plots for all heavy metals had higher coefficients of determination,  $R^2$ , than the Freundlich, suggesting that the Langmuir isotherm is a good model for the adsorption of the studied metal ions onto CHB and CHB-GLA-CA. It means that the uptake of metal ions occurs on a homogeneous surface by monolayer adsorption. Parameters of the Langmuir isotherms for all metal ions are given in Table 1.

**Table 1.** Parameters of the Langmuir isotherms for the adsorption of Pb(II), Cu(II), Zn(II), Cd(II) and Cr(VI) ions onto CHB and CHB-GLA-CA.

Adsorbent	CHB			CHB-GLA-CA			
	Metal	$q_m$ , $mg\ g^{-1}$	$K_L$ , $dm^3\ mg^{-1}$	$R^2$	$q_m$ , $mg\ g^{-1}$	$K_L$ , $dm^3\ mg^{-1}$	$R^2$
Cu(II)		24.9	0.82	0.9702	42.5	1.21	0.9758
Pb(II)		21.6	0.74	0.9803	20.7	6.92	0.9833
Cd(II)		5.8	0.38	0.9969	7.9	0.10	0.9638
Zn(II)		4.9	0.39	0.9846	14.8	0.07	0.9778
Cr(VI)		110.7	0.07	0.9820	131.0	0.16	0.9888

Obviously, CHB-GLA-CA beads exhibited better adsorption performance compared to CHB, which could be ascribed to the supplemental functional groups (-COOH) attached to the surface of the CHB-GLA-CA adsorbent.

Adsorption of Pb(II), Cu(II), Zn(II), Cd(II) and Cr(VI) ions onto CHB-GLA-CA in fixed-bed column was conducted at constant operating conditions and the obtained breakthrough curves for the two, Pb(II) and Cd(II), out of five ions are presented in Figure 2a and b, respectively. The ADR equation was used to describe the breakthrough curves with the aid of COMSOL Multiphysics software as simulation and numerical tool. As can be seen in Fig. 2, good agreement between the predicted theoretical breakthrough curves and the experimental results can be observed for both metal ions. Similar results were obtained for the other three metals.

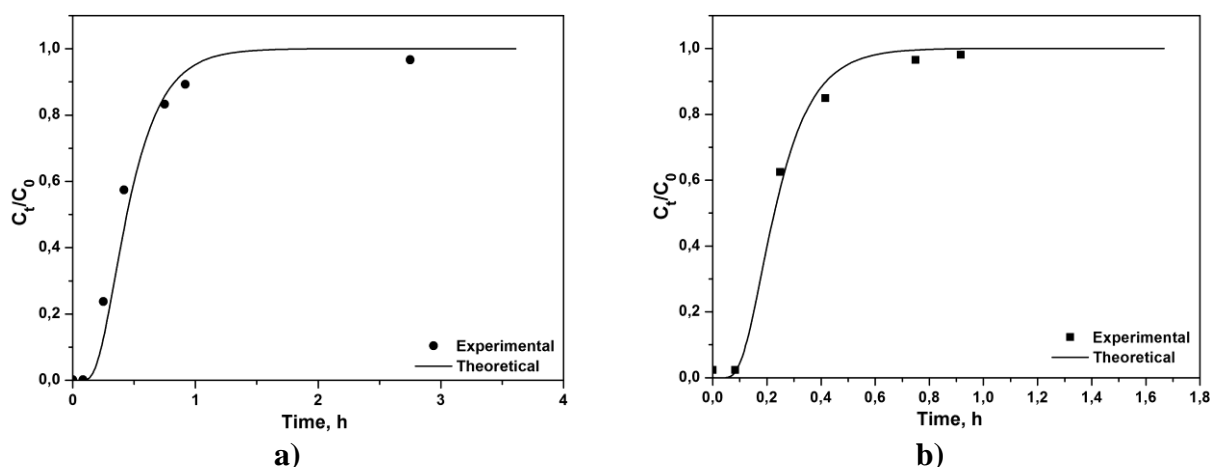


**Figure 2.** Breakthrough curves for adsorption of a) Pb(II) and b) Cd(II) ions onto CHB-GLA-CA adsorbent.

## CONCLUSION

Chitosan-based hydrogel beads modified with glutaraldehyde and citric acid remarkably enhanced the adsorption capacity of all investigated heavy metal ions. Maximum removal efficiency was achieved in the pH ranges of 4.0 - 6.5 and 2.0 - 3.5 for divalent cations and Cr(VI) oxyanion, respectively. The equilibrium adsorption data were best fitted by the Langmuir isotherm model and the maximum adsorption capacity for all metal ions was 20% higher for CHB-GLA-CA compared to CHB. Hence, it can be concluded that CHB-GLA-CA could be efficiently used for the removal of heavy metal ions from wastewaters.

Preliminary continuous fixed-bed adsorption experiments showed that predicted and experimentally obtained breakthrough curves for all heavy metal ions are in good agreement, proving that COMSOL Multiphysics software potentially could be used as numerical tool to predict breakthrough curves for real dynamic systems operated under different conditions.

## Acknowledgement

The research was funded by the Ministry of Education, Science and Technological Development of the Republic of Serbia.

## REFERENCES

- [1] B. Qu, Y. Luo, International Journal of Biological Macromolecules, 2020, 152, 437-448.
- [2] C. Shi, C. Lv, L. Wu, X. Hou, Journal of Hazardous Materials, 2017, 338, 231-249.
- [3] L. Zhang, Y. Zeng, Z. Cheng, Journal of Molecular Liquids, 2016, 214, 175-191.

## PARTITIONING OF DIFFERENT POLARITY PESTICIDES, DELTAMETHRIN AND DICAMBA, IN AQUEOUS BIPHASE SYSTEMS WITH IONIC LIQUIDS

A. Jocić, S. Marić, J. Milićević and A. Dimitrijević

*Vinča Institute of Nuclear Sciences, University of Belgrade, P.O. Box 522, 11001 Belgrade, Serbia  
(sladjana.maric@vin.bg.ac.rs)*

### ABSTRACT

An aqueous biphasic system (ABS) composed of the imidazolium and choline based ionic liquids mixed with potassium phosphate salt ( $K_3PO_4$ ) was suggested as the ABS system suitable for extraction of two different polarity pesticides deltamethrin (DLT) and dicamba (DCM). The influence of two ionic liquid (IL) cations on the partitioning behavior of examined pesticides from aqueous solution was evaluated. The results showed that both pesticides, DLT and DCM preferably migrate to the more hydrophobic, IL-rich phase. The higher DLT partition coefficient was obtained for more hydrophobic imidazolium-IL enriched ABS phase ( $\log K_{DLT}=2.59$ ) compared to ABS with choline IL ( $\log K_{DLT}=2.25$ ). On the other hand, less hydrophobic DCM distributes more in the IL-rich phase of choline-based ABS ( $\log K_{DCM}=0.85$ ) in relation to imidazolium-based ABS ( $\log K_{DCM}=0.33$ ).

### INTRODUCTION

Deltamethrin (DLT) is a very efficient insecticide that is extensively used to control agricultural insects and ectoparasites in animals, also control human disease vectors, such as mosquitoes [1]. Dicamba (DCM) is a selective systemic herbicide widely used to kill broadleaf weeds that infest farmlands [2]. Increasing the use of pesticides in agricultural practices for controlling weed growth and reducing the loss of crops is a major contamination source for both surface and groundwater resources. Besides the agricultural activities, pesticides can enter into the environment through industrial waste, storage tank leakage, landfills leaching, sewer, and many other sources [3]. During recent years, international concern has arisen on a wide range of toxic side effects of pesticides to non-target organisms such as humans and animals. Therefore, it is important to develop reliable, highly sensitive, and easily operated methods to monitor their concentration in the environment and food. Pretreatment of samples is the first step in every analytical method of pesticide determination. Liquid-liquid extraction (LLE) is the oldest pretreatment technique prescribed in many standard analytical methods for the separation and extraction of pesticides. However, conventional LLEs are based on the utilization of a large amount of hazardous organic solvents and also a large volume of sample is often required for trace analysis. Aqueous biphasic system (ABS) is an environmentally safe alternative to classic LLE and can be formed by mixing aqueous solutions of two water-soluble components at appropriate concentrations or a particular temperature. High water content in both phases, as well as biodegradable, recyclable, non-toxic, and nonflammable components, constitutes the most valuable environmental advantage of the ABS. Ionic liquids (ILs) are organic salts with unique properties such as liquid states at low temperature, negligible vapor pressure, high thermal stability, and they as novel, greener solvents have been strategically introduced as components to ABS [3].

This study aims to evaluate the partitioning of two different polarity pesticides (DLT and DCM) in ABS composed of IL, inorganic salt and water. The influence of ILs cation on the partitioning of the targeted pesticide was investigated using two ILs: 1-butyl-3-methylimidazolium chloride,  $[C_4mim]Cl$ , and choline chloride,  $[Ch]Cl$ .

## METHODS

A ternary mixture was prepared within the biphasic region containing 30 wt% [C<sub>4</sub>mim]Cl, 11 wt% of K<sub>3</sub>PO<sub>4</sub>, and 59 wt% of an aqueous solution of examined pesticide (DLT or DCM). For [Ch]Cl a composition of 21 wt% of K<sub>3</sub>PO<sub>4</sub>, 30 wt% of IL, and 49 wt% of the aqueous solution of DLT or DCM was used due to the smaller two-phase region of ABS with this IL. The ternary mixtures compositions were chosen based on the phase diagrams of each IL earlier reported [4,5]. Each mixture was vigorously vortex-stirred at 2500 rpm and allowed to reach equilibrium by the separation of both phases for 12 h and at 25°C. After a careful separation of both phases, the amount of targeted pesticide at each aqueous phase was quantified by measuring the absorbance at 264 nm with the UV spectrometer (Spectrophotometer LLG-uniSPEC2). Possible interferences of both the inorganic salt and the IL with the analytical method were taken into account and blank controls were employed. The partition coefficients of deltamethrin and dicamba (DLT and DCM),  $K_{DLT}$ , and  $K_{DCM}$ , were determined as the ratio of the concentration of DLT or DCM in the IL-rich and the inorganic salt (K<sub>3</sub>PO<sub>4</sub>)-rich phase. For both the ternary mixtures evaluated, the top phase is the IL-rich phase while the bottom phase is the K<sub>3</sub>PO<sub>4</sub>-rich phase.

## RESULTS AND DISCUSSION

The liquid-liquid equilibrium data for IL-based ABS (IL + K<sub>3</sub>PO<sub>4</sub> + H<sub>2</sub>O) obtained at T = 25 °C and atmospheric pressure (p = 0.1 MPa) are shown in Figure 1a. For a fixed concentration of IL (30 wt%), a lower amount of inorganic salt is needed to form the [C<sub>4</sub>mim]Cl–K<sub>3</sub>PO<sub>4</sub> ABS compared with ABS based on [Ch]Cl–K<sub>3</sub>PO<sub>4</sub>. This is a consequence of the higher hydrophobicity of the imidazolium cation compared to hydrophilic choline cation, being thus the [C<sub>4</sub>mim]Cl more easily excluded for a second liquid phase. These ternary phase diagrams were used for determining the mixture compositions in the two phases range used for extraction experiments.

The values of the partition coefficients of pesticide between the two phases are dependent on the specific and favorable interaction of the pesticide with each of the components present in the system. The obtained partition coefficients of pesticide in the IL-based ABS at 25°C are presented in Figure 1b. In both systems, it is observed a preferential partitioning of pesticides for the more hydrophobic IL-rich phase with partition coefficients larger than 1 ( $\log K > 0$ ). Pesticides are different polarity, the logarithm of octanol/water partition coefficient,  $\log(K_{ow})$  is 4.60 and –1.88 for DLM and DCM, respectively, so their partitioning is mainly related to the relative hydrophobicity of ABS phases. From the results, it is clear that DLM, has higher partition coefficients, owing to its higher hydrophobicity, compared to DCM. The results show that the  $\log K_{DTM}$  values increase with the increasing hydrophobic character of ILs. Therefore, the better results ( $\log K_{DLT}=2.59$ ) are obtained with [C<sub>4</sub>mim]Cl as the more hydrophobic IL, compared to [Ch]Cl ( $\log K_{DLM}=2.25$ ). On the contrary, the lower partitioning was obtained for more hydrophilic pesticide DCM with partition coefficients  $\log K_{DCM}=0.33$  in [C<sub>4</sub>mim]Cl based ABS and  $\log K_{DCM}=0.85$  in [Ch]Cl based system.

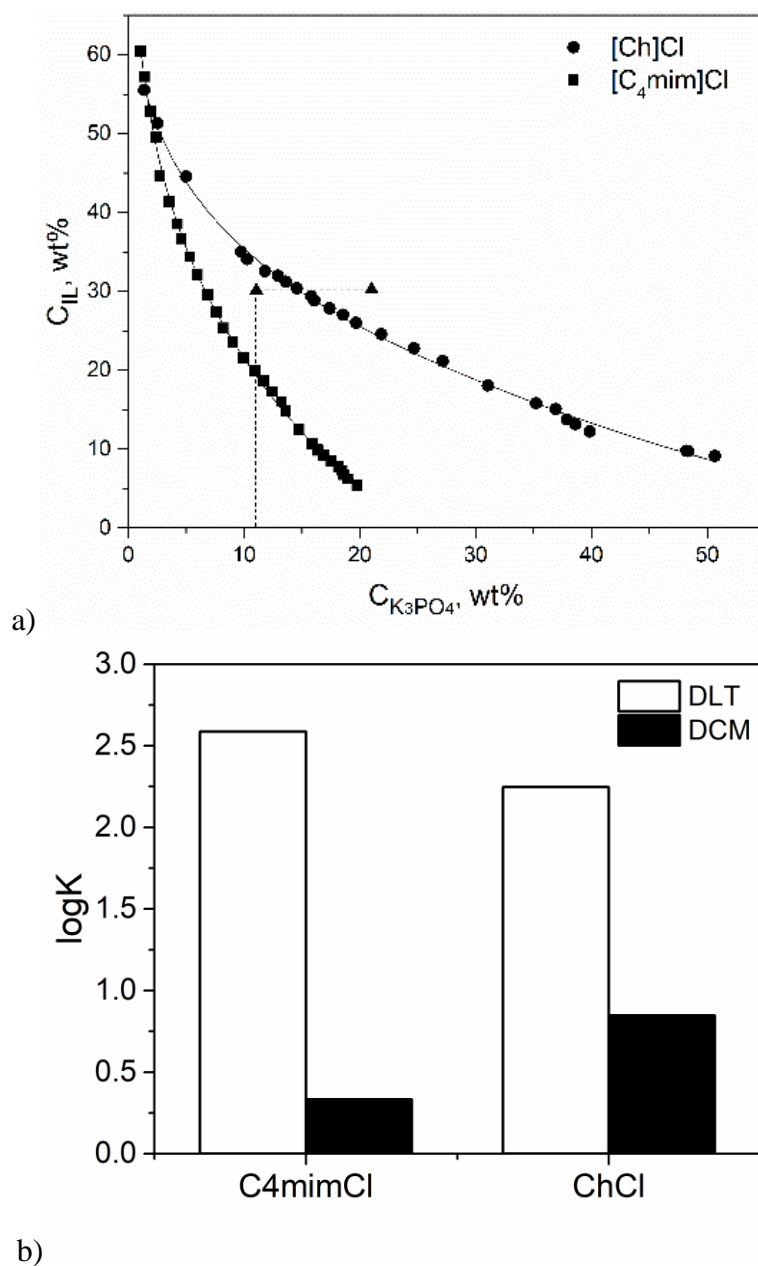


**Figure 1.** a) Phase diagrams of the ABS composed of  $[C_4mim]Cl + K_3PO_4 + H_2O$  (■) and  $[Ch]Cl + K_3PO_4 + H_2O$  (●) as well as the ternary mixture compositions used for extraction (▲) at  $T=25^\circ C$  and  $p=0.1$  MPa .

b) Logarithmic function of partition coefficient ( $\log K$ ) of deltamethrin (DLT) and dicamba (DCM) in the IL-based ABS at  $25^\circ C$ .

## CONCLUSION

In this study, the partitioning of the two pesticides, deltamethrin and dicamba, in the aqueous biphasic system (ABS) based on different ILs ( $[C_4mim]Cl$  and  $[Ch]Cl$ ) in combination with potassium phosphate salt was investigated. It was found that pesticides preferably migrate to the IL-rich phase in both studied systems. Highly hydrophobic DLM shows a high partition coefficient in the  $[C_4mim]Cl-K_3PO_4-H_2O$  ABS that makes this system suitable for its extraction. On the contrary,  $[Ch]Cl$ -based ABS is a more suitable system for the extraction of less hydrophobic DCM. It can be concluded that studied aqueous biphasic platform has great potential for extraction and preconcentration of targeted pesticide, but further optimization studies (which include evaluation of the influence of various operational parameters such as temperature, pH, pesticide content, different ABS mixture composition) are needed to reach adequate analytical performance.

**Acknowledgement**

This work was supported by the Ministry for Science of the Republic of Serbia (Grant no. 451–03–9/2021–14/200017).

**REFERENCES**

- [1] Q. Lu, Y. Sun, I. Ares, A. Anadón, M. Martínez, Z. Yuan, X. Wang, *Environmental Research*, 2019, 170, 260–281.
- [2] H. A. Isiyaka, K. Jumbri, N. S. Sambudi, Z. U. Zango, N. Ain, F. Abdullah, B. Saad, A. Mustapha, *RSC Advances Open*, 2020, 10 43213.
- [3] A. Dimitrijević, L. Ignjatović, A. Tot, M. Vraneš, N. Zec, S. Gadžurić, T. Trtić-Petrović, *Journal of Molecular Liquids*, 2017, 243, 646–653
- [4] P. H. S. Calhau, R. C. S. Sousa, I. J. B. Santos, S. M. Silva, J.S.R. Coimbra, *Journal of Chemical and Engineerin Data*, 2019, 64, 3781–3785.
- [5] F. Pourebrahim, S. Shahriari, M. Salehifar, H. Mozafari, *Bulletin of the Chemical Society of Japan*, 2015, 88, 1494–1499.

# SYNTHESIS OF ACTIVATED CARBONS FROM WATER HYACINT BIOMASS AND ITS APPLICATIONS AS ADSORBENTS FOR HERBICIDE GLYPHOSATE

A. Hakky Mohammad and M. Kijevcanin

*University of Belgrade, Faculty of Technology and Metallurgy,  
Karnegijeva 4, 11000 Belgrade, Serbia*

## ABSTRACT

In this work the activated carbons were synthesized from hyacinth biomass by chemical activation with  $ZnCl_2$ , followed by carbonization in temperature range from  $400^\circ C$  to  $700^\circ C$ . The content of C, H and N was estimated by elemental analysis while the textural properties of samples were obtained from adsorption-desorption isotherms of  $N_2$  at  $-196^\circ C$ . The obtained activated carbons were applied as adsorbents of herbicide glyphosate.

## INTRODUCTION

Due to rapid growth and formation of dense mat, water hyacinth causing a variety of negative effects on surface fresh waters [1]. Utilization of water hyacinth biomass as source of lignocellulose to produce activated carbon can be one of the strategies of water pollution control.

Organophosphate herbicide glyphosate [N-(phosphonomethyl)-glycine], has been widely used although the phosphonates may have a significant impact on human health [2]. In this study activated carbons were synthesized from water hyacinth biomass and tested as herbicide glyphosate adsorbents.

## EXPERIMENTAL

### *Materials*

The water hyacinth (WH) plant (Karbala, Iraq) was used as raw material for obtaining of activated carbons. The raw WH was washed with distilled water. The roots and stalks without leaves were chopped and naturally dried on air for 14 days. The dry WH was crushed and ground in rotary mill, and finally sieved in order to obtain particle size 1.4 – 2.0 mm.

The  $ZnCl_2$  ( $\geq 98\%$ ), supplied from Sigma-Aldrich, was used as activating agent in activated carbons synthesis. The herbicide glyphosate – GPh ( $\geq 99\%$ ), used in adsorption study, was purchased from Merck.

### *Preparation of activated carbon*

The activated carbons based on dry water hyacinth biomass were prepared by chemical activation of dry WH with  $ZnCl_2$  according to procedure described in literature [3]. The mass ratio of  $ZnCl_2$  and WH during impregnation was 2:1. The 40 g of dry WH sample was added to 150 ml of solution with appropriate mass of  $ZnCl_2$  and stirred at  $60^\circ C$  during 4 hours. The solid and liquid phases were separated by filtration through Buchner funnel and dried at  $105^\circ C$  during 24h. The carbonization of activated WH was carried out in electrical furnace with nitrogen flowing ( $150\text{ cm}^3\text{ min}^{-1}$ ) and heating rate of  $15^\circ C\text{ min}^{-1}$ . The carbonization during 60 min was conducted at temperature range from  $400$  to  $700^\circ C$ . The obtained activated carbons were rinsed with 0.5 M HCl in order to remove activating agent, and finally washed with hot distilled water until neutral pH. The activated carbons were denoted according to carbonization temperature ( $AC_{400}$ ,  $AC_{500}$ ,  $AC_{600}$  and  $AC_{700}$ ).

### *Methods*

The elemental analysis (C,H,N) of activated carbons was performed using elemental analyzer instrument (Thermo Scientific - FlashEA1112 Automatic Elemental Analyzers). The textural properties (specific surface area -  $S_{BET}$ , the total pore volume -  $V_T$ , micropores volume -  $V_{mic}$  and

mesopores volume –  $V_{\text{meso}}$ ) of activated carbons were obtained from adsorption-desorption nitrogen isotherms at  $-196\text{ }^{\circ}\text{C}$  (Micromeritics' ASAP® 2020).

During adsorption study, the glyphosate concentration was determined by spectrophotometer (UV-VIS 1800 Shimadzu) at  $\lambda_{\text{max}}=264\text{ nm}$ . The adsorption study was carried out at  $25\text{ }^{\circ}\text{C}$ ; the concentration of GPh was  $100\text{ mg dm}^{-3}$ . The volume of GPh solution of  $75.0\text{ cm}^3$  was introduced into the glass flasks and mixed with  $20\text{ mg}$  of adsorbents. At predetermined time intervals between  $5\text{ min}$  and  $240\text{ min}$ , the GPh concentration in the supernatant was analyzed, with previous separation of the solid phase by centrifugation at  $12000\text{ rpm}$ .

The adsorbed amount of the pollutant ( $q_t$ ) was calculated according to Eq.1.

$$q_t = \frac{(C_i - C_t) \cdot V}{m} \quad (1)$$

where  $q_t$  is the amount of GPh adsorbed at time  $t$  ( $\text{mg g}^{-1}$ ),  $C_i$  – initial concentration of GPh ( $\text{mg dm}^{-3}$ ), and  $C_t$  – concentration of GPh in solution in time  $t$  ( $\text{mg dm}^{-3}$ ).

## RESULTS AND DISCUSSION

The result of the elemental analysis of dry WH and activated carbons are presented in Table 1. The major organic elements in all investigated samples are carbon and oxygen. The WH has higher content of ash, consisting mainly from silica-oxides and metal-oxides.

**Table 1.** The results of elemental analysis

Sample	Content of elements (wt%)				
	C	H	O <sup>a</sup>	N	Ash
Dry WH	41.22	6.23	47.07	1.54	3.94
AC <sub>400</sub>	80.31	3.37	15.16	0.32	0.84
AC <sub>500</sub>	81.57	3.15	14.20	0.27	0.81
AC <sub>600</sub>	83.24	2.98	12.79	0.24	0.75
AC <sub>700</sub>	84.15	2.75	12.23	0.19	0.68

<sup>a</sup>The oxygen content was calculated by difference

The treatment with HCl after activation process led to leaching of metal cations and therefore reduced the ash content. During carbonization process, with temperature increases the content of carbon increased, which was expected. These results are in agreement with the results described in literature [3].

The surface area, total pore volume, volume of micropores and mesopores of activated carbons are shown in Table 2.

**Table 2.** Surface area and pore volumes of activated carbons obtained at different temperatures

Temperature ( $^{\circ}\text{C}$ )	$S_{\text{BET}}$ ( $\text{m}^2\text{ g}^{-1}$ )	$V_{\text{tot}}$ ( $\text{cm}^3\text{g}^{-1}$ )	$V_{\text{mic}}$ ( $\text{cm}^3\text{g}^{-1}$ )	$V_{\text{meso}}$ ( $\text{cm}^3\text{g}^{-1}$ )
400	1154	0.602	0.298	0.298
500	1317	0.697	0.152	0.541
600	1284	0.670	0.135	0.527
700	1163	0.605	0.113	0.485

$S_{\text{BET}}$ -specific surface area according to BET method;  $V_{\text{tot}}$ -total pore volume;  $V_{\text{mic}}$ -micropore volume;  $V_{\text{meso}}$ -mesopore volume

The surface areas and pore volumes of activated carbons increased with increasing final carbonization temperature from 400°C to 500°C, while further increasing of temperature led to  $S_{\text{BET}}$  decreasing. It was also observed that higher carbonization temperatures reduced microporosity, and had positive impact on mesoporosity development, which was in agreement with literature data [4, 5].

The activated carbons were applied as adsorbents of herbicide GPh. The effect of contact time on the amount of adsorbed GPh was shown at Fig. 1.

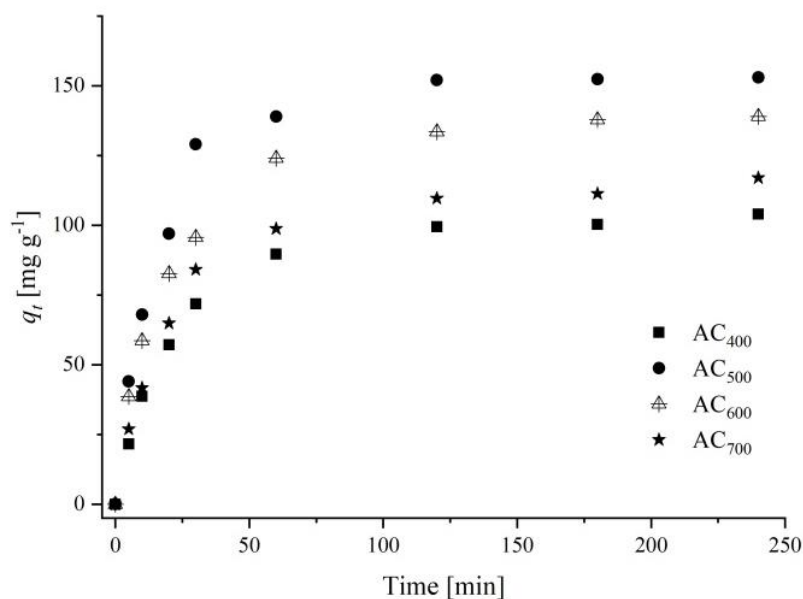


**Figure 1.** The effect of contact time on GPh adsorption onto activated carbons obtained at different carbonization temperature

The adsorption results reveal that amount of adsorbed GPh is in correlation with surface development. The AC<sub>500</sub> adsorbed the highest amount of GPh, with value of  $q_{120}=153.4 \text{ mg g}^{-1}$ . For investigated adsorption processes, the 120 min can be considered as equilibrium time, since there is no significant change in amount of adsorbed GPh for longer times.

## CONCLUSION

The activated carbons were obtained from water hyacinth biomass by process of chemical activation with  $\text{ZnCl}_2$  on carbonization temperature in range from 400 °C to 700 °C. The activated carbon obtained at 500 °C shown best develop surface area of  $1317 \text{ m}^2 \text{ g}^{-1}$  as well as highest value for amount of adsorbed glyphosate of  $153.4 \text{ mg g}^{-1}$ . This study confirmed that water hyacinth waste biomass can be successfully converted to useful adsorbent.

## Acknowledgement

Authors acknowledge Prof. Dr. Yarub Al-Douri, Nanotechnology and Catalysis Research Centre, University of Malaysia, for experimental work support.

## REFERENCES

- [1] V. Tobias, J. Conrad, B. Mahardja, *Biol. Invasions*, 2019, 21, 3479–3490.

- [2] S. Bradberry, A. Proudfoot, J. Vale, 2004, *Toxicol. Rev.* 23, 159-167.
- [3] T. H. Liou, 2010, *Chem. Eng. J.*, 158, 129–142.
- [4] M. Gómez-Tamayo, A. Macías-García, M.A. Díez, E.M. Cuerda-Correa, 2008, *J. Hazard. Mater.*, 153, 28–36.
- [5] Q. Qian, M. Mochida, H. Tatsumoto, 2007, *Bioresour. Technol.* 98, 353–360.

## ISOLATION OF ACETAMINOPHEN FROM IONIC LIQUID RICH-PHASE OF THE AQUEOUS BIPHASIC SYSTEM

S. Marić, A. Jocić, A. Dimitrijević

*Vinča Institute of Nuclear Sciences, University of Belgrade, P.O. Box 522, 11001 Belgrade, Serbia  
(sladjana.maric@vin.bg.ac.rs)*

### ABSTRACT

In this work, extraction of acetaminophen using an aqueous biphasic system and its isolation from the ionic liquid-rich phase through precipitation with the anti-solvents were studied. The obtained result show that system composed of 1-butyl-3-methylimidazolium chloride and copolymer is able to extract acetaminophen to ionic liquid phase. Also, the results indicate that the isolation of acetaminophen from ionic liquid phase is possible by the addition of potassium chloride in appropriate volume ratio. The results obtained can be used in the development of process for the recovery of valuable drugs from pharmaceutical wastes.

### INTRODUCTION

Pharmaceutical waste can be regarded as a source of valuable compounds because about 90% of the Active Pharmaceutical Ingredients (APIs) are still in its active form past the expiration date [1]. For the recovery of various compounds from different matrices, the most commonly used method is Liquid-Liquid Extraction (LLE). Given that this method uses toxic volatile organic solvents, Aqueous Biphasic Systems (ABSs), as a water-based systems formed by combinations of compounds such as polymer-polymer, polymer-salt and ionic liquid (IL)-salt pairs of phase-forming components, have proven to be a good alternative to the traditional LLE. Ionic Liquids (ILs) as components of ABS, due to their unique properties and tunable characteristics, have been widely investigated for the extraction of alkaloids, antibiotics and amino acids. IL-based ABS offering simpler, quicker, greener, and highly more efficient procedures [2]. Recently researchers proposed three step processes for the recovery of target drugs from pharmaceutical wastes which consist of solid-liquid extraction of the APIs from unused pills, its extraction and purification using the IL-based ABS and the APIs isolation by precipitation with anti-solvent [1]. One of the most used APIs in analgesic drug acetaminophen (ACF), also known as paracetamol, can be extract from pharmaceutical waste using IL-based ABS [3]. Among the most investigated IL is certainly 1-butyl-3-methylimidazolium chloride [C<sub>4</sub>mim]Cl [4] mainly because of its non-toxic character and some very interesting properties such as the possibility to dissolve cellulose. Acetaminophen has two strong hydrogen donor sites, the amide group (N-H) and the hydroxyl group (O-H). The amide group additionally contains a C=O interaction site that may interact favorably with the aromatic ring hydrogens of [C<sub>4</sub>mim]<sup>+</sup> leading the preference of the ACF to IL-rich phase [5]. For the isolation of the target compounds extracted, precipitation by anti-solvents is the process most used due to its simple operation and scalability [4]. In this paper, extraction of ACF to IL-phase was performed using ABS composed of [C<sub>4</sub>mim]Cl and copolymer (Pluronic PE6200). The main objective of this work was to find the effective anti-solvent for isolation of ACF from IL.

### METHODS

**Extraction of ACF.** The phase diagram of the ABS composed of [C<sub>4</sub>mim]Cl (Sigma, USA) and PE6200 (BASF, Germany) was determined through the cloud point titration method at 25°C and atmospheric pressure [6]. ABS with the composition of 45 wt% of [C<sub>4</sub>mim]Cl + 32 wt% of PE6200 + 23 wt% deionized H<sub>2</sub>O and appropriate amounts of ACF (Sigma, USA) was mixed and centrifuged.

After separating the phases, concentrations of ACF in each phase, determined by means UV spectroscopy at 250 nm (Spectrophotometer LLG-uniSPEC2), were used to calculate ACF extraction recovery efficiency (RE %).

**Isolation of ACF.** Acetaminophen isolation from the 40 wt% aqueous solution of [C<sub>4</sub>mim]Cl was conducted through precipitation with anti-solvents, namely potassium chloride (KCl) and aluminum sulfate (Al<sub>2</sub>(SO<sub>4</sub>)<sub>3</sub>). The mass of ACF added was that at which saturation of the solution was achieved. Aqueous solutions of KCl (Alkaloid, Skopje) at 25 wt%, Al<sub>2</sub>(SO<sub>4</sub>)<sub>3</sub>·18H<sub>2</sub>O (Pliva, Zagreb) at both 10 wt% and 15 wt% were added in the proportion 1 : 2 (volume of initial solution : volume of anti-solvent). After the addition of the anti-solvent, a precipitate was formed, left 1h and then was centrifuged at 7000 rpm for 5 min. The same procedure was repeated for an aqueous solution of KCl in the proportions 1 : 1, 1 : 2 and 1 : 4 (volume of initial solution : volume of KCl). Isolation efficiencies of ACF were calculated from the equation:

$$IE (\%) = 100 - \left( \frac{m_{\text{antisol}}^{\text{ACF}}}{m_{\text{solution}}^{\text{ACF}}} \times 100 \right) \quad (1)$$

where  $m_{\text{antisol}}^{\text{ACF}}$  is the mass of ACF in the solution after addition of anti-solvent and  $m_{\text{solution}}^{\text{ACF}}$  is mass of ACF in the initial solution [4].

## RESULTS AND DISCUSSION

For the selected extraction point (which is located in the biphasic region of the phase diagram), RE of ACF toward the [C<sub>4</sub>mim]Cl-rich phase was higher than 70%, showing the capacity of the studied ABS to concentrate the ACF in IL-phase. The isolation of ACF from [C<sub>4</sub>mim]Cl with both KCl and Al<sub>2</sub>(SO<sub>4</sub>)<sub>3</sub>, has been achieved. KCl was selected to avoid introduction of new ionic species into the solution (since Cl<sup>-</sup> were already parts of the system) and Al<sub>2</sub>(SO<sub>4</sub>)<sub>3</sub> was selected because of the strong “salting-out” effect of this salt.

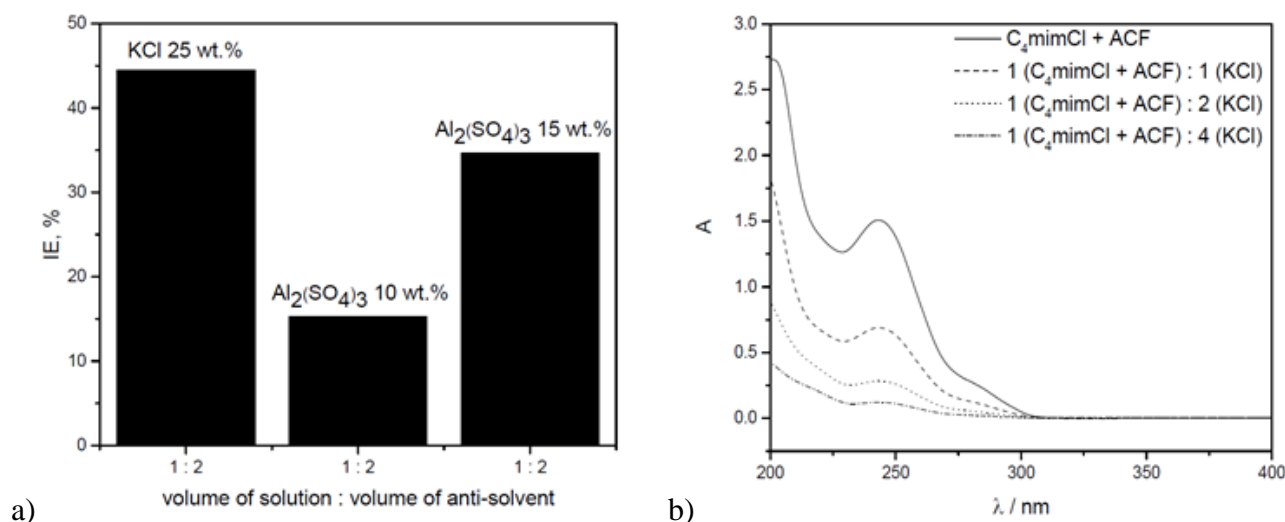


**Figure 1.** a) Isolation efficiency of ACF using three different anti-solvent composition (25 wt% KCl, 10 wt% and 15 wt% Al<sub>2</sub>(SO<sub>4</sub>)<sub>3</sub>) added in the proportion 1 : 2 (solution volume : anti-solvent volume) b) UV spectrum of ACF at different proportion of volume [C<sub>4</sub>mim]Cl solution to volume of KCl.

By comparing the results, Figure 1.a., of IE for anti-solvents (with different mass fraction) added in the same volume ratio, it can be concluded that KCl at 25 wt% is a better precipitating reagent. Consequently, the isolation of ACF by 25 wt% KCl was investigated additionally.

**Table 1.** Isolation efficiency of ACF obtained through precipitation of ACF from 40 wt. % aqueous solution of [C<sub>4</sub>mim]Cl with different anti-solvents.

Ratio of solution and anti-solvent	IE / %
<i>Potassium chloride at 25 wt%</i>	
1 : 1	8.66
1 : 2	44.49
1 : 4	61.60
<i>Aluminum sulfate at 10 wt%</i>	
1 : 2	15.29
<i>Aluminum sulfate at 15 wt%</i>	
1 : 2	34.69

Thus, from UV spectra of ACF in 40 wt% aqueous solution of [C<sub>4</sub>mim]Cl with KCl obtained for different volume ratio of [C<sub>4</sub>mim]Cl solution to volume of KCl (Figure 1.b), IE of ACF were calculated. Obtained results of isolation efficiency of ACF (equation 1) acquired during the ACF isolation step through precipitation with anti-solvents, are showed in Table 1. The highest isolation efficiencies of 61.60%, were obtained when the volume of the KCl is 4 times larger than the volume of initial solution. Thus, the change in the ionic strength of the medium caused by the introduction of anti-solvent in the system, reduce the interactions between ACF and the components of the solution leading to its precipitation.

## CONCLUSION

In this study, extraction of acetaminophen to IL-rich phase of ABS and its isolation from the same phase were investigated. It has been shown that, by using a system composed of ionic liquid and copolymer, acetaminophen can be extracted into an IL-rich phase. It has also been shown that using KCl as anti-solvent, acetaminophen can be isolated from IL-rich phase. The obtained results, extraction recovery efficiency higher than 70% and isolation efficiency higher than 60%, suggest that the described process can be used for recovery of ACF from pharmaceutical waste.

## Acknowledgement

The research was funded by the Ministry of Education, Science and Technological Development of the Republic of Serbia.

## REFERENCES

- [1] M. Zawadzki, F.A.E. Silva, U. Domańska, J.A.P. Coutinho, S.P.M. Ventura, *Green Chemistry*, 2016, 18, 3527–3536.
- [2] S.P.M. Ventura, F.A. E Silva, M. V. Quental, D. Mondal, M.G. Freire, J.A.P. Coutinho, *Chemical Reviews*, 2017, 117, 6984–7052.
- [3] F.A. E Silva, T. Sintra, S.P.M. Ventura, J.A.P. Coutinho, *Separation and Purification Technology*, 2014, 122, 315–322.

- 
- [4] F.A. E Silva, M. Caban, M. Kholany, P. Stepnowski, J.A.P. Coutinho, S.P.M. Ventura, *ACS Sustainable Chemistry & Engineering*, 2018, 6, 4574–4585.
- [5] A.S. Paluch, T.C. Lourenç, F. Han, L.T. Costa, *The Journal of Physical Chemistry B*, 2016, 120, 3360–3369.
- [6] M.G. Freire, A.F.M. Cláudio, J.M.M. Araújo, J.A.P. Coutinho, I.M. Marrucho, J.N. Canongia Lopes, L.P.N. Rebelo, *Chemical Society Reviews*, 2012, 41, 4966–4995.

## APPLICATION OF CHLORINE DIOXIDE FOR PHARMACEUTICAL DEGRADATION

M. V. Pergal <sup>1</sup>, I. D. Kodranov <sup>2</sup>, M. Krpić <sup>2</sup>, D. D. Manojlović <sup>2,3</sup>

<sup>1</sup> *University of Belgrade, Institute of Chemistry, Technology and Metallurgy, Njegoševa 12, 11000 Belgrade, Serbia. (marijav@chem.bg.ac.rs)*

<sup>2</sup> *Faculty of Chemistry, University of Belgrade, Studentski trg 12-16, 11000 Belgrade, Serbia. ikodranov@gmail.com*

<sup>3</sup> *South Ural State University, Lenin prospekt 76, 454080 Chelyabinsk, Russia.*

### ABSTRACT

This study investigated degradation of ibuprofen in deionized and river waters using chlorine dioxide treatment. The degradation degree of ibuprofen was monitored by high-performance liquid chromatography (HPLC) analysis. The toxicity effect of degradation products was determined by *Daphnia magna* bioassay. The results showed that alkaline condition favors the degradation of ibuprofen and high concentration of chlorine dioxide is required for very efficient degradation of ibuprofen. Degree of degradation in the real water sample is relatively low and ranged from 42% to 47% compared to the degree of degradation in deionized water (99%). The results of toxicity tests showed that degradation products of ibuprofen belong to class III as acutely toxic.

### INTRODUCTION

Chlorine dioxide (ClO<sub>2</sub>) is a powerful one-electron oxidant ( $E_0 = 0.936$  V), known for its ability to oxidize organic and inorganic pollutants [1]. Previous studies have reported the oxidative degradation of several pharmaceutical contaminants via ClO<sub>2</sub> such as estrogenic 17 $\alpha$ -ethinylestradiol, antibiotic sulfamethoxazole, roxithromycin, b-lactams and fluoroquinolones. ClO<sub>2</sub> is generally considered as effective treatment for oxidizing pharmaceuticals and other organic contaminants [1]. Pharmaceutical residues have been detected frequently in the aquatic environment at very low concentrations (ng/L to  $\mu$ g/L) [2]. Nevertheless, due to designed persistence and biological activity, their long-term presence poses real environmental risks. Ibuprofen (Fig. 1) is a widely used non-steroidal anti-inflammatory drug, consumed in high amounts in both human and domestic animal practices or farming [2]. Toxicological effects of ibuprofen metabolites (human or microbial origin) in the aquatic environment have been reported to influence cyclooxygenase reactions and therefore could affect not only the reproduction of aquatic animals, but also the photosynthesis of aquatic plants. Degradation of ibuprofen using Fenton reaction, dielectric barrier discharge (DBD), electrochemical and microbial degradation was reported in the literature up to now.

In this paper, effectiveness of ibuprofen degradation in water solutions using ClO<sub>2</sub> was examined. The degradation degree was assessed by HPLC analysis, while toxicity of degradation products was determined by *Daphnia magna* bioassay.

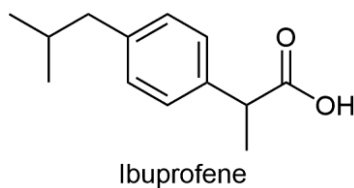


**Figure 1.** Chemical structure of ibuprofen

## METHODS

Ibuprofen was supplied by Hemofarm. The pure stock solution of chlorine dioxide ( $3 \text{ g/dm}^3$ ) was prepared by mixing sodium chlorite (Superior Water Disinfection Power, TwinOxide®) and sodium bisulphate (Superior Water Disinfection Power, TwinOxide®), in  $1 \text{ dm}^3$  of deionized water. The exact concentration of chlorine dioxide in the stock solution was quantified using 4500- $\text{ClO}_2$  DPD method according to the Standard Method [3].

Degradation of ibuprofen in deionized and river waters under light condition by  $\text{ClO}_2$  was previously described [4]. Experiments consisted of adding the ibuprofen to deionized waters to achieve a concentration of ibuprofen of  $10 \text{ mg/L}$ , and pH was adjusted to be 10.00 and after that, stock solution of chlorine dioxide was added resulting in concentrations of  $15 \text{ mg/L}$ . The degradation was followed from 0.5 to 24 h.

River water was collected on 30 May 2019 from the Sava River at Makiš “Reni Bunar 17” ( $44^\circ 26' \text{ N}$ ,  $20^\circ 22' \text{ E}$ ) in Belgrade, Serbia.

Degradation efficiency was measured by high-performance liquid chromatography (HPLC) analysis. Degradation efficiency was calculated, and compounds were separated chromatographically using the equipment, and mobile phase as previously described [4]. Analysis and data processing were done using Chromeleon v 6.8 (ThermoFisher Scientific).

For toxicity bioassay, *Daphnia magna* was used as a test organism and toxicity test was performed on the same way as previously described [4].  $\text{LC}_{50}$  (lethal concentration which causes 50% mortality in the daphnids) was based on the number of dead specimens, with 95% confidence intervals determined by regression model: Spearman-Kärber using TesTox software, version 1.0.

## RESULTS AND DISCUSSION

The results of HPLC analysis (Fig. 2) showed that the highest degree of degradation was obtained at an ibuprofen concentration of  $10 \text{ mg/L}$  when treated with  $15 \text{ mg/L}$   $\text{ClO}_2$  under light condition after 24 h  $\text{ClO}_2$  treatment. With increasing reaction time, degree of degradation increased. Degree of degradation of ibuprofen occurs in the range of 96-99% (0.5 h, 96.0%; 1 h, 97.1%; 2 h, 97.1%; 3 h, 97.3%; 6 h, 97.4%; 24 h, 98.6%).

HPLC analysis of ibuprofen degradation in Sava River water was performed to determine the degradation efficiency in a real water sample. The real sample from the Sava River has a certain pH value that we did not adjust, unlike the sample of ibuprofen in deionized water. Ibuprofen was treated with  $15 \text{ mg/L}$   $\text{ClO}_2$ , without changing its pH value (pH = 7.75), because it is a real sample from the Sava River.

HPLC analysis of degradation of ibuprofen in the water from the Sava River showed that the best degradation result was obtained after 24 h of  $\text{ClO}_2$  treatment and it was 47%. The shorter the time exposure of ibuprofen to  $\text{ClO}_2$ , the lower the percentage of degradation of ibuprofen was obtained (6 h, 45.8%; 3 h, 45.6%; 2 h, 45.2%; 1 h, 42.7%; 0.5 h, 42.1%).

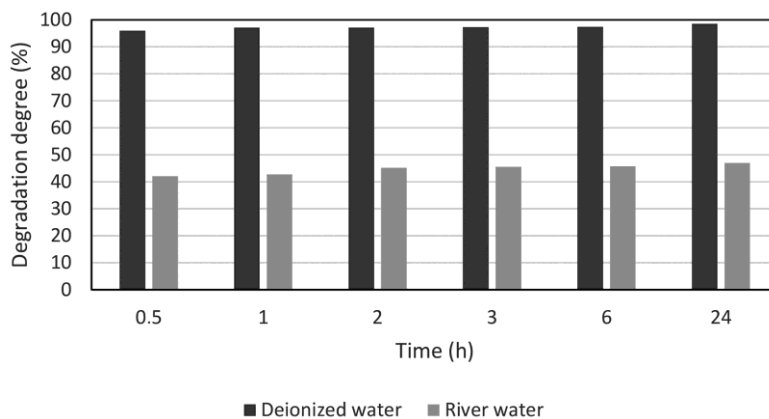


**Figure 2.** Degradation degree of ibuprofen in deionized and River water

Toxicity tests of initial ibuprofen and degradation products obtained under conditions that led the highest degradation degree of ibuprofen (15 mg/L  $\text{ClO}_2$ , pH 10.00 and after 24 h  $\text{ClO}_2$  treatment) was evaluated. The  $\text{LC}_{50}$  value of degradation products was 89.09% after 24 h test period, while after 48 h test period,  $\text{LC}_{50}$  value was 53.59%. This result obtained for 24 h test period showed that solution of degradation products belongs to class III of acute toxicity with a value of toxic unit (TU) = 1.1, while the result for 48 h test period showed that solution of degradation products belong to the same class with a value of TU = 1.9.  $\text{LC}_{50}$  value for initial ibuprofen cannot be expressed because mortality for *Daphnia Magna* is 0% at a concentration of 100% ibuprofen. Since  $\text{TU} < 1$  for initial solution of ibuprofen, the initial ibuprofen solution can be considered weakly toxic to non-toxic [5]. From the obtained results, it can be concluded that degradation products are much more toxic than the initial solution of ibuprofen. The obtained results are in agreement with results for toxicity of ibuprofen and its degradation products presented in the literature [6].

## CONCLUSION

A high degree of degradation (99%) in deionized water was obtained after treatment of ibuprofen with 15 mg/L  $\text{ClO}_2$ , at pH = 10, after 24 h of  $\text{ClO}_2$  treatment. Under the same conditions in real water sample, the percentage of degradation is relatively low and ranged from 42% to 47% depending on the reaction duration. Based on the toxicity test, it can be concluded that in the case of initial ibuprofen solution can be considered weakly toxic to non-toxic, while in the case of solution of degradation products of ibuprofen it was shown that they can cause acute toxicity.

## Acknowledgement

The authors would like to thank the Ministry of Education, Science and Technological Development (Grant No: 451-03-9/2021-14/200026; 451-03-9/2021-14/200168) and TwinOxide-RS d.o.o.

## REFERENCES

- [1] Y. Wang, H. Liu, Y. Xie, T. Ni, G. Liu, Chemical Engineering Journal, 2015, 279 409-415.
- [2] M. Markovic, M. Jovic, D. Stankovic, V. Kovacevic et al., Science of the Total Environment, 2015, 505, 1148-1155.
- [3] APHA (American Public Health Association) American Water Works Association, and Water Environment Federation, Standard Methods for the Examination of Water and Wastewater, 20 th ed. American Public Health Association, Washington DC, 1998.
- [4] M.V. Pergal, I.D. Kodranov, M.P. Pergal, B.P. Dojčinović, D.S. Stanković, B.B. Petković, D.D. Manojlović, Water Air Soil Pollution, 2018, 229, 310.

- [5] G. Persoone, B. Marsalek, I. Blinova, A. Törökne, D. Zarina, L. Manusadzianas, G. Nalecz Jawecki, L. Tofan, N. Stepanova, L. Tothova, B.A. Kolar, *Environmental Toxicology*, 2003, 18, 395-402.
- [6] G. H. Han, H. G. Hur, S. D. Kim, *Environmental Toxicology and Chemistry*, 2006, 25, 265-271.

## THE LIFETIMES OF $^{238}\text{U}$ NUCLEI, THE ESCAPING ATTEMPTS OF THEIR ALPHA PARTICLES AND THE GEIGER-NUTTAL LAW

P. I. Premović

Laboratory for Geochemistry, Cosmochemistry and Astrochemistry,  
University of Niš, P.O. Box 224, 18000 Niš, Serbia

### ABSTRACT

We consider here the large populations of  $^{238}\text{U}$  nuclei and their emitted alpha particles. The main points are: (a) a time interval for which alpha particle of  $^{238}\text{U}$  nucleus makes one attempt to escape is approximately  $10^{-21}$  second; (b) the number of the mean escape attempts is  $\sim 2 \times 10^{38}$ ; (c) contribution of the tunneling time of  $^{238}\text{U}$  nucleus to the mean time and to the lifetime of each individual nuclei is negligible; (d) the sum of the lifetimes of  $^{238}\text{U}$  nuclei and the sum of the number of escape attempts of their alpha particles are constant. Consequently, the ratio of these two sums is also constant, and is about  $10^{-21}$  seconds; and, (e) a new mathematical form of the Geiger-Nuttall law is derived using a very simple theoretical approach.

### INTRODUCTION

Radioactive decay is a purely statistical (random) process. If the number of radioactive nuclei is large enough then the total number of radioactive nuclei  $N_t$ , that have not yet been transformed at a time  $t$ , can be obtained from the following equation

$$N_t = N_0 e^{-\lambda t} \quad \dots \quad (1)$$

where  $N_0$  is the number of radioactive nuclei at a time  $t = 0$  and  $\lambda$  is the decay constant. This equation is the final mathematical representation of the radioactive decay law, and it applies to all decays. The decay pattern of a large number of radioactive nuclei is easy to predict using eqn. (1). For practical purposes, we will be using *Avogadro's number*  $N$  ( $= 6.022 \times 10^{23}$ ) as a reasonable approximation for a large number of radioactive nuclei.

In general, there are two ways to measure the time for which a radioactive nucleus is stable: half-life  $t_{1/2}$  and the mean lifetime  $\tau$ . By the definition of the term half-life, when  $N_t = 1/2 N_0$  then  $t = t_{1/2}$ . In accordance with the definition of the term half-life, when  $N_t = 1/2 N_0$  then  $t = t_{1/2}$ . A simple algebra of eqn. (1) shows that  $t_{1/2} = (\ln 2)/\lambda$ .

The quantity  $\tau$  is the reciprocal of the decay constant  $\lambda$  or  $\tau = 1/\lambda$ ;  $\tau$  is usually estimated from the measured  $t_{1/2}$  using the following relation  $\tau = 1.44 t_{1/2}$ . Of course,  $\lambda$ ,  $t_{1/2}$  and  $\tau$  have only meaning for a large population of radioactive nuclei (of the same type, of course).

We will concentrate on the lifetimes of a large population of the decayed  $^{238}\text{U}$  nuclei, as well as on the escaping times of their emitted  $\alpha$ -particles.

### DERIVATIONS, RESULTS AND DISCUSSION

If there is an initial population of  $N$  radioactive, the sum of their *all* individual *lifetimes* divided by  $N$  is the *mean lifetime*  $\tau$ . mathematically speaking,  $\tau$  is the *arithmetic mean of lifetimes* of all  $N$  individual nuclei

$$\tau = (\tau_1 + \tau_2 + \dots + \tau_{N-1} + \tau_N)/N$$

where  $i$  and  $\tau_i$  denote, respectively, individual radioactive nuclei and their lifetimes.

Rearranging this equation gives

$$N\tau = (\tau_1 + \tau_2 + \dots + \tau_{N-1} + \tau_N) \quad \dots \quad (2).$$

After a bit of algebra and estimation, we found that about 62.5 % of  $\tau_i$  is smaller than  $1.44t_{1/2}$  or  $\tau$ . Therefore, for a large population of radioactive nuclei about 37.5 % of  $\tau_i$  exceeds  $\tau$ .

Consider alpha ( $\alpha$ -) decay of (parent)  $^{238}\text{U}$  (initially at rest) with  $\tau$  of about  $2 \times 10^{17}$  second to (daughter)  $^{234}\text{Th}$ . It is assumed that the parent  $^{238}\text{U}$  nucleus before decay consists of the daughter  $^{234}\text{Th}$  and  $\alpha$ -particle. This particle is in a free (non-bound) state, otherwise, the decay could not occur. The emitted  $\alpha$ -particle whose mass  $m_\alpha$  is ca.  $6.65 \times 10^{-27}$  kg has a speed  $v_\alpha = 1.42 \times 10^7$  m sec $^{-1}$ . This speed is determined from its non-relativistic kinetic energy  $E_\alpha = 1/2 m_\alpha v_\alpha^2$ , ca. 4.2 MeV. In fact,  $v_\alpha$  is its speed when  $\alpha$ -particle escapes from the  $^{238}\text{U}$  nucleus.

According to classic mechanics,  $\alpha$ -particle with the  $E_\alpha$  of ca. 4.2 MeV could never be able to overcome the Coulomb potential barrier of  $^{238}\text{U}$ ,  $V_C$ , which is probably about 20 MeV [1] and to escape the nucleus. Quantum mechanics provides an explanation based upon the concept of tunneling where this particle can be found in a classically forbidden (outside) region of the nucleus.

The size (diameter)  $d$  of the nucleus of the heaviest atoms, such as uranium (U), is about  $15 \times 10^{-15}$  m or 15 fm. In fact, an  $\alpha$ -particle must make many attempts back and forth across  $^{238}\text{U}$  nucleus before it can escape; in fact, this particle oscillates along the diameter of nucleus. A time interval for which the  $\alpha$ -particle of  $^{238}\text{U}$  nucleus makes one "try" to escape is approximately given by  $d/v_\alpha = 10^{-21}$  seconds. In other words,  $\alpha$ -particle effectively attempts to tunnel through the Coulomb barrier  $v_\alpha/d = 10^{21}$  times per second. Denote now with  $n$  and  $n_i$ , respectively, the mean escape attempts and the individual escape attempts of the  $\alpha$ -particle before leaving  $^{238}\text{U}$  nucleus. Let also  $t(e)$  and  $t_i(e)$  stand for the mean escaping time and the escaping time, respectively. Simple reasoning indicates that  $t(e) \sim \tau$  and  $t_i(e) \sim \tau_i$  because the tunneling time  $T$  could contribute to these escaping times.

A question that goes along with tunneling is: how long it takes for  $\alpha$ -particle to tunnel the Coulomb barrier. The tunneling time problem is one of the long-standing and controversial problems in quantum mechanics. There are numerous attempts to solve it but none of them gives a flawless answer to this question [2].

The width of the barrier  $w$  through which an  $\alpha$ -particle must tunnel can be roughly calculated using the following equation:  $w = (V_C/E_\alpha)d - d$  [1]. Inserting in this equation the values for  $V_C$ ,  $E_\alpha$  and  $d$  we obtain  $w \sim 57$  fm which is probably much smaller about 30 fm [1]. Of course, the speed of this particle during the tunneling process cannot exceed the speed of light  $c$ , therefore, the lower limit for the tunneling time  $T = w/c \sim 1 \times 10^{-22}$  second; its upper limit  $w/v_\alpha \sim 1.5 \times 10^{-21}$  second. Therefore, contribution of the tunneling time to  $\tau$  is negligible. Consequently,  $t(e) \sim \tau = nd/v_\alpha$  then the number of the mean escape attempts

$$n = \tau v_\alpha / d \quad \dots \quad (3).$$

We know that  $\tau$  is about  $2 \times 10^{17}$  sec and  $v_\alpha = 1.42 \times 10^7$  m sec $^{-1}$  for  $^{238}\text{U}$  so  $n \sim 2 \times 10^{38}$  is the constant characteristic for this uranium isotope. In general,  $n$  of eqn. (3) is the constant characteristic for any isotope  $\alpha$ -emitter of the heaviest atom (including any uranium isotope  $\alpha$ -emitter, of course). Since  $T$  contributes to each then  $t_i(e) = n_i d / v_\alpha + T = 10^{-21} n_i + T$ . Of course, the maximum contribution of  $T$  is about  $1.5 \times 10^{-21}$  second and the maximum  $\tau_i = 10^{-21} n_i + 1.5 \times 10^{-21}$  second. For  $n_i \geq 100$  we can practically take that  $\tau_i = 10^{-21} n_i$ . By inserting this  $\tau_i$  into eqn. (2) we obtain

$$N\tau = 10^{-21}(n_1 + n_2 + \dots + n_{N-1} + n_N) \quad \dots \quad (4).$$

Plugging the values for  $N$  and  $\tau$  into the equations (2) and (4) we get

$$\tau_1 + \tau_2 + \dots + \tau_{N-1} + \tau_N = 1.2 \times 10^{41} \text{ seconds}$$

and

$$(n_1 + n_2 + \dots + n_{N-1} + n_N) = 1.2 \times 10^{62}.$$

Thus, the sums of lifetimes of a large population of  $^{238}\text{U}$  nuclei and the number of escape attempts of their  $\alpha$ -particles are fixed. A similar conclusion is true for other appropriate radioactive isotopes. If the number of decayed  $^{238}\text{U}$  nuclei is  $k$  times greater or smaller (but still large) then the above sums would be  $k$  times higher or lower. However, the ratio of eqns. (2) and (4) is constant and equals:  $\tau/n = \tau_i/n_i = 10^{-21}$  second even if  $k \rightarrow \infty$ , of course. This is of some importance. Any single  $^{238}\text{U}$  nucleus which we observe is not all alone in the Universe and it belongs to an infinitely large total number ( $k \rightarrow \infty$ ) of its  $^{238}\text{U}$  nuclei. Therefore, the ratio  $\tau/n$  of  $^{238}\text{U}$  of about  $10^{-21}$  seconds is one of the “magic” units of time of the Universe.

Geiger-Nuttall law [3, 4] is a semi-empirical law that expresses the half-life of a heavy  $\alpha$ -emitter in terms of the kinetic energy of its released  $\alpha$ -particle. In its modern natural logarithm (LN) form this law is:  $\ln t_{1/2} = a + b/\sqrt{Q_\alpha}$ ,  $\ln t_{1/2} = a + b/\sqrt{Q_\alpha}$  where  $Q_\alpha$  is the  $\alpha$ -decay energy  $a$  and  $b$  are the constants that can be determined by fitting to experimental data for each isotopic series. The kinetic energy,  $E_\alpha$ , of the emitted  $\alpha$ -particle is rather slightly less than  $Q_\alpha$ .<sup>4</sup> Therefore, the above equation can be rewritten as  $\ln t_{1/2} = a + b/\sqrt{E_\alpha}$ . The quantum tunneling enables one to obtain the Geiger-Nuttall law, including coefficients, via direct calculation.

We know that  $n = \tau v_\alpha/d$  and  $v_\alpha = \sqrt{2E_\alpha/m_\alpha}$ . Combining these two equations and after a bit of algebra, we get  $\tau = nd \times \sqrt{(m_\alpha/2)}/\sqrt{E_\alpha}$ . Substituting in this equation  $1.44t_{1/2}$  instead  $\tau$ ,  $u$  instead  $(nd/1.44)$  and  $w$  instead  $\sqrt{(m_\alpha/2)}$  we obtain

$$t_{1/2} = u \times w \times \sqrt{1/\sqrt{E_\alpha}} \quad \dots \quad (5)$$

where  $u$  and  $w$  are the constants. Its LN form is

$$\ln t_{1/2} = \ln u + \ln w + \ln(1/\sqrt{E_\alpha}) \quad \dots \quad (6).$$

Evidently,  $u$  and  $w$  are also the constants. This equation is a linear function of  $\ln t_{1/2}$  vs.  $\ln(1/\sqrt{E_\alpha})$ . To illustrate this, we will use some experimental data for uranium isotopes  $^{228}\text{U} - ^{238}\text{U}$  given in Table 1. The plot  $\ln t_{1/2}$  vs.  $\ln(1/\sqrt{E_\alpha})$  for these isotopes gives a straight line, Fig. 1. Of course, it is before necessary to convert seconds (sec) to years (yr) and joules (J) into MeV of this equation.

Uranium isotope	$E_\alpha$ [MeV]	$t_{1/2}$
238	4.198	$4.468 \times 10^9$ yr
236	4.494	$2.342 \times 10^7$ yr
235	4.395	$7.037 \times 10^8$ yr
234	4.775	$2.455 \times 10^5$ yr
232	5.320	69.8 yr
230	5.888	20.8 day
228	6.680	9.1 min
226	7.570	0.35 sec

**Table 1.** Some experimental data of uranium isotopes  $^{226}\text{U} - ^{238}\text{U}$  [5-8].

It appears that the above new form of the semi-empirical Geiger-Nuttall law represents until now the simplest theoretical way to derive this law. It is also possibly applicable to other  $\alpha$ -emitters of the heaviest atom isotopes.

We know that  $m_\alpha = 6.65 \times 10^{-27}$ ,  $1 \text{ yr} = 3.15 \times 10^7$  sec and that  $1 \text{ J} = 6.24 \times 10^{12}$  MeV. After a simple algebra the eqn. (5) can be written as follows

<sup>4</sup> The kinetic energy of the recoiling  $^{234}\text{Th}$  nucleus produced in the decay of  $^{238}\text{U}$  is 0.070 MeV.

$$t_{1/2} = nd/1.44 \times (3.15 \times 10^7) \times \sqrt{[(6.25 \times 10^{12}) \times m_{\alpha}/2](1/\sqrt{E_{\alpha}})} \quad \dots \quad (7).$$

In the case of  $^{238}\text{U}$ , for example, plugging into this equation the values for  $n$  ( $= 2 \times 10^{-38}$ ),  $d$  ( $= 15 \times 10^{-15}$  m),  $m_{\alpha}$  ( $= 6.65 \times 10^{-27}$  kg) and  $E_{\alpha}$  ( $= 4.198$  MeV) we calculate  $t_{1/2} \sim 4.74 \times 10^9$  years. The experimental value for  $t_{1/2}$  is  $\sim 4.47 \times 10^9$  years, Table 1. Our theoretical approach is therefore not “too” bad. A detailed consideration of eqn. (7) will be a subject of the next author’s study.

For the sake of clarity, let us consider briefly  $u$  and  $w$  of eqn. (5). According to eqn. (7), the constant  $u$  is a product of two variable terms:  $n$  and  $d$  and the constant  $w$  consist of three fixed terms:  $m_{\alpha}$  and two conversion factors  $J$  into MeV ( $6.25 \times 10^{12}$ ) and sec into yr ( $3.15 \times 10^7$ ). Therefore in this equation  $u$  ( $= nd/1.44$ ) is the constant which is characteristic for each of the isotope  $\alpha$ -emitters of the heaviest atoms and  $w$  [ $= 1/(3.15 \times 10^7) \times \sqrt{(6.25 \times 10^{12} \times m_{\alpha}/2)}$ ] is the general constant, the same for all of these  $\alpha$ -emitters. In contrast, the  $a$  and  $b$  constants in the original mathematical form of the Geiger-Nuttall are characteristic for each isotopic series.

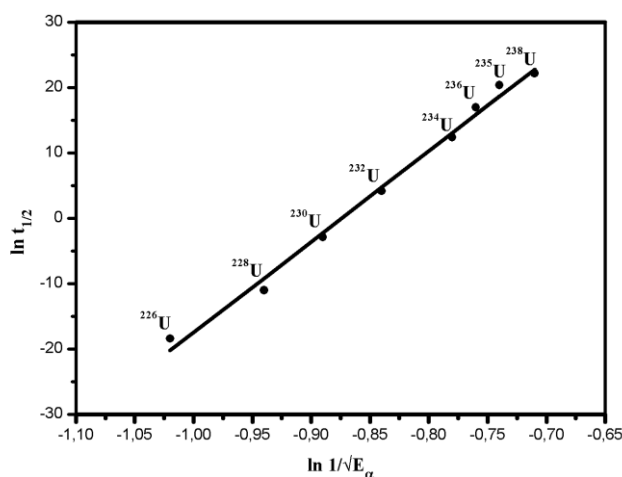


**Figure 2.** A comparison of the eqn. (6) with experimental data for  $^{226}\text{U} - ^{238}\text{U}$  [5-8]. The linear fit to the values is shown by the solid line.

## CONCLUSION

A new expression for the Geiger-Nuttall law is reproduced on a very simple way.

## REFERENCES

- [1] S. T. Thornton, A. Rex, *Modern Physics for Scientists and Engineers* (4th Edition), Cengage Learning, 2012.
- [2] N. L. Chuprikov, ArXiv,1303.6181v4 [quant-ph], 24 Mar 2014.
- [3] H. Geiger and J.M. Nuttall, *Phil. Mag.*, 1911, 22, 613-621.
- [4] H. Geiger and J.M. Nuttall, *Phil. Mag.*, 1912, 23, 439-445.
- [5] D. Ferreira and R. Pinto, <https://fenix.tecnico.ulisboa.pt/downloadFile/3779576931836/Ex8seriel>.
- [6] N. E. Holden, *The uranium half-lives: a critical review*, National nuclear data center Brookhaven National Laboratory, 1981.
- [7] J. Elkenberg, *Radium Isotope Systematics in Nature: Applications in Geochronology and Hydrogeochemistry*. Habilitation Thesis, Earth Science Department, Swiss Federal Institute of Technology, Zürich, 2002.
- [8] Uranium isotopes. Wikipedia, the free encyclopedia.

## QUANTITATIVE DETERMINATION OF DEHP BY FOURIER TRANSFORM INFRARED SPECTROSCOPY

T. Anđelković<sup>1</sup>, D. Bogdanović<sup>1</sup>, I. Kostić<sup>1</sup>, G. Nikolić<sup>2</sup>, B. Kostić<sup>2</sup>,  
and R. Pavlović<sup>3</sup>

<sup>1</sup>University of Niš, Faculty of Science and Mathematics, Department of Chemistry, Višegradska 33,  
18000 Niš, Serbia

<sup>2</sup>University of Niš, Faculty of Technology, Department of Chemistry and Chemical Technology,  
Bulevar oslobođenja 124, 16000 Leskovac, Serbia

<sup>3</sup>University of Milan, Department of Veterinary Science and Public Health, Via Celoria 10, 20133  
Milan, Italy

(Corresponding author: e-mail: dannica.milojkovic@gmail.com)

### ABSTRACT

Phthalates are chemical substances that are widely used as plasticizers that are added to PVC to improve their properties. Because of phthalate tendency to migrate to environment and their harmful effect on human health, the aim of this paper is quantification of di(2-ethylhexyl)phthalate (DEHP) in PVC pharmaceutical contact materials (PCM articles) using Fourier transform infrared spectroscopy (FTIR). Quantification was performed based on obtained linear calibration curve for DEHP within the mass concentration range from 0 to 50% in relation to mass of PVC article for two monitored ranges on the FTIR spectrum ( $720\text{-}760\text{ cm}^{-1}$  and  $1560\text{-}1610\text{ cm}^{-1}$ ). The results showed that the investigated transfusion set and tubing for transfusion contains the most DEHP (27.50%), followed by quadrupole bag with 24.1%, transfer bag with 22.9% and sag-M bag for transfusion with 4.98%.

### INTRODUCTION

Phthalates are synthetic chemical esters of phthalic acid, also called plasticizers, because their most common use is related to the softening of the polymeric materials, which makes plastic more elastic and flexible to use. Phthalates represent a large group of compounds, where each phthalate is characterized by a specific chemical and toxicological profile. The most known phthalate, for its most common use, is DEHP. Annual production of all phthalates amounted to 8.4 million tons and production of DEHP was about 37% of the total phthalates which is because the plastic can contain up to 40% DEHP by weight [1]. Studies have shown that phthalates have a harmful effect on human health [2, 3], so monitoring of the phthalates in various media is of great importance.

FTIR spectroscopy has found its application in identification or characterization of many unknown materials, and PVC among the other samples. FTIR spectroscopy is often used in prescreening of PVC samples because operation of the instrument is simple and easy, sample does not require pretreatment, enables spectrum measurement in a short time and has a low running cost.

The aim of this study is quantitative determination of DEHP in PVC PCM articles after calibration using FTIR technique, which was preceded removal of total amount of phthalates from PVC PCM article by precipitation method and spiking of the free-phthalates PVC PCM with the exact amount of DEHP.

### METHODS

The tetrahydrofuran (THF) (HPLC grade) was purchased from Fischer scientific (USA). The *n*-hexane (HPLC grade) was purchased from Carlo Erba (France). Bis(2-ethylhexyl) phthalate was purchased, purity 99.7%, from Sigma–Aldrich (USA).

The PVC PCM articles used for this investigation were transfusion set with transfer bag, quadrupole blood bag, Sag-M bag and coupled transfusion tubing (TIANHE Pharmaceutical, Chine). The PVC PCM articles were taken from local Clinical Center Niš (Serbia).

The Laser Fourier Transform Infrared Spectroscop (BOMEM Hartman & Braun-Michelson MB series 100) was used to record FTIR spectra. The manual hydraulic press (Graseby Specac) designed to create pellet samples which can then be processed using FTIR was used. Amalgamator (Wig-L-Bug) was used for mixing a variety of materials including PVC precipitates from this analysis.

Preparation of the calibration standards for FTIR analysis was done by spiking the PVC PCM articles from which the total phthalate content was removed by the previous precipitation method. In order to obtain PVC precipitate without phthalates, *n*-hexane was added to the THF solution of PVC article. The PVC precipitate without phthalates was separated from the aliquot by centrifugation and after drying was mixed with KBr. Obtained pellets, formed by manual hydraulic press, were scanned by FTIR for confirmation of completely release of phthalates from PVC article.

Obtained free-phthalate PVC pellets were spiked with DEHP so each obtained PVC standards contains 0%, 5%, 10%, 20%, 30%, 40% and 50% DEHP in relation to the mass of PVC. Obtained PVC standards were dissolved in THF and after dissolving these calibration solutions were poured into evaporating dishes. After evaporation, obtained calibration standards in the form of a thin polymer film were recorded using FTIR technique.

Preparation of PVC samples for FTIR analysis included dissolving PVC articles in THF, evaporation of this solution, and after evaporation applying thin polymer film to a sample holder and then directing infrared light through it to obtain a FTIR spectrum.

## RESULTS AND DISCUSSION

On the FTIR spectrum the phthalates have distinctive peaks at  $743\text{ cm}^{-1}$  (characteristic for their *ortho*-substituted aromatic ring) and peaks at  $1599$  and  $1579\text{ cm}^{-1}$  (typical for the aromatic ring quadrant stretching vibration). Other useful characteristic FTIR spectra absorption bands for PVC were:  $2960\text{ cm}^{-1}$  (for -C-H bond),  $1718\text{ cm}^{-1}$  (for the phthalate ester),  $1450\text{ cm}^{-1}$  (for -CH<sub>2</sub>- and -CH<sub>3</sub>),  $1278\text{ cm}^{-1}$  (for -CH<sub>2</sub>-),  $1073\text{ cm}^{-1}$  (for -CH<sub>3</sub>).

The presence of these characteristic bands on the FTIR spectra of investigated PVC samples indicated that these PVC PCM articles contained phthalates. Also, the absence of these peaks on the FTIR spectra of PVC samples from which phthalates have been removed by precipitation method, indicated the absence of phthalates. PVC samples free of phthalates were spiked with exact known DEHP concentration and used for further analysis, calibration and quantification.

In order to quantitative determine DEHP in PVC PCM articles, first of all the calibration standards were recorded on the FTIR instrument. The areas of the obtained bands on FTIR spectrum were calculated and the calibration diagrams  $P=f(c)$  were made, where  $P$  was peak area and  $c$  was mass concentration of DEHP (%). The obtained calibration curves for DEHP within the concentration range from 0 to 50 mass%, for two monitored ranges on the FTIR spectrum are shown in Figure 1, with characteristics given in Table 1.

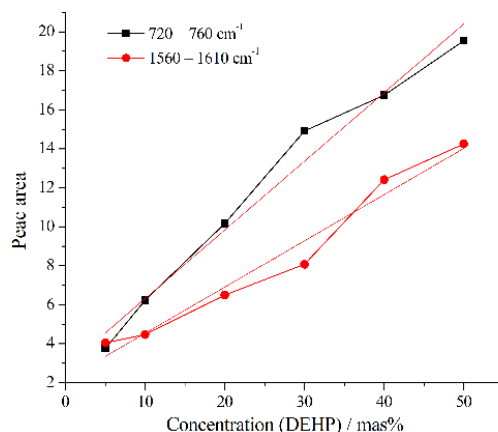


**Figure 1.** Calibration curves for DEHP within the concentration range from 0 to 50 mass%, for two monitored areas on the FTIR spectrum

**Table 1.** Linear equations and correlation coefficient of obtained calibration curves for DEHP

Range (cm <sup>-1</sup> )	Linear equation	Correlation coefficient, R <sup>2</sup>
720-760	$y=(2,80\pm0,77)+(0,34\pm0,03)x$	0,997
1560-1610	$y=(2,17\pm0,65)+(0,24\pm0,02)x$	0,996

Based on the calibration and peak areas of bands in the specified ranges on FTIR spectra of investigated PVC PCM articles, the DEHP content of each PVC PCM article was calculated and given in Table 2.

**Table 2.** Mass concentration of DEHP in PVC PCM articles

PVC PCM articles	Mass concentration of DEHP (%)
Tubing for transfusion	27.5±0.6
Quadrupole bag	24.1±0.2
Transfer bag	22.9±0.2
Sag-M	4.98±0.17

## CONCLUSION

The precipitation method was efficient method for removing phthalates from the PVC articles. FTIR method is a fast, efficient and reliable method for the determination of phthalates. The disadvantage of this method was that it is not a selective method due to determination of total phthalates in PVC article. Transfusion tubing contained the highest amount of DEHP, as much as 27.5% by weight of PVC, which is reasonable since tubing was the most flexible. The following are the transfusion bags from the quadrupole bag with 24.1%, followed by transfer bag with 22.9% and sag-M bag with 4.98%.

## Acknowledgement

This study was performed within the research program – Contract No. 451-03-9/2021-14/200124.

**REFERENCES**

- [1] European Council for Plasticisers and Intermediates (ECPI), *Weichmacher & weich – PVC*, Factsheet, 2016
- [2] J.D. Meeker, S. Sathyanarayana, S. Swan, *Phil. Trans. R. Soc. B*, 2009, **364**, 2097–2113.
- [3] R. Hauser, A. Calafat, *Occup Environ Med*, 2005, **62**(11), 806-818.

## PHTHALATES DETERMINATION IN CHILDREN TOYS BY GAS CHROMATOGRAPHY-MASS SPECTROMETRY

T. Anđelković<sup>1</sup>, D. Bogdanović<sup>1</sup>, I. Kostić<sup>1</sup>, G. Kocić<sup>2</sup> and R. Pavlović<sup>3</sup>

<sup>1</sup>*University of Niš, Faculty of Science and Mathematics, Department of Chemistry, Višegradaska 33, 18000 Niš, Serbia*

<sup>2</sup>*University of Niš, Faculty of Medicine Department of Biochemistry, Bulevar dr Zorana Đinđića 81, 18000 Niš, Serbia*

<sup>3</sup>*University of Milan, Department of Veterinary Science and Public Health, Via Celoria 10, 20133 Milan, Italy*

(Corresponding author: e-mail: [dannica.milojkovic@gmail.com](mailto:dannica.milojkovic@gmail.com))

### ABSTRACT

The aim of this work was qualitative and quantitative determination of dimethyl phthalate (DMP), di-*n*-butyl phthalate (DnBP), benzyl butyl phthalate (BBP), di(2-ethylhexyl)phthalate (DEHP), di-*n*-octyl phthalate (DnOP) in plastic children toys using the GC-MS technique. Phthalates were isolated from the PVC toys by tetrahydrofuran and then polymer was precipitated by the addition of an excess of *n*-hexane. Based on presence or absence of peaks at the specific retention time in the obtained GC-MS chromatogram of PVC toys, the existence of phthalates in the PVC toys was checked. Based on the obtained calibration curve with correlation coefficient 0.999 for DEHP, the only phthalate qualitatively detected in toys, the mass percentage of DEHP in each toy was determined. The amount of DEHP in the 13 analyzed PVC toys was in the range from 9.47 to 53.24 % by weight of PVC article. The five analyzed PVC articles did not contain noted five tested phthalates, while one plastic toy was not made of PVC. The obtained results indicated that some children toys have high amount of DEHP, which certainly exceeds the allowable DEHP concentration.

### INTRODUCTION

Phthalates are phthalic acid esters, whose main purpose is to soften polyvinyl chloride (PVC) are also called plasticizers. The most commonly used phthalates are dimethyl phthalate (DMP), di-*n*-butyl phthalate (DBP), benzyl butyl phthalate (BBP), di(2-ethylhexyl) phthalate (DEHP) and di-*n*-octyl phthalate (DOP). Since many toys are made of PVC and phthalates can leach out from plastic over time, because they are not bonded by chemical bonding to plastics, phthalates can reach the mouth of children and thus harm their health, according to research [1]. According to Directive 2005/84/EC, products containing 0.1% DEHP, DnBP and BBP (individually or together) by weight of a plastic product may not be placed on the market [2]. However, when it comes to toys the European Commission has banned the use of DEHP, DBP and BBP as plasticizers in children's toys and childcare products, while the use of DINP, DIDP and DNOP has been restricted and the restriction applies only to toys that children can put on in the mouth [3]. Noting the restrictions imposed by the European Union on the use of phthalates, monitoring of phthalate concentration in toys is essential, for which different techniques are applied.

The aim of this work was to determine DMP, DBP, BBP, DEHP and DOP in children's plastic toys that children can place in the mouth, which were not labeled from which plastics they are made, using GC-MS technique.

## METHODS

All used reagents were of HPLC grade purity: tetrahydrofuran (THF) (Fischer scientific (USA)), *n*-hexane (Carlo Erba (France)), phthalates - DMP, DBP, BBP, DEHP, DOP (Sigma–Aldrich (USA)) and dibutyl adipate (DBA) (Fluka (Switzerland)).

Gas chromatographic analysis was performed on gas chromatograph 6890 (Hewlett-Packard, USA) equipped with a mass selective detector (MSD) 5973 (Hewlett-Packard, USA) and Autosampler 7683 (Agilent, USA) and SGE 25QC2/BPX5 0.25 capillary column (25 m×0.22 mm×0.25 μm, non-polar). The MSD was used in single ion-monitoring mode (SIM), the quantification ion is  $m/z$  149 for DBP, BBP, DEHP and DOP,  $m/z$  163 for DMP and ion  $m/z$  185 was chosen as representative ion for DBA. The identification of target compounds was based on the relative retention time, the presence of target ions and their relative abundance.

The calibration standard series in a concentration range of 0.25 to 2.50 μg mL<sup>-1</sup> of each phthalate with DBA at a concentration of 1 μg mL<sup>-1</sup> was obtained by diluting the stock standard solutions of each phthalate with *n*-hexane and their mixing.

In this study, 19 different plastic soft and flexible toys that children could put in their mouths were analyzed. All tested toys without specifying which plastics they were made from were purchased in the Serbian market.

The measured mass of the plastic toy was dissolved in 5 ml of THF. The THF solution was treated with 10 ml of *n*-hexane. This way the polymer was transferred to the precipitate while the dissolved phthalates were transferred to the supernatant. Further, the supernatant was filtered through the 0.45 μm PTFE and after proper dilution with *n*-hexane and addition of DBA, was recorded using GC-MS technique.

## RESULTS AND DISCUSSION

The chromatogram of a standard solution of investigated phthalates and DBA, given in Figure 1, shows good separation of five phthalates and DBA occurred within a running time of 13.5 min. The calibration curves were linear in the range from 0.25 to 2.5 μg mL<sup>-1</sup> with correlation coefficient of calibration curves 0.990.

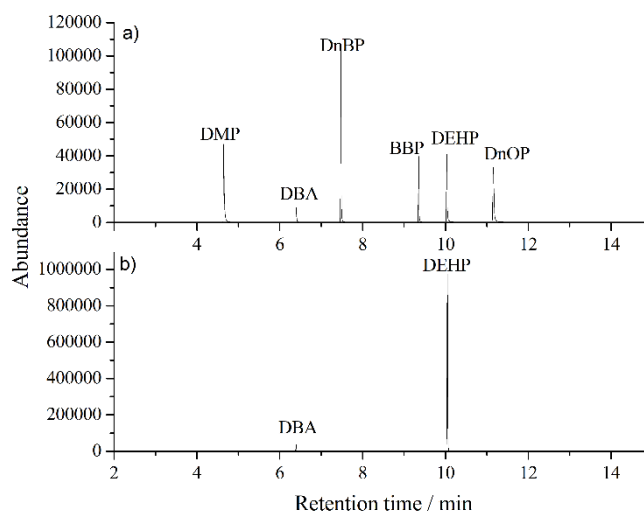


**Figure 1.** a) GC-MS chromatogram of a standard solution of investigated phthalates and DBA in a concentration of 1.5 μg mL<sup>-1</sup> and 1.00 μg mL<sup>-1</sup>, respectively; b) GC-MS chromatogram of the analyzed PVC article (1)

Based on the obtained chromatograms for each article, qualitative determination of phthalates was performed. The results showed the presence of DEHP and the absence of the remaining four tested phthalates in 13 analyzed PVC toys. The five remaining toys did not contain these investigated phthalates even though they are made of PVC, which means that they either contain some other phthalate used to soften the PVC, or that the toys are made in accordance with the applicable regulations that plastic toys do not contain phthalates. One of the 19 tested toys was not PVC, since it did not dissolve in THF and was not further analyzed.

Based on the performed DEHP calibration, the quantification of the 13 samples was performed and the obtained results are given in Table 1. The samples are marked with number 1 through 13.

The results show that the amount of DEHP in 13 PVC toys is very high and ranges from 10.27 to 53.24 % by weight of PVC samples. These are the expected results since it is known that phthalates are added to the PVC to soften it, and that DEHP is the most commonly used phthalate. On the other hand, these results are unexpected given the fact that phthalates are prohibited plasticizers when it comes to children's toys.

**Table 1.** Mass % of DEHP in PVC toys

PVC article	Mass % of DEHP in PVC samples
1	53,24 ± 2,72
2	43,00 ± 0,94
3	40,69 ± 0,92
4	40,24 ± 1,12
5	40,01 ± 1,95
6	36,87 ± 1,61
7	36,87 ± 1,61
8	36,82 ± 1,17
9	36,44 ± 0,64
10	31,34 ± 1,11
11	29,50 ± 0,63
12	27,04 ± 1,92
13	10,27 ± 0,31

## CONCLUSION

Considering the impact of phthalates on human health and total or partial ban on the use of certain phthalates as plasticizers in plastic toys constant monitoring of phthalate content in PVC toys is of great importance. The results of GC-MS analyze showed that 13 from 19 analyzed children toys contained DEHP in mass concentration range from 9.47 to 53.24 %. Given obtained results using GC-MS method it could be concluded that these toys made of PVC containing a considerable amount of DEHP are being sold in Serbia, despite the ban of the European Commission, which directly endangers the youngest population.

***Acknowledgement***

This study was performed within the research program – Contract No. 451-03-9/2021-14/200124.

**REFERENCES**

- [1] J. M. Braun, S. Sathyanarayana, R. Hauser, *Curr Opin Pediatr*, 2014, 25(2), 247-254
- [2] Directive 2005/84/EC of the European Parliament and of the Council, *Official Journal of the European Union*, 2005
- [3] EUROPA, Permanent ban of phthalates: Commission hails long-term safety for children's toys, *EUROPA Rapid Press Release*, 2005

## INFLUENCE OF UV RADIATION TO DEHP CONCENTRATION IN PVC CHILDREN TOYS

T. Anđelković<sup>1</sup>, D. Bogdanović<sup>1</sup>, I. Kostić<sup>1</sup>, G. Kocić<sup>2</sup> and R. Pavlović<sup>3</sup>

<sup>1</sup>University of Niš, Faculty of Science and Mathematics, Department of Chemistry, Višegradska 33, 18000 Niš, Serbia

<sup>2</sup>University of Niš, Faculty of Medicine Department of Biochemistry, Bulevar dr Zorana Đinđića 81, 18000 Niš, Serbia

<sup>3</sup>University of Milan, Department of Veterinary Science and Public Health, Via Celoria 10, 20133 Milan, Italy

(Corresponding author: e-mail: dannica.milojkovic@gmail.com)

### ABSTRACT

In order to determine the influence of UV-A and UV-C radiation on the structure of polymers in PVC toys, and therefore on the bond strength between DEHP and polymer, the concentration of DEHP in PVC toys was determined after irradiation of PVC toys using UV-A and UV-C light for a certain period. After performed calibration, DEHP quantification in two irradiated PVC toys was done using GC-MS technique. The obtained results indicated that UV-A and UV-C light influenced on DEHP migration from PVC toys into environment, which further affected the decrease in DEHP concentration in PVC toys. With increasing duration of radiation of these toys, the mass concentration of DEHP in the toys decreased, and for toy 1 was decreased from 27.04 to 19.58 mass%, while for toy 2 this decrease was from 36.82 to 30.81 mass%.

### INTRODUCTION

Phthalates are compounds that are most widely used in the form of plasticizers, which serve to soften, increase flexibility, extend life and stabilize the smell of plastic materials, and as plasticizers can make up to 50% by weight of plastic article [1]. Di-2-ethylhexyl phthalate (DEHP) is the most used phthalate due to its market price [2]. Although DEHP production decreases over time, DEHP remains one of the “biggest” pollutants, as plastics can contain from 1 to 40% DEHP [3]. As plasticizers, phthalates are also added to polyvinyl chloride (PVC), from which children's toys and products intended for children's use are further produced – pacifiers, baby bottles, teethers [4]. Therefore, plastic children's toys, that contain phthalates, are a potential source of phthalates. Due to the contact with the mentioned toys, due to the fast metabolism and small body weight, children are exposed to the action of phthalates from plastic toys at the earliest stage of their development. There is great concern about the use of these articles, especially articles such as teethers and other toys that can be placed in the mouth, due to more intensive migration of phthalates from plastic due to mechanical pressure on the teeth.

The aim of this paper is to examine the effect of UV light on the migration of DEHP from PVC toys, and thus on the reducing concentration of DEHP in the toys, and on the enrichment with DEHP of the environment to which DEHP migrated. Determination of DEHP concentration in PVC toys was performed using the GC-MS technique.

### METHODS

All used reagents were HPLC grade purity: Tetrahydrofuran (THF) (Fischer scientific (USA)), *n*-hexane (Carlo Erba (France)), DEHP (Sigma–Aldrich (USA)) and dibutyl adipate (DBA) (Fluka (Switzerland)).

Gas chromatograph 6890 (Hewlett-Packard, USA) equipped with a mass selective detector (MSD) 5973 (Hewlett-Packard, USA) and Autosampler 7683 (Agilent, USA) and SGE 25QC2/BPX5 0.25 capillary column (25 m×0.22 mm×0.25 μm, non-polar) was used for gas chromatographic analysis. The MSD was used in single ion-monitoring mode (SIM), the quantification ion is  $m/z$  149 for DEHP and ion  $m/z$  185 was chosen as representative ion for DBA. The identification of DEHP was based on the relative retention time, the presence of target ion and its relative abundance.

The calibration standard series in a concentration range of 0.25 to 2.50 μg mL<sup>-1</sup> of DEHP with DBA at a concentration of 1 μg mL<sup>-1</sup> was obtained by diluting the stock standard solution of DEHP with *n*-hexane.

Two toys in which the DEHP content was determined in a previous study were irradiated with UV-A light and UV-C light for a certain time interval, in order to analyze the influence of UV-A and UV-C light on the change in the polymer structure of PVC articles, and on the migration of phthalates from PVC toys. UV chamber was used as a source of UV-A radiation with a wavelength of 365 nm and UV photo reactor with low pressure mercury lamps, 28 W, with a maximum radiation at 254 nm, manufactured by Philips (Netherlands) was used as a source of UV-C radiation. The toys were placed at 5 cm from these lamps. The UV-A radiation somewhat imitated solar radiation, while the UV-C radiation was set experimentally, for comparison the effects of these two radiations on the migration of phthalates from PVC toys. PVC toys were irradiated with UV-A light for 1, 2, 4, 6, 12, 24 h, while PVC toys were irradiated with UV-C light for 1 and 2 h.

The quantification of DEHP in irradiated PVC toys was performed after each radiation time, in the following manner. In order polymer precipitating and DEHP retaining in the supernatant, 5 mL of THF solution of the irradiated plastic toy was treated with 10 mL of *n*-hexane. After filtering of the supernatant through the 0.45 μm PTFE and after proper dilution with *n*-hexane and addition of DBA, analyze of prepared samples were performed using GC-MS technique.

## RESULTS AND DISCUSSION

The calibration curve for DEHP was linear in the range from 0.25 to 2.5 μg mL<sup>-1</sup> with calibration equation  $y = (3,418 \pm 0,044) x - (0,275 \pm 0,062)$  and correlation coefficient of calibration curve 0.999. Based on the performed DEHP calibration, the quantification of the DEHP in irradiated toys after dissolving these toys in THF was performed using GC-MS technique and the obtained results were given in Table 1. Figure 1 shows the chromatograms of non-irradiated and irradiated toys with UVC light for 2 h.

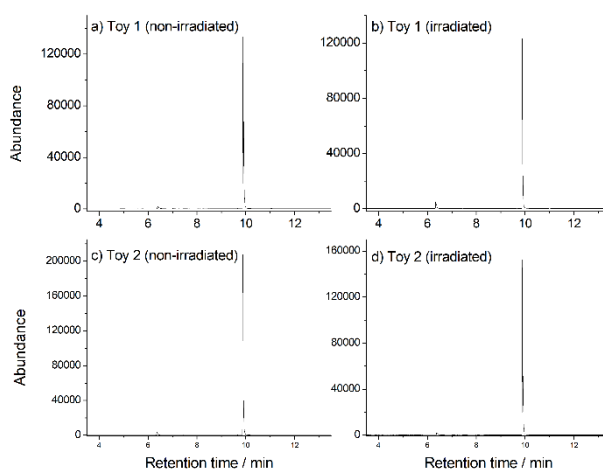


**Figure 1.** GC-MS chromatogram of non-irradiated and irradiated toys with UVC light for 2 h

**Table 1.** GC-MS quantification of DEHP in irradiated PVC toys

PVC Toy	Type of radiation	Time of radiation (h)	Content of DEHP in PVC toy (mass %)	
1	–	0	27,04±1,92	
		2	21,87±2,25	
	UV-A	4	21,45±1,08	
		6	20,75±2,46	
		12	21,67±1,12	
		24	21,13±1,13	
		UV-C	1	20,03±0,11
	2		19,58±0,17	
	2	–	0	36,82±1,17
			1	33,75±0,21
UV-A		2	33,32±0,75	
		4	33,59±1,02	
		6	33,50±1,98	
		12	33,04±1,41	
		24	33,39±1,12	
		UV-C	1	31,22±0,17
2			30,81±0,19	

The results showed that the weight percentages of DEHP in Toy 1 decreased from 27.04 to 19.58 mass%, while this range for Toy 2 ranged from 36.82 to 30.81 mass%. Therefore, with increasing radiation time, the bond between DEHP and the polymer weakened, because of which DEHP migrated more easily from the PVC toy to the outside environment, whereby the DEHP content decreased in PVC toys with radiation time. UV-A radiation for 2 h caused the strongest change in the DEHP content of PVC toys, while further radiation reduced the percentage composition of DEHP gradually.

## CONCLUSION

Due to the results presented in the paper, there should be concerns for children's health due to the high concentration of phthalates in toys, as well as the weakening of the bond between DEHP and polymers due to UV-A and UV-C light, which affects the potentially easier DEHP migration and the concentration of migrated DEHP into the atmosphere.

## Acknowledgement

This study was performed within the research program – Contract No. 451-03-9/2021-14/200124.

**REFERENCES**

- [1] A. O. Earls, I. P. Axford, J. H. Braybrook, *J Chromatogr A*, 2003, 983, 237-246.
- [2] T. J. Wams, *Sci Total Environ*, 1987, 66, 1-16.
- [3] R. Rudel, L. Perovich, *Atmos Environ*, 2008, 43(1), 170-81.
- [4] S. Saeidnia, Phthalates, *Encyclopedia of Toxicology*, 928–933, (3<sup>rd</sup> ed.), Academic Press, Elsevier Inc., London, 2014.

## CADMIUM TRANSLOCATION EFFICIENCY IN WATER LETTUCE

D. Anđelković<sup>1</sup>, M. Branković<sup>2</sup> and B. Zlatković<sup>3</sup>

<sup>1</sup> University of Niš, Agricultural faculty, Kosančićeva 4, 37000 Kruševac, Serbia

<sup>2</sup> University of Niš, Faculty of Sciences and Mathematics, Department of Chemistry, Višegradska 33, 18000 Niš, Serbia (milica.chem@outlook.com)

<sup>3</sup> University of Niš, Faculty of Sciences and Mathematics, Department of Biology, Višegradska 33, 18000 Niš, Serbia

### ABSTRACT

Heavy metals commonly found in waters are As, Pb, Hg, Cd, Ni and Cr. The major cost of heavy metal pollution is their bioaccumulation. Phytoremediation of waters and soils refers to the use of pollutant-accumulating plants to extract and accumulate contaminants from contaminated medium. The main objective of this study was to estimate the translocation efficiency and response of *P. stratiotes* on increased cadmium levels in water. Estimation of translocation efficiency was performed for a nutrient-free water polluted with 1, 5, 10, 15 and 20 ppm of cadmium, over 15 days of growth. High translocation efficiency was observed for plants grown up to five days in water with the two lowest levels of tested cadmium contamination.

### INTRODUCTION

Plants, animals and ultimately humans are negatively affected by heavy metal pollution of water supplies. Heavy metals such as As, Pb, Hg, Cd, Ni and Cr are commonly found in waters. One of the major consequences of this kind of pollution is bioaccumulation of heavy metals. There are many functional changes that can be observed in plants, after being exposed to heavy metals, such as plant membrane damage due to the formation of reactive oxygen species and radicals, disrupted metabolic activities or growth retardations. For example, the accumulation of cadmium in *P. stratiotes* stimulates malondialdehyde production, indicating that cadmium indirectly leads to production of superoxide radicals and increases lipid peroxidative products and oxidative stress [1]. However, toxicity degree of non-essential metals such as Cd, Pb, Hg depends on their concentration.

Important sources of cadmium contamination are atmospheric decomposition derived from mining, smelting, and fuel combustion, as well as the use of phosphate fertilizers and sewage sludge, batteries, pigments, metal coatings, and plastics [2].

Phytoremediation of waters and soils from heavy metals refers to the use of pollutant-accumulating plants to extract and accumulate contaminants to the harvestable parts and is increasingly being considered as an environmentally friendly, easy, and cost-effective solution to clean up soils and wetlands contaminated by heavy metals [1].

The main objective of this study was to estimate the translocation efficiency and response of *P. stratiotes* on increased cadmium levels in a non-nutrient solution.

### METHODS

Reagents: the source of cadmium was the 72.958  $\mu\text{g mL}^{-1}$  solution of cadmium-chloride [ $\text{CdCl}_2$ ]. Nutrients for plant growth were not used.

Bio-sorbent: The samples of aquatic macrophyte *P. stratiotes* were handpicked from the natural freshwater habitat in Ostrovica, near Niš (Serbia), in the mid-June 2017.

Experimental setup: Collected plant samples were washed with tap water to eliminate the remains of pond sediments and particulate matter, placed in five different 35 L plastic tanks (labeled from I to V) and filled with tap water. Each tank contained 15 specimens of *P. stratiotes* and different amount

of  $\text{Cd}^{2+}$  ion, as given in Table 1. Plants were grown during 15 days in contaminated media. One plant per day was removed from each tank and analyzed.

**Sample preparation:** After removal from tanks, samples of *P. stratiotes* were washed out of excessive substrate solution with fresh water and left to dry indoor at ambient temperature until complete dryness. Afterwards, to remove possible residual humidity, plants were additionally dried in a laboratory oven, at 100 °C for 30 minutes, prior to weighing. Leaves and root of each plant specimen were separated, weighted, cut in small pieces and pulverized. A weight of each specimen sample was then digested with 15 mL of a mixture (v/v 3:1) of concentrated 63% nitric acid and 30% hydrogen peroxide and solution was evaporated until dryness. The solid residue was re-dissolved in 13 mL of 0.1 mol/dm<sup>3</sup> nitric acid, filtered through filter paper, then through microfilter (0.45 μm), after which the mineralized plant material was ready for instrumental analysis.

**Instrumental analysis:** To determine the metal content in plant material, obtained extracts were analyzed by atomic absorption spectroscopy (AAS) using VARIAN Aanalyst 300 with acetylene/air flame.

**Calculation of translocation factor and translocation efficiency:** The ratio of heavy metal concentration in the shoot (mgkg<sup>-1</sup>) to that in the root of the plant (mgkg<sup>-1</sup>) is defined as the translocation factor (TF). The efficiency of translocation (in %) depicts the ability of the plant to translocate the metal species from roots to leaves at different concentrations. It is calculated by multiplying TF with 100.

**Table 1.** Concentration of  $\text{CdCl}_2$  and  $\text{Cd}^{2+}$  ion and amount of plant material in each tank.

Tank No.	I	II	III	IV	V
$\text{Cd}^{2+}$ ion concentration, ppm	1	5	10	15	20
$\text{Cd}^{2+}$ ion mass, mg	35	175	350	525	700
$\text{CdCl}_2$ concentration, ppm	1.631	8.154	16.307	24.461	32.615
Total mass of plant material at start of experiment (fresh weight), g	490	480	528	426	522
Total mass of plant material at the end of experiment (fresh weight), g	402	355	388	292	349

## RESULTS AND DISCUSSION

An ideal hyperaccumulator plant would have shoots with a high capacity to accumulate heavy metals/metalloids, high biomass, and rapid growth, and bioconcentration factor (BCF) and translocation factor (TF) values higher than 1 [2].

As determined within this study the translocation factor *i.e.*, the translocation efficiency of *P. Stratiotes* towards cadmium was highest after first day of growth in medium containing 5 ppm  $\text{Cd}^{2+}$ . In fact, among the days of cultivation the highest translocation efficiency was observed after 1<sup>st</sup> day, ranging from 24.09% for plants from water polluted with 15 ppm to 248.52% for plants from water polluted with 5 ppm of cadmium. After that period, a straight decline and then uniformity in TF was observed.

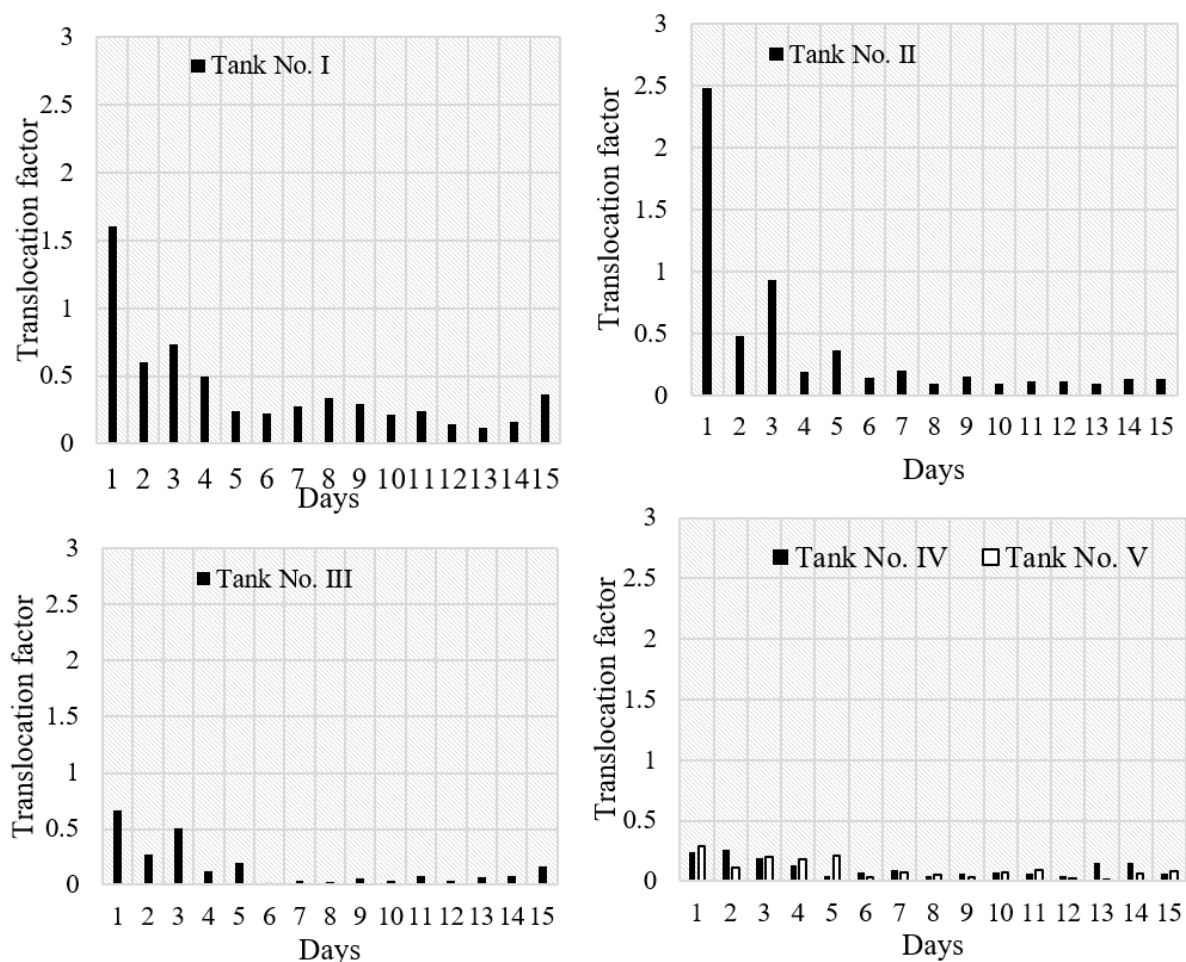


**Figure 1.** Translocation factor as a measure of *P. Stratiotes* ability for root-to-shoot Cd distribution.

Regarding the previously mentioned criteria, TF is higher than 1 only in waters polluted with 1 and 5 ppm of cadmium. With increased cadmium pollution (10 to 20 ppm) TF decreased. The highest value observed was 0.66 after 1<sup>st</sup> day of growth in 10 ppm-polluted water.

## CONCLUSION

Estimation of translocation factor/translocation efficiency of *P. Stratiotes* towards cadmium was performed for several levels of a nutrient-free cadmium-polluted water, over the 15 days of growth. The translocation efficiency was highest after the first day of growth in water containing 5 ppm Cd<sup>2+</sup>. Moreover, TF was higher than 1 only in waters polluted with 1 and 5 ppm of cadmium. With increased cadmium pollution (10 to 20 ppm) TF decreased. Regarding the growth period, from the 1<sup>st</sup> to the 5<sup>th</sup> day a decline in TF was observed, after which it was uniform.

## Acknowledgement

This study was supported by the Ministry of Education, Science and Technological Development of the Republic of Serbia (contract no. 451-03-9/2021-14/200383 and 451-03-9/2021-14/200124)

**REFERENCES**

- [1] Y. Li, S. Zhang, W. Jiang, D. Liu, *Environmental Science and Pollution Research*, 2013, 20, 1117–1123.
- [2] S. Das, S. Goswami, A. Das Talukdar, *Bulletin of Environmental Contamination and Toxicology*, 2014, 92, 169–174.

## WASTE COTTON/POLYESTER YARN AS AN ADSORBENT FOR THE REMOVAL OF HEAVY METALS FROM WASTEWATER

S. Mihajlović<sup>1</sup>, M. Vukčević<sup>1</sup>, M. Maletić<sup>2</sup>, B. Pejić<sup>1</sup>, A. Perić Grujić<sup>1</sup>, M. Ristić<sup>1</sup>, K. Trivunac<sup>1</sup>

<sup>1</sup>University of Belgrade, Faculty of Technology and Metallurgy, Karnegijeva 4, 11000 Belgrade, Serbia.

<sup>2</sup>Innovation Center of the Faculty of Technology and Metallurgy, Karnegijeva 4, 11000 Belgrade, Serbia.

### ABSTRACT

Waste cotton/polyester yarn was used for the removal of Pb(II), Cd(II), Cr(III) and As(V) ions from aqueous solution. In attempt to increase the adsorption efficiency, cotton/polyester yarn was modified by sodium hydroxide solution. Characterization of examined yarns was performed by scanning electron microscopy, Fourier transform infrared spectroscopy and streaming potential method for determination of the isoelectric point. It was shown that applied treatments slightly affected the surface acidity due to increased availability of ester groups and changes in cellulose-derived groups. These changes in surface chemistry of modified cotton/polyester yarns did not improve their adsorption capacity for Cd(II), Cr(III) and As(V) ions. However, both unmodified and modified waste cotton/polyester yarns could be used for efficient removal of lead ions from wastewater.

### INTRODUCTION

Nowadays, the most widely used material for cloth manufacturing is cotton. In order to improve physical, mechanical and comfortable characteristics of clothing, decorative fabrics and textile products, mixture of cotton and polyester yarns are often used. The increase in textile production caused by frequent changes in fashion trends leads to the formation of large amounts of textile waste that can have a negative impact on the quality of the environment. Therefore, the possibility of reusing the waste textile, fibers and yarns are increasingly investigated in the past years. Following the general trend of using waste materials as adsorbents [1], in this work, cotton/polyester yarns obtained as a waste from textile industry, were used as cheap and efficient sorbent for removal of lead, chromium, cadmium and arsenic ions from wastewater.

### MATERIAL AND METHODS

Waste cotton/polyester yarn (C/PES) was obtained from textile factory SIMPO Dekor (Serbia, Vranje). C/PES was modified by NaOH solutions, for one hour at room temperature, and two alkali treated samples were obtained: C/PES<sub>10</sub> (10 % NaOH) and C/PES<sub>18</sub> (18 % NaOH).

The morphological characteristics of yarn samples were assessed by scanning electron microscopy (Mira3, Tescan). FTIR spectra of the samples, within a range of 400-4000 cm<sup>-1</sup>, were recorded using a Nicolet™ iS™ 10 FT-IR Spectrometer (ThermoFisherSCIENTIFIC). Zeta potential ( $\zeta$ ) of cotton yarn samples was measured using the streaming potential method (SurPASS electrokinetic analyzer, Anton Paar GmbH), as described in the literature [1]. Isoelectric point (IEP) was determined by extrapolation of experimental data.

Adsorption of Pb(II), Cd(II), Cr(III) and As(V) by unmodified and modified C/PES samples were performed from aqueous solutions, in the batch system at 25 °C. Fixed amount of unmodified and modified C/PES samples (0.02 g) was added in 20 cm<sup>3</sup> of metal ions solution at initial concentrations ranging from 100 to 1000  $\mu\text{g dm}^{-3}$ , per each ion. Concentration of selected metal ions in the solution was measured by inductively coupled plasma-mass spectrometry (ICP-MS Agilent 7500e).

## RESULTS AND DISCUSSION

The structure and surface morphology of C/PES sample, composed from cotton and PES components, is visible on Fig. 1a.

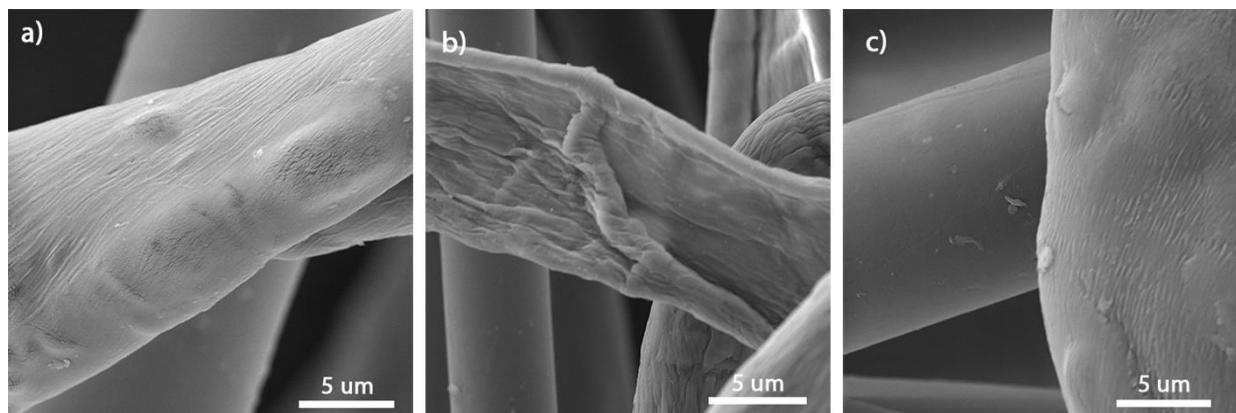


**Figure 1.** SEM photographs of a) C/PES, b) C/PES<sub>10</sub> and c) C/PES<sub>18</sub>

Cotton component consists from spirally twisted cotton fibers, with distinctly rough surface, featured by longitudinal cracks along the fiber. On the other hand, PES component is characterized by straight, untwisted, filament, with noticeably smooth surface. Applied treatments do not affect the morphology of modified C/PES samples (Fig. 1b and 1c).

FTIR spectra for unmodified and modified C/PES samples are shown in Fig. 2a. The wide band between 3350 and 3250  $\text{cm}^{-1}$  is assignable to the stretching vibrations of O-H bond (hydroxyl groups), whereas the bands around 2920 and 2850  $\text{cm}^{-1}$  are to be ascribed to asymmetric and symmetric C-H stretching vibrations, respectively.

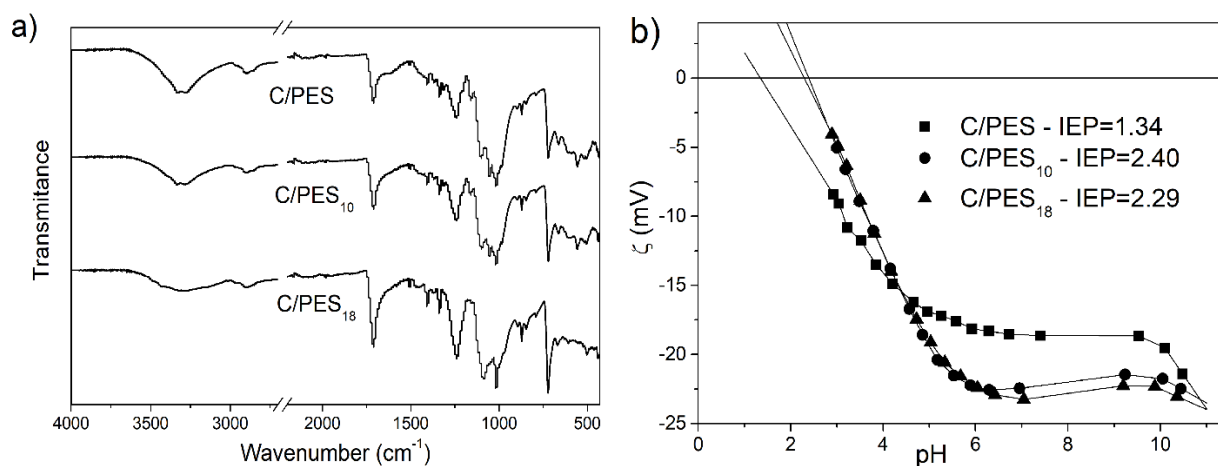


**Figure 2.** Characterization of C/PES samples: a) FTIR spectra and b) point of zero charge

The broad peak around 1630  $\text{cm}^{-1}$  can be attributed to the aromatic skeletal vibration, or C=O stretching vibrations of carbonyl groups [2]. The bands in region 1150-1000  $\text{cm}^{-1}$  are assigned to cellulose, indicating C-O and C-C stretching. Peaks at 1710 and 1240  $\text{cm}^{-1}$  originated from ester group, while peak at 1505  $\text{cm}^{-1}$  originated from aromatic systems in polyester chains [3].

Applied modification, and increase in NaOH concentration, lead to the increase in intensity of bands at  $1710$  and  $1240\text{ cm}^{-1}$ , and alter the surface chemistry of cotton component (changes in the region  $1150\text{--}1000\text{ cm}^{-1}$ ). Applied treatments induce opening of the yarns structure, making ester groups more available. Increased accessibility of ester groups made surface less acidic, which is visible from increase in the IEP values (Fig. 2b).

All C/PES samples showed high adsorption efficiency for lead ions, which were the most competitive (Fig. 3). However, increased accessibility of less acidic ester groups on the surface of C/PES<sub>10</sub> and C/PES<sub>18</sub> negatively affected the adsorption of less competitive ions (Cd(II), Cr (III) and As(V)). Therefore, the adsorption of heavy metals was studied through adsorption kinetics and isotherms using unmodified C/PES as adsorbent (Fig. 4).

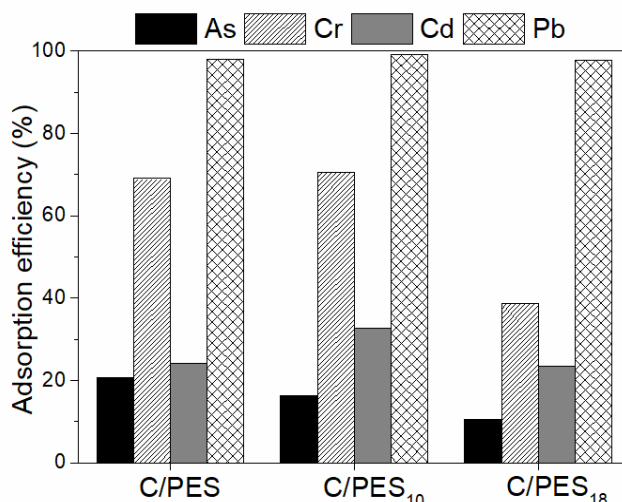


**Figure 3.** Adsorption efficiency of C/PES samples

adsorption of less competitive ions (Cd(II), Cr (III) and As(V)). Therefore, the adsorption of heavy metals was studied through adsorption kinetics and isotherms using unmodified C/PES as adsorbent (Fig. 4).

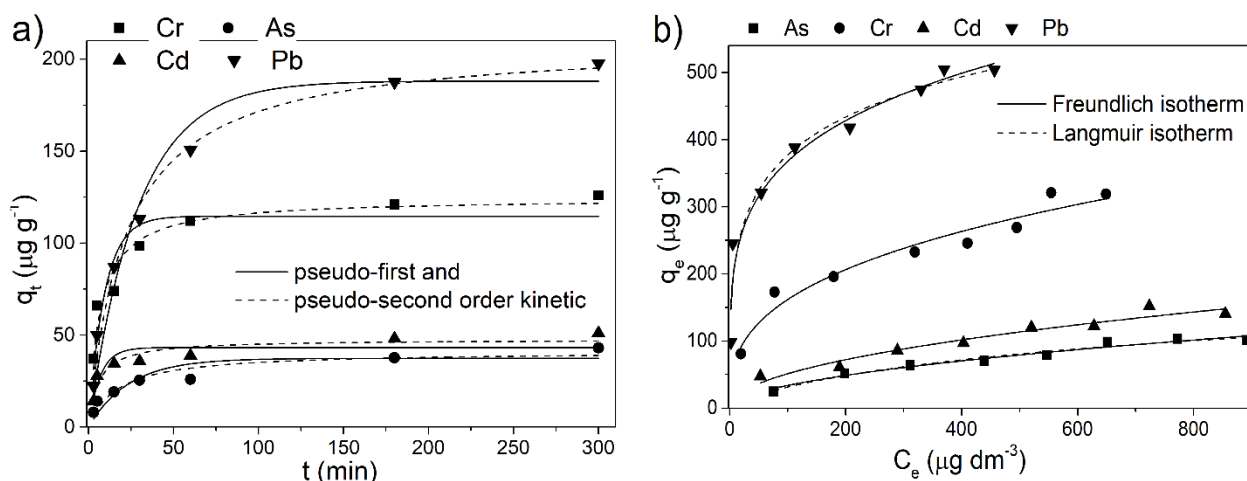


**Figure 4.** Effect of time (a) and initial concentration (b) on heavy metals adsorption onto C/PES sample

Adsorption of tested heavy metals on C/PES better fits with pseudo-second order kinetic model, suggesting that adsorption process is characterized by chemisorption. Adsorption equilibrium data showed equally good fitting with both, Freundlich and Langmuir isotherm models.

## CONCLUSION

Chemical modification with NaOH opened the yarn structure, making its surface groups more available. This apparent increase in ester groups number, along with the alteration of cellulose surface chemistry from cotton component, changed the acidity of yarn surface. Applied treatments did not improve the capacity of C/PES yarns for adsorption of Cd(II), Cr (III) and As(V). Nevertheless, it has been shown that lead ions can be efficiently removed from wastewater by adsorption onto both, unmodified and modified waste cotton/polyester yarns.

***Acknowledgement***

The research was funded by the Ministry of Education, Science and Technological Development of the Republic of Serbia (Contract No. 451-03-9/2021-14/200135 and Contract No. 451-03-9/2021-14/200287).

**REFERENCES**

- [1] S. Mihajlović, M. Vukčević, B. Pejić, A. Perić Grujić, M. Ristić, *Environ. Sci. Pollut. Res.*, 2020, **27**, 35769–35781.
- [2] H. Zhang, R. Ming, G. Yang, Y. Li, Q. Li, H. Shao, *Polym. Eng. Sci.*, 2015, **55**, 2553–2558.
- [3] A.A. Younis, *Egypt. J. Pet.*, 2016, **25**, 161-169.



*L - Phase Boundaries,  
Colloids,  
Liquid Crystals,  
Surface-Active Substances*



## NITROGEN DOPED CARBON CRYOGEL AS A SORBENT FOR HEAVY METAL IONS (ZN, CD, HG)

A. Krstić<sup>1</sup>, T. Minović Arsić<sup>1</sup>, M. Mirković<sup>1</sup>, A. Lolić<sup>2</sup>, A. Kalijadis<sup>1</sup>

<sup>1</sup>University of Belgrade, Vinca Institute of Nuclear Sciences - National Institute of the Republic of Serbia, Mike Petrovića Alasa 12-14, Belgrade, Serbia

<sup>2</sup>University of Belgrade, Faculty of Chemistry, Studentski trg 12-16, Belgrade, Serbia  
E-mail: aleksandar.krstic@vinca.rs

### ABSTRACT

Heteroatom incorporated into carbon material structure may result an increase of specific surface area, amount of surface functional groups, formation of new functional groups and an increase of charge which are important for improvement of adsorption process. The aim of this work was to investigate possible application of nitrogen doped carbon cryogels (CCN) for heavy metals removal from waste water. Adsorption kinetics and influence of pH value on adsorption were investigated. In order to describe the adsorption mechanism on carbon cryogel, the adsorption isotherms were determined. The obtained results showed that the incorporation of nitrogen into the carbon cryogel structure leads to an increase in the specific surface area and oxygen content. Adsorption study showed that the samples with the highest concentration of incorporated nitrogen showed better adsorption characteristic and faster adsorption equilibria compared to undoped carbon cryogel. Also, pH decrease of water solutions leads to stronger  $\pi$ - $\pi$  interaction between functional group on carbon surface and metal ions from solution that leads to a better metal removal from water.

### INTRODUCTION

Carbon aerogel (CC), xerogel and cryogel are types of carbon materials prepared by sol-gel polycondensation of organic matter (resorcinol and formaldehyde) in the presence of  $\text{Na}_2\text{CO}_3$  as a catalyst [1]. Wet gels drying can be performed by supercritical drying, lyophilization and solvent evaporation at atmospheric pressure [2]. Carbonization in the inert gas stream was used for obtaining final carbon material. Due to their characteristics such as porosity, good electrical and thermal conductivity, these materials have found application as adsorbents for removal pollutants from water, energy storage cells, electrode and catalyst carriers. Porosity is crucial characteristic for their application in the heavy metal adsorption process. Incorporation of heteroatom (N, S, B, P) in carbon structure may affect physico-chemical properties, and electrochemical properties [3]. Nitrogen doping has significant impact on structural and surface characteristics of carbon material. Due to its electronic structure the redistribution of charge in the carbon structure occurs during incorporation of nitrogen. Nitrogen in carbon structure is an electron donor that can affect the formation of new functional groups on carbon surface which, in addition to the specific surface area, are crucial for adsorption process.

### METHODS

Carbon cryogels (CC) samples were synthesized by polycondensation of resorcinole and formaldehyde in water with base catalyst  $\text{Na}_2\text{CO}_3$ . Sample was dried by liophylization and carbonized at  $900^\circ\text{C}$ . Melamine was used as nitrogen source which was added to a precursor solution to obtained nitrogen nominal concentrations of 2 wt%, 6 wt%, and 10 wt% [4]. CC samples were characterized by elemental and BET analysis. Kinetics and equilibrium adsorption studies were investigated using a batch experimental approach. A mixture of hydrate salts ( $\text{Zn}(\text{NO}_3)_2$ ,  $\text{Cd}(\text{NO}_3)_2$  and  $\text{Hg}(\text{NO}_3)_2$ ) concentration of 10 ppm was used as adsorbate. The mass of adsorbent used for the

experiment was 50 mg. Concentration of heavy metal were determinate by ICP-OES spectrometer, model ICAP 7400 *duo* Thermofisher Scientific. All the experiments were performed at room temperature (25°C).

## RESULTS AND DISCUSSION

The addition of melamine into CC precursor resulted that nitrogen was incorporated in final materials up to 1,15 wt%. Results presented in Table 1 show that the specific surface area values are in the range 592-928 m<sup>2</sup>/g. Nitrogen incorporation leads to increase of specific surface area values, compare to pristine CC<sub>0</sub> sample, especially for CCN<sub>2</sub> sample but mesoporosity for all samples is saved [4].

**Table 1:** Elemental analysis and porous properties of CC samples doped with nitrogen [4]

Sample	C (wt%)	N (wt%)	O (wt%)	H (wt%)	S <sub>BET</sub> m <sup>2</sup> /g	S <sub>meso</sub> m <sup>2</sup> /g
CC <sub>0</sub>	88,47	0,00	10,04	1,49	592	318
CCN <sub>1</sub>	84,85	0,45	12,80	1,90	887	513
CCN <sub>2</sub>	81,58	0,72	15,82	1,88	928	561
CCN <sub>3</sub>	82,44	1,15	14,72	1,69	676	305

Investigation of adsorption kinetics was carried out in the interval 0-24h and results showed significantly better adsorption characteristic for all CCN samples. The equilibration time for CC<sub>0</sub> was reached after 3h with adsorption maximum of 82% for zinc, 75% for cadmium and 86% for Hg. Equilibration time of CCN samples was shorter (1h) than the CC<sub>0</sub> sample. The adsorption maximum of all CCN samples was higher than the CC<sub>0</sub> sample (Figure 1). After 1h equilibration, CCN<sub>2</sub> sample was adsorbed 92%, 85% and 89% of Zn, Cd and Hg, respectively. For CCN<sub>1</sub> and CCN<sub>2</sub> those values are similar. After 24h all doped samples adsorbed more than 94% of pollutants. Insignificant differences in adsorption process between doped samples were observed and indicate that more developed specific surface is not crucial for higher adsorption capacity. The obtained results can be explained that the nitrogen incorporation leads to the redistribution of charge on carbon surface, an increase of electron density which leads to stronger electrostatic interaction and dipole-dipole interaction between metal ions from the adsorbate solution and functional groups from the carbon surface.

Influence pH was investigated in the range 2-12 pH units for Zn and Cd, and in the range 2-8 pH units for Hg adsorption. Initial concentration of adsorbate was 10 ppm, and equilibration time was 3h for CC<sub>0</sub> sample and 1h for all CCN samples. Initial pH value of mix adsorbate solution was 5.5. Cd was strongly adsorbed in the pH range 4-8. For Zn and Hg, results are similar. Since pH of adsorbate is at about 5.5, this value is optimal for the removal all three compounds. At this pH, the adsorption of all metals was highest (more than 95%). Stronger acidic condition is unfavorable for adsorption because of competition between H<sup>+</sup> ions and metal ions in solution.

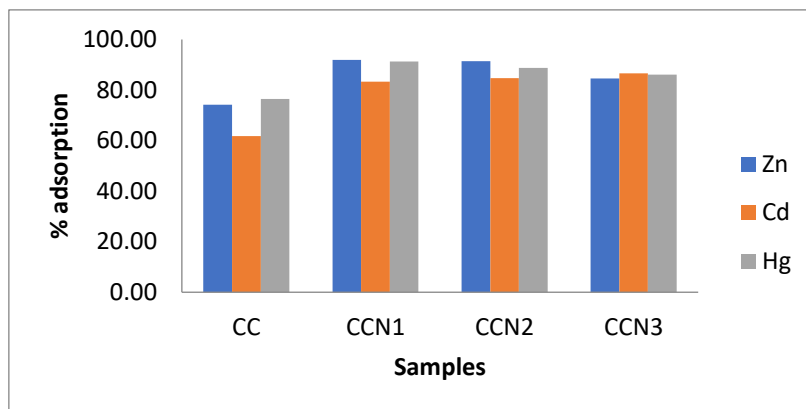


**Figure 1:** Adsorption of metals after 1h of equilibration on samples CC<sub>0</sub>, CCN<sub>1</sub>, CCN<sub>2</sub> and CCN<sub>3</sub>

**Table 2:** Langmuir and Freundlich isotherm parameters for metals ions adsorption on tested samples

Sample	Heavy metal	Langmuir isotherm		Freundlich isotherm		
		$R^2$	$Q_0$ (mg/g)	$R^2$	$K_F$ ((mg g <sup>-1</sup> ) (dm <sup>3</sup> mg <sup>-1</sup> ) <sup>1/n</sup> )	1/n
CC	Zn	0.9678	6.11	0.7784	3.86	0.2115
	Cd	0.8573	3.56	0.0817	2.34	0.0364
	Hg	0.9959	27,93	0.8853	5.92	0.3743
CCN <sub>1</sub>	Zn	0.9986	10.00	0.7988	4.26	0.2356
	Cd	0.9925	3.09	0.5826	2.48	0.0529
	Hg	0.9976	34.25	0.9510	1.77	0.5703
CCN <sub>2</sub>	Zn	0.9997	13.57	0.8234	4.65	0.2906
	Cd	0.844	4.53	0.3739	2.73	0.0877
	Hg	0.9812	34.84	0.9733	3.66	0.6006
CCN <sub>3</sub>	Zn	0.9988	9.29	0.6791	4.29	0.2112
	Cd	0.9154	3.32	0.8247	1.04	0.2458
	Hg	0.9577	30,25	0.8732	6.94	0.3718

Under the optimum condition, the interaction between the examined metals and CC samples was investigated. The initial concentration of metals in the solution was varied and the adsorption isotherms were determined. The obtained experimental adsorption isotherms for all samples were treated according to the Langmuir and Freundlich model. The assumption of the Langmuir model adsorption isotherms is that there is initially fixed number of adsorption sites on the surface and that adsorption is limited to monolayer coverage. The Freundlich model isotherms differ from the Langmuir and assumes that multilayer adsorption occurs on a heterogeneous adsorbent that has different active sites with varying adsorption energies. Based the  $R^2$  values, equilibrium data obtained for all three metals, fitted well with Langmuir isotherms for all examined samples. Maximum adsorption capacity and  $R^2$  of all CCN samples are higher than  $R^2$  value of CC<sub>0</sub> which means better agreement with Langmuir equation, which implies the homogenous distribution of active sites on carbon surface.

## CONCLUSION

This work investigated a possible application of nitrogen doped carbon cryogels for removal of different heavy metals from waste water. The obtained result confirmed presence of nitrogen in carbon structure and showed that the nitrogen incorporation leads to increase a specific surface area and oxygen content. This increase is a greatest for sample with an intermediate concentration of incorporated nitrogen. The investigation of adsorption kinetics, effect of pH and adsorption isotherms showed better adsorption characteristic for nitrogen doped carbon cryogel samples. Finally, based on results in this work, it can be concluded that nitrogen doped carbon cryogel could be potentially used as a sorbent for zinc, cadmium, and mercury in water remediation treatment.

## Acknowledgement

All authors thank to the Ministry of Education, Science and Technological Development of the Republic of Serbia for the financial support of the research through institutional funding (contract number 451-03-9/2021-14/200017).

## REFERENCES

- [1] R. W. Pekala, C. T. Alviso, X. Lu, J. Gross, J. Fricke, New organic aerogels based upon a phenolic-furfural reaction, *J. Non-Cryst. Solids* 188 (1995) 34–40.
- [2] B. Babić, B. Kaludjerović, Lj. Vračar, N. Krstajić, Characterization of carbon cryogel synthesized by sol–gel polycondensation and freeze-drying, *Carbon* 42 (2004) 2617–2624.
- [3] D. Geng, S. Yanga, Y. Zhang, J. Yang, J. Liu, R. Li, T.-K. Sham, X. Suna, S. Ye, S. Knights, Nitrogen doping effects on the structure of graphene, *Appl. Surf. Sci.* 257 (2011) 9193– 9198.
- [4] Ana Kalijadis, Nemanja Gavrilov, Bojan Jokić, Martina Gilić, Aleksandar Krstić, Igor Pašti, Biljana Babić, Composition, Structure and Potential Energy Application of Nitrogen Doped Carbon Cryogels, *Mater. Chem. Phys.* 239 (2019). 122120

## INFLUENCE OF SEC-ALKAN SULFONATE ON DISHWASHING ANIONIC SURFACTANTS MIXTURE

S. N. Blagojević<sup>1</sup>, S. M. Blagojević<sup>2</sup> and N. Pejić<sup>2</sup>

<sup>1</sup>*Institute of General and Physical Chemistry, Studentski trg 12/V, Belgrade*

<sup>2</sup>*University of Belgrade – Faculty of Pharmacy, Department of Physical Chemistry and Instrumental Methods, Vojvode Stepe 450, Belgrade, Serbia*

### ABSTRACT

Surface active properties and foamability of anionic surfactants mixtures (sodium lauryl ether sulfate (SLES), sec-alkan sulfonate (sodium C14–17 alkyl sec sulfonate (SAS)), cocamidopropyl betaine (CB) and cocodiethanolamide (DEA) were studied. Investigated features of particular anionic surfactants mixture were critical micelle concentration (CMC), surface tension ( $\gamma$ ) and foam volume. The aqueous mixture composition, containing SLES, CB and DEA in ratio 10:1:0.5 (expressed in mass percent) were base anionic surfactants mixture. With the addition of SAS to the SLES/CB/DEA surfactants mixture, both CMC and  $\gamma$  were decreased, as well as foaming properties of SLES/CB/DEA were improved. All those indicate that SAS surfactant can be used to produce better cleaning products.

### INTRODUCTION

Dishwashing in aqueous wash liquor is a complex process which involves the interaction of numerous physical and chemical parameters. In the broadest sense, washing can be defined as both the removal by water or aqueous surfactant solution of poorly soluble dirt and the dissolution in water [1]. The main and most important ingredient in dishwashing liquids are surfactants which molecule are consisted of a long hydrocarbon “tail” that dissolves in organic and other non-polar solvents, and a hydrophilic “headgroup” that dissolves in polar solvents, and the most important for usage, water. Because of its dual affinity, surfactants in water based solvents show more or less marked tendency to the spontaneous accumulation in the phase boundary surfaces by reducing the surface tension of the solution, and forming micelles. When a dishwashing liquid that have sufficient amount of surfactant is dissolved in water, several bulk solution properties are significantly changed, decreasing the surface tension and increasing the ability of the solution to solubilize hydrocarbons. Those changes are happened only when certain surfactant concentration, termed the critical micelle concentration (CMC) is reached. The thermodynamically stable micelles, which can be formed beyond CMC, are in equilibrium with the monomers in the solution and are characteristic of the ability of surfactants to solubilize hydrophobic substances.

Modern dishwashing liquid formulation has a mixture of surfactants, mainly anionic and in some formulations with addition of nonionic. SAS possesses good wetting properties and high degreasing effect are also compatible with other anionic surfactants [1]. The main expectation of those products is to have a high foam, good detergency and wetting, and for estimating of quality of detergent it is important to determine CMC, surface tension and foaming [2].

This work focused on the effect of SAS on the detergency performance of base anionic surfactants (sodium lauryl ether sulfate, coco betaine and coco amide) mixture. Thus, the foaming behavior of mixed anionic surfactants systems (SLES/CB/DEA) was characterized as a function of SAS concentration added in the SLES/CB/DEA. The micellization and surface activity of examined anionic surfactants mixtures were investigated by conductometric and stalagmometric method at  $23.0 \pm 0.1$  °C, whereas foaming properties of the mixtures were determined by standard measurement method.

## EXPERIMENTAL

All commercial chemical raw materials used in this study were obtained from the stated suppliers and used without any further treatment: SLES (Cosmacol AES-70-2-24, Sasol, Italy), SAS (Hostapur SAS 60, Clariant, Switzerland), CB (Empigen BS/FA, Huntsman, USA) and DEA (Empilan 2502, Huntsman, USA). All examined surfactant mixture solutions were prepared in a 100 mL volumetric flask and diluted to desired concentration with deionized water ( $18 \text{ M}\Omega \text{ cm}^{-1}$ , Milli Q, Millipore).

The conductivity measurements were applied to determine the CMC in various surfactant systems combinations: SLES, CB and DEA in mass percent ratio 10:1:0.5 (base surfactants mixture, SLES/CB/DEA) as well as SLES/CB/DEA and SAS (SLES/CB/DEA/SAS) which was added to the SLES/CB/DEA in different concentration. The specific conductance were measured using a digital conductivity meter SensION 5 (Hach, USA) with an accuracy of  $\pm 0.5\%$ , and with the matching 51975 conductivity probe that uses the 4-ring method. The break in specific conductivity *versus* concentration curve indicated the onset of the micellization process. The CMC determination error did not exceed 3%. The surface tension of each mixed surfactant solutions system was determined with a Traube stalagmometer (Neubert-Glass), using drop counting method. Evaluation of foamability of mixed surfactant solution systems was done by foam volume measuring after free flows from 1 m of 0.4% dishwashing formulations without soil with total volume of 5 L [3]. The reservoir was placed in such a way that the outlet tube was positioned in the centre of the basin at 1 m height.

## RESULTS AND DISCUSSION

The CMC values of examined mixtures of anionic surfactants were determined from inflections in plots of specific conductivity ( $\kappa$ ) vs. concentration of surfactant mixture ( $c$ ). The obtained graphical dependence is a curve which consists of two segments (premicellar and postmicellar). Each plot shows the single break point. The CMC is obtained from the intersection of the fitting lines of the  $\kappa$ - $c$  plots above and below the break point. In addition to the conventional procedure (William's method [4]), in order to improve the quality of the calculated CMC, the method proposed by Carpena [5] was also used. Surface tension measurements were performed at 23.0 °C for 0.1% water solutions of surfactant mixture. Four samples of surfactants mixture and their mixing ratio, the CMC,  $\gamma$  and foam volume, were all summarized in Table 1.

Surface tension and CMC were found to be  $26.1 \text{ mN m}^{-1}$  and  $0.25 \text{ g L}^{-1}$  for SLES/CB/DEA surfactants mixture in their mass percent ratio 10:1:0.5 (sample 1). It is obvious that addition of SAS to the base surfactants mixture (samples 2-4), in such a concentration that the sum of mass percent of SLES and SAS was 10% in all samples, reduced both  $\gamma$  and CMC and make better foaming with no drainage. Also, the sample 4 which include SAS in its highest concentration, showed the best performance among the surfactant mixtures. This suggest a smaller micelle formation between few type of surfactants, i.e. several anionic surfactants, and all better performances of surfactant mixtures can be attributed to the interaction of hydrophilic and hydrophobic groups, and better mixing on the air-water surface for foaming.

**Table 1.** Property of anionic surfactants mixture: mixing ratio, critical micelle concentration (CMC), surface tension ( $\gamma$ ) and foam volume

Sample number	Surfactants mixture	Ratio <sup>a</sup>	CMC <sup>b</sup> (g L <sup>-1</sup> )	$\gamma$ (mN m <sup>-1</sup> )	Foam volume (mL)
base anionic surfactants mixture					
1	SLES/CB/DEA	10:1:0.5	0.25	26.1	210
base surfactants mixture/SAS					
2	SLES/CB/DEA/SAS	7:1:0.5:3	0.20	24.1	235
3	SLES/AOS/CB/SAS	5:1:0.5:5	0.12	23.0	250
4	SLES/AOS/CB/SAS	3:1:0.5:7	0.09	20.5	265

<sup>a</sup>expressed as mass percent; <sup>b</sup>trials were repeated (n = 3) for reproducibility.

The micelle formation and the adsorption on the interface for a single surfactant is a typical property determined by the length of its hydrophobic chain. When SAS surfactant are used in combination with anionic surfactants mixture, foaming of the formulations are improved.

Mixtures of two and more anionic surfactants show specific behavior because the charge interaction between surfactants enhances the surface activity, i.e. significant reduces CMC, and that leads to lower surface tension and better foaming. It is due to the fact that in the mixed anionic micelles, the polar head group of the anionic surfactant is located further than the polar group in micelles of a single anionic surfactant, and therefore, the repulsion energy between the charged groups is smaller.

## CONCLUSION

Anionic sec-alkan sulfonate SAS has a great influence on the critical micellar concentration, surface tension and foaming of the examined anionic surfactant mixtures, i.e. mixture of SLES, CB and DEA. Thus, base anionic surfactants mixture with SAS (SLES/CB/DEA/SAS) can be used in a lower concentration. Because of the charge interaction between surfactants of the same type, the surface properties of mixtures (CMC and surface tension) were enhanced and foaming ability was improved. However, the low CMC values of those surfactants mixtures indicate that they display high detergency performance even at relatively low concentrations.

## Acknowledgement

This work was partially supported by the Ministry for Education, Science and Technological Development of the Republic of Serbia.

## REFERENCES

- [1] J. Falbe, Surfactants in consumer products, Springer, Berlin, 1987.
- [2] C. Nitsch, G. Huttmann, SOFW J, 2002, 128, 5, 11–15.
- [3] Annual book of ASTM standards, 2015, vol. 15.04, ASTM D1173–07.

[4] R. Williams, J. N. Phillips, K. J. Mysels, *Trans. Faraday. Soc.*, 1955, 51, 728–737.

[5] P. Carpena, J. Aguiar, P. Bernaola–Galván, C. Carnero Ruiz, *Langmuir*, 2002, 18, 6054–6058.

# *M - Complex Compounds*



## CRYSTAL STRUCTURE OF THE MACROCYCLIC COMPLEX [Co<sub>2</sub>(μ-pht)tpmc](ClO<sub>4</sub>)<sub>2</sub>·H<sub>2</sub>O

M. Antonijević Nikolić<sup>1</sup>, M. Rodić<sup>2</sup>, B. Dražić<sup>3</sup>, S. Tanasković<sup>3</sup>

<sup>1</sup> Academy of Applied Studies, Šabac, Serbia

<sup>2</sup> Faculty of Sciences, University of Novi Sad, Novi Sad, Serbia

<sup>3</sup> Faculty of Pharmacy, University of Belgrade, Belgrade, Serbia

### ABSTRACT

The crystal structure of the Co(II) complex [Co<sub>2</sub>(pht)tpmc](ClO<sub>4</sub>)<sub>2</sub>·H<sub>2</sub>O (pht= phthalate dianion; tpmc= *N,N',N'',N'''*-tetrakis(2-pyridylmethyl)-1,4,8,11-tetraazacyclotetradecane) was determined by X-ray diffraction method. The complex crystallizes in monoclinic crystal system, *C2/c* space group. The geometries around both Co(II) atoms are highly distorted octahedral. The Co(II) ions exhibit CoN<sub>4</sub>O<sub>2</sub> coordination environments with the four nitrogen donor atoms of the tpmc ligand and two oxygen atoms belonging to the one carboxylate group of pht<sup>2-</sup> ligand. The carboxylate groups of pht<sup>2-</sup> are coordinated in an *endo*-bidentate mode. The tpmc ligand adopted a *boat* conformation in which the two coordinated Co(II) atoms are located on the same side of the ring, with Co...Co distance amounting 5.4799(5) Å.

### INTRODUCTION

Tetraazamacrocyclic ligand with four pendant arms, *N,N',N'',N'''*-tetrakis(2-pyridylmethyl)-1,4,8,11-tetraazacyclotetradecane (tpmc), forms mono-, bi-, or tetranuclear complexes having various structures depending on the metal center and the number of co-ligands. Metal centers are coordinated with tpmc in *exo* or *endo* mode. In bi- and tetranuclear complexes, depending on the number, type, and size of donor atoms of additional ligands, metal centers, as well as the reaction conditions, different modes of macrocyclic conformations were found. Macrocyclic ligand adopts *boat* conformation when the additional ligand is bonded in a bridged or a combined chelate-bridged manner and a *chair* conformation when two other ligands are independently bonded in *trans* position. Metal centers are also bridged with N-(CH<sub>2</sub>)<sub>3</sub>-N fragments of the macrocyclic ring. Many macrocyclic mixed ligand Co(II) complexes were previously described [13–19]

In order to get better insight into the coordination chemistry of cobalt(II) complexes, in this paper we present structural characterization of the [Co<sub>2</sub>(μ-pht)tpmc](ClO<sub>4</sub>)<sub>2</sub>·H<sub>2</sub>O complex.

### METHODS

#### Preparation

The starting material for the single crystals was complex [Co<sub>2</sub>(pht)tpmc](ClO<sub>4</sub>)<sub>2</sub>·2H<sub>2</sub>O prepared according to the procedure given in our earlier paper [1]. Pure product, twice recrystallized from the mixture CH<sub>3</sub>CN–H<sub>2</sub>O (1:1; v/v) was dissolved in mixture EtOH/H<sub>2</sub>O (1:1; v/v), *c*=4·10<sup>-3</sup> M. After staying for about seven days at room temperature blue single crystals appeared.

#### Measurements

Diffraction data from the suitable single crystal were obtained on a Gemini S (Oxford Diffraction) single crystal diffractometer, using MoKα X-radiation. Instrument control and data processing were performed using CrysAlisPro [6]. The crystal structure was solved with the SHELXT [7], and refined with the SHELXL [8]. The ShelXle [9] was used as a GUI for the refinement procedures.

Crystal data: C<sub>42</sub>H<sub>50</sub>Cl<sub>2</sub>Co<sub>2</sub>N<sub>8</sub>O<sub>13</sub>, *M* = 1063.66 g mol<sup>-1</sup>, monoclinic crystal system, *C2/c* space group, *a*=38.5666(7) Å, *b*=8.4069(2) Å, *c*=29.5531(6) Å, β=98.102(2)°, *V*=9486.2(3) Å<sup>3</sup>, *Z*=8.

Diffraction data set (99.95% complete up to  $(\sin \theta)/\lambda = 0.6 \text{ \AA}^{-1}$ ) consisted of 50304 measured reflections, 11662 of which were unique ( $R_{\text{int}}=0.026$ ). Refinement of 677 parameters against all unique reflections and 173 restraints converged at  $R(\text{all data})=0.071$ ,  $R(I>2\sigma(I))=0.057$ ,  $wR(\text{all data})=0.188$ ,  $wR(I>2\sigma(I))=0.174$ ,  $\text{Goof}=1.083$ .

## RESULTS AND DISCUSSION

The molecular structure of the dinuclear complex cation  $[\text{Co}_2(\mu\text{-pht})\text{tpmc}]^{2+}$  is presented in Fig. 1. Dinuclear complex cation  $[\text{Co}_2(\mu\text{-pht})\text{tpmc}]^{2+}$  is comprised of two hexacoordinated Co(II) atoms, one octadentately coordinated tpmc molecule and one tetradentately coordinated  $\text{pht}^{2-}$  anion. Macrocycle tpmc is octadentately coordinated in a symmetrical bridging mode. One side of the ligand coordinates Co(II) by two cyclam nitrogen atoms and two pyridine nitrogen atoms so that three fused five-membered metallocycles are formed. The tpmc ligand adopts an overall boat-like conformation in which the two coordinated Co(II) atoms are located on the same side of the ring with  $\text{Co}\cdots\text{Co}$  distance reaching  $5.4799(5) \text{ \AA}$ .

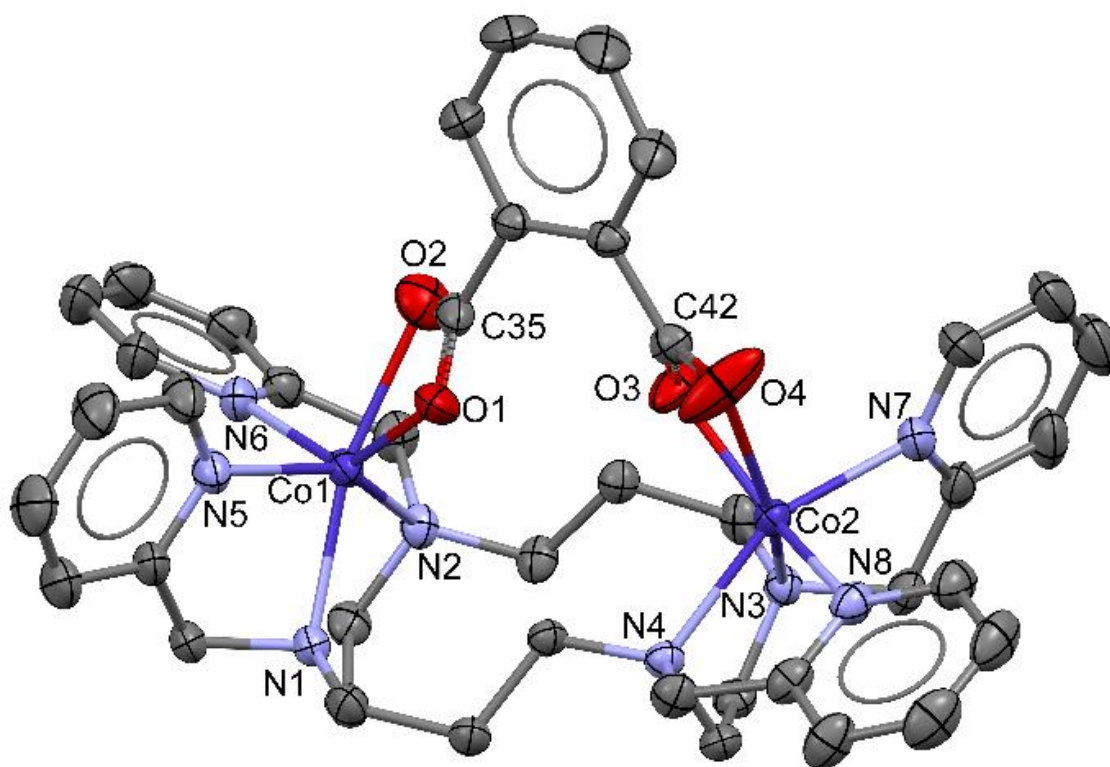


**Figure 1.** Molecular structure of the complex cation  $[\text{Co}_2(\mu\text{-pht})\text{tpmc}]^{2+}$ . Thermal ellipsoids are drawn at the 30 % probability level.

Coordination environments around both Co(II) atoms are highly distorted octahedra. Bond lengths between nitrogen atoms of tpmc and Co1 are somewhat longer compared to those involving Co2. The tpmc ligand adopts an overall *boat*-like conformation in which the two coordinated Co(II) atoms are located on the same side of the ring.

The observed coordination mode is evidently caused by bridging coordination of  $\text{pht}^{2-}$  ligand. Carboxylate groups of  $\text{pht}^{2-}$  coordinated in an endo-bidentate mode, with a different degree in bonding asymmetry. Namely, significantly larger difference in Co–O bond lengths are found for carboxylate group coordinated to Co2 ( $d(\text{Co2}-\text{O3}) = 2.018(2) \text{ \AA}$ ,  $d(\text{Co2}-\text{O4}) = 2.372(3) \text{ \AA}$ ) compared to that coordinated to Co1 ( $d(\text{Co1}-\text{O1}) = 2.148(3) \text{ \AA}$ ,  $d(\text{Co1}-\text{O2}) = 2.228(3) \text{ \AA}$ ). Carboxylate groups

are twisted opposed to phthalate ring, and corresponding dihedral angles subtended by mean planes through carboxylate group atoms and mean plane through phthalate ring carbon atoms are  $50.0(3)^\circ$  (for O1–C35–O2) and  $40.1(4)^\circ$  (for O3–C42–O4).

## CONCLUSION

In this paper, we presented the crystal structure of the complex cation  $[\text{Co}_2(\mu\text{-pht})\text{tpmc}]^{2+}$  studied by X-ray diffraction analysis. It is a first complex where the tpmc ligand adopts an overall *boat*-like conformation in which the two coordinated Co(II) atoms are located on the same side of the ring, with Co...Co distance amounting  $5.4799(5)$  Å. Coordination environments around both Co(II) atoms are highly distorted octahedra. Dinuclear complex cation  $[\text{Co}_2(\mu\text{-pht})\text{tpmc}]^{2+}$  is comprised of two hexacoordinated Co(II) atoms, one octadentately coordinated tpmc molecule, and one tetradentately coordinated  $\text{pht}^{2-}$  anion. Macrocycle tpmc is octadentately coordinated in the symmetrical bridging mode.

## Acknowledgement

The authors acknowledge financial support of the Ministry of Education, Science and Technological Development of the Republic of Serbia (Grants No. 451-03-68/2020-14/200125 and No. 451-03-68/2020-14/200161).

## REFERENCES

- [1] G. Vučković, V. Stanić, S.P. Sovilj, M. Antonijević-Nikolić, J. Mrozinski. *J. Serb. Chem. Soc.*, 2005, 70, 1121-1129.
- [2] S.B. Tanasković, G. Vučković, M. Antonijević-Nikolić, T. Stanojković, G. Gojgić-Cvijović. *J. Mol. Struct.*, 2012, 1029, 1-7.
- [3] G. Vučković, S. B. Tanasković, U. Rychlewska, D. D. Radanović, J. Mroziński, M. Korabik, J. *Mol. Struct.*, 2007, 827, 80-87.
- [4] M. Antonijević Nikolić, J. Antić Stanković, S. B. Tanasković, *J. of Coord. Chem.*, 2018, 71, 1542-1559.
- [5] G. Vučković, S. B. Tanasković, Z .M. Miodragović, V. Stanić, *J. Serb. Chem. Soc.*, 2007, 72 (12), 1295-1308.
- [6] Rigaku Oxford Diffraction, *CrysAlisPro Software system*, Rigaku Corporation, Wroclaw, Poland, 2019.
- [7] G. M. Sheldrick, *Acta Crystallogr. Sect. A Found. Adv.*, 2015, 71, 3-8.
- [8] G. M. Sheldrick, *Acta Crystallogr. Sect. C Struct. Chem.*, 2015, 71, 3-8.
- [9] C. B. Hübschle, G. M. Sheldrick, B. Dittrich, *Appl. Crystallogr.*, 2011, 44, 1281-1284.

## STABILITY CONSTANTS OF FOUR BINUCLEAR Co(II) COMPLEXES WITH A MACROCYCLE AND DIFFERENT CARBOXYLATO CO-LIGANDS

B. Dražić<sup>1</sup>, M. Antonijević Nikolić<sup>2</sup>, S. Tanasković<sup>1</sup>,

<sup>1</sup>Faculty of Pharmacy, University of Belgrade, Belgrade, Serbia (bdrazic@pharmacy.bg.ac.rs)

<sup>2</sup>Academy of applied studies Šabac, Department for medical, business and technological studies, Šabac, Serbia

### ABSTRACT

The complexation reaction between  $\text{Co}^{2+}$  with the tpmc = N,N',N'',N'''-tetrakis(2-pyridylmethyl)-1,4,8,11-tetraazacyclotetradecane and carboxylate/dicarboxylate co-ligands, was studied using spectrophotometric method. The stoichiometric composition and stability constants of four mixed-ligand Co(II) complexes of formulas  $[\text{Co}_2(\text{benz})_2\text{tpmc}](\text{ClO}_4)_2$  (**1**),  $\text{benz}^-$  = benzoate anion;  $[\text{Co}_2(\text{L})\text{tpmc}](\text{ClO}_4)_2$ , L =  $\text{pht}^{2-}$  (phthalate dianion) (**2**), L =  $\text{ipht}^{2-}$  (isophthalate dianion) (**3**) and L =  $\text{tpht}^{2-}$  (terephthalate dianion) (**4**) are reported. The stoichiometric ratio of the compounds was determined spectrophotometrically at 20 °C and constant ionic strength of 0.1 mol dm<sup>-3</sup> (KNO<sub>3</sub>) in ethanol–water mixtures as the solvent using Job's methods of continuous variation. The values of stability constants K and Gibbs free energy  $\Delta G$  were calculated.

### INTRODUCTION

Mixed ligand complexes containing macrocyclic ligand cyclam (1,4,8,11-tetraazacyclotetradecane) or its derivatives like tpmc (N, N', N'', N''' - tetrakis (2-pyridylmethyl) -1,4,8,11-tetraazacyclotetradecane) have broad spectrum of application e.g. in catalysis [1], as corrosion inhibitors [2], antitumors [3], antiviral [4], antibacterial, antifungal or antimalarial agents [5]. The flexible macrocyclic ring usually coordinates two metal ions in exo-coordination mode and could accommodate different additional ligands in a variety of coordination modes, giving stable complexes. Usually, additional monodentate ligands coordinate to the metal centers in trans position or bidentate ligands bridge the central atoms.

Mixed complexes of Co (II) with tpmc (Fig. 1) and one or two additional ligands of different species are the research focus due to their specific structural, chemical and biological properties [7]. The basis of this research is the study of the relationship between structure and reactivity. The stability constant is one of the crucial physicochemical parameters, necessary for the correct interpretation of the complex and determination of the metal-ligand reaction properties.

In our previous studies [8,9], series of four mixed-ligand complexes with formulas:  $[\text{Co}_2(\text{benz})_2\text{tpmc}](\text{ClO}_4)_2$  (**1**),  $[\text{Co}_2(\text{L})\text{tpmc}](\text{ClO}_4)_2$  (L =  $\text{pht}^{2-}$ ,  $\text{ipht}^{2-}$  and  $\text{tpht}^{2-}$ ) (**2–4**) were synthesized and characterized by elemental analyses, electrical conductivities, VIS and IR spectroscopy and magnetic as well as cyclic voltammetric measurements. To study how the structure of these ligands (Fig. 2) is related to the stability of the formed complexes we analyzed the reaction conditions of the complex formation. The aim of this study was to confirm the molar ratio required for the complete reaction of these metals

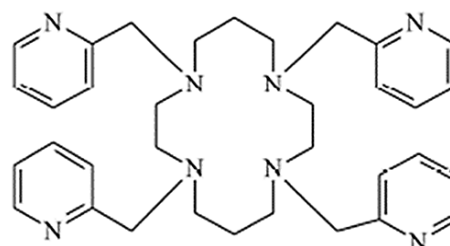


**Figure 1.** Structure of tpmc (N,N',N'',N'''-tetrakis(2-pyridylmethyl)-1,4,8,11-tetraazacyclotetradecane)

and ligands, and to determine the stoichiometric composition and stability constants of these previously described complexes.

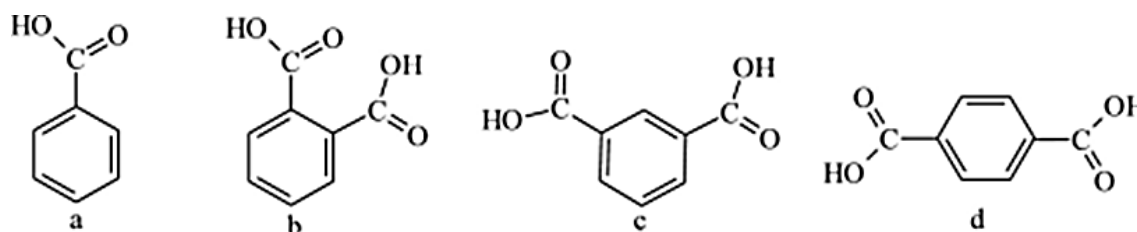


**Figure 2.** Structures of Hbenz (a), H<sub>2</sub>pht (b), H<sub>2</sub>ipht (c) and H<sub>2</sub>tpht (d)

## METHODS

For the spectrophotometric study of the stoichiometric composition and the stability constants of the complexes **1–4** during the reaction, the Job's method of continuous variation was applied. [10,11]. UV/Vis spectra were recorded using Thermo Scientific Evolution 60S UV-Visible Spectrophotometer.

Series of equimolar solutions were prepared for the investigated complexes as specified by the general procedure by mixing different volumes of Co(II) aqueous solutions ( $c = 5 \cdot 10^{-3} \text{ mol dm}^{-3}$ ) and mixed-ligand ( $L_m = L + \text{tpmc}$ ) ethanol solutions ( $c = 1.5 \cdot 10^{-2} \text{ mol dm}^{-3}$ ) [12]. The final volumes of 10 ml were maintained constant by adding water. All solutions were prepared by keeping the same total concentration ( $c = 4 \cdot 10^{-3} \text{ M}$ ), while changing the mole fraction of these two components, Co(II) ion and mixed-ligand. The constant ionic strength of the solutions was adjusted with  $0.1 \text{ mol dm}^{-3}$  KNO<sub>3</sub> (prepared in distilled water). The solution of mixed-ligand ( $L_m$ ) for complex **1**, where  $L = \text{Hbenz}$ , were prepared by mixed ligands  $L_m = \text{Hbenz}/\text{tpmc}$  in the molar ratio of 2:1. The solutions of mixed-ligands ( $L_m$ ) for complexes **2–4** with dicarboxylate co-ligands ( $L = \text{KHpht}$ ; H<sub>2</sub>ipht or H<sub>2</sub>tpht) have  $L_m = L/\text{tpmc}$  molar ratio of 1:1.

The absorption spectra were recorded over the wavelength range of 200–900 nm. To prove the stability of the absorbance, the spectra of the solutions were recorded immediately after the preparation and repeated after 15 min, 30 min, 60 min, and 2h. The absorbance maximum remained constant after 15 min and no change in the concentration of the complex or color intensity was observed. Also, because in the pH range of 6–7 only slight change in the wavelength values was observed, a pH of 6.5 without buffer was chosen for all experiments.

## RESULTS AND DISCUSSION

The composition and stability constant values of the formed complexes were determined by UV–Vis absorption spectroscopy in ethanol–water mixtures as the solvent at  $I = 0.10 \text{ mol dm}^{-3}$  (KNO<sub>3</sub>) and at a constant temperature of 20 °C using the Job's method of continuous variation. The Job's curves were obtained using series of solutions of two components Co(II) ion and mixed-ligand  $L_m$ . The analytical concentration sum of the two components was constant but their mole fractions were varied. The absorbance for each solution was determined calculating the complexes maximum absorbance, initially determined by varying the wavelength from 200 to 900 nm. Under the same conditions, at the investigated wavelength, metal and ligands did not absorb significantly. The wavelength of the maximum absorbance for complexes **1–4** was found to be  $\lambda_{\text{max}} = 529(\mathbf{1})$ ,  $530(\mathbf{2})$ ,  $520(\mathbf{3})$ , and  $527(\mathbf{4})$  nm respectively and was used as  $\lambda_{\text{max}}$  for the analytical measurements. The electronic spectra of the complexes formed during the reaction (Fig.3.) were the same as those for

the separately synthesized complexes. The spectra of complexes **1** – **4**, same concentration ( $c = 1 \cdot 10^{-3} \text{ mol dm}^{-3}$ ) in DMF were described in detail in previous work [8,9].

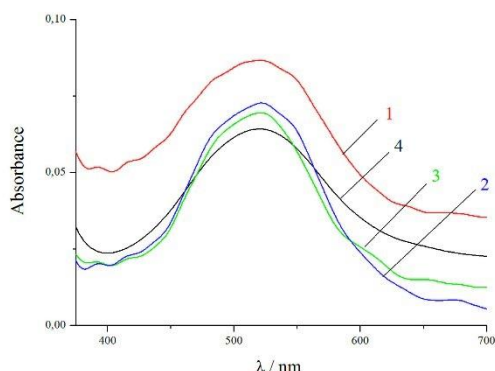


**Figure 3.** UV/Vis spectra of the Co(II) complexes **1** – **4** ( $c = 1 \cdot 10^{-3} \text{ mol dm}^{-3}$ ) in ethanol–water mixtures as the solvent at 20 °C and pH 6.5. The numbers designate the numbers of the complexes.

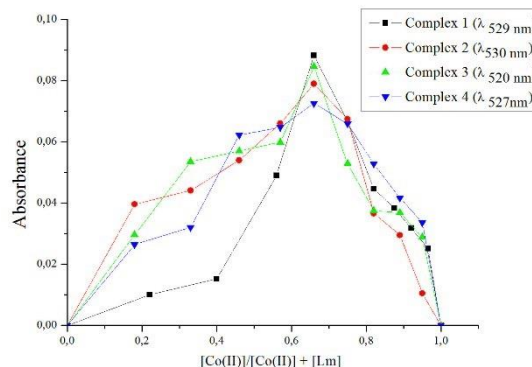
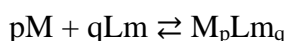


**Figure 4.** Dependence of absorption maximum of the mole fraction  $[\text{Co(II)}]/\{[\text{Co(II)}] + [\text{Lm}]\}$ .

The perpetual change graph was plotted after the necessary absorbance adjustment was made and is illustrated in Fig. 4. The measured absorbances were corrected for the absorbances of reactants. The resulting absorbance showed a maximum at the mole fraction corresponding to their complex and indicates the stoichiometry of the complex. These results confirmed the 2:1 stoichiometry for all the investigated complexes, which reached a maximum at  $[\text{M}^{2+}]/([\text{M}^{2+}] + [\text{Lm}])$  molar ratio of  $\sim 0.66$ . Two molecules of Co (II) ion reacted with a single molecule of the mixed ligand group. The stability constant ( $K$ ) of the reaction:



at the 2:1 metal-to-mixed ligand ratio was calculated using equation (1) [13]:

$$K = \frac{[\text{M}_2\text{Lm}]}{([\text{M}]_t - 2[\text{M}_2\text{Lm}])^2([\text{Lm}]_t - [\text{M}_2\text{Lm}])} \quad (1)$$

Where  $[\text{M}]_t$  is the total concentration of the metal and  $[\text{Lm}]_t$  is the total concentration of the mixed-ligand at the initial stage.

For all the investigated complexes, the stability constants were calculated based on the spectral experiments data using a computerized iterative method of successive approximation and taking into account the average value of three independent measurements [14]. The  $\Delta G$  values for the formation of the complexes **1**–**4** were calculated using Eq. (2) [15]:

$$\Delta G = -2.303 RT \log K \quad (2)$$

were  $R$  is the gas constant ( $8.314 \text{ J mol}^{-1} \text{ K}^{-1}$ ),  $T$  is the temperature (293.16 K) and  $K$  is the stability constant. The values of  $\log K$  and  $\Delta G$  for the complexes **1–4** are presented in Table 1.

**Table 1.** Values of  $\log K$  (stability constant) and  $\Delta G$  (Gibbs free energy) for complexes 1–4 with SD (standard errors).

Compound	$\log K \pm \text{SD}$	$\Delta G \text{ (kJmol}^{-1}\text{)}$
$[\text{Co}_2(\text{benz})_2\text{tpmc}](\text{ClO}_4)_2$ ( <b>1</b> )	$5.28 \pm 0,12$	$-29.64 \pm 0,31$
$[\text{Co}_2(\text{pht})\text{tpmc}](\text{ClO}_4)_2$ ( <b>2</b> )	$5.37 \pm 0,09$	$-30.14 \pm 0,41$
$[\text{Co}_2(\text{ipht})\text{tpmc}](\text{ClO}_4)_2$ ( <b>3</b> )	$5.35 \pm 0,08$	$-30.03 \pm 0,40$
$[\text{Co}_2(\text{tpht})\text{tpmc}](\text{ClO}_4)_2$ ( <b>4</b> )	$5.25 \pm 0,09$	$-29.46 \pm 0,20$

## CONCLUSION

The composition and stability of the for Co(II) complexes have been investigated using spectrophotometric method at  $20^\circ \text{C}$  and constant ionic strength of  $0.1 \text{ mol dm}^{-3}$  ( $\text{KNO}_3$ ) in ethanol–water mixtures as the solvent. The obtained results confirmed the formation of  $\text{M}_2\text{Lm}$  for all of the investigated Co(II) complexes, and the corresponding formula of the complexes is in accordance with the previously published results. The determined stability constants have very similar  $\log K$  values in the range 5.25 to 5.37. Finally, the  $\Delta G$  values of all investigated complexes were negative, meaning that the kinetic process is a spontaneous one in all cases.

## Acknowledgement

The authors acknowledge the financial support of the Ministry of Education, Science and Technological Development of the Republic of Serbia (Grants No: 451-03-9/2021-14/200161)

## REFERENCES

- [1] S.P. Sovilj, G. Vučković, K. Babić, N. Matsumoto, M. Avramov-Ivić, V.M. Jovanović, J. Coord. Chem. 1994, **31**, 167–179.
- [2] K. Babic-Samardžija, N. Hackerman, S.P. Sovilj, V.M. Jovanovic, J. Solid State Electrochem. 2008, **12**, 155–163.
- [3] W. Sibert, A.H. Cory, J.G. Cory, J. Chem. Soc., Chem. Commun. 2002, 2, 154–155.
- [4] S.J. Paisey, P.J. Sadler, Chem. Commun. 2004, **3**, 306–307.
- [5] J. Patole, S. Dutta, S. Pathye, E. Sinn, Inorg. Chim. Acta 2001, **318**, 207–211,
- [6] Y.A. Zolotov, Macrocyclic Compounds in Analytical Chemistry, Chemical Analysis, John Wiley & Sons Inc, New York, 1997.
- [7] S. J. Paisey, P. J. Sadler, 2004, **3**, 306-307.
- [8] G. Vučković, V. Stanić, S. P. Sovilj, M. Antonijević-Nikolić, J. Mrozinski, J. Serb. Chem. Soc 2005, **70** (8–9), 1121-1129.
- [9] G. Vučković, S. B. Tanasković, Z.M. Miodragović, V. Stanić, J. Serb. Chem. Soc., 2007, **72** (12), 1295-1308.
- [10] P. Job, Ann.Chm., 1928 **9** (10) 113–203
- [11] K.K. Sen Gupta, S.P. Moulik, K. Dey, Z. Anorg. Allg. Chem., 1970, 379, 72–78.
- [12] Özlen, S., Mehtap, J. Mol. Struct., 2017, **1149**, 307–314
- [13] N.J. Rose, R.S. Drago, J. Am. Chem. Soc., 1959, **81**, 6138–6141A.
- [14] K. Hirose, J. Inclusion Phenom. Macrocyclic Chem., 2001, **39**, 193–209,
- [15] J.W. Moore, R.G. Pearson, in: Kinetic and Mechanisms, John Wiley & Sons, New York, 1981.

## EFFECT OF TRANS SUBSTITUENT ONTO HYDROGEN BOND INTERACTION IN SQUARE-PLANAR PLATINUM (II) COMPLEXES

J. M. Živković

*Innovative Centre of Department of Chemistry, Studentski trg 12-16, 11000 Belgrade  
(andric\_jelena@chem.bg.ac.rs)*

### ABSTRACT

The influence of *trans* substituent onto hydrogen bond interaction energies was studied. The interaction energies for neutral, singly and doubly charged platinum(II) complexes with water molecule were calculated at M06L-GD3/def2tzvpp level. The results on interaction energies have shown that ligands in *trans* position to interacting water molecule does not show the same trend in different molecules.

### INTRODUCTION

Hydrogen bonds are important interactions that are widely studied. The hydrogen bond interaction between totally optimized water dimers calculated at CCSD(T)/CBS is -4.84 kcal/mol.[1] During coordination of water molecules, strength of hydrogen bond increases from -5.4 kcal/mol for neutral complex to -18.7 kcal/mol for doubly charged octahedral complexes.[1] Interaction energies become even stronger when water molecule is coordinated in tetrahedral complexes, from -9.2 kcal/mol for neutral complex to -24.0 kcal/mol for doubly charged complexes.[2]

Hydrogen bond interactions of coordinated water of hexaaqua complexes with different nucleic acid bases are also strong and span from -6.7 kcal/mol to -49.9 kcal/mol.[3] These interaction energies are several times stronger than for non-coordinated water-nucleic acid bases (-4.6 to -8.7 kcal/mol).[3] Additionally, the calculated energies are stronger for the double-charged  $[\text{Mg}(\text{H}_2\text{O})_6]^{2+}$  complex (-12.9 to -49.9 kcal/mol) than for the single charged  $[\text{Na}(\text{H}_2\text{O})_6]^+$  complex (-6.6 to -19.6 kcal/mol). [3]

The square-planar complexes of platinum(II) have been in focus for many years, especially cisplatin.[4] In the twenties of the last century, *trans* effect has been observed by studying platinum complexes.[5-8] *Trans* effect was defined as effect of a coordinated group on the rate of substitution reactions of ligands *trans* to itself. [5]The experimental values measured by increase in the rate of substitution of the *trans* ligand are in following order:

$\text{F}^-; \text{H}_2\text{O}; \text{OH}^- < \text{NH}_3 < \text{py} < \text{Cl}^- < \text{Br}^- < \text{I}^-; \text{SCN}^-; \text{NO}_2^-; \text{SC}(\text{NH}_2)_2; \text{Ph} < \text{SO}_3^{2-} < \text{PR}_3; \text{AsR}_3; \text{SR}_2; \text{CH}_3 < \text{H}^-; \text{NO}; \text{CO}; \text{CN}^-; \text{C}_2\text{H}_4$

After observing *trans* effect in the twenties of the last centuries, the „*trans*-influence“ of a ligand in a metal complex was defined in sixties [9-12] as the extent to which ligand weakens the bond *trans* to itself in the equilibrium state of that complex.

### METHODS

In order to calculate interaction energies between coordinated water and free water molecules, the monomer geometries were optimized at M06L-GD3/def2tzvpp level. The energy of hydrogen bond was calculated using the same M06L-GD3/def2-tzvpp level, since it gives result that are in good agreement with the CCSD(T)/CBS what is considered as gold standard in quantum chemistry. Namely, the CCSD(T)/CBS calculated for  $[\text{Pt}(\text{H}_2\text{O})_4]^{2+} \cdots \text{H}_2\text{O}$  interaction energy is -25.0 kcal/mol and the M06L-GD3/def2-tzvpp interaction energy is -24.9 kcal/mol. The interaction energies were calculated for model systems with rigid monomers, where  $d_{\text{OO}}$  distance was varied. The electrostatic potential was also calculated at M06L-GD3/def2-tzvpp level, on surfaces defined as the 0.001 au

(electronbohr<sup>-3</sup>) contours of the electronic densities. The values of positive potentials on interacting hydrogen atom on coordinated water (Vs) molecules prior to interaction were also calculated.

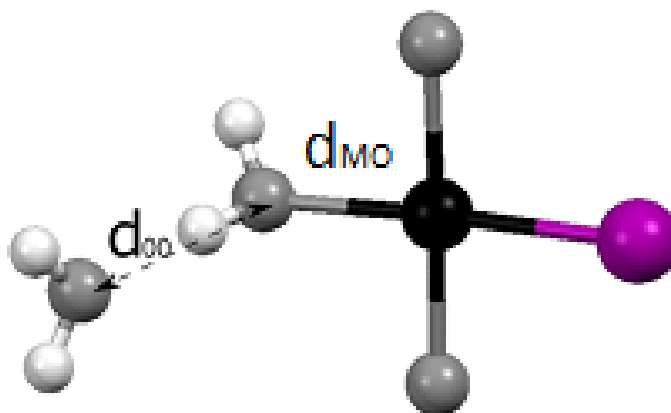


**Figure 1.** The model system used for calculation of hydrogen bond interaction for square-planar platinum(II) complex. The  $d_{oo}$  is distance between two oxygen atoms of interacting water molecules and  $d_{MO}$  is distance between metal and oxygen atoms of interacting ligand. The purple color denotes ligand in *trans* position.

## RESULTS AND DISCUSSION

The influence of *trans* ligand onto hydrogen bond strength was studied for platinum(II) complexes and water molecule (**Figure 1**). The platinum(II) complexes with different ligands and charges were considered. For neutral complexes, hydrogen bond interaction increases in following order: *trans*-[Pt(H<sub>2</sub>O)(CO)Cl<sub>2</sub>]/H<sub>2</sub>O, [Pt(H<sub>2</sub>O)<sub>2</sub>ICl]/H<sub>2</sub>O, [Pt(H<sub>2</sub>O)BrCl]/H<sub>2</sub>O, [Pt(H<sub>2</sub>O)<sub>2</sub>(NO<sub>2</sub>)Cl]/H<sub>2</sub>O, [Pt(H<sub>2</sub>O)<sub>2</sub>FCl]/H<sub>2</sub>O, [Pt(H<sub>2</sub>O)<sub>2</sub>CNCl]/H<sub>2</sub>O, *trans*-[Pt(H<sub>2</sub>O)<sub>2</sub>Cl<sub>2</sub>]/H<sub>2</sub>O and *trans*-[Pt(H<sub>2</sub>O)(NH<sub>3</sub>)Cl<sub>2</sub>]/H<sub>2</sub>O and interaction energies are -8.1 kcal/mol, -8.2 kcal/mol, -8.3 kcal/mol, -8.5 kcal/mol, -8.6 kcal/mol, -8.6 kcal/mol, -8.6 kcal/mol and -8.9 kcal/mol, respectively. The interaction energies are increasing in next order of *trans* ligands CO < I<sup>-</sup> < Br<sup>-</sup> < NO<sub>2</sub><sup>-</sup> < F<sup>-</sup> < CN<sup>-</sup> < Cl<sup>-</sup> < NH<sub>3</sub>. The interaction energies do not follow sequence of the elongation of  $d_{MO}$  distance. The correlation between interaction energy and Vs value is very poor ( $R^2 = 0.0015$ ), due to pronounced influence of chlorine atom on intramolecular interaction as well as side repulsive interaction.

The interaction energies for singly charged platinum(II) complexes [Pt(H<sub>2</sub>O)<sub>3</sub>I]<sup>+</sup>/H<sub>2</sub>O, [Pt(H<sub>2</sub>O)<sub>2</sub>(NH<sub>3</sub>)Cl]<sup>+</sup>/H<sub>2</sub>O, [Pt(H<sub>2</sub>O)<sub>3</sub>Br]<sup>+</sup>/H<sub>2</sub>O, [Pt(H<sub>2</sub>O)<sub>3</sub>CN]<sup>+</sup>/H<sub>2</sub>O, [Pt(H<sub>2</sub>O)<sub>3</sub>NO<sub>2</sub>]<sup>+</sup>/H<sub>2</sub>O, [Pt(H<sub>2</sub>O)<sub>3</sub>F]<sup>+</sup>/H<sub>2</sub>O, [Pt(H<sub>2</sub>O)<sub>3</sub>Cl]<sup>+</sup>/H<sub>2</sub>O and [Pt(H<sub>2</sub>O)<sub>2</sub>Cl(CO)]<sup>+</sup>/H<sub>2</sub>O are -14.4 kcal/mol, -14.7 kcal/mol, -15.0 kcal/mol, -15.4 kcal/mol, -15.6 kcal/mol, -15.8 kcal/mol, -16.3 kcal/mol and -16.6 kcal/mol, respectively. The interaction energies for singly charged complexes increase from I<sup>-</sup> to CO in following order; I<sup>-</sup> < NH<sub>3</sub> < Br<sup>-</sup> < CN<sup>-</sup> < NO<sub>2</sub><sup>-</sup> < F<sup>-</sup> < Cl<sup>-</sup> < CO. As for neutral complexes, increasing of hydrogen bond strength does not correspond to elongation of *trans* ligand bond ( $d_{MO}$ ). The trend in interaction energy does not fit well with the increasing potential (Vs) on hydrogen atom ( $R^2 = 0.2703$ ). The interaction energies for [Pt(H<sub>2</sub>O)<sub>3</sub>(NH<sub>3</sub>)]<sup>2+</sup>/H<sub>2</sub>O, [Pt(H<sub>2</sub>O)<sub>4</sub>]<sup>2+</sup>/H<sub>2</sub>O and [Pt(H<sub>2</sub>O)<sub>3</sub>(CO)]<sup>2+</sup>/H<sub>2</sub>O are -22.7 kcal/mol, -24.9 kcal/mol and -27.9 kcal/mol, respectively. Thus, the increasing trend in interaction energies follows *trans* ligands as NH<sub>3</sub> < H<sub>2</sub>O < CO. Platinum(II) *trans* ligand bond elongation ( $d_{MO}$ ) follows sequence H<sub>2</sub>O < NH<sub>3</sub> < CO. This trend is in accordance with increasing electrostatic potential on interacting hydrogen (Vs) prior to interaction ( $R^2 = 0.8687$ ).

## CONCLUSION

The results of the study on the effect of *trans* ligand in metal complex onto hydrogen bond interactions of coordinated water molecule show that *trans* ligand does not influence increasing of hydrogen bond strength in the same order for three types of the platinum(II) square planar aqua complexes, neutral, single charged and double charged. Also, the order of the *trans* ligands in any of these complexes is not the same as the order of the ligands observed in the literature for *trans* effect in ligand substitution reactions.[5] Beside this, there is no correlation of hydrogen bond strength with elongation of M-O bond as well as with  $V_s$  for neutral and singly charged complexes. One of the reasons for lack of correlation could be side interactions of free water molecule with coordinated chlorine atoms.

## Acknowledgement

This work was supported by the Serbian Ministry of Education, Science and Technological Development (Contract numbers: 451-03-9/2021-14/ 200288).

## REFERENCES

- [1] J. M. Andrić, G. V. Janjić, D. B. Ninković, S. D. Zarić, Phys. Chem. Chem. Phys., 2012, **21**, 10896-10898.
- [2] J. M. Andrić, M. Z. Misini-Ignjatović, J.S. Murray, P. Politzer, S.D. Zarić Ninković, ChemPhysChem, 2016, **17**, 2035-2042.
- [3] J. M. Andrić, I. M. Stanković, S. D. Zarić, Acta Crystallogr. A, 2019, **B75**, 301-309.
- [4] J. M. Hill, E. Loeb, A. S. Maclellan, N. O. Hill, A. Khan, J. J. King, Cancer Chemo. Rep., 1975, **59**, 647-659.
- [5] I. I. Chernyaev, Ann Inst Platine, 1926, **4**, 243-275.
- [6] J. Gažo, I B. Bersuker, J. Garaj, M. Kabešová, J. Kohout, H. Langfelderová, M. Melník, M.Serator, F.Valach, Coord. Chem. Rev., 1976, **19**, 253-297.
- [7] M. Melník, Coord. Chem. Rev., 1982, **47**, 239-261.
- [8] F. Basolo, RG Pearson, Prog. Inorg. Chem. 1962, **3**, 381-453.
- [9] A. Pidcock, R. E. Richards, L. M. Venanzi, J. Chem. Soc. A, 1966, 1707-1710.
- [10] L. M. Venanzi, Chem. in Britain, 1968, **4**, 162-167.
- [11] T. G. Appleton, H.C. Clark, L.E. Manzer, Coord. Chem. Rev. 1973, 335- 422.
- [12] R. Herak, N. Juranić, M. B. Čelap, J. Chem. Soc., Chem Comm., 1980,**14**, 660-661,

*N - General Physical Chemistry*



## APTAMER-SMALL-MOLECULE TARGET STRUCTURE-ACTIVITY RELATIONSHIPS: FROM GROUP FREE BINDING ENERGY CONTRIBUTIONS TO ELECTRON TRANSFER RATES

M. N. Stojanović

*Division of Experimental Therapeutics, Irving Medical Center, Columbia University,  
mns18@cumc.columbia.edu*

### ABSTRACT

Aptamers (oligonucleotide-based receptors) are isolated from random libraries through cycles of enrichment based on binding to a target coupled with amplifications. There are two fundamental advantages of aptamers over antibodies: (1) We can select aptamers for small molecules ignored by the immune system even when haptenized, *e.g.*, in the past we targeted neurotransmitters and amino acids and (2) Aptamers are readily engineered to undergo gross conformational changes upon ligand binding, which makes them perfect receptors for biosensor applications. However, despite these important advantages, clinical applications have been largely precluded by the paucity of aptameric receptors achieving clinically relevant affinities and specificity.

I will present our recent systematic studies using group free energy of binding contributions that led us to a comprehensive approach based on functional group analysis to overcome traditional barriers to isolation of high-quality aptamers. I will specifically discuss new multi-step approaches to three challenging small molecule targets. The same thinking enabled us to develop some new methods to engineer aptamers in a way that maximized conformational changes occurring near electrode surfaces leading to optimal receptors for electrochemical aptamer-based sensors (E-AB).

## VARIANTS OF THE 3D COMPUTER MODEL OF THE LiF-KF-RbF T-x-y DIAGRAM

V. Vorob'eva , A. Zelenaya , V. Lutsyk and M. Lamueva

*Institute of Physical Materials Science (Siberian Branch of the Russian Academy of Sciences), 6  
Sahyanova st., 670047 Ulan-Ude, Russia. (vluts@ipms.bscnet.ru)*

### ABSTRACT

Because of the many contradictions, connected with the literature data about the binary systems, which form the ternary LiF-KF-RbF one, three possible versions of the T-x-y diagram geometric structure of this system were proposed and their three-dimensional computer models had been designed.

### INTRODUCTION

The fluoride systems of alkaline and alkaline-earth metals together with the fluorides of uranium, plutonium, and lanthanum are proposed as the assumed components for the IV generation nuclear reactor fuel [1, 2].

It is found that LiF-KF-RbF and LiF-RbF-MgF<sub>2</sub> systems are effective eutectic compositions for dissolution of the fuel fluoride as these ternary mixtures have suitable nuclear properties and also favorable melting points, e.g., {0.40 mol LiF + 0.33 mol KF + 0.27 mol RbF}, MP = 440 K; 0.46 mol LiF + 0.04 mol MgF<sub>2</sub> + 0.50 mol RbF}, MP = 462.3 K [3].

The binary KF-LiF system is the simple eutectic one, and it is confirmed as by the experimental data [4] (at 492°C, 50% mol KF), so by the thermodynamic calculations [3, 5].

According to the experimental investigations of the KF-RbF system, its T-x diagram is the continuous series of solid solutions, moreover in [4] – without a minimum. The RbF melting point, defined as 780°C in the same work, is 13-15°C lower than in the works of other authors [2, 5, 6]. Reference [7] gives data, in which there is the minimum of liquidus curve at 770°C, 72% mol RbF. The formation of minimum is confirmed by works based on the thermodynamic calculation methods [2, 5, 6].

The LiF-RbF binary system has the greatest contradictions. Experimentally studied [4] two branches of liquidus intersect in the eutectic point at 450°C, 50% mol RbF. Besides the eutectic (470°C, 56% mol RbF) it is shown in [7] the formation of the incongruently melting compound LiRbF<sub>2</sub> of the constant composition in the peritectic reaction and with the coordination of the peritectic point at 475°C, 53% mol RbF. Data, obtained as a result of the thermodynamic calculations, are distinguished too. Thermodynamic calculations [1] confirmed the eutectic at 474°C, 54% mol RbF, but with the decomposition of the LiRbF<sub>2</sub> compound below 407°C.

The peritectic reaction with the formation of the LiRbF<sub>2</sub> compound, existing in the very narrow temperature interval (it is for some reason named as the congruently melting compound in the paper conclusion), precede to the eutectic reaction in the LiF-RbF system in the later work [3].

### METHODS

The description of the ternary system also has a number of essential divergences.

It is assumed in [4] that there are no ternary invariant reactions and the liquidus consists of two surfaces, which correspond to LiF and the crystallization field of the the continuous solid solution of KF and RbF in the LiF-KF-RbF system (Figure 1a).

Since the presence of the minimum in the KF-RbF T-x diagram is the fact established, it is logical to assume the ternary eutectic E point (its coordinates are given into [7]) on the univariant curve,

connecting two binary eutectics, and the fold outgoing from it in the direction of the minimum (Figure 1b). And, of course, it is not possible to disregard the formation of the  $\text{LiRbF}_2$  compound in the sub-solidus in both versions of the T-x-y diagram.

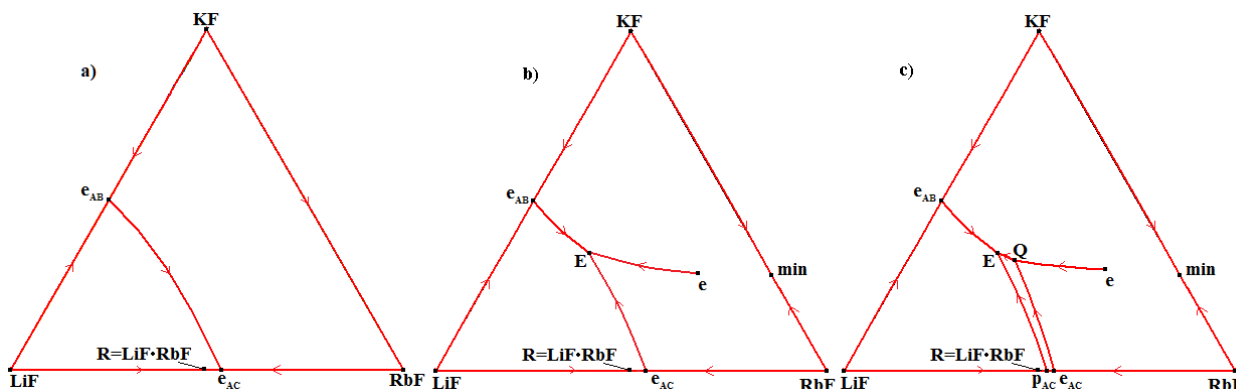


**Figure 1.** Variants of liquidus structure of the LiF-KF-RbF T-x-y diagram: according to [4] (a), hypothetical with the fold eE (b), by data [7] (c).

Formation of the ternary eutectic E:  $L \rightarrow \text{LiF} + \text{KF} + \text{LiRbF}_2$  at  $440 \pm 10^\circ\text{C}$ , 40% mol LiF, 32.5% mol KF, 27.5% mol RbF is discussed in [7], where quasi-peritectic reaction Q:  $L + \text{RbF} \rightarrow \text{KF} + \text{LiRbF}_2$  precede at  $450^\circ\text{C}$  (Figure 1c). The univariant curve eQ of the mutual crystallization of KF and RbF is the fold on the solid solution  $\text{KF}(\text{LiF})$  liquidus surface because of the minimum in the KF-RbF system.

The special reference was comprised on the basis of analysis and classification of phase diagrams of basic topological types [8]. It includes 3D computer models of T-x-y diagrams: - with uni- and invariant transformations, given by one, two or three binary miscibility gaps of eutectic or peritectic type; - with binary and ternary compounds, melting congruently or incongruently, with the endo- or exothermic phases; - with the polymorphism of one, two or three components in different temperature intervals; - with the uni- and invariant monotectic and syntectic transformations at liquid immiscibility.

The Reference includes also the cases of univariant transformations along the fold in liquidus, when the T-x-y diagram is given by binary systems with the continuous series of solid solutions and one system is the eutectic (Figure 1a) or peritectic one. Since the ternary system, combined from two binary eutectic systems and third system with the continuous solid solutions, may includes the four-phase transformation, in this case the eutectic fold disappears on the liquidus surface (Figure 1b). This type of T-x-y diagram (Figure 1c) is included to the Reference too, as the case with the binary incongruently melting compound, invariant four-phase transformation and the fold on the liquidus.

Each computer model is the phase diagram template, which is converted into the real system 3D model after input its experimental parameters (concentrations and temperatures of binary and ternary points, the characteristics of surface curvature, represented in isopleths and isothermal sections).

This Reference of Computer Models is recommended to use when it is necessary to design 3D model of T-x-y of diagram, presented it as the combination of different topological types.

For instance, it is obvious, that it is convenient to use the Reference Book in order to select the suitable geometric types and to design one of the T-x-y diagram from three in Figure 1 as the combination of two types. So, both versions of the eutectic uni- (Figure 1a) or invariant (Figure 1b) transformations can be “combined” with a diagram with intermediate compound  $\text{LiRbF}_2$  formation in the sub-solidus.

## RESULTS AND DISCUSSION

After the analysis of the published data about the binary systems of fluorides of lithium, potassium and rubidium it is possible to conclude that the system KF-LiF is eutectic, and KF-RbF – with the continuous rows of solid solutions and the minimum. As for the LiF-RbF system, than it accurately has the eutectic, and contradictions relate to the conditions of formation and existence of the LiRbF<sub>2</sub> compound. It either is formed below the eutectic and exists in the sub-solidus or is the incongruently melting one and is formed in the peritectic reaction. The data of other authors about the fact that it is decomposed at low temperatures are not sufficiently reliable.

As a result, the special Reference of the 3D computer models the T-x-y diagrams of basic topological types [8] open the opportunities to construct three versions of phase diagram for this system. These space models make it possible to design any isopleths and isothermal sections, and also to analyze the processes of the melt solidification and microstructure formation. And these 3D models of T-x-y diagrams for the LiF-KF-RbF system are ready for comparison with the analogous experimental sections to verify and to validate the adequacy of one of three variants.

## CONCLUSION

Three versions of the 3D computer models of the LiF-KF-RbF T-x-y diagram have been constructed after combining of the corresponding 3D models of T-x-y diagrams from the Reference [8]. The final answer - which of these versions is the singularly accurate one, the experiment will give.

### *Acknowledgement*

This work was been performed under the program of fundamental research SB RAS (project 0270-2021-0002) and it was partially supported by the RFBR project 19-38-90035.

## REFERENCES

- [1] O. Beneš, J. P. M. Meer, R. J. M. Konings, CALPHAD, 2007, **31**, 209 - 216; <https://doi.org/10.1016/j.calphad.2006.12.004>.
- [2] O. Beneš O, Thermodynamics of Molten Salts for Nuclear Applications, Dissertation, Prague, 2008.
- [3] M. Sumanta, D. Smruti, J. Solid State Electrochem., 2017, **21**, 3589 -3597; <https://doi.org/10.1007/s10967-017-5330-y>.
- [4] E. P. Dergunov, Rep. of the Academy of Sciences of the USSR, 1947, **LVIII** (7), 1369 - 1372.
- [5] J. Sangster, A. D. Pelton, J. Physical and Chemical Reference Data, 1987, **16**, 509 - 561; <https://doi.org/10.1063/1.555803>.
- [6] H. Q. Yin, S. Wu, X. Wang, et al, J. Fluorine Chemistry, 2019, **217**, 90 -96; <https://doi.org/10.1016/j.jfluchem.2018.09.008>.
- [7] R. E. Thoma, Reactor Chemistry Division. Phase Diagrams of Nuclear Reactor Materials, USA, 1959.
- [8] V. I. Lutsyk, V. P. Vorob'eva, A. E. Zelenaya, Solid State Phenomena, 2015, **230**, 51 - 54; [10.4028/www.scientific.net/SSP.230.51](https://doi.org/10.4028/www.scientific.net/SSP.230.51).

## THEORETICAL STUDY OF GEOMETRIES AND ENERGIES OF THE Pt $\cdots$ H INTERACTIONS

D. Ž. Veljković<sup>1</sup>, D.S. Kretić<sup>1</sup>, D. Vojislavljević-Vasilev<sup>2</sup> and S.D. Zarić<sup>1</sup>

<sup>1</sup> University of Belgrade – Faculty of Chemistry, Studentski trg 12 – 16, 11000 Belgrade, Serbia

<sup>2</sup> Innovation center of the Faculty of Chemistry, Studentski trg 12-16, 11000 Belgrade, Serbia  
e-mail:vdusan@chem.bg.ac.rs

### ABSTRACT

Geometries and energies of Pt $\cdots$ H interactions were studied using analysis of crystallographic data and quantum chemical calculations. Cambridge Structural Database (CSD) was searched for all crystal structures containing X-Pt $\cdots$ H-OH interactions. Analysis of geometrical parameters in crystal structures showed that in majority of crystal structures X-Pt $\cdots$ H interactions do not have tendency for linear arrangement. Based on the results of analysis of geometrical parameters, model systems for quantum chemical calculations were made. Results of quantum chemical calculations showed that in case of linear X-Pt $\cdots$ H arrangement (angle X-Pt-H = 180°) between PtS molecule and water calculated intermolecular interactions are repulsive, while in case of X-Pt $\cdots$ H interaction with the X-Pt-H angle value of 90° the interaction is attractive ( $\Delta E = -2.42$  kcal/mol). These results of quantum chemical calculations are in good agreement with the results of the analysis of crystallographic data.

### INTRODUCTION

Existence of the intramolecular interactions in which transition metal atom act as a proton acceptor was proposed six decades ago. [1] First examples of metal-hydrogen interactions were found in crystal structures of platinum compounds. [1] In recent years, interest for this type of hydrogen bonds significantly increased since these interactions can play very important role in many areas of chemistry, from C-H bond activation to the material design and bioinorganic chemistry. [2] Hydrogen-platinum interactions were also extensively studied by quantum chemical calculations. [3-5]

In our recent work, we showed that there are significant differences in the energies of X-H $\cdots$ Pt interactions between cisplatin and transplatin molecules. [6] Results of quantum chemical calculations performed on model systems containing cisplatin/transplatin molecules and water showed that energy of O-H $\cdots$ Pt interaction between cisplatin molecule and water is  $\Delta E_{\text{MP2/aug-cc-PVDZ}} = -5.97$  kcal/mol, while for transplatin/water system energy of O-H $\cdots$ Pt interaction is  $\Delta E_{\text{MP2/aug-cc-PVDZ}} = -4.43$  kcal/mol. [6]

### METHODS

Cambridge Structural Database (CSD – version 5.39) was searched using ConQuest software. [7] All crystal structures containing Pt $\cdots$ H distances in the interval 2.00 – 5.00 Å and X-Pt-H angle in the interval 90° - 180° were extracted and analyzed.

Quantum chemical calculations were performed to calculate Pt $\cdots$ H interaction energies in PtS/H<sub>2</sub>O model systems (**Figure 1**). Two orientations were considered: orientation A in which angle S-Pt-H is 90° and orientation B in which atoms S, Pt and H are linearly arranged. Interaction energies were calculated using MP2 method and aug-cc-PVDZ basis set (for Pt atom aug-cc-PVDZ-pp basis set was used). All quantum chemical calculations were done using Gaussian09 software.

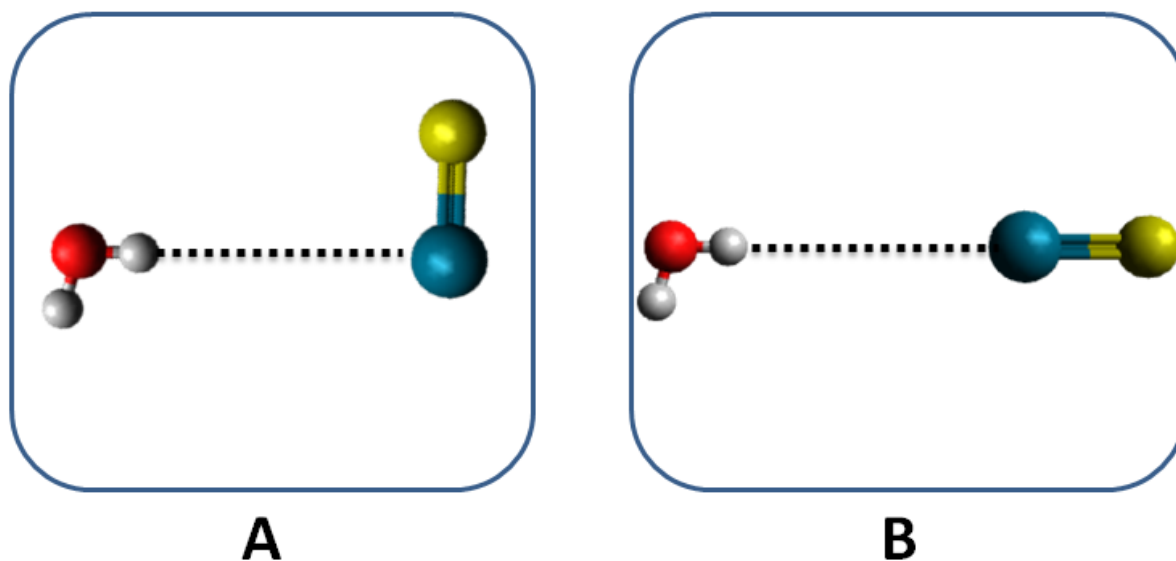


**Figure 1.** Model system for calculation of Pt···H interaction energies between Pts and H<sub>2</sub>O. Two orientations were considered: A) orientation in which S-Pt-H angle is 90° and B) orientation in which S-Pt-H angle is 180°.

## RESULTS AND DISCUSSION

Using criteria given in methodology section, 97083 crystal structures containing Pt···H contacts were extracted. Distribution of X-H-Pt angle was analysed (**Figure 2**). Results showed that in extracted crystal structures hydrogen-platinum interactions are not linear: in majority of analysed structures values of X-H-Pt angle are in the interval 90° - 130°. Results also showed that the least abundant crystal structures are those in which Pt···H interactions are linear (X-Pt-H angle values in the interval 170° - 180°). Based on the results of the analysis of angle X-Pt-H values in extracted crystal structures, model systems for quantum chemical calculations were made (**Figure 1**).

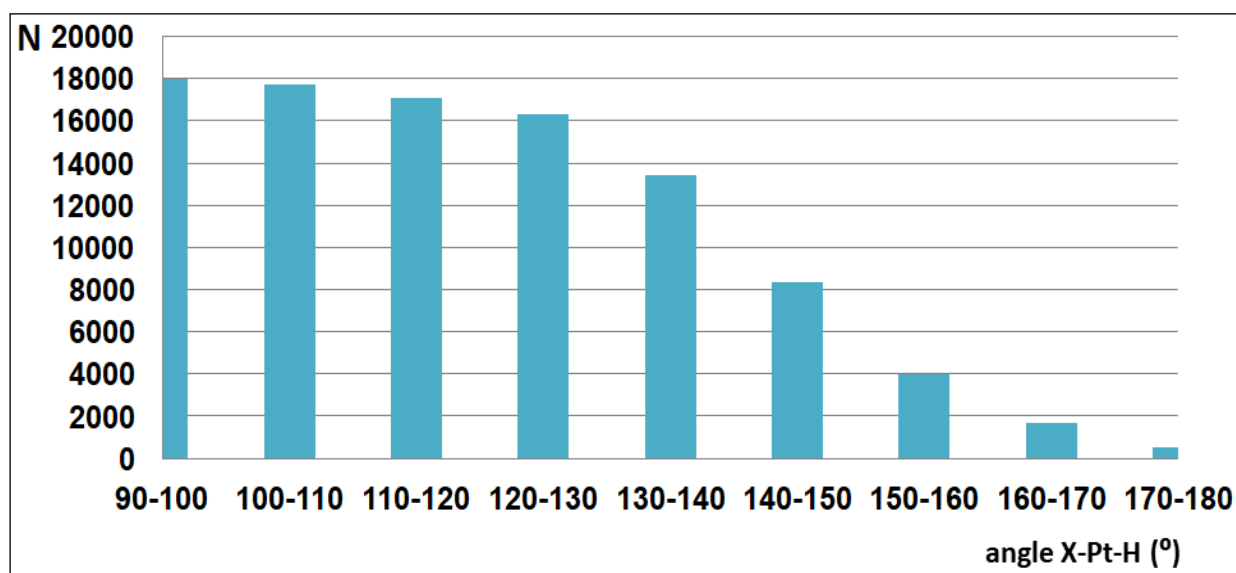


**Figure 2.** Distribution of angle X-Pt-H values in crystal structures extracted from CSD.

Results of quantum chemical calculations showed that in case of linear arrangement (model system B), Pt···H interactions are repulsive. For the model system A, results of interaction energies calculations (**Figure 3**) showed that in this orientation very strong Pt···H interactions occur ( $\Delta E_{\text{MP2/aug-cc-PVDZ/aug-cc-PVDZ-pp}} = -2.42$  kcal/mol).

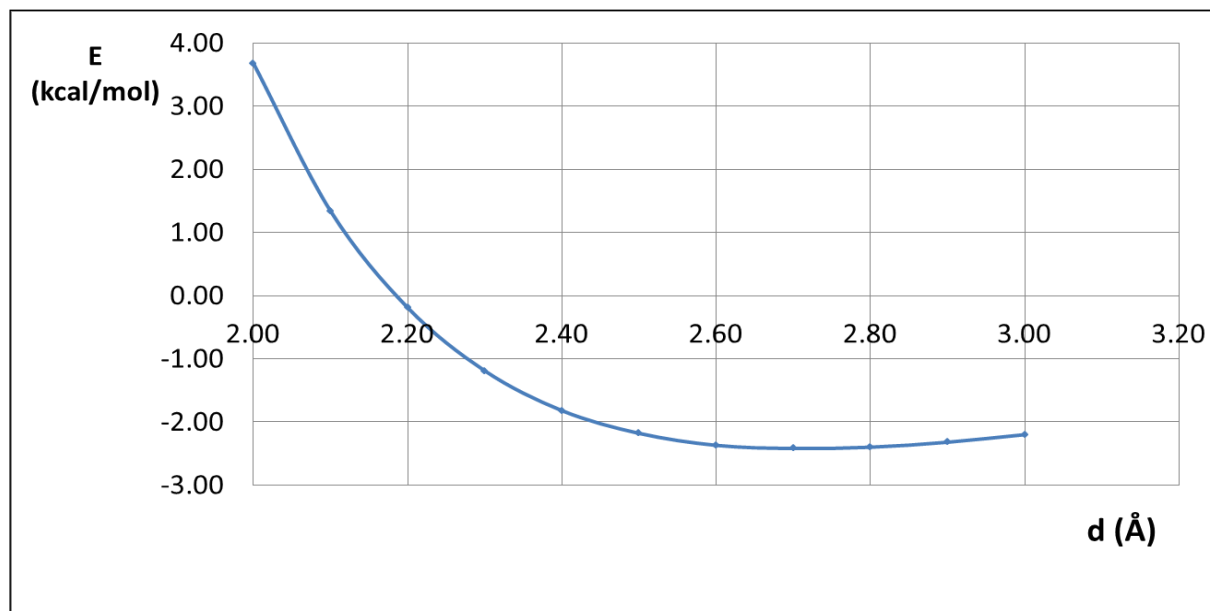


**Figure 3.** Calculated energies and Pt···H distances in X-Pt···H interactions between PtS and H<sub>2</sub>O molecules for model system B.

The Pt···H distance that corresponds to the strongest calculated X-Pt···H interaction in model system B is 2.70 Å, which is shorter than the sum of van der Waals radii for these elements (2.95 Å).

## CONCLUSION

In this work energies and geometries of Pt···H interactions were studied in crystal structures extracted from CSD and by quantum chemical calculations. Results of the analysis of geometrical parameters from extracted crystal structures indicated that Pt···H interactions do not have preference for linear interactions. Quantum chemical calculations performed on PtS/H<sub>2</sub>O model systems showed that interactions in model system B (linear arrangement of S, Pt and H atoms) are repulsive, while interactions in model system A are relatively strong ( $\Delta E_{\text{MP2/aug-cc-PVDZ/aug-cc-PVDZ-pp}} = -2.42$  kcal/mol). Results of quantum chemical calculations were in good agreement with the results of analysis of crystallographic data.

## Acknowledgement

This work was supported by the Serbian Ministry of Education, Science and Technological Development (Contract numbers: 451-03-9/2021-14/200168 and 451-03-9/2021-14/200288).

## REFERENCES

- [1] E. R. T. Tiekink, *Coord. Chem. Rev.*, 2017, 345, 209–228.
- [2] E. S. Tabei, H. Samoueia, M. Rashidi, *Dalton Trans.*, 2011, 40, 11385–11388.
- [3] S. Rizzato, J. Berges, S. A. Mason, A. Albinati, J. Kozelka, *Angew. Chem. Int. Ed.* 2010, 49, 7440–7443.
- [4] O. Kroutil, M. Předota, Z. Chval, *Inorg. Chem.* 2016, 55, 3252 – 3264.

- 
- [5] G. V. Janjić, M. D. Milosavljević, D. Ž. Veljković, S. D. Zarić, *Phys. Chem. Chem. Phys.* 2017, 19, 8657–8660
- [6] D. Ž. Veljković, A. B. Đunović, S. D. Zarić, *ChemistrySelect* 2019, 4, 12909– 12914.
- [7] I. J. Bruno, J. C. Cole, P. R. Edgington, M. Kessler, C. F. Macrae, P. McCabe, J. Pearson, R. Taylor, *Acta Crystallogr., Sect. B: Struct. Sci., Cryst. Eng. Mater.*, 2002, B58, 389–397.

## SYNERGISM IN THE EXTRACTION OF CATECHOL AND HYDROQUINONE FROM AQUEOUS SOLUTIONS BY THE DIETHYL ETHER/1-BUTANOL MIXTURES

G.M. Nikolić<sup>1</sup>, J.V. Živković<sup>1</sup>, J. Pupazić<sup>2</sup> and M.G. Nikolić<sup>3</sup>

<sup>1</sup>University of Niš, Faculty of Medicine, Department of Chemistry, 18000 Niš  
(e-mail : goranhem@yahoo.com)

<sup>2</sup>University of Niš, Faculty of Medicine, Department of Pharmacy

<sup>3</sup> University of Niš, Faculty of Sciences and Mathematics, Department of Chemistry

### ABSTRACT

Synergic effect in the extraction of catechol and hydroquinone from aqueous solutions by the diethyl ether/1-butanol solvent mixtures was investigated. Higher distribution ratios for both catechol and hydroquinone were obtained in the whole composition range of the diethyl ether/1-butanol binary mixture in comparison to extraction with pure solvents. For the same organic phases distribution ratios for catechol were higher than for hydroquinone, but the values of synergic coefficients were higher for hydroquinone.

### INTRODUCTION

Phenolic compounds and among them catechol (1,2- dihydroxybenzene) and hydroquinone (1,4-dihydroxybenzene) can be found as the major pollutants in various types of wastewaters, to name coal gasification wastewater as an typical example [1]. Since simple polyphenols are toxic for bacteria, currently liquid-liquid extraction is commonly used to remove phenolic compounds before biochemical treatment of such wastewaters [2]. Like in the case of other poorly extractable compounds, greater extraction efficacy of simple polyphenols is achieved by the use of mixed solvents instead of single solvents due to the synergic effect [1-4]. In this paper we present the results for synergic effects in the extraction of catechol and hydroquinone from aqueous solutions by the diethyl ether/1-butanol (DEE/1-BuOH) solvent mixtures.

### MATERIALS AND METHODS

All the chemicals used in this work were obtained from commercial suppliers, were of analytical grade (p.a.) purity, and have been used as received. Stock solutions of catechol and hydroquinone (0.01 mol dm<sup>-3</sup>) were prepared by dissolving exactly weighted amount of pure substances in doubly distilled water. In order to avoid autoxidation of dissolved phenols on standing, 1 mol dm<sup>-3</sup> solution of HCl was added to stock solutions to adjust their pH value to ≈2. Working solutions of phenols prepared by the tenfold dilution of stock solutions were extracted by the shake-flask method with organic phases of various compositions. All extractions were performed in duplicate for the same composition of organic phase.

Evolution 60 UV/Vis scanning spectrophotometer (Thermo Scientific, USA) was used for measuring absorbances of aqueous phases at the  $\lambda_{\max}$  which was 276 nm for catechol and 288 nm for hydroquinone. UV spectra of catechol and hydroquinone are shown on Fig. 1.

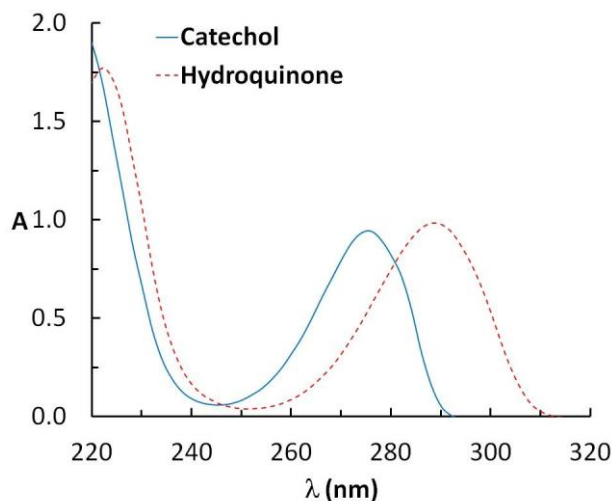


**Figure 1.** UV spectra of catechol and hydroquinone ( $0.4 \text{ mmol dm}^{-3}$ ).

Distribution ratios ( $D$ ) were calculated by using the equation

$$D = \frac{A_0 - A}{A} \times \frac{V_{aq}}{V_{org}}$$

where  $A_0$  and  $A$  were aqueous phase absorbances before and after extraction, and  $V_{aq}$  and  $V_{org}$  were the volumes of aqueous and organic phase, respectively. Synergic coefficient,  $K_c$ , which presents the quantitative measure of synergic effect, was calculated according to the equation

$$K_c = \log(D_{mix}/D_{add})$$

where  $D_{mix}$  represents experimentally measured and  $D_{add}$  theoretically calculated distribution ratio values, respectively. Theoretically calculated distribution ratios were obtained from the following equation

$$D_{add} = D_1\phi_1 + D_2(1 - \phi_1)$$

where  $D_1$  and  $D_2$  represent distribution ratios of phenolic solutes for pure solvents and  $\phi_1$  is the volume fraction of one pure solvent in binary mixture.

## RESULTS AND DISCUSSION

The dependence of catechol and hydroquinone distribution ratios on the composition of diethyl ether/1-butanol binary mixture is shown in Fig. 2.

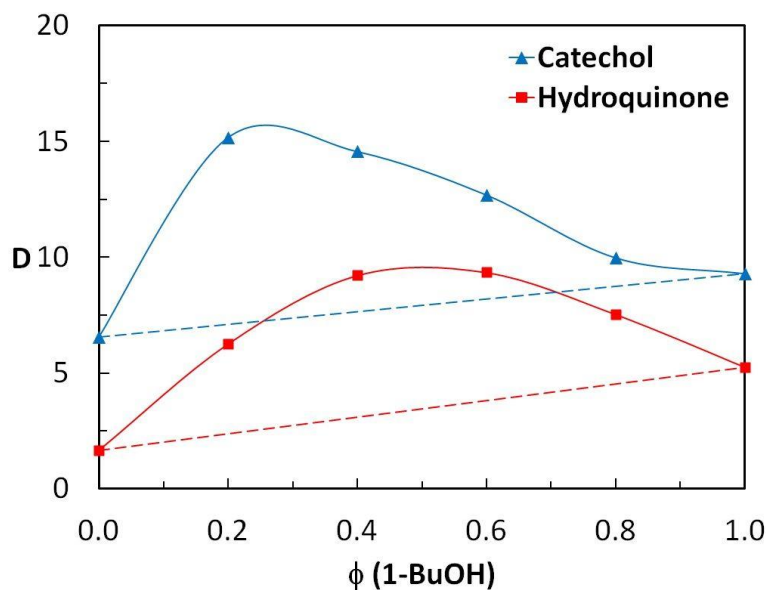


**Figure 2.** Distribution ratios dependence on the binary DEE/1-BuOH solvent mixture composition for catechol (blue triangles) and hydroquinone (red squares). Dashed lines represent theoretically calculated values.

Distribution rate and synergic coefficient values for the extraction of catechol and hydroquinone are given in Table 1.

**Table 1.** The distribution rate and synergic coefficient values for the extraction of catechol and hydroquinone.

$\phi$ (1-BuOH)	Catechol			Hydroquinone		
	D	$D_{\text{mix}}/D_{\text{add}}$	$K_c$	D	$D_{\text{mix}}/D_{\text{add}}$	$K_c$
0	6.56	-	-	1.66	-	-
0.2	15.17	2.134	0.329	6.52	2.747	0.439
0.4	14.56	1.902	0.279	9.21	2.979	0.474
0.6	12.69	1.547	0.189	9.34	2.452	0.390
0.8	9.98	1.140	0.057	7.53	1.662	0.221
1	9.29	-	-	5.25	-	-

Distribution ratios of both catechol and hydroquinone were higher than theoretically predicted values in the whole composition range of the diethyl ether/1-butanol binary mixtures. The maximum value of distribution ratio for catechol was obtained with the binary mixture containing an excess of diethyl ether, the compound that can be only hydrogen bond acceptor, and that is similar to the extraction of simple polyphenols with ketone (MPK or MIBK)/*n*-pentanol or diisopropyl ether/*n*-pentanol binary mixtures [1,5]. On the other side, the highest distribution ratio values for hydroquinone were obtained by using diethyl ether/1-butanol binary mixtures with about equal volume fractions of both components which is similar to the hydroquinone extraction with *n*-propyl acetate/*n*-pentanol binary mixtures [5].

Distribution ratio values for catechol were higher than the values for hydroquinone for the same composition of organic phases which may be the consequence of the possibility of intramolecular hydrogen bond formation in catechol. However, the values of synergic coefficient were higher for hydroquinone.

## CONCLUSION

Synergic effect was observed in the extraction of catechol and hydroquinone from aqueous solutions with the diethyl ether/1-butanol binary mixtures in the whole range of their compositions. Although the distribution ratio values for catechol were higher for the same organic phase compositions, the synergic coefficient values were higher for hydroquinone.

## Acknowledgement

This work was partially supported by the Ministry of Education, Science and Technological Development of the Republic of Serbia.

## REFERENCES

- [1] C. Guo, Q. Cao, B. Chen, S. Yang, Y. Qian, *J. Cleaner Prod.*, 2019, **211**, 380-386.
- [2] S. Yang, D. Ma, P. Cui, *J. Chem. Eng. Data*, 2018, **63**, 63-68.
- [3] N. Ya. Mokoshina, O.V. Erina, O.A. Pakhomova, R.V. Savushkin, *Russ. J. Phys. Chem. A*, 2007, **81**, 2181-2185.
- [4] G.M. Nikolić, J.V. Živković, D.S. Atanasković, M.G. Nikolić, *Russ. J. Phys. Chem. A*, 2013, **87**, 2191-2194.
- [5] C. Guo, Y. Zhang, Y. Qian, S. Yang, *Ind. Eng. Chem. Res.*, 2018, **57**, 11374-11380.

*O - Pharmaceutical Physical Chemistry*



## THE EFFECT OF NONIONIC BRIJ 35 MICELLES ON IONIZATION OF SIX ACE INHIBITORS

M. Popović-Nikolić<sup>1</sup>, G. Popović<sup>2</sup> and D. Obradović<sup>1</sup>

<sup>1</sup> University of Belgrade, Faculty of Pharmacy, Department of Pharmaceutical Chemistry, Vojvode Stepe 450, 11000 Belgrade, Serbia. (majap@pharmacy.bg.ac.rs)

<sup>2</sup> University of Belgrade, Faculty of Pharmacy, Department of General and Inorganic Chemistry, Vojvode Stepe 450, 11000 Belgrade, Serbia.

### ABSTRACT

The  $pK_a$  values of six ACE inhibitors (ACEI); captopril (Cp), cilazapril (Cz), enalapril (En), lisinopril (Ls), quinapril (Qp) and ramipril (Rp) have been potentiometrically determined in micellar solutions of Brij 35. Nonionic micelles affected the ionization of ACEI from -3.44 to +1.9 pK units in comparison to “pure” water. The change in distribution of equilibrium forms is significantly expressed at pH values of biopharmaceutical importance which may indicate on potential interactions with noncharged but polar molecules under the physiological conditions.

### INTRODUCTION

ACEI are drugs applied in the treatment of different cardiovascular disorders, primarily in the therapy of hypertension and congestive cardiac insufficiency.

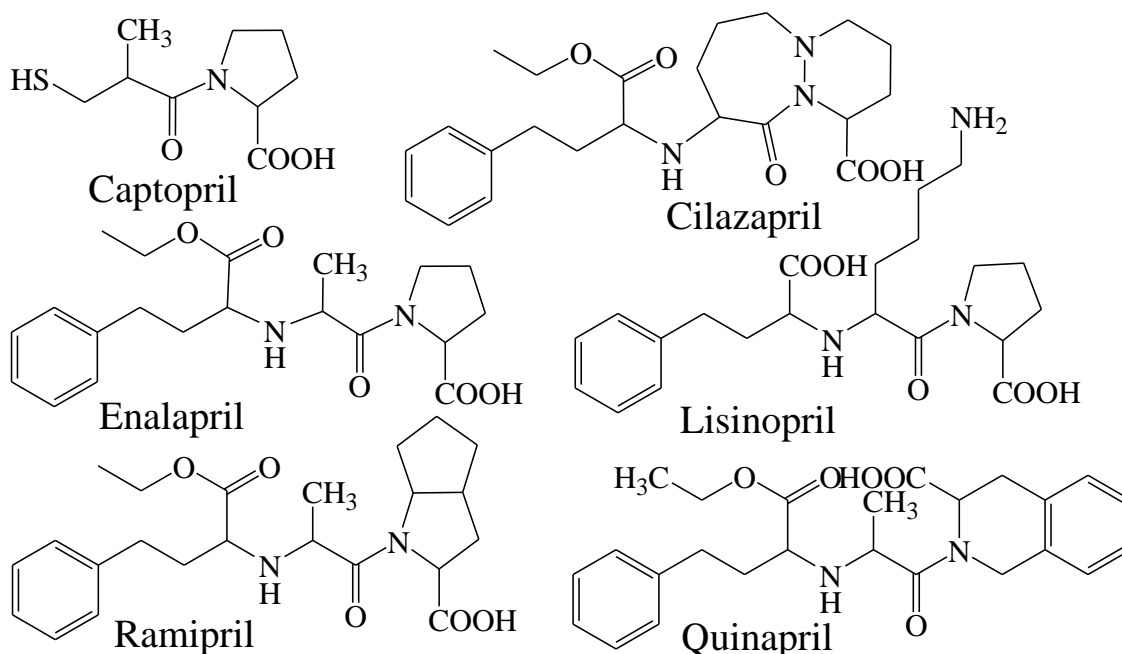


**Figure 1.** Chemical structures of investigated ACEI

Chemically, investigated ACEI are diacid (Cp), with carboxyl and thiol group, and amphotiles (Cz, En, Qp, Rp) containing one acidic (carboxylic) and one basic (secondary amino) functional group (Figure 1). Ls is an amphotile with four ionizable centers, two acidic groups (carboxylic) and two basic groups (primary and secondary amino group). Ionizable functional groups of ACEI play an important role in drug interaction with the active site of ACE enzyme [1]. By investigating the

interactions of drugs with biomembrane mimetic systems, such as micelles [2], a better insight into the behavior of drugs under physiological conditions could be provided. In this work the protolytic equilibria of six ACEI have been investigated in micellar solutions of nonionic surfactant polyoxyethylene (23) lauryl ether (Brij 35).

## METHODS

All solutions of examined ACEI ( $10^{-3}$  M) in  $10^{-2}$  M micellar solutions of nonionic surfactant Brij 35 were titrated with 0.0998 M NaOH at a 25 °C and a constant ionic strength (0.1 M NaCl). Experimental data obtained by potentiometric titrations were analyzed by the computer program Hyperquad.

## RESULTS AND DISCUSSION

The difference between  $pK_a$  values determined with and without [3] the micelles is expressed as  $\Delta pK$  (Table 1).

**Table 1.** The  $pK_a$  values of investigated ACEI potentiometrically determined in  $10^{-2}$  M micellar solutions of Brij 35 and differences ( $\Delta pK_a$ ) with respect to values determined in surfactant free solutions [3].

ACEI	$pK_{a1}$	$\Delta pK_{a1}$	$pK_{a2}$	$\Delta pK_{a2}$	$pK_{a3}$	$\Delta pK_{a3}$	$pK_{a4}$	$\Delta pK_{a4}$
Cp	5.40 $\pm 0.02$	+1.90	6.55 $\pm 0.02$	-3.44				
Cz	3.54 $\pm 0.07$	+0.17	5.85 $\pm 0.07$	-0.62				
En	3.06 $\pm 0.01$	+0.12	5.10 $\pm 0.02$	-0.31				
Ls	2.22 $\pm 0.09$	+0.79	2.90 $\pm 0.08$	-0.25	6.16 $\pm 0.03$	-1.04	10.52 $\pm 0.03$	-0.38
Rp	3.81 $\pm 0.07$	+0.46	5.32 $\pm 0.08$	-0.45				
Qp	1.44 $\pm 0.01$	-1.68	3.86 $\pm 0.01$	-1.54				

The effect of Brij 35 micelles ( $\Delta pK_a$ ) ranges from -1.68 to +1.9 on carboxyl group (the  $pK_{a1}$  and the  $pK_{a2}$  of Ls; and the  $pK_{a1}$  for the other examined ACEI) and from -1.54 to -0.31 on secondary amino group (the  $pK_{a3}$  of Ls and the  $pK_{a2}$  of Cz, En, Qp and Rp). The  $pK_{a4}$  of the primary amino group of Ls is shifted for -0.38 while the  $pK_{a2}$  of the thiol function of Cp is the most significantly affected, for -3.44. Generally, the shift in protolytic equilibria is most evident in the cases of Cp and Qp. Observed shift in protolytic equilibria in a relation to surfactant free media can be mainly explained in terms of properties of Brij 35 micelles. The nonionic micelles do not have a charge and counterions but Brij 35 micelles are characterized by a higher degree of hydration in the palisade layer which allows high water penetration. Changes in ionization mode led to the conclusion that the ionizable functional groups of ACEI are involved in interactions with polar oxygen groups and molecules of water in palisade layer of Brij 35 micelles, which include hydrogen bond formation and dipole interactions.

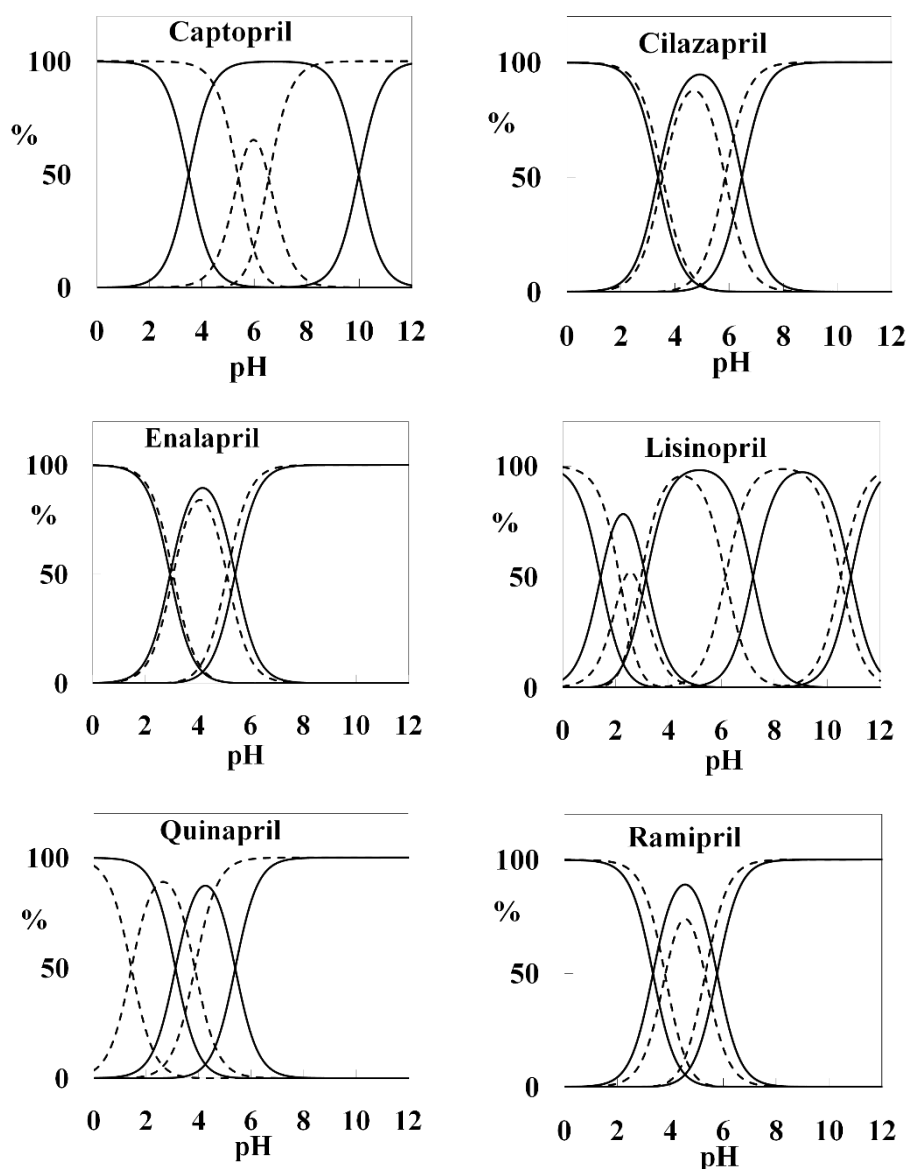


**Figure 2.** Distribution of investigated ACEI equilibrium forms as a function of pH. Solid line – „pure“ water media; dash line - Brij 35 micelles media.

Distribution diagrams of ACEI indicate that significant shift in ionization can be observed at the pH values of biopharmaceutical importance (Figure 2). This finding could be considered for potential interactions with biomolecules in physiological conditions.

## CONCLUSION

The shift in protolytic equilibria of six ACEI have been observed in the presence of Brij 35 micelles as a membrane mimicking system indicating that their ionizable groups are involved in interactions with palisade layer of nonionic micelles which can be considered for interactions with biomolecules present in physiological conditions.

***Acknowledgement***

This research was funded by the Ministry of Education, Science and Technological Development, Republic of Serbia through Grant Agreement with University of Belgrade-Faculty of Pharmacy No: 451-03-9/2021-14/200161.

**REFERENCES**

- [1] Lemke T. L., Williams D. A., Roche V. F., Zito S. W., Foye's Principles of Medicinal Chemistry, Lippincott Williams & Wilkins: Philadelphia, 2013.
- [2] Fendler, J. H. Chem. Rev. 1987, 87, 877–899.
- [3] Popović M. R., Popović G. V., Agbaba D. D. J. Chem. Eng. Data 2013, 58, 2567-2573.

## THE EFFECT OF NONIONIC SURFACTANTS ON IRBESARTAN AND LOSARTAN SOLUBILITY

M. Popović-Nikolić<sup>1</sup>, G. Popović<sup>2</sup>, M. Grujić<sup>2</sup> and D. Agbaba<sup>1</sup>

<sup>1</sup> Department of Pharmaceutical Chemistry,  
(majap@pharmacy.bg.ac.rs)

<sup>2</sup> Department of General and Inorganic Chemistry, Faculty of Pharmacy, University of Belgrade,  
Vojvode Stepe 450, 11000 Belgrade, Serbia

### ABSTRACT

The solubility of two structurally similar sartans, irbesartan and losartan, were investigated at pH 4.5 (acetate buffer) in surfactant free media and in the presence of nonionic surfactants Brij 35 and TX-100 ( $10^{-3}$  mol/L). The solubility of both compounds is of the same order of magnitude in surfactant free media. The nonionic surfactants caused significant increase in losartan solubility (more than 100 times) but very slight increase in irbesartan solubility (only 2 times). The obtained results point out that imidazole moiety, where the main difference between chemical structures of examined sartans can be observed, could be responsible for interaction with the micelles of nonionic surfactants.

### INTRODUCTION

Irbesartan and losartan belongs to the class of angiotensin II receptor blockers (sartans) that act as competitive and selective antagonists of angiotensin II at the angiotensin AT<sub>1</sub> receptors and are used in the treatment of hypertension, cardiac insufficiency, myocardial infarction, and diabetic nephropathy [1]. Accurate mechanism of interaction with AT<sub>1</sub> receptor is still not completely resolved, but available data indicate that not only the conformation of active form of the sartans is important for the activity, but also the ionization state in physiological conditions as well as interaction with biomembranes [2]. Irbesartan and losartan are quite similar in their chemical structure, containing the tetrazole ring linked to the biphenyl group (Figure 1). The main difference is located in the imidazole moiety, whereby losartan contains chlorine and hydroxymethyl substituents, while 4,5-dihydro-5-oxo-1H-imidazole is part of irbesartan. Examined compounds are ampholytes with one acidic centre (tetrazole) and one basic centre (nitrogen of the imidazole moiety).

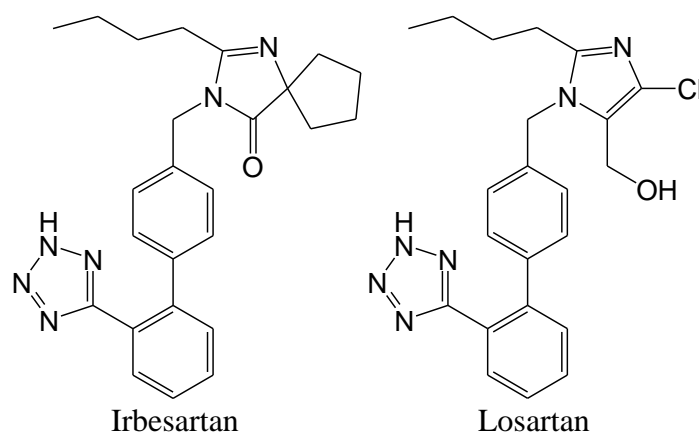


Figure 1. Chemical structures of examined sartans

Solubility and the  $pK_a$  are the most important physico-chemical parameters that affect permeability and absorption of drugs. The knowledge of these parameters is necessary for the estimation of pharmacokinetic properties of drugs, during the analytical procedures and in development of pharmaceutical dosage forms. Under the physiological conditions the ionization and solubility profile of drugs may be affected by the interactions with biomolecules of different charge and polarity. Micellar solutions of surfactants have been used as the biomembrane mimetic systems [3] which act to increase the solubility of poorly soluble drugs. We have previously [4] shown that the ionization centers of losartan ( $pK_{a1}$  3.27 and  $pK_{a2}$  4.60) are directly involved in the interactions with nonionic micelles, unlike the irbesartan ( $pK_{a1}$  3.88 and  $pK_{a2}$  4.55), although both molecules share a similar structure. The aim of this study was to investigate the solubility of irbesartan and losartan in micellar solutions of nonionic surfactants (4-octylphenol polyethoxylate - TX-100 and polyoxyethylene lauryl ether - Brij 35) as biomembrane mimetic systems.

## EXPERIMENTAL

Spectrophotometric measurements were carried out on the UV-Vis spectrophotometer Cintra 20 (GBC, Australia). Automatic titrator 798 MPT Titrino (Metrohm, Switzerland) with a combined electrode LL unitrode Pt 1000 (Metrohm, Switzerland) was used for potentiometric measurements. Irbesartan hydrochloride and losartan potassium were kindly donated from Medicines and Medical Devices Agency of Serbia (Belgrade, Serbia). The nonionic surfactants, TX-100 (Acros Organic) and Brij 35 (Sigma–Aldrich) were used for the preparation of micellar solutions. All solutions were prepared in double distilled water.

Saturated solutions of irbesartan and losartan were prepared in 0.01 mol/L acetate buffer pH 4.5. For this purpose, 2 mg of losartan potassium or irbesartan hydrochloride was dissolved in 40 mL of 0.0044 mol/L sodium acetate solution, and then the corresponding sartan was precipitated by the addition of 0.56 mL of 0.4 mol/L acetic acid. The pH value of 4.5 was adjusted with the addition of 0.4 mol/L acetic acid. Suspensions were thermostated at 25 °C, with occasional stirring for 24 h, and then filtered through 0.22  $\mu$ m membrane filter. The aliquots of the filtrates were diluted, made alkaline (pH 11) by adding NaOH solution and actual concentrations of anionic form of the sartans were determined spectrophotometrically at 250 nm. Saturated solutions of examined sartans in the presence of  $10^{-3}$  mol/L micellar solutions of Brij 35 and TX-100 were prepared by the same procedure applied for determinations in surfactant-free solutions, but with a higher mass of losartan potassium or irbesartan hydrochloride (5 mg). A higher mass of sartan was required due to the expected higher solubility in the micellar media. Further procedure, equilibration, filtration and dilution of the filtrate were the same as in the determination in surfactant-free media. The absorbances of the solutions were measured at 250 nm (when investigating the influence of Brij 35) and 244 nm (when investigating the influence of TX-100) against corresponding blanks. At wavelength 244 nm TX-100 shows minimum absorption. The absorption spectra of irbesartan and losartan are shown in Figure 2.

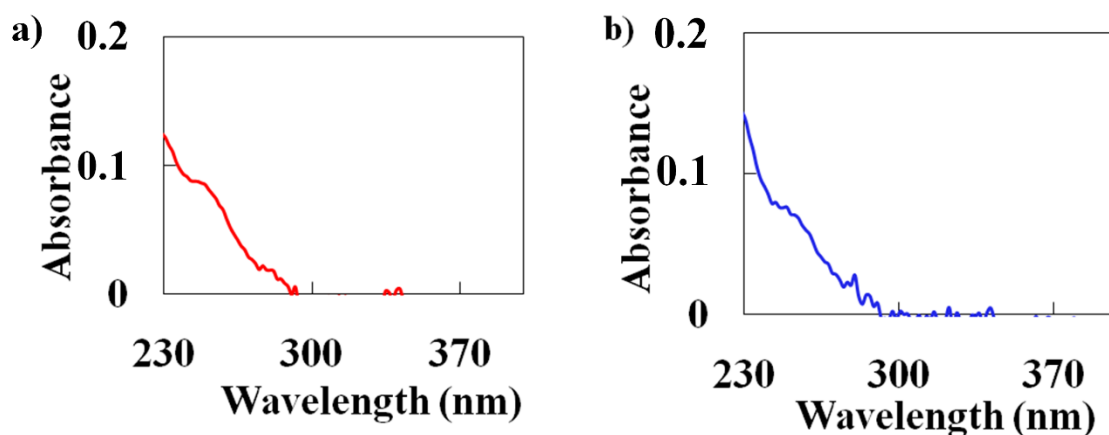


**Figure 2.** Absorption spectra of  $5 \times 10^{-6}$  M a) irbesartan and b) losartan prepared in acetate buffer pH 4.5.

## RESULTS AND DISCUSSION

We have previously shown that the protolytic equilibria of losartan is affected by the presence of nonionic micelles ( $\Delta pK_a$  from -0.86 to 0.69) wherein the influence is most pronounced at biopharmaceutically important pH 4.5 [4]. It was not feasible to estimate the effect on irbesartan ionization because its solubility in micellar solutions of nonionic surfactants was lower than the concentration required for potentiometric determination ( $5 \times 10^{-4}$  mol/L). In order to investigate the differences in interaction of structurally similar compounds with the nonionic micelles, the solubility of irbesartan and losartan were determined in surfactant free and surfactant supplied solutions ( $10^{-3}$  mol/L of Brij 35 and TX-100) at pH 4.5 (Table 1). In surfactant free media the solubility of both compounds is of the same order of magnitude. However, significant differences can be observed among the values determined in the presence of surfactants. With their solubilizing effect micellar solutions have contributed to the significant increase in losartan solubility, more than 100 times. On the other hand, the solubility of irbesartan increased in the presence of micelles approximately 2 times. The nonionic micelles are not charged but consist of hydrophilic surface layer with the polar oxygen atoms where the hydrogen bond forming and dipole interactions are possible with polar groups of drugs. This could indicate that the interactions of sartans with nonionic micelles potentially depend on the substituent of the imidazole group. That part of the irbesartan molecule is more hydrophobic than in losartan which could be the reason for lacking the interactions of irbesartan with the nonionic micelles.

**Table 1.** The solubility of irbesartan and losartan (mol/L) at pH 4.5 determined in the absence and the presence of  $10^{-3}$  mol/L surfactants (Brij 35 and TX-100) at 25 °C.

Sartan	Surfactant free	Brij 35	TX-100
Irbesartan	$6.4 \times 10^{-6}$	$1.2 \times 10^{-5}$	$1.1 \times 10^{-5}$
Losartan	$5.2 \times 10^{-6}$	$>5 \times 10^{-4}$	$>5 \times 10^{-4}$

## CONCLUSION

Obtained results indicate that there is no significant difference in irbesartan and losartan solubility in surfactant free solutions. Significant solubility increase has been observed for losartan in  $10^{-3}$  mol/L solutions of Brij 35 and TX-100. On the other hand, micellar solutions did not show pronounced solubilizing effect on irbesartan. On the basis of observed results it can be assumed that the hydrophobic imidazole moiety of irbesartan could be responsible for lacking the interactions with nonionic micelles.

## Acknowledgement

This research was funded by the Ministry of Education, Science and Technological Development, Republic of Serbia through Grant Agreement with University of Belgrade-Faculty of Pharmacy No: 451-03-9/2021-14/200161.

## REFERENCES

- [1] Lemke T. L., Williams D. A., Roche V. F., Zito S. W., Foye's Principles of Medicinal Chemistry, Lippincott Williams & Wilkins: Philadelphia, 2013.
- [2] Zoumpoulakis, P., Daliani, I., Zervou, M., et al. Chem. Phys. Lipids. 2003,125, 13-25.
- [3] Fendler, J. H. Chem. Rev. 1987, 87, 877–899.
- [4] Grujić, M., Popović, M., Popović, G., Nikolic, K., Agbaba, D. J. Pharm. Sci. 2016, 105, 2444-2452.

*Q - Food Physical Chemistry*



## ENERGY DISTRIBUTION BETWEEN MAIZE AND WEEDS

V. Dragičević, M. Simić, and M. Brankov

*Maize Research Institute Zemun Polje, Slobodana Bajića 1, 11185 Zemun Polje – Belgrade, Serbia.  
(vdragicevic@mrizp.rs)*

### ABSTRACT

The aim of the study was to investigate the variations in accumulation of dry substance and water in maize and weeds, induced by two herbicide types (applied pre- and post-emergence). Weeds tend to captivate higher energy amounts than crop plants. Greater free energy of water indicated increased energy consumption for non-spontaneous processes in weeds. Relatively unchanged net heat of combustion of maize and lower net heat of combustion of weeds indicated herbicide ability to reduce energy accumulation by weeds and to remain it constant in maize plants.

### INTRODUCTION

Plant growth is result of gradual accumulation of dry substance and water. Process of photosynthesis is the main factor of energy conversion into the dry substance, while the water enables environment for chemical reactions and homeostasis upholding. Crop plants and weeds, which live at the same field are competitors, combat each with other for resources, such as sunlight, water, nutrients, etc. [1]. Weed control could be obtained by application of different measures, including herbicides. Some of them could have positive effect on chlorophyll synthesis, as well as energy balance of crops [2,3].

The objective of this study was to investigate the variations in accumulation of dry substance and water in maize plants and weeds, under the influence of two herbicide types (applied pre sowing and after sowing).

### METHODS

The experiment was established in the experimental field of the Maize Research Institute Zemun Polje, Serbia. The maize hybrid ZPSC 388 was sown in the second half of April in 2014, 2015 and 2016. Two herbicides were tested: pre-emergence (pre-em; applied immediately after sowing) and post-emergence (post-em; applied in maize phase 5-8 leaves). Weeds and maize plants were sampled 3 weeks after post- and 6 weeks after pre-emergence herbicide application. Total fresh and dry substance (after drying at 60 °C) of weeds per 0.25 m<sup>2</sup> area and fresh and dry substance of five whole maize plants were measured. Based on subtraction between fresh and dry substance, free energy of free water ( $\Delta G$  for maize  $\Delta G_M$  and weeds  $\Delta G_W$ ) was calculated using sorption isotherm [4, 6]:

$$\Delta G = -RT \ln(a_w)$$

The net heat of combustion (NHC) was calculated after dry substance combustion, using loss-on-ignition method [5], by multiplying with coefficients 16.52 MJ kg<sup>-1</sup> for maize (NHC<sub>M</sub>) [6] and 17.33 MJ kg<sup>-1</sup> for weeds (NHC<sub>W</sub>) [7]. The chlorophyll content in maize leaves was measured with a SPAD-502 Plus chlorophyll meter (Minolta, Tokyo, Japan) and leaf area index (LAI) with LI – 3100 area meter (LI Cor, Lincoln, NE). The grain yield (GY) was measured at the end of the maize growing period.

The data are presented with standard deviation (SD) and the dependences between examined parameters were obtained by correlation (Pearson's coefficients).

**RESULTS AND DISCUSSION**

The values of water based free energy of maize and weeds (Fig. 1) were mainly lower in both herbicide treatments: Nevertheless, when  $\Delta G_W$  and  $\Delta G_M$  were compared,  $\Delta G_M$  was lower, with exception of 2016, when  $\Delta G_M$  was higher in regard to  $\Delta G_W$ , indicating stress and energy consumption for non-spontaneous processes to maintain equilibrium [3, 4].

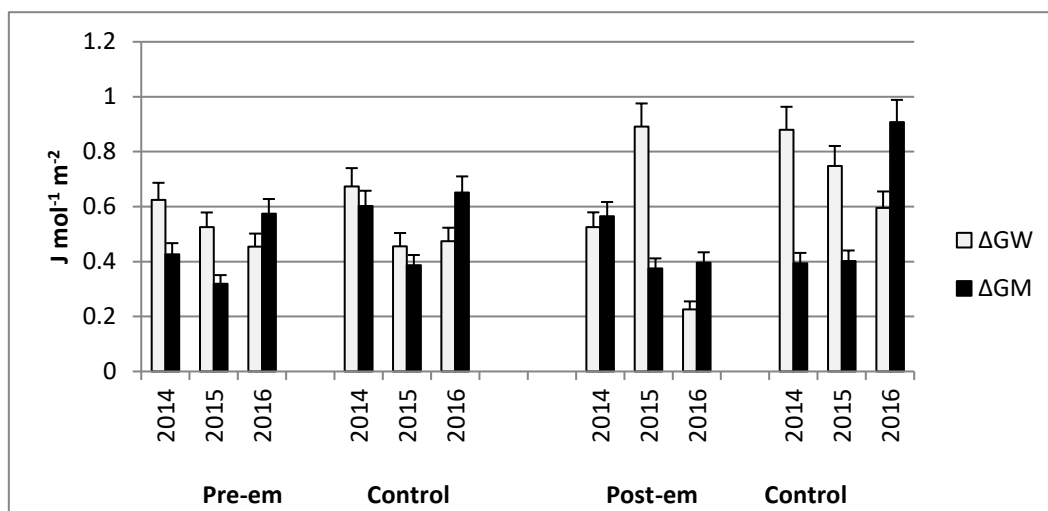


**Figure 1.** The influence of year and applied herbicides on free energy of weeds ( $\Delta G_W$ ) and maize ( $\Delta G_M$ )

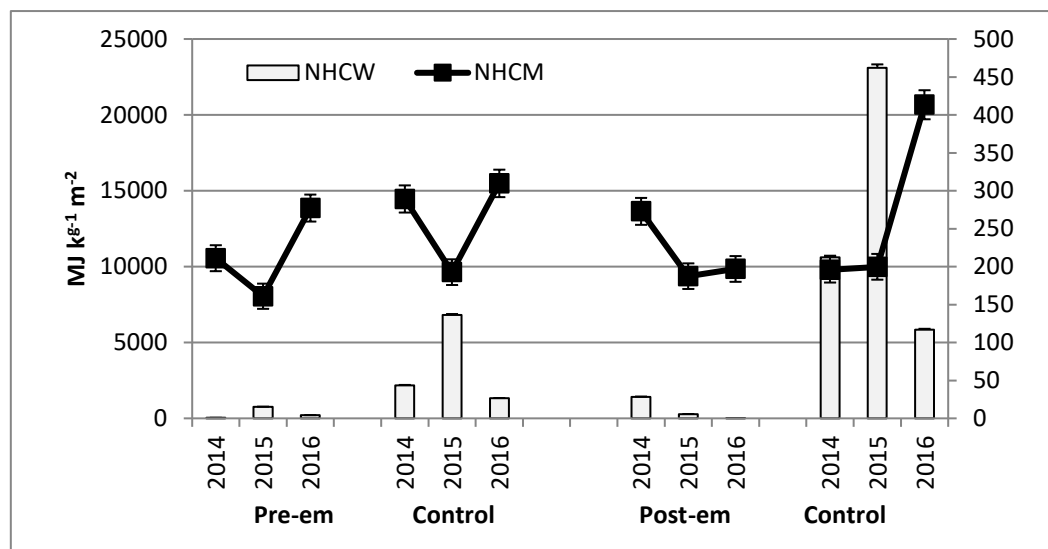


**Figure 2.** The influence of year and applied herbicides on net heat of combustion of weeds ( $NHC_W$ ) and maize ( $NHC_M$ )

The general difference between maize and weeds was present in net heat of combustion, having greater values in weed samples. Relatively lower  $NHC_W$  values in treatments with herbicides, particularly post-em herbicide, indicated that herbicide induced stress increased energy consumption on biochemical processes in weeds [3]. On the other hand, average values of  $NHC_M$  mainly remained constant, with variations present between years. Only in post-em control in 2016,  $NHC_M$  and  $\Delta G_M$  had the highest values.

**Table 1.** Correlation between leaf area index (LAI), grain yield (GY) and chlorophyll content (Chl.) and free energy of weeds ( $\Delta G_W$ ) and maize ( $\Delta G_M$ ), as well as net heat of combustion of weeds ( $NHC_W$ ) and maize ( $NHC_M$ ) (Pearson's correlation coefficients)

	LAI	GY (t ha <sup>-1</sup> )	Chl. (SPAD units)
$\Delta G_W$ (J mol <sup>-1</sup> m <sup>-2</sup> )	-0.371*	-0.415*	-0.257
$\Delta G_M$ (J mol <sup>-1</sup> m <sup>-2</sup> )	0.005	0.205	0.357*
$NHC_W$ (MJ kg <sup>-1</sup> m <sup>-2</sup> )	-0.685*	-0.678*	-0.726*
$NHC_M$ (MJ kg <sup>-1</sup> m <sup>-2</sup> )	0.013	0.214	0.365*

\*Significant at 5% probability level

The correlation between maize growth parameters (leaf area index, grain yield and chlorophyll content) and energy parameters of maize and weeds ( $\Delta G_M$ ,  $\Delta G_W$ ,  $NHC_M$  and  $NHC_W$ ) revealed significant and negative interdependence between  $\Delta G_W$  and  $NHC_W$  in regard to leaf area index and grain yield (Tab. 1), testifying about negative impact of weeds and their ability to captivate higher energy amounts than crop plants, thus affecting crop energy balance and yield potential [1]. Positive correlation between chlorophyll content and energy parameters of maize ( $\Delta G_M$  and  $NHC_M$ ) supports standpoint that photosynthesis is main factor of crop energy production, as well as yield potential [8].

## CONCLUSION

Weeds tend to captivate higher energy amounts than crop plants, thus decreasing maize yield parameters. Greater  $\Delta G_W$  values indicated increased energy consumption for non-spontaneous processes in weeds. Lower values of  $NHC_W$  and relatively invariable  $NHC_M$ , particularly in post-em treatment indicated herbicide ability to reduce energy accumulation by weeds and to keep it constant in maize plants.

## Acknowledgement

This work was supported by the Ministry of Education, Science and Technological Development of the Republic of Serbia (Grant no. TR-31037).

## REFERENCES

- [1] M. Simić, L. Stefanović, *Acta Biologica Iugoslavica G: Acta Herbologica*, 2008, 17, 7-21.
- [2] I. Spasojević, V. Dragičević, M. Simić, D. Kovačević, M. Brankov, *Pesticides and Phytomedicine*, 2014, 29, 45-54.
- [3] V. Dragicevic in: *Thermodynamics of seed and plant growth*. Ed. M. Gorji-Bandpy, INTECH, Rijeka, Croatia, 2015, 195-221.

- 
- [4] W.Q. Sun, in: *Desiccation and Survival in Plants: Drying Without Dying*, Black M. & Pritchard H. W. (Ed.), CABI Publishing, New York, USA, 2002, 47-91.
- [5] M.K. Matthiessen, F.J. Larney, L. Brent Selinger, A.F. Olson, *Communications in Soil Science and Plant Analysis* 2005, 36, 2561-2573.
- [6] E.S. Domalski, T.L. Jr. Jobe, T.A. Milne, *Thermodynamic data for biomass conversion and waste incineration*. National Bureau of Standards And Solar Energy Research Institute, 1986.
- [7] S.P. Bermejo, A. Prado-Guerra, A.I. García Perez, L.F. Calvo Prieto, *Renewable Energy*, 2020, 146, 2224e2233.
- [8] D. Li, Z. Zhang, D. Zheng, L. Jiang, Y. Wang, *Journal of Northeast Agricultural University*, 2012, 19, 3, 14-19.

## UHPLC-DAD-ESI-MS ANALYSIS OF THE ETHANOLIC REISHI/PROPOLIS EXTRACT

S. S. Konstantinović<sup>1</sup>, M. Stefanović<sup>1</sup>, D. Z. Troter<sup>1</sup>, J. B. Zvezdanović<sup>1</sup>, D. M. Stojiljković<sup>2</sup> and V. B. Veljković<sup>1,3</sup>

<sup>1</sup> University of Niš, Faculty of Technology, Bulevar oslobođenja 124, 16000 Leskovac, Serbia (sakisandra12@yahoo.com).

<sup>2</sup> Super Natura, Južnomoravskih brigada 156E, 16000 Leskovac, Serbia.

<sup>3</sup> Serbian Academy of Sciences and Arts, Knez Mihailova 35, 11000 Belgrade, Serbia.

### ABSTRACT

Ultrahigh performance liquid chromatography coupled with diode array and mass spectrometry detectors (UHPLC-DAD-ESI-MS) was used for analyzing the composition of an ethanolic Reishi/Propolis extract (70:30 v/v). The extract contains a significant amount of polyphenols with the major contribution of flavonoids and phenolic acids, suggesting its potential role as an antimicrobial and antioxidant agent.

### INTRODUCTION

Reishi (*Ganoderma lucidum*) is a medicinal mushroom with a long history of use for promoting health and longevity in China, Japan, and other Asian countries. Various parts of Reishi are available as powders, dietary supplements, and tea. The presence of diverse chemical compounds in Reishi is correlated with the various pharmaceutical properties and health benefits [1]. Propolis, a resinous substance provided by honeybees from different plants, is another natural product used in traditional medicine. Due to their numerous pharmacological properties, different propolis preparations are highly appreciated [2]. Combining pure Reishi extract with another natural and biologically active extract can enhance its antioxidant and antimicrobial activities. The aim of this study was to evaluate the chemical composition of the ethanolic Reishi/Propolis extract (70:30 v/v) by the UHPLC-DAD-ESI-MS analytical technique.

### EXPERIMENTAL

#### Material and methods

A commercial ethanolic Reishi/Propolis (70:30 v/v) extract was provided by Super Natura (Leskovac, Serbia). Standards of quercetin, rutin, and apigenin were obtained from Sigma Chemical Company (St. Louis, USA). The solvents used in the UHPLC-experiments were of HPLC or LC/MS grade. A volume of the extract (100 ml) was evaporated under vacuum at 40 °C until dry and further dried at 50 °C until constant weight ( $\gamma = 4 \text{ mg/cm}^3$ ). The chromatographic separation was performed on a Hypersil gold C18 column (50 × 2.1 mm, 1.9 μm) at 25 °C using a Dionex Ultimate 3000 UHPLC+ system equipped with a diode array (DAD) detector and an LCQ Fleet Ion Trap Mass Spectrometer, Thermo Fisher Scientific, USA. A mobile phase consisted of two solvents, 0.1%, v/v, formic acid in water and methanol with a gradient program at 0.25 ml·min<sup>-1</sup> flow rate [3]. The injection volume was 1.0 μl. Absorption UV/Vis spectra were recorded on a DAD-detector with a total spectral range between 200 and 800 nm. The mass spectrometric analysis was performed using a 3D-ion trap with electrospray ionization (ESI) in the negative ion mode. MS-spectra were acquired by a full range acquisition of  $m/z$  130-1300, with a tandem mass spectrometry analysis performed by a data-dependent scan – the collision-induced dissociation (CID) of the detected molecular ions peaks ( $[M-H]^-$ ) with the normalized collision energy set at 25 eV. Xcalibur software (version 2.1) was used for instrument control, data acquisition, and data analysis.

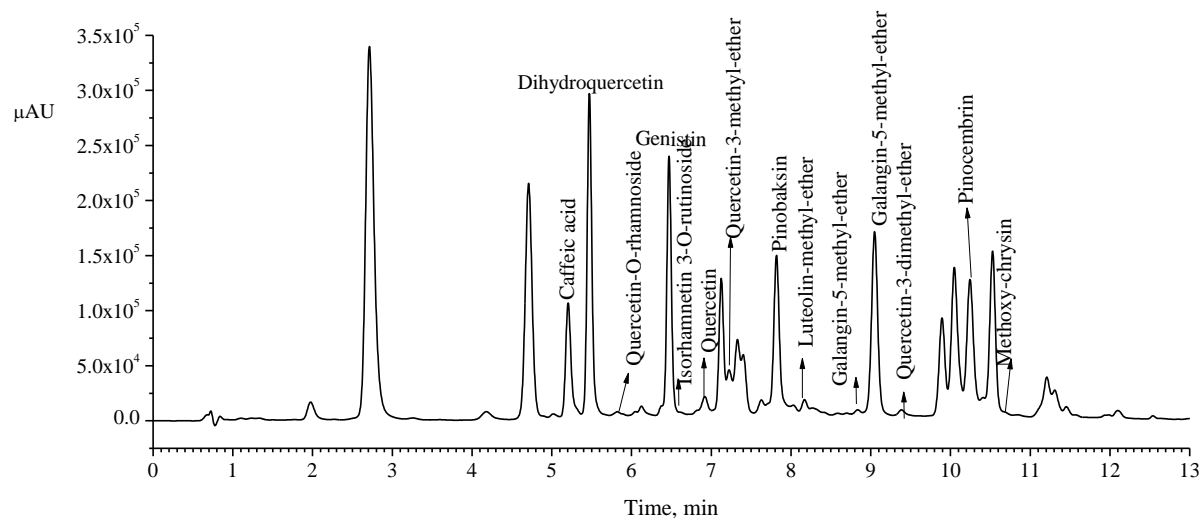


**Figure 1.** UHPLC-DAD chromatogram of Reishi/Propolis extract at DAD signal  $\lambda_{\text{det}} = 300 \text{ nm}$ .

## RESULTS AND DISCUSSION

Caffeic acid ( $[\text{M-H}]^-$ ,  $179 \text{ m/z}$ ) was detected as a peak No. 2 in the UHPLC-DAD chromatogram (Figure 1). The corresponding UV/Vis spectrum (Figure 2) contains two absorption maxima (at  $\lambda_{\text{max}} = 290 \text{ nm}$  and  $\lambda_{\text{max}} = 323 \text{ nm}$ ).

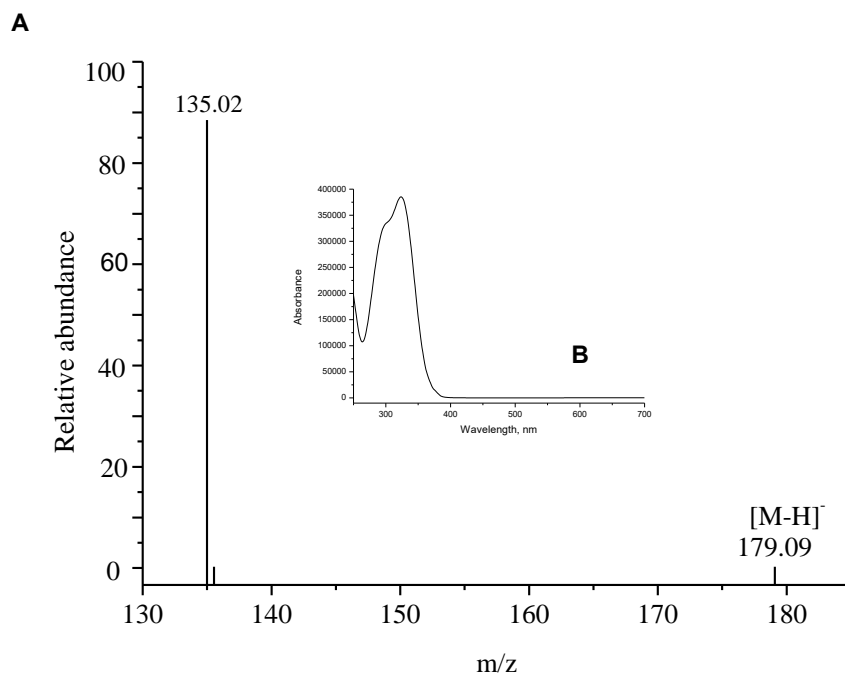


**Figure 2.** Mass (A) and UV-Vis (B) spectra of caffeic acid.

An appropriate MS/MS-fragmentation pattern in the negative mode (Figure 2) confirmed the suggested compound, with a molecular ion at  $m/z$  179  $[M-H]^-$  and the corresponding fragment ion detected at  $m/z$  135 [4,5]. Caffeic acid derivatives were detected by peaks No. 4, 20, 21, and 22 [5-9]. UHPLC-DAD chromatogram also revealed quercetin and its derivatives dihydroquercetin, quercetin-*O*-rhamnoside, quercetin-3-methyl-ether, and quercetin-3-dimethyl-ether (peaks No. 9, 5, 7, 11 and 19) with molecular ion peaks found at  $m/z$  301, 303, 447, 300, and 329, respectively (Figure 1) [4,6]. Genistin, a well-known isoflavone, was identified as a signal No. 8 ( $[M-H]^-$ ,  $m/z$  431) (Figure 1). The extract was also rich in pinobanksin (No. 15,  $m/z$  135), its 5-methyl-ether derivate and 3-*O*-derivatives (acetate, butyrate, propionate and pentanoate), as well as methoxy-chrysin, luteolin-methyl-ether, galangin-5-methyl-ether, and isorhamnetin 3-*O*-rutinoside [7,8,10]. The extract also contained pinocembrin ( $[M-H]^-$ , 255  $m/z$ , the peak No. 23, Fig. 1), flavanone, a natural precursor of pinobanksin. The corresponding UV/Vis and MS/MS-fragmentation patterns confirmed the suggested compound [7]. The peaks No. 12, 13, 18, and 26 were the unidentified derivatives of phenolic acids and flavonoids.

## CONCLUSION

The composition of the Reishi/Propolis ethanolic extract (70:30 v/v) analyzed by the UHPLC-DAD-ESI-MS/MS analysis confirmed the presence of a significant amount of polyphenols with the dominant contribution of flavonoids and phenolic acids. This study strongly suggests using the extract as antimicrobial and antioxidant agent in the development of new drugs of natural origin.

## Acknowledgement

This work was funded by the Ministry of Education, Science, and Technological Development of the Republic of Serbia (Project assigned to the Faculty of Technology, Leskovac, University of Niš, the researchers' groups III 45001 and TR 34012, No. 451-03-68/2020-14/200133).

## REFERENCES

- [1] S. Wachtel-Galor, J. Yuen, J. A. Buswell, I. F. F. Benzie in: Herbal Medicine: Biomolecular and Clinical Aspects. 2nd edition, Chapter 9, *Ganoderma lucidum* (Lingzhi or Reishi), A Medicinal Mushroom, I. F. F. Benzie and S. Wachtel-Galor (Eds.), CRC Press/Taylor & Francis, Boca Raton, Florida, USA, 2011.
- [2] M. Barbarić, K. Mišković, M. Bojić, M. B. Lončar, A. Smolčić-Bubalo, Ž. Debeljak, M. Medić-Šarić, Journal of Ethnopharmacology, 2011, 135, 772-778.
- [3] V. Tadić, I. Arsić, J. Zvezdanović, A. Zugić, D. Cvetković, S. Pavkov, Journal of Ethnopharmacology, 2017, 199, 138-148.
- [4] H.-Y. Zhao, J.-H. Sun, M.-X. Fan, L. Fan, L. Zhou, Z. Li, J. Han, B.-R. Wang, D.-A. Guo, Journal of Chromatography A, 2008, 1190, 157-181.
- [5] J.-P. Cornard, C. Lapouge, The Journal of Physical Chemistry A, 2006, 110, 7159-7166.
- [6] M. Ye, W.-Z. Yang, K.-D. Liu, X. Qiao, B.-J. Li, J. Cheng, J. Feng, D.-A. Guo, Y.-Y. Zhao, Journal of Pharmaceutical Analysis, 2012, 2, 35-42.
- [7] S. I. Falcão, M. Vilas-Boas, L. M. Estevinho, C. Barros, M. R. M. Domingues, S. M. Cardoso, Analytical and Bioanalytical Chemistry, 2010, 396, 887-897.
- [8] F. Pellati, G. Orlandini, D. Pinetti, S. Benvenuti, Journal of Pharmaceutical and Biomedical Analysis, 2011, 55, 934-948.
- [9] MassBank at <http://www.massbank.jp>
- [10] J. M. Fuentes-Alventosa, S. Jaramillo, G. Rodríguez-Gutiérrez, P. Cermeño, J. A. Espejo, A. Jiménez-Araujo, R. Guillén-Bejarano, J. Fernández-Bolaños, R. Rodríguez-Arcos, Journal of Agricultural and Food Chemistry, 2008, 56, 6977-6984.

## LABORATORY SCALED EVALUATION OF SORPTION BEHAVIOR FOR FIVE PESTICIDES IN APPLE PEEL: EFFECT OF PESTICIDE CONCENTRATION

D. Anđelković<sup>1</sup>, M. Branković<sup>2</sup>, and G. Kocić<sup>3</sup>

<sup>1</sup> *University of Niš, Agricultural Faculty, Kosančićeva 4, 37000 Kruševac, Serbia*

<sup>2</sup> *University of Niš, Faculty of Sciences and Mathematics, Department of Chemistry, Višegradska 33, 18000 Niš, Serbia (milica.chem@outlook.com)*

<sup>3</sup> *University of Niš, Faculty of Medicine, Bulevar dr Zorana Đinđića 81, 18108 Niš, Serbia*

### ABSTRACT

Apples are frequently exposed to pesticides. Pesticide interaction with peel (cuticle and waxes) starts *via* absorption mechanisms. Sorption behavior affects the fate and persistence of the pesticides. This laboratory scaled study was designed to determine the residue levels of four fungicides and one insecticide in apple peel after fruit immersion in commercial pesticide solutions of several concentrations. The study showed that when increasing the pesticide concentration in solution, the in-peel amount of the fungicides and the insecticide increases exponentially and linearly, respectively.

### INTRODUCTION

The first point of contact of pesticide molecule and fruit is the peel. Peel is considered to have an ability to accumulate most of the applied pesticides. The main reason for this consideration is the cuticle and its structure and composition. Cuticle represents an extracellular coating comprising a polymeric matrix of cutin and soluble cuticular waxes. The waxy part mainly consists of C16–C18 chain compounds, *i.e.* saturated and unsaturated dihydroxy hexadecenoic, trihydroxy and epoxy hydroxy octadecanoic acids, and a triterpenoid-rich cuticular wax mixture [1].

Pesticide interaction with the cuticle and the cuticular waxes starts *via* absorption mechanisms. Although there are many factors (pesticide formulation applied, the applying conditions etc.), absorption and its magnitude ultimately depend on the pesticide and the peel wax characteristics. This includes the polarity characteristics of pesticides and their mode of action (penetrating, non-penetrating), the maturity stage of apple fruit, the growth season and even the apple variety. Sorption behavior tends to affect the fate of the pesticide as well as its persistence in the fruit.

This study was designed to determine the residue levels of four fungicides and one insecticide in apple peel after fruit immersion in commercial pesticide solutions of different concentrations and thus to assess if the sorption process is concentration-dependent.

### METHODS

#### Experiment set-up

Apples of the *Granny Smith* variety were chosen at the open-air market (JP “Tržnica”, city of Niš, Serbia). The average mass of 15 apple units used in this study was 183.02±9.20g.

Apples were cleaned from any visible dirtiness after which each fruit was soaked for 1.50 min in an aqueous solution (300 mL) fortified with five commercial pesticides (pyrimethanil (*Botrystock*®), cyprodinil (*Cormax*®), boscalid (*Bosco*®), trifloxystrobin (*Zato 50 WG*®), and bifenthrin (*Talstar 10 EC*®)) with final concentrations as follows: 1.00, 5.00, 10.00, 15.00, and 20.00 mg·L<sup>-1</sup>. Each submersion was performed in triplicates.

Apples were peeled immediately after the submersion. To check for the possible migration of pesticides during the immersion period, the first layer of flesh (approx. 1 mm) was peeled and analyzed. The analysis procedure is schematically presented in Figure 1.

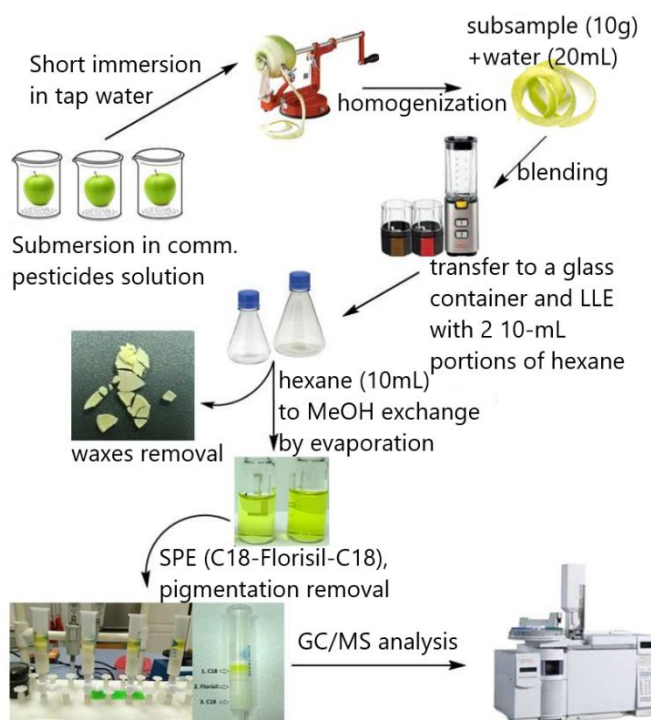


**Figure 1.** Experiment setup and sample preparation procedure

### Instruments

**GC/MS analysis.** The gas chromatographic analysis was performed on Agilent 6890 gas chromatograph equipped with a 5973 Mass Selective Detector (MSD) and 7683 autosampler and SGE 25QC2/BPX5 0.25 capillary column (25m×0.22mm×0.25μm, non-polar). The target compounds were identified in scan mode ( $m/z$  50–400) and analyzed in selected ion monitoring (SIM) mode with confirmation ions as given in Figure 2. Both data acquisition and processing were completed by Agilent MSD ChemStation® D.02.00.275 software.

Pesticide	<i>Pyrimethanil</i>	<i>Cyprodinil</i>	<i>Trifloxystrobin</i>	<i>Bifenthrin</i>	<i>Boscalid</i>	<sup>a</sup> Maximum residual level (the highest level of a pesticide residue that is legally tolerated in or on food or feed when pesticides are applied correctly (Good Agricultural Practice))
Class	Fungicide	Fungicide	Fungicide	Insecticide	Fungicide	
Structure	Anilino pyrimidine	Anilino pyrimidine	Strobilurin	Pyrethroid ester	Pyridine-carboxamide	
<u>MRL</u> <sup>a</sup> mg kg <sup>-1</sup>	15	2	0.7	0.01	2	
Molecular mass	199.25	225.28	408.37	422.86	343.2	
Log <u>K<sub>ow</sub></u>	2.84	3.59	4.5	6	2.96	
Retention time, min	6.79	7.95	9.06	9.61	12.08	
Characteristic ions, $m/z$	<b>198</b> <sup>b</sup>	<b>224</b> <sup>b</sup>	<b>116, 131, 145</b>	<b>181, 166, 165</b>	<b>140, 342, 112</b>	

**Figure 2.** Properties and qualification parameters of investigated pesticides (quantifier ion is given in bold)

**RESULTS AND DISCUSSION**

Pyrimethanil amounts in peel range from 0.092 mg·kg<sup>-1</sup> (1.00 mg·L<sup>-1</sup>) to 4.051 mg·kg<sup>-1</sup> (20.00 mg·L<sup>-1</sup>). Cyprodinil, trifloxystrobin, and bifenthrin amounts range from 0.542 to 6.135 mg·kg<sup>-1</sup>, from 0.176 to 0.643 mg·kg<sup>-1</sup> and from 0.293 to 0.745 mg·kg<sup>-1</sup>, respectively. After immersion in 1.00 mg·L<sup>-1</sup> solution, the amount of boscalid is below evaluated mLOD, that is 0.010 mg·kg<sup>-1</sup>, but within 5.00 – 20.00 mg·L<sup>-1</sup> solution concentration range it ranges from 0.070 to 0.354 mg·kg<sup>-1</sup>.

The amount of pyrimethanil, cyprodinil, trifloxystrobin, and boscalid in peel increases exponentially with the pesticide concentrations in immersion solution with a high correlation degree (Figure 3). Change in bifenthrin amount in peel shows no obvious correlation with the concentration in immersion solution (Figure 3) since 5.00 – 15.00 mg·L<sup>-1</sup> concentration increment did not result in a significant increase of pesticide amount. However, if the amount change is monitored over three solution concentration levels (1.00, 10.00, and 20.00 mg·L<sup>-1</sup>), a strong linear correlation can be observed (R<sup>2</sup> = 0.9991).

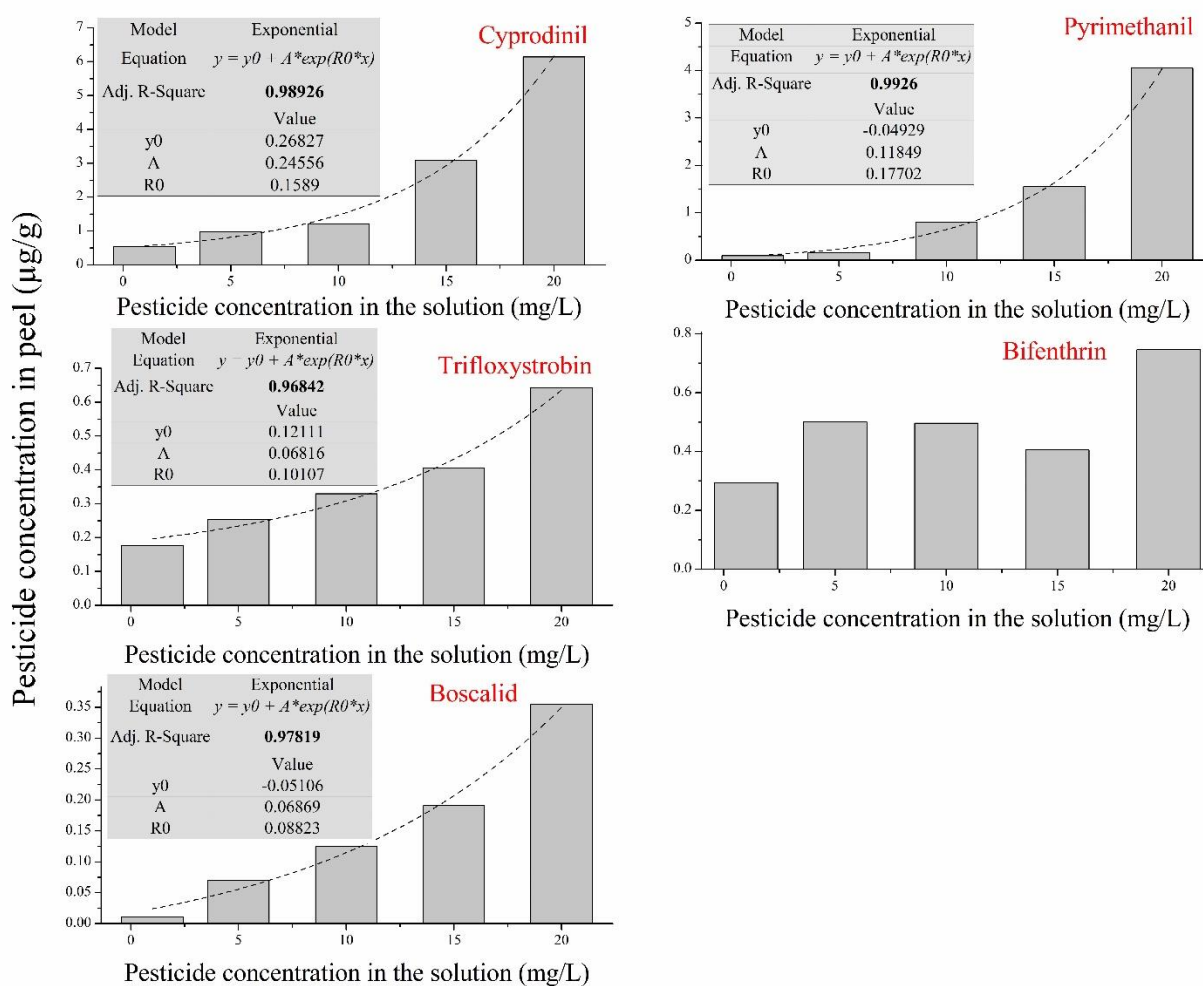


**Figure 3.** Correlation between pesticide amount measured in peel and added to the solution

**CONCLUSION**

In-peel amounts of fungicides increase exponentially with an increase in pesticide concentrations in immersion solution; sorption rate decreases in the following order: pyrimethanil, cyprodinil > trifloxystrobin > boscalid. In-peel amount of bifenthrin is steady over the 5.00 – 15.00 mg·L<sup>-1</sup>

concentration range in the solution, but when monitored over the larger concentration increment (1.00, 10.00, and 20.00 mg·L<sup>-1</sup>) strong linear correlation can be observed.

***Acknowledgement***

This study was supported by the Ministry of Education, Science and Technological Development of the Republic of Serbia (contracts no. 451-03-9/2021-14/200383 and 451-03-9/2021-14/200124).

**REFERENCES**

- [1] J. Leide, X. de Souza, I. Papp, M. Riederer, *Scientia Horticulturae*, 2018, 229, 137–147.

## COMPOSITION OF BUCKWHEAT EXTRACTS DETERMINED BY UHPLC-LTQ OrbiTrap MS

M. Nešović<sup>1</sup>, U. Gašić<sup>2</sup>, N. Nedić<sup>3</sup>, S. Blagojević<sup>1</sup>, Lj. Ignjatović<sup>4</sup>, Ž. Tešić<sup>5</sup>

<sup>1</sup> *Institute of General and Physical Chemistry, Studentski trg 12-16/V, 11158 Belgrade, Serbia, (milicaffh@yahoo.com)*

<sup>2</sup> *University of Belgrade, Department of Plant Physiology, Institute for Biological Research "Siniša Stanković", National Institute of Republic of Serbia, Bulevar despota Stefana 142, 11060 Belgrade, Serbia.*

<sup>3</sup> *University of Belgrade, Faculty of Agricultural Department, Nemanjina 6, 11080 Belgrade - Zemun, Serbia.*

<sup>4</sup> *University of Belgrade, Faculty of Physical Chemistry, Studentski trg 12-16, 11158 Belgrade, Serbia.*

<sup>5</sup> *University of Belgrade, Faculty of Chemistry, Studentski trg 12-16, 11158 Belgrade, Serbia.*

### ABSTRACT

Buckwheat is a high nutritional plant. It has great potential for the prevention of many diseases, mostly due to its antioxidant properties. As a functional food, it is recognized as a valuable plant for research. Ultra-high performance liquid chromatography coupled to linear trap quadrupole of a mass spectrometer and equipped with ion trap OrbiTrap (UHPLC-LTQ OrbiTrap MS) has been used to investigate the existence of polyphenols in buckwheat leaf, stem, flower and grain. It was shown that extracts of a different part of buckwheat, obtained by the solid phase extraction (SPE) method, possess a notable number of polyphenols. Prominent compounds were quercetin and its derivatives (rutin, quercitrin) and *p*-hydroxybenzoic acid. Compounds such as monomeric flavanol 3-ols (epicatechin and its galloylated derivatives) and dimers (B type procyanidins) are identified in all four analyzed buckwheat samples, with dominant portion in buckwheat grain.

### INTRODUCTION

Common buckwheat (*Fagopyrum esculentum*) is a pseudo-cereal plant from the *Polygonaceae* family. Buckwheat is a multipurpose plant and it is recognized as a functional food [1]. Commercial products of buckwheat are tea (made from leaves or flowers), flour and meals (from grains) and honey. Firstly, buckwheat was cultivated due to a higher protein value of its grains compared to cereals, which as well do not contain rutin [1]. Many consumers are relying on buckwheat dishes made from grains such as porridge, bread, various types of meals. Buckwheat grains are often used to fill pillows, which are characterized by a specific aroma obtained from volatile compounds distinctive for buckwheat [2]. Buckwheat leaves and flowers are also highly valued, but their use is mainly in traditional medicine in China. Buckwheat flowers are a rich source of nectar used by bees who made strong flavored honey with high quality. Buckwheat contains proteins that have high nutritional value, dietary fiber, many minerals and vitamins [3]. It represents a valuable food source and a good choice of food for people intolerant to gluten.

Phenolic compounds, as secondary metabolites of plants, are responsible for the useful priority of buckwheat. Buckwheat attracts considerable interest due to its positive effect on hypertension, dyslipidemia, hyperglycemia [1], and shows anti-inflammatory and anticancer effects [3]. These properties have been attributed mostly to the presence of specific polyphenols. It was reported that rutin was the main component found in all parts of buckwheat [4]. Furthermore, monomeric flavanol 3-ols (catechin and epicatechin) with its dimers derivatives (procyanidins) were proposed as markers for buckwheat [5].

The aim of this study was to analyze polyphenols content in different parts of buckwheat. As the content of polyphenols is not uniform in all parts of the plant and differs in certain stages of plant development, the analysis of leaf, stem, flower and grain, could show the transport of these phytochemicals through the plant. Furthermore, detected polyphenols could show a reason for various uses of different parts of buckwheat.

## METHODS

For this study, different parts of common buckwheat (*Fagopyrum esculentum* Moench) were analyzed. Four samples (leaf, stem, flower, grain) were collected from buckwheat species "Novosadska" cultivated in Western Serbia, locality Radojevići (43°23'31" N, 19°52'20" E), during 2017.

The drying of buckwheat samples performed in the dark at room temperature for 15 days. Isolation of phenolic compounds from samples was carried out by using SPE. The preparation of sample extracts and standard solutions for phenolic profile analysis was achieved by following the procedure described by Gašić et al. [6].

The identification of phenolic compounds was carried out by UHPLC-LTQ OrbiTrap MS system (Thermo Fisher Scientific, Bremen, Germany). Chromatographic and spectrometric conditions, as well the instruction for fragmentation study, were previously described by Gašić et al. [6]. The presence of phenolic compounds was confirmed using available phenolic standards and published data. Verifying the presence of phenolic compounds was based on its fragmentation pathways, comparison of its accurate mass to the calculated mass, and retention time.

## RESULTS AND DISCUSSION

With UHPLC-LTQ OrbiTrap MS it was detected 59 phenolic compounds, of which phenolic acids were dominant. Figure 1 shows chromatogram of some identified polyphenols in buckwheat leaf.

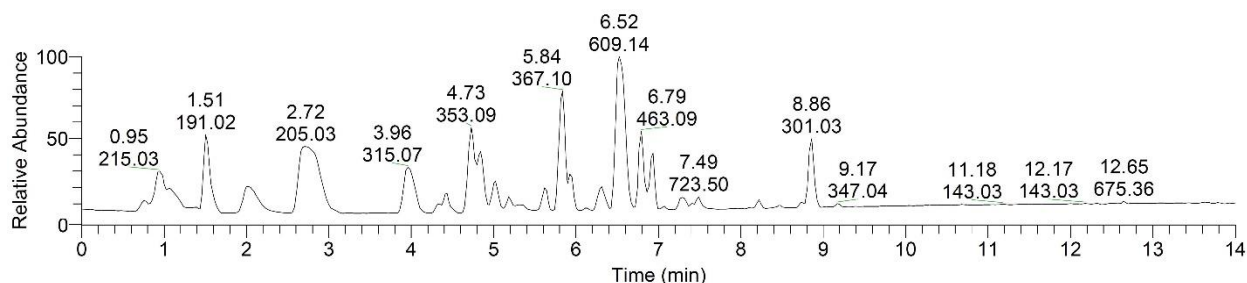


**Figure.1.** Base peak chromatogram of buckwheat leaf extract sample.

All analyzed samples show the presence of quercetin ( $m/z$  301) and its derivatives. The highest intensity of quercetin ( $m/z$  301) was noted in flower, followed by leaf, grain and stem, while the intensity of quercetin glycoside rutin (quercetin 3-*O*-(6"-rhamnosyl)-hexoside) ( $m/z$  609) was as follows: leaf, flower, stem and grain. The presence of rutin in a different part of buckwheat was also noted by other authors [1,3,4]. Zhang et al. [1] noted the highest content of rutin in buckwheat flowers and state that free quercetin occurs in flowers and achenes of *Fagopyrum esculentum*. It was noted that all quercetin derivatives give fragment ion at  $m/z$  301, which corresponds to the deprotonated molecular ion of quercetin.

Dominant compounds in four analyzed buckwheat samples were (epi)catechin ( $m/z$  289) and (epi)catechin gallate ( $m/z$  441), while procyanidins were found in buckwheat leaf, flower and grain, but not in buckwheat stem sample. These compounds are reported as characteristic for buckwheat [5], with its higher presence than in cereals. Confirming the presence of procyanidins in our analyzed

buckwheat samples, it contributes to the positive health application of buckwheat. Buckwheat grain sample shows a dominant number of flavan-3-ols and dimers, and a lower number of polyphenols that belong to cinnamic acid derivatives. Relying to the observations noted by Pasini et al. [2] who proposed *p*-coumaric and *p*-hydroxybenzoic acid as markers of buckwheat, their presence was confirmed in analyzed samples.

As the process of photosynthesis mostly takes place in the leaves, the highest number of compounds could be expected in analyzed buckwheat leaf sample. However, a high number of phenolic compounds was noted in the buckwheat flower sample too, but still, the buckwheat leaf possessed the highest number of phenolic acids. Contrary to these samples, in the buckwheat stem sample was noted two times lower number of phenolic compounds. Regardless of a different number of identified phenolic compounds, the importance of the biological activity of each part of buckwheat occurs due to the synergism of phenolic compounds.

## CONCLUSION

According to the obtained results, samples of buckwheat leaf, stem, flower and grain contain a significant number of polyphenols. Identification of 59 polyphenols in different parts of buckwheat indicates the high value of this plant. Due to the knowledge of using buckwheat in the prevention of many diseases, the examination of polyphenols content has a great influence on the health-protective effects of buckwheat. Further, these results could increase the importance of different parts of buckwheat, as well as buckwheat itself. Since buckwheat is a multi-purpose plant, this type of study contributes to higher utilization of buckwheat as a functional food, which certainly needs to be used more.

## Acknowledgement

This work has been supported by Ministry of Education, Science and Technological Development of Republic of Serbia (Contract number: 451-03-9/2021-14/200051, 451-03-9/2021-14/200007, 451-03-68/2020-14/200168).

## REFERENCES

- [1] Z.-L. Zhang, M.-L. Zhou, Y. Tang, F.-L. Li, Y.-X. Tang, J.-R. Shao, W.-T. Xue, Y.-M. Wu, *Food Res. Int.*, 2012, 49, 389–395.
- [2] F. Pasini, S. Gardini, G.L. Marcazzan, M.F. Caboni M. F., *Food Chem*, 2013, 141, 2802–2811.
- [3] J.A. Giménez-Bastida, H. Zieliński, *J. Agric. Food Chem.*, 2015, 63, 7896–7913.
- [4] J. Kalinova, J. Triska, N. Vrchotova, *J. Agr. Food Chem.*, 2006, 54(15), 5330-5335.
- [5] K. Bittner, S. Rzeppa, H.-U. Humpf, *J. of Agric. Food Chem.*, 2013, 61, 9148-9154.
- [6] G. Gašić, B. Šikoparija, T. Tosti, J. Trifković, D. Milojković-Opsenica, M. Natić, Ž. Tešić, *J. AOAC Int.*, 2014, 97(5), 1259-1267.

## RESEARCH OF QUALITY AND ANTIOXIDANT POTENTIAL OF HUMAN MILK AND INFANT FORMULA FOR LACTOSE-INTOLERANT INFANTS

N. Lugonja<sup>1</sup>, J. Avdalović<sup>1</sup>, D. Stanković<sup>2,3</sup>, J. Milić<sup>1</sup>, M.M. Vrvic<sup>4</sup>  
and S. Spasić<sup>1</sup>

<sup>1</sup> *University of Belgrade, Institute of Chemistry, Technology and Metallurgy, Belgrade, Serbia. (jelena.avdalovic@ihtm.bg.ac.rs)*

<sup>2</sup> *University of Belgrade, Faculty of Chemistry, Belgrade, Serbia*

<sup>3</sup> *Vinča Institute of Nuclear Sciences, National Institute of the Republic of Serbia, Belgrade, Serbia*

<sup>4</sup> *BREM GROUP Ltd, Str. Oslobođenja 39b, 11090 Belgrade, Serbia*

### ABSTRACT

Infant food is a crucial component of development and normal growth of infants. Nutritive characteristics and methods for determination of the antioxidant potential of the infant food were compared in order to test the quality and biological value of human milk and infant formula with and without lactose. The antioxidant potential was determined using cyclic and differential pulse voltammetry, and electron paramagnetic resonance spectroscopy. Used electrochemical methods revealed high antioxidant potential of infant formula compared to human milk, while electron paramagnetic resonant spectroscopy revealed that the infant food possesses a significant capability to capture  $\cdot\text{OH}$  radicals and form carbon-centred radical in Fenton reaction. Lactose-free infant formula has high antioxidant potential and its application is important during diarrhea because infant food contributes to the reduction of pathogens by changing redox state of the environment in the infant's gastrointestinal tract.

### INTRODUCTION

Adequate nutrition is essential for growth, development and protection against oxidative stress of infants. Human milk is considered to be the optimal food and the “gold standard” in infant nutrition. However, when mother is not able to breastfeed, infant formula provides adequate substitute, with macronutrients, vitamins, minerals, prebiotic fibres and antioxidants necessary for growth and development of infants [1, 2]. Special lactose-free infant formula (IF FL) can be used for nutrition of infants and young children suffering from lactose intolerance and diarrhea as it provides adequate nutrients respecting principles and characteristics of the target group. Quality of the special infant formula is determined by its nutritive value and total antioxidant capacity (TAC). Lactose-free infant formula contains less lactose and lower concentration of fat, more protein and a certain amino acid profile with antioxidants, and as a functional food, it plays a key role in the body's physiological and antioxidant activities. Oxidation process occurs during cellular signalling and contributes the most to the overall physiological function. Oxidative stress occurs when homeostasis of a biosystem's redox status, which represents the relative level of oxidation of biological molecules and structures, is disturbed [2]. Tests for determination of antioxidant protection effects in biological fluids and infant food are useful for determining food quality and the level of prevention of oxidative stress in infants [3].

The aim of this paper is to provide new important data on infant food in terms of the prevention of oxidative stress and available methods for testing quality and antioxidant potential of human milk, infant formula and special lactose-free infant formula in order to prevent oxidative stress.

## METHODS

The TAC was determined in milk of mothers of term infants (MM) and two infant formulas (Impamil, Serbia): IF 1 – infant formula for term infants from birth to 6 months of age and IF FL – a special lactose-free infant formula for nutrition of infants and young children suffering from lactose intolerance and diarrhea, without gluten and saccharose. IF FL contains digestible maltodextrin instead of lactose, with optimal mineral and vitamin content. Macronutrient content of infant food was determined in the following manner: protein content by Bradford method, while lactose and D-galactose content were determined according to Megazyme Lactose kit methods, using specific enzyme-test, such as K-LACGAR 12/05 (lactose and D-galactose); Total lipid content was determined by Weibull–Berntrop gravimetric method (ISO 8262-1|IDF 124-1:2005) for infant foods. TAC of infant food was estimated by electrochemical methods cyclic and differential pulse voltammetry. Voltammograms were recorded with three electrode system using a CHI760B instrument (CHInstruments, Austin, USA) [3]. For these methods total charge (C) was parameter of interest and changes in the charge during oxidation were monitored. Potentiometric titration was done by Pt electrode in the solution made of 1:1 v/v milk and phosphate buffer (0.1 M pH 6.7), after constant volumes of the redox mediator 0.1 M I<sup>-</sup>/I<sub>2</sub>. Portions of 10 µl of titrant were added into 50 mL of solutions every 90 s and changes in EMF (mV) were monitored. Electron paramagnetic resonance spin-trapping spectroscopy (EPR) was applied to examine the ability of human milk to scavenge hydroxyl radical ( $\cdot$ OH) and to establish reactive products of oxidation of milk constituents. The signal intensity of the BMPO adduct with carbon-centered radical was detected [1].

## RESULTS AND DISCUSSION

Table 1 shows nutritional and antioxidant profile of the tested infant food. Declared nutritive values of IF 1 approximately correspond to the composition of breast milk, with higher protein and galactose content, while special IF FL for infants and young children suffering from lactose intolerance and diarrhea has significantly lower content of lactose and galactose.

**Table 1.** Nutritional characteristics and antioxidant potential of infant food

Infant food	Protein content (g/100 mL)	Fat content (g/100m L)	Lactose content (g/100 mL)	Galactose content (mg/100 mL)	CV (10 <sup>7</sup> C)	DPV (10 <sup>7</sup> C)	POT (mV)	EPR (BMPO /OH spin adduct of OH)
MM	1.21±0.03	3.7±0.7	6.99±0.22	2.80± 0.2	3.9±0.4	15±1	250±8	81±10
IF 1	1.49±0.01	3.5±0.3	6.95±0.35	4.60±0.1	2.7±0.2	10±1	180±5	108±11
IF FL	1.79±0.01	3.3±0.2	0.01±0.01	93.70±0.3	2.9±0.1	12±1	190±7	145±16

By comparing potentiometric titration and voltametric measurements of redox changes in antioxidant potential, it can be noticed that breast milk has higher antioxidant potential compared to IF 1, while IF FL has a higher TAC compared to standard IF 1 for infant nutrition, which indicates the special purposes of this type of IF in acute diarrhea when electrolyte balance is disturbed and oxidative stress is increased. The applied differential pulse and cyclic voltammetry showed a higher

TAC of IF FL compared to IF 1 (Fig 1 A, B). Figure 1C shows EPR spectra of infant formula IF1 and IF FL. Spectra obtained in the Fenton system showed that hydroxyl radical reacted with protein and ascorbate biomolecules in food to produce ascorbyl and carbon-centered radicals. The radicals were stabilized with BMPO spin trap. The intensities of the signal of BMPO adducts were presented in Table 1. IF has carbon-centered radical similar to MM, while level of ascorbyl radical is higher in IF, suggesting human milk possesses stronger antioxidant potential compared to IF.

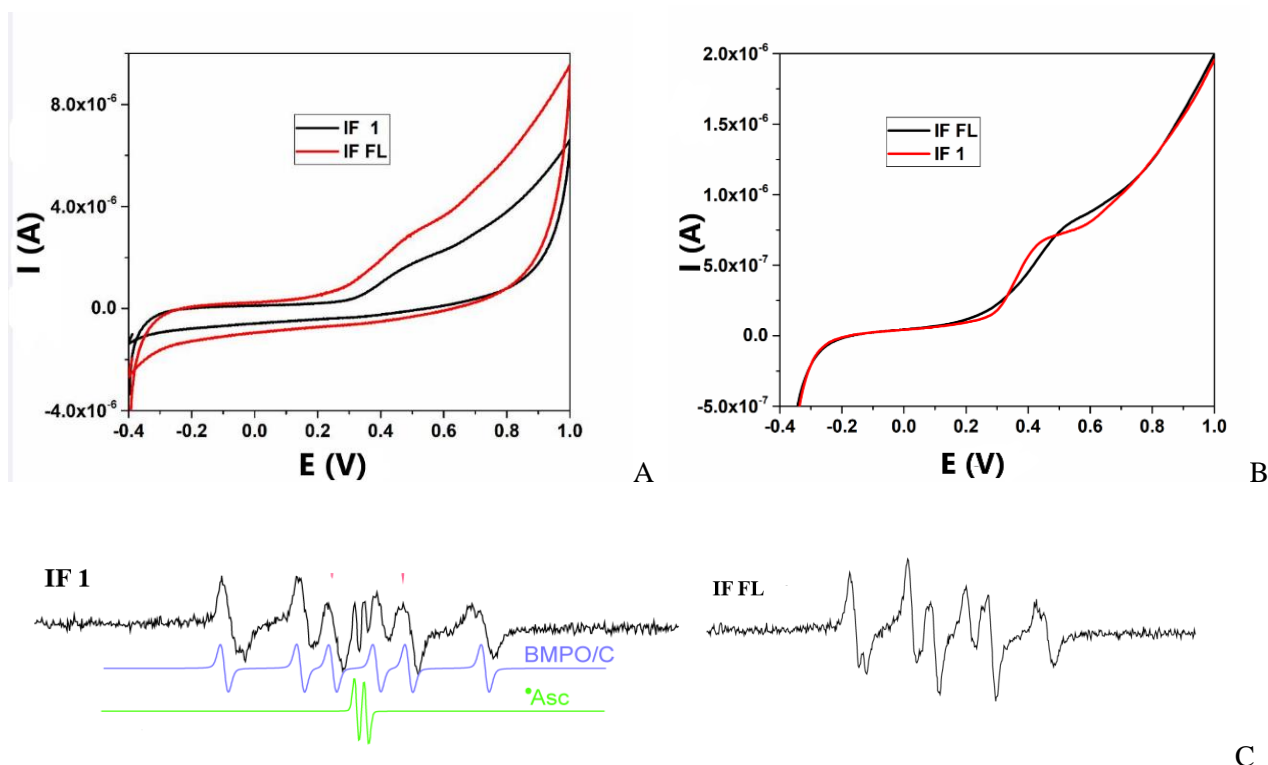


**Figure 1.** Methods for determination of TAC in infant food: A) Cyclic voltammetry; B) Differential pulse voltammetry; C) Electron paramagnetic resonance spin-trapping spectroscopy (EPR)

## CONCLUSION

Human milk is a synergistic mixture of several interacting components which provide the greatest functional and antioxidant benefit to infant. Herein applied electrochemical and EPR methods can be used to determine TAC of infant food. Special IF FL has higher TAC compared to IF, which is important in cases of diarrhea when increased TAC of infant food contributes to the reduction of pathogens by changing redox state of the environment in infant gastrointestinal tract.

## Acknowledgement

This work is supported by the Ministry of Education, Science and Technological Development of the Republic of Serbia (Grants No. 451-03-9/2021-14/200026).

## REFERENCES

- [1] N. Lugonja, S. Spasic, O. Laugier, A. Nikolic-Kokic, I. Spasojevic, Z. Orescanin –Dusic, M. Vrvic, *Nutrition*, 2013, 29, 431-35.

- [2] V. Marinkovic, M. Rankovic-Janevski, S. Spasic, A. Nikolic-Kokic, N. Lugonja, D. Djurovic, S. Miletic, M. Vrvic, I. Spasojevic, *Journal of Pediatric Gastroenterology and Nutrition*, 2016, 62, 901–906.
- [3] N. Lugonja, D. Stankovic, B. Milicic, S. Spasic, V. Marinkovic, M. Vrvic, *Food Chemistry*, 2018, 240, 567-572.

## EXAMINATION OF PROOXIDATIVE ACTIVITY OF RED WINE IN MELANOMA CELLS

N. Đorđević<sup>1</sup>, L. Korićanac<sup>1</sup>, J. Žakula<sup>1</sup>, N. Todorović Vukotić<sup>1</sup>, S. Pejić<sup>1</sup>, V. Tešević<sup>2</sup> and S. B. Pajović<sup>1</sup>

<sup>1</sup> *University of Belgrade, Institute of Nuclear Sciences Vinča, National Institute of the Republic of Serbia, Laboratory of Molecular Biology and Endocrinology, 11001 Belgrade, Serbia. (neda@vin.bg.ac.rs)*

<sup>2</sup> *University of Belgrade, Faculty of Chemistry, 11000 Belgrade, Serbia.*

### ABSTRACT

Melanoma is responsible for 75% of all deaths from skin cancer. Its lethality arises from its rapid progression, easy metastasis and drug-resistance as well. Red wine is a natural product rich in polyphenolic compounds with potent anticancer activities. It seems that in cancer cells these compounds behave as prooxidants initiating reactive oxygen species mediated cellular DNA breakage and consequent cell death. The aim of this study was to investigate prooxidative activity of red wine samples (Merlot variety, commercial as well as VCR1 and VCR101 clonal wines) in melanoma A375 cells, through measuring the relationship of reduced and oxidized form of glutathione (GSH/GSSG) and comparison with the GSH/GSSG ratio in control (untreated melanoma cells). The data obtained showed that tested red wine samples decrease GSH/GSSG ratio in A375 cells compared to control ( $4.6 \pm 0$ ), with the largest decrease noticed in treatment with VCR101 wine ( $0.66 \pm 0.05$ ).

### INTRODUCTION

Wine is a natural product with well-known beneficial effects on human health. Especially the red one is rich with the polyphenols, compounds with wide range of biological activities, like antioxidant, anti-inflammatory and chemopreventive activities. Since novel studies pointed out a connection between inflammation and cancer development, consumption of phenolic rich natural products, like red wine, could be very useful for cancer prevention [1].

Antioxidant activity of the polyphenolic compounds is one of the most important features related to biological activity of these compounds in healthy cells. On the other hand, polyphenols exert a wide variety of anticancer effects. They modulate activities of ROS-scavenging enzymes, take part in arresting the cell cycle, induce apoptosis, autophagy, and suppress cancer cell proliferation and invasiveness [2]. An increasing number of data indicate that polyphenols can act as prooxidants due to the action of reactive oxygen species, and thus initiate the breakdown of cellular DNA, and therefore cell death [3].

Melanoma is less common, but the most malignant skin tumor. It belongs to one of the most malignant tumors in humans. The incidence of melanoma is constantly increasing in recent decades, so for the last 20 years an increase of up to 200% over has been reported [4]. This report investigated prooxidative activity of commercial and red wine obtained from specific vine clones (VCR1 and VCR101) of Merlot variety in melanoma A375 cells aiming to complete biological characterization of specific vine clones.

### METHODS

In order to examine the prooxidative effect of red wine in cancer cells, melanoma A375 cells were treated with 5% concentration of analysed wine in exponential growth phase. The wines used in this study were of Merlot variety, both, commercial wine and wines obtained from two vine clones (VCR1 and VCR101). The melanoma cells were prepared according to method of Rahman et al. [5]. After

24 h incubation, A375 cells were washed with 3 mL of cold 0.1 M phosphate buffer pH 7.4. Thereafter, cells were trypsinized with 0.5 mL Try-EDTA for 5 min at room temperature and collected in 2 mL of cold medium. After centrifugation for 3 min at 2000 g on room temperature, the supernatant was pour off and the residue was resuspended in 2 mL of 0.1 M phosphate buffer pH 7.4. The cells were again centrifuged at 4000 g, 10 min and resuspended in 500  $\mu$ L of extraction buffer (0,1 M potassium phosphate buffer pH 7,5 with 5 mM EDTA, 0,1% Triton X100 and 0.6% sulfosalicylic acid). Finally, melanoma cells were lysed for 30 min on ice with vortexing. After centrifugation at 4000 g, 20 min at 4 °C, the resulting supernatant was collected in chilled tubes.

The content of reduced and oxidized glutathione was determined according to modified method of Salbitani et al. [6]. The reaction mixture (sample) contained 600  $\mu$ L of extraction buffer, 40  $\mu$ L 0.4% DTNB and 50  $\mu$ L of cell extract/GSH standard. Blank contained 650  $\mu$ L of extraction buffer and 40  $\mu$ L 0.4% DTNB. After 5 min of incubation at room temperature, the absorbance was measured on 412 nm. The content of GSH was calculated from standard curve. Thereafter, 50  $\mu$ L 0.4% NADPH and 1  $\mu$ L 0.5 U of glutathione reductase were added in reaction mixture. After 30 min of incubation at room temperature, the absorbance at 412 nm was measured, and the concentration of total glutathione was calculated from the standard curve for GSH. The concentration of GSSG was determined by subtraction of the content of GSH from the determined concentration of total glutathione. The obtained GSH/GSSG ratio in analysed samples was compared with the GSH/GSSG ratio in control (untreated melanoma cells). All data were displayed as mean value  $\pm$  SD and analyzed by two-way ANOVA followed by Tukey's HSD test.

## RESULTS AND DISCUSSION

The obtained data revealed that GSH/GSSG ratio in melanoma A375 cells treated with all three samples of analysed wines was significantly lower ( $p < 0.001$ ) than GSH/GSSG ratio in control cells ( $4.6 \pm 0$ ). This ratio was lower in melanoma cells treated with clonal (VCR1 and VCR101) wines compared to commercial wine. Furthermore, the treatment of melanoma cells with VCR101 clonal wine mostly reduces the GSH/GSSG ratio ( $0.66 \pm 0.05$ ). Prooxidative effect of wine samples could be attributed to their polyphenolic compounds. Previous literature data have just pointed out prooxidative activity of some polyphenols, mostly flavonoids, through their various ways of cytotoxic effects on cancer cells [7,8]. On the other hand, previous research has also shown that red wine and its polyphenols increase GSH intracellular level in human erythrocytes of healthy donors mainly due to the elevated activity of glutathione reductase [9,10]. Namely, flavonoids are potent antioxidants under normal and pro-oxidants under pathological conditions, when they can target apoptotic signalling cascade activating apoptosis and also can suppress proliferation and inflammation.

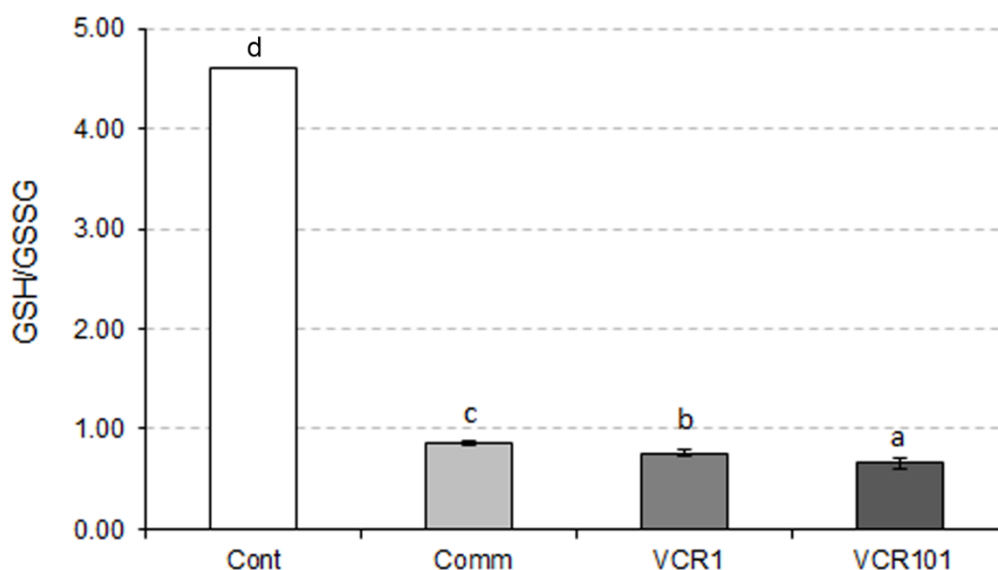


**Figure 1.** GSH/GSSG ratio in control A375 cells (Cont) and A375 cells treated with Merlot red wine samples, commercial wine (Comm) and wine obtained from two vine clones VCR1 and VCR101. All measurements were done in triplicate and the obtained results are expressed as mean value  $\pm$  SD. Different letters show significant differences between obtained values ( $p < 0.05$ ), according to Tukey's HSD test.

The obtained results further complement previously published results about chemical composition and biological activity of specific red wine clones of Merlot variety, VCR1 and VCR101 [11]. These results also further recommended mentioned clones for use in standard vinification procedures.

## CONCLUSION

From the obtained results, it can be concluded that the cause of the shifted GSH/GSSG balance towards GSSG is probably due to the prooxidative effect of red wines in A375 cells. This result is very important having in mind the chemo- and radio-resistance of melanoma cells. The given conclusion is in accordance with the previous scientific assumptions and findings that polyphenolic compounds of plant origin exhibit their anticancer activity by prooxidative action. Finally, this study highlights red wine itself as polyphenolic-rich food that, in moderate consumption, could reduce the risk of cancer.

## Acknowledgement

This work was supported by the Ministry of Education, Science and Technological Development of the Republic of Serbia (Grant No. 451-03-9/2021-14/200017).

## REFERENCES

- [1] T. I. Pavel, C. Chircov, M. Rădulescu, A. M. Grumezescu, Regenerative wound dressings for skin cancer, *Cancers*, 2020, 12, 1-22.
- [2] C. Rodríguez-García, C. Sánchez-Quesada, J. J. Gaforio, Dietary flavonoids as cancer chemopreventive agents: An updated review of human studies, *Antioxidants*, 2019, 8, 137.
- [3] H. Y. Khan, S. M. Hadi, R. M. Mohammad, A. S. Azmi, Prooxidant anticancer activity of plant-derived polyphenolic compounds: An underappreciated phenomenon, *Functional Foods in Cancer Prevention and Therapy*, 2020, 221-236.

- [4] A. Višnjić, P. Kovačević, A. Veličkov, M. Stojanović, S. Mladenović, Head and neck cutaneous melanoma: 5-year survival analysis in a Serbian university center, *World Journal of Surgical Oncology*, 2020, 18, 1-8.
- [5] I. Rahman, A. Kode, S. K. Biswas, Assay for quantitative determination of glutathione and glutathione disulfide levels using enzymatic recycling method, *Nature Protocols*, 2006, 1, 3159-3161.
- [6] G. Salbitani, C. Bottone, S. Carfagna, *Bio-protocol*, 2017, 7, e2372.
- [7] V. Stepanić, A. Čipak Gašparović, K. Gall Troselj, D. Amic, N. Žarković, Selected attributes of polyphenols in targeting oxidative stress in cancer, *Current Topics in Medicinal Chemistry*, 2015, 15, 1-14.
- [8] D. M. Kopustinskiene, V. Jakstas, A. Savickas, J. Ernatoniene, Flavonoids as anticancer agents, *Nutrients*, 2020, 12, 457.
- [9] I. Tedesco, S. Moccia, S. Volpe, G. Alfieri, D. Strollo, S. Bilotto, C. Spagnuolo, M. Di Renzo, R. P. Aquino, G. L. Russo, Red wine activates plasma membrane redox system in human erythrocytes, *Free Radical Research*, 2016, 50, 557-569.
- [10] I. Tedesco, C. Spagnuolo, S. Moccia, G. L. Russo, M. Russo, C. Cervellera, The pro-oxidant activity of red wine polyphenols induces an adaptive antioxidant response in human erythrocytes, *Antioxidants*, 2021, 10, 800.
- [11] N. O. Đorđević, N. Todorović, I. T. Novaković, L. L. Pezo, B. Pejin, V. Maraš, V. V. Tešević, S. B. Pajović, Antioxidant activity of selected polyphenolics in yeast cells: The case study of Montenegrin Merlot wine, *Molecules*, 2018, 23, 1971.

# *R - Physico-Chemical Analysis*



## DETECTION AND ISOTOPIC DISTRIBUTION OF OXAPROZINE COMPLEX CONTAINING CU(II) IONS BY LDI MASS SPECTROMETRY

F. Veljković<sup>1</sup>, B. Božić<sup>2</sup>, M. Stoiljković<sup>1</sup>, I. Radović<sup>1</sup>, B. Janković<sup>1</sup>, M. Ćurčić<sup>1</sup> and S. Veličković<sup>1</sup>

<sup>1</sup>*VINČA Institute of Nuclear Sciences - National institute of the Republic of Serbia, University of Belgrade, P.O.Box 522, 11001 Belgrade, Republic of Serbia.  
(filipveljkovic@vin.bg.ac.rs)*

<sup>2</sup>*University of Belgrade, Faculty of biology, Studentski trg 16, 11158 Belgrade, Republic of Serbia.*

### ABSTRACT

An oxa complex containing transition metal ions is potentially a great medication in anticancer therapies. In this work we used laser desorption/ionization (LDI) on a commercial matrix-assisted LDI time of flight mass spectrometry (MS) instrument to demonstrate possibilities for direct detection and obtainment of isotopic distribution of Oxaprozin metal complex with Cu(II) ions. Results show that the molecular ion of Oxaprozin metal complex with Cu(II) ions were detected at  $m/z$  711.14, 712.13, 713.13, 714.13, 715.13, 716.10, at the range of laser intensity from 3300 to 3700 a.u., the accelerating voltage of 25000 V, the grid voltage of 60%, and the range extraction delay time from 100 to 300 ns. For the above mentioned instrumental parameters, the experimental isotopic distribution of Oxaprozin metal complex with Cu(II) ions is in a good agreement with its theoretical values. The LDI MS appears to be a promising method for characterization of new organometallic species.

### INTRODUCTION

Oxaprozin (3-(4,5-diphenyl-1,3-oxazol-2-yl)propanoic acid) is classified as non-steroidal anti-inflammatory drug (NSAIDs) that shows analgesic and antipyretic properties [1-3]. Various studies have highlighted that continuous therapy with NSAIDs makes the real promise of chemoprevention and additional therapy for cancer patients [4-5]. Transition metal ions have attracted major interest since they are trace elements present in the reactive centers of many enzymes [6-10]. Transition metal ions form complexes of NSAIDs that are more active than their parent drugs and exhibit lesser side-effects [11]. For instance, a square planar Cu(II) complex with ketoprofen [(*R,S*)-2-(3-benzoylphenyl)propanoic acid] has shown good anti proliferative effects against human breast cancer cell line T47D rich in progesterone receptors [12].

Matrix assisted laser desorption/ionization time of flight mass spectrometry (MALDI-TOF) is widely applied for the analysis of high-molecular and non-stable compounds, including bioorganic and organometallic species [13]. On the other hand, MALDI without matrix i.e., laser desorption/ionization (LDI) method can be useful tool for the detection and characterization of metal compounds (coordination and organometallic complexes and inorganic species).

As previously emphasized, the careful selection of the instrumental parameters of the LDI mass spectrometer could provide less ion fragmentation, i.e., detection of the accurate mass of any in-stable organometallic compounds (which represents their essential information) [14]. The major advantage of LDI is that the ionization technique creates primarily singly charged ions, so, even relatively complex mixtures, can be analyzed [15].

The main goal of this study was the detection of fingerprint tail of the oxaprozin metal complex with Cu(II) ions by varying the instrumental parameters of the LDI mass spectrometer.

Considering the limited amount of data on how instrumental parameters affect the LDI mass spectra of an organometallic complex, the results of this study are of significant importance.

## METHODS

0.35 mg of previously synthesized Cu(II) complexes with oxaprozin [1-3] was dissolved in 25  $\mu$ L of DMSO (Dimethyl sulfoxide). Analyte and solvent were mechanically mixed and transferred to the plate of stainless steel. A volume of 0.5  $\mu$ L of this suspension was dried and transferred in the high vacuum conditions of mass spectrometer. A MALDI target plate with samples on it was inserted into the instrument.

Measurements were performed on the commercial Voyager-DE PRO mass spectrometer acquired from Sciex (USA) equipped with TOF analyzer, operating in the positive reflection mode with pulsed extraction. Ions were formed by a pulsed UV laser beam (nitrogen laser, 337 nm, 3 ns pulse width, and operating at 20.00 Hz), and 200 shots were summed. The laser attenuator is device that controls laser intensity, while the laser attenuator was controlled by using the slider controls on the Manual Laser Control page, which has range of 0-4600 a.u. (arbitrary units). Hence, this relative scale will be used hereafter for the laser intensity. The stoichiometry of the ion species was determined via comparison of experimental isotopic envelopes with the theoretical models.

## RESULTS AND DISCUSSION

The effect of instrumental parameters of the LDI TOF mass spectrometer for detection of the previously synthesized Cu(II) complex with Oxaprozin has been examined in this study.

The following instrumental parameters were varied during the experiment: the laser intensity from 2000 a.u. to 4000 a.u., the accelerating voltage from 9000 to 25000 V, the grid voltage from 40 to 90 %, and the extraction delay time from 100 to 300 ns.

The positive mode LDI mass spectrum of the complex of Cu(II) with Oxaprozin is shown in **Figure 1**. Since negative mode showed higher level of the fragmentation and spectra complexity, focus was on the positive ion mode. The negative mode of Cu(II) complex with Oxaprozin will be the subject of further researches.

The mass spectra were analyzed via a comparison of experimental isotopic patterns with its theoretical models. The recognition of Cu- oxaprozine peaks in a mass spectrum is straight forward since Cu element exists in nature as a two-isotope mixture, while oxaprozine have three Under the LDI mass spectrometric conditions, all isotopic peaks were well-resolved.

Mean experimental values of the relative ratio of the intensity of an individual combination of isotopes are shown in **Figure 1**., together with the standard deviation, their corresponding theoretical values and relative error of experimental measurements which are given in **Table 1**.

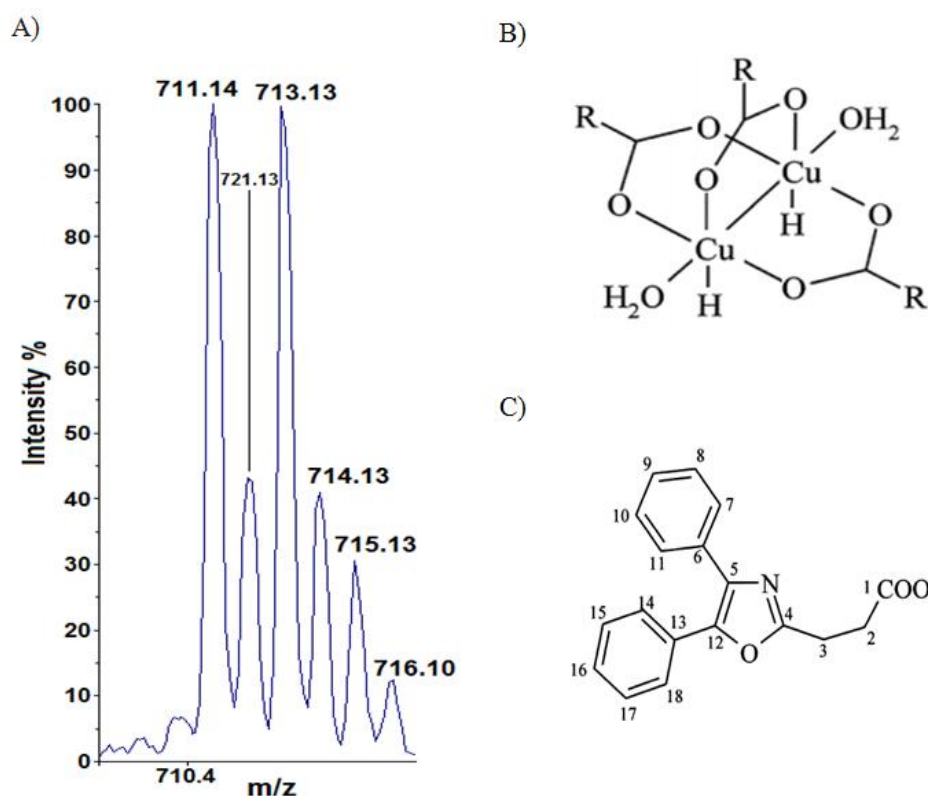


**Figure 1.** Experimentally obtained mass spectrum of Cu(II) complexes with Oxaprozin (A), proposed structure of the Cu (II) oxa ligand labeled with R (B) and structure of oxa ligand (C).

**Table 1.** Mean experimental values of the relative ratio of the intensity of an individual combination of isotopes together with the standard deviation, their corresponding theoretical values and relative error of experimental measurements

Experimental peak position m/z	Relative abundance of isotopes by S/N in LDI spectra	Calculated m/z	Theoretical values of relative abundances	Measurement error %
711.14	$31.59 \pm 2.03$	711.06	31.98	1.23
712.13	$13.42 \pm 1.48$	712.06	12.83	4.58
713.13	$30.24 \pm 1.93$	713.06	31.36	3.60
714.13	$12.51 \pm 1.57$	714.06	11.92	4.91
715.13	$9.42 \pm 0.47$	715.06	9.00	4.58
716.10	$2.83 \pm 0.42$	716.06	2.98	5.19

The molecular ion of Oxaprozin metal complex with Cu(II) ions ( $m/z$  711.14, 712.13, 713.13, 714.13, 715.13, 716.10, **Figure 1.**) was detected on three values of the laser intensity (3300, 3500, and 3700 a.u). It was observed that the relative intensity of these peaks increases with the rise of laser intensity from 3300 to 3700 a.u. The optimal value of the accelerating voltage was 25000V, the grid voltage 60%, and the extraction delay time from 100 to 300 ns. Variation of extraction delay time didn't show noticeable impact as previous three variables did.

Measurement error of isotopic distribution is in the range of acceptable level (under 5%) for all mass peaks except for mass 716, which is expected since its least abundant isotope.

The isotopic distribution of Oxaprozin metal complex with Cu(II) ions is in good agreement with its theoretical calculation on the above mentioned experimental conditions.

## CONCLUSION

In this work, the possibility of using LDI-TOF MS for detecting Cu(II) organometallic complex with commercially available NSAID has been investigated.

The positive mode of LDI mass spectra measured at the laser intensity range of 3300-3700 a.u. ensures that the experimental isotopic distribution is in a good agreement with its theoretical values.

The LDI MS can be a useful method for future research of various organometallic complexes containing other metals such as Mn(II), Co(II), Ni(II), Zn(II), etc.

## Acknowledgement

This work was financially supported by the the Ministry of Education, Science and Technological Development of the Republic of Serbia, contract number: 451-03-9 / 2021-14 / 200017and 451-03-9/2021-14/200178.

## REFERENCES

- [1] M. A. al-Faks, M. C. Pugh, *Orthop. Rev.*, 1992, **21**, 558–563.
- [2] J. J. Talley, D. L. Brown, J. S. Carter, M. J. Graneto, C. M. Koboldt., J. L. Masferrer, W. E. Perkins, R. S. Rogers, A. F. Shaffer, Y. Y. Zhang, B. S. Zweifel, K. Seibert, *J. Med. Chem.*, 2000, **43**, 775–777.
- [3] B. D.Bozic, J. R. Rogan, D. D.Poleti, N. P.Trisovic, G. S.Uscumlic,*Chem Pharm Bull.*, 2012, **60**, 865–9.
- [4] J. A. Baron, *Prog Exp Tumor Res.*, 2003, **37**, 1–24.
- [5] R. Ettarh, A. Cullen, A. Calamai, *Pharmaceuticals (Ott.)*, 2010, **3**, 2007–2021.
- [6] Y. Iizuka, E. Sakurai, Y. Tanaka, *Riken Review*, 2001, **35**, 3–4.
- [7] S. J. Lippard, J. M. Berg, “Principles of Bioinorganic Chemistry”, University Science Books, Mill Valley, 1994.
- [8] R.K. Szilagy, P. A. Bryngelson, M. J. Maroney, B. Hedman, K. O. Hodgson, E. I. Solomon, *J Am Chem Soc.*, 2004, **126**, 3018–3019.
- [9] M. H. Stipanuk, “Biochemical, Physiological & Molecular Aspects of Human Nutrition,” 2nd ed., W. B. Saunders Company, New York, 2006.
- [10] M. Kobayashi, S. Shimizu, *Eur J Biochem.*, 1999, **261**, 1–9.
- [11] P. Lay, T. Hambley, WO Patent 109843, 2007.
- [12] D. K. Saha, S. Padhye, S. Padhye, *Met Based Drugs*, 2001, **8**, 73–77.
- [13] J. H. Banoub, R. P. Newton, E. Esmans, D. F. Ewing, G. Mackenzie, *Chem. Rev.*, 2005, **105**, 1869.
- [14] M. Wyatt, *J. Mass Spec.*, 2011, **46**, 712.
- [15] W. Henderson, J. S. McIndoe, *Mass Spectrometry of Inorganic, Coordination and Organometallic Compounds*, 2005.

## ON POSSIBILITIES OF MINERAL PIGMENTS CHARACTERISATION USING LDI-MS: THE IRON-RICH EARTHY OCHER CASE

M. Stoiljković, S. Veličković, I. Radović, and F. Veljković

*Department of physical chemistry, VINČA Institute of Nuclear Sciences – National institute of the Republic of Serbia, University of Belgrade, P.O.Box 522, 11001 Belgrade, Republic of Serbia. (filipveljkovic@vin.bg.ac.rs)*

### ABSTRACT

Earthy ochre sample originating from the Devil's Town, a rocky geological formation in the South Serbia region, was described using a laser desorption/ionization time-of-flight mass spectrometry (LDI-ToF-MS). Obtained laser desorption/ionization mass spectrum consisted dominantly of the series of chromium and iron (such as  $\text{Fe}_{1-3}\text{O}_{1-3}$ ,  $\text{Fe}_{1-2}(\text{OH})_{1-2}$ ,  $\text{Fe}_{1-3}\text{O}(\text{OH})_{2-3}$ ,  $\text{Cr}_{1-3}\text{O}_{2-9}$ ,  $\text{Cr}(\text{OH})$ ,  $\text{CrO}(\text{H}_2\text{O})$ ,  $\text{CrO}(\text{OH})_4$ ,  $\text{Cr}_2\text{O}_2(\text{OH})$ ). These oxides, hydroxides and oxyhydroxides species of chromium and iron indicates at presence  $\text{Cr}_2\text{O}_3$ ,  $\text{CrO}_3$ ,  $\text{Fe}_2\text{O}_3$  and  $\text{Fe}_3\text{O}_4$  in the sample.

### INTRODUCTION

Ochres are earthy, metal oxide- or metal oxide-hydroxide, which forms deposits in the surface or near-surface. The most common ochreous deposits are iron-rich and, by definition, are impure contains a mixture of mineral components. Red ochres dominate by hematite and, yellow ochres typically dominate by goethite. Ochre deposits formed as natural acid rock drainage and acid mine drainage tend to revert to goethite. Such deposits are concentrating in streams and rivers and, their locations are remarkable (**Figure 1a**). Yellow, through red, and brown pigments for painting may be derived from these kinds of native deposits [1]. Classified as the most common natural pigments red and yellow ochres at the same time constitute the major components of the color palette used in a fine art including pottery.

Earlier papers have shown that the mass spectrometry offers much information useful to the characterization of solid materials. For example, Robertson-Honecker have developed a pulsed glow discharge mass spectrometry method for the direct speciation of Cr(III) and Cr(IV) in the solid sample [2]. To date, **the laser desorption/ionization mass spectrometry** has been used to characterize pure nanoparticles of  $\text{Fe}_2\text{O}_3$  and  $\text{Fe}_3\text{O}_4$  ferrite [3].

This paper demonstrates that the LDI MS can be to use for the characterization of mineral pigment of natural origin. It is a non-destructive technique needed a minimal amount of sample and no prior preparation. To fully support the sample description a multi-analytical approach was also implemented encompassing chemical, mineralogical, and structural composition.

### METHODS

An amount of ochre mud dried at  $105\text{ }^\circ\text{C}$  for two hours, crushed, and sieved. A drop of sample suspension in deionized water is transferred onto the sample plate and, no matrix is added. The dried spot was measured in positive reflection modes on mass spectrometer MALDI-TOF, Voyager-DE PRO (USA) equipped with 3 ns laser at 337 nm. The ions stoichiometries were obtained via comparison of experimental isotopic pattern with the theoretical models.

A sample aliquot is dissolved in heated aqua regia for elemental analysis. Quantification is obtained using an optical emission spectrometer ICP-OES, iCAP 7000 Series, Thermo Scientific.

## RESULTS AND DISCUSSION

The drainage site is shown on **Figure 1**. The SEM images indicate the diversity in raw material morphology, meaning different sizes and surface areas, which may affect the laser desorption/ionization efficiency.

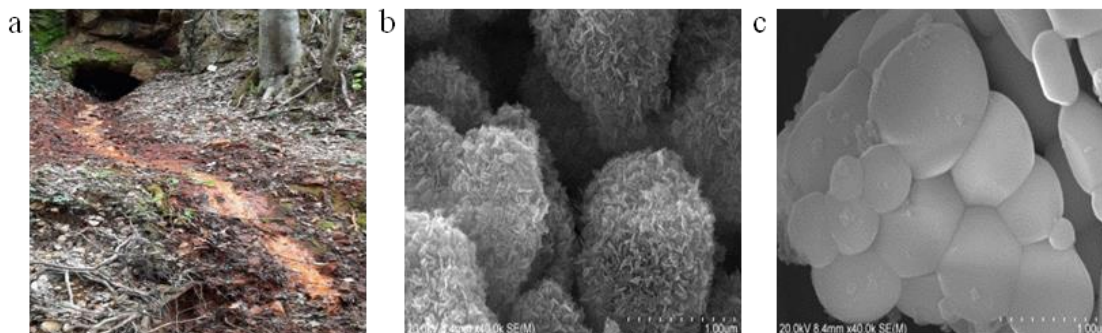


**Figure 1.** a) An drainage called Red Well at the locality Devil's town, South Serbia; b) and c) SEM images of dried and sieved sample.

The positive mode LDI mass spectra were recorded in the  $m/z$  range 20-200 (**Figure 2**).

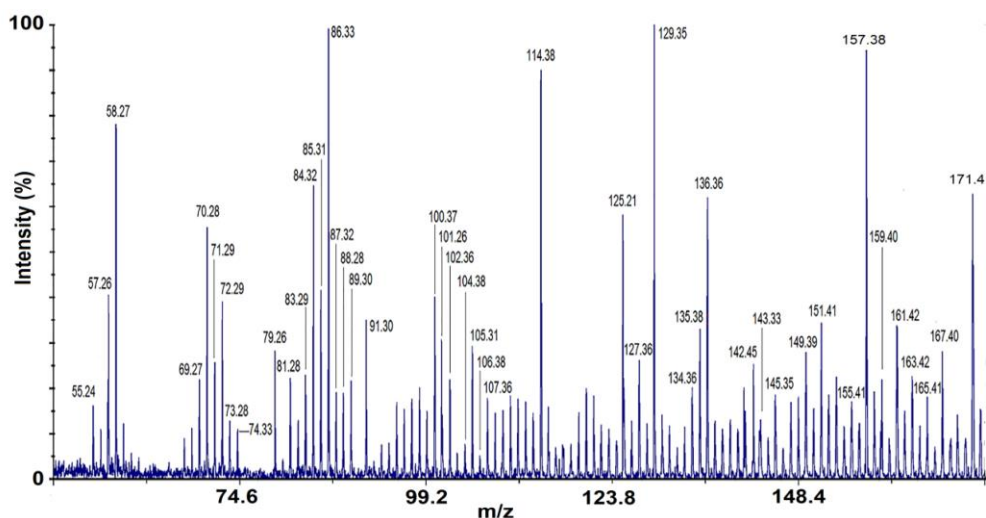


**Figure 2.** The positive mode LDI mass spectra of the sample. Conditions: positive ion mode, laser energy of 3400 a.u.

A numerous positively charged  $\text{FeO}^+$ ,  $\text{FeO}_2^+$ ,  $\text{FeO}_3^+$ ,  $\text{Fe}_2\text{O}^+$ ,  $\text{Fe}_2\text{O}_2^+$ ,  $\text{Fe}_3\text{O}_3^+$  and their hydrogen adducts suggests the presence  $\text{Fe}_2\text{O}_3$  and  $\text{Fe}_3\text{O}_4$  oxide in the sample. Ions of  $(\text{FeH})_2^+$ ,  $\text{FeO}(\text{OH})_2^+$ ,  $\text{Fe}(\text{OH})_3^+$ ,  $\text{Fe}_2(\text{OH})_2^+$ ,  $\text{Fe}_3\text{O}(\text{OH})_2^+$  originates from these iron oxides, too. The specific dominant ion species is identified as  $\text{FeCrO}_4\text{H}^+$  at  $m/z$  173.40, while the positive ions at  $m/z$  155.41 (calcd 155.86), 157.38 (calcd 156.87), 171.41, and 189.39 (188.86) is identified as  $\text{FeCrO}_3^+$ ,  $\text{FeCrO}_3\text{H}^+/\text{FeCrO}_2(\text{OH})^+$ ,  $\text{FeCrO}_4^+$ , and  $\text{FeCrO}_4(\text{OH})^+$ .

Similar to previous, presence of  $\text{Cr}^{2+}$  and vast of  $\text{Cr}_x\text{O}_y^+$  ( $x=1-3$ ,  $y=2-9$ ) cluster ions indicates the presence chromium Cr(III) and Cr(VI) oxide. Because the formation of hydride and hydrated type ions, e.g.,  $\text{MH}^+$  and  $\text{M}(\text{H}_2\text{O})^+$  are expected in the mass spectrum, it can be concluded that the positive

ions such as  $\text{CrO}(\text{OH})^+$ ,  $\text{CrO}(\text{H}_2\text{O})^+$ ,  $\text{CrO}(\text{OH})_4^+$ ,  $\text{Cr}_2\text{O}_2(\text{OH})^+$ ,  $\text{Cr}_3\text{O}_6\text{H}^+/\text{Cr}_3\text{O}_6(\text{OH})^+$ ,  $\text{Cr}_3\text{O}_7(\text{OH})_2^+/\text{Cr}_3\text{O}_8(\text{OH})\text{H}^+$ , also originated from  $\text{Cr}_2\text{O}_3$  and  $\text{CrO}_3$  oxide.

The signals observed in the positive mode LDI mass spectrum in the Figure 2 are listed in **Table 1**.

**Table 1.** Overview of ion species generated by the positive mode LDI MS from the sample from The Devil's Town (Natural Landmark in the Republic of Serbia).

<i>IONS</i>	<i>m/z</i> of the most abundant isotopic peak with their theoretical values	<i>IONS</i>	<i>m/z</i> of the most abundant isotopic peak with their theoretical values
$\text{CrOH}^+$	69.27 (68.94)	$\text{Fe}(\text{OH})_3^+$	107.36 (106.94)
$\text{Cr}(\text{H}_2\text{O})^+$	70.28 (69.95)	$(\text{FeH})_2^+$	114.38 (113.88)
$\text{FeO}^+$	72.29 (71.93)	$\text{FeO}(\text{OH})(\text{H}_2\text{O})_2^+$	125.21 (124.95)
$\text{FeOH}^+$	73.28 (72.94)	$\text{Fe}_2\text{O}^+$	127.36 (127.86)
$\text{Fe}(\text{H}_2\text{O})^+$	74.33 (73.95)	$\text{Fe}_2\text{OH}^+$	129.35 (128.87)
$\text{CrO}_2^+$	84.32 (83.93)	$\text{Cr}_2\text{O}_2/\text{CrO}(\text{OH})_4$	136.36 (135.95)
$\text{CrO}_2\text{H}^+$	85.31 (84.94)	$\text{Fe}_2\text{O}_2^+$	143.33 (143.86)
$\text{CrO}(\text{OH})\text{H}^+$	86.33 (85.95)	$\text{Fe}_2(\text{OH})_2^+$	145.33 (145.88)
$\text{FeO}_2^+$	88.28 (87.92)	$\text{Cr}_2\text{O}_3^+$	151.41 (151.86)
$\text{FeO}_2\text{H}^+$	89.30 (88.93)	$\text{Cr}_2\text{O}_3\text{H}^+$	153.41 (152.87)
$\text{AlO}_4^+$	91.31 (90.96)	$\text{FeCrO}_3^+$	155.41 (155.86)
$\text{CrO}_3^+$	100.37 (99.92)	$\text{FeCrO}_3\text{H}^+$	157.38 (156.87)
$\text{CrO}_3\text{H}^+$	101.37 (100.97)	$\text{Cr}_2\text{O}_4^+$	167.40 (167.86)
$\text{Al}_2\text{O}_3^+$	102.36 (101.95)	$\text{FeCrO}_4^+$	171.41 (171.86)
$\text{FeO}_3^+$ or $\text{Cr}_2^+$	104.38 (103.92/103.89)	$\text{FeCrO}_4\text{H}^+$	173.40 (172.86)
$\text{FeO}_3\text{H}^+$	105.31 (104.93)	$\text{Cr}_2\text{O}_5^+$	183.42 (183.86)
$\text{FeO}(\text{OH})_2^+$	106.38 (105.94)	$\text{Cr}_2\text{O}_6^+$	199.45 (199.85)

Finds of various ferrous/ferric oxide and oxide-hydroxide ions corresponds to ICP-OES elemental analysis results since the iron concentration is found to be 48 mass percentages, meaning about 70% of iron oxide.

Group of detected Fe-Cr-based (hydro)oxide and Cr-based (hydro)oxide ions confirmed by found chromium content of 1.25 ppm which gives Cr/Fe mass ratio of 0.25%. However, even measured in quantities of 1.25 and 2.5 ppm, Mn and Mg were not recorded in mass spectra under the conditions applied. The same is valid for phosphorous measured to be 3.5 ppm. However,  $\text{Al}_2\text{O}_3^+$  and  $(\text{AlO})_3(\text{SiO}_3)_3(\text{H}_2\text{O})_4^+$  ions are identified in the positive mode mass spectrum and, the aluminum content of 2.3 ppm is determined by ICP-OES.

As is known from the literature during its crystallization iron (hydr)oxides could immobilize heavy metal ions by process strongly dependent on pH in surrounding environment. Chromium as Cr(VI) immobilizes forming a complex compound with hydroxyl groups of goethite, a common natural iron oxide hydrate [4]. This fact explains presence of Fe-Cr (hydro)oxide ions in the mass spectra but not Mn and Mg. The mineral goethite makes up the largest part in the sample composition as confirmed by FTIR spectroscopy.

## CONCLUSION

In this work, it has been demonstrated the possibilities of the positive mode LDI-TOF-MS technique for the identification complex composition of the natural sample of ochre from the Devil's Town. It was interestingly found that the positive ions of Fe-Cr based (hydr)oxides found in the mass spectra says about the chromium origin and its chemical bonding in the mineral. It is also possible to obtain indications of the geochemical processes in the environment from which the sample originates. Finally, the sample ochre mineral as a pigment can be classified.

## *Acknowledgement*

This work was financed by the Ministry of the Education, Science and Technological Development of the Republic of Serbia, the contracts No 451-03-9/2021-14/ 200017

## REFERENCES

- [1] R. Siddall, Minerals, 2008, **8**(5), 201.
- [2] J. N. Robertson-Honecker, N. Zhang, A. Pavkovich, F. L. King. J. Anal. At. Spectrom., 2008, **23**, 1508.
- [3] A. T. de Ville d'Avray, E. E. Carpenter, C. J. O'Connor, R. B. Cole, Eur. Mass.Spectrom., 1998, **4**, 441-449.
- [4] X. Wang, N. Chen, L. Zhang, Environ. Sci.: Nano, 2019, **6**, 2185.

## DEVELOPING OF A METHOD FOR DETERMINING ASCORBIC ACID USING A SMARTPHONE AS A DETECTOR

A. Ivanković<sup>1</sup>, A. Martinović Bevanda<sup>2</sup>, M. Pehar<sup>2</sup>, A. Stipanović<sup>1</sup>, S. Talić<sup>2</sup> and D. Petrović<sup>1</sup>

<sup>1</sup> University of Mostar, Faculty of Agronomy and Food technology,

Biskupa Čule bb, 88000 Mostar, Bosnia and Herzegovina. (anita.ivankovic@apf.sum.ba)

<sup>2</sup> University of Mostar, Department of Chemistry, Faculty of Science and Education, Bosnia and Herzegovina, Matice hrvatske bb, 88000 Mostar, Bosnia and Herzegovina

### ABSTRACT

The development of a method for the determination of ascorbic acid based on the reaction with Cu (II) -neocuproin using a smartphone is described. The absorbance of the reaction solution prepared from Cu (II) -neocuproin solution and standards / samples at a wavelength of 458 nm was measured spectrophotometrically. The solutions in the cuvettes were then imaged using a smartphone. The samples in the cuvettes were placed on a white background and photographed in daylight. During spectrophotometric and smartphone determination, ascorbic acid achieved a linear dynamic range of  $2 \times 10^{-5}$  -  $1 \times 10^{-3}$  mol L<sup>-1</sup>. The analytical usability of the method was checked, using a spectrophotometer and a smartphone, in the analysis of real samples.

### INTRODUCTION

Smartphones besides telecommunication services have many different application possibilities. Today, they are increasingly used as cameras.

The main trends in the development of analytical instrumentation include the design of measuring instruments that are able to provide as much analytical information about the analyzed material, but at the same time simplify and reduce analytical instruments to possible use directly by users without specialized training. The use of mobile phones in the modification of analytical devices for remote and personal use can be considered a very effective way to improve access to personal analytical devices, for example in bioanalytical applications, biosensors based on smartphones, and the integration of fluid microdevices and smartphones [1, 2].

L-ascorbic acid or vitamin C (L-threo-hex-2-enone-1,4-lactone) is a water-soluble vitamin with pronounced antioxidant properties. It is found in a variety of fruits and vegetables such as oranges, lemons, pomegranates, cabbage, broccoli, peppers, kale, potatoes. It is one of the first isolated vitamins. Ascorbic acid participates as a cofactor of two enzymes, prolyl hydroxylase and lysyl hydroxylase. These two enzymes are responsible for the hydroxylation of lysine and proline in collagen, resulting in hydroxyproline and hydroxylysine which are important in stabilizing bonds in collagen. In the absence of ascorbic acid, the stability of collagen is disturbed and scurvy occurs [3].

The aim of this paper is to optimize the method of determining ascorbic acid using a smartphone, and then test the application of the method in the analysis of real samples. Based on the obtained results, an attempt will be made to show the possibility of replacing the spectrophotometer with a smartphone.

### METHODS

The preparation of twelve 50 mL plastic measuring cuvettes, in which we prepared the following concentrations of standards:  $2 \times 10^{-5}$ ,  $3 \times 10^{-5}$ ,  $6 \times 10^{-5}$ ,  $8 \times 10^{-5}$ ,  $1 \times 10^{-4}$ ,  $2 \times 10^{-4}$ ,  $3 \times 10^{-4}$ ,  $4 \times 10^{-4}$ ,  $6 \times 10^{-4}$ ,  $8 \times 10^{-4}$ ,  $1 \times 10^{-3}$ ,  $1 \times 10^{-2}$ . The stock solution to prepare these working solutions is  $1 \times 10^{-3}$  mol L<sup>-1</sup>. Then prepare reaction solutions of 2 mL of standard, 2 mL of reagent and make up the residue to a total volume of 5 mL with buffer, pH = 5. Reaction solutions were prepared in 15 mL plastic cuvettes. The

absorbance measured in the visible part of the electromagnetic radiation at a wavelength of 458 nm. The obtained values are recorded and the calibration direction is created on the computer in Excel.

The optimal conditions for taking photographs of the prepared reaction solutions were determined. The cuvettes were photographed on a white clean background in daylight and laboratory lighting. The cuvettes were placed against the background and the mobile device was placed at a distance of  $12 \text{ cm} \pm 2 \text{ cm}$ . After the cuvettes are photographed, the values of the three channels (R, G and B) can be obtained in the RGB program, which is installed on the mobile device [4]. A calibration direction is created in Excel.

When two graphs are obtained based on the described experiments, they were compared based on the repeatability, the slope of the direction, and the R-value (which must be in the range of 0.900 - 0.999).

For real samples, pharmaceutical preparations of ascorbic acid tablets, vitamin C (500 mg), (manufacturer Alkaloid Skopje), and BioC (500 mg), (Dietpharm, manufacturer Fidifarm) were used. Bio C 500 tablets contain bioflavonoids, natural substances from plants that significantly enhance the positive effects of vitamin C.

The mass of 5 tablets is calculated and the average mass of one tablet is calculated. The average mass of each tablet is 0.54624 g, which is dissolved in a 50 mL volumetric flask in distilled water. From this solution we made a working solution. The working solution was prepared with the addition of neocuproin and supplemented with buffer  $\text{pH} = 5$  to a total volume of 5 mL.

In preparing the film tablet sample solution, additional comminution and filtration of the sample stock solution was required.

## RESULTS AND DISCUSSION

The results of the experiments indicate very small differences in the measurements obtained with the spectrophotometer and the smartphone. Linearity was obtained between the measured signal and the concentration in the same concentration range. It cannot be claimed that one method is more accurate or precise than the other. The errors observed in the results are a combination of random and systematic errors that are part of each measurement, and cannot be exclusively attributed to the shortcomings of the selected detectors.

**Table 1.** Comparison of results obtained using spectrophotometer and using a smartphone

	Taken, $\text{mol L}^{-1}$	Added, $\text{mol L}^{-1}$	Utilization, %	
			Spectrophotometer	Smart phone
Vitamin C	$2,227 \times 10^{-4}$	$1,136 \times 10^{-4}$	95,90%	96,12%
Alkaloid		$1,136 \times 10^{-3}$	92,31%	92,02%
BioC		$1,136 \times 10^{-2}$	89,31%	90,21%
Dietpharm	$2,227 \times 10^{-4}$	$1,136 \times 10^{-4}$	73,05%	88,96%
		$1,136 \times 10^{-3}$	86,52%	93,34%
		$1,136 \times 10^{-2}$	75,93%	91,12%

Under the same optimal reaction conditions, yields of 109.2% and 146.6% were obtained when using a spectrophotometer as a detector, and 111.8% and 152.21% when using a smartphone.

In the field of economy, maintenance, device calibration, device size, device radiation, the smartphone can very easily replace the spectrophotometer. However, there are currently no suitable software that can facilitate the processing of results, ie images, with the aim of collecting qualitative

and quantitative information. Software for analytical determinations is being developed using smartphones that will give quality results in a very short time. The method can be further optimized and should not be neglected as we are in the age of modern mobile phones and at this time several billion people are using mobile phones for various purposes.

## CONCLUSION

A simple and inexpensive method for the determination of L-ascorbic acid based on the reaction with neocuproin was developed and applied, using a spectrophotometer and a smartphone as detectors. Conditions were optimized: pH, volume of added reagent, volume of added analyte, possible interferences were tested. Under optimally selected conditions, LDP was achieved:  $1 \times 10^{-5} - 1 \times 10^{-3}$  mol L<sup>-1</sup> for both detectors used. The method has shown satisfactory applicability in the analysis of real samples. Vitamin C, an Alkaloid, has shown better yield, a possible reason for this is the lower probability of error simpler matrix. Bio C contains additional substances, such as bioflavonoids, that have shown an interfering effect.

## Acknowledgement

This work was supported by the Federal Ministry of Education and Science of the Federation of Bosnia and Herzegovina (Grants No. 05-39-22637-2/19, November 4<sup>th</sup> 2019).

## REFERENCES

- [1] D., Hernández, J., Marty and R., Guerrero, Smartphone as a Portable Detector, Analytical Device, or Instrument Interface, InTech, 2017, DOI: 10.5772/intechopen.69678.
- [2] N., Kallay, S., Žalac, D., Kovačević, T., Peročanin and A., Čop, Physico-chemical practicum, Department of Physics and Chemistry, Department of Chemistry, Faculty of Science, University of Zagreb, 2002.
- [3] L., Pachla, D., Reynolds and P., Kissinger, Analytical Methods for Determining Ascorbic Acid in Biological Samples, Food Products, and Pharmaceuticals, Journal of Association of Official Analytical Chemists, Vol 68, Iss 1, 1985, pp 1–12, <https://doi.org/10.1093/jaoac/68.1.1>.
- [4] M., Pohanka, Photography by Cameras Integrated in Smartphones as a Tool for Analytical Chemistry Represented by an Butyrylcholinesterase Activity Assay, Sensors, 15, 13752-13762, 2015, doi:10.3390/s150613752

## GC/MS PESTICIDES ANALYSIS IN APPLE PEEL: A METHOD FOR WAXES ELIMINATION

D. Anđelković<sup>1</sup> and M. Branković<sup>2</sup>

<sup>1</sup> *University of Niš, Agricultural Faculty, Kosančićeva 4, 37000 Kruševac, Serbia*

<sup>2</sup> *University of Niš, Faculty of Sciences and Mathematics, Department of Chemistry, Višegradska 33, 18000 Niš, Serbia (milica.chem@outlook.com)*

### ABSTRACT

Apple peel as a natural barrier can retain some amount of applied pesticides and thus serve as an indicator of their presence. This study was conducted to establish a sample preparation method for GC/MS pesticide residue analysis in apple peel, which results in the elimination of waxes. The developed procedure is time- and cost-effective and does not implement the usage of sorbent or any other expensive consumables.

### INTRODUCTION

Apple peel represents a significant part of a consumers' diet. It is a source of a range of phenolic acids, such as chlorogenic, caffeic, p-coumaric and protocatechuic acids [1] and shows potent antioxidant and antiproliferative activity, likely linked to the triterpenes, since these are mostly found in peels [2].

Apple peel is frequently exposed to pesticide treatment, especially in the latest stages of the IPM practice. Since it has barrier properties, peel can accumulate most of the applied pesticides. Thus, the analysis of a peel, instead of whole fruit, can give an indication of the pesticide residue level.

The aim of this study was to establish and evaluate a rapid method for pesticide residue analysis by GC-MS in apple peel. The fact that usual extractors in GC/MS-based analysis are water-immiscible solvents, such as hexane, dichloromethane, or dimethyl ether, places a problem on the start since the extraction of peel results in the high amount of co-extracted waxes. Beside the potential effect on analyte(s) response and thus the quantification – which is known as the matrix effect – a significant amount of low-volatile waxes can cause instrument performance troubles such as column overload or even blocking. This study also explored the effectiveness of simple physical processes, such as freezing, in the removal of waxes, contrary to the widely implemented practice of sorbent employment.

### METHODS

#### Sample preparation procedure

**Extraction procedure.** Water (20 mL) was added to the peel portion ( $10 \pm 0.1$  g) and blended. The sample was quantitatively transferred to a glass container with an additional 5 mL of water. Afterward, solvent extraction was performed with hexane (two 10 mL portions). The organic phase was separated from the solids-water dispersion by centrifugation (5 min/3500 rpm).

**Clean-up procedure.** Hexane extract (10 mL) was evaporated to dryness under a stream of nitrogen, in a water bath set at 40°C. Methanol (1 mL) was added to the solid residue and left for 10 min. Afterward, it was mixed on a vortex (1 min), stored in freezer at -15°C (30 min), filtered (0.45 µm microfilter) and analyzed.

## Instruments

**GC/MS analysis.** The gas chromatographic analysis was performed on Agilent 6890 gas chromatograph equipped with a 5973 Mass Selective Detector (MSD) and 7683 autosampler and SGE 25QC2/BPX5 0.25 capillary column (25m×0.22mm×0.25μm, non-polar). Both data acquisition and processing were completed by Agilent MSD ChemStation® D.02.00.275 software.

## RESULTS AND DISCUSSION

The non-cleaned hexane extract of apple peel contains high amounts of compounds with aliphatic chain fragments (retention times 8.10 and 12.38 min), as confirmed by the mass spectra (Figure 1). These compounds can be recognized as groups of waxes that usually prevail in the peel. Many wax compounds were identified in the apple peel, among them hydrocarbons, sterols, terpenes, and fatty acids [3,4].

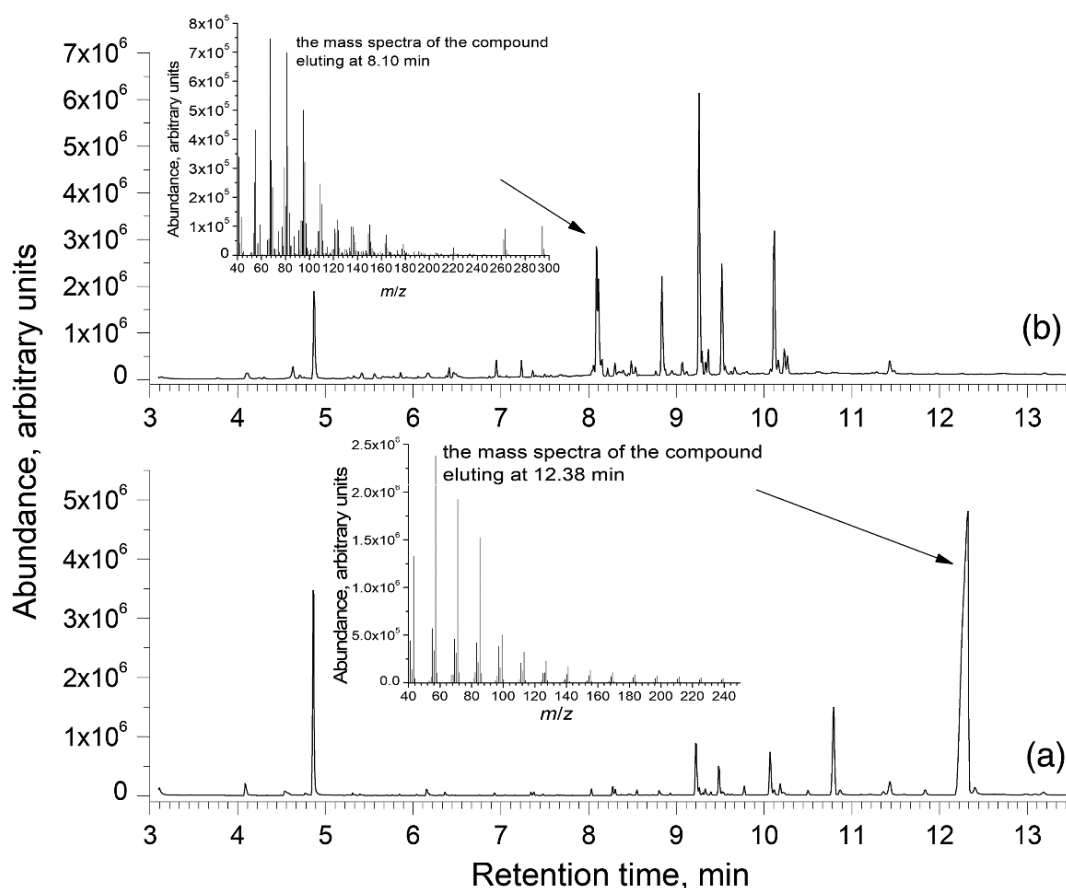


**Figure 1.** Chromatograms of nonfortified Idared peel extract prior (a) and after the SE/LTP step (b) in scan acquisition mode.

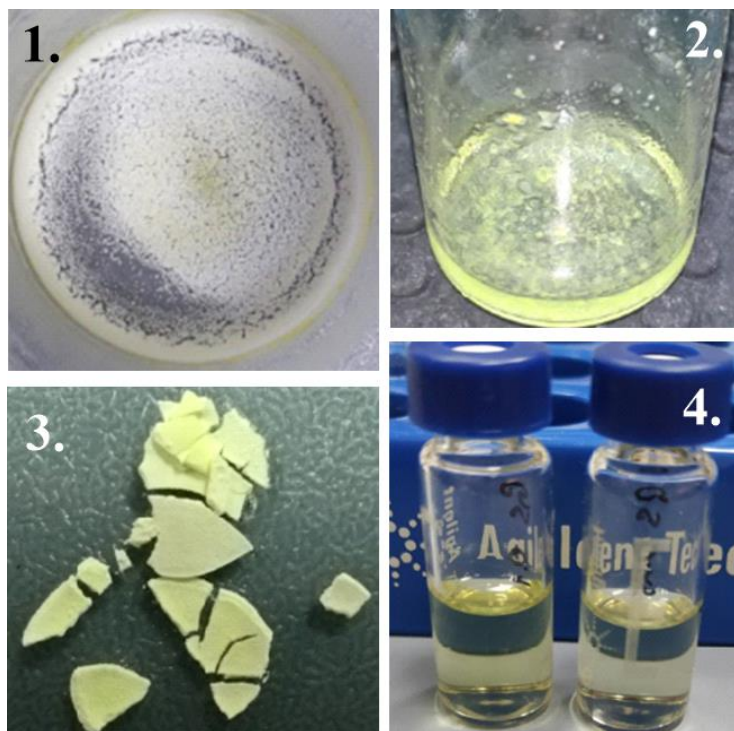


**Figure 2.** Illustration of the SE/LTP step: 1. After the evaporation; 2. After the methanol addition; 3. The removed precipitate (waxes); 4. Final peel extract.

The main goal of the sample preparation procedure was to eliminate low-volatility waxes to assist GC column performance, *i.e.*, to prevent column blocking or contamination.

The sample preparation procedure consisted of two steps: solvent exchange and low-temperature precipitation by freezing. Freezing enables partial removal of some co-extractives with limited solubility in polar solvents, and it initiates solidification and precipitation of most fats and waxes [5].

After the hexane–methanol exchange, the dry residue did not completely dissolve in methanol, *i.e.*, a white-coloured deposit remained in the solution (Figure 2-2). After the freezing, the amount of deposit increased, leading to the complete removal of waxes (Figure 2-3), which can also be evidenced in the chromatogram by the disappearance of aliphatic compound peaks (Figure 1).

## CONCLUSION

The developed sample preparation procedure consisted of the hexane-to-methanol exchange and subsequent low-temperature precipitation by freezing. The combination resulted in the complete removal of the waxes from apple peel extract and thus eliminated the instrument performance problems. The sample preparation procedure does not implement the usage of sorbents; that is, it is cost-effective.

## Acknowledgement

This study was supported by the Ministry of Education, Science and Technological Development of the Republic of Serbia (contracts no. 451-03-9/2021-14/200383 and 451-03-9/2021-14/200124).

## REFERENCES

- [1] J. Lee, B. L. Chan, A. E. Mitchell, *Food Chemistry*, 2017, 215, 301–310.
- [2] J. Viškelis, N. Uselis, M. Liaudanskas, V. Janulis, P. Bielicki, T. Univer, D. Kviklys, *Zemdirbyste-Agriculture*, 2018, 105, 71–78.
- [3] J. Wu, H. Gao, L. Zhao, X. Liao, F. Chen, Z. Wang, X. Hu, *Food Chemistry*, 2007, 103, 88–93.

- [4] B. Klein, F. R. Thewes, A. Rogerio de Oliveira, A. Brackmann, J. S. Barin, A. J. Cichoski, R. Wagner, *Food Research International*, 2019, 116, 611–619.
- [5] K. Madej, T. K. Kalenik, W. Piekoszewski, *Food Chemistry*, 2018, 269, 527–541.

## CHARACTERISATION 1,4-DISUBSTITUTED 2,5-DIKETOPIPERAZINES BY ESI MASS SPECTROMETRY

F. Veljković<sup>1</sup>, R. Masnikosa<sup>1</sup>, B. Perić<sup>2</sup>, N. Pantalon Juraj<sup>2</sup>, J. Georgijević<sup>1</sup>, S. I. Kirin<sup>2</sup>, and S. Veličković<sup>1</sup>

<sup>1</sup>VINČA Institute of Nuclear Sciences - National institute of the Republic of Serbia, University of Belgrade, P.O.Box 522, 11001 Belgrade, Republic of Serbia. (filipveljkovic@vin.bg.ac.rs)

<sup>2</sup>Ruđer Bošković Institute, Bijenička cesta 54, HR-10000 Zagreb, Croatia

### ABSTRACT

The diketopiperazines have been steadily attracting researchers' attention in pharmaceutical chemistry due to their potential biological effects. Electrospray ionization mass spectrometry (ESI MS) is known to be a versatile analytical technique for detection of very low concentrations of various diketopiperazines in different samples. Hence, we characterized our p-disubstituted phenyldiketopiperazines **1** ( $R = H$ ), **2** ( $R = NO_2$ ) and **3** ( $R = -N(CH_3)$ ) by ESI MS. We have shown that the majority of the fragment ions in the ESI mass spectra originated from reactions initiated by one of the nitrogen atoms of the piperazine ring.

### INTRODUCTION

Ubiquitous in nature, bioactive cyclodipeptides, such as 2,5-diketopiperazines, are potential drug candidates because of their proven antibacterial, antiviral, herbicidal, and anticancer properties [1-4].

In our previous work, we have prepared three compounds: bis(phenyl)-2,5-piperazinedione (**1**),  $NO_2$ (**2**) and  $(CH_3)_2N$  (**3**) para-substituted analogues with the aim to study the electrophilic aromatic substitution effect on *para*- position of bis(phenyl)-2,5-piperazinediones. Their structures were characterized in detail using combined power of X-ray diffraction, solid-state NMR measurements, and DFT computations (NMR-crystallography) [5]. Their single-crystal structures showed asymmetry breaking in **1**, a symmetric structure in **2** and a disorder in **3**. Although we confirmed their identities using both ESI-MS and matrix-assisted laser desorption ionization (MALDI) MS [5], the analysis of their fragmentation(s) and potential dimerization in solution is lacking. To this end, we conducted a thorough analysis of the ESI mass spectra of 1,4-bis(4-(dimethylamino)phenyl)piperazine-2,5-dione (compound **1**); 1,4-bis(4 nitrophenyl)piperazine-2,5-dione (compound **2**), and 1,4-bis(4-(dimethylamino)phenyl)piperazine-2,5-dione (compound **3**). The information obtained herein can also be used to confirm the structures of the aforementioned compounds.

### METHODS

Mass spectra were acquired using triple quadrupole ESI MS instrument (Agilent Technologies 6420 QqQ, Agilent, USA). Compounds were dissolved in water-methanol 50:50 (v/v) mixture (HPLC grade methanol, miliQ water), at a concentration of 10 mg/mL. The instrument settings were as detailed previously [5].

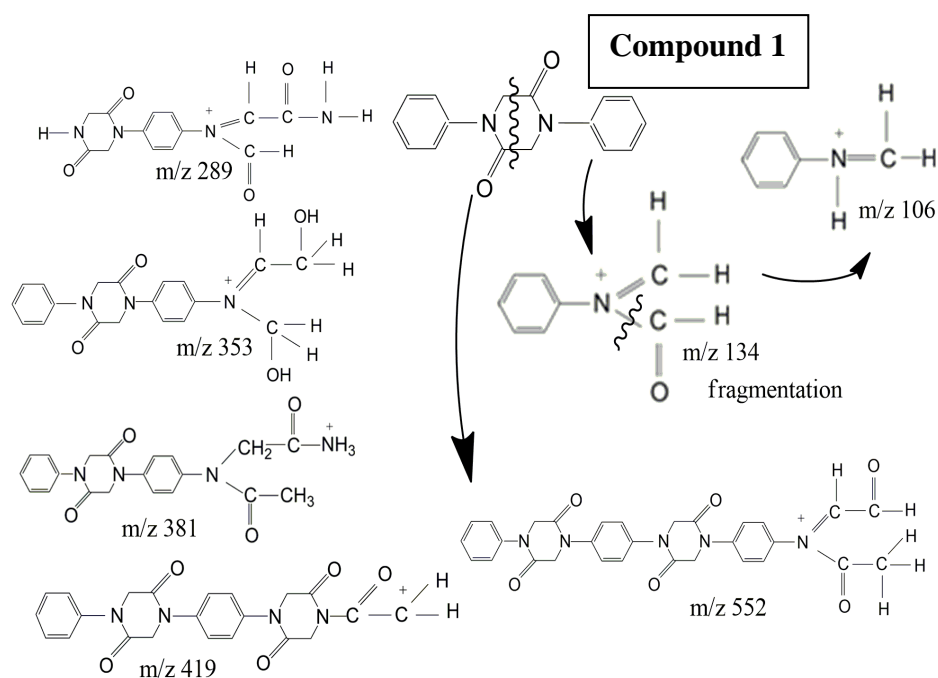
### RESULTS AND DISCUSSION

**Table 1.** displays  $m/z$  of ions produced by the ESI MS in the positive mode: compound **1**- $C_{16}H_{14}N_2O_2$ ,  $m/z$  266.1133, compound **2** -  $C_{16}H_{12}N_4O_6$ ,  $m/z$  356.0835, and compound **3** -  $C_{20}H_{24}N_4O_2$ ,  $m/z$  352.1978.

**Table 1.** List of  $m/z$  of ions obtained by the ESI MS in the positive mode for compounds **1**, **2** and **3**.

Compound 1		Compound 2		Compound 3	
$m/z$	intensity	$m/z$	intensity	$m/z$	intensity
106.1	62986.46	85.1	8333.76	133.2	46731.95
134.1	31619.44	239.2	6676.79	134.2	231521.23
<b>267.2*</b>	<b>325111.06</b>	267.3	11974.29	148.2	93076.55
268.2	68040.05	341.3	6098.14	149.2	48465.06
289.2	148325.80	353.3	19519.82	162.2	168952.30
290.2	28904.46	364.3	7676.46	164.2	48050.20
353.3	33476.13	381.3	20225.43	169.7	99561.70
381.3	33724.99	397.3	6235.02	179.2	51624.39
419.2	27281.88	415.3	8614.17	<b>353.3*</b>	<b>633195.19</b>
552.2	28639.02	443.3	7714.58	354.3	155874.31

The possible routes to generation of ions listed in Table 1 are shown in **Figure 1**, **Figure 2**, and **Figure 3**.

**Figure 1.** Proposed routes to fragment and dimer ions derived from 1,4-bis(4-(dimethylamino)phenyl)piperazine-2,5-dione (compound 1).

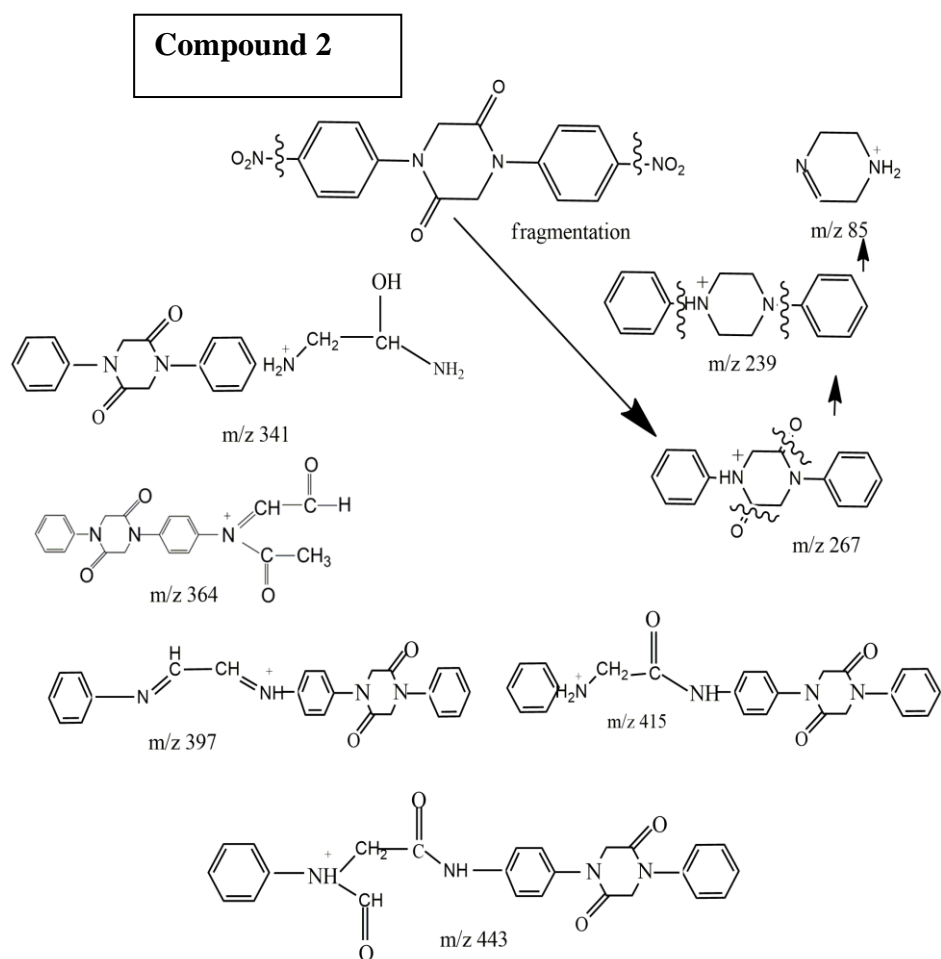


**Figure 2.** Proposed routes to fragment and dimer ions derived from 1,4-bis(4-nitrophenyl)piperazine-2,5-dione (compound 2).

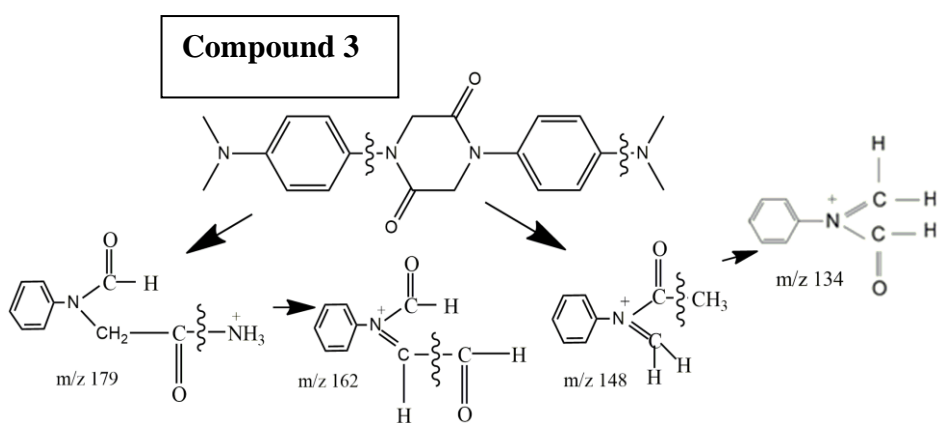


**Figure 3.** Proposed routes to fragment and dimer ions derived from 1,4-bis(4-(dimethylamino)phenyl)piperazine-2,5-dione (compound 3).

The protonated molecular ions,  $[M+H]^+$ , detected in the spectra of **1** and **3**, are marked with an asterisk.  $[M+H]^+$  were not detected in the spectra of **2**.

Only two fragment ions derived directly from **1** were detected. Other fragment ions in the spectra of **1** were most likely formed by fragmentation of its dimer (**Figure 1**). The absence of  $[M+H]^+$  ion in the spectra of **2** indicates its instability under the applied ESIMS conditions. However, both the ion at  $m/z$  267 (compound **2** lacking both  $\text{NO}_2$  groups) and its fragment ions were detected. Fragment ions derived from the corresponding dimers were also identified (**Figure 2**). In the case of **3**, we found not only the  $[M+H]^+$  ion but also four fragments (**Figure 3**).

## CONCLUSION

In the ESI mass spectra of p-disubstituted phenyldiketopiperazines **1** ( $R = H$ ), and **3** ( $R = -\text{N}(\text{CH}_3)$ ) both their fragment ions and the fragment ions derived from their dimers were identified. Nitro groups make 1,4-bis(4 nitrophenyl)piperazine-2,5-dione unstable under the ESIMS conditions.

## Acknowledgement

This work was partially supported by the Ministry for Science of the Republic of Serbia (grant no. 451-03-9/2021-14/200017) and in part by the Croatian-Serbian bilateral project (grant no. 337-00-205/2019-09/17).

## REFERENCES

- [1] S. Hirano, S. Ichikawa, A. Matsuda, *Bioorg. Med. Chem.*, 2008, **16**, 428-436.
- [2] E. Van Der Merwe, D. Huang, D. Petersen, G. Kilian, P. J. Milne, M. Van de Venter, C. Frost, *Peptides*, 2008, **29**, 1305-1311.
- [3] R. R. King, L. A. Calhoun, *Phytochemistry*, 2009, **70**, 833-841.
- [4] S. Sinha, R. Srivastava, E. D. Clercq, R. K. Singh, *Nucleosides, Nucleic Acids*, 2004, **23**, 1815-1824.
- [5] B. Perić, N. PantalonJuraj, G. Szalontai, S. R. Veličković, F. M. Veljković, D. Vikić-Topić, S. I. Kirin, *J. Mol. Structure*, 2021, **1234**, 130157-130166.



*Author index*



Abakumov A.A.	122	Bubanja I.N.	238, 445
Abazović N.	143, 147, 180	Bychko I.B.	122
Abramović B.	143, 147	Caballero A.	193
Aćimović D.	283, 287	Cherkezova-Zheleva Z.	109
Agan B.	493	Cvetković V.S.	275, 279
Agbaba D.	675	Cvjetičanin N.	291
Ajduković M.	151, 187, 388	Červený J.	236
Aleksić M.	294	Čolović M.B.	406, 410, 414
Aleksieva K.	167, 174, 177	Čomor M.	143, 147, 180
Amić A.	129	Čučulović A.	561
Anđelković D.	624, 688, 716	Čučulović R.	561
Anđelković T.	612, 616, 620	Čudina O.	294
Anićijević V.	547	Čupić Ž.	199, 246, 254
Antić B.	483	Ćirić-Marjanović G.	121
Antić N.	569	Ćurčić M.	705
Antonijević M.	347, 351, 355	Daković A.	380, 525
Antonijević Nikolić M.	645, 648	Danilov P.A.	369
Armaković S.	143, 147	Despotović V.	143, 147
Aroguz A.Z.	489, 493	Devečerski A.	580, 584, 588
Ashkenasy G.	18	Devic G.	533, 537
Avdalović J.	551, 554, 695	Dietrich J.W.	215
Avdović E.	95, 351, 355	Dimić D.	95, 99, 316
Bajuk-Bogdanović D.	121, 418, 445	Dimitrić Marković J.M.	95, 129, 316
Baldinelli L.	10	Dimitrijević A.	592, 600
Bandela A.K.	18	Dinić I.	399
Banković P.	132, 184, 388	Dobričić V.	294
Bartolić D.	336	Dojčinović B.	184, 483
Bartolomei B.	10	Dostanić J.	155, 159
Barudžija T.S.	275	Dragić M.	320
Barykin A.V.	47	Dragičević V.	681
Bašćarević Z.	438	Drakulić D.	25, 308, 324, 572
Bassil B.S.	121	Dražić B.	645, 648
Bauman Yu.	115	Džambaski Z.	328, 332
Beškoski V.	445	Džunuzović E.	501
Blagojević D.	25	Džunuzović J.V.	497, 501, 505
Blagojević Filipović J.P.	61, 103	Đorđević D.M.	512
Blagojević J.	139	Đorđević I.	132
Blagojević S.M.	639	Đorđević N.	308, 699
Blagojević S.N.	298, 639, 692	Đorović J.	351
Blagojević V.A.	359	Đorović Jovanović J.	99, 347
Bogdanović D.	612, 616, 620	Đurkić T.	529, 541, 569
Bojić A.	468, 472, 476	Egerić M.	580, 584
Bojić D.	472, 476	Erceg T.	489
Bondžić A.M.	328, 332	Escosura A.	18
Bondžić B.P.	114, 328, 332	Feldhaus D.	275
Boshkov N.	190	Filipović N.	572
Boshkova N.	190	Filipović Tričković J.	442
Božić B.	92, 705	Finčur N.	143, 147
Brankov M.	681	Friedrich B.	275
Branković M.	624, 688, 716	Fulczyk A.	208, 261
Brborić J.	294	Gabrovska M.	163
Brdarić T.	283, 287	Gajski G.	414
Brkljačić J.	480	Gaković B.	369

Gašić U.	692	Jović-Jovičić N.	151, 187, 465
Gavrilov N.	294, 301	Kačarević-Popović Z.	426, 434
Gavrilović L.	308	Kadinov G.	167, 174
Gentili P.L.	10	Kalijadis A.	635
Georgijević J.	720	Kaluđerović G.	95
Gerić M.	414	Kaluđerović G.N.	23
Gizdavić-Nikolaidis M.	445	Kandić I.	576
Gojgić-Cvijović G.	445	Kapustin R.V.	62, 66
Goldbeter A.	3	Karakirova Y.	163, 177
Górecki J.	201	Katnić Dj.	442
Govedarica M.	565	Khan M.S.	135
Govedarica O.	139, 489	Khattak R.	135
Grce A.	438, 442	Kholdeeva O.A.	121
Grinvald I.I.	62, 66	Kijevcanin M.	596
Grković I.	25, 320, 324	Kirin S.I. 110,	720
Grujić D.	395	Knežević N.Ž.	480
Grujić M.	675	Knyazev A.V.	43, 47
Grujić S.	430, 541, 569	Knyazeva S.S.	43
Gulicovski J.	576	Kocić G.	616, 620, 688
Gusarova E.V.	43	Kodranov I.D.	480, 483, 604
Gusevac Stojanović I.	52, 324, 572	Kokunešoski M.	438, 442
Gvozdić E.	541	Kolar-Anić Lj.	199, 246, 250
Habuda-Stanić M.	465	Kolev H.	163, 174, 193
Hakky Mohammad A.	596	Konstantinović S.S.	685
Hauser M.J.B	4	Korićanac L.	699
Hercigonja R.	291	Kortz U.	121, 406, 410, 414
Holgado J.P.	193	Kostić B.	612
Ignjatović Lj.	692	Kostić I.	612, 616, 620
Ilić I.	187, 465,	Kostić M.	468, 472, 476
Ilić M.	533, 554	Kowalska T.	208, 261
Ilić S.	438, 442	Kragović M.	576
Ionin. A.A.	369	Krajišnik D.	525
Isaković A.	406, 410	Krasheninnikova O.V.	47
Ivanković A.	713	Kretić D.S.	661
Ivanović T.	51	Krpić M.	604
Ivanović-Šašić A.	184, 187, 199, 246	Krstić A.	635
Janićijević D.	418	Krstić D.Z.	406, 410, 414
Janjić G.	132	Krstić J.	151, 163
Janković B.	705	Krstić N.S.	457
Janković M.	139	Krstić S.	580
Janković-Častvan I.	399, 529	Kudryashov S.I.	369
Janošević D.	312	Kumrić K.	580, 584, 588
Janošević Ležaić A.	301	Kusutkina A.M.	43
Ječmenica Dučić M.	283, 287	Kuzmanović M.	74, 74, 82
Jerala J.	21	Lacin D.	489, 493
Jevremović A.	418, 422	Lađarević J.	92
Jocić A.	592, 600	Lamueva M.	658
Joksimović K.	551	Łata E.	208, 261
Joksović Lj.	449	Lazarević M.	143, 147
Jovanović D.	332	Lazarević-Pašti T.	544, 547
Jovanović M.	258	Leach J.	242
Jović A.	291	Lente G.	123
Jovićević J.N.	275, 279	Leskovac A. R.	332

Lindeboom R.	170	Milenković D.	129, 347, 351
Lješević M.	445	Miletić J.	308
Logacheva A.S.	43	Miletić S.	533
Lolić A.	635	Milić J.	551, 554, 695
Lončar A.	269, 316	Milićević J.	592
Lončarević B.	445	Milojević Rakić M.	418, 422
Lončarević D.	155, 159	Milojković J.	551
Lopičić Z.	551	Milošević I.R.	384, 521
Lugonja N.	551, 554, 695	Milošević K.	159
Lukić M.	551	Milovanović B.	151, 388
Lutsyk V.	658	Milovanović D.	369
Ma T.	406, 410, 414	Milovanović M.R.	61
Ma X.	406, 410, 414	Milutinović-Nikolić A.	132, 151, 187
Maćešić S.	199, 250, 254	Minić D.M.	402
Machado T.D.	399	Minić D.M.	402
Maksimchuk N.V.	121	Minović Arsić T.	635
Maksimović J.	70, 449	Mirković M.	635
Maksimović J.P.	269	Mishakov I.	115
Maksimović T.	449	Misirlić-Denčić S.	406, 410
Maksin D.	287	Mitrović A.Lj.	312
Malenov D.P.	61, 453	Mitrović J.	468, 476
Maletić M.	529, 628	Mitrović N.	25, 320, 324
Mančić L.	399	Mladenović M.	57
Manojlović D.D.	480, 604	Mojović Z.	180
Manojlović V.	258	Momčilović M.	283, 521
Marega C.	501	Morozova-Roche L.A.	307
Marić S.	592, 600	Mouille G.	312
Marinković B.A.	399	Mudrinić T.	132, 184, 388
Marinović S.	132, 184, 388	Murić B.	395
Marković B.M.	497, 501, 505	Muzika F.	201, 236
Marković D.M.	521	Najdanović S.	468, 472
Marković I.D.	521	Nastasović A.	497, 501
Marković M.	82, 380, 525	Nedeljković A.	576
Marković S.	399	Nedić N.	692
Marković Z.	129, 347, 351, 355	Nedić Vasiljević B.	418, 422
Martinović Bevanda A.	713	Nedić Z.	449
Martinović J.	25, 320, 324	Negrojević L.	269, 316
Maselko J.	33	Nešović M.	692
Masnikosa R.	720	Nestorović S.	561
Mašojević D.	391	Nikolić G.	612
Matić Bujagić I.	541	Nikolić G.M.	457, 665
Matijašević S.	430	Nikolić J.	430
Matković A.	384	Nikolić Lj.B.	509
Matović Lj.	584, 588	Nikolić M.G.	457, 665
Mau J.	20	Nikolić N.	298, 426, 434
Medaković V.M.	61	Nikolić Z.S.	373, 377
Mercader J.P.	8	Nikolova D.	163
Mihajlović S.	628	Ninković D.B.	61
Mijajlović M.	170	Nišić N.	576
Mijin D.	89, 92	Novakovic K.	230, 242, 250
Miladinović J.M.	51	Novaković T.	180, 184
Miladinović Z.P.	51	Obradović D.	671
Milanović Ž.	95, 347, 355	Obradović M.	380, 525

Ognjanović M.	483	Radović I.	705, 709
Oliwa P.	237	Radović Vučić M.	468, 472, 476
Omerašević M.	580	Radulović A.	369
Onjia E.	505	Radulović K.	151
Orlik M.	237	Rakić A.A.	99
Ostojić S.	483	Randjelović B.M.	373, 377
Otoničar M.	391	Ranković D.	74, 78, 82
Pagnacco M. 70,	449	Rašović A.	359, 363
Pajović S.B.	308, 699	Ristić M.	628
Panova A.A.	43	Ristić N.	576
Pantalon Juraj N.	720	Ristivojević N.	99
Pantelić D.	395	Rodić M.	645
Pantić N.	340	Rottinghaus G.E.	380, 525
Parac Vogt T.	328	Rupar J.	294, 301
Pavličević J.	139, 489, 493	Sadihov H.	18
Pavlović R.	612, 616, 620	Sajewicz M.	208, 261
Pehar M.	713	Sandić Z.P.	497, 505
Pejić B.	628	Savić B.	283, 287
Pejić N.	639	Savić Biserčić M.	82
Pejić S.	25, 308, 699	Savić D.S.	509, 512, 515
Perez-Merkader J.	8	Savić D.S.	515
Pergal M.	537	Savić S.R.	515
Pergal M.V.	480, 483, 604	Savić T.D.	143, 147, 180
Perić B.	720	Savić V.	430
Perić Grujić A.	628	Savović J.	74, 78, 82
Perović I.	283, 287	Schmitz G.E.	222
Petković M.	291	Schreiber I.	236
Petrović D.	713	Senčanski J.	70, 298, 449
Petrović Đ.	584, 588	Shipilova A.S.	43
Petrović M.	468, 472, 476	Shopska M.	167, 174
Plavšić M.B.	512	Shtereva I.	167, 174
Plavšić M.M.	509, 512, 515	Simić M.	681
Popadić M.	132	Simonović Radosavljević J.	312
Popović D.Ž.	51	Sinadinović-Fišer S.	139
Popović G.	671, 675	Smiljanić D.	380, 525
Popović N.	308	Smiljanić S.	430
Popović-Nikolić M.	671, 675	Spasić A.M.	258
Pošarc-Marković M.	438	Spasić S.	695
Potkonjak N.	544, 547	Spasojević D.	340
Premović P.I.	558, 608	Spasojević J.	426, 434
Prodanović O.	340	Spasojević M.	380, 525
Prodanović R.	340	Sretenović D.	95
Prokić D.	529	Stambolova I.	190
Prokopijević M.	336, 340	Stamenović U.	391
Pupazić J.	665	Stanisavljev D.	238, 445
Radaković N.	561	Stanković D.	483, 695
Radenković M.	565	Stanković I.M.	61
Radić N.	190	Stanković K.	588
Radić R.	565	Stanković M.	336
Radmilović M.	395	Stanković S.	580, 584
Radonjić V.	163	Stanojević A.	246
Radosavljević A.	426, 434	Stanojković A.	422
Radotić K.	312, 336, 340	Stanojković J.	561

Stefanović I.S.	497, 501, 505	Trivunac K.	628
Stefanović M.	685	Troter D.Z.	685
Stevanović G.	151, 388	Trtica M.	74, 82
Stipanović A.	713	Tsvetkov P.	163
Stjepanović M.	465	Uskoković Marković S.	418
Stoiljković M.	78, 705, 709	Uzelac M.	143, 147
Stojanovic M.N.	657	Valenta Šobot A.	442, 438
Stojanović Z.	572	Vasić Anićijević D.	283, 287
Stojić I.	78	Vasić B.	384
Stojiljković A.S.	246	Vasić M.M.	402
Stojiljković D.M.	685	Vedyagin A.	115
Stojiljković V.	308	Velić N.	465
Stojković Simatović I.	291, 298	Veličković S.	705, 709, 720
Stojmenović M.	576	Velinov N.	468, 472, 476
Stoyanova D.	190	Veljković D.Ž.	661
Strizhak P.E.	122	Veljković F.	705, 709, 720
Stroppa A.	22	Veljković I.S.	61, 453
Sundar A.	121	Veljković V.B.	685
Suručić Lj.T.	497, 505	Veljković Ž.	61
Syrov E.V.	47	Veselinović D.	561
Szabó R.	123	Veselinović Lj.	399
Szakacs Zs.	461	Veselinović M.	521
Šajić A.	78	Vidojkovic S.	170
Šalipur H.	155	Višnjić-Jeftić Ž.	521
Šaponjić A.	438, 442	Vitnik V.	86, 89, 92
Škapin S.D.	391	Vitnik Ž.	86, 89, 92
Šljukić B.	291	Vodnik V.	391
Šojić Merkulov D.	143, 147	Vojislavljević-Vasilev D.	61, 661
Šolević Knudsen T.	554	Vorob'eva V.	658
Špirkova M.	480	Vrvić M.M.	533, 554, 695
Tadić J.	89	Vujasin R.	580, 584, 588
Tadić T.T.	497, 501, 505	Vujin J.	384
Talić S.	713	Vukčević M.	529, 628
Talik E.	208, 261	Vukić N. 139,	489
Tanasković S.	645, 648	Vukićević N.M.	275, 279
Tančić P.	449	Vuković Z.	388
Tasić T.	544	Wagner N.	18
Tatalović N.	25	Zalomaeva O.V.	121
Telečki I.	588	Zarić M.	25, 320, 324
Teofilović V.	139, 489, 493	Zarić S.D.	61, 103, 453, 661
Tešević V.	699	Zarkov B.	395
Tešić Ž.	692	Zdravković S.	265
Thomas M.	19	Zeković S.	265
Todoran D.	461	Zelenaya A.	658
Todoran R.	461	Zildžović S.	430
Todorova S.	174, 177, 193	Zlatković B.	624
Todorović A.	25, 308, 572	Zvezdanović J.B.	685
Todorović Vukotić N.	308, 699	Žakula J.	699
Tolić Stojadinović Lj.	569	Žerajić S.A.	509, 515
Topalović D.	565	Živanović S.C.	457
Topalović V.	430	Živković J.M.	61, 652, 665
Tóth A.	200	Živković S.	521
Tovilović-Kovačević G.	480		

CIP - Каталогизација у публикацији  
Народна библиотека Србије, Београд

544(082)

66.017/.018(082)

502/504(082)

343.98(082)

**INTERNATIONAL Conference on Fundamental and Applied Aspects of Physical Chemistry  
(15; 2021; Beograd)**

Physical Chemistry 2021: proceedings: the Conference is dedicated to the 30th Anniversary of the founding of the Society of Physical Chemists of Serbia and 100th Anniversary of Bray-Liebhafsky reaction. Vol. 2 / 15th International Conference on Fundamental and Applied Aspects of Physical Chemistry, September 20-24, 2021, Belgrade, Serbia; [organized by The Society of Physical Chemists of Serbia in cooperation with Institute of Catalysis Bulgarian Academy of Sciences ... [et al.]]; [editors Željko Čupić and Slobodan Anić]. - Belgrade: Society of Physical Chemists of Serbia, 2021 (Belgrade: Jovan). - VI str., str. 347-732: ilustr.; 30 cm

Tiraž 200. - Bibliografija uz svaki rad. - Registar.

ISBN 978-86-82475-39-2

ISBN 978-86-82475-40-8 (niz)

а) Физичка хемија -- Зборници б) Наука о материјалима -- Зборници в) Животна средина -- Зборници  
г) Форензика -- Зборници

COBISS.SR-ID 53325065